Photometry of Elliptical Galaxies in Crowded Starfields

[Part I / III: Dissertation]

KARSTEN MARKUS

Department of Astronomy

University of Cape Town

Republic of South Africa

Cape Town & Berlin

01.12.2006

Abstract

Observations of nearby large-scale structures in the Zone of Avoidance have revealed a number of important findings. Amongst these were large-scale structures like the Norma cluster and the surmised Norma Supercluster. However, various difficulties arise when extragalactic objects are investigated close to the band of stars, dust and gas that form the Milky Way. The most severe of these problems, star crowding and Galactic extinction, are analysed in this study. Stars superimposed on a galaxy can cause significant deviations in the established surface brightness profiles of these galaxies. Furthermore, the light received from these galaxies is reduced by the increasing amount of dust and gas in the line of sight towards lower Galactic latitudes. In this study, a set of thirty elliptical galaxies in the central Norma cluster region was analysed by means of high quality optical and near infrared observational data. It is found that the determination and application of a pixel mask for interfering parts in the image offers sufficiently good results for moderate numbers of foreground stars and with relatively little effort. For heavy star crowding and awkwardly positioned stars or even other galaxies close to the investigated galaxy, a more accurate method was developed: the stars were modelled with a point spread function and thereafter subtracted. Subsequently, the $(R_c - K_s)$ colour (which is relatively insensitive to the choice of Galactic reddening law) and the colour excess were obtained. These were then compared with the most commonly used measure of extinction, the DIRBE/IRAS dust maps. The latter are, however, poorly calibrated at low Galactic latitude and are believed to overestimate the Galactic extinction at lower latitudes. The results obtained here do in fact show that the DIRBE/IRAS dust maps already slightly overestimate the Galactic extinction at the position of the central Norma cluster region.

Dedication

This thesis is dedicated to my parents,

ELISABETH JOHANNA MARKUS
– neé Bonnekessen –

and

RUDOLF BERNHARD MARKUS.

This thesis is also dedicated to the approximately 7 million South Africans who are expected to die within the next 10 years due to HIV and AIDS.

May the loss of wisdom and culture due to their deaths bring new thoughts and insights to the following generations.

Acknowledgments

Ubuntu ungamntu ngabanye abantu. [1]

There are innumerable people that – in one way or another – had influence on the positive outcome of my studies, and this dissertation in particular. Unfortunately, I will have to limit this little demonstration of gratitude to the most immediate supporters.

Professor Anthony – Tony – Patrick Fairall and Dr. Patrick Alan Woudt from the Astronomy Department at the University of Cape Town (UCT) will be the first ones to be mentioned. Both took very good care of me – against all odds. Tony, thanks a lot for being open to listening to me and for not getting tired of dealing with the various problems that occurred on and on. I also would like to emphasize that I have very much enjoyed your very good skills of 'explaining the local universe' and your interest in good quality education. Meeting you has left a deep impression on me. Patrick, the same holds for you. If it wasn't about your abilities to multitask and to turn problems into opportunities, the whole department would come to stand still. I will always be grateful to both of you for being your student and I am looking forward to working together with you in the future.

I would also like to mention Dr. Anja Schröder, who was a visiting astronomer at the UCT Astronomy Department in 2001. She may not have realised, but in her very kind way, she made me feel good about the things I was working on.

[1] Xhosa proverb: Ubuntu ungamntu ngabanye abantu – A person is only a person through other people; meaning that to develop as persons, we need to be empowered by others (Shuttle, 1995)

Meeting her has certainly put scientific work into a new perspective for me – Thank you!

Dr. Wolfgang Hasse from the Wilhelm-Foerster-Observatory (WFO) in Berlin, Germany, introduced me to quite a different scientific philosophy. Not only did I benefit from his theoretical knowledge, but also from his kind offer to join his working group at the WFO. Being a theoretical cosmologist, he showed great interest in my work and the discussions with him not seldomly opened my eyes as to where I was standing – literally. For this, a big "Danke!".

The most important person in my life, however, has been my friend and wife, Wilnelia Edith Adams. She was and still is the most valuable source of inspiration I have. Meeting her at UCT was a lucky chance in my life and I am happy that she offered me the opportunity of getting to know her better. Wilnelia, you may not be aware of this, but I do not regret a minute of the time I spent with you, be it in good or in bad times!

In terms of non-scientific support, I would first like to thank my family, and in particular my parents, Rudolf Markus and Elisabeth Markus. They never stopped believing in me and they supported me as much as they could. I will never forget this and I am proud to be your son!

Moreover, many friends and colleagues have been very encouraging in various ways. I will briefly mention a few representative names here, but the list is obviously incomplete. May those who are not mentioned forgive me for not doing so. I certainly should have mentioned you!

Joan **A**dams	Olivia Adams	Robert Adams
Rory Adams	William Adams	Wilnelia Adams
Marguerite Armstrong		
Frank **B**eier	Daniel Bendix	Andrea Bierau
Herrmann Bonnekessen	Franz Bonnekessen	Hannah Bohle
Stefan Bubenzer	Prof. Buffler	
Michelle **C**luver	Lisa Crause	
Britta **D**eutsch	Hans-Joachim Döbler	
Prof. **F**airall	Prof. Feast	Julia Frantz
Jörn **G**reving		
Katrin **H**ammerstein	Dr. Hasse	Björn Heggemann
Dr. Hempel	Ulrike Hentschel	Frank Hermes
Prof. Hunklinger		
Lesley **J**ennings	Birgit Joest	
Robert **K**astl	Volker Kathöfer	Dr. Kirstein
Thorsten Koch	Andreas Köster	Prof. Kraan-Korteweg
Katya Kumkova-Wolpert		
Regine **L**ord		
Anna **M**arkus	Elisabeth Markus	Oliver Markus
Rudolf Markus	Tanja Markus	Johannes Meier
Sabine Morgner		
Dr. **N**ickel	Sandra Nikolic	Prof. Nordmeier
Mark **P**ollmeier	Mellanie Pollmeier	Retha Pretorius
Tobias **R**odäbel		
Prof. **S**ahm	Katrin Sailer	Christian Schäfers
Christine Siewert	Dr. Schreiber	Dr. Schröder
Ralf Staudemeyer		
Helmut **T**hieke	Mia Thieke	Prof. Thomsen
Prof. **U**lmschneider		
Prof. **W**arner	Kerstin Wagner	Florian Weißbach
Dr. Woudt		

Utilised Data Sources

ArXiv e-print service:

See *http://lanl.arxiv.org/*.

Astrophysics Data System:

See *http://adswww.harvard.edu/*.

Coma cluster data:

Generously supplied by Dr. J. Lucey, Department of Physics, *University of Durham*, United Kingdom, see *http://www.dur.ac.uk/john.lucey/*.

Near infrared Norma cluster data:

Data obtained with *European Southern Observatory* facilities and generously supplied by Dr. A. C. Schröder, Department of Physics & Astronomy, *University of Leicester*, United Kingdom.

Milky Way image:

Generously supplied by Dr. A. Mellinger, see Mellinger (2000) and *http://home.arcor-online.de/axel.mellinger/*.

NED database:

NASA/IPAC Extragalactic Database, see *http://nedwww.ipac.caltech.edu/*.

Optical Norma cluster data:

Data obtained with *European Southern Observatory* facilities and generously supplied by Dr. P. A. Woudt, Astronomy Department, *University of Cape Town*, Republic of South Africa, see *http://mensa.ast.uct.ac.za/~pwoudt/*.

Redshift data:

Obtained with the *Anglo Australian Observatory 2dF* instrument and generously supplied by Dr. J. Lucey, Department of Physics, *University of Durham*, United Kingdom, see *http://www.dur.ac.uk/john.lucey/*.

SIMBAD database:

This research has made use of the *SIMBAD* database, operated at the *Centre de Données astronomiques de Strasbourg*, France, see *http://simbad.u-strasbg.fr/*.

ViZieR service:

This research has made use of the *ViZieR* service, operated at the *Centre de Données astronomiques de Strasbourg*, France,
see Ochsenbein et al. (2000) and *http://vizier.u-strasbg.fr/*.

Utilised Software

GALFIT software:

See *http://zwicky.as.arizona.edu/~cyp/work/galfit/galfit.html* and Peng et al. (2002).

GNUPlot software:

See *http://www.gnuplot.info/*.

Hierarch28 software:

Provided by the *European Southern Observatory*, see *http://archive.eso.org/saft/*.

IRAF software:

IRAF is distributed by the *National Optical Astronomy Observatories*, which are operated by the *Association of Universities for Research in Astronomy, Inc.*, under cooperative agreement with the *National Science Foundation*. See *http://iraf.noao.edu/* and Tody (1986, 1993).

Killall software:

I kindly acknowledge Prof. McCall for the use of the *Killall* software,
also see Buta and McCall (1999).

Mac OS:

Developed by *Apple Computer, Inc.*, see *http://www.apple.com/*.

Physica software:

Provided by the *TRIUMPH Computing Services Group*,
see *http://www.triumf.ca/physica/html/homepage.html*.

RedHat Linux :

Provided by *Red Hat, Inc.*, See *http://www.redhat.com/*.

SAOImage DS9 software:

This research has made use of *SAOImage DS9*, developed by *Smithsonian Astrophysical Observatory*, see *http://hea-www.harvard.edu/RD/ds9/* and Joye and Mandel (2003).

SkyCat software:

Provided by the *European Southern Observatory*, see *http://archive.eso.org/skycat/*.

SM software:

Previously known as *SuperMongo*, see *http://www.astro.princeton.edu/~rhl/sm/* and Lupton and Monger (1997).

STSDAS & TABLES packages:

Products of the *Space Telescope Science Institute*, which is operated by *Association of Universities for Research in Astronomy, Inc.*, for *NASA*,
see *http://www.stsci.edu/resources/software_hardware/*.

Contents

List of Tables

List of Figures

Chapter 1

Introduction

This introductory chapter first gives an overview over historic developments which led to the discovery of the Large-Scale Structures in the universe (Section 1.1). The subsequent discovery of the Great Attractor behind the Zone of Avoidance and the surveys conducted in this area are reviewed thereafter (Section 1.2). A brief description on the effects of the foreground extinction caused by our own galaxy is given (Section 1.3), followed by the motivation and an outline of this dissertation (Section 1.4).

1.1 Historical Background

Friedrich Wilhelm Herschel, who grew up in the area around Hanover, Germany, before later moving to England, was an extraordinary man. Born in 1738, he passed away in 1822, at the age of 83. Probably best known to the public at the time for his work as a composer, he is, however, remembered best for his scientific contributions. William – as he was called in later times – worked as an astronomer, and in this capacity built the most advanced telescopes of his time; he discovered the planet Uranus and some of its moons, discovered infrared radiation, located numerous double stars – and about 2500 nebulae (latin: clouds), which appeared as fuzzy patches of light seen

in the night sky. Due to the lack of a method for distance determination at the time, these could either have been Galactic gas clouds or extragalactic objects, i.e. galaxies.

John (Frederick William) Herschel – William's son – not only followed in his father's footsteps by resurveying all of his father's nebulae, but he added some five hundred more, before he relocated his telescope to the southern hemisphere, specifically to the Cape of Good Hope in Southern Africa. In 1864, he published his *General Catalogue of Nebulae* of about 4600 nebulae (Herschel, 1864) of which only about ten percent had been observed before. In the 18^{th} century, Charles Messier observed about hundred of these (Messier, 1781).

At first, William had correctly interpreted many of the nebulae he observed as stellar systems, although they were too distant to allow him to identify individual stars. He made these findings in accordance with the philosophical concept of 'island universes' (Kant, 1798). A 'great debate' spanned the 18^{th} to the 20^{th} century, on whether the universe was populated by multiple stellar systems – so-called 'island universes' – or by a single stellar system. It was not clear until the 1920s whether nebulae were in fact Galactic gás clouds or extragalactic objects, i.e. galaxies.

Later in life, William changed his opinion with regard to the view that nebulae were simply gas clouds in our Galaxy, possibly in the process of forming new stars. Interestingly, his son John also believed in the idea of 'island universes', but, realising that he had no convincing evidence, he too went along with the more conservative alternative view of gas clouds in the Galaxy.

As we know today, the great majority of nebulae in the *General Catalogue of Nebulae* are in fact galaxies, and the catalogue therefore provided the first revelation of the universe on a large scale. John saw that about a third of all nebulae were concentrated into an eighth of the sky; the distribution was irregular, with branches – or protuberances – running outwards from the core and centred on the constellation of Virgo. He deduced that our Galaxy

lay far from this core, but was "... involved within its outlying members ..." and "... forms an element of some of its protuberances ..." (Herschel, 1858). This was the first account of a large-scale structure of the universe, namely the Virgo Supercluster.

Richard Proctor, who opposed the island universe idea, made sky plots of Herschel's *General Catalogue of Nebulae*, which showed empty voids surrounded by the nebulae (Proctor, 1878). However, since the general congregation of galaxies towards Virgo matched the Galactic pole, he argued that this was too much of a coincidence and therefore in contradiction with having no favoured alignment to the nebular system, i.e. the Milky Way. It took the development of photographic emulsions and the development of the 100-inch telescope at the Mount Wilson Observatory to see the galaxies for what they are: external stellar systems. In 1924, Edwin Hubble was able to identify Cepheid variable stars in the Andromeda Galaxy, the closest of the spiral galaxies. This was proof that galaxies were stellar systems in their own right. Moreover, by using Cepheids as distance indicators, Hubble could show that these island universes were too distant to be part of our own Galaxy (Hubble, 1925). In the following years, Hubble produced a relationship that showed the expansion of the Universe by combining his distance estimates with the radial velocities measured by Vesto Slipher (Hubble, 1929, 1936).

In the 1930s, Harlow Shapley claimed that clouds of very distant galaxies existed in the southern sky. This distribution of 'metagalaxies' was contrary to Hubble's claim of a more or less uniform, but random distribution of galaxies. Hubble had examined over a thousand photographs of the 100-inch Mount Wilson telescope, on which he identified about 44000 galaxies. However, each photograph was small in extent and probed relatively deep, deeper than the presently known nearby large-scale structures. Shapley, in contrast, recognized the Metagalaxies on wide field photographs (Shapley, 1934).

In the late 1970s, Jaan Einasto presented a paper at an international conference in which he asked whether the Universe had a cellular structure,

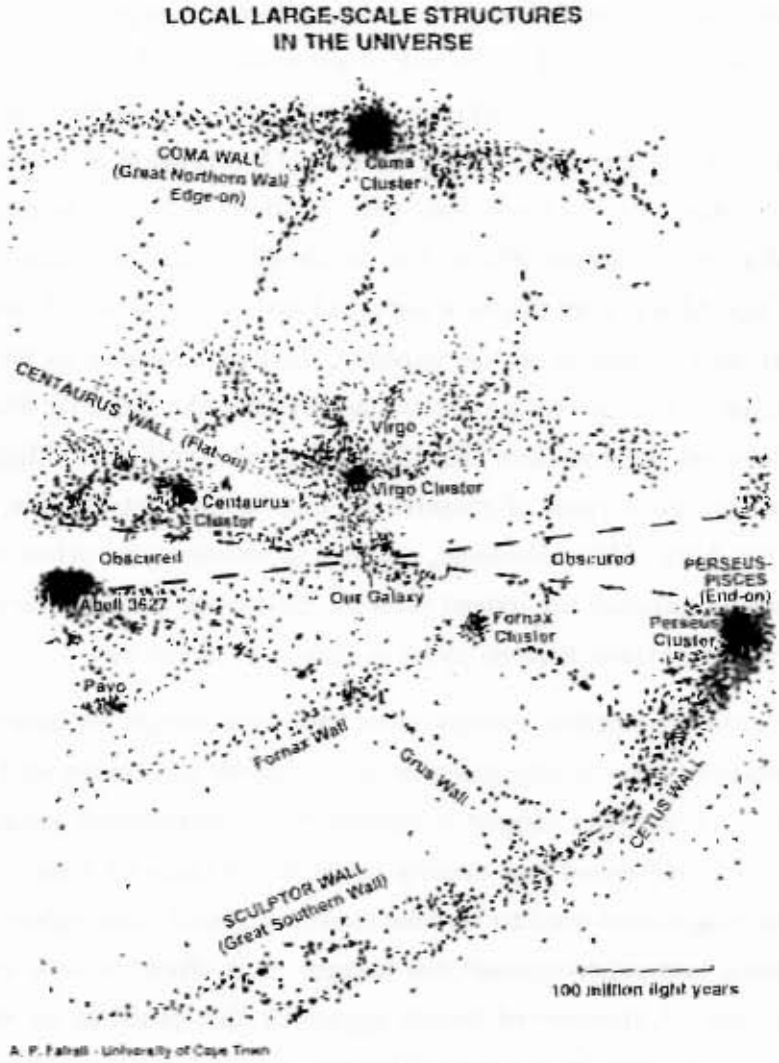

Figure 1.1: A schematic diagram of nearby large-scale structures within about 7000 km/s of the position of our Galaxy. The three-dimensional structures are projected onto two dimensions: the Supergalactic Plane of Gerard de Vaucouleurs. Most of the major nearby condensations tend toward this plane. The part of the visible universe that is obscured by the Milky Way is indicated. The figure is taken from (Fairall, 1998, p. 75), with permission.

In 1878, Richard Proctor had already recognised the "Zone of few Nebulae", i.e. the area in the sky where few nebulae – or galaxies – are visible. When Edwin Hubble did his survey of galaxies in 1935, he found hardly any galaxies in a broad band spanning the entire sky. He coined the term Zone of Avoidance for this area, though Zone of Obscuration seems a more accurate description, due to the foreground obscuration by our own Galaxy. The Milky Way covers about 20% of the visible night sky, and dust, gas and the stars in the Milky Way act as a natural barrier to studies of the large-scale structure and dynamics of the universe. Galaxies appear to be fainter and smaller due to the increasing extinction towards the Galactic Plane. All optically selected surveys show this classic Zone of Avoidance. Magnitude- and diameter-limited surveys of galaxies are increasingly incomplete, as they approach the Milky Way. However, surveys in wavelengths other than optical, do show that galaxies are indeed present. Moreover, some of the most nearby large-scale structures happen to lie in this part of the sky.

A number of optical surveys have therefore sought to narrow the Zone of Avoidance by accepting galaxies with smaller diameters and lower magnitudes. However, the biggest complication for automated galaxy detection is the greatly increased star density towards the Galactic Plane. Automated scanning procedures tend to become confused about faint galaxy images and overlapping and superimposed star images, as is often the case at low Galactic latitudes. A number of people approach this problem by scanning sky survey photographs by eye very diligently under high magnification. These searches uncover large numbers of partially obscured galaxies down to extinction levels in the B band of 5 magnitudes or less. Today, we can give an almost complete account of the nearby structures due to the success in tracing continuous structures from one side of the Galactic Plane to the other. See Kraan-Korteweg and Lahav (2000) for a detailed description of the different surveys conducted in the Zone of Avoidance and Fairall and Woudt (2005) for newer results.

In order to trace the unveiled apparent large-scale structures in redshift-

space, dedicated follow-up redshift surveys have been performed by various research groups[1] (Kraan-Korteweg and Lahav, 2000). However, there are some difficulties in obtaining reliable redshifts with optical observations at low Galactic latitudes, due to the general faintness of the galaxies. In some cases, a star is superimposed directly on top of the nucleus of a galaxy, which is very difficult to resolve spectroscopically, and in about 10% of these cases, this is actually impossible.

A few degrees wide, the Milky Way remains totally opaque to optical surveys. It is only possible to detect galaxies within this area by means of radio observations, mainly HIand in the hard X-rays. The radio and X-ray telescopes have to be aimed blindly, since the galaxies cannot be seen. However, with the use of multibeam instruments, this is no longer a problem, and many galaxies have been detected so far. Observing in the X-rays is particularly interesting, as the hot gas in large galaxy clusters radiates in this part of the spectrum. Thus, it is possible to detect these clusters behind the Milky Way.

For a detailed overview of the large-scale structures in the universe and the historic developments of their discovery, the reader is referred to the excellent description in Fairall (1998).

1.2 Local Dynamics and the Great Attractor Region

When it became apparent that galaxies are not distributed randomly in redshift-space, alternative ways of measuring their distance were developed

[1] A very good overview over the different groupings and their research can be obtained from the three conference proceedings for the "Unveiling Large-Scale Structures behind the Milky Way", "Mapping the Hidden Universe: The Universe behind the Milky Way in HI" and the "Nearby Large-Scale Structures and the Zone of Avoidance" conferences, held in Paris (1994), Guanajuato (2000) and Cape Town (2004), respectively. The proceedings were published in the Astronomical Society of the Pacific Conference Series, Volumes 67, 218 and 329, respectively.

and applied. For spiral galaxies, the Tully-Fisher relation proved to be a good way of estimating the distance (Tully and Fisher, 1977). Though not very precise for individual galaxies, this method is nonetheless quite accurate when applied to groups of galaxies that are assumed to be at relatively similar distances from the observer, such as galaxies in clusters. Similarly for elliptical galaxies, a strong correlation between luminosity L in the galaxy and the central velocity dispersion σ_0 exists:

$$L \propto \sigma_0^4 , \tag{1.1}$$

known as the Faber-Jackson relation. However, this relation does not have exactly the same slope for all luminosities. For example, cD galaxies have a velocity dispersion σ_0 less than the predictions of the $\approx L^{1/4}$ curve. The central velocity dispersion of the bulges of spiral galaxies also follows the Faber-Jackson relation (Faber and Jackson, 1976).

A collaboration of British and American astronomers, known as the 'Seven Samurai'[2], used detailed photometric and spectroscopic data from elliptical galaxies to find a relationship for their intrinsic luminosity. They discovered that, in a three-dimensional plot of velocity dispersion within the galaxy, total brightness and average surface brightness, the galaxies showed a nearly planar distribution and thus the D_n-σ_0 relation was born. It is based on the 'Donald Diameter' D_n, the diameter of the isophote within which the surface brightness averages to a given level, and the central velocity dispersion σ_0 of the stars in the galaxy. With this new relation, relative distances can be derived, and it was applied to a sample of elliptical galaxies by the Seven Samurai. They compared the derived distances with the ones from galaxy redshifts and came to the conclusion that this newly developed method was not only a redshift independent way for estimating the distance of galaxies, but it could also be used to show large-scale motions in the nearby universe. Their stunning result was what appeared to be an infall

[2]David Burstein, Alan Dressler, Sandy Faber, Roger Davies, Donald Lynden-Bell, Roberto Terlevich and Gary Wegner. A nice description of this collaboration and their research is given in Dressler (1997).

pattern towards (gal. l, gal. b, cz) $\sim (307°, 9°, 4350\,\mathrm{km/s})$ which is driven by a rather large mass concentration – the discovery of what Dressler called the 'Great Attractor' (Dressler et al., 1987; Lynden-Bell et al., 1988). This is a dynamically important overdensity of galaxies in the local universe (Kolatt et al., 1995; Lynden-Bell et al., 1988; Tonry et al., 2000).

Given that the luminous matter in the universe is not randomly scattered, as scientists such as Hubble assumed at the beginning of the 20^{th} century, questions arose on where the large-scale structure of the universe originated. Obviously, the structure itself contains information about its origins, and therefore information about the conditions and the formation processes in the early universe. This information must be incorporated into the existing cosmological models, constraining the possible scenarios.

However, many of the known nearby large-scale structures are partially obscured by the Galactic Plane. For instance, the accurate extent and masses of the Local Supercluster, the Perseus-Pisces chain, and the Great Attractor overdensity are not known. Moreover, the two major superclusters in the local universe, Perseus-Pisces and the Great Attractor, are at opposite positions, but at similar distances from the local group of Galaxies, yet both are partly obscured by the foreground Milky Way. It still has to be established, how much each mass agglomeration is contributing to the gravitational pull on the Local Group, and whether other massive structures may be hidden behind the Zone of Avoidance, for which no indication exists so far.

A possible contradiction might arise, for instance, if the Great Wall and the Perseus-Pisces chain were found to be connected across the Zone of Avoidance (Giovanelli and Haynes, 1982; Marzke et al., 1996). This would indicate structures of a size bigger than $140\,\mathrm{h}_{70}^{-1}\,\mathrm{Mpc}$, which would be incompatible with the angular extent of fluctuations measured in the Cosmic Microwave Background radiation, which are considered to be the initial stages of the large-scale structures observed today.

Another result obtained from measurements of the Cosmic Microwave Background is the dipole anisotropy. This is explained by a peculiar motion

at $v_p = 627\,km/s$ of the Local Group relative to the Cosmic Microwave Background towards gal. $l = 276°$, gal. $b = 30°$ (Kogut et al., 1993). It is thought that this motion is caused by the distribution of matter in the universe and the gravitational pull thereof.

When determining the gravity field at the position of the Local Group, i.e. the acceleration of the Local Group by, for instance, using theoretical reconstruction methods as described later, it is crucial to include the (unknown) mass distribution that lies hidden behind the Zone of Avoidance (Kolatt et al., 1995). Confirmation of the vector measured in the Cosmic Microwave Background with the motion of the Local Group determined from the matter distribution, i.e. its direction as well as its convergence distance, will lead to constraints on the cosmological parameter Ω_0. To be able to model the gravity field without knowing the hidden mass, a uniformly filled Zone of Avoidance is often assumed, using for instance Poisson statistics. The well-mapped regions adjacent to the Zone of Avoidance can also be extrapolated – or even interpolated – into the Zone of Avoidance, or one can use spherical harmonic analyses. However, due to inhomogeneous data coverage, incorrect assumptions on the galaxy distribution in the Zone of Avoidance or false assumptions on the mask to be filled in the Zone of Avoidance, the lack of data remains one of the main uncertainties in current dipole determinations, since this introduces nonexisting flow fields (Rowan-Robinson et al., 2000).

A significant effect on the Local Group is not only caused by large, distant mass agglomerations, but also by smaller, yet somewhat closer masses. In fact, since in linear theory the peculiar velocity v_p of the Local Group is assumed to be proportional to the net gravity field, the nearby entities become quite important. One can determine this net gravity field from the sum of the masses M_i of all galaxies divided by the distance r_i squared:

$$v_p \propto \frac{\Omega_0^{0.6}}{b} \sum_i \frac{M_i}{r_i^2} \cdot \hat{\mathbf{r}}_i \,, \tag{1.2}$$

(Kraan-Korteweg and Lahav, 2000), where Ω_0 is the density parameter and

b the bias parameter. This can be directly determined, for instance, from the sum of the observed galaxies in the sky, assuming a constant mass-to-light ratio (Kraan-Korteweg and Lahav, 2000), since both the flux of a galaxy as well as gravity decreases with r^{-2}:

$$v_{\rm p} \propto \sum_i 10^{-0.4\,{\rm m}} \cdot \hat{\mathbf{r}}_i \,. \tag{1.3}$$

It would be highly significant if nearby galaxies hidden behind the Galactic Plane were still to be found, as this would have an important impact on the existing models. Six of the nine apparently brightest (extinction-corrected) galaxies are located in the Zone of Avoidance (Buta and McCall, 1999; Kraan-Korteweg et al., 1994), and it is therefore not unrealistic to expect further nearby galaxies to be found behind the Milky Way.

The discovery of a large nearby galaxy behind the Milky Way would have a large impact on currently existing models of the dynamics of the Local Group of galaxies. Assuming that the Milky Way and its massive companion M31 separated from the Hubble flow at the time of their formation and that they behaved dynamically like an isolated binary system ever since, one can use the distances and motions of nearby galaxies to constrain the total mass of the Milky Way and M31 pair, and the dynamical age of the Local Group (Kahn and Woltjer, 1959; Lynden-Bell, 1982). However, this method, known as 'Local Group timing', would be affected significantly, if, for instance, the dominant members of the IC 342/Maffei Group were massive and near enough (McCall, 1989; Valtonen et al., 1993). By tracing the orbits of the Local Group galaxies back in time, using the 'least action principle' for instance, this method can be extended (Dunn and Laflamme, 1995; Peebles, 1990). Yet, this implies an accurate knowledge of the number, distance and mass of all nearby galaxies, which can only be achieved with a sound knowledge of the nearby universe in the Zone of Avoidance, the Galactic extinction and the effects that extinction has on the measured parameters, like galaxy diameters (Cameron, 1990; Nagayama et al., 2005).

One way of uncovering structures that are hidden behind the Galactic

Plane is by reconstructing them from the adjacent data that has been found thus far. There are two methods that are most commonly used to reconstruct the galaxy distribution behind the Milky Way. The POTENT method uses the peculiar velocities of galaxies to reconstruct the mass density field (Bertschinger and Dekel, 1989; Dekel, 1994). One assumes that the motions of galaxies are a result of gravitational fields of the underlying mass distribution. The galaxies act as test particles, similar to the orbital velocities of stars in a galaxy, which seem to indicate the presence of a massive halo (Rubin and Ford, 1970). The dynamics of the galaxies should reveal the presence of massive structures, quite independently of whether they are visible or not. The analysis, using a software package called POTENT (Bertschinger and Dekel, 1989), creates a smoothed velocity map, which is used to reconstruct the underlying mass-density field. It is assumed that the flows of galaxies are effectively laminar and free of vortex motion. Mathematically, this can be expressed by assuming the velocity field to be irrotational:

$$\nabla \times \mathbf{v} = 0. \tag{1.4}$$

Using this, the velocity field $\mathbf{v}(x)$ can be derived from a scalar potential $\phi(x)$:

$$\mathbf{v}(x) = -\nabla \cdot \phi(x) \tag{1.5}$$

The potential is obtained by integrating over the radial velocity field, as only the radial component is available. The practice is complicated by noise, errors and incompleteness of the data, which largely has to be smoothed, often on the scales of $7 - 17\,\mathrm{h}_{70}^{-1}\,\mathrm{Mpc}$, due to the irregular rather than uniformly dense manner in which the velocity field is sampled. Because of this, all reconstruction methods only trace structures on the very largest scales, i.e. on a supercluster level. However, various large-scale structures are confirmed entirely from the peculiar motion of galaxies, while the POTENT maps gradually improve as more data becomes available. Using POTENT and its counterparts, one can map peculiar flows over a surrounding region of $cz \approx 6000\,\mathrm{km/s}$ (Kraan-Korteweg and Lahav, 2000).

A statistical approach on reconstructing the galaxy distribution behind the Galactic Plane is the Wiener Filter method (Hoffman, 2000; Zaroubi, 2000). This is particularly suited to dealing with sparse, noisy and incomplete data, but requires a prior knowledge of the relation between the mass and the observed galaxy distribution. It is possible to use positional information only, by using a 2-dimensional Wiener Filter reconstruction method, or positional and redshift information, by using a 3-dimensional method. Several structures found by using the Wiener Filter technique have been independently confirmed, for instance, the Vela Supercluster and more recently some major superclusters and large local voids (Erdogdu et al., 2004; Hoffman, 1994; Kraan-Korteweg and Woudt, 1993; Lahav, 2005; Saunders et al., 1991; Strauss et al., 1992).

For a general description, and for reconstructions in the Zone of Avoidance, see Fisher et al. (1995), Hoffman (1994) and Lahav (1994), respectively. A comprehensive review of the various reconstruction methods, their results and a comparison with the observed distribution of unveiled galaxies in the Zone of Avoidance is given in Kraan-Korteweg and Lahav (2000).

It is possible to trace the galaxy distribution behind the Milky Way from direct observations at various wavelengths. However, it can also be inferred indirectly by analysing the peculiar motions of galaxies, using the POTENT or Wiener Filter methods, and assuming that these arise from the irregular mass density field in the local universe. It is even possible to infer cosmological parameters, such as Ω_0, when comparing the directly observed distribution with its reconstructed mass density field (Dekel, 1994; Sigad et al., 1998).

When applying the reconstruction methods, both the POTENT and the Wiener Filter methods show the Great Attractor as a main feature, amongst others, like the Perseus-Pisces Supercluster at gal. $l \approx 130°$ (Kolatt et al., 1995). As a significant mass excess, located close to or behind the southern Milky Way, the Great Attractor is clearly visible. It is roughly positioned at a distance of $r \approx 57\, h_{70}^{-1}$ Mpc and gal. $l \approx 320°$, gal. $b \approx 0°$. However, because

of measurement errors in the observations, scatter and zero-point uncertainty in the adopted distance relations and the large smoothing of cz $\approx$ 1200 km/s of the sparsely sampled field, the location of this peak is poorly defined. Although the best evidence for the existence of the Great Attractor comes from the reconstructed galaxy/mass distribution, the nature and extent of the Great Attractor have been interpreted somewhat contradictorily (Dressler, 1988; Hudson, 1993a,b; Jahoda and Mushotzky, 1989; Lynden-Bell, 1991; Rowin-Robinson et al., 1990), due to the less than perfect match between the observed galaxy distribution and the reconstructed mass density field (Dekel, 1994).

Although the rich galaxy cluster ACO 3627 – also known as the Norma cluster – has been known since 1989 (Abell et al., 1989), it was only identified as a dominant cluster in 1996 (Kraan-Korteweg et al., 1996; Woudt, 1998), when a large number of redshifts were obtained, revealing a large velocity dispersion and thus a high mass. It is centrally situated within the Centaurus Wall structure and occurs just where the Centaurus Wall is seen to cross the plane of our Galaxy. Although the size of the Norma cluster is comparable to the somewhat more distant Coma cluster, and although it is the most dominant cluster in the Centaurus Wall, it is not an obvious structure in the sky, as large parts of it are hidden behind the southern Milky Way. The position of the Norma cluster at gal. $l \approx 325°$, gal. $b \approx -7°$ and cz $\approx$ 4848 km/s coincides closely with the predicted position of the Great Attractor, but its mass is an order of magnitude too low for the cluster to be the Great Attractor itself. It must therefore be concluded that the Great Attractor remains a more extended mass overdensity, but it is likely that the massive Norma cluster holds a central position as the bottom of an extended gravitational well, similar to the Coma cluster in the Great Wall.

Observations in different wavebands are necessary to penetrate the Zone of Avoidance effectively. Each waveband is best suited for the detection of particular types of objects, e.g. HI-rich spiral galaxies can be observed throughout the Zone of Avoidance in the Radio (HI) band, while galaxy

clusters behind the Galactic Plane can be detected with X-ray surveys. As a result, many dedicated surveys – Radio (HI), far infrared, near infrared, optical and X-ray – were initiated and combined to search for a galaxy excess associated with the Great Attractor. Many of these searches complement each other in the galaxy population that they trace. An overview of the advantages and limitations of each of these methods is given by Woudt (1998) and a complete overview of surveys in the entire Zone of Avoidance up to the year 2000 is given in Kraan-Korteweg and Lahav (2000). More details on recent results can be found in the proceedings of the *Nearby Large-Scale Structures and the Zone of Avoidance* conference, held 2004 in Cape Town, South Africa (Fairall and Woudt, 2005). Most of the information given in this chapter on the surveys that were conducted in the Great Attractor region was extracted from these references.

For HI-rich galaxies, the least affected method of searching for galaxies behind the Galactic Plane is by searching for the redshifted 21 cm emission line of neutral hydrogen. The Galaxy is fully transparent to this kind of radiation. However, gas-poor early-type galaxies as tracers of massive groups and clusters will be missed in these surveys. Similarly, galaxies close to radio continuum sources will not be included, nor will nearby extragalactic sources with low redshift or even blueshift, since their spectral HI emission falls into the Galactic emission line of neutral hydrogen (Henning et al., 1998, 2000; Kerr and Henning, 1987).

Conveniently, detecting HI signals makes it possible not only to ascertain the redshift of the object, but also its rotational velocity. This provides further insight into the intrinsic Galactic properties and can furthermore be used to relate redshift-space to real space, e.g. by applying the Tully-Fisher relation.

In the southern Zone of Avoidance, which includes the Great Attractor region, a systematic blind HI survey has been performed, covering a velocity range from $-1200\,\mathrm{km/s}$ up to $12700\,\mathrm{km/s}$ with a channel spacing of $13.2\,\mathrm{km/s}$ per channel (Henning et al., 2005, 1999, 2000; Kraan-

Korteweg et al., 1999; Staveley-Smith et al., 1998). The observations were performed in driftscan mode, using the 64 m radio telescope of Parkes and a specifically constructed Multibeam receiver with 13 beams in the focal array (Staveley-Smith et al., 1996). In the Great Attractor region around ($300° \geq$ gal. $l \geq 332°$, gal. $|b| \leq 5.5°$), the survey was already analysed, and 236 galaxies above the $3\,\sigma$ detection level of 25 mJy have been uncovered (Juraszek et al., 2000). About 70% of these detections had not been previously identified. These new findings show that structures can be traced all the way across the Milky Way, which supports the view that the Great Attractor overdensity appears to be a wall-like structure, starting close to the Pavo cluster and having its core at the Norma cluster.

The negligible effect of extinction in the long wavelengths of the far infrared makes it possible to do a sky survey without an imposed magnitude- or diameter-limit close to the Galactic Plane. Thus, in 1983, the *Infrared Astronomical Satellite* (IRAS)[3] surveyed 96% of the whole sky in the far infrared. However, this survey does not consist of images, but of the fluxes at 4 IRAS passbands in the FIR, at 12, 25, 60 and 100 μm only. The resulting *IRAS Point Source Catalogue* (IRAS PSC), (Meurs et al., 1988), containing 250 000 point sources, was extensively used to identify galaxies.

These identifications of possible galaxy candidates are based on flux ratios only, for instance using $f_{60} > 0.6$ Jy, $f_{60}^2 > f_{12} \cdot f_{25}$, and $0.8 < f_{100}/f_{60} < 0.5$ as selection criteria (Yamada et al., 1993). Together with the small effect of the extinction on the flux at these long wavelengths, the homogeneous sky coverage of the data obtained with only one experiment is an obvious advantage. Nonetheless, it remains difficult to probe the inner part of the Zone of Avoidance with IRAS data because of cool cirrus sources and high source counts of Galactic objects in the Galaxy, which have the same IRAS characteristics as external galaxies. The upper cut-off in the third criterion mentioned above was imposed to minimize the contamination of identified

[3]For a description of the abbreviations used in this dissertation, the reader is referred to Section B in the Appendix on page 247.

potential galaxies with cool cirrus sources and young stellar objects within our Galaxy (Yamada et al., 1993). By doing this, however, the IRAS surveys become less complete for nearby galaxies (Woudt, 1998). Furthermore, mainly normal spiral galaxies and starburst galaxies can be identified by using these flux and colour criteria. As a result, the IRAS galaxy sample contained hardly any dwarf galaxies, nor the dustless elliptical galaxies. The general difficulties in identifying galaxies at low latitudes are shown by Yamada et al. (1993). In their systematic IRAS galaxy survey of the southern Milky Way, they found a dramatic and unrealistic increase in possible galaxies close to the Galactic Plane with $|b| \leq 15°$. Similarly it was found that the detection rate of IRAS galaxy candidates decreases significantly as a function of Galactic latitude from $|b| = 16°$ to $|b| = 2°$ (Lu et al., 1990). These results can only be explained by faulty galaxy identifications and therefore cause a limit of 84% in the sky coverage in which reliable IRAS galaxy identifications can be made (Kraan-Korteweg and Lahav, 2000).

IRAS is insensitive to the dustless elliptical galaxies, as they do not radiate in the far infrared, and IRAS is therefore also insensitive to galaxy clusters. However, galaxy clusters mark the peaks in mass density distributions. Furthermore, the broad IRAS luminosity function does result in a more diluted galaxy distribution, since a larger fraction of distant galaxies will enter a flux-limited sample compared to an optical galaxy sample, i.e. images taken in various optical wavelenghts. These factors are causing the observed density enhancements in IRAS galaxy samples to be rather weak.

Despite these limitations, various dedicated searches for large-scale clustering within the whole Zone of Avoidance, i.e. $|b| \leq 15°$, have been done, see Takata et al. (1996) for a summary. In these surveys, various filamentary features and connections across the Zone of Avoidance could be identified. Most of these coincide with structures uncovered in optical work, although they can be more prominent in the near infrared, as can be seen, for instance, in both crossings of the Perseus-Pisces arms into the Zone of Avoidance. New structures have been identified, too, like the Cygnus-Lyra filament at

gal. $l \approx 60° - 90°$; gal. $b \approx 0°$; cz $\approx 4000\,\mathrm{km/s}$. It was furthermore possible to confirm the three general concentrations of galaxies around Puppis (gal. $l = 245°$), the Hydra-Antilia extension (gal. $l = 280°$) and the Centaurus Wall (gal. $l = 315°$) (Kraan-Korteweg et al., 1995). However, the Great Attractor is not prominent in these IRAS observations, compared to the optical or the POTENT reconstructions, and the Norma cluster is not visible at all. This is due to the fact that these observations suffer from the same limitations in highly obscured regions as optical surveys do, as IRAS colour criteria were used to select galaxy candidates, which were then verified by visually examining sky surveys like the *Palomar Observatory Sky Survey* (POSS) for the northern and *European Southern Observatory / United Kingdom Science Research Council* (ESO/SRC) Sky Atlas for the southern sky. Furthermore, IRAS galaxy samples have been used to reconstruct the large-scale structure across the Galactic Plane, as well as to determine the peculiar motion of the Local Group, using the two-dimensional IRAS galaxy distribution as well as the galaxy distribution in redshift-space. The available redshift-data for IRAS galaxies have increased rapidly in the last years (Fisher et al., 1995; Strauss et al., 1992), resulting in the PSC catalogue of 15411 galaxies complete to $f_{60} = 0.6\,\mathrm{Jy}$ with 84% sky coverage and a depth of $20000\,\mathrm{km/s}$ (Saunders et al., 2000b). Analysis of this *Infrared Astronomical Satellite Point Source Catalogue Redshift Survey* (IRAS PSCz) data reveals that the acceleration vector of the Local Group points about 15° away from the Cosmic Microwave Background dipole (Rowan-Robinson et al., 2000; Schmoldt et al., 1999). Assuming full convergence at the sample boundary, about 2/3 of the measured acceleration is generated within $4000\,\mathrm{km/s}$. There is, however, a non-negligible contribution out to $14000\,\mathrm{km/s}$, after which the acceleration amplitude seems to have converged. Many of the prominent large-scale structures like superclusters and voids are located behind the Milky Way. Saunders and collaborators found that the 16% coverage of the sky missing in the IRAS PSCz catalogue causes significant uncertainty. As a result, they initiated the 'Behind the Plane' (BTP) survey to increase the sky cov-

erage by optimizing their colour criteria to $f_{60}/f_{25} > 2.0$; $f_{60}/f_{12} > 4.0$ and $1.0 < f_{100}/f_{60} < 5.0$, and therefore minimizing contamination by Galactic sources, and by taking K′ band images of all new galaxy candidates found. This resulted in roughly another thousand galaxies being added to the IRAS PSCz sample and a reduction of the coverage gap to a mere 7% of the sky (Saunders et al., 2000a). In this IRAS PSCz plus BTP survey with 16400 galaxies, large-scale structures across most of the Galactic Plane can be identified, including the Great Attractor region, where the galaxies can be traced to the rich galaxy cluster ACO 3627.

Two systematic surveys were recently conducted in the near infrared spectrum. The *Deep New Infrared Southern Sky Survey* (DENIS) imaged the southern sky in Galactic latitude from $-88°$ up to $+2°$ in the I_c (0.8 μm), J (1.25 μm) and K_s (2.15 μm) bands. The second survey covered the whole sky in the J (1.25 μm), H (1.65 μm) and K_s (2.15 μm) bands and was called the *2 Micron All Sky Survey* (2MASS). Both surveys mapped the sky in declination strips that are 30° in length and 12 arcmin wide for DENIS, and $6 \times 8.5\,\mathrm{arcmin}^2$ for 2MASS.

For $|b| > 10°$, the DENIS completeness limits for highly reliable automated galaxy extraction, given in total magnitudes, are $I_c = 16.5^m$, $J = 14.8^m$ and $K_s = 12.0^m$ (Mamon, 1998). Similarly for 2MASS, the completeness limits, given in isophotal magnitudes, are $J = 15.0^m$, $H = 14.2^m$ and $K_s = 13.5^m$. The main characteristics of the two surveys and their respective completeness limits for extended sources are given by Epchtein and Skruskie (Epchtein, 1998; Epchtein et al., 1997; Skrutskie, 1998; Skrutskie et al., 1997). See also Cutri et al. (2003); Jarrett et al. (2000).

Compared to the optical B band, the extinction for the I_c, J, H and K_s bands are only 45%, 21%, 14% and 9%, respectively, causing the decrease in galaxy number counts towards lower Galactic latitudes to be considerably slower in the near infrared, compared to the optical. However, dependencies on morphological types, surface brightness, intrinsic colour, orientation and star-crowding lower the number of detectable galaxies. The near infrared

surveys appear to be particularly useful for the mapping of massive early-type galaxies – tracers of density peaks in the mass distribution – and therefore complement the far infrared and HI observations, which are better suited to detecting spiral galaxies (Kraan-Korteweg and Lahav, 2000).

The efficiency of uncovering galaxies at high extinction was analysed using DENIS images in the regions of the rich Norma cluster at gal. $(l, b) = (325.3°, -7.2°)$, with extinction A_B on this area varying from 1.2^m to 2.0^m, and the suspected extension of the Norma Supercluster across the Galactic Plane (Kraan-Korteweg et al., 1999, 1998; Schröder et al., 1998, 1997).

In practice, however, the B band was found to be superior to the identification of galaxies on DENIS images to extinction levels of at least $A_B = 2.0^m$ (Kraan-Korteweg and Lahav, 2000), and optical surveys do remain the most efficient in identifying obscured galaxies for extinction levels of $A_B \gtrsim 1^m$ - 3^m. The near infrared surveys become more efficient at lower Galactic latitudes, i.e. for $A_B \gtrsim 3^m.0$, due to higher extinction close to the Galactic Plane and therefore the increasing incompleteness of deep optical searches. Below latitudes of gal. $|b| \simeq 1°$ - $2°$, the expectation that no galaxies could be identified due to the heavy star-crowding, was confirmed (Mamon, 1994). The lowest Galactic latitude where galaxies were identified was at gal. $b \simeq 1.2°$ and $A_B \simeq 11^m$. These results were verified in more recent comparisons of optical and near infrared observations, using the *2MASS Extended Source Catalogue* (Kraan-Korteweg and Jarrett, 2005).

Deep near infrared surveys in the Great Attractor region, using the SIRIUS instrument attached to the Infrared Survey Facility in South Africa, the Wide Field Imager of the ESO/MPG 2.2 m-telescope at La Silla, Chile, and using DENIS observations, seem to suggest that a potential galaxy cluster around PKS1343-601 is not as rich as the Pavo or Centaurus clusters (Kraan-Korteweg et al., 2005; Nagayama et al., 2004, 2005; Schröder et al., 2005). However, the observations show that the Cen-Crux cluster (CIZAJ1324.7-5736) is a rich galaxy cluster.

Due to the advantages of optical surveys for identifying galaxies without

a bias towards particular morphological type at extinction levels $A_B \gtrsim 1^m$ - 3^m, systematic deep searches for partially obscured galaxies have been performed on existing sky surveys. Furthermore, new surveys were conducted in the Galactic Plane by various collaborations, which proved that large-scale structures can be traced to much lower Galactic latitudes despite the foreground obscuration. Since the earliest successful attempts of narrowing the Zone of Avoidance in 1956 (Böhm-Vitense, 1956) and the first systematic galaxy search in 1980 (Weinberger, 1980), almost the complete range in Galactic longitude has been covered by searches for hidden galaxies behind the Milky Way. Down to obscuration layers of about three magnitudes in the B band, the Zone of Avoidance could be considerably narrowed. Galaxies were found at even larger extinction levels of $A_B = 5.0^m$ and higher, possibly indicating holes in the foreground dust layer.

Unfortunately, galaxy and star images cannot yet be separated by automated measuring machines like COSMOS or APM on a viable basis below gal. $|b| \lesssim 10°$ to $15°$ (Drinkwater et al., 1995; Lewis and Irwin, 1996). Even with the application of artificial neural networks, results are promising, but not yet satisfying. Applying high latitude fields as training examples resulted in acceptable hit-rates of found galaxies of 80% to 96%, albeit with a similar number of false alarms. Conversely, the use of low latitude training-fields resulted in almost no false alarms, but a low hit-rate of about 30% to 40% (Naim, 1995).

Optical surveys have uncovered various important large-scale structures, one of which is the extreme galaxy overdensity centred on the Norma cluster at around gal. $(l, b) \sim (325°, 7°)$, the most massive galaxy cluster in the nearby universe. A deep optical galaxy search and subsequent redshift observations (Kraan-Korteweg et al., 1999; Woudt, 1998) showed that this cluster most likely marks the previously unidentified but predicted density-peak at the bottom of the potential well of the Great Attractor overdensity. It is similar in size, richness and mass to the Coma cluster and is shown to be at rest with respect to the rest frame of the Cosmic Microwave Background

(Woudt, 1998). Two more clusters were identified in the Great Attractor region. Relatively close to the Norma cluster is the Cen-Crux cluster at gal. $(l, b) \approx (306°, 6°)$, cz $\approx 6000\,\mathrm{km/s}$. More distant is the Ara cluster at gal. $(l, b) \approx (329°, -9°)$, cz $\approx 15000\,\mathrm{km/s}$ (Woudt, 1998).

A more recent discovery (Kraan-Korteweg and Woudt, 1999) is the suspected rich galaxy cluster centred on the second brightest extragalactic radio source PKS1343-601 (McAdam, 1991), which can be identified as a giant elliptical galaxy at cz $\sim 3900\,\mathrm{km/s}$ (West and Tarenghi, 1989). The area surrounding this galaxy at gal. $(l, b) \sim (310°, 2°)$ lies behind an obscuration layer of about twelve magnitudes in the optical B band, as estimated by the DIRBE/IRAS extinction maps (Schlegel et al., 1998). Observations in the near infrared are therefore more suitable for locating galaxies in this area.

The X-ray band seems to be ideally suited for looking for rich galaxy clusters behind the Milky Way. Rich clusters are strong X-ray emitters, and their X-ray luminosity is roughly proportional to the cluster mass. Moreover, the Milky Way is transparent for hard X-ray emission above a few keV. Limitations exist mainly for soft X-ray close to the Galactic Plane due to the photoelectric absorption by Galactic hydrogen atoms. Furthermore, rich galaxy cluster surveys are a good extension to the existing radio, near and far infrared surveys, as described earlier, because these clusters are mainly composed of early-type galaxies, which cannot be properly observed at long wavelengths. They are generally located at the centres of superclusters and Great-Wall-like structures, and they mark the density peaks and the deepest potential wells within these structures, due to their high mass-to-light ratios. Consequently, identifying the positions of these clusters can help us to understand the observed velocity flow fields introduced by these overdensities and to trace the large-scale structures.

Despite these prospects and the fact that four of the seven most X-ray luminous clusters in the 2-10 keV range lie at latitudes below ($|b| < 20°$) (Edge et al., 1990; Fabian, 1994), a systematic search in the X-ray band for galaxy clusters behind the Milky Way has only recently begun (Ebeling

et al., 1999, 2000). This *Clusters in the Zone of Avoidance* (CIZA) project is utilising the ROSAT All Sky Survey Source Catalogue (Ebeling et al., 2002; Voges et al., 1999). Of the 1901 X-ray sources with nominal X-ray fluxes within the CIZA study area, 191 galaxy clusters could be identified so far (Ebeling et al., 2005).

The disadvantage of ROSAT is that the measurements are affected by the photonic absorption by the Galactic hydrogen atoms close to the Galactic Plane, due to its observing region in the soft X-rays ($0.1 - 2.4$keV). Despite this shortcoming, it does have an advantage over the first experiments, like Uhuru, Ariel V and HEAO-1, since it has a better angular resolution, which reduces the problem of confusing Galactic sources with clusters. This had happened, for instance, with the Norma cluster, the 6th brightest cluster in the ROSAT X-ray All Sky Survey (Böhringer et al., 1996; Tamura et al., 1998), which was – due to the low angular resolution of the used HEAO-1 all-sky data – confused with the neighbouring X-ray bright Galactic X-ray binary 1H1556-605 in the first attempt to identify galaxy clusters in the Zone of Avoidance by means of their X-ray emission (Jahoda and Mushotzky, 1989).

An on-going *XMM-Newton* survey of galaxy clusters at $z < 0.075$ located within a 40×40 square degree region around the approximate location of the Great Attractor shows that the Cen-Crux cluster is about one-third as massive as the Norma cluster (Böhringer et al., 1996; Mullis et al., 2005; Tamura et al., 1998). However, although X-ray emission in the area around PKS1343-601 has been shown before (Tashiro et al., 1998), the lack of emission detection in the CIZA survey seems to suggest that no large galaxy-cluster will be found at this position (Ebeling et al., 2002, 2005).

Newer results from the CIZA project suggest that a potential component of the Great Attractor is an extended triangular structure that is viewed almost edge on. It is centred at $cz \approx 4500\,\mathrm{km/s}$ and formed by the Cen-Crux cluster (CIZAJ1324.7-5736), the Norma cluster and the Centaurus cluster (Ebeling et al., 2002). Another large-scale structure was identified with CIZA

at a distance of cz $\approx$ 15000 km/s. This structure appears to be a chain of X-ray selected clusters that starts from the Triangulum Australis Cluster and crosses the Galactic Plane northward up to the Shapley Supercluster. This may well be the reason for the lack of observational evidence for backside infall into the Great Attractor at cz $\approx$ 4500 km/s. Therefore, estimates of the masses of the CIZA clusters in this structure have to be critically assessed (Ebeling et al., 2005; Mullis et al., 2005).

To get a whole sky coverage of bright X-ray clusters, a combination of several cluster samples is planned, using the final CIZA cluster sample, the ROSAT Brightest Cluster Sample at $|b| \geq 20°$ and $\delta \geq 0°$ (Ebeling et al., 2000, 1998) and the REFLEX sample at $|b| \geq 20°$ and $\delta \leq 2.5°$ (Böhringer et al., 2004). The resulting list of clusters will be ideally suited to studying large-scale structures, and especially the connectivity of clusters and walls across the Galactic Plane, as well as assessing the Cosmic Microwave Dipole Anisotropy (Kocevski et al., 2005).

Whereas observations in different wavebands were conducted to narrow the obscuration layer of the Milky Way to a smaller latitude, a number of spectroscopic surveys were carried out to map the distribution of galaxies in redshift-space (Lahav, 2005). Redshift surveys have become very powerful nowadays. The *Two degree Field* facility (2dF) at the Anglo Australian Telescope is a 400-fibre optical spectrograph with a 2°-diameter field of view, which can deliver up to 400 spectra during one single observation. Over 220 000 redshifts have thus been obtained in the 2dF Galaxy Redshift Survey (2dFGRS).

In the Great Attractor region, a deep redshift survey was conducted in the Norma cluster area (Woudt, 1998; Woudt and Kraan-Korteweg, 2000; Woudt et al., 1999, 2000a,b) and more recently, results from the *Two degree Field* facility have become available for this particular region (Colless et al., 2001; Lewis et al., 2002). This will be followed soon by data becoming available from the *Six degree Field* facility (6dF) survey, which will give even further detailed information on the redshift distribution of galaxies (Huchra et al.,

2005; Jones et al., 2004, 2005).

The distribution in redshift-space clearly shows the large-scale structures in the nearby universe and – when presented and analysed appropriately – the data can help to identify new structures (Fairall et al., 2005a,b; Huchra et al., 2005). However, due to the peculiar velocities of the galaxies, it does not represent the exact spatial galaxy distribution; see Fairall (1998) for a good illustration.

As mentioned earlier, redshift-independent distances can be obtained by making use of the Tully-Fisher (Tully and Fisher, 1977) and the Faber-Jackson relations (Faber and Jackson, 1976). Both can be used to determine the total amount of light we receive from a galaxy. However, much of it comes from the faint outer parts; thus distances derived from the Faber-Jackson relation are not very precise. Nowadays, the latter of the two is replaced by the more efficient D_n-σ_0 relation (Dressler et al., 1987).

The Faber-Jackson relation has residuals that are clearly correlated with galaxy properties. There exists a linear relation between the logarithm of three main properties of ellipticals that form what is called the Fundamental Plane. These quantities can be the effective radius r_e, the central velocity dispersion σ_0 and the mean surface brightness μ_e, or some related quantities such as the 'Donald Diameter' D_n enclosing a mean surface brightness with a particular value, i.e. the ratio of the flux within an isophote to the area encompassed by the isophote (Djorgovski and Davis, 1987; Dressler et al., 1987). The equations of this plane can be used for more precise distance determinations than the Faber-Jackson relation. A good overview over the origin and use of the Fundamental Plane is given in Hogg (2001).

1.3 The Galactic Foreground Extinction

In conclusion, then, to be able to explore the extragalactic sky in the Zone of Avoidance, one needs an exact knowledge of the foreground extinction caused by the Milky Way and a clear understanding of the effects of this extinction

on the observed parameters. The latter issue was partly investigated in the optical wavelengths and the near infrared (Cameron, 1990; Nagayama et al., 2004), but it does need further attention, especially for other wavelengths.

Since the Galactic foreground extinction is a function of the wavelength, the mean extinction at a given wavelength A_λ, compared to the visual extinction A_V, can be expressed as:

$$A_\lambda / A_\mathrm{V} = a(1/\lambda) + b(1/\lambda)/R_\mathrm{V}. \tag{1.6}$$

The value of the interstellar extinction is a function of the ratio of total to selective extinction $R_\mathrm{V} \equiv A_\mathrm{V}/\mathrm{E(B-V)}$, and depends on the environment along the line of sight through the galaxy (Cardelli et al., 1989). A standard value of $R_\mathrm{V} = 3.1$ is applied for the diffuse interstellar medium, but for dense molecular clouds, this value can be higher ($R_\mathrm{V} \geq 4$). However, shifts in effective wavelength are being ignored in observations that look for the ratio of total to selective extinction, although it is known that these depend on reddening and the intrinsic colours. This can lead to significant errors in both magnitudes and distances for galaxies that are heavily reddened by dust in the Milky Way (McCall and Armour, 2000). For an overview of interstellar dust in the Galaxy, see Mathis (1990).

Until the end of the 20^{th} century, the Galactic extinction in the Zone of Avoidance has been estimated by means of Galactic neutral hydrogen column density maps (Burstein and Heiles, 1982). Although these maps do not cover the Zone of Avoidance ($|b| < 10°$), they can be extrapolated by assuming a constant gas-to-dust ratio:

$$\mathrm{E(B-V)} = \left(\frac{\mathrm{N_{HI}}}{2.23 \cdot 10^{18}} \right) \cdot 4.43 \cdot 10^{-4} - 0.055, \tag{1.7}$$

using the Galactic column densities $\mathrm{N_{HI}}$ (Hartmannn and Burton, 1997; Kerr et al., 1986).

However, the gas-to-dust ratio varies, and for some regions, e.g. $230° \leq l \leq 310°$ and $-20° \leq b \leq 20°$, the Great Attractor region, increases of up to a factor of two have been suggested, resulting in a severe overestimation

of the extinction (Burstein et al., 1987). Furthermore, the HI line might be saturated close to the Galactic Plane ($|b| \lesssim 2°$), resulting in underestimation of the extinction (Kraan-Korteweg and Lahav, 2000). This, however, can be avoided by using the Galactic CO as a tracer of extinction at these low latitudes (Dame et al., 1987).

An improved estimate of the Galactic foreground extinction is given by the 100 μm extinction maps from the DIRBE/IRAS experiment (Schlegel et al., 1998). These maps have a better resolution of 6.1′, rather than $\sim$ 20′ - 30′ for the HI maps, and claim to be of factor of two better at low and moderate extinction, compared to the previously used neutral hydrogen maps (Schlegel et al., 1998). However, the DIRBE/IRAS maps are only calibrated by extinction measurements away from the Galactic Plane, and the accuracy of these maps still needs to be established close to the Galactic Plane ($|b| \leq 10°$) (Schlegel et al., 1998). By using photometry and measurements of the colour-Mg_2 relation (Bender et al., 1993), a pilot study on 18 early-type galaxies has shown that the DIRBE/IRAS maps provide a good estimate of the Galactic extinction at least down to a Galactic extinction of $E(B-V) \leq 0.5\,\mathrm{mag}$ (Woudt, 1998). Although a systematic underestimation by a factor of $f = 0.86$ for moderate to high DIRBE/IRAS reddening was found, this finding is based on only a few galaxies in a small region of the Zone of Avoidance, and it therefore seems too early to incorporate these results into the DIRBE/IRAS maps. Further calibrations of the DIRBE/IRAS maps have already been done (Nagayama et al., 2005; Saito et al., 2000; Schröder et al., 2005; Temporin et al., 2000; Woudt et al., 2005). In particular, the colours of the galaxies in the Zone of Avoidance as identified with the near infrared surveys DENIS and 2MASS provide a large database for the calibration of the DIRBE/IRAS maps at low Galactic latitudes (Schröder et al., 2005). Despite these calibrations, there are still uncertainties regarding the accuracy of the DIRBE/IRAS maps (Arce and Goodman, 1999; Burstein, 2003, 2005; Hudson, 1999; Nagayama et al., 2004; Woudt et al., 2005).

1.4 Motivation and Outline of this Dissertation

The rich Norma cluster can be used to address some outstanding issues regarding the Great Attractor region and the large-scale structures surrounding it. It is still not known, whether the Great Attractor is a nearby overdensity at cz $\approx$ 3200 km/s (Tonry et al., 2000) or if it is more distant at cz $\approx$ 4500 km/s (Kolatt et al., 1995). The Norma cluster might also be located at the bottom of the potential well of the Great Attractor. Furthermore, the Great Attractor itself may take part in a flow on even larger scales.

In order to approach these problems, peculiar motions of galaxies in the Great Attractor region need to be identified. This, however, is not a trivial task, as the many problems that occur need careful consideration (McCall and Armour, 2000). Some of these uncertainties are caused by the Galactic foreground extinction (Hudson, 1999) which affects the correction of observed parameters like magnitudes and isophotal diameters (Cameron, 1990; Nagayama et al., 2005). Another difficulty arises at low latitudes as a result of the rising numbers of stars. The effect of star-crowding not only makes automatic identification and classification of galaxies difficult, but also influences the photometry obtained of the partially obscured galaxies (Buta and McCall, 1999), e.g. for galaxy searches in the near infrared, the heavy star-crowding becomes a significant delimiting factor (Kraan-Korteweg, 2005).

This dissertation attempts to address these questions, by using a sample of 32 early-type galaxies within the inner part of the Norma cluster. High signal-to-noise spectra have been obtained with the 2dF system, as well as deep R_c band photometry of the entire Norma cluster within its Abell radius, and K_s band photometry for selected galaxies.

Various methods to account for the heavy star-crowding were tested and compared in this dissertation. By either 'clipping' or masking out the stars, or by modelling their shape, followed by subtracting modelled artificial stars, the

images were prepared, so that the galaxies in the images could be examined independently of the numerous foreground stars. At times, the high stellar-density (e.g. several ten thousand stars per square degree brighter than 20^{th} magnitude in R_c) resulted in obvious deviations in the surface brightness profiles obtained. After determination of the best reduction method, accurate R_c and K_s magnitudes were derived for the sample.

These results were then compared with data obtained from 2MASS, and the $(R_c - K_s)$ colours of these galaxies were determined and used to examine the Galactic reddening. By making use of relations that link the Mg_2 indices and σ_0 to the intrinsic colours of galaxies, the Galactic reddening was determined to provide an accurate measure of the extinction (Bender et al., 1993), independently of the assumed reddening law. This was then used to compare the foreground extinction around the central region of the Norma cluster with the predictions from the existing DIRBE/IRAS extinction maps (Schlegel et al., 1998).

The presented account of the work done here is divided into three parts, or volumes, of which the first one is considered to be the dissertation itself. The second and third parts are appendices to the first part and were detached from the first part due to the extended volume of their content.

The second part contains supplementary results in the form of a catalogue of images and plots of the galaxies that were investigated. It offers further insight into the data set, which will be relevant for further analysis. The third part contains a detailed description in the form of a tutorial that explains some of the techniques that were developed and applied to the work displayed here. Although an overview of all the procedures adopted in this dissertation is given in the main part, the reader can gain more insight into the work by looking at the detailed third part.

The first part of this dissertation continues in the next chapter by describing the data that were obtained (Sections 2.1 to 2.3) and setting out how these data were reduced (Sections 2.4 to 2.6).

As one of the main tasks of the work presented here, four procedures for

overcoming the heavy foreground star-crowding were developed and applied to the data. In the third chapter, Sections 3.1 to 3.4, each of these four methods is described in detail. This is followed by an internal comparison of the corresponding results in Section 3.5.

In Chapter 4, the extraction of various attributes from the data is illustrated. The sky brightness for the optical and infrared data is determined in Section 4.1. Sections 4.2 and 4.3 outline the establishment of surface brightness profiles, subsequently resulting in the determination of integrated magnitudes, and the determination of circular aperture photometry for the galaxies, respectively. This is followed by an internal comparison of the subsequent results for the eight different CCDs of the *Wide Field Imager* instrument in Section 4.4. For the results obtained in the near infrared, an external comparison with data from the *2 Micron All Sky Survey* is given in Section 4.5. Details in Section 4.6, about how the effective radii and magnitudes for each galaxy were obtained, are followed by an account on the determination of the apparent galaxy colours in Section 4.8. Lastly, the photometric corrections that had to be applied to the data are described in Section 4.9.

The principal results from the work described in the previous three chapters are given in Sections 5.1 and 5.2. Secondary results are given in the second part of this dissertation. In Section 5.1, the obtained properties of the galaxies are given, while the colour excess in the central Norma cluster region is investigated in Section 5.2.

Finally, in the last chapter, the developed methods and the obtained results are put into a general context, and a brief outline of future prospects is given.

Chapter 2

Observations and Reductions

This chapter first determines the selected set of galaxies (Section 2.1), and then gives a description of the instruments that were used (Section 2.2). The observations and the reductions thereof are illustrated (Sections 2.3 and 2.4, respectively), and an explanation of the photometric calibration and a brief report on the astrometry are given at the end of this chapter (Sections 2.5 and 2.6, respectively).

2.1 Dataset

The mechanisms developed in this dissertation, e.g. to derive properties such as galaxy brightness in severely star-crowded regions, ought to be tested and compared based on a reasonably large set of data. Similarly, the application of the obtained magnitudes, e.g. to calculate the $(R_c - K_s)$ colours and Galactic extinction and to derive an initial Fundamental Plane of the Norma cluster, determined the selection criteria for the galaxies that were chosen. The following first selection rules were applied to obtain an initial set of galaxies:

1. position – galaxies within a radius of 100 arcmin of the centre of the Norma cluster at gal. $(l, b) = (325.3, -7.2)$, as defined by the strong radio galaxy PKS 1610-608,

2. galaxy type – elliptical and lenticular galaxies,

3. brightness – the brightest galaxies in apparent magnitude in the B_J band, with a limit of 17.5^m, and

4. redshift – confirmed cluster members based on a reliable redshift measurement within the range $2500 < cz < 7000\,km/s$.

To find the galaxies that fulfilled these criteria, the service from the *ViZieR*[1] catalogue access tool and the *SIMBAD*[2] database were used in connection with data presented by Woudt (1998). *ViZieR* allows one to restrict searches for objects to a circular area of chosen radius at a given position and includes the most recent information about the objects, taken in this case from Woudt (1998) through *SIMBAD*. The application of the described selection rules resulted in a preliminary dataset of 64 galaxies.

When the work on this set started, further restrictions were applied, related to the data that were going to be used. Since new accurate redshifts were available from observations obtained with the *Two degree Field* (2dF)[3] spectrograph (Dr. Lucey, priv. comm.), these were given preference. However, this reduced the dataset to about half the previous number. On the already prepared R_c and K_s band exposures (cf. Section 2.4 on page 39), each galaxy was examined visually to confirm that each object was indeed an elliptical or lenticular galaxy. Table A.1 on page 193 in Appendix A.1 shows the galaxies that were excluded from the initial set.

The final subset of galaxies used in this dissertation consists of a mere 32 galaxies that were left after the described selection process. An overview of positions of galaxies in this set is given in Figure 2.1 on page 33, plotted in equatorial and galactic coordinates, respectively. The tabulated data can be found in Appendix A.1, Table A.2 on page 194. However, for two galaxies shown in this Table, the magnitudes for only one filter were obtained.

[1] http://vizier.u-strasbg.fr/

[2] http://simbad.u-strasbg.fr/

[3] For a description of the abbreviations used in this dissertation, the reader is referred to Section B in the Appendix on page 247.

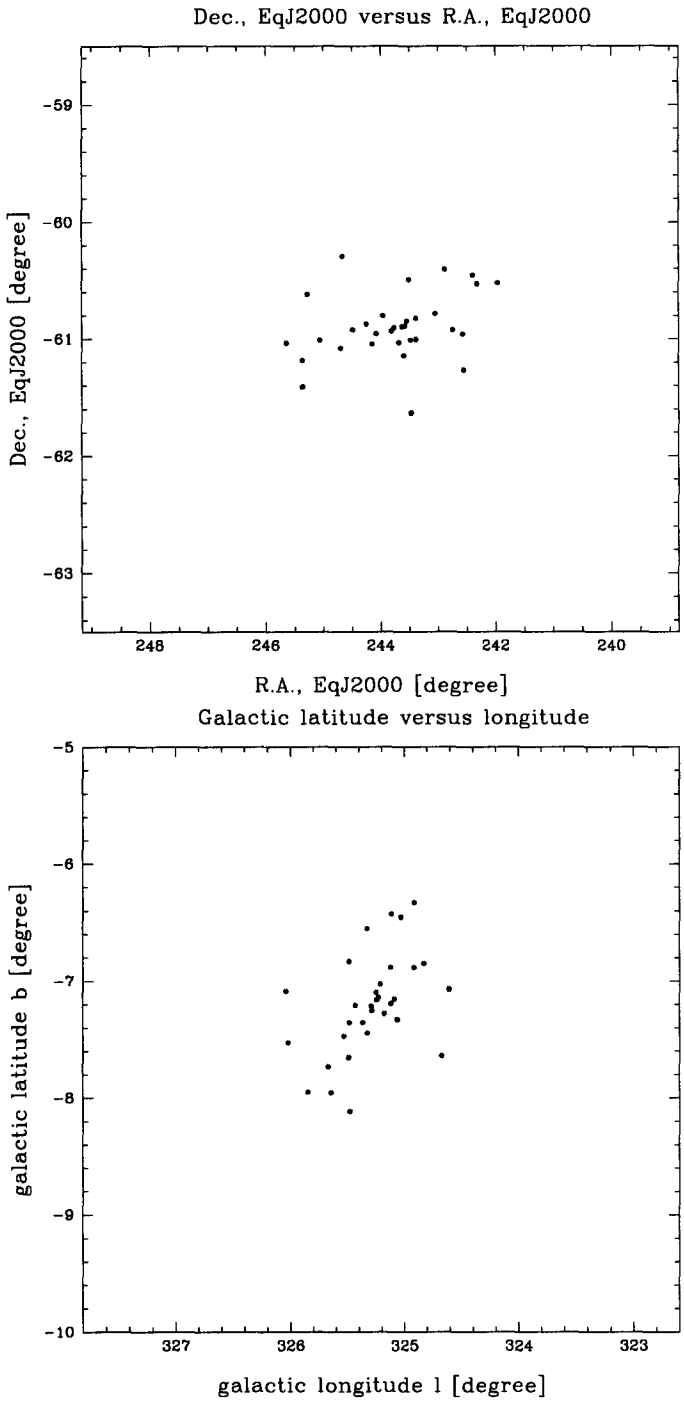

Figure 2.1: Position plots of final galaxy set as shown in Table A.2 on page 194 in Appendix A.1. Equatorial coordinates are shown at the top and galactic coordinates at the bottom. Compare also with Figures 5.2 and 5.3 on pages 151 and 152, respectively, in Section 5.2.

The galaxy WKK 6075 remained in the sample by mistake, although no K_s data were available, and for the galaxy WKK 6116, the radius for modelling the galaxy was not extended far enough to derive the R_{c23} magnitude (cf. Section 3.4 on page 65). The magnitudes derived for these two galaxies were therefore not used for colours and extinction. More details about each galaxy in the set can be found in Chapter 5 on page 121 and in Part II of this dissertation.

2.2 Telescopes and Instruments

High quality photometric data from two photometric bands were used to obtain the magnitudes and colours for the galaxies in the final galaxy set. Both of these, the R_c band and the K_s band, lie at the long wavelength end of the optical and near infrared spectrum, respectively, and are therefore the filters that are the least effected by the Galactic extinction in their spectral range. Furthermore, the $(R_c - K_s)$ colour is relatively independent of the assumed reddening law. However, one should note that the R_c is very broad and the reddening law used by Schlegel et al. (1998) and in this dissertation is founded upon broad-band photometry (Cardelli et al., 1989). Now, Bessel (1990) has stated that the effective wavelength shifts significantly with spectral type and Fitzpatrick (1999) has indicated that the R_c band is where monochromatic and broad-band reddening laws differ significantly, primarily because of the sensitivity of the band to effective wavelength shifts.

The telescope that was used for the optical observations was the *Max Planck Gesellschaft / European Southern Observatory* (MPG/ESO) 2.2 m or *2p2* telescope situated in La Silla, Chile. The telescope has a focal reducer-type camera mounted permanently at its Cassegrain focus. This *Wide Field Imager* (WFI) instrument consists of a mosaic of 4×2 CCD detectors with narrow inter-chip gaps, plus one CCD for the auto-guider. It has a detector coverage of $34' \times 33'$ and therefore a field of view with a diameter of almost $0.8\,^\circ$. Each chip consists of 2048×4096 pixels and offers excellent sensitiv-

ity from the atmospheric ultraviolet cut-off at around 320 nm to the near infrared. Only under the most superb seeing conditions will the pixel size of 0.238 arcsec undersample the point spread function. The WFI instrument is a joint project between the ESO, the *Max Planck Institut für Astronomie* in Heidelberg, Germany, and the *Osservatorio Astronomico di Capodimonte* in Naples, Italy (Baade, 1999).

Near infrared observations were obtained using the *Son of ISAAC*[4] (SOFI) instrument attached to the ESO 3.6 m *New Technology Telescope* (NTT). This telescope has an alt-azimuth mount and is housed in a rotating building with excellent in-built thermal control. It has a thin main mirror that enables the mirror's shape to be preserved in all telescope positions by altering the pressure from the mirror's support structure – the so-called active optics[5] system.

SOFI is the infrared spectrograph and imaging camera attached to the NTT. It is equipped with a 1024×1024 pixel *Hawaii HgCdTe* array, manufactured by *Rockwell Scientific*, and the instrument offers multiple observing modes, namely low and medium resolution spectroscopy with varying slit sizes, imaging polarimetry and imaging with different plate scales and broad and narrow band filters. For the data in this dissertation, only the Large Field imaging observing mode was used. This gives a scale of about 0.288 arcsec/pixel and a field of view of $4.94' \times 4.94'$.

In addition to the optical and near infrared data, spectral observations were conducted by the *Anglo-Australian Observatory* (AAO) (Dr. Lucey, priv. comm.). Initially, the spectroscopy was to come from the South African Astronomical Observatory 1.9 m telescope, but these data were superseded by the higher quality *Two Degree Field* system (2dF) data obtained subsequently. The 2dF is a complex astronomical instrument that is designed to

[4] *Infrared Spectrometer and Array Camera* (ISAAC) - the 'father' of the SOFI instrument.

[5] Active optics means that the shape of the mirror is maintained in each position of the telescope, unlike adaptive optics where the shape of the mirror is correcting for atmospheric turbulences.

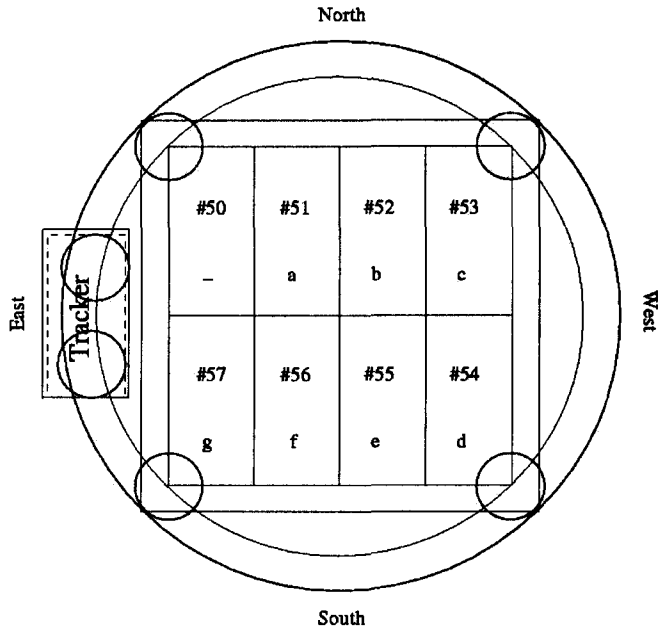

Figure 2.2: Orientation and labelling of the WFI CCDs. The picture is taken from *http://www.ls.eso.org/*, with permission.

allow the acquisition of up to 400 simultaneous spectra of objects anywhere within a two degree field in the sky. It consists of a wide field corrector, an atmospheric dispersion compensator, a robot gantry that positions optical fibres with up to 15 microns or 0.25 arcsec accuracy, and two spectrographs, each of which accepts 200 of these fibres to produce low to medium resolution spectra. Each spectrograph contains a science-grade *TEK* 1024 × 1024 pixel CCD with focus of 2 to 2.5 pixels over the entire chip and without bad columns. A tumbling mechanism with two field plates allows the next field to be configured while the current field is being observed.

The 2dF system is mounted at the prime focus of the *Anglo-Australian Telescope* (AAT), a 3.9 m optical telescope situated at Siding Spring, New South Wales, Australia.

2.3 Observations

The optical data used in this dissertation are taken from observations with the ESO *2p2* telescope, conducted by Dr. Woudt during three nights from the 18th until the 21st of May 1999. Deep R_c band photometry was obtained, using the filter ESO #844, which corresponds to the Cousins R photometric band (R_c) (Baade, 1999).

The entire Norma cluster was observed out to the Abell radius ($\equiv 3h_{50}^{-1}\,\mathrm{Mpc} = 2.1h_{70}^{-1}\,\mathrm{Mpc}$), which, at the redshift distance of $cz \approx 4800\,\mathrm{km/s}$ of the Norma cluster, corresponds to about 1.75 degrees in the sky. The resulting exposures cover about 10 square degrees of the sky. For each of the observed fields, five exposures were taken, which were slightly shifted with respect to each other. This technique is effectively used to reduce the effect of differences in sensitivity on the CCDs and in the optical pathway of the telescope, like bad and hot pixels, and to eliminate the gaps between the CCDs, allowing full coverage. Every two hours, standard stars from the Landolt selected areas were observed (Landolt, 1992) to be able to calibrate the data photometrically. A contamination problem of the CCDs on the WFI occurred during the time of the observations. This problem was apparent as a progressive loss of sensitivity, but it has not, however, compromised the quality of the data observed (Dr. Woudt, priv. comm.).

An overview of the data extracted from the optical observations related to the galaxy set described in Section 2.1 on page 31 is shown in Table A.3 on page 196 in Appendix A.1. The number of each observation field was defined by Dr. Woudt (priv. comm.) whereas the CCD number and the observing date were extracted from the FITS file header. The exposure time and airmass stated were calculated from the FITS header information, and the FWHM was obtained by using the *IRAF* task `imexamine`. For each galaxy, the sky brightness μ_{Rc}^{sky} was calculated as described in Section 4.1 on page 86. For observation fields that included more than one object, the calculated mean is shown in in Table A.3.

A selection of galaxies in the Norma cluster was observed by Dr. Schröder

with the ESO NTT during four consecutive nights from the 9^{th} of June 20000 onwards. For each galaxy a series of 10×4 exposures with each 7.5 s was observed with the K_s band filter of the SOFI instrument. For the same reasons as for the optical observations, the telescope position was slightly changed every 30 seconds (after 4 repeated 7.5 s exposures), resulting in 10 shifted images. During the two photometric nights (9^{th} to the 11^{th} of June 2000), standard stars from Persson et al. (1998) were observed approximately two hours apart throughout the night. In analogy to the galaxy observations described, the standard stars were observed at four slightly shifted telescope pointings, each time for 10×7.5 seconds (Dr. Woudt, priv. comm.).

An overview of the data extracted from the near infrared observations related to the galaxy set described in Section 2.1 on page 31 is summarised in Table A.4 on page 200 in Appendix A.1. The observing date was extracted from the FITS file header. The exposure time was 7.5 seconds for each exposure, and the airmass stated was calculated from FITS header information. The FWHM was obtained by using the *IRAF* task `imexamine`. For each galaxy, the sky brightness μ_{Ks}^{sky} was calculated as described in Section 4.1 on page 86.

As part of the preparatory work for this dissertation, proper astrometry on visually identified galaxies in the Great Attractor region had to be established by Dr. Woudt, the author and others (cf. Section 2.6 on page 44). The determined galaxy positions were then used by the AAO to measure the galaxy spectra and to determine the radial velocity or redshift and the velocity dispersion for each galaxy. The results concerning the whole Great Attractor region will be published elsewhere in a new galaxy catalogue (cf. Section 6 on page 167). In this dissertation, only the velocity dispersions obtained for the selected set of galaxies (cf. Section 2.1 on page 31) were used to get a reddening -independent estimate of the galaxy colours and the Galactic extinction, cf. Section 5.2 on page 149. An overview of the data used from the 2dF is given in Table A.5 on page 202 in Appendix A.1. It was generously provided by Dr. Lucey and will be published in full elsewhere (Dr. Lucey,

priv. comm.).

2.4 Data Reduction

The optical data obtained by means of the WFI has been flatfielded and bias-subtracted using the *MSCRED* package in *IRAF*. However, considerable variations in the background of up to 10% remained after flatfielding, with varying patterns for each of the eight CCDs. By removing all of the brighter stars from the object frames and by median-combining these images using a sigma-clipping technique, a superflat was created. After correcting the data with the superflat, the variations in the background level were reduced to less than 1%. For each of the observed fields, five exposures were taken, each slightly shifted in relation to the others, but centred on one exposure. These five images were combined and aligned, using the tasks `imcombine` and `imalign` within *IRAF*, whereby the 'ccdclip'-option in `imcombine` was effectively used to clip out the bad and hot pixels on the WFI CCDs. Since the ESO hierarchical keywords in the FITS header information are unfortunately not compatible with many FITS readers, e.g. *IRAF*, the necessary conversions had to be conducted using the program `hierarch28` available from the ESO[6]. After this conversion, all relevant information necessary for the data-processing could be calculated with the *IRAF* task `asthedit` and inserted into the FITS-header by using `hedit` (Davis, 1994; Jones and Valdes, 2000). Once this had been done, smaller sub-images were cut out from each image for each galaxy of about 800×800 pixels, centred on the galaxy.

The near infrared data from the SOFI instrument were flatfielded and reduced by Dr. Woudt (priv. comm.) and the 2dF spectra were processed by Dr. Lucey (priv. comm.). A few header keywords needed to be updated in the SOFI FITS-files; the updated information was entered into the header with the *IRAF* task `hedit` (Davis, 1994).

[6] *http://archive.eso.org/saft/*

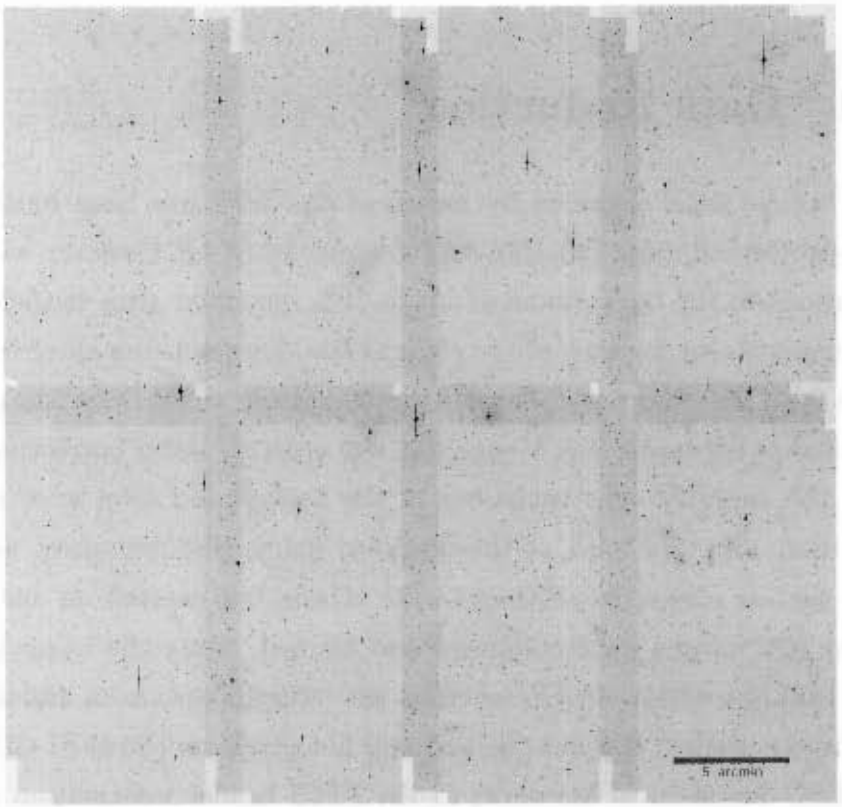

Figure 2.3: The central field of the Wide Field Imager observations. The five exposures that were taken for each CCD were combined into one image. This resulted in an overlap of the exposures, thereby covering the whole area without leaving gaps between the CCDs. This – plus the overlapping of the observation fields during the observation – made it possible to observe several galaxies with more than one CCD, which was used for the internal comparison of the CCDs in Chapter 5 on page 121. The scale indicated at the bottom right corresponds to 300 arcsec. The width and height of this combined image is 35.6 arcmin and 34.8 arcmin, respectively, resulting in a diagonal of 0.829 degree. North is at the top and East is on the left side. Also compare this with Figures 2.2 and 2.4 on pages 36 and 41 respectively.

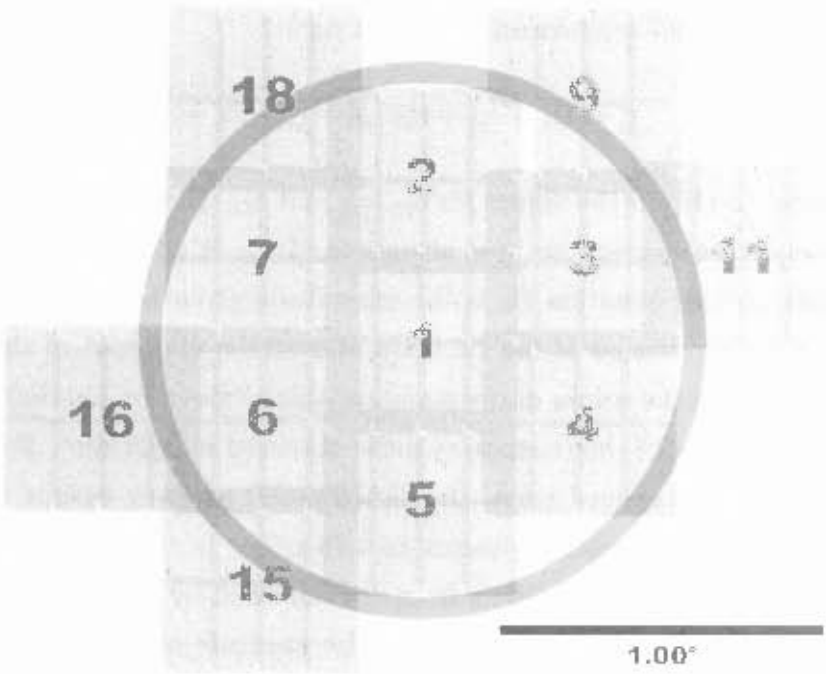

Figure 2.4: The WFI observations used in this dissertation. The 16 fields used here are a subset of the 46 fields observed in total, covering the whole Norma cluster. The indicated circle marks half the Abell radius and has a diameter of about 1.75 degree. Furthermore, the overlap of each field and each CCD exposure can be seen. Also compare this with Figures 2.2 and 2.3 on pages 36 and 40 respectively.

2.5 Photometric Calibration

Every two hours apart during each night of observing with the WFI instrument, standard stars from the Landolt *Selected Areas* (SA) were observed (Landolt, 1992). This appeared to be the most efficient way to determine the characteristics of each of the eight CCDs of the WFI, considering the large field of view. Out of the Landolt SAs, SA104, SA107, SA110 and SA113 were observed.

Based on Massey and Davis (1992), for each WFI CCD and for each

observed night, the transformation equation

$$r_c = R_c + c_{r1} + c_{r2} \cdot X + c_{r3} \cdot (V - R) \tag{2.1}$$

was solved to obtain the values for c_{r1}, c_{r2} and c_{r3}. Here c_{r1} is the zero-point offset, c_{r2} is the extinction per airmass and c_{r3} is the colour term. Furthermore, in this equation R_c is the magnitude given by Landolt (Landolt, 1992), X is the airmass of the standard star at the midpoint of the observation, $(V - R_c)$ is the colour of the standard star as given by Landolt (Landolt, 1992) and $r_c = -2.5 \cdot \log(\text{counts/s})$ is the observed magnitude[7]. For the photometry of the standard stars, the *DAOPHOT* package within *IRAF* and an aperture of 20 pixels, equivalent to 4.76 arcsec in the images, were used. This chosen aperture size differs from the one used by Landolt. However, as can be seen in Figure 2.5 on page 43, the aperture of 14 arcsec applied by Landolt would have been ill chosen for the WFI data. No significant light distribution exists for radii larger than about 5 arcsec and thus a large part of the sky would have entered into the photometry, which then would have increased the noise (Howell, 1989; Stetson, 1990).

Once the parameters c_{r1}, c_{r2} and c_{r3} had been fitted simultaneously as free parameters for each of the eight WFI CCDs, a mean value for the extinction per airmass (c_{r2}) was determined for each night of observation. The derived mean extinctions per airmass ($\overline{c_{r2}}$) are 0.082 ± 0.009 mag/airmass, 0.088 ± 0.012 mag/airmass and 0.092 ± 0.009 mag/airmass for each of the three observing nights from the 18^{th} to 19^{th}, 19^{th} to 20^{th} and 20^{th} to 21^{st} in May 1999, respectively. Using these values for the mean extinction per airmass, the parameters c_{r1} and c_{r3} were again fitted simultaneously as free parameters for each WFI CCD, but this time keeping c_{r2} fixed at the appropriate value, i.e. $\overline{c_{r2}}$ for each night of observation. It is assumed that the resulting values for c_{r1} and c_{r3} are hardware dependent only and that they do not vary over a period of a few days. They were therefore averaged over the three nights, giving a well-defined set of $\overline{c_{r1}}$- and $\overline{c_{r3}}$-values for each of

[7] In this dissertation, the 'log' is referring to the common logarithm to the base 10.

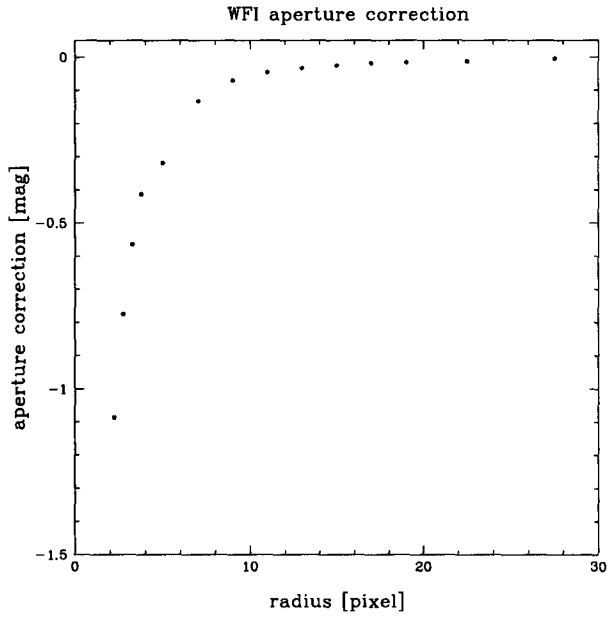

Figure 2.5: The aperture correction that should to be applied for the WFI standard stars. The magnitude values shown need to be added to the determined standard star magnitudes, and depend on the chosen aperture size. As can be seen, no significant light distribution exists beyond about 5 arcsec. The task `mkapfile` in the package *PHOTCAL* within *IRAF* was used to determine the shown aperture corrections. The data was derived for a standard star in the field SA110 which had a peak count of about 20,000.

the eight WFI CCDs. The resulting mean values $\overline{c_{r1}}$ and $\overline{c_{r3}}$ plus the number of standard star measurements that were used to derive these values are summarised in Table 2.1 on page 44.

Residuals (function − fit) from fitting the transformation equations are shown in Figure 2.6 on page 45 for two of the eight WFI CCDs. In the Appendix, Figures A.1 to A.3 on pages 204 to 206 show the residuals for the other six CCDs. The residuals are shown for different standard star brightness, airmass at time of observation, colour of the standard star and observation time. The slight shift that can be seen for each day is due to

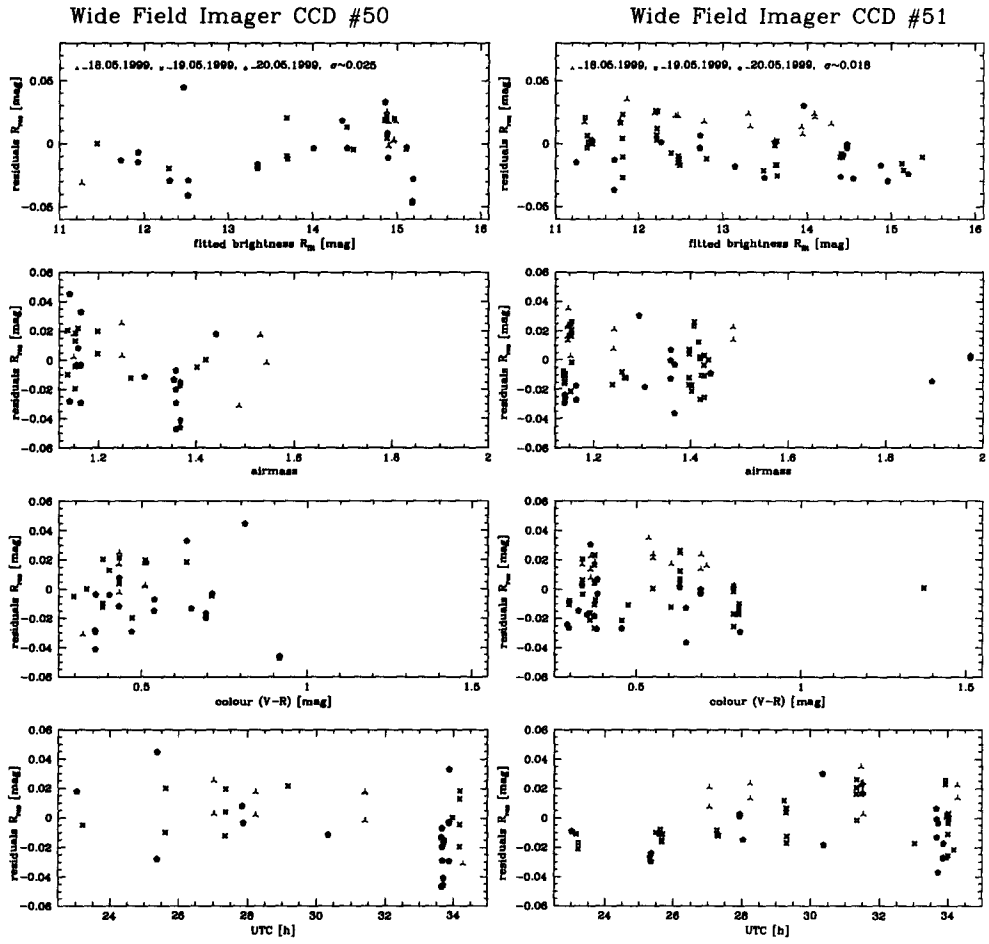

Figure 2.6: Residuals (function − fit) from the R_c standard star solution for the WFI CCDs #50 and #51. In the Appendix, Figures A.1 to A.3 on pages 204 to 206 show the residuals for the other six CCDs. The residuals are shown for different standard star brightness, airmass at time of observation, colour of the standard star and observation time. The slight shift that can be seen for each day is due to the data being fitted for each night, while for the resulting function the coefficients c_{r1} and c_{r3} were averaged over all the days, as described in the text.

Since many of the stars were overexposed, the 'spikes' were used as a kind of reticle (Dr. Woudt, priv. comm.).

Consequently, the positions, types and sizes of all of the galaxies that could be visually identified on the obtained WFI exposures were determined. To be able to see even the faintest galaxies in the images, the program *SkyCat*[8] was used to zoom into the images. The contrast and cut-levels could be adjusted, making it possible to find and identify different types of objects. Using this technique, Dr. Woudt, Dr. Hempel[9] and I spent several weeks successfully browsing through the exposures. A few thousand new galaxies were found and catalogued, as well as improved positions for the galaxies that were already known. Most of these data will be part of a new detailed catalogue of galaxies in the Great Attractor region, published elsewhere (Dr. Woudt, priv. comm.), and will include the redshift data obtained from 2dF (Dr. Lucey, priv. comm.).

[8]Provided by the ESO, see *http://archive.eso.org/skycat/*.

[9]Dr. M. Hempel, Physics and Astronomy Department, Michigan State University, United States of America.

Chapter 3

Separating Galaxies from the Foreground Starfield

The main focus of this study was to take foreground stars into account, when determining the photometric properties of elliptical galaxies. Thus, four different techniques were developed here and investigated to approach this problem. The four methods are called *σ-Clipping*, *PSF-Fitting*, *Star-Masking*, and *iPSF-Fitting*. They are described in detail in this chapter, Sections 3.1, 3.2, 3.3 and 3.4, respectively. An internal comparison of the results obtained by applying these procedures is given in Section 3.5.

In terms of determining surface brightness profiles, early-type galaxies have an inherent advantage over late-type and irregular galaxies. Their brightness as well as their structure can be modelled by a series of consecutive ellipses of constant surface brightness, i.e. isophotes. Variation of the ellipticity, position angle, centre and radius makes it possible to reduce almost every elliptical galaxy to a set of isophotes. Within *IRAF*[1], the `ellipse` task is well suited for this procedure.

[1]For a description of the abbreviations used in this dissertation, the reader is referred to Section B in the Appendix on page 247.

There are, however, several factors that influence whether the model produced is an appropriate representation of the real view of the galaxy. Many of these factors result from our position as observers within our own Galaxy. For instance, the closer the observations lie to the plane of the Milky Way, the more apparent become the extinction and reddening effects, which are caused by dust and gas in our Galaxy. This problem is often approached by doing observing in different wavebands and thus being able to estimate the wavelength-dependent extinction.

Another factor that becomes important at lower latitudes is the appearance of many foreground stars that populate our Galaxy. Observations far away from the Galactic Plane often only have to account for few relatively bright stars from our sun's immediate neighbourhood. At the position of the Great Attractor, however, several tens of thousands of stars per square degree brighter than 20^{th} magnitude in R_c can be resolved. These stars not only crowd any extragalactic object, but their light can also contribute to (and thus exaggerate) the measured brightness of any object. This is partly due to the effects of seeing, which can be reduced by using telescopes that are less affected by the Earth's atmosphere, like the *Hubble Space Telescope* (González et al., 2005). However, the observing time at these facilities is limited and most observers will have to rely on earth-bound telescopes for their observations.

Newly built telescopes can produce high resolution images in the optical as well as the near infrared wavebands. This makes it possible to conduct observations in different wavebands and thus to overcome the effects of Galactic extinction to some extent. The problem of star-crowding, however, is still a serious one and, for instance in the K_s band, it is one of the limiting factors for extragalactic observations at extinction levels of about $A_B \approx 10^{\text{m}}$ (Kraan-Korteweg, 2005).

Determining galaxy models independently of the foreground starfield for galaxies at low Galactic latitude was thus a main part of the work presented in this dissertation. The usual approach of using the k-sigma-clipping within

the `ellipse` task was examined, as was the approach of producing a pixel-mask for masking out the stars (Busko, 1996; Jedrzejewski, 1987). A newer approach of modelling the stars with point spread functions (PSF), followed by subtracting of the model from each single star was tested as well (Buta and McCall, 1999). The experience gained resulted in the development of a new procedure of treating the data in order to generate the best possible surface brightness profiles for early-type galaxies.

3.1 *σ-Clipping*

To obtain surface brightness profiles of elliptical galaxies, one can use the `ellipse` task, which is part of *IRAF*. This task works well for images with a few stars on top of the galaxy. However, in star-crowded fields, with many stars in front of the galaxy, one has to account for the `ellipse` modelling of a galaxy being influenced by many and possibly bright stars.

One way of approaching this problem is by using the k-sigma-clipping option from within the `ellipse` task itself. This was done here as a first measure to account for the star-crowding. The principle behind this is to determine the best fitted isophotal ellipse for a given radius. All intensity counts that are higher or lower than the average by a certain amount within each ellipse are cut – or 'clipped'. This process is repeated several times in an iterative manner – to establish the best possible fit.

The upper and lower amount for which clipping would occur was adjusted in the `usclip` and `lsclip` parameters. The numbers given were multiplied by the sigma value as stated in `daophot.datapars`. This would then determine the upper and lower limits, respectively. The value entered into the `nclip` parameter gives the number of iterations applied to the k-sigma-clipping. Here, this method is called '*σ-Clipping*'. An overview of this approach is given in Figure 3.1 on page 50.

The `ellipse` models were established by starting at a given distance from the estimated centre of the galaxy, usually at a radius of around ten

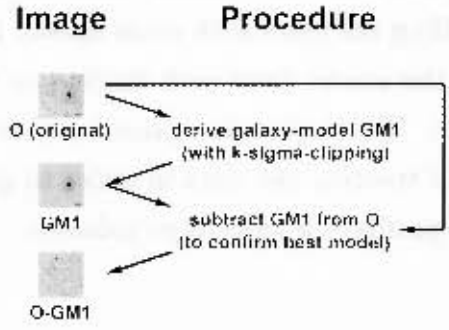

Figure 3.1: Diagram of the *σ-Clipping* method as described in this chapter. See also Figures 3.2 and 3.3. The example images are shown for the K_s band and the galaxy WKK 5920. The arrows indicate causal dependencies.

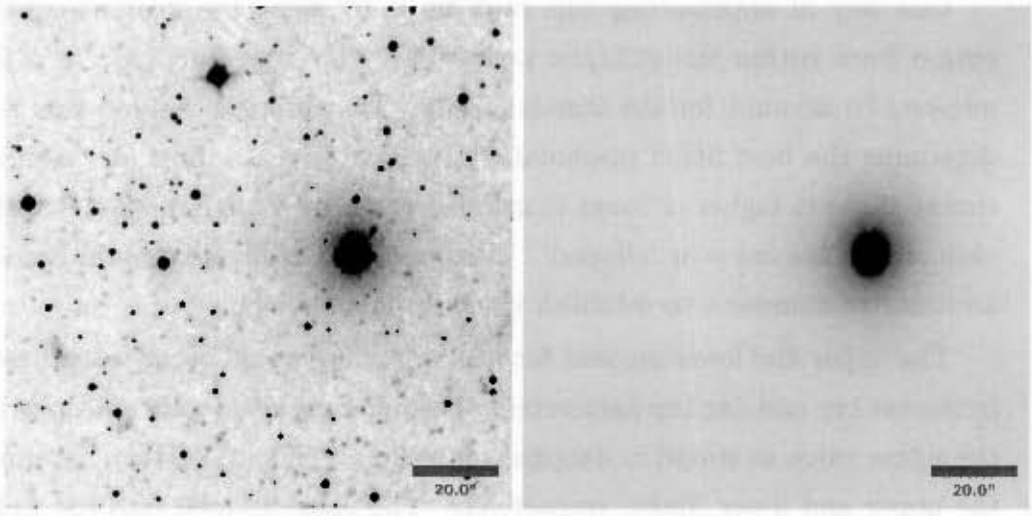

Figure 3.2: Galaxy WKK 5920, the original K_s band image (left), and the *σ-Clipping* model of the galaxy (GM1, right) as produced with the `ellipse` and `bmodel` tasks.

pixels from the centre. First the elliptical isophotes were determined from a given radius outwards, i.e. towards an increasing radius, and then inwards, to model the central region of the galaxy. The largest possible radius was to ensure that the `ellipse` model would reach the background. If possible, the position angle and ellipticity parameters were not kept fixed, neither were the parameters for the suspected centre of the galaxy. However, it was often necessary to keep one or more of these parameters constant in order to obtain a proper galaxy model, particularly in the case of the model obtained by applying the *σ-Clipping* method only.

In order to judge whether the determined model might be appropriate, an artificial galaxy was modelled for each object by using the result of the `ellipse` task. The output of the `bmodel` task within *IRAF* is a FITS image containing the galaxy model, which is based on the output of the `ellipse` task. See the right side of Figure 3.2 on page 50 for an illustration. Note that the rings visible in Figure 3.2 are artefacts of the method used to remove the galaxy. These rings will also be visible for some of the following images and several images in Part II of this dissertation. By using `imarith` within *IRAF*, the image was then subtracted from the original image, which contained the 'real' image of the galaxy and the stars. The resulting original-minus-galaxy model image (O-GM1)[2] was inspected by eye to see whether there were indeed as few residuals visible as possible (see left side of Figure 3.3 on page 52). If the results were not satisfying, the whole process was repeated from the editing of the parameter files that feed into the `ellipse` task to the re-modelling of the galaxy. Furthermore, the `backgr` value within the `bmodel` task often had to be adjusted, since this gives the background, which is added to the galaxy model. This was especially important if the resulting O-GM1 images were to be used for further analysis, as will be described in Sections 3.2, 3.3 and 3.4 on pages 53, 62 and 65, respectively. The whole process was repeated until the results could not be improved any further. Once the best model was subtracted from the original image, the part of

[2]Compare with Figure 3.1.

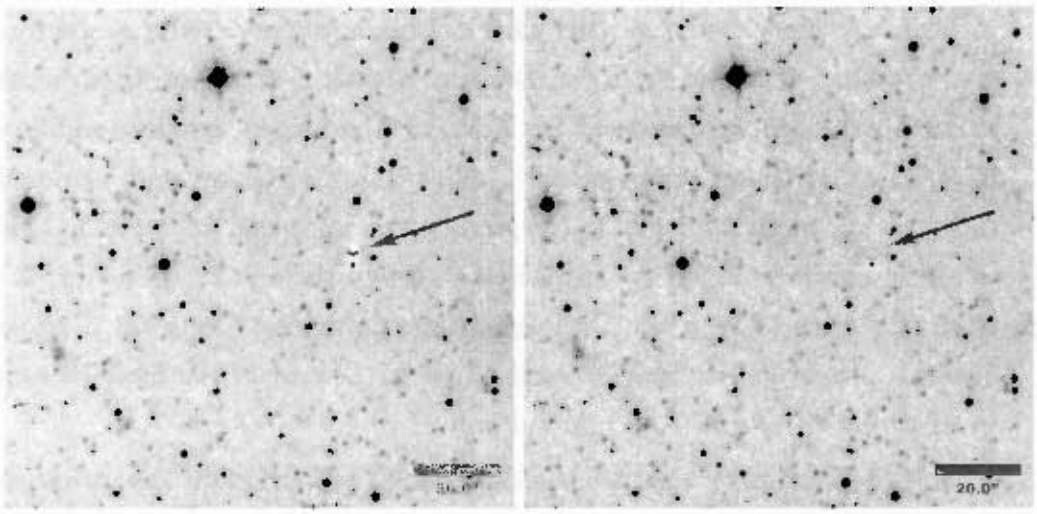

Figure 3.3: Galaxy WKK 5920, the original image minus the *σ-Clipping* galaxy model (left), and the resulting clean image without a trace of the galaxy (O-GM1, right).

the resulting image was cleaned where the galaxy core was situated. As this central region of the galaxy is difficult to model with `ellipse`, this cleaning was necessary for the methods still to be described. The cleaning was conducted by either copying an empty part (i.e. without stars) of the image from far away from the galaxy, using `imcopy`, or by editing the area interactively with `imedit`. Compare the images on the left and the right in Figure 3.2. Whenever the O-GM1 image from the *σ-Clipping* is mentioned in the following sections, it is this 'cleaned' image that is referred to.

Note that all those parts of the images, where galaxies have been analysed, were inspected by eye beforehand. This was to ensure that there were no significant deviations in the background, as all the applied methods described in this Chapter do not allow for backgrounds that are not smooth. However, no significant deviations in the background, e.g. due to insufficient flat fielding, have been found on the scales on which the galaxies were analysed. Furthermore, no diffuse emission from the Milky Way, like the H_{alpha} emission that is indeed visible in some parts of the R_c band images, could be

observed near to the relevant areas of these images.

Since all of this was done 'by hand' and as an iterative process, in the worst cases it could take up to several hours per galaxy[3]. To reduce the time spent by the user, an *IRAF* script is being developed to allow the user to process many galaxy models simultaneously. However, as this scripting is still very much a 'work-in-progress', it is not included in this dissertation (cf. Section 6 on page 170). A more detailed description of how to conduct the *σ-Clipping* is given in Part III of this dissertation.

3.2 *PSF-Fitting*

To allow for the shortcomings of determining the galaxy surface brightness profiles with the implemented k-sigma-clipping of the `ellipse` task, three further methods were employed to improve the galaxy models obtained. All three methods use the `ellipse` task to model the galaxy and are based on the results from the *σ-Clipping* as described in Section 3.1 on page 49. However, they try to remove the stars and other artefacts without relying on the `ellipse`-internal k-sigma-clipping only. The *PSF-Fitting* method described in this section models and subtracts the stars. The following method simply masks out all stars and artefacts, and is therefore called the *Star-Masking* method, cf. Section 3.3 on page 62. Stars and artefacts are removed completely in the *improved PSF-Fitting* method described in Section 3.4 on page 65.

The *PSF-Fitting* procedure described in this section was the first improvement to the use of the `ellipse`-internal k-sigma-clipping only. It soon became apparent, however, that more accurate and simpler, less time-intensive methods had to be developed. The *PSF-Fitting* method is therefore seen

[3]The absolute worst case that was processed during the course of this research, was an image on which one elliptical galaxy was partly covered by another (WKK 6305a, 6305b). The two galaxy models were subtracted in an alternating interactive manner to obtain good models for both galaxies. Images resulting from application of the *iPSF-Fitting* are shown in Appendix A.4 on page 213.

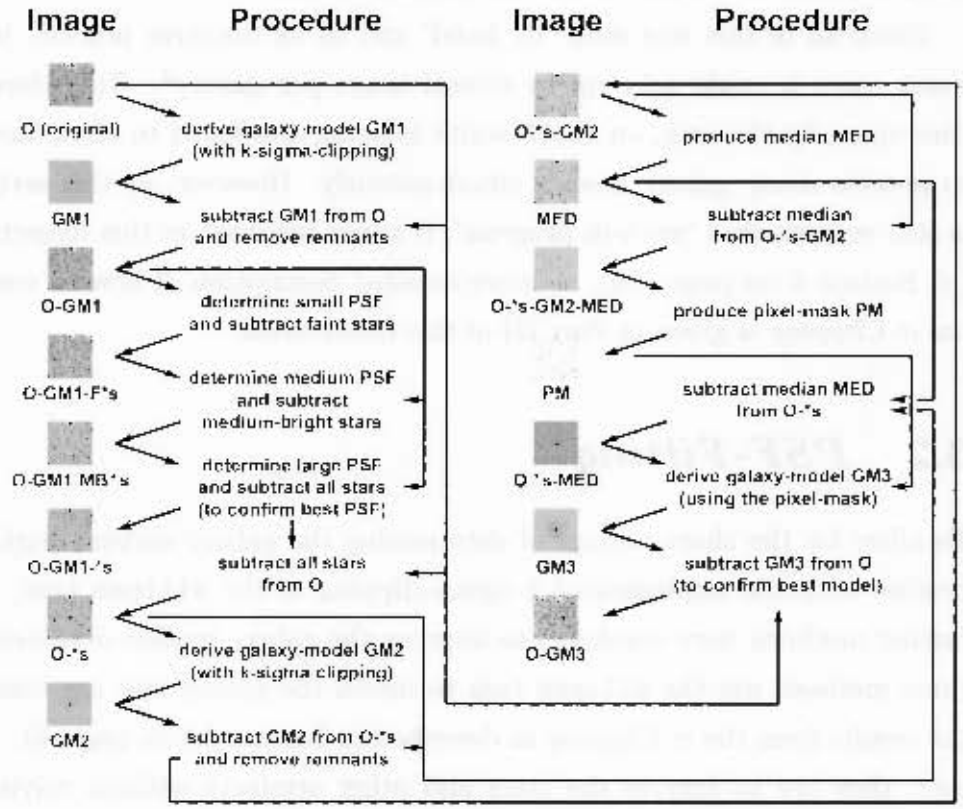

Figure 3.4: Diagram of the *PSF-Fitting* method as described in this chapter. See also Figures 3.5 to 3.12. The example images are shown for the R_c band and the galaxy WKK 6600. The arrows indicate causal dependencies.

as a prototype for testing various methods of processing the data and is only mentioned for reasons of completeness. Despite the fact that it is only mentioned for the sake of completeness, a comparison was intended for this dissertation, of the data obtained from applying the *PSF-Fitting* with the results from the other three data processing methods set out in Sections 3.1, 3.3 and 3.4 on pages 49, 62 and 65, respectively. Unfortunately, most of the resulting data were lost in a computer crash *and* the subsequent failure of the backup drive, making a reasonable comparison impossible.

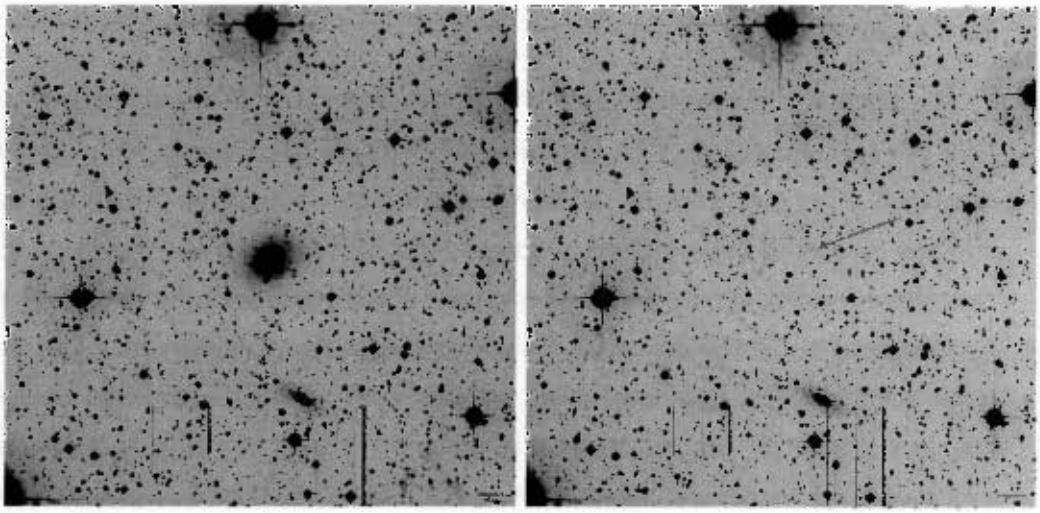

Figure 3.5: Galaxy WKK 6600, the original R_c band image (left), and the clean image without the galaxy (O-GM1, right), after repeated *σ-Clipping* as described in Chapter 3.1 on page 49.

An overview of the procedure is given in Figure 3.4 on page 54. As mentioned earlier, the first step in processing the data was to obtain an image with a rough galaxy model (GM1) subtracted from the original. It was obtained by following the *σ-Clipping* procedure described in the previous section. This resulted in an image with the galaxy model subtracted and the least possible remnants of this subtraction visible in the image (O-GM1, see right side of Figure 3.5 on page 55). Once this image had been obtained, it was used to subtract the stars found. Thereafter, the remaining hot pixels and bad columns were eliminated. Lastly the remains from the star-subtraction as well as overlooked faint stars and very bright, often overexposed stars were removed, too.

In the galaxy-subtracted image (O-GM1), the remnants left at the position of the centre of the subtracted galaxy had to be erased first. These remnants occur more or less prominently for all galaxies due to seeing effects. They can either be replaced by an empty area, i.e. without stars, from a different section of the image, using `imcopy`, or by editing the area interactively

with `imedit`.

To obtain a well-established PSF one needs to use many bright stars that are not saturated. The environment of these stars needs to be clean of artefacts, stars etc. This was achieved here by removing first the fainter stars and the remnants before determining the final PSF. Thus, the positions of all the stars in the image had to be identified, which could be done automatically by means of the `daofind` task. However, it often happened that some stars were not identified, whereas other objects were wrongly identified as stars, e.g. hot pixels or central regions of galaxies. The identification of these objects could be altered interactively with `tvmark`. Once the positions of all the stars in the image had been determined, their relative brightness was determined with the `phot` task. The resulting list of stars was sorted with `pselect` into four 'brightness bins': three bins for the faintest, medium-bright and brightest stars, respectively, and one bin for the saturated stars, including other stars for which the relative brightness could not be identified by the `phot` task, e.g. if they were too close to the edge of the image.

For each set of stars, i.e. the bright, the medium-bright and the faint stars, the point spread function is determined with the `psf` task, starting with the faint stars. When the PSF for the faint stars had been established, they were subtracted from the O-GM1 image (see left side of Figure 3.6). To do the subtraction, the `nstar`, `group` and `substar` tasks were used. From the resulting image, the PSF for the medium-bright stars was determined subsequently. The medium-bright stars were then subtracted again from the O-GM1 image, together with the faint stars. This time, however, the larger PSF derived from the medium-bright stars was used (see right side of Figure 3.6). This procedure was then repeated in a similar manner for the bright stars, until a proper PSF for the bright stars had been established (see left side of Figure 3.7). For each of the consecutive determinations of the PSF, i.e. for the stars with different brightnesses and radii, the PSF-radius in `daophot.daopars` was increased, for instance from 15 pixels for the faint stars up to 45 pixels for the bright stars, depending on the sizes of the stars.

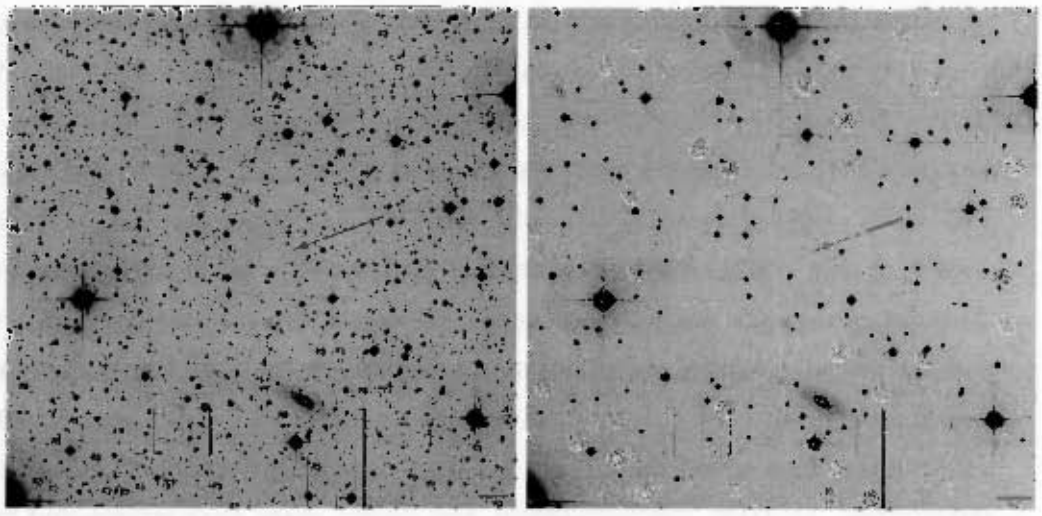

Figure 3.6: Galaxy WKK 6600, an image with galaxy and stars subtracted, after the first iteration of determining an appropriate PSF (O-GM2-F*s, left), and an image with galaxy and stars subtracted, after the second iteration of determining an appropriate PSF (O-GM2-MB*s, right).

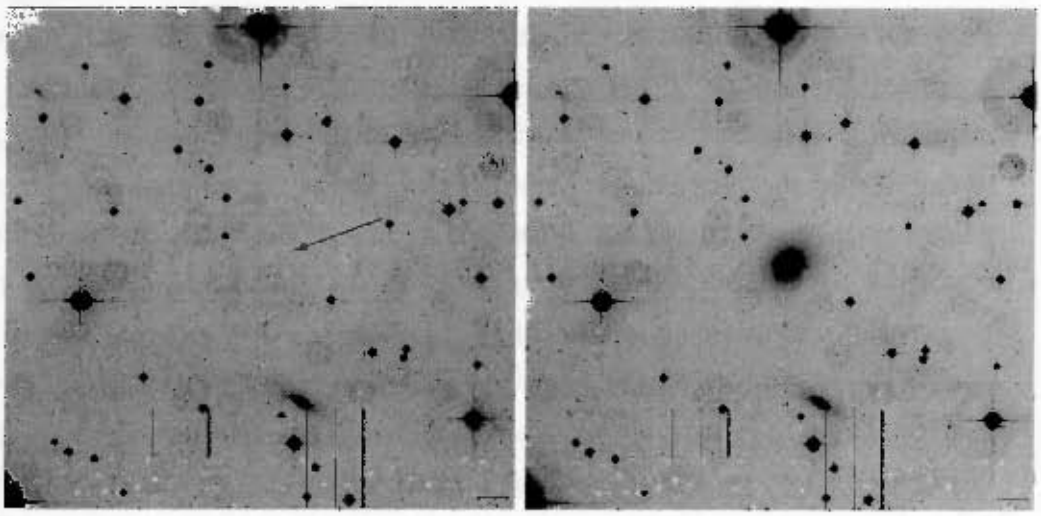

Figure 3.7: Galaxy WKK 6600, the image with galaxy and stars subtracted, after the third iteration of determining an appropriate PSF (O-GM1-*s, left), and the original image with stars subtracted (O-*s, right).

Sometimes, it was necessary to repeat the entire PSF determination process, due to a bad selection of stars, which were used to produce the PSF. This was especially the case at the beginning of the project. After some experience had been gained with the selection of stars, this became necessary less often. Other factors that influenced the outcome had to be considered too. For instance, it was necessary to lower the `datamin` parameter in `daophot.datapars` each time a new PSF was to be established. This was due to the increase in the standard deviation ('noise') of the background, which in turn affected the good minimum data in the images after each star-subtraction that could been used. Once a reasonably good PSF had been determined, all faint, medium-bright and bright stars were subtracted from the original image (O-*1) by means of `substar`, i.e. from the image containing both the stars and the galaxy (see right side of Figure 3.7).

With the `ellipse` and `bmodel` tasks, a new galaxy model (GM2) was established. To see whether this model was a good one, it was subtracted with `imarith` from the image with all stars subtracted (see left image in Figure 3.8). Thereafter, the internal k-sigma-clipping within `ellipse` was activated once more. Once it was apparent that the model could not be improved any further, it was subtracted from the original image (see right image in Figure 3.8). The remnants in the central region of the subtracted galaxy were erased, using either `imcopy` or `imedit`, as described before (O-GM2, see left side of Figure 3.9 on page 60). All faint, medium-bright and bright stars were subtracted from the O-GM2 image with `substar`, using the good PSF determined earlier (see right side of Figure 3.9 on page 60). From the resulting O-GM2-*s image, a median image was produced (see left side of Figure 3.10 on page 60), using the `median` task. This was then subtracted from the same image with `imarith` (O-GM2-*s-MED, see right side of Figure 3.10 on page 60) to account for the remnants left from subtracting the stars. All remaining artefacts, e.g. from overexposed stars, hot pixels etc., were masked out. The pixels with higher or lower intensity than about $\pm 3\,\sigma$ were raised with `imreplace` to a very high intensity, e.g. 65000 counts. This

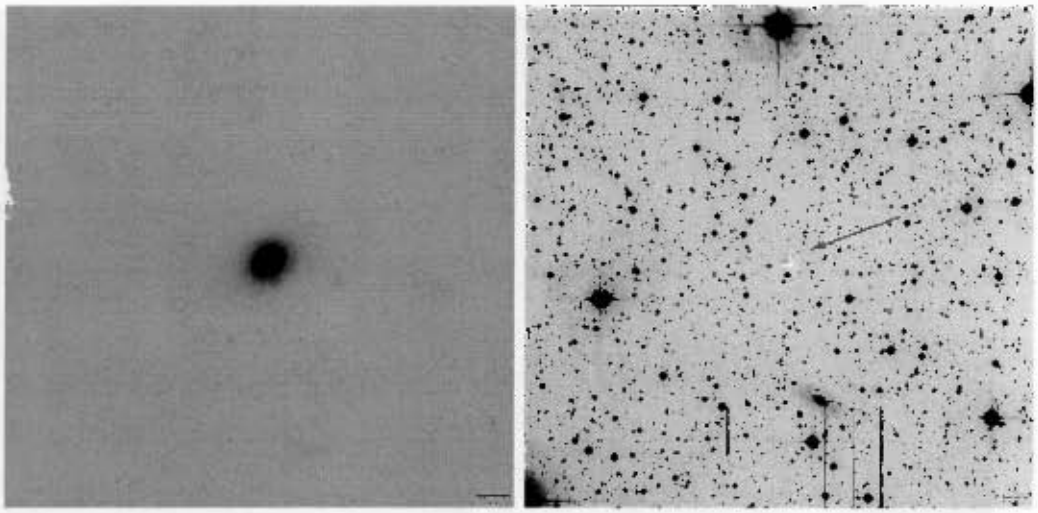

Figure 3.8: Galaxy WKK 6600, the galaxy model after subtracting the stars using the determined PSF (GM2, left), and the image after subtracting the new galaxy model (right).

made it possible to produce a pixel-mask with the `ccdmask` task (see left side of Figure 3.11 on page 61). As running `ccdmask` can take hours, the process was usually run as a background task, while working on another image.

The final galaxy model was obtained by subtracting the median image from the O-*s image (see right side of Figure 3.11 on page 61). A new galaxy model could now be established with the `ellipse` task. This time, however, this was done without using the internal k-sigma-clipping, but instead with applying the pixel-mask (GM3, see left side of Figure 3.12 on page 61). The `ellipse` parameters were adjusted after applying `bmodel` and `imarith`. Viewing the remnants of the subtracted galaxy model and adjusting the ellipse parameters made it possible to obtain the best possible galaxy model (see right side of Figure 3.12 on page 61). The data in the *STSDAS* tables produced by `ellipse` were exported into ASCII tables with `tdump` to process the results further (cf. Section 4.2 on page 91). A more detailed description of how to conduct *PSF-Fitting* is given in Part III of this dissertation.

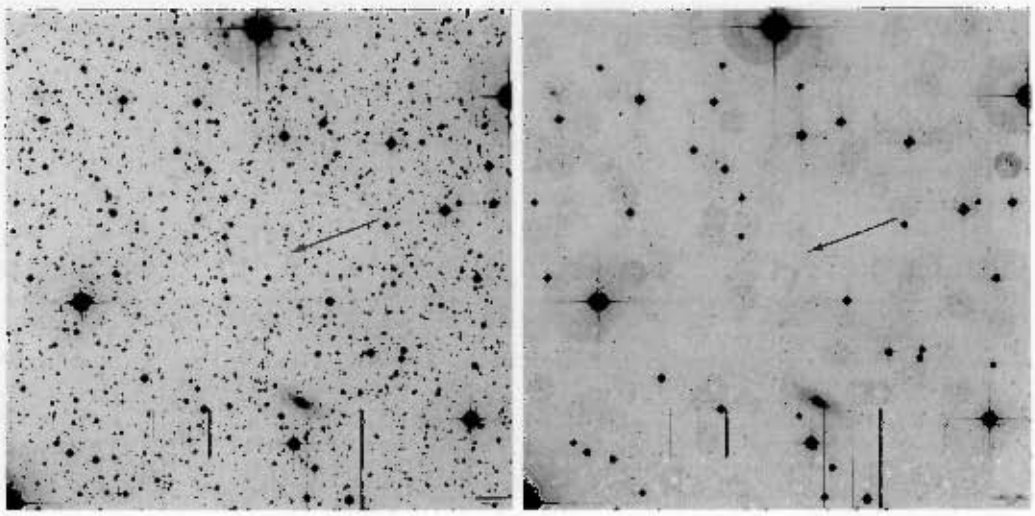

Figure 3.9: Galaxy WKK 6600, the new clean image without galaxy remnants, after subtracting the new galaxy model (left), and the new clean image, after subtracting the new galaxy model and the stars using the determined PSF (O-*s-GM2, right).

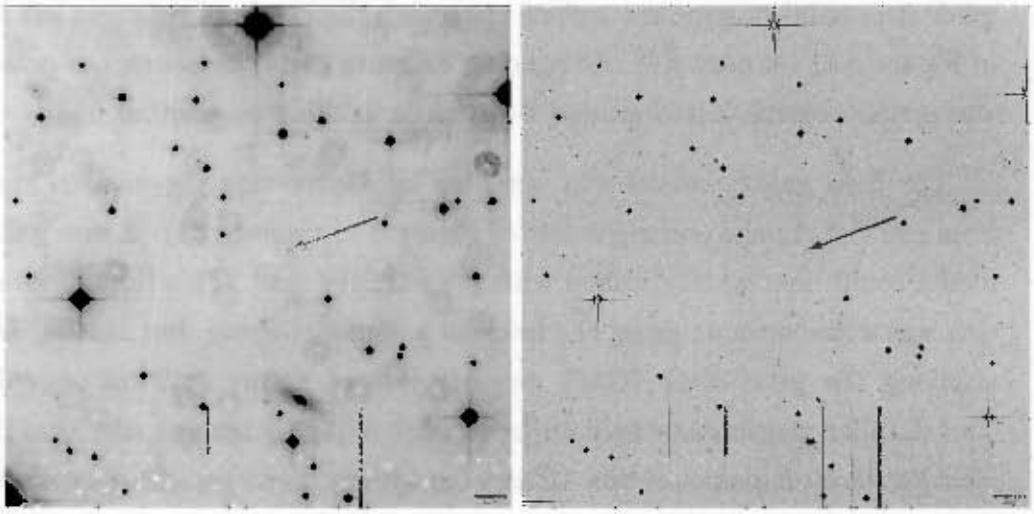

Figure 3.10: Galaxy WKK 6600, median image obtained from the image with subtracted stars and galaxy (MED, left), and the galaxy-, star- and median-subtracted image (O-*s-GM2-MED, right).

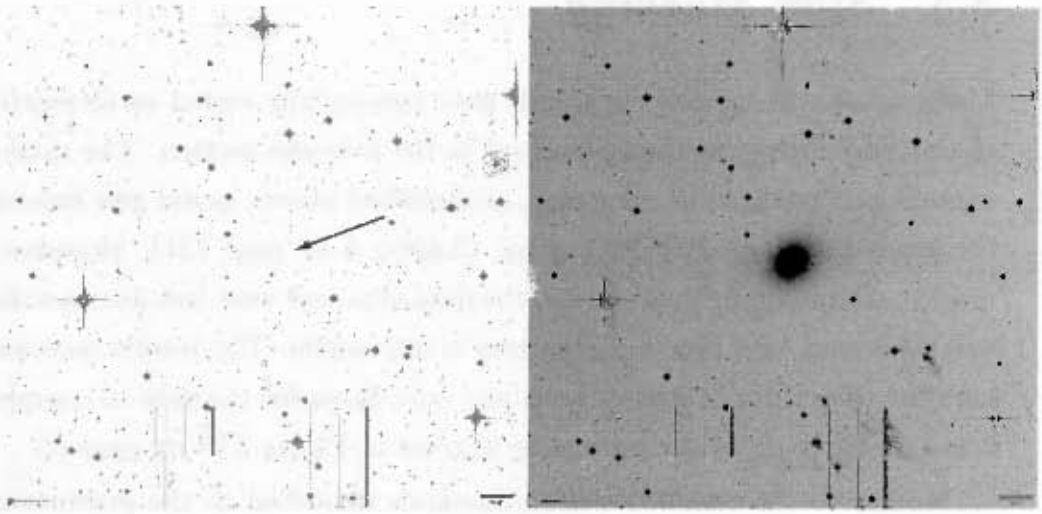

Figure 3.11: Galaxy WKK 6600, the pixel-mask derived from the frame with galaxy model, stars and median image subtracted (PM, left), and the original image with the stars and the median subtracted (O-*s-MED, right).

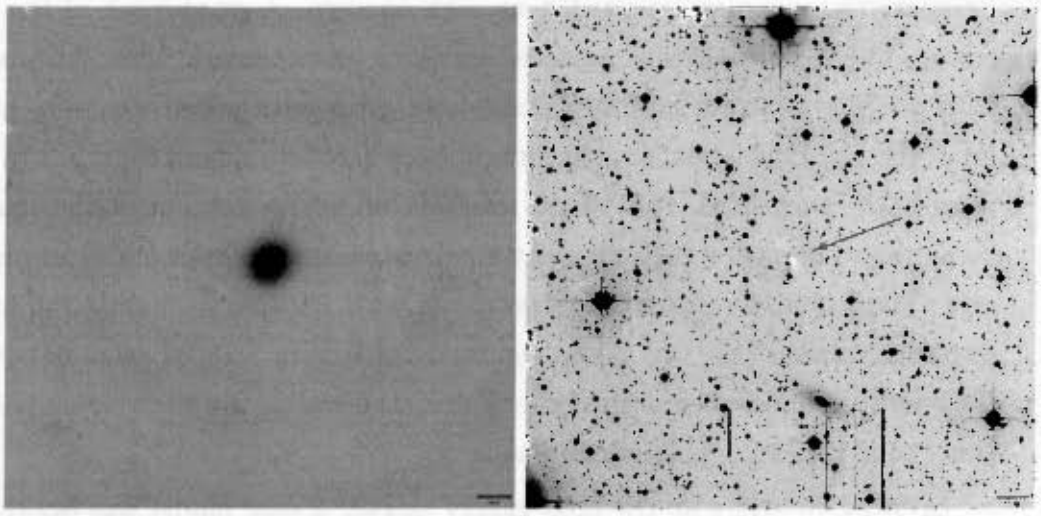

Figure 3.12: Galaxy WKK 6600, the *PSF-Fitting* model of the galaxy as produced with the `ellipse`- and `bmodel` tasks (GM3, left), and the original image minus the *PSF-Fitting* galaxy model (O-GM3, right).

3.3 *Star-Masking*

Much simpler and quicker methods were successfully tested as alternatives to the *PSF-Fitting* method described in the previous section. The masking of stars and artefacts in the image, as described above, would give results of the same quality as *PSF-Fitting* (cf. Chapter 5 on page 121). However, as mentioned in the previous section, the data obtained were lost due to unforeseeable events, and thus a comparison is impossible. The results mentioned here are thus without proper basis and only given for the sake of completeness. An overview of the processing is given in Figure 3.13 on page 63.

Similar to the two *PSF-Fitting* methods described in the previous and the following sections, one starts with the results obtained by means of σ-*Clipping*, described in Section 3.1 on page 49. An image with the galaxy model subtracted as thoroughly as possible from the original was obtained (O-GM1[4], see right side of Figure 3.14 on page 64). Next, the remnants at the central position of the subtracted galaxy model (GM1) were removed interactively, using either `imedit` or with `imcopy`. A pixel-mask of the resulting O-GM1 image was produced by using the `ccdmask` task. All pixels with a higher or lower intensity than about $\pm 5\,\sigma$ were raised to a very high intensity, e.g. 65000 counts, using `imreplace` (see left side of Figure 3.15 on page 64). Sometimes, this would result in an entire column of the image being raised to such a high intensity that `ccdmask` was not able to run properly. Thus, a copy of the image was made with `imcopy`, excluding the high intensity column (see top of the right side of Figure 3.15 on page 64). On the resulting image, the `ccdmask` task was then run in the background, as it could take hours for `ccdmask` to finish.

In order to arrive at the final galaxy model, a new model was obtained from the original image with the `ellipse` task, although this time without the internal k-sigma-clipping, but instead by using the pixel-mask obtained previously (see left side of Figure 3.16 on page 65). The `bmodel` task was used

[4]Compare with Figure 3.13 on page 63.

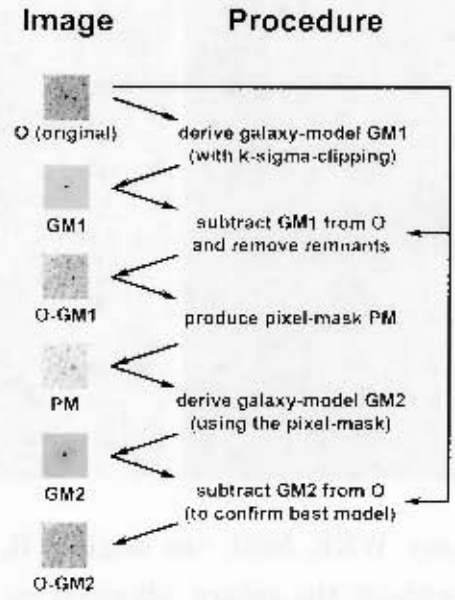

Figure 3.13: Diagram of the *Star-Masking* method as described in this chapter. See also Figures 3.14 to 3.16. The example images are shown for the R_c band and the galaxy WKK 5920. The arrows indicate causal dependencies.

to produce a model image of the galaxy model (GM2). By subtracting the resulting model image from the original image with `imarith`, it was possible to assess whether the model accurately resembled the galaxy (see right side of Figure 3.16 on page 65). The best possible model was created by adjusting the parameters in the `ellipse` task and re-modelling the galaxy – if necessary, several times. To be able to process the results further (cf. Section 4.2 on page 91), the data in the *STSDAS* tables produced by the `ellipse` task were exported into ASCII tables by using `tdump`. A more detailed description of how to conduct *Star-Masking* is given in Part III of this dissertation.

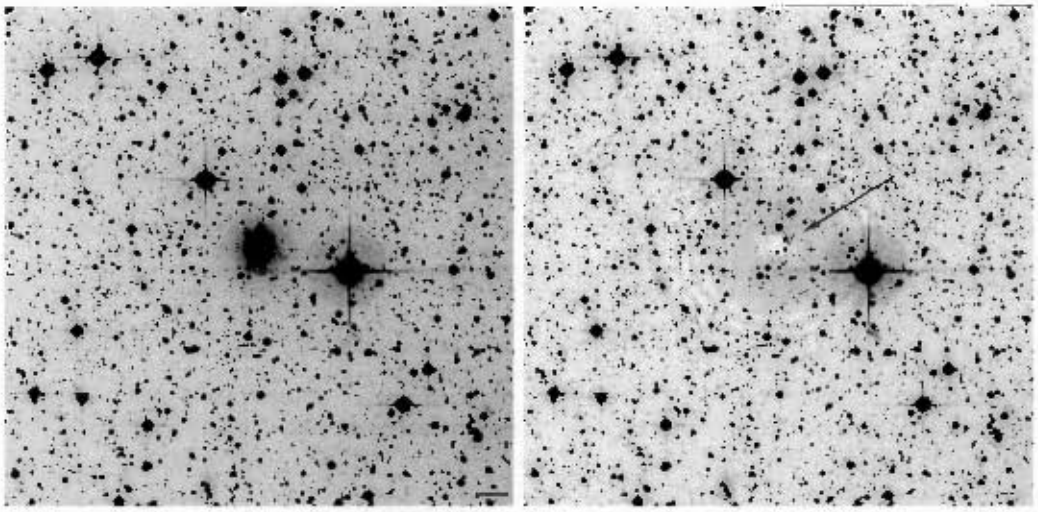

Figure 3.14: Galaxy WKK 5920, the original R_c band image (left), and the clean image without the galaxy, obtained by applying the *σ-Clipping* described in Chapter 3.1 on page 49 (O-GM1, right).

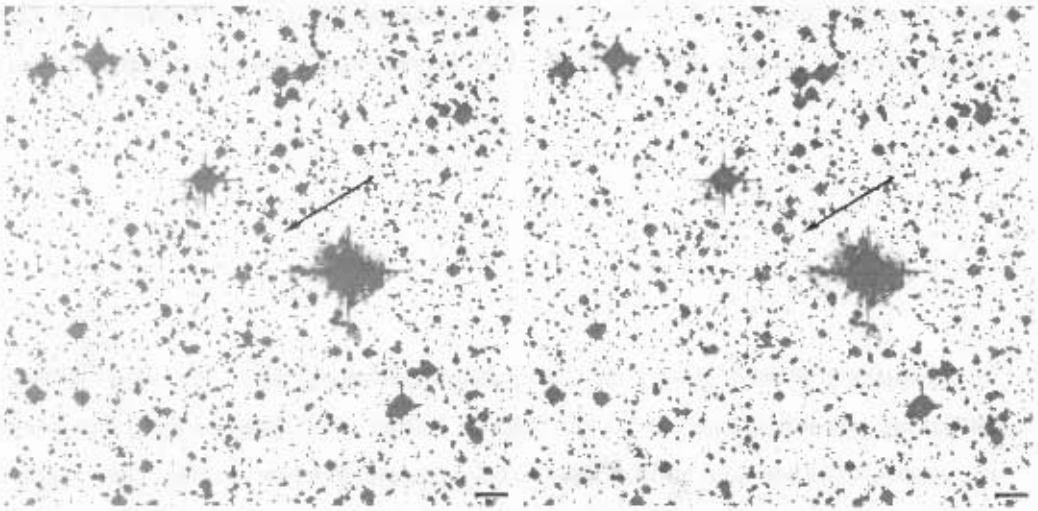

Figure 3.15: Galaxy WKK 5920, the pixel-mask derived from the image with the *σ-Clipping* galaxy model subtracted (left), and the pixel-mask derived from the image with the *σ-Clipping* galaxy model subtracted and bad pixel-columns removed (right).

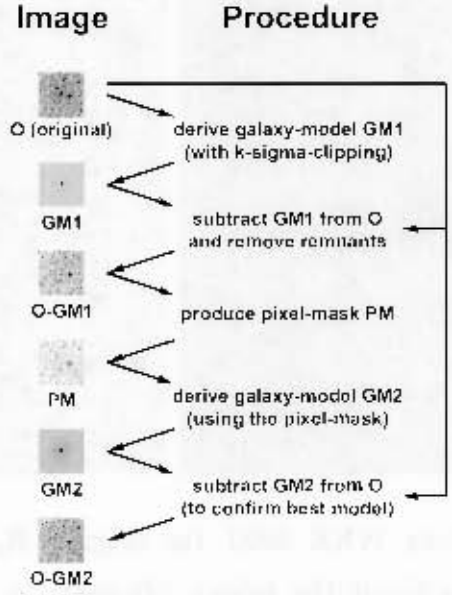

Figure 3.13: Diagram of the *Star-Masking* method as described in this chapter. See also Figures 3.14 to 3.16. The example images are shown for the R_c band and the galaxy WKK 5920. The arrows indicate causal dependencies.

to produce a model image of the galaxy model (GM2). By subtracting the resulting model image from the original image with `imarith`, it was possible to assess whether the model accurately resembled the galaxy (see right side of Figure 3.16 on page 65). The best possible model was created by adjusting the parameters in the `ellipse` task and re-modelling the galaxy – if necessary, several times. To be able to process the results further (cf. Section 4.2 on page 91), the data in the *STSDAS* tables produced by the `ellipse` task were exported into ASCII tables by using `tdump`. A more detailed description of how to conduct *Star-Masking* is given in Part III of this dissertation.

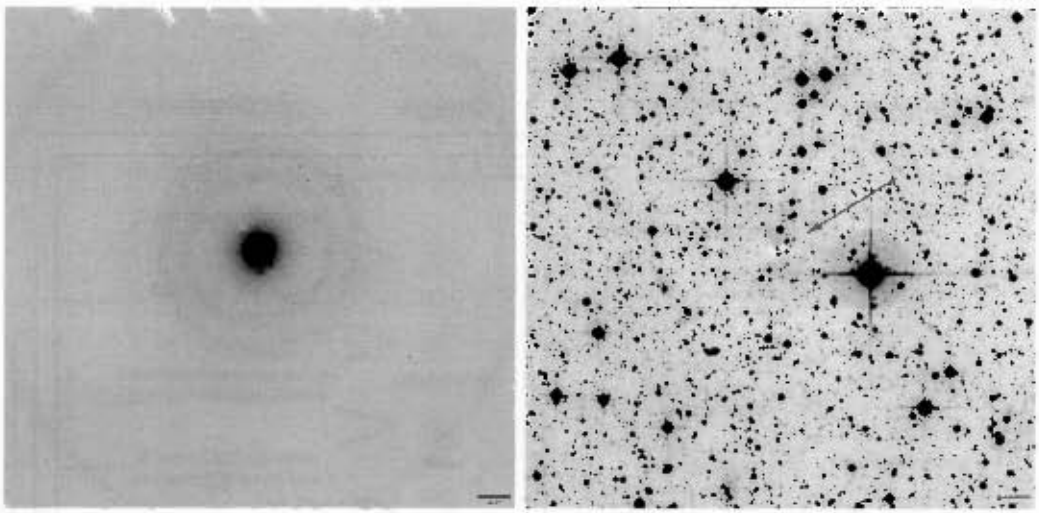

Figure 3.16: Galaxy WKK 5920, the *Star Masking* model of the galaxy as produced with the `ellipse`- and `bmodel` tasks (GM2, left), and the original image minus the *Star-Masking* galaxy model (O-GM2, right).

3.4 *Improved PSF-Fitting*

Despite some shortcomings of the *PSF-Fitting* and *Star-Masking* methods, both appear to be efficient enough to allow accurate determination of the surface brightness of the galaxies. However, most of the data that were obtained by means of these methods were lost, due to a computer crash and a faulty backup tape, as mentioned before. Consequently, as the data had to be analysed again, a new and improved method for obtaining even better surface brightness of the galaxies was developed subsequently. This method will be described in this section. Out of all four data reduction methods described in this chapter, it is considered to offer the best results. An overview of the processing is given in Figure 3.17 on page 66.

The *improved PSF-Fitting* or *iPSF-Fitting* method is based on the *PSF-Fitting* method described in Section 3.2 on page 53. The method was based on the realisation that a PSF would be able to model and remove all stars in the image. However, the ways in which the PSF was obtained were varied,

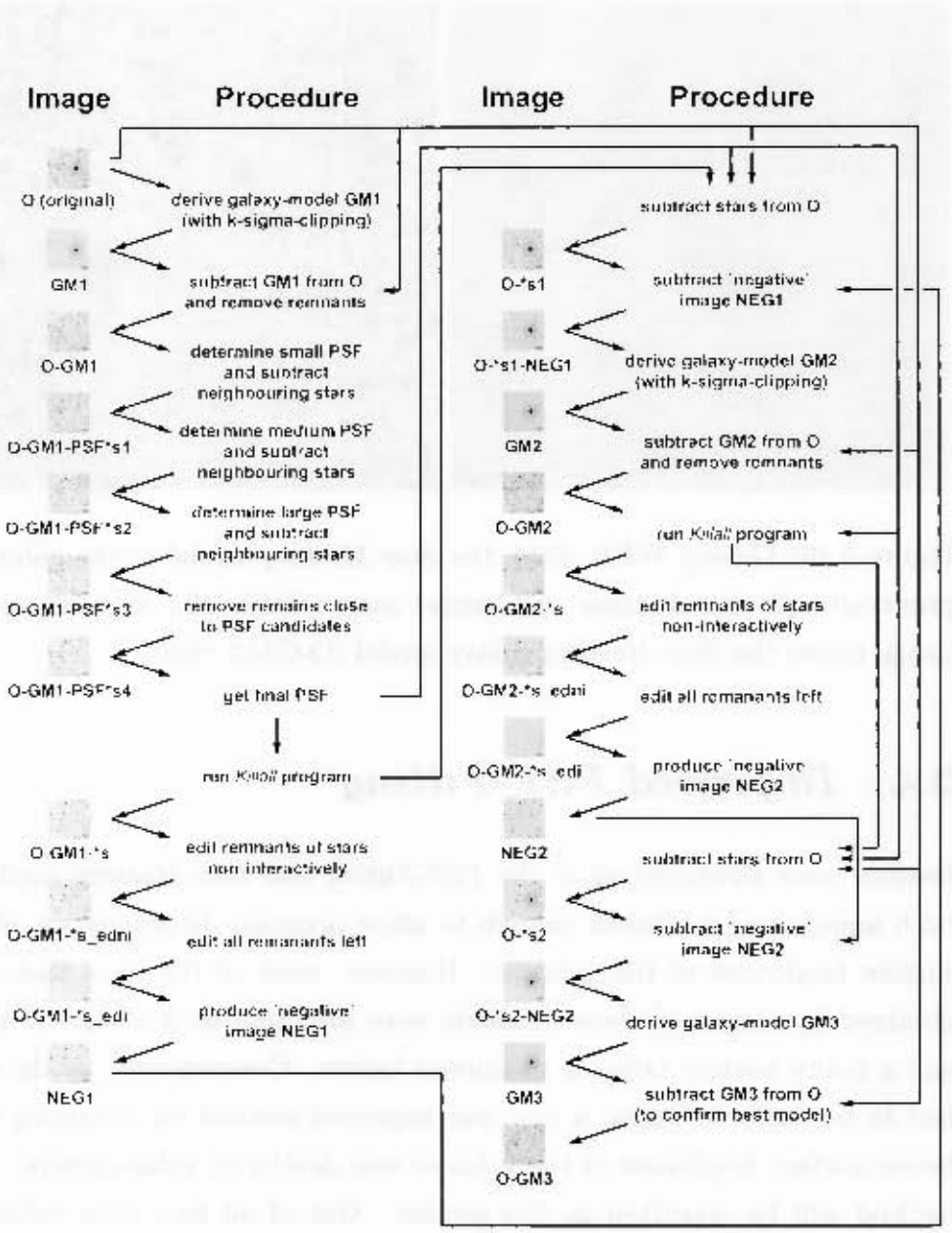

Figure 3.17: Diagram of the *iPSF-Fitting* method as described in this chapter. See also Figures 3.18 to 3.32. The example images are shown for the K_s band and the galaxy WKK 5920. The arrows indicate causal dependencies.

and the procedure to remove the stars was changed completely in the newer iPSF-Fitting method. A program called *Killall*[5] was used to significantly improve the removal of the stars as well as other remnants of the image that may have influenced the assessment of proper surface brightness profiles (Buta and McCall, 1999).

The starting point for *iPSF-Fitting* is the galaxy-subtracted image obtained by applying the *σ-Clipping* described in Section 3.1 on page 49. As it was done for the *PSF-Fitting* and *Star-Masking* methods, the central region of the removed galaxy had to be edited out by either using `imedit`, to edit the area interactively, or by using `imcopy`, to replace the region with a different clean part of the image. This resulted in an image with the model of the galaxy subtracted and ideally no remnants of this subtraction visible in the image (O-GM1[6], see right side of Figure 3.3 on page 52).

Within this image, the positions of all stars in the image needed to be identified. This was done automatically with the `daofind` task. However, some stars were not found and some objects were wrongly identified as stars, e.g. hot pixels or central regions of galaxies. The identification of these objects thus had to be altered interactively with `tvmark`. Once the positions of all the stars in the image had been determined, their relative brightnesses were determined with the `phot` task. Using the `psolect` task, the brightest non-saturated stars were then selected from the list of stars obtained with `phot`.

A proper PSF was obtained by selecting PSF candidate stars, followed by interactively removing the neighbours to determine a better PSF. To do so, a subset of the bright stars first had to be selected as PSF candidates, before generating a first PSF, using the `psf` task. This PSF was used to subtract all close neighbours from the PSF candidates. The close neighbouring stars were listed in a file as the output of the `psf` task. The tasks `nstar` and `substar` were then used to remove these neighbouring stars from the image of the

[5] I kindly acknowledge Prof. McCall for the use of the *Killall* software (Buta and McCall, 1999).

[6] Compare with Figure 3.17 on page 66.

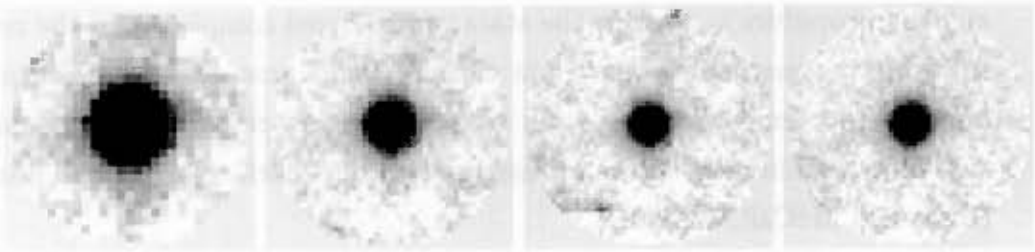

Figure 3.18: Galaxy WKK 5920, the evolution of a PSF. From left to right, the resulting PSFs are shown after the first, second, third and fourth run of `psf`. The radius increases from left to right from 14, 20 to 26 pixels, respectively, with both images on the right having a radius of 26 pixels.

original-minus-galaxy model (O-GM1) (cf. Figure 3.18 on page 68 and the left side of Figure 3.19 on page 70). On the resulting image, i.e. without the neighbouring stars, a new PSF was modelled. The same PSF candidates, or a subset thereof, were used. However, the PSF-radius in `daophot.daopars` was increased. This new PSF was in turn used to subtract the neighbours of the PSF candidates from the O-GM1 image (cf. Figure 3.18 and the right side of Figure 3.19). As the PSF-radius had been raised, the number of neighbours increased, too. Therefore more stars had to be removed when applying the `nstar` and `substar` tasks to the O-GM1 image. This procedure was performed a third time (cf. Figure 3.18 and the left side of Figure 3.20 on page 71). The PSF-radius in `daophot.daopars` was increased each time a new PSF was determined, e.g. from 14 pixels for the faint stars up to 26 pixels for the bright stars, depending on the sizes of the stars. By doing so, more and more neighbours were included. Furthermore, the `datamin` parameter in `daophot.datapars` had to be raised each time, due to additional noise in the images, which was produced by removing the neighbouring stars. After the neighbours of the PSF candidates had been subtracted for the third time, `imedit` was used to remove any remains close to the PSF candidates (cf. Figure 3.18 and the left side of Figure 3.20 on page 71). Once the surrounding of the PSF candidate stars had been 'cleaned' in this way, the

final PSF was determined with psf (cf. Figure 3.18).

This final PSF was now used as input for the *Killall* program. *Killall* was originally written by Buta and McCall (1999) to remove stars from star-crowded images. It offers a way of obtaining a relatively clean image of a star-crowded galaxy. The program interactively subdivides the image, finds the stars, carries out an initial photometry, flattens the background, fits the stars, subtracts the stars and reassembles the star-subtracted subsections (Buta and McCall, 1999). However, the program sometimes also removes parts of the galaxy. It was therefore only used to determine the proper positions of the stars and to remove the stars from the O-GM1 image.

Running *Killall* on the O-GM1 image resulted in several output files, one of which was an image with all except the saturated stars removed (cf. right side of Figure 3.21 on page 72). This file was edited with imedit to remove all remnants that might still have been apparent from the star-removing process. At first imedit was run non-interactively, using the output file of *Killall* that contained the positions of all except the saturated stars in the original image (cf. right side of Figure 3.22 on page 73). This usually took quite some time, depending on the hardware that was being used. When this had been completed, the resulting image was edited interactively with imedit to delete all saturated stars, bad columns etc. Everything was removed that might have influenced the determination of an accurate surface brightness profile of the particular galaxy.

It should be noted that no significant deviations of the PSF have been observed across the analysed parts of the R_c band images. This was possible, because small portions of the field of view of the WFI were extracted for each galaxy. However, a variation of the PSFs were indeed be observed across the wide-field array of CCDs of the WFI.

This produced an image that contained neither the galaxy, nor the stars, nor any saturated stars or bad columns nor anything else that might have influenced the resulting surface brightness profile (cf. left side of Figure 3.23 on page 74). To be able to obtain an image with similar properties, but

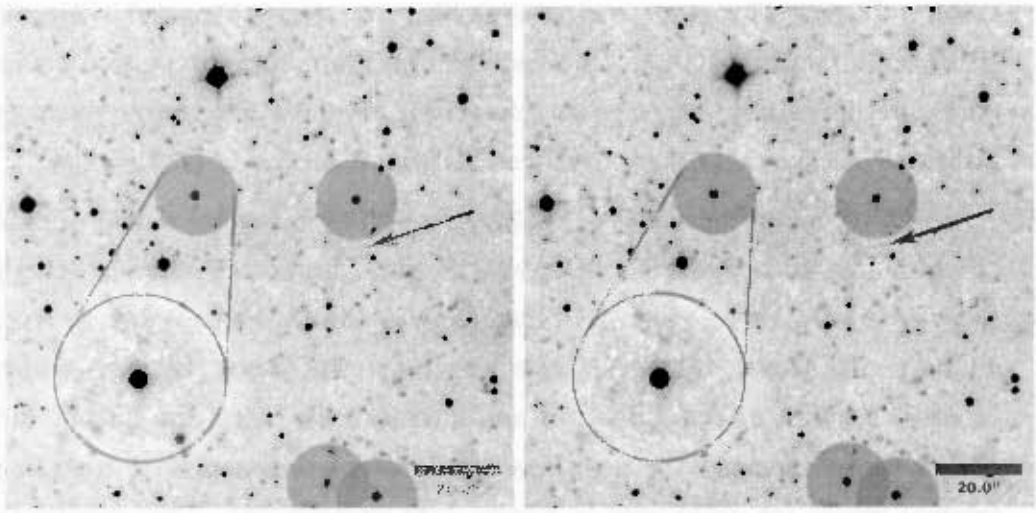

Figure 3.19: Galaxy WKK 5920, after first and second run of `psf`. The closest neighbours of the selected PSF stars were removed using the first PSF model (O-GM1-PSF*s1, left) and. Thereafter, the close neighbours of the selected PSF stars were removed using the second PSF model (O-GM1-PSF*s2, right). In these images, the surroundings of the selected PSF stars are highlighted by circular areas with a radius of 70 pixels. One such area is magnified by a factor of two.

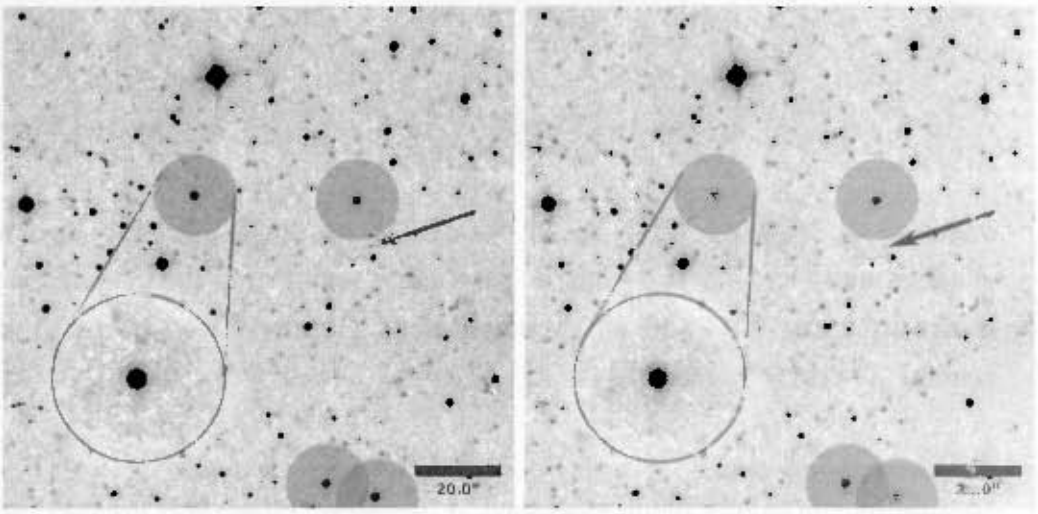

Figure 3.20: Galaxy WKK 5920, after third run of `psf` and PSF stars cleaned. The neighbours of the selected PSF stars were removed using the third PSF model (O-GM1-PSF*s3, left), and thereafter the surroundings of the PSF stars were cleaned with `imedit` (O-GM1-PSF*s4, right). In these images, the surroundings of the selected PSF stars are highlighted by circular areas with a radius of 70 pixels. One such area is magnified by a factor of two.

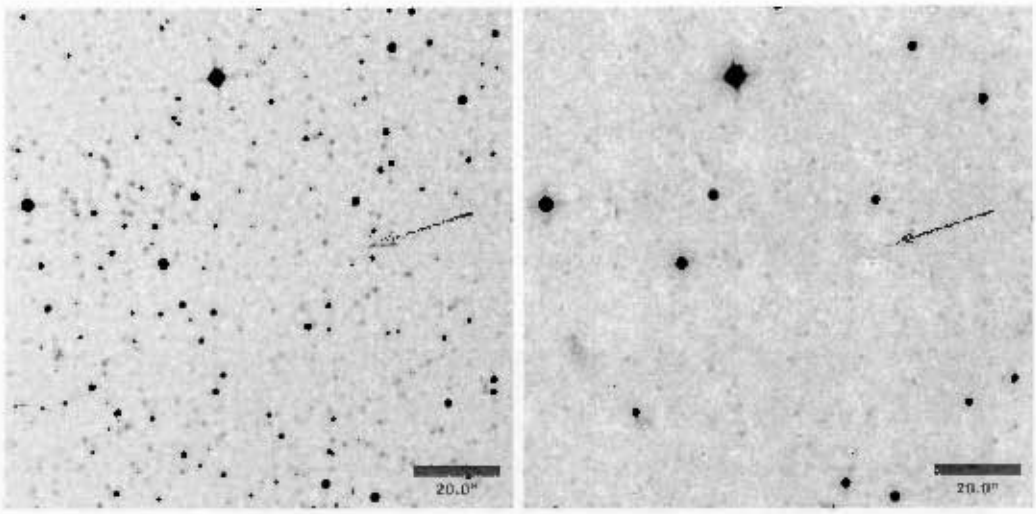

Figure 3.21: Galaxy WKK 5920, the *Killall* output image with the 'sky' (background) and all stars left in the image (left), and the *Killall* output image with the 'sky' and all stars removed. However, the saturated stars remain (O-GM1-*s, right).

containing the galaxy being examined, a 'negative' image was created. With the `imarith` task, one produced an image containing the differences between the *Killall* output, i.e. an image without stars but with remnants, and the edited clean image (cf. right side of Figure 3.23 on page 74).

A first improved star-subtracted image of the galaxy could then be obtained by using `substar` to subtract all stars from the original image, i.e. the image containing all stars and the galaxy (cf. left side of Figure 3.24 on page 74). The position file obtained with *Killall* served as an input file for `substar`. From this star-subtracted original image, the 'negative' image was subtracted, using `imarith`. The result was an image containing the galaxy but without any stars or other unwanted features (cf. right side of Figure 3.24 on page 74). It was therefore ideally suited for determining a new, better galaxy model. With the `ellipse` and `bmodel` tasks, a new model of the galaxy was obtained (cf. left side of Figure 3.25 on page 75) and then subtracted from the original image with `imarith` (cf. left side of Figure 3.26 on

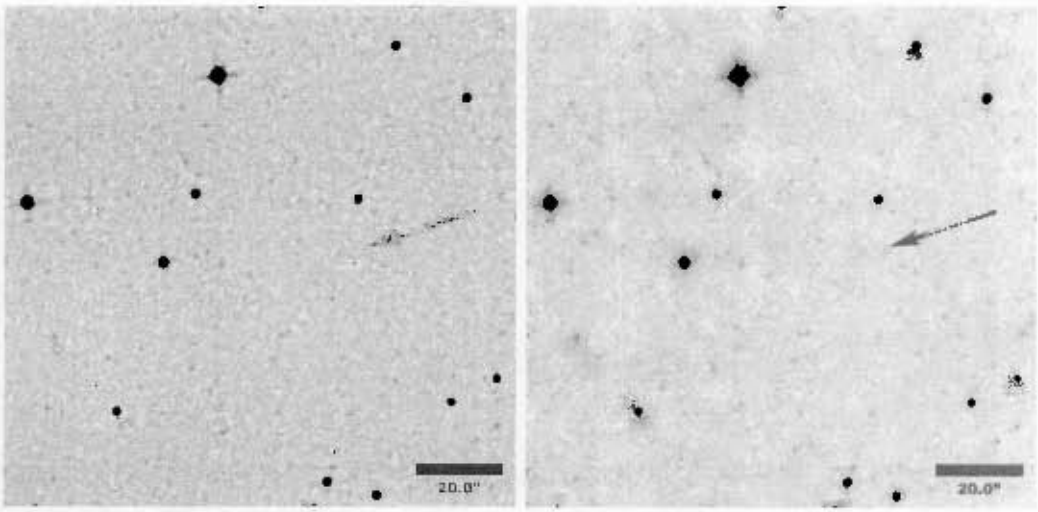

Figure 3.22: Galaxy WKK 5920, the *Killall* output image with all stars removed, excluding the saturated ones, and with the 'sky' (background) remaining in the image (left), and after non-interactively cleaning the image using the `imedit` task (O-GM1-*s_edni, right).

page 75). The central remnants were removed or replaced as described before, which resulted in a new image without the galaxy and the least visible remnants thereof (cf. right side of Figure 3.26 on page 75).

This new O-GM2 image again served as input to the *Killall* programme, cf. page 69. The whole process described was repeated one more time, until a new even better model of the galaxy was obtained (cf. Figures 3.27 to 3.30 on pages 76 to 78). This time, however, it was done without using the internal k-sigma-clipping option within `ellipse`. This last model was then the final result (cf. left side of Figure 3.31 on page 79), and the data in the *STSDAS* tables produced by `ellipse` had to be exported to ASCII tables to be able to process the results further (cf. Section 4.2 on page 91). This was done by means of the `tdump` task. A more detailed description of how to conduct the *iPSF Fitting* is given in Part III of this dissertation.

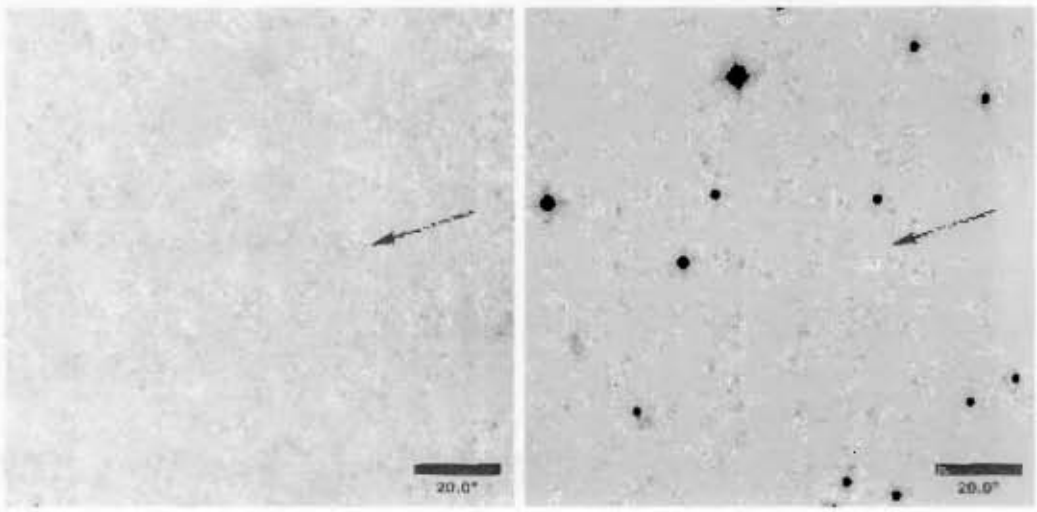

Figure 3.23: Galaxy WKK 5920, after interactively cleaning the image using the imedit task (O-GM1-*s_edi, left), and the 'negative' image of the remains that were left after running *Kilhill* and cleaning the resulting image, i.e. the areas that were removed interactively (NEG1, right).

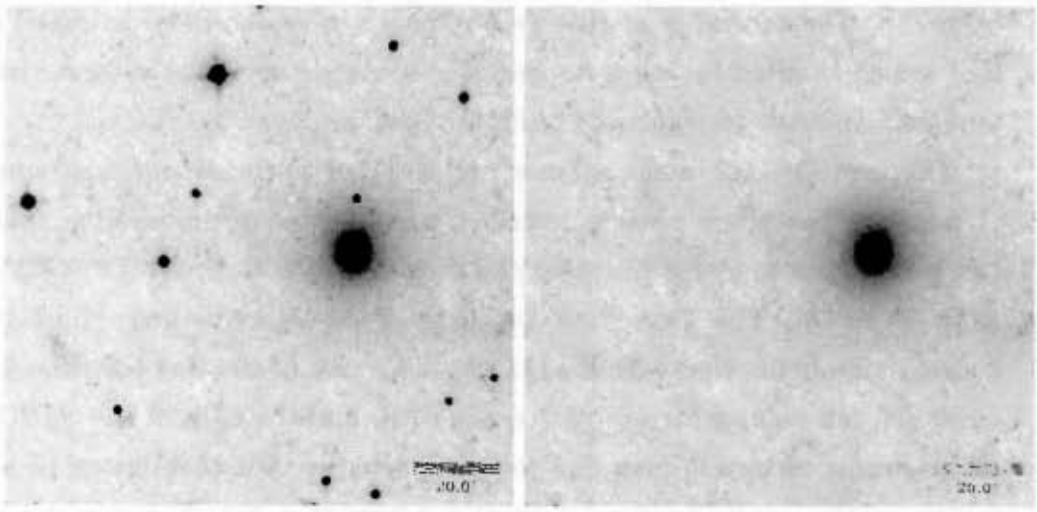

Figure 3.24: Galaxy WKK 5920, the original image with the stars subtracted (O-*s1, left), and the original image after it was cleaned, i.e. with the 'negative' image subtracted (O-*s1-NEG1, right).

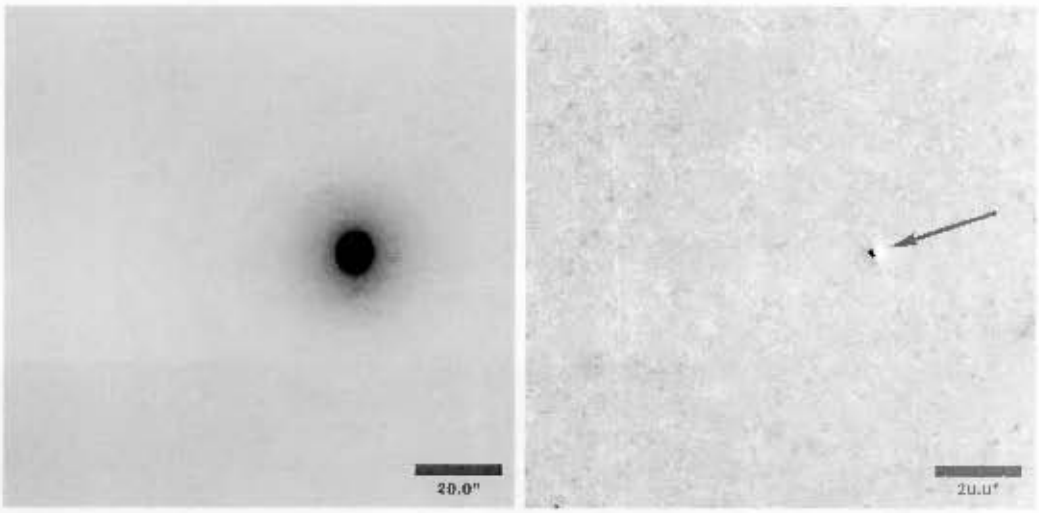

Figure 3.25: Galaxy WKK 5920, the improved galaxy model (GM2, left), and the clean image minus the improved galaxy model (right).

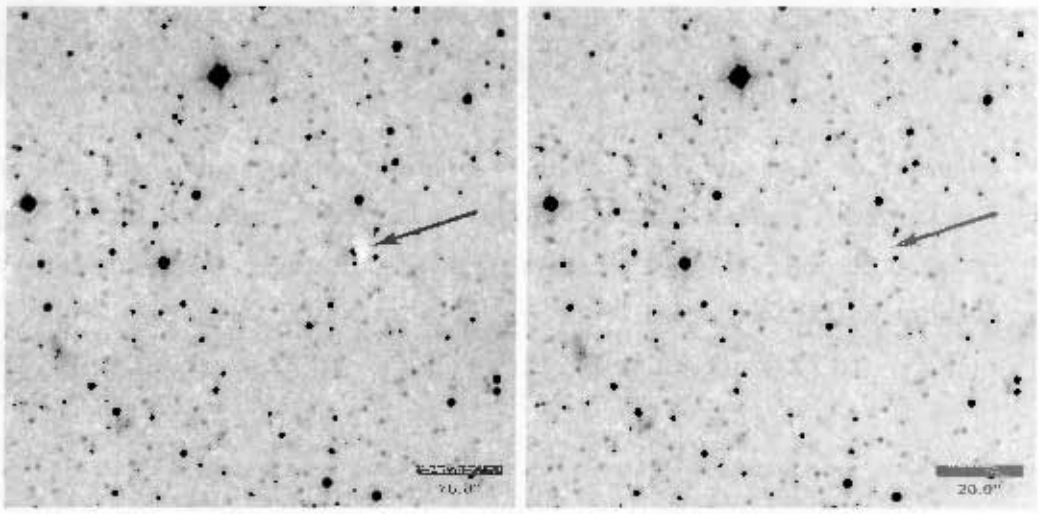

Figure 3.26: Galaxy WKK 5920, the original K_s band image minus the improved galaxy model (left), and the original K_s band image minus the improved galaxy model and the removed remains in the centre (O-GM2, right).

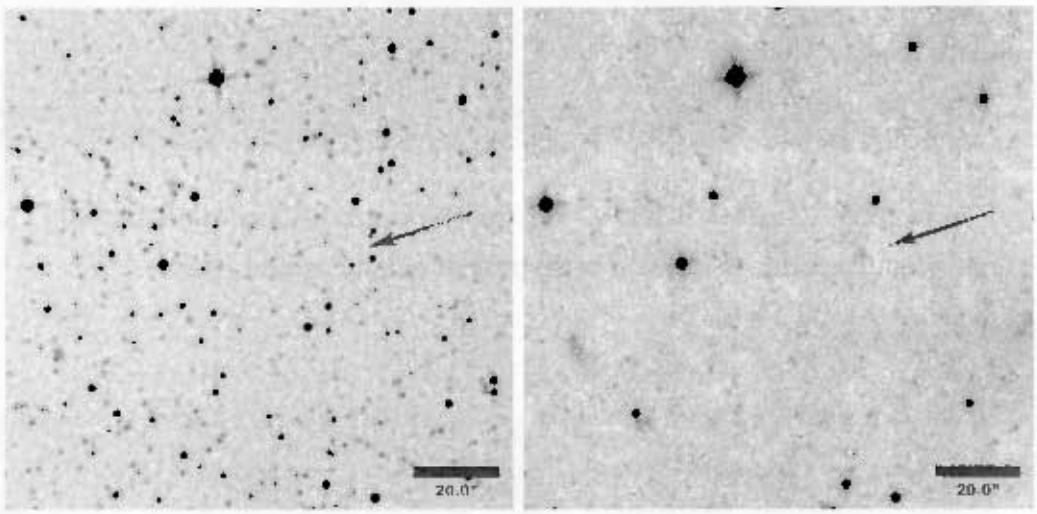

Figure 3.27: Galaxy WKK 5920, the *Killall* output image with the 'sky' (background) and all stars left in the image (left), and the *Killall* output image with the 'sky' and all stars removed. However, the saturated stars remain (O GM2 *s, right).

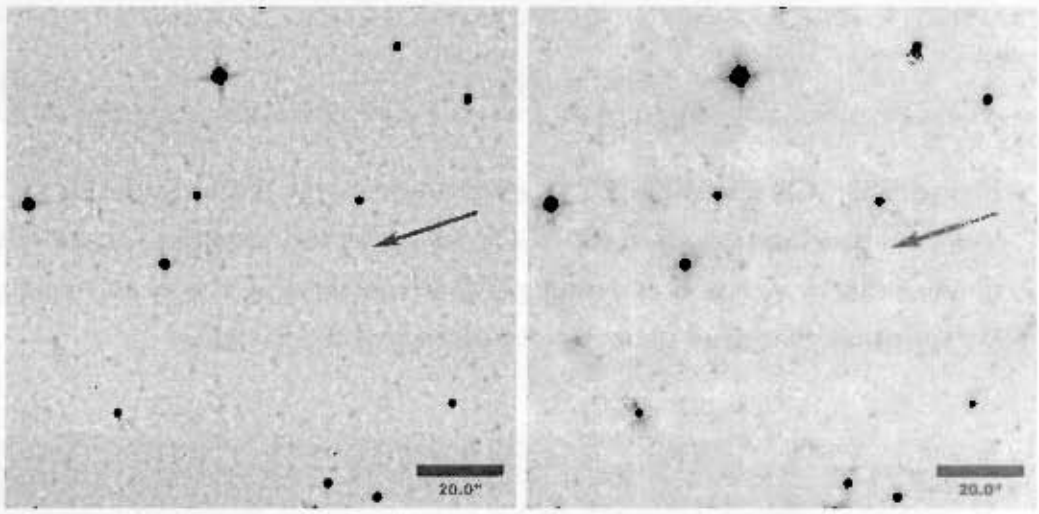

Figure 3.28: Galaxy WKK 5920, the *Killall* output image with all stars removed, excluding the saturated ones, and with the 'sky' (background) remaining in the image (left), and after non-interactively cleaning the image using the `imedit` task (O-GM2-*s_edni, right).

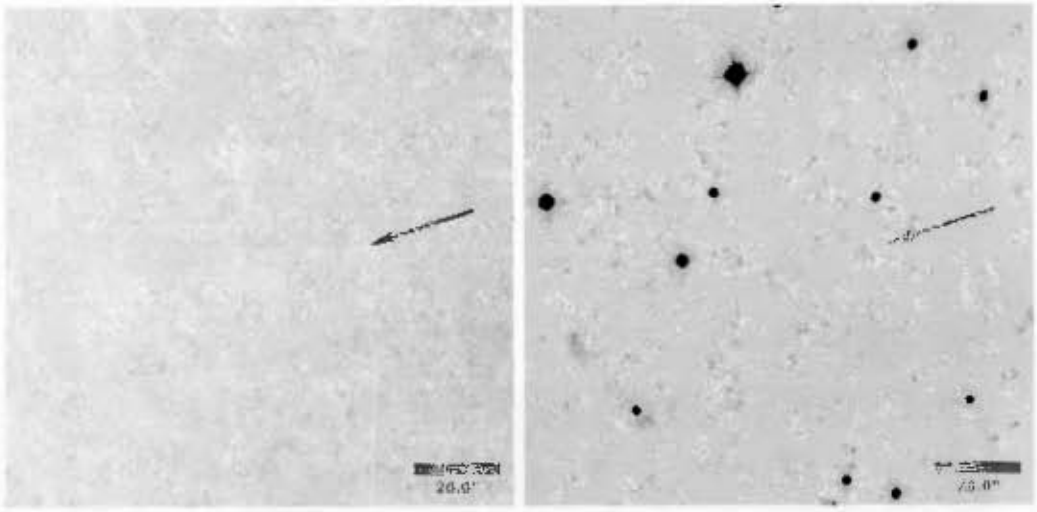

Figure 3.29: Galaxy WKK 5920, after interactively cleaning the image by using the `imedit` task (O-GM2-*s.edi, left), and the 'negative' image of the remains that were left after running *Killall* and cleaning the resulting image, i.e. the areas that were removed interactively (NEG2, right).

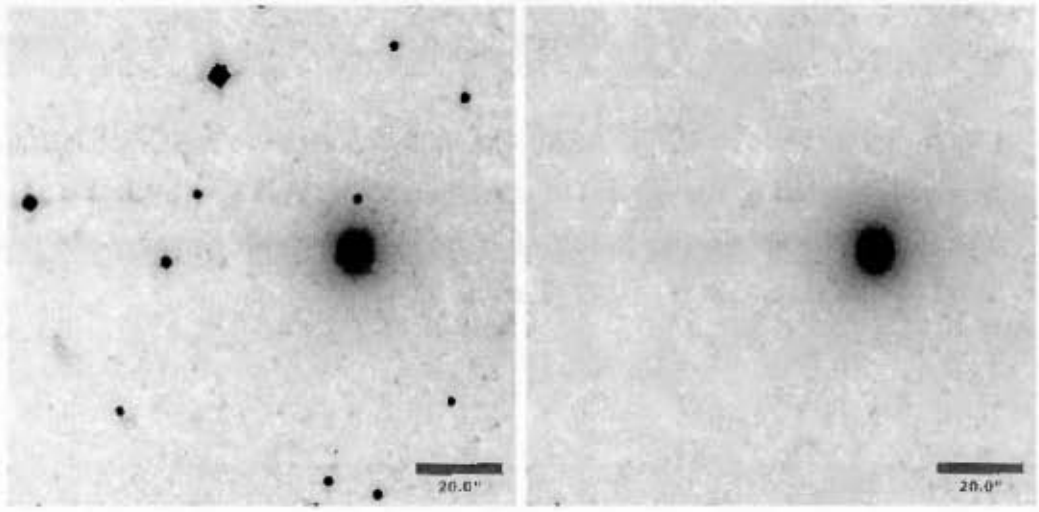

Figure 3.30: Galaxy WKK 5920, the original image with the stars subtracted (O-*s2, left), and the original image after it was cleaned, i.e. with the 'negative' image subtracted (O-*s2-NEG2, right).

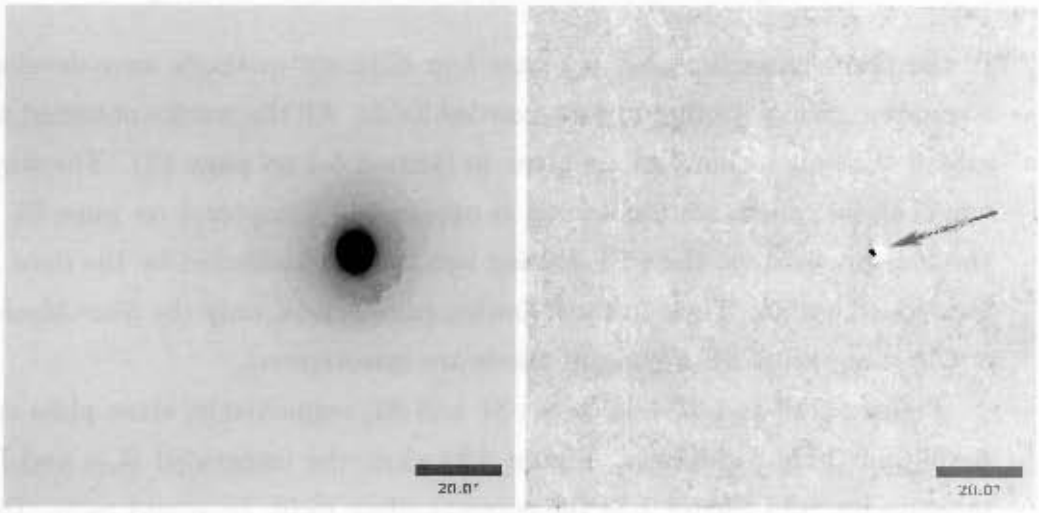

Figure 3.31: Galaxy WKK 5920, the final galaxy model (GM3, left), and the clean image minus the final galaxy model (right).

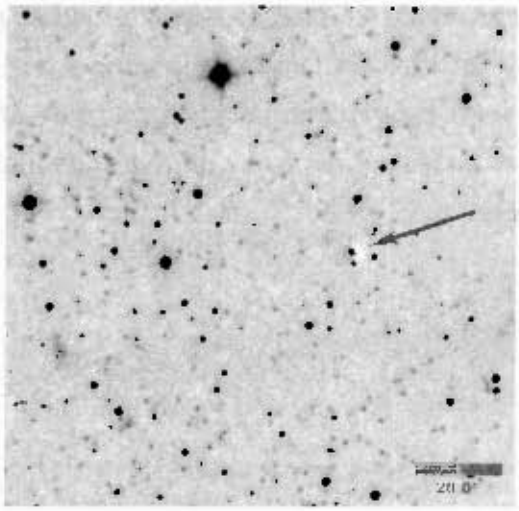

Figure 3.32: Galaxy WKK 5920, original K_s band image minus the final galaxy model (O-GM3).

3.5 Comparison of the four Techniques

In the previous sections, all together four different methods were developed to analyse galaxy profiles in star crowded fields. All the results obtained with any of the four techniques are given in Section 5.1 on page 121. The way in which these results were obtained is outlined in Chapter 4 on page 85. Of the four procedures, the *PSF-Fitting* was the most affected by the data loss mentioned earlier. Thus, in the following comparison, only the *Star-Masking*, *σ-Clipping* and *iPSF-Fitting* methods are investigated.

Figures 3.33 and 3.34 on pages 81 and 82, respectively, show plots comparing all three techniques. Figure 3.33 plots the integrated K_{s20} and R_{c23} magnitudes, and Figure 3.34 the corresponding radii, r_{Ks20} and r_{Rc23}. To be able to compare the results for the R_c and K_s bands, the R_c data that were used in this comparison were integrated up to larger radii, compared to the K_s data. Table 3.1 on page 83 gives the fitted differences in magnitudes and radii for each pair of the three procedures.

From the comparison of the *iPSF-Fitting* method with the *σ-Clipping* method, it becomes apparent that the determined brightness for all galaxies is higher for the latter, and the corresponding radii are therefore larger. The same holds for a comparison between the *Star-Masking* and *σ-Clipping* procedures: the galaxies appear to be fainter and smaller when applying the *Star-Masking* technique.

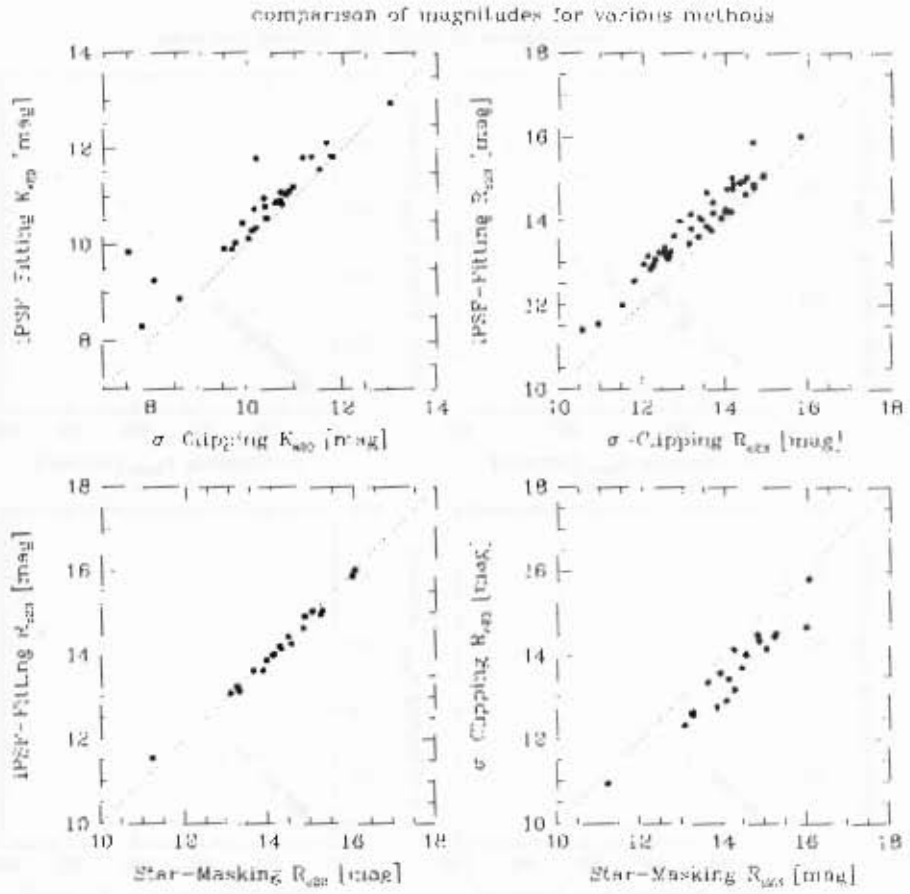

Figure 3.33: The determined integrated magnitudes R_{c23} compared for all four methods.

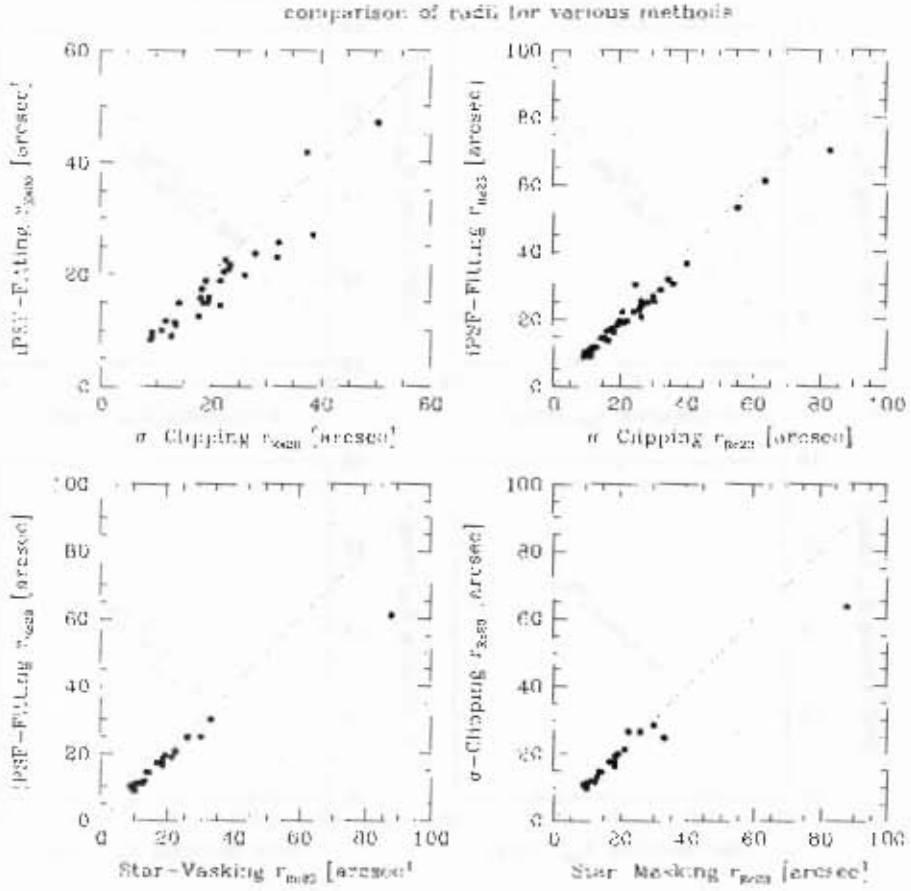

Figure 3.34: The determined r_{Re23} radii compared for all four methods.

Table 3.1: The mean differences of magnitudes and radii for the developed procedures described in the previous sections. Here, the $\sigma_{\rm fit}$ are the derived root mean squares of the residuals.

difference of procedures	filter	brightness [mag]	radius [arcsec]	number of galaxies	$\sigma_{\rm fit}^{\rm brightness}$ [mag]	$\sigma_{\rm fit}^{\rm radius}$ [arcsec]
iPSF-Fit.−σ-Clip.	K_s	$0.431 + 0.090$	$-2.875 - 0.599$	30	0.491	3.225
iPSF-Fit.−σ-Clip.	R_c	0.564 ± 0.043	-1.523 ± 0.279	48	0.297	1.894
iPSF-Fit.−Star-Mask.	R_c	0.075 ± 0.029	$0.999 \perp 0.336$	21	0.132	1.502
σ-Clip.−Star-Mask.	R_c	0.660 ± 0.072	$0.083 \perp 0.533$	21	0.328	2.381

It is therefore possible to conclude that the *σ Clipping* method offers the worst results of all three methods. The lower brightness parts of stars and other objects are probably not clipped out completely, causing a general shift to brighter magnitudes and larger radii. Using the *Star-Masking* method seems to offer better results. However, a small shift to fainter magnitudes and to larger radii can be observed. As part of the *Star-Masking* procedure, all count rates are masked out, that are several sigma larger than the average background. When the masked area includes large parts of the galaxy, it may cause a shift towards smaller counts, and thus towards fainter magnitudes. Similarly, the masking of counts that are several sigma lower than the average background may cause a shift to positive counts for the fainter parts of the galaxy, thus resulting in larger radii. However, it is not entirely understood where these shifts originate from, and further investigation would be helpful.

Based on the above comparison, it is possible to conclude that the *iPSF-Fitting* method offers the best results. This observation is further strengthened in Section 4.5 on page 104 by an external comparison of 2MASS data with the derived integrated K_{s20} magnitudes and the corresponding r_{Ks20} radii obtained from the *iPSF-Fitting* and the *σ-Clipping* procedures. This comparison shows good agreement of the derived *iPSF-Fitting* magnitudes and radii with the 2MASS data.

Chapter 4

Galaxy Profiles and Parameters

Various parameters are extracted from the observed images and galaxies. The derived sky brightness for the R_c and K_s band images is given in Section 4.1. Surface brightness profiles are calculated for all galaxies, which makes it possible to determine integrated magnitudes and corresponding radii for these galaxies (Section 4.2). For all galaxies, circular aperture photometry is obtained as well (Section 4.3). The results are then investigated for the different WFI CCDs and furthermore compared externally with 2MASS data (Sections 4.4 and 4.5, respectively). From fitting a de Vaucouleur $r^{1/4}$ profile, effective magnitudes and radii are established (Section 4.6), and additionally the total magnitudes by fitting a Sèrsic r^{1/n_s} function (Section 4.7). For each galaxy, $(R_c - K_s)$ colours are determined (Section 4.8). Lastly, Section 4.9 describes the photometric corrections that were applied to the data.

By obtaining the clean galaxy images in the previous chapter, the foundation was laid for determining various properties of the galaxies under study. As all the stars and other artefacts in the images had been removed, accurate parameters concerning the geometry and photometry of the galaxies could be established, e.g. surface brightness and colour profiles.

4.1 Sky Brightness

For each of the galaxies in the selected sample (cf. Section 2.1 on page 31 and Table A.2 on page 194 in Appendix A.1), the sky brightness in the R_c and K_s bands were determined. In order to obtain the surface brightness profiles, the count rate of the background in each image was measured in the area surrounding each galaxy, using the `imexamine` task from within *IRAF*[1]. At ten different positions scattered all over the image, the mean count rate was calculated in a squared field with the size of 10×10 pixels. Where applicable, the image used for this was the resulting image with all the stars subtracted. Otherwise, the positions were inspected by eye beforehand to ensure that they were in between the stars and far away from any galaxy or nebula. Also note that no significant deviations in the background, e.g. due to insufficient flat fielding, have been found on the scales on which the galaxies were analysed. Furthermore, no diffuse emission from the Milky Way, like the H_{alpha} emission that is indeed visible in some parts of the R_c band images, could be observed near to the relevant areas of these images.

This method seems to work better in star-crowded fields than the background fitting that is often used to establish the sky brightness in observations far away from the Galactic Plane (Jørgensen et al., 1992). The background fitting can, for instance, be done by making use of the results obtained in the previous chapter. Ideally, the count rates determined by means of the `ellipse` task decrease from its maximum at the centre of the galaxy towards the sky-value with increasing radius or semi-major axis. The region where the count rate reaches the sky level can be fitted by a function, so that the counts of the sky background can be estimated. The statistical method described above, where the sky was estimated by measuring the count rate at different positions, was applied to all data obtained in this dissertation. However, for a sample of galaxies in the R_c band, the background fitting was

[1]For a description of the abbreviations used in this dissertation, the reader is referred to Section B in the Appendix on page 247.

tested as well. The following two equations were used as fitting functions,

$$N = n_{sky1} + o_1/(r_{sma}^{Rc})^2 \tag{4.1}$$

and

$$N = n_{sky2} + o_2/(r_{sma}^{Rc})^3 . \tag{4.2}$$

The fitting was done for two different lengths along the semi-major axis by making use of the *Physica*[2] software. The resulting background would then, for instance, be the mean of the two fits, i.e. $n_{sky} = (n_{sky1} + n_{sky2})/2$. The o_1 and o_2 are arbitrary factors that were fitted, and N is the total number of counts for each isophote, as derived with `ellipse` in the previous chapter (Jørgensen et al., 1992). The radius r_{sma}^{Rc} will be defined by Equation 4.9 on page 93.

The resulting values n_{sky} would then be used in Equations 4.3 and 4.4 below to determine the brightness of the background. The fits of the fitted galaxies are presented in Appendix A.3 on page 207. The data were obtained with the `ellipse` task and by applying the *Star-Masking* method described in Section 3.3 on page 62. As an example, the plot showing the fit for WKK 5920 can be seen in Figure 4.1 on page 88.

The results obtained from the standard star solution were used to determine the sky brightness from the derived background counts (cf. Section 2.5 on page 41). The measured count rates from the fitting described above, or the `imexamine` measurements mentioned earlier, were used in one of the two equations

$$\mu_{Rc}^{sky} = \mu_{Rc}^{offset} - 2.5 \cdot \log(n_{sky}) \tag{4.3}$$

or

$$\mu_{Ks}^{sky} = \mu_{Ks}^{offset} - 2.5 \cdot \log(n_{sky}) , \tag{4.4}$$

to determine the sky brightness for the R_c band and K_s band observations, respectively[3]. Here, n_{sky} is the number of counts of the sky. The offsets

[2]Provided by the TRIUMPH Computing Services Group.

see *http://www.triumf.ca/physica/html/homepage.html*.

[3]In this dissertation, the 'log' is referring to the common logarithm to the base 10.

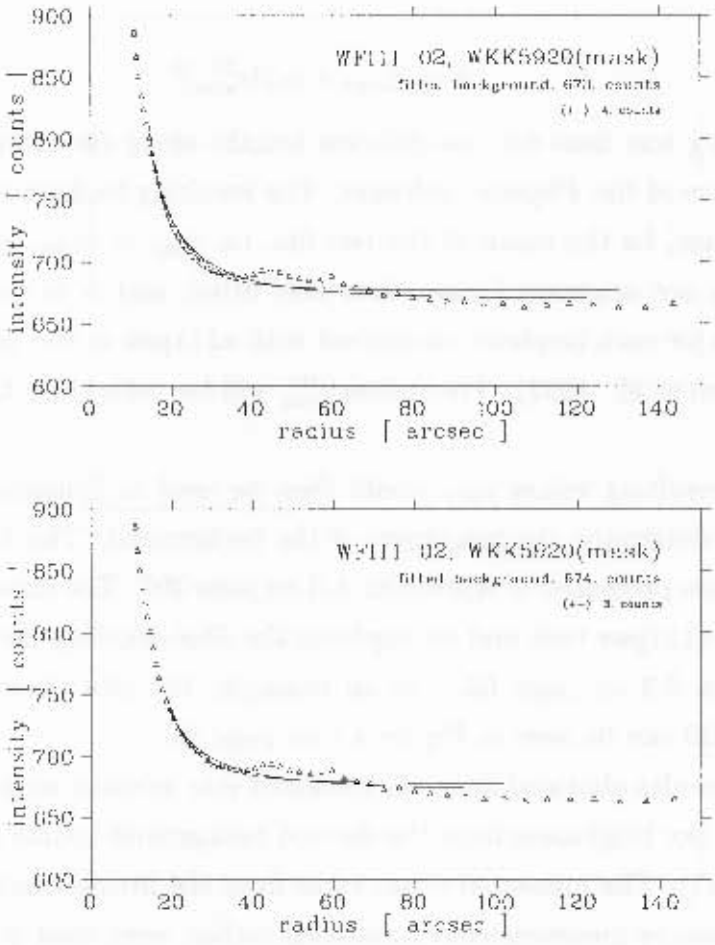

Figure 4.1: Galaxy WKK 5920, WFI background fit as described in the text. The radius refers to the semi-major axis length. The fit shown in the plot on the top was conducted over a larger range in radius than in the plot at the bottom. Similar plots for 21 galaxies in total are shown in Appendix A.3 on page 207.

$\mu^{\mathrm{Ic}}_{\mathrm{offset}}$ and $\mu^{\mathrm{Ks}}_{\mathrm{offset}}$ were calculated by using the transformation coefficients that resulted from the photometric calibration:

$$\mu^{\mathrm{offset}}_{\mathrm{Rc}} = 2.5 \cdot \log(t^{\mathrm{exp}}_{\mathrm{Rc}} \cdot A^{\mathrm{WFI}}_{\mathrm{Rc}}) - \overline{c_{\mathrm{r1}}} - \overline{c_{\mathrm{r2}}} \cdot X_{\mathrm{Rc}} - \overline{c_{\mathrm{r3}}} \cdot (\mathrm{V} - \mathrm{R_c}) \qquad (4.5)$$

and

$$\mu^{\mathrm{offset}}_{\mathrm{Ks}} = 2.5 \cdot \log(t^{\mathrm{exp}}_{\mathrm{Ks}} \cdot A^{\mathrm{SOFI}}_{\mathrm{Ks}}) - c_{\mathrm{k1}} - c_{\mathrm{k2}} \cdot X_{\mathrm{Ks}} - c_{\mathrm{k3}} \cdot (\mathrm{J} - \mathrm{K_s}) \qquad (4.6)$$

The transformation coefficients $\overline{c_{\mathrm{r1}}}$, $\overline{c_{\mathrm{r2}}}$, $\overline{c_{\mathrm{r3}}}$, c_{k1}, c_{k2} and c_{k3} were derived in Section 2.5 on page 41. The exposure times are given by $t^{\mathrm{exp}}_{\mathrm{Rc}}$ and $t^{\mathrm{exp}}_{\mathrm{Ks}}$, while $A^{\mathrm{WFI}}_{\mathrm{Rc}} = 0.0566\,\mathrm{arcsec}^2$ and $A^{\mathrm{SOFI}}_{\mathrm{Ks}} = 0.0829\,\mathrm{arcsec}^2$ are the areas of the sky that are projected onto each pixel of the WFI and SOFI, respectively. X_{Rc} and X_{Ks} are the airmasses of the observations and $(\mathrm{V} - \mathrm{R_c})$ and $(\mathrm{J} - \mathrm{K_s})$ the colours, which are assumed to be zero for the sky. The established sky backgrounds are given in Tables A.3 and A.4 on pages 196 and 200 in Appendix A.1. In Table A.3, the average is stated for the observed fields where the sky brightness was calculated for more than one galaxy.

In Figure 4.2, the results from either using the background fitting or the statistical technique are compared. Both methods were applied to the results from the *Star-Masking* procedure as described in Section 3.3 on page 62. As can be clearly seen, the determined background counts from the background fitting appear to give higher count rates for all measurements, compared to the statistical method. The average difference in counts of the fitting method minus the statistical method $\Delta R_{\mathrm{c23,(fitting-statistics)}}$ is $9.18 + 1.17$, as indicated by the dashed line in Figure 4.2. Depending on the overall sky level, this effect could cause shifts in background determination of a few hundredth of a magnitude.

It can be argued, that these differences are caused by a selection effect when examining the background statistics. After all, determining the areas of the sky without visible objects may result in selecting inherently darker regions in the sky. This can hardly be the case, however, when large foreground star numbers in the images are apparent, as was the case with the

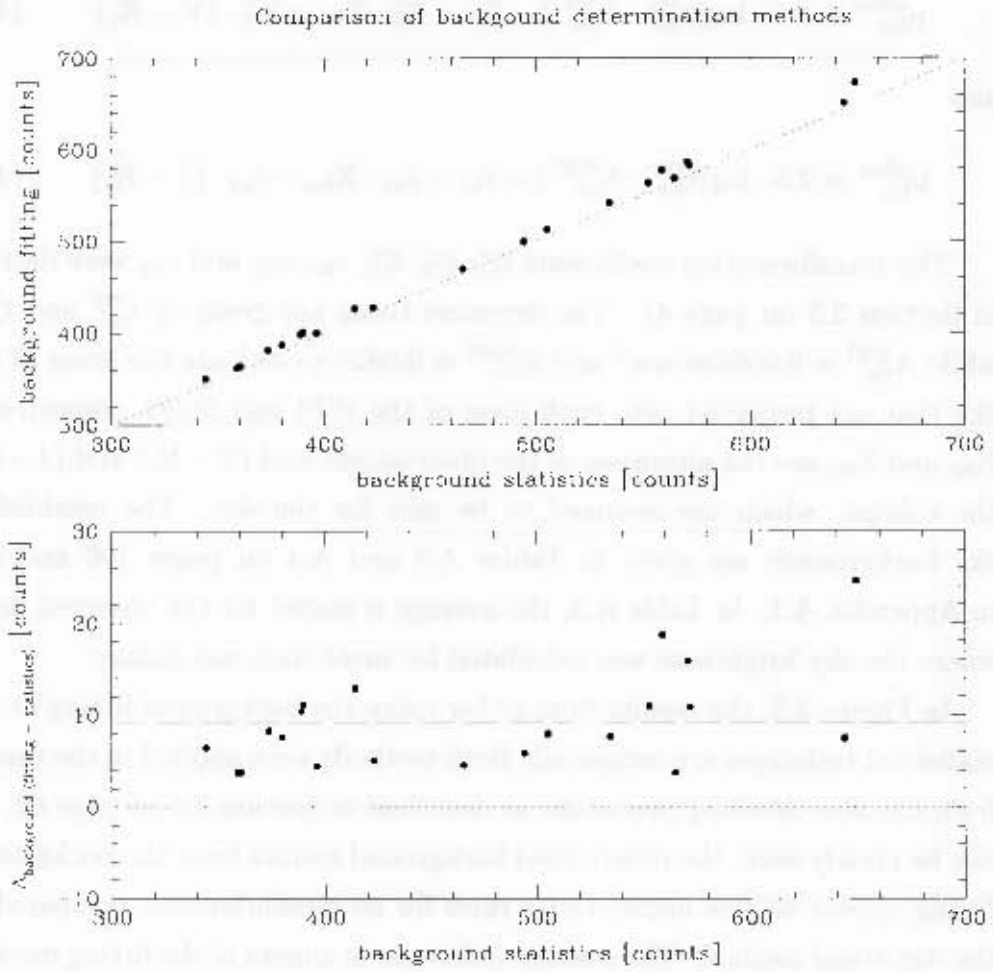

Figure 4.2: Comparison of background values derived from either using a statistical method or by fitting galaxy profiles using the *Star-Masking* method as described in Section 3.3 on page 62. The average $\Delta R_{c20,(fitting-statistics)}$ is $9.18 \perp 1.17$, as indicated by the dashed line.

data analysed in this study. Empty areas in the sky are rare in practice, and thus an unconscious selection of areas with low sky levels seems unlikely.

The reason for the difference in background counts more likely lies with the fact that the masking applied in the *Star-Masking* method is only conduced for count rates several σ higher and lower than the median background. Thus, the outer parts of stars and other low-intensity objects in the images are not masked out when applying the `ellipse` task. Objects with low brightness, such as faint stars, are not masked out at all. All these objects contribute to the apparent brightness of the sky and thus result in a shift towards positive count rates for the background fitting procedure.

This effect may not be relevant when examining galaxies with low star densities away from the Galactic Plane. In such cases, it appears to be sufficient to choose a mask large enough for each object, to ensure that even the outer parts are masked out properly. However, when looking at star-crowded areas of the sky, masking seems to become less efficient, due to the large number of faint objects. This is why the statistical method appears to be better suited for estimating the sky brightness and was therefore applied for all the work done in this dissertation.

4.2 Surface Brightness Profiles

The results obtained by means of the `ellipse` task within *IRAF* in Chapter 3 on page 47 were used to find the surface brightness profiles for each galaxy in each observed field, as well as their ellipticity and position angle.

The `ellipse` task determines a model of a galaxy by deriving ellipses with increasing radii – or rather semi-major axis lengths. These consecutive ellipses – or isophotes – are determined by contours of constant surface brightness, meaning the mean surface brightness in an elliptical annulus in the limit where the width of the annulus shrinks to zero. This makes it then possible to examine each of these isophotes in terms of their calculated properties, e.g. the number of counts and the flux within the ellipse, the position

angle and the ellipticity.

The `ellipse` models were established by starting at a given distance from the estimated centre of the galaxy, usually at a radius of around ten pixels from the centre. First the elliptical isophotes were determined from a given radius outwards, i.e. towards an increasing radius, and then inwards. The largest possible radius was to ensure that the `ellipse` model would reach the background. If possible, the position angle and ellipticity parameters were not kept fixed, neither were the parameters for the suspected centre of the galaxy. However, it was often necessary to keep one or more of these parameters constant in order to obtain a proper galaxy model.

Similar to the determination of the sky brightness, as discussed earlier, the count rate within each of the ellipses was used to determine the surface brightness of the galaxy. For each of the isophotes calculated by the `ellipse` task, the isophotal magnitudes were obtained by entering the corresponding count rates into one of these two equations:

$$\mu_{\mathrm{Rc}} = \mu_{\mathrm{Rc}}^{\mathrm{offset}} - 2.5 \cdot \log(N - \mathrm{n_{sky}}) \tag{4.7}$$

or

$$\mu_{\mathrm{Ks}} = \mu_{\mathrm{Ks}}^{\mathrm{offset}} - 2.5 \cdot \log(N - \mathrm{n_{sky}})\,, \tag{4.8}$$

for either the $\mathrm{R_c}$ or the $\mathrm{K_s}$ band, respectively. As in Equations 4.3 and 4.4, the $\mathrm{n_{sky}}$ stands for the number of counts of the sky, as derived for each galaxy (cf. Section 4.1 on page 86), while N is the number of counts within the isophote as derived by means of `ellipse` task in Chapter 3. The offsets $\mu_{\mathrm{offset}}^{\mathrm{Rc}}$ and $\mu_{\mathrm{offset}}^{\mathrm{Ks}}$ were calculated by using the transformation coefficients that resulted from the photometric calibration (cf. Section 2.5 on page 41), and are given by Equations 4.5 and 4.6, for the $\mathrm{R_c}$ band and the $\mathrm{K_s}$ band data, respectively. Since the exact colours for each object were not known beforehand, literature values for $(\mathrm{V}-\mathrm{R_c})$ and $(\mathrm{J}-\mathrm{K_s})$ colours were assumed, i.e. 0.65^{m} and 1.0^{m}, respectively (Dr. Woudt, priv. comm.).

The resulting isophotal magnitudes were plotted against the semi-major axis of the galaxy as given by the `ellipse` task. The distance on the semi-

major axis was calculated by using

$$r_{\rm sma}^{\rm Rc} = r_{\rm sma,pix}^{\rm Rc} \cdot 0.238\,\text{arcsec} \tag{4.9}$$

and

$$r_{\rm sma}^{\rm Ks} = r_{\rm sma,pix}^{\rm Ks} \cdot 0.288\,\text{arcsec}\,, \tag{4.10}$$

according to the different lengths in the sky projected onto each pixel for the WFI and SOFI CCDs, respectively. In these equations, $r_{\rm sma,pix}^{\rm Rc}$ and $r_{\rm sma,pix}^{\rm Ks}$ stand for the semi-major axis lengths of the ellipses in number of pixels, as derived by the `ellipse` task. The $r_{\rm sma}^{\rm Rc}$ and $r_{\rm sma}^{\rm Ks}$ stand for the same semi-major axis converted into arcsec.

Once the isophotal magnitudes had been calculated, the semi-major axis lengths $r_{\rm Rc23}$ and $r_{\rm Ks20}$ of the isophotes were determined from the calculated data. These are the semi-major axis lengths for which the surface brightness reached the 23$^{\rm rd}$ and 20$^{\rm th}$ magnitude per unit area, for the R_c and K_s data, respectively. The integrated magnitudes R_{c23} and K_{s20} were established by adding up the isophotal magnitudes up to the given semi-major axis length, using

$$R_c\mu = \mu_{\rm Rc}^{\rm offset} - 2.5 \cdot \log(L_{\rm Rc}) - 2.5 \cdot \log(A_{\rm Rc}^{\rm WFI}) \tag{4.11}$$

and

$$K_s\mu = \mu_{\rm Ks}^{\rm offset} - 2.5 \cdot \log(L_{\rm Ks}) - 2.5 \cdot \log(A_{\rm Ks}^{\rm SOFI})\,. \tag{4.12}$$

The offsets $\mu_{\rm Rc}^{\rm offset}$ and $\mu_{\rm Ks}^{\rm offset}$ are given by Equations 4.5 and 4.6, respectively. $L_{\rm Rc}$ and $L_{\rm Ks}$ are the fluxes through the given ellipses as derived by `ellipse`, which are reduced by the sky, i.e. $(n_{\rm sky} \cdot A_{\rm Rc}^{\rm WFI} \cdot n_A)$ and $(n_{\rm sky} \cdot A_{\rm Ks}^{\rm SOFI} \cdot n_A)$ for Equations 4.11 and 4.12, respectively. The counts of the sky $n_{\rm sky}$ were determined earlier (cf. Section 4.1 on page 86) and the area n_A, over which the flux had been determined, was given by the `ellipse` task.

Example plots of the isophotal as well as the integrated magnitudes for R_c and K_s with respect to the semi-major axis length are shown for WKK 5920 in Figure 4.3 on page 94. These plots were derived for the data from the *iPSF-Fitting* method described in Section 3.4 on page 65. All plots obtained

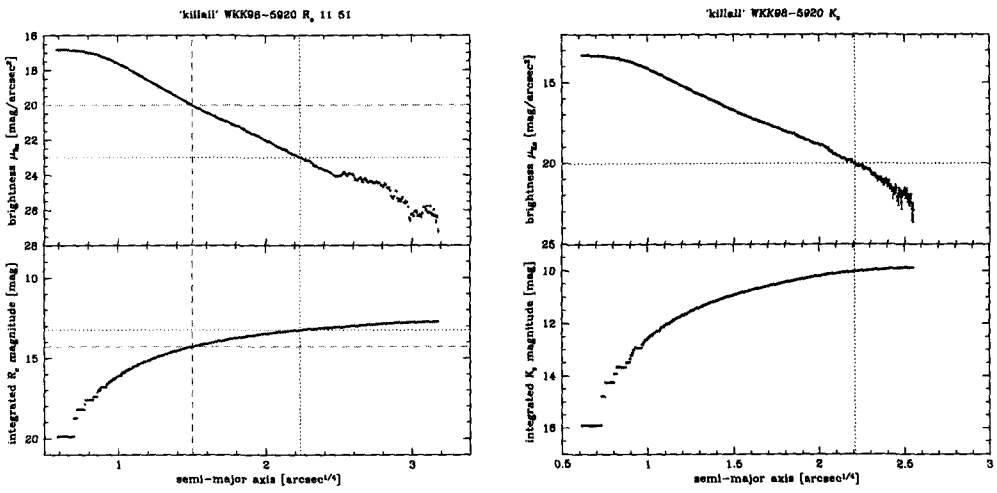

Figure 4.3: Galaxy WKK 5920, isophotal and integrated magnitude plots for R_c and K_s as determined with the *iPSF-Fitting* method described in Section 3.4 on page 65. The horizontal dotted lines indicate where the isophotal magnitudes μ_{Rc} and μ_{Ks} are reaching the 23^{rd} and the 20^{th} magnitude per arc second squared, respectively. A dashed horizontal line is indicating where the isophotal magnitude μ_{Rc} is reaching the 20^{th} magnitude per arc second squared. The vertical lines indicate the corresponding radii. Similar plots for all galaxies can be found in Part II of this dissertation.

with the *σ-Clipping* and the *iPSF-Fitting* methods are shown for all galaxies in Part II of this dissertation. The plots obtained for the *Star-Masking* and the *PSF-Fitting* methods can be seen in Appendix A.5 on page 215.

In addition to the mentioned magnitude plots, the ellipticity and the position angle were derived for each isophote by using `ellipse`. They were plotted against the semi-major axis distance for each galaxy and for each observed field, see corresponding figures in Part II of this dissertation. Example *SM*-scripts for how the plots were derived from the data are given in Part III of this dissertation.

4.3 Circular Aperture Photometry

One of the goals of this study was to establish the colour excess of the galaxies in the central Norma cluster area. This was possible through a comparison with external photometry derived from Coma cluster galaxies. However, this external data was obtained by making use of a circular aperture with a radius of 10 arcsec. Thus, for the data processed earlier by applying the *iPSF-Fitting* method (cf. Section 3.4 on page 65), similar circular aperture photometry had to be derived. To further be able to make a comparison with the obtained data, the chosen aperture radius had to be adjusted to 14 arcsec, since the Norma cluster is assumed to be about 1.4 times closer than the Coma cluster. This was necessary to avoid a bias towards redder colours and thus a too large colour excess, due to the radial colour gradients that exist for elliptical galaxies (cf. Section 5.2 on page 149). Furthermore, the derived circular aperture magnitudes were also used for comparing the eight different WFI CCDs, independently of the derived galaxy model (cf. Section 4.4 on page 95). To obtain these magnitudes, the *IRAF* task `phot` in the *DAOPHOT* package was used to get the flux within the circular apertures. This was then adjusted by using the previously mentioned Equations 4.11 and 4.12, on page 93, for the R_c and the K_s band, respectively. However, with the L_{Rc} and L_{Ks} representing the fluxes through the sky-subtracted circular apertures with radii of 14 arcsec.

4.4 Magnitudes and Radii for different WFI CCDs

Of the 31 galaxies for which the integrated magnitudes like R_{c23} were determined, 14 galaxies were observed with more than one CCD. Two of these were even observed with three CCDs. Thanks to the slight shifting of the telescope between exposures, as described in Section 2.3 on page 37, parts of the sky were recorded more than once. This made it possible to check for in-

ternal accuracy of the magnitudes and radii derived for the WFI instrument.

In Figures 4.4 and 4.5 on pages 97 and 98, respectively, the integrated magnitudes R_{c23} and corresponding r_{Rc23} radii are compared, respectively. These two properties are strongly coupled. For each CCD, the variations with respect to the other seven CCDs are shown. The corresponding numerical results can be found in Section 5.1 on page 121. The differences found when comparing each CCD with its counterparts can be seen in Table 4.1. Figures 4.6 and 4.7 on pages 99 and 100, respectively, show these deviations for each pair of CCDs.

It can be seen from Figures 4.4 to 4.7 and Table 4.1 that the magnitudes and radii in general agree well. However, a closer look reveals slight shifts between the CCDs in the order of a few tenth of a magnitude. These shifts may partly be caused by the shifts already mentioned in Section 2.5 on page 41, and would thus be results of averaging some of the photometric parameters. e.g. for each night of observations. This effect, however, could not solely cause such large offsets. Two more reasons could account for the

difference WFI CCDs	brightness [mag]	radius [arcsec]	number of galaxies
#5x−#50	-0.050 ± 0.055	0.058 ± 0.819	4
#5x−#51[a]	−0.093	0.629	1
#5x−#52	0.185 ± 0.017	-2.234 ± 1.170	8
#5x−#53	-0.104 ± 0.048	1.143 ± 0.707	8
#5x−#54	-0.093 ± 0.049	0.444 ± 0.631	4
#5x−#55	-0.114 ± 0.042	1.691 ± 1.892	5
#5x−#56	0.007 ± 0.086	0.771 ± 1.400	2
#5x−#57	0.142 ± 0.024	-0.977 ± 0.500	4

[a]No standard deviation can be calculated, since only one set of data is available.

Table 4.1: The mean differences of magnitudes and radii from the determination of surface brightness profiles (cf. Section 4.2 on page 91), for each WFI CCD compared to the other seven CCDs.

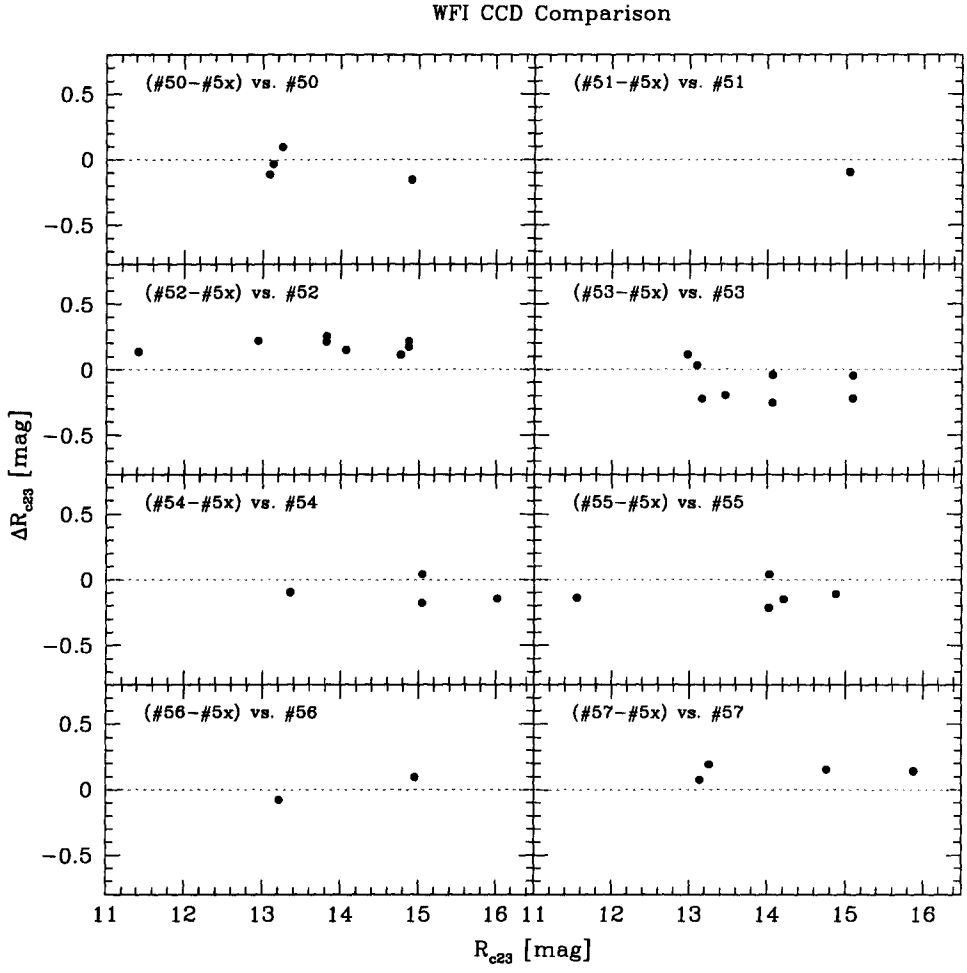

Figure 4.4: Comparison of the derived galaxy magnitudes for all eight WFI CCDs. The magnitudes were derived using the *iPSF-Fitting* method as described in Section 3.4 on page 65, and from the determination of surface brightness profiles, cf. Section 4.2 on page 91.

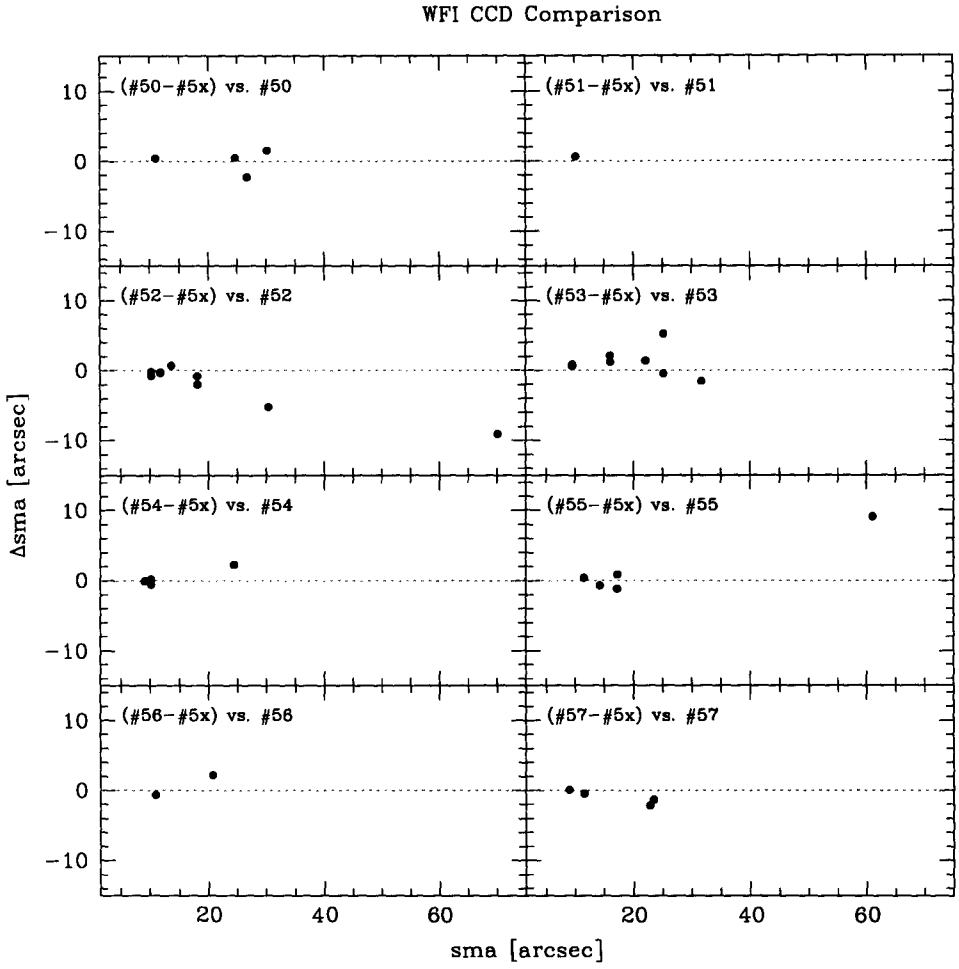

Figure 4.5: Comparison of the derived galaxy radii for all eight WFI CCDs. The radii were derived using the *iPSF-Fitting* method as described in Section 3.4 on page 65, and from the determination of surface brightness profiles, cf. Section 4.2 on page 91.

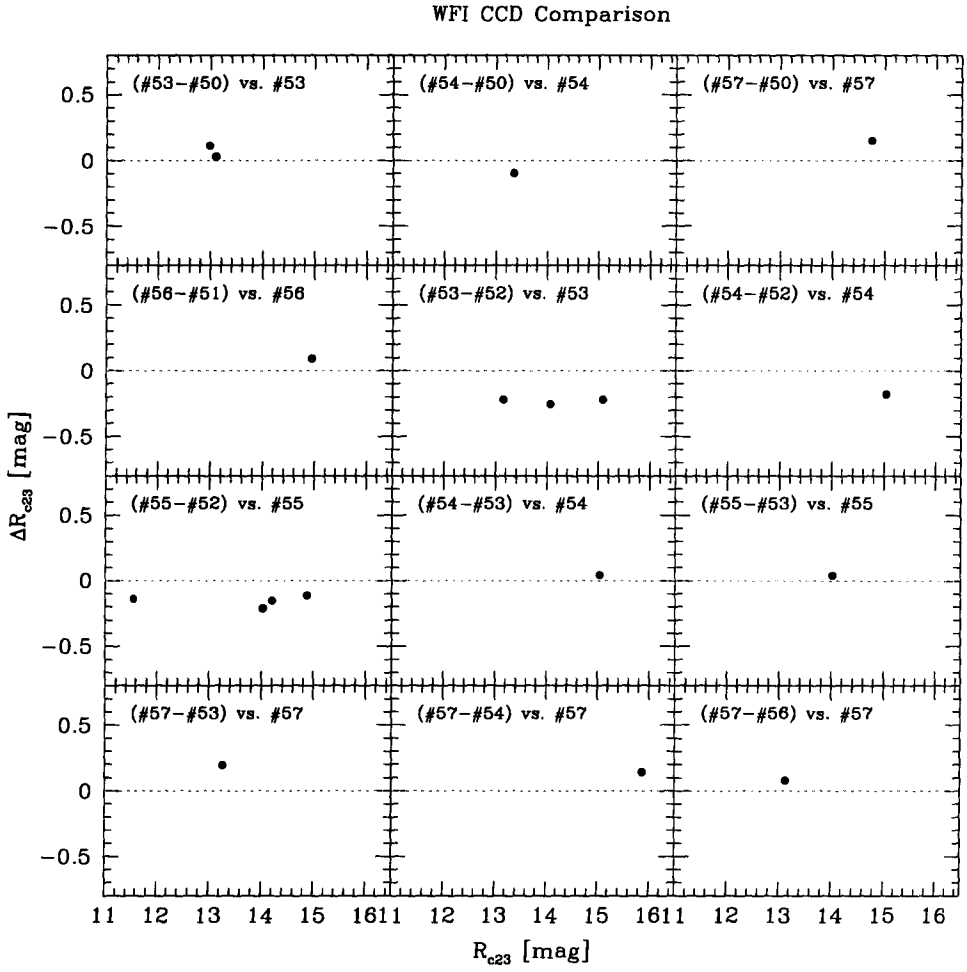

Figure 4.6: Comparison of the derived galaxy magnitudes for each pair of the eight WFI CCDs. The magnitudes were derived using the *iPSF-Fitting* method as described in Section 3.4 on page 65, and from the determination of surface brightness profiles, cf. Section 4.2 on page 91.

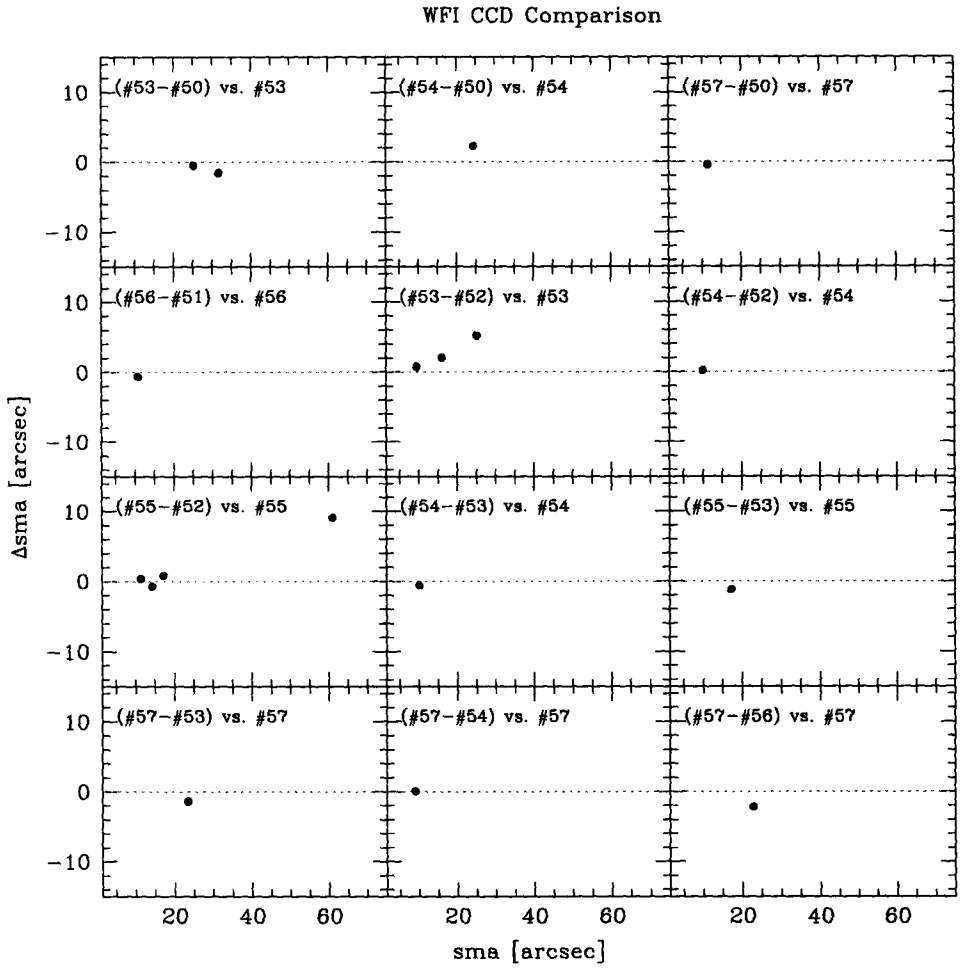

Figure 4.7: Comparison of the derived galaxy radii for each pair of the eight WFI CCDs. The radii were derived using the *iPSF-Fitting* method as described in Section 3.4 on page 65, and from the determination of surface brightness profiles, cf. Section 4.2 on page 91.

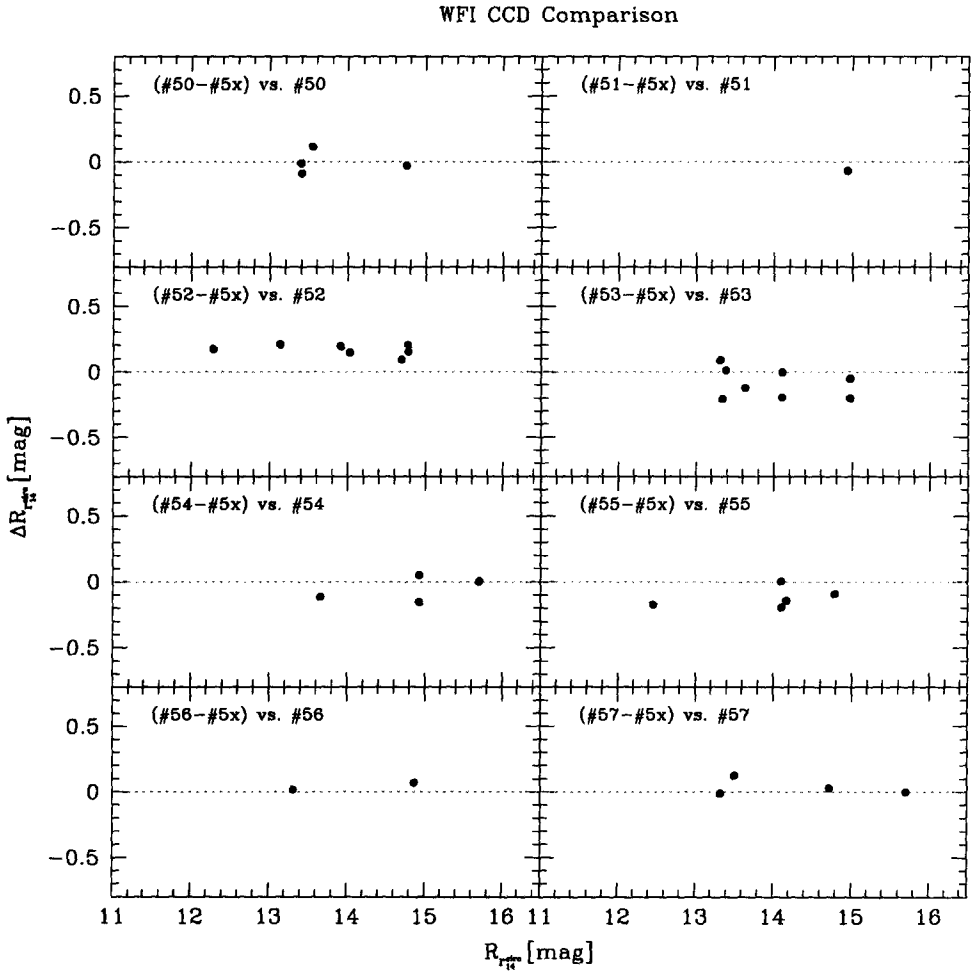

Figure 4.8: Comparison of the derived galaxy magnitudes for all eight WFI CCDs, using circular apertures. The magnitudes were derived as described in Section 4.3 on page 95, using the results from the *iPSF-Fitting*, cf. Section 3.4 on page 65.

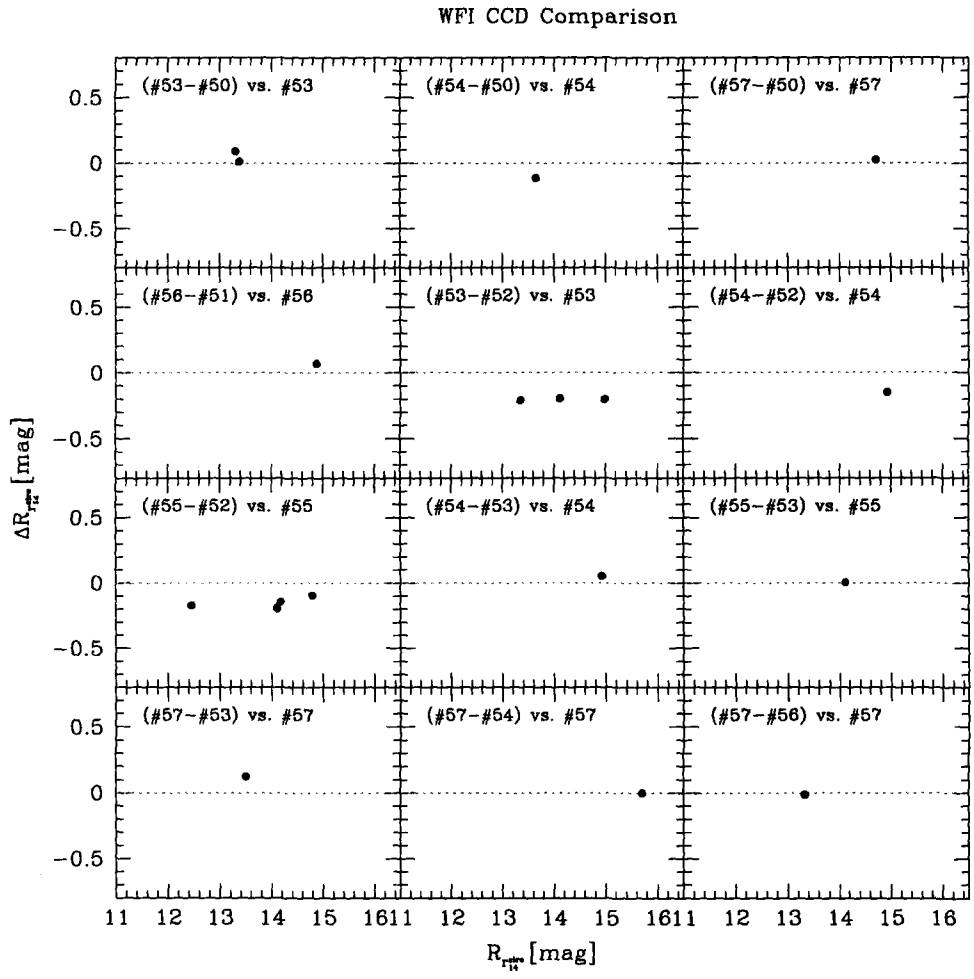

Figure 4.9: Comparison of the derived galaxy magnitudes for each pair of the eight WFI CCDs, using circular apertures. The magnitudes were derived as described in Section 4.3 on page 95, using the results from the *iPSF-Fitting*, cf. Section 3.4 on page 65.

difference WFI CCDs	brightness [mag]	number of galaxies
#5x−#50	-0.003 ± 0.043	4
#5x−#51[a]	−0.093	1
#5x−#52	0.170 ± 0.014	8
#5x−#53	-0.085 ± 0.040	8
#5x−#54	-0.054 ± 0.048	4
#5x−#55	-0.120 ± 0.035	5
#5x−#56	0.041 ± 0.027	2
#5x−#57	0.033 ± 0.031	4

[a]No standard deviation can be calculated, since only one set of data is available.

Table 4.2: The mean differences of circular aperture magnitudes for each WFI CCD compared to the other seven CCDs.

discrepancies. Since all the investigated galaxies lie close to the edge of a set of combined images, the different models made of the galaxy could deviate from CCD to CCD, because parts of the galaxy can be missing. Furthermore, the differences in intensity of up to 50 counts at the edges from one CCD to the next can cause variations in the determined magnitudes and radii, especially for the low intensity parts of the galaxies. These variations in intensity are caused by the background variation of about 1% for each exposure, which was mentioned in Section 2.4 on page 39. This causes variations at the edges due to the adding of several exposures into one image, as described in Section 2.4. Obtaining different models seems inevitable for the galaxies that are positioned at the edge of different images, e.g. when some of the lower intensity parts of a particular galaxy are missing in each image. To ensure that the shown differences in magnitudes and radii are not caused by slightly different galaxy models, the circular aperture photometry obtained earlier (cf. Section 4.3 on page 95) was investigated as well. All the double and triple magnitude sets were compared for the eight WFI CCDs. The results are shown in Figures 4.8 and 4.9 on pages 101 and 102, respectively.

The fitted offsets can be found in Table 4.2. It can be seen that the elliptical photometry and the circular aperture photometry do agree very well. This indicates that the fitted differences in magnitudes for the WFI CCDs do not result from the determination of different galaxy models for different CCDs. The differences in intensity could nevertheless still account for the shown offsets between the CCDs.

4.5 External Comparison of Magnitudes and Radii

In order to verify the accuracy of the described methods, the magnitudes and radii that were determined need to be compared with external data. Particularly suitable galaxy magnitudes and radii in the near infrared are available from the *2 Micron All Sky Survey* (2MASS), e.g. for the K_s band. 2MASS offers high accuracy and coverage of the entire sky. The correlation of K_s band data from this study and from 2MASS are thus investigated in this section.

Figures 4.10 and 4.11 on pages 105 and 106, respectively, show the relation between 2MASS and the SOFI K_{s20} and r_{Ks20} data as derived by means of the *σ-Clipping* method described in Section 3.1 on page 49. Similarly, Figures 4.12 and 4.13 on pages 107 and 108, respectively, show these relations for the *iPSF-Fitting* method described in Section 3.4 on page 65. The tabulated magnitudes, radii and other galaxy properties that were determined with the methods described in the previous section can be found in Section 5.1 on page 121. The data taken from 2MASS for these comparisons are given in Table A.8 on page 229.

For each of the two procedures, the differences $\Delta K_{s20,2MASS-SOFI}$ and $\Delta r_{Ks20,2MASS-SOFI}$ are plotted in Figures 4.10 to 4.13 on pages 105 to 108, respectively. Two functions are fitted, using the *Gnuplot* implementation of the nonlinear least-squares Marquardt-Levenberg algorithm. The fitted

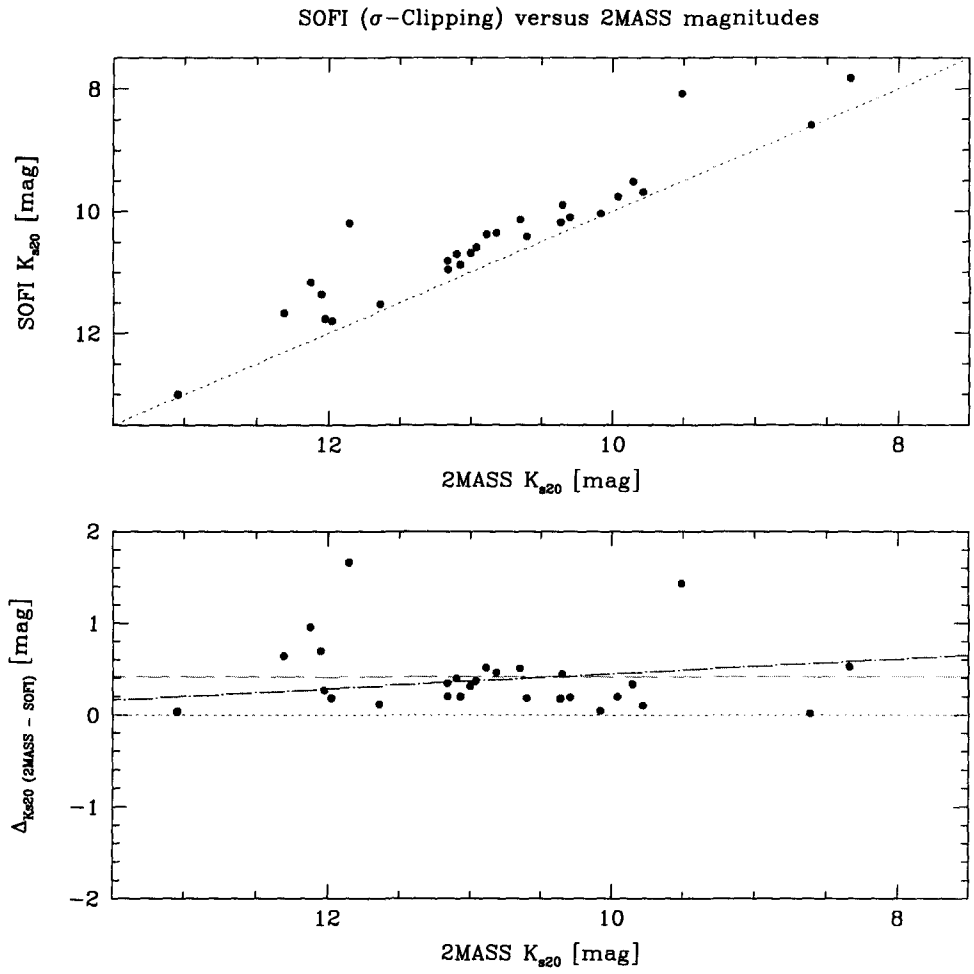

Figure 4.10: Comparison of K_{s20} galaxy magnitudes derived by means of the *σ-Clipping* procedure for SOFI vs. K_{s20} galaxy magnitudes from the 2MASS catalogue. The dashed lines represent the fitted Funtions 4.13 and 4.14 on page 105, using the results shown in Table 4.3 on page 109.

functions are

$$g(x) = a \cdot x + b \tag{4.13}$$

and

$$h(x) = c\,. \tag{4.14}$$

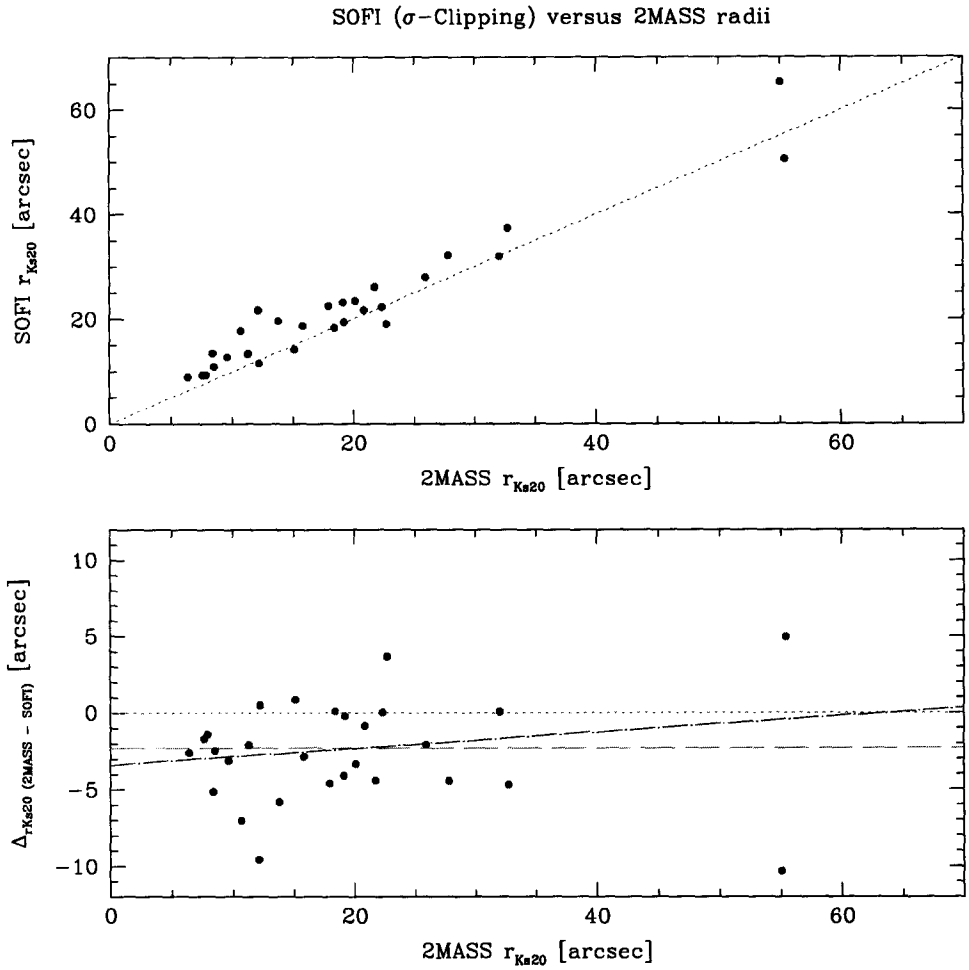

Figure 4.11: Comparison of r_{Ks20} galaxy radii derived by means of the σ-*Clipping* procedure for SOFI vs. r_{Ks20} galaxy radii from the 2MASS catalogue. The dashed lines represent the fitted Funtions 4.13 and 4.14 on page 105, using the results shown in Table 4.3 on page 109.

Here x is either the 2MASS magnitude or the radius, depending on the fit. For the fitting parameters a, b and c, the resulting values are given in Table 4.3 on page 109. The fitted functions are indicated in the plots.

As can be seen from the fitted values as well as the plots, the brightness for the σ-*Clipping* method appears to be too high compared with the

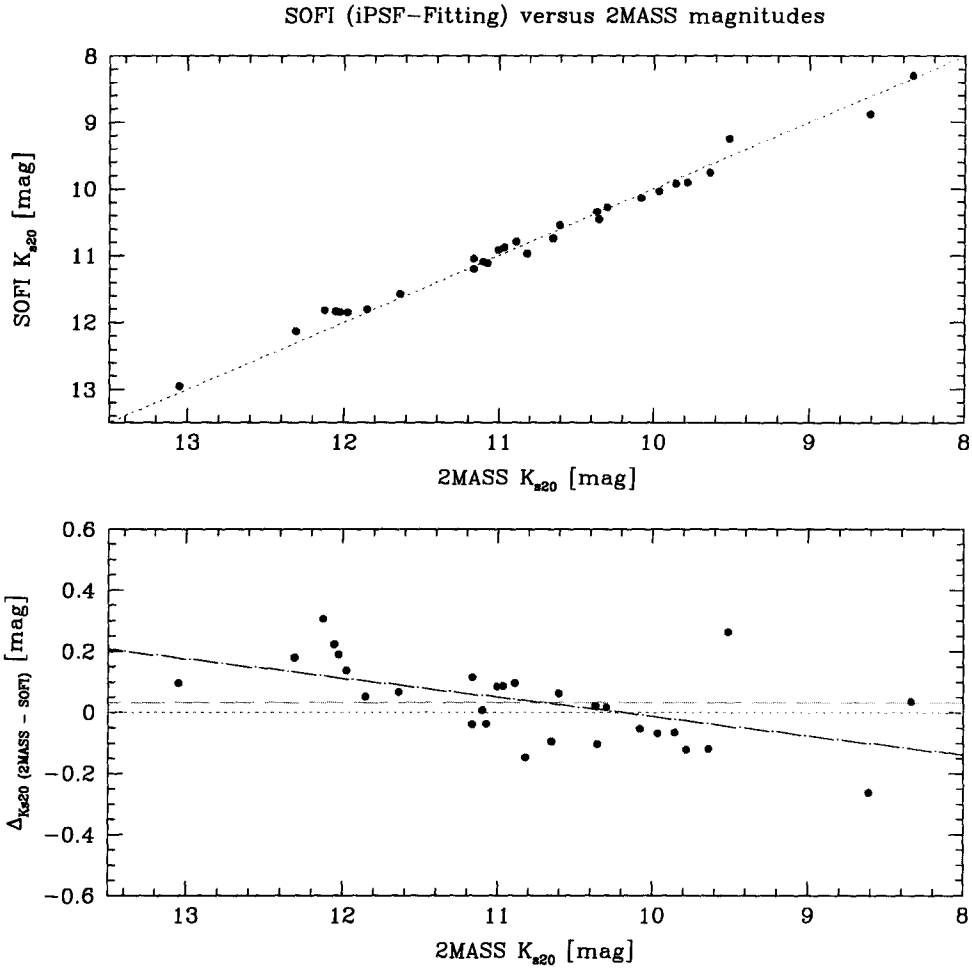

Figure 4.12: Comparison of K_{s20} galaxy magnitudes derived by means of the *iPSF-Fitting* procedure for SOFI vs. K_{s20} galaxy magnitudes from the 2MASS catalogue. The dashed lines represent the fitted Funtions 4.13 and 4.14 on page 105, using the results shown in Table 4.3 on page 109.

2MASS data, and the corresponding radii appear to be too large. This corresponds well with the results discussed in Section 3.5 on page 80, with regard to the comparison of the data derived from the different procedures. Conversely, the brightness and radii determined with the *iPSF-Fitting* method agree quite well with the data from 2MASS. Also, a much smaller scatter in

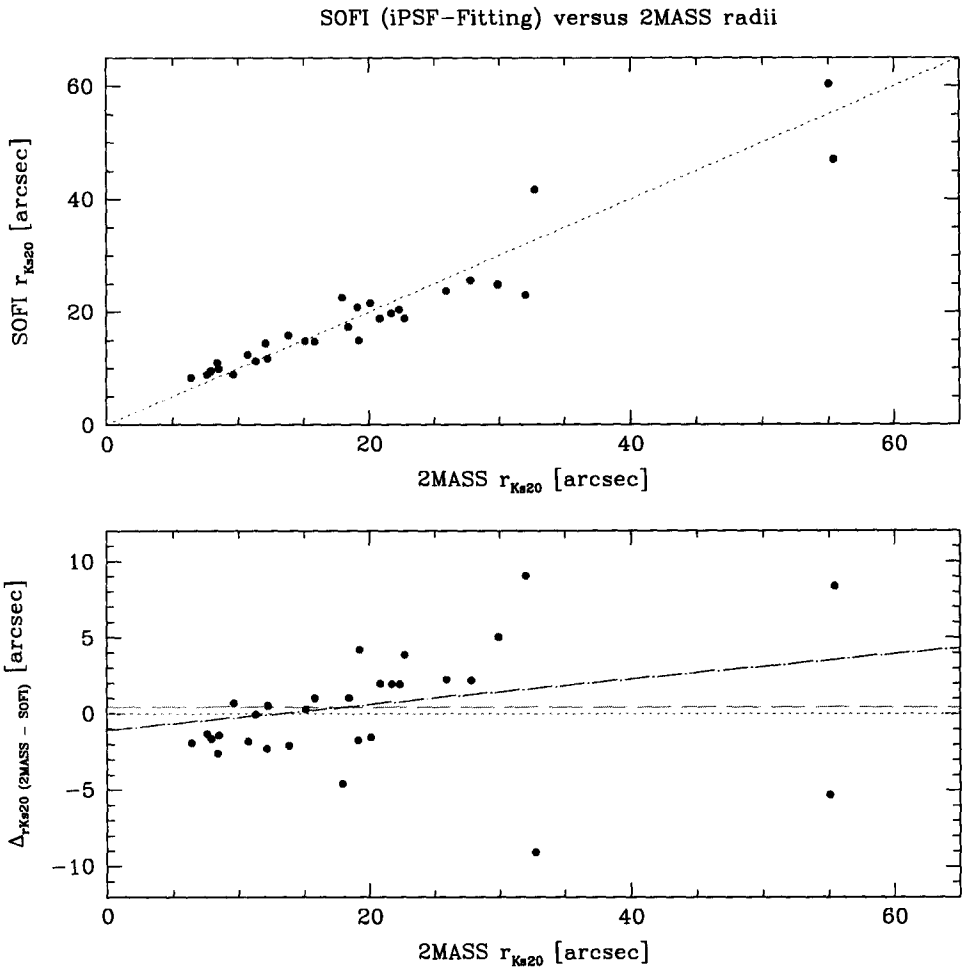

Figure 4.13: Comparison of r_{Ks20} galaxy radii derived by means of the *iPSF-Fitting* procedure for SOFI vs. r_{Ks20} galaxy radii from the 2MASS catalogue. The dashed lines represent the fitted Funtions 4.13 and 4.14 on page 105, using the results shown in Table 4.3 on page 109.

magnitude range can be observed for the *iPSF-Fitting* method compared to the σ-*Clipping* method. These results seems to suggest that the former technique is indeed a very good approach for dealing with galaxies in crowded starfields.

Table 4.3: Results from fitting the $\Delta K_{s20,2MASS-SOFI}$ and $\Delta r_{Ks20,2MASS-SOFI}$ for the two methods, *σ-Clipping* and *iPSF-Fitting*. The fitted functions are given in Equations 4.13 and 4.14 on page 105, using the fitting parameters a, b and c. Here, the σ_{fit} are the derived root mean squares of the residuals. The number of galaxies used for the fitting are 28 for the *σ-Clipping* method and 29 for the *iPSF-Fitting* method.

method	fitted property	a	b	c	$\sigma_{fit}^{g(x)}$	$\sigma_{fit}^{h(x)}$
σ-Clipping	magnitudes	-0.082 ± 0.067	1.266 ± 0.697	0.413 ± 0.074	0.385	0.389
σ-Clipping	radii	0.053 ± 0.065	-3.405 ± 1.470	-2.312 ± 0.599	3.130	3.110
iPSF-Fitting	magnitudes	0.063 ± 0.022	-0.643 ± 0.233	0.033 ± 0.024	0.117	0.131
iPSF-Fitting	radii	0.083 ± 0.078	-1.094 ± 1.590	0.429 ± 0.697	3.677	3.686

Assuming this to be the case, another effect can be seen in the plots and in the fits. For fainter galaxies, the SOFI data seems to produce brighter galaxies, whereas this relation is reversed for brighter galaxies, with a turning point at a magnitude of about 10.5^{m}. Consequently, the determined radii are smaller for SOFI than for 2MASS in the case of small (faint) galaxies and larger for galaxies larger than about 15 arcsec. This result may need further investigation on a larger set of data. If true, however, this could be caused by the fact that the SOFI data have a higher angular resolution than the 2MASS data. For instance, a deviation of the elliptical profile in the 2MASS data due to the comparably large FWHM could cause smaller and fainter galaxies to be 'smeared out', hence causing such galaxies to appear slightly fainter. The differences could also be a result from the way 2MASS is dealing with star crowding. However, to confirm such a relation, a closer investigation on a larger data set ought be undertaken, also, because this relation does not seem to be visible for the *σ-Clipping* data.

4.6 Effective Radii and Magnitudes

Two further properties were extracted from the galaxy data that had been derived earlier with `ellipse`. Again, only the results from Section 3.4 on page 65 were used here, since the *iPSF-Fitting* method is considered to offer the best results, compared to the methods described in Sections 3.1 to 3.3 on pages 49 to 62.

The parameters of interest in this regard are the effective surface brightness μ_e and the effective radius r_e. From the fitting of a function to the surface brightness profiles of each galaxy, as described in Section 4.2 on page 91, the radius can be determined, within which half of the total light of the galaxy is assumed to be emitted. This radius is called the effective radius r_e, and the isophote at this particular radius gives the effective surface brightness μ_e. A major advantage of effective radii compared to radii of isophotes is, that they are independent of the surface brightness scale and are thus not

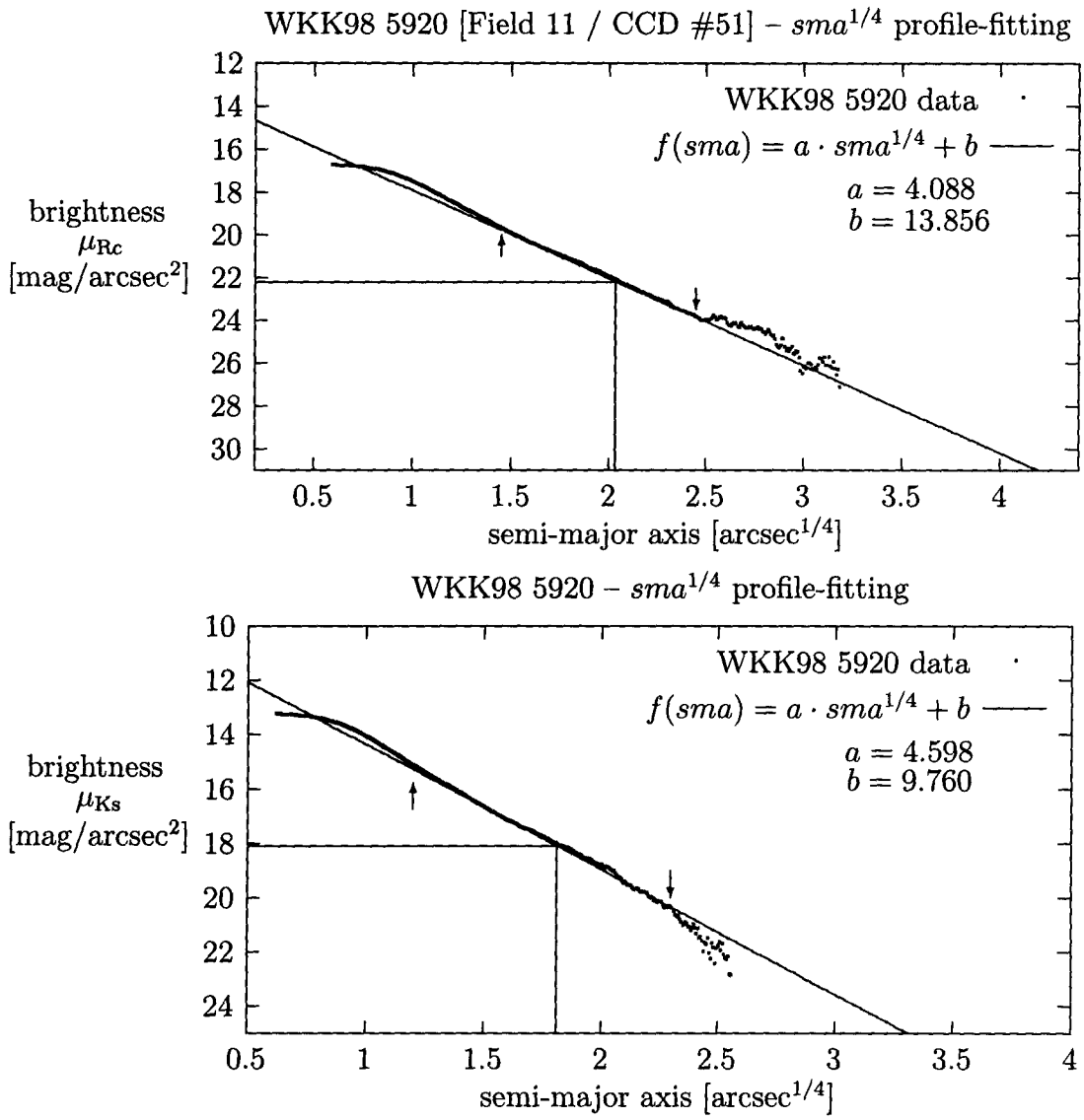

Figure 4.14: Galaxy WKK 5920, plots of brightness (μ_{R_c} and μ_{K_s}) versus semi-major axis ($sma^{1/4}$) to demonstrate the profile fitting with the *Gnuplot* implementation of the nonlinear least-squares Marquardt-Levenberg algorithm. The arrows point to the upper and lower limit of the data set that was used for the fit. The abscissa is scaled with $(\mathrm{sma})^{1/4}$ to account for the de Vaucouleur $r^{1/4}$ relation (see text for further explanation of this). The resulting effective (half-light) radius $r_e^{1/4}$ and effective (half-light) surface brightness μ_e are indicated by straight lines. Similar plots for all galaxies can be found in Part II of this dissertation.

affected by extinction.

The ideal function to be fitted to the surface brightness profile of early-type galaxies and even for the central regions of spiral galaxies appears to be the Sèrsic r^{1/n_s} function (Sèrsic, 1968), although, until today, the de Vaucouleur $r^{1/4}$ function is often used to do the fitting (de Vaucouleur, 1948, 1959; Hogg, 2001; Jørgensen et al., 1992). In this dissertation, the $r^{1/4}$ function was applied, in order to enable the comparison of results from different sources and for reasons of simplicity, as the resulting function given by

$$\mu = \mu_e + k \cdot \left[\left(\frac{sma}{r_e} \right)^{1/4} - 1 \right] \tag{4.15}$$

can be reduced to a linear function and easily fitted (Caon et al., 1993; Hogg, 2001). To do this, the surface brightness was plotted against the semi-major axis length $sma^{1/4}$ and fitted with the function $f(sma^{1/4}) = a \cdot sma^{1/4} + b$. However, the profiles were inspected by eye and only the parts were used for the fitting, that were considered to be not affected by seeing effects or that deviated too strongly from the straight line, see Figure 4.14 on page 111 for an example. The *Gnuplot* implementation of the nonlinear least-squares Marquardt-Levenberg algorithm was used for the fitting. When comparing the fitted function with Equation 4.15, one can find the relations for the effective (half-light) radius r_e and the effective (half-light) surface brightness μ_e;

$$r_e = (k/a)^4 \tag{4.16}$$

and

$$\mu_e = b + k\,, \tag{4.17}$$

respectively. k for the de Vaucouleur $r^{1/4}$ function is found to be 8.3268 (Hogg, 2001), and thus r_e and μ_e can be obtained from the fit.

The obtained r_e and μ_e are shown in Table 5.3 on page 129 in Chapter 5. It must be noted that the results differ a lot for some double sets of galaxy measurements, e.g. for WKK 6180, WKK 6242, WKK 6615 etc. The same reasons apply here that caused the deviations in galaxy magnitudes and radii

for different WFI CCDs, as described in Section 4.4 on page 95. However, the method for obtaining the effective magnitudes and radii is much more sensitive to deviations in intensity, and therefore the discrepancies appear much more serious. The shown error in Table 5.3 can not account for this, since it is based on the fit of a small portion of the surface brightness profile only.

4.7 Total Magnitudes derived with GALFIT

An important property of galaxies are total magnitudes. They are derived within the faintest visible isophote, but are corrected for the missing light by extrapolating the surface brightness profile out to infinity. The main advantage of total compared to isophotal magnitudes is, that the extinction only affects the magnitude, since the radius has been integrated out of the determination. Total magnitudes can for instance be used for a Fundamental Plane analysis. However, the total magnitude data derived in this dissertation are not used for any analysis presented here. They are only stated for reasons fo completeness.

To derive the total magnitudes for all galaxies, a software called *GALFIT* has been used. This program makes it possible, to easily derive many different parameters from images that are containing galaxies (Peng et al., 2002). Some of the derived parameters, namely the total magnitudes R_c^{total} and K_s^{total}, the effective radii $r_{e,Rc}^{GALFIT}$ and $r_{e,Ks}^{GALFIT}$, and the Sèrsic indices $n_{s,Rc}$ and $n_{s,Ks}$ (Sèrsic, 1968), are shown in Table 5.7 on page 139 in Chapter 5. *GALFIT* was applied to the images that were resulting from the data processing described in Section 3.4 on page 65, because the *iPSF-Fitting* method is considered to offer the best results, compared to the methods described in Sections 3.1 to 3.3 on pages 49 to 62. Note that for the total magnitudes shown in Table 5.7, the photometric corrections described in Section 4.9 on page 116 have not been applied yet.

4.8 Apparent Galaxy Colours

Since photometry was obtained for two filters, it was possible to calculate the differences in their intensities. These $(R_c - K_s)$ colours were obtained by using the integrated magnitudes of the galaxies as described in Section 4.2 on page 91.

For the R_c band, the integrated magnitude at r_{Ks20} was calculated, i.e. at the semi-major axis length for which the surface brightness μ in the K_s band

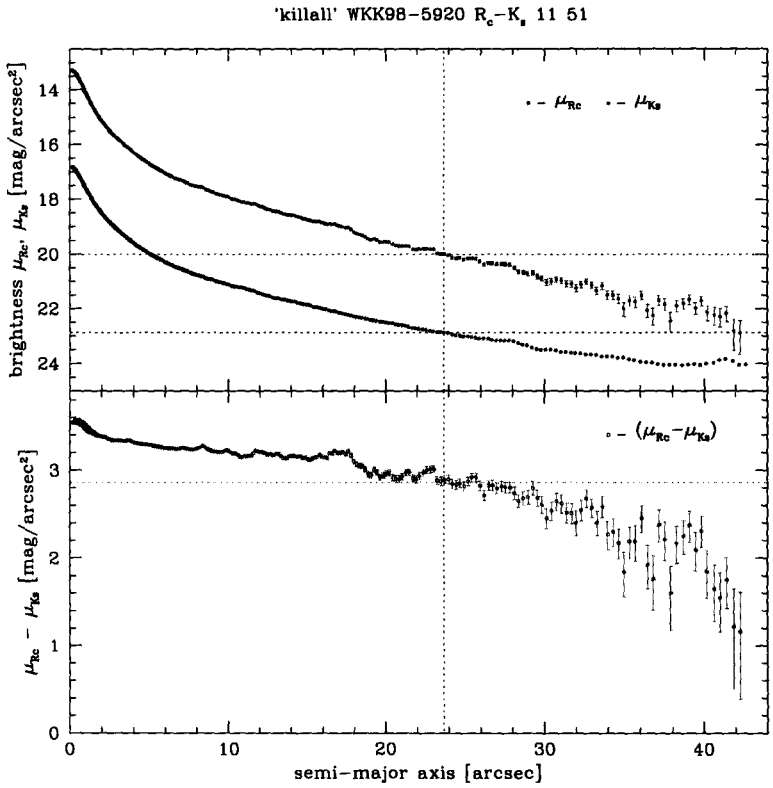

Figure 4.15: Galaxy WKK 5920, $(\mu_{R_c} - \mu_{K_s})$ magnitude plot. The vertical line indicates the radius for which the K_s band isophote reaches the 20^{th} magnitude per square arc second. The sharp fall-off for large radii is due to the K_s band data reaching the background. Similar plots for all galaxies can be found in Part II of this dissertation.

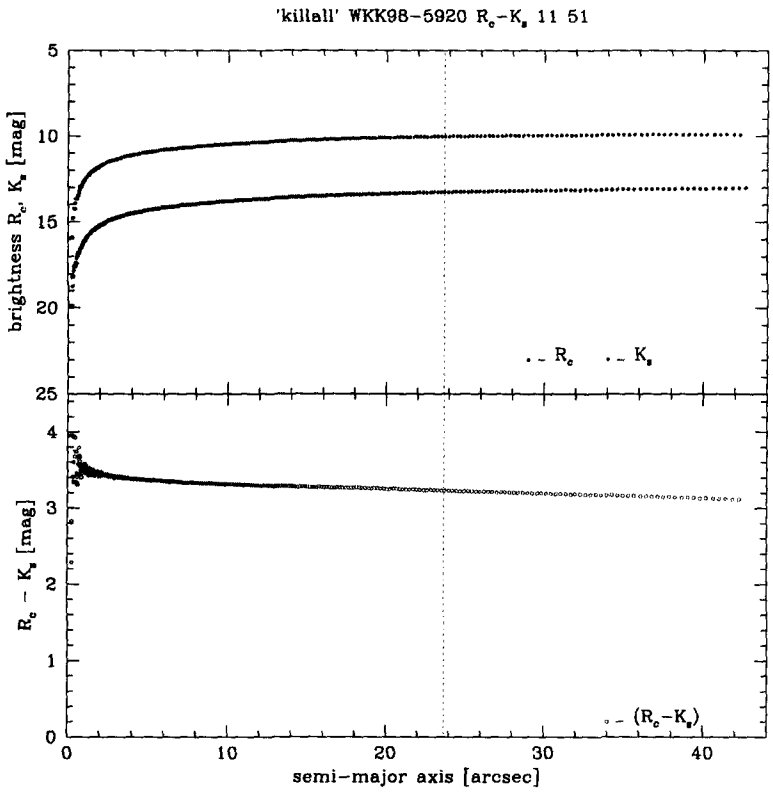

Figure 4.16: Galaxy WKK 5920, $(R_c - K_s)^{r_{Ks20}}$ magnitude plot as described in Section 4.8 on page 114. The vertical line indicates the radius for which the K_s band isophote reaches the 20^{th} magnitude per square arc second. Similar plots for all galaxies can be found in Part II of this dissertation.

reaches the 20^{th} magnitude per unit area. This is demonstrated in Figure 4.16 on page 115 for WKK 5920. Similar plots for all galaxies can be found in Part II of this dissertation. The difference in integrated magnitudes between the two bands (R_c and K_s) results in the $(R_c - K_s)^{r_{Ks20}}$ colour. Similarly, the $(R_c - K_s)^{r_e^{Ks}}$ colours were obtained from the R_c and K_s integrated magnitudes at the effective radii r_e^{Ks}, as determined in the previous section.

The results from Section 3.4 on page 65 are considered to offer the best results, compared to the methods described in Sections 3.1 to 3.3 on pages 49

to 62. Therefore only the data resulting from applying the *iPSF-Fitting* method were used.

Subsequently, another set of $(R_c - K_s)^{r_{14}^{circ}}$ colours were derived, to be able to do a comparison with external data (cf. Section 5.2 on page 149). The used circular aperture magnitudes were obtained with the **phot** task according to the description given in Section 4.3 on page 95.

4.9 Photometric Corrections

To be able to work with and compare the derived galaxy brightness, one has to apply a series of corrections. These transformations cause the galaxies to be virtually moved towards the observer. The corrections were applied to the derived $(R_c - K_s)$ colours shown in Section 5.1 in Tables 5.4 and 5.6 on pages 133 and 137, respectively and to the Coma cluster data given in Appendix A.8 in Table A.11 on page 241. Likewise, for the integrated magnitudes as derived by means of the *iPSF-Fitting* procedure as well as for the effective surface brightness μ_e in Section 5.1 in Tables 5.9 and 5.3 on pages 147 and 129, respectively, such corrections were applied according to

$$m_{corr} = m_{obs} - A_x - SBC - EVC - KC\,. \tag{4.18}$$

Here, m_{obs} is the observed and m_{corr} the corrected integrated magnitude. The applied corrections are:

A_x: The extinction correction, derived from the DIRBE/IRAS dust maps by Schlegel et al. (1998). They were extracted from the *Nasa/IPAC Extragalactic Database*[4] (NED) for each object. The extinction corrections given in the NED are calculated according to the method described in the Appendix of Schlegel et al. (1998). For the data used here, the magnitude corrections A_{Rc} and A_{Ks} were applied. However, it is not yet clear, whether the extinction derived by Schlegel et al. (1998) is accurate at low latitudes, e.g. due to its low resolution compared

[4]See *http://nedwww.ipac.caltech.edu/*.

to the patchiness of the dust in the foreground Milky Way (Burstein, 2005). It has also been suggested that Schlegel et al. (1998) have overestimated the extinction close to the Galactic Plane (Arce and Goodman, 1999; Dutra et al., 2002; Nagayama et al., 2004). Thus, the precision of the extinction maps in the investigated area must still be ascertained. On a large scale, however, it is the most accurate measurement for extinction today.

SBC: The surface brightness of a galaxy, i.e. the flux per unit area, diminishes with distance, due to the expansion of the universe, i.e. the area from which the flux is emitted. To correct for the missing light, a correction of SBC $= 10 \cdot \log(1 + \overline{z}_{\mathrm{cluster}})$ has to be applied, with $\overline{z}_{\mathrm{cluster}}$ being the assumed redshift of the galaxy cluster (Sparkle and Gallagher, 2000). The redshift $\overline{z}_{\mathrm{cluster}}$ of the cluster is assumed to lie close to the mean $\overline{z}$ determined from using the galaxy spectra of the cluster member galaxies. For the Norma cluster galaxy set used in this dissertation, the average $\overline{z}_{\mathrm{Norma}}$ is about 0.017. For the Coma cluster data used in Section 5.2 on page 149, the average $\overline{z}_{\mathrm{Coma}}$ is about 0.0227.

KC: Also caused by the expansion of the universe is a redshift of the observed light. The spectrum emitted from a galaxy is shifted to longer wavelengths. However, every observation is limited to a range of frequencies or photon energies. Thus, when keeping the observed photon range fixed, the observed part of a galaxy spectrum moves towards the shorter wavelength part for more distant galaxies. This effect increases with redshift and depends on the shape of the spectrum (galaxy type) that is observed. For a small range in redshift, this relation can be approximated linearly for each galaxy type and observed filter band. According to Poggianti (1997), the relationship applied here is

$$\mathrm{KC} = c_{\mathrm{K}} \cdot z\,, \tag{4.19}$$

with $c_{\mathrm{K}} = -1.5$ for the K_s band and $c_{\mathrm{K}} = 1.1$ for the R_c band. Here z is the individual redshift for each galaxy, taken from the galaxy spectrum.

The described correction is often referred to as the *k-correction.*

EVC: Since light travels with finite velocity, everything we observe has happened in the past. This effect may not be relevant for nearby observations, but it becomes an important factor when considering the large-scale structures of the universe. The distribution of stars within a galaxy as well as their spectra change over time. Since galaxies are basically an agglomeration of stars, the spectrum of galaxies evolves with time, too. This makes it necessary to apply an evolutionary correction to distant galaxies. The observed waveband and galaxy types have to be taken into account. For a small range in redshift, this relation can be approximated linearly for each galaxy type and observed filter band. According to Poggianti (1997), the corrections were derived with

$$\mathrm{EVC} = c_{\mathrm{EV}} \cdot \overline{z}_{\mathrm{cluster}}\,, \tag{4.20}$$

where $c_{\mathrm{EV}} = -1.4$ for the K_s band and $c_{\mathrm{EV}} = -1.2$ for the R_c band. Again, $\overline{z}_{\mathrm{cluster}}$ is the assumed redshift of the galaxy cluster, i.e. either $\overline{z}_{\mathrm{Norma}} \approx 0.017$ or $\overline{z}_{\mathrm{Coma}} \approx 0.0227$, for the Norma cluster and the Coma cluster, respectively.

A further two corrections ought to be applied, but were neglected here. The first correction is due to effects of the seeing on the galaxy profiles. Although it can be seen that the central parts of the surface brightness profiles are affected by the seeing, this effect is considered to be negligible, because the central parts of the galaxies were not used for any analysis in this dissertation. This was possible, because of the good photometry that was obtained, and because the investigated galaxies are large compared to the effects of seeing (FWHM < 2 arcsec; see the determined FWHM for the WFI and SOFI observations in Appendix A.1, Tables A.3 and A.4 on pages 196 and 200, respectively). The second correction needs to be investigated first. The argument is that the radius of galaxies is reduced by Galactic extinction and that thus more light would be received if the galaxy was not concealed by dust and gas in the foreground. The extinction correction applied according

to Schlegel et al. (1998), described earlier, only accounts for the reduction of brightness, but not for the light that is missed due to smaller radii. This correction was not adopted here, but should be applied, once this subject has been analysed more closely. Similar to the corrections suggested for the B band and K_s band by Cameron (1990) and Nagayama et al. (2004), respectively, corrections for other bands must still be derived.

Chapter 5

Results

The primary results from applying the developed techniques are shown in this chapter. Section 5.1 consists of tables of the various galaxy properties extracted, such as galaxy brightness and size. The observed colour, the colour excess and the colour gradients of the galaxies are investigated in Section 5.2.

Establishing a method to determine accurate galaxy photometry in crowded starfields was one of the main goals of this study. Descriptions of the developed procedures are given in Chapter 3 on page 47. In accordance with these procedures, various types of information about the galaxies at hand were extracted using the methods described in Chapter 4 on page 85. This resulted in a series of principal and supplementary results, which will be outlined and discussed briefly in this chapter.

5.1 Properties of the Galaxy-Set

The main results from deriving surface brightness profiles and integrating over a given area, resulted in particular magnitudes and radii, depending on the criteria for which these values were derived. The criteria applied here are described in detail in Section 4.2 on page 91. For the *σ-Clipping* and *iPSF-Fitting* procedures, the resulting galaxy properties are listed in Tables 5.1

and 5.2 on pages 124 and 126, respectively. These are the principal results for this study. They were used to compare the developed procedures internally and with external data taken from 2MASS, as set out in Sections 3.5 and 4.5, on pages 80 and 104, respectively. The tabulated results for the *Star-Masking* and *PSF-Fitting* methods are considered to be less important and can be found in Appendix A.6 in Tables A.6 and A.7 on pages 227 and 228, respectively. For all these magnitudes, the photometric corrections described in Section 4.9 on page 116 have not been applied. For the corrected *iPSF-Fitting* magnitudes, see Table 5.9 on page 147. The surface brightness profiles for all the galaxies in the galaxy set outlined in Section 2.1 on page 31 are shown in Part II of this dissertation.

For all galaxies, the effective radii r_e and effective magnitudes μ_e were determined by fitting a de Vaucouleur $r^{1/4}$ function to the galaxy surface brightness profiles. This is described in more detail in Section 4.6 on page 110. The derived values plus their fitting errors can be found in Table 5.3 on page 129. The obtained magnitudes and colours were corrected photometrically, as described in Section 4.9 on page 116.

Furthermore, circular aperture photometry was obtained for all galaxies by making use of the *IRAF* task `phot`, as described in Section 4.3 on page 95. The derived magnitudes and colours were corrected photometrically, as described in Section 4.9 on page 116, and can be found in Table 5.5 on page 135.

It should be mentioned again, that for some double sets of galaxy measurements, the results do differ a lot, e.g. for WKK 6180, WKK 6242, WKK 6615 etc. in Table 5.3 on page 129. Possible reasons for these deviations are given in Sections 4.4 and 4.6 on pages 95 and 110, respectively.

For the *iPSF-Fitting* procedure, the apparent colours were determined according to the methods described in Section 4.8 on page 114. The colours were established for two different radii for the elliptical aperture photometry, namely the radius at which the surface brightness in the K_s band reaches the 20^{th} magnitude and the effective radius $r_{e,Ks}$ in the K_s band, as derived in

Sections 4.4 and 4.6 on pages 95 and 110, respectively. Similarly, the circular aperture photometry was obtained for a radius of 10 arcsec for the Coma cluster data and a radius of 14 arcsec or the Norma cluster (cf. Section 4.3 on page 95). All the derived colours are shown in Tables 5.4, 5.5 and 5.6 on pages 133, 135 and 137, respectively. The magnitudes and colours were corrected photometrically, as described in Section 4.9 on page 116. However, the extinction correction was not applied. The integrated magnitudes $R_{r_{Ks20}}$ for the R_c band at r_{Ks20} radius, and the integrated magnitudes $R_{r_{e,Ks}}$ and $K_{r_{e,Ks}}$ at the effective radius $r_{e,Ks}$ for the K_s band are given in the tables as well. Likewise, the circular aperture magnitudes $R_{r_{14}^{circ}}$ and $K_{r_{14}^{circ}}$ are shown. See Figures 4.15 and 4.16 on pages 114 and 115, respectively, for a demonstration of how the colours were determined from the surface brightness profiles. Similar figures for all the other galaxies are presented in Part II of this dissertation.

Total magnitudes have been derived for all galaxies with the *GALFIT* software. This program allows one to derive many parameters for galaxies, some of which are shown in Table 5.7 on page 139. All the tabulated data were derived as described in Section 4.7 on page 113, but are, however, not used for any analysis in this dissertation. The data are rather stated for reasons of completeness only. Also note that for the total magnitudes shown in Table 5.7, the photometric corrections described in Section 4.9 on page 116 have not been applied yet.

In Table 5.8 on page 143, the ellipticities and position angles are given for each galaxy. However, deriving these values was not straightforward. They were extracted from the plots as shown in Part II of this dissertation. Only rough values could be estimated, since the ellipticities as well as the position angle parameters were often kept variable during the isophote fitting. For instance, deriving the values was often based on sections where the position angle stayed roughly constant when observed radially outward. Furthermore, the numbers given here for the position angles were adjusted to a coordinate system, where 0° would point northwards and 90° points to

the east (i.e. increasing counter-clockwise) and the semi-major axis would be the pointer. Compare also with the images given for each galaxy in Part II of this dissertation, where northwards and westwards are at the top and the right side, respectively. This adjustment was necessary, because orientation of the images was only adapted to the same coordinate system after the isophote fitting had been conducted. Furthermore, for the plotting, the angles were sometimes rotated by 180°. Galaxy types for each galaxy are proposed as well and are stated in Table 5.8. These classifications are based on the shown ellipticities and on visual inspections of the galaxy, e.g. on the images presented for each galaxy in Part II of this dissertation.

Table 5.1: Magnitudes and radii obtained by applying the *σ-Clipping* procedure. For these magnitudes, the photometric corrections described in Section 4.9 on page 116 have not yet been applied. The data are sorted and displayed according to photometrically corrected K_{s20}^{corr} brightness, as derived with the *iPSF-Fitting* procedure (cf. Table 5.9 on page 147).

WKK* ident.	obs. field.†	WFI CCD‡	R_{c23} [mag]	r_{R23}§ [arcsec]	K_{s20} [mag]	r_{Ks20}§ [arcsec]
6269	01	52	10.568	83.072	7.815	65.329
	01	55	10.953	63.510		
6318	01	51	11.532	55.221	8.592	50.442
6204	01	54	11.814	40.136	8.072	37.402
6116	03	56	12.213	32.248	n.a.	n.a.
5987	03	53	12.633	26.459	7.527	38.565
	11	50	12.657	26.459		
6019	04	53	12.159	30.394	9.680	31.924
	04	52	12.266	36.030		
5972	03	53	12.043	34.582	9.517	32.248
	11	50	12.333	24.685		
5920	11	51	12.612	28.375	9.760	27.984
6360	01	57	12.595	25.903	10.031	19.007
	01	56	12.560	26.459		
6600	07	50	13.356	19.821	10.100	21.647

Table 5.1: (continued) Magnitudes and radii obtained by applying the σ-*Clipping* procedure.

WKK* ident.	obs. field.†	WFI CCD‡	R_{c23} [mag]	r_{R23}§ [arcsec]	K_{s20} [mag]	r_{Ks20}§ [arcsec]
6183	03	57	12.698	26.180	10.189	23.425
	01	53	13.137	24.202		
6180	04	50	12.419	30.085	9.902	26.134
	01	54	12.554	26.976		
6250	01	55	13.669	20.816	10.416	23.213
6679	16	52	12.773	19.411	10.141	19.411
6221	02	54	12.914	21.248	10.376	22.297
6242	01	52	13.906	16.551	10.733	18.078
	01	55	14.140	14.400		
6431	06	53	13.562	16.225	10.596	21.647
6383	01	50	13.709	22.092	10.692	22.503
6342	01	56	13.184	14.698	10.358	14.253
6012	04	54	14.014	15.308	10.817	19.597
6235	05	52	13.190	19.227	10.706	18.646
	05	53	13.385	18.290		
	01	55	13.435	17.765		
6555	06	51	14.013	17.592	10.877	18.290
6282	01	55	13.704	13.170	10.963	11.688
6229	01	53	14.693	9.124	11.523	9.293
6075	09	56	14.446	10.685	n.a.	n.a.
	03	51	14.520	10.900		
6198	05	54	13.547	15.463	10.188	17.730
6047	04	52	14.051	12.046	11.167	13.420
	03	55	14.190	12.281		
6477	06	52	14.490	11.815	11.760	10.996
6473	18	55	14.161	11.240	11.358	13.561
6233	01	52	14.679	11.020	11.794	9.293
	01	54	14.901	9.487		
	01	53	14.925	10.175		
6615	06	57	14.173	12.545	11.665	12.760
	15	50	14.350	11.462		
6620	06	57	14.669	11.240	13.006	9.020

Table 5.1: (continued) Magnitudes and radii obtained by applying the *σ-Clipping* procedure.

WKK* ident.	obs. field.†	WFI CCD‡	R_{c23} [mag]	r_{R23}§ [arcsec]	K_{s20} [mag]	r_{Ks20}§ [arcsec]
	16	54	15.814	9.595		

*Taken from Woudt (1998).

†As defined by Dr. Woudt (priv. comm.).

‡Extracted from the FITS header.

§Stated as semi-major axis length

Table 5.2: Magnitudes and radii obtained by applying the *iPSF-Fitting* procedure. For these magnitudes, the photometric corrections described in Section 4.9 on page 116 have not yet been applied. For the data with corrections applied, see Table 5.9 on page 147. The data in the table below are sorted and displayed according to K_{s20}^{corr} brightness, as derived by means of the *iPSF-Fitting* procedure (cf. Table 5.9 on page 147).

WKK* ident.	obs. field.†	WFI CCD‡	R_{c23} [mag]	r_{R23}§ [arcsec]	K_{s20} [mag]	r_{Ks20}§ [arcsec]
6269	01	52	11.416	70.145	8.302	60.332
	01	55	11.554	61.028		
6318	01	51	11.993	53.065	8.874	47.048
6204	01	54	12.576	36.384	9.249	41.754
6116	03	56	12.857	28.622	9.757	24.863
5987	03	53	13.104	25.176	9.841	26.929
	11	50	13.135	24.685		
6019	04	53	13.163	25.176	9.904	22.961
	04	52	12.941	30.394		
5972	03	53	12.975	31.656	9.918	25.629
	11	50	13.087	30.085		
5920	11	51	13.242	24.908	10.031	23.682
6360	01	57	13.139	22.793	10.131	18.826
	01	56	13.217	20.622		

Table 5.2: (continued) Magnitudes and radii obtained by applying the *iPSF-Fitting* procedure.

WKK* ident.	obs. field.†	WFI CCD‡	R_{c23} [mag]	r_{R23}§ [arcsec]	K_{s20} [mag]	r_{Ks20}§ [arcsec]
6600	07	50	13.621	19.411	10.280	18.826
6183	03	57	13.264	23.468	10.345	21.647
	01	53	13.457	22.092		
6180	04	50	13.256	26.693	10.455	19.784
	01	54	13.353	24.421		
6250	01	55	13.771	22.092	10.540	20.816
6679	16	52	13.628	18.290	10.744	14.970
6221	02	54	13.999	18.862	10.790	20.391
6242	01	52	14.063	13.590	10.849	15.746
	01	55	14.213	14.282		
6431	06	53	13.869	16.387	10.875	14.400
6383	01	50	14.180	19.411	10.917	22.503
6342	01	56	14.150	14.400	10.965	14.818
6012	04	54	14.213	14.548	11.047	15.904
6235	05	52	13.814	18.113	11.092	14.818
	05	53	14.067	16.064		
	01	55	14.026	17.251		
6555	06	51	14.275	17.251	11.109	17.387
6282	01	55	14.440	11.688	11.203	11.688
6229	01	53	14.790	8.773	11.574	8.937
6075	09	56	14.954	10.804	n.a.	n.a.
	03	51	15.047	10.175		
6198	05	54	14.669	13.990	11.800	12.519
6047	04	52	14.766	11.815	11.819	11.338
	03	55	14.878	11.462		
6477	06	52	14.639	11.240	11.837	9.949
6473	18	55	15.031	9.595	11.830	10.996
6233	01	52	14.872	10.266	11.839	9.573
	01	54	15.047	10.084		
	01	53	15.092	9.487		
6615	06	57	14.759	11.462	12.129	8.937
	15	50	14.913	11.020		

Table 5.2: (continued) Magnitudes and radii obtained by applying the *iPSF-Fitting* procedure.

WKK* ident.	obs. field.†	WFI CCD‡	R_{c23} [mag]	r_{R23}§ [arcsec]	K_{s20} [mag]	r_{Ks20}§ [arcsec]
6620	06	57	15.875	8.937	12.950	8.332
	16	54	16.019	9.020		

*Taken from Woudt (1998).

†As defined by Dr. Woudt (priv. comm.).

‡Extracted from the FITS header.

§Stated as semi-major axis length

Table 5.3: Effective surface brightness and effective radii obtained by applying the *iPSF-Fitting* procedure and fitting the resulting surface brightness profiles (cf. Section 4.6 on page 110). For these magnitudes, the photometric corrections described in Section 4.9 on page 116 have been applied. The data in the table below are sorted and displayed according to photometrically corrected K_{s20}^{corr} brightness, as derived by means of the *iPSF-Fitting* procedure (cf. Table 5.9 on page 147).

WKK* ident.	obs. field.†	WFI CCD‡	$\mu_{e,Rc}$ [mag]	$\mu_{e,Rc}^{err}$ [mag]	$r_{e,Rc}$§ [arcsec]	$r_{e,Rc}^{err}$§ [arcsec]	$\mu_{e,Ks}$ [mag]	$\mu_{e,Ks}^{err}$ [mag]	$r_{e,Ks}$§ [arcsec]	$r_{e,Ks}^{err}$§ [arcsec]
6269	01	52	22.028	0.030	57.798	0.613	18.348	0.029	30.401	0.244
	01	55	22.113	0.029	53.872	0.518				
6318	01	51	22.000	0.025	44.132	0.407	18.575	0.009	28.589	0.079
6204	01	54	21.659	0.030	26.729	0.241	19.047	0.044	26.387	0.357
6116	03	56	21.574	0.031	20.027	0.197	17.006	0.030	7.143	0.053
5987	03	53	21.360	0.035	16.740	0.166	18.738	0.034	17.142	0.174
	11	50	20.954	0.022	13.651	0.084				
6019	04	53	20.136	0.039	10.501	0.103	16.409	0.076	6.170	0.099
	04	52	20.183	0.055	13.212	0.191				
5972	03	53	21.188	0.026	19.208	0.150	17.235	0.035	9.040	0.076

Table 5.3: (continued) Effective surface brightness and effective radii obtained by applying the *iPSF-Fitting* procedure and fitting the resulting surface brightness profiles.

WKK* ident.	obs. field.†	WFI CCD‡	$\mu_{e,Rc}$ [mag]	$\mu^{err}_{e,Rc}$ [mag]	$r_{e,Rc}$§ [arcsec]	$r^{err}_{e,Rc}$§ [arcsec]	$\mu_{e,Ks}$ [mag]	$\mu^{err}_{e,Ks}$ [mag]	$r_{e,Ks}$§ [arcsec]	$r^{err}_{e,Ks}$§ [arcsec]
	11	50	21.130	0.024	17.712	0.118				
5920	11	51	21.354	0.022	17.218	0.122	17.912	0.043	10.759	0.131
6360	01	57	19.535	0.028	6.600	0.048	16.092	0.019	4.285	0.019
	01	56	19.458	0.020	6.185	0.031				
6600	07	50	19.877	0.162	6.341	0.248	18.424	0.087	11.185	0.272
6183	03	57	20.820	0.033	11.516	0.103	17.310	0.064	6.745	0.101
	01	53	21.247	0.029	13.129	0.105				
6180	04	50	22.700	0.060	33.940	0.707	18.109	0.033	9.735	0.090
	01	54	22.038	0.035	21.412	0.242				
6250	01	55	19.606	0.043	7.202	0.079	18.246	0.087	15.023	0.423
6679	16	52	20.188	0.023	7.327	0.042	17.454	0.040	6.131	0.065
6221	02	54	21.485	0.046	13.258	0.183	19.806	0.039	25.621	0.429
6242	01	52	16.835	0.067	1.743	0.018	17.114	0.041	5.981	0.061
	01	55	19.784	0.113	5.744	0.177				
6431	06	53	19.716	0.020	5.605	0.029	17.062	0.064	4.815	0.066

Table 5.3: (continued) Effective surface brightness and effective radii obtained by applying the *iPSF-Fitting* procedure and fitting the resulting surface brightness profiles.

WKK* ident.	obs. field.†	WFI CCD‡	$\mu_{e,Rc}$ [mag]	$\mu^{err}_{e,Rc}$ [mag]	$r_{e,Rc}$§ [arcsec]	$r^{err}_{e,Rc}$§ [arcsec]	$\mu_{e,Ks}$ [mag]	$\mu^{err}_{e,Ks}$ [mag]	$r_{e,Ks}$§ [arcsec]	$r^{err}_{e,Ks}$§ [arcsec]
6383	01	50	20.756	0.036	9.653	0.096	18.243	0.037	10.694	0.108
6342	01	56	19.797	0.083	5.057	0.101	16.640	0.063	3.889	0.052
6012	04	54	19.914	0.067	5.488	0.089	19.070	0.105	11.199	0.326
6235	05	52	20.994	0.031	10.322	0.095	17.694	0.070	6.047	0.107
	05	53	20.611	0.033	7.632	0.066				
	01	55	21.227	0.050	10.639	0.156				
6555	06	51	20.847	0.062	8.473	0.153	18.041	0.062	7.482	0.120
6282	01	55	19.907	0.148	4.228	0.161	17.736	0.103	5.554	0.151
6229	01	53	16.806	0.062	1.116	0.011	13.927	0.153	1.042	0.020
6075	09	56	17.225	0.163	1.575	0.044	n.a.	n.a.	n.a.	n.a.
	03	51	17.871	0.083	1.905	0.027				
6198	05	54	21.954	0.089	10.704	0.267	19.167	0.110	9.008	0.274
6047	04	52	19.821	0.101	3.966	0.082	18.492	0.110	6.440	0.194
	03	55	19.769	0.097	3.718	0.081				
6477	06	52	19.540	0.042	3.511	0.034	16.969	0.053	3.056	0.035

Table 5.3: (continued) Effective surface brightness and effective radii obtained by applying the *iPSF-Fitting* procedure and fitting the resulting surface brightness profiles.

WKK* ident.	obs. field.†	WFI CCD‡	$\mu_{e,Rc}$ [mag]	$\mu^{err}_{e,Rc}$ [mag]	$r_{e,Rc}$§ [arcsec]	$r^{err}_{e,Rc}$§ [arcsec]	$\mu_{e,Ks}$ [mag]	$\mu^{err}_{e,Ks}$ [mag]	$r_{e,Ks}$§ [arcsec]	$r^{err}_{e,Ks}$§ [arcsec]
6473	18	55	17.567	0.153	1.523	0.043	16.241	0.129	2.645	0.066
6233	01	52	18.701	0.070	2.238	0.031	16.242	0.081	2.205	0.037
	01	54	19.668	0.027	3.193	0.019				
	01	53	19.639	0.046	3.058	0.032				
6615	06	57	21.601	0.045	7.944	0.104	17.034	0.112	2.642	0.066
	15	50	23.396	0.069	18.716	0.426				
6620	06	57	18.896	0.270	2.375	0.119	14.239	0.423	1.078	0.060
	16	54	19.423	0.237	2.726	0.130				

*Taken from Woudt (1998).

†As defined by Dr. Woudt (priv. comm.).

‡Extracted from the FITS header.

§Stated as semi-major axis length.

Table 5.4: Magnitudes and colours obtained by applying the *iPSF-Fitting* procedure. For these magnitudes, all except the extinction correction of the photometric corrections described in Section 4.9 on page 116 have been applied. The data in the table below are sorted and displayed according to K_{s20}^{corr} brightness, as derived by means of the *iPSF-Fitting* procedure (cf. Table 5.9 on page 147).

WKK* ident.	obs. field.†	WFI CCD‡	R_{c23} [mag]	$R_{r_{Ks20}}$§ [mag]	K_{s20} [mag]	$(R_c - K_s)^{r_{Ks20}}$§ [mag]
6269	01	52	11.343	11.403	8.280	3.123
	01	55	11.481	11.487		3.207
6318	01	51	11.928	12.003	8.842	3.161
6204	01	54	12.506	12.446	9.223	3.223
6116	03	56	12.790	12.854	9.727	3.127
5987	03	53	13.033	13.003	9.816	3.188
	11	50	13.064	13.275		3.460
6019	04	53	13.090	13.122	9.882	3.239
	04	52	12.868	12.966		3.083
5972	03	53	12.902	13.002	9.896	3.106
	11	50	13.014	13.092		3.196
5920	11	51	13.172	13.196	10.005	3.190
6360	01	57	13.063	13.125	10.113	3.013
	01	56	13.141	13.168		3.056
6600	07	50	13.550	13.561	10.256	3.305
6183	03	57	13.189	13.222	10.325	2.897
	01	53	13.382	13.390		3.065
6180	04	50	13.186	13.354	10.429	2.926
	01	54	13.283	13.398		2.970
6250	01	55	13.696	13.715	10.521	3.193
6679	16	52	13.558	13.633	10.718	2.915
6221	02	54	13.925	13.887	10.770	3.117
6242	01	52	13.991	13.965	10.826	3.139
	01	55	14.141	14.120		3.294
6431	06	53	13.803	13.847	10.843	3.004
6383	01	50	14.107	14.057	10.895	3.162
6342	01	56	14.079	14.070	10.940	3.131

Table 5.4: (continued) Magnitudes and colours obtained by applying the *iPSF-Fitting* procedure.

WKK* ident.	obs. field.†	WFI CCD‡	R_{c23} [mag]	R_{rKs20}§ [mag]	K_{s20} [mag]	$(R_c - K_s)^{rKs20}$§ [mag]
6012	04	54	14.144	14.113	11.019	3.094
6235	05	52	13.746	13.836	11.063	2.774
	05	53	13.999	14.033		2.971
	01	55	13.958	14.030		2.968
6555	06	51	14.204	14.199	11.084	3.115
6282	01	55	14.369	14.369	11.178	3.191
6229	01	53	14.718	14.713	11.551	3.162
6075	09	56	14.882	n.a.	n.a.	n.a.
	03	51	14.975	n.a.		n.a.
6198	05	54	14.599	14.647	11.774	2.873
6047	04	52	14.693	14.708	11.797	2.912
	03	55	14.805	14.810		3.014
6477	06	52	14.571	14.615	11.808	2.808
6473	18	55	14.958	14.921	11.809	3.112
6233	01	52	14.800	14.823	11.815	3.008
	01	54	14.975	14.993		3.178
	01	53	15.020	15.017		3.202
6615	06	57	14.691	14.806	12.100	2.705
	15	50	14.845	14.942		2.841
6620	06	57	15.799	15.834	12.932	2.902
	16	54	15.943	15.977		3.045

*Taken from Woudt (1998).

†As defined by Dr. Woudt (priv. comm.).

‡Extracted from the FITS header.

§See Section 4.8 on page 114.

Table 5.5: Corrected integrated magnitudes and colours for the circular apertures obtained with the `phot` task. The average was used if more than one measurement was available from the R band data analysis. For these magnitudes, all except the extinction correction of the photometric corrections described in Section 4.9 on page 116 have been applied. The data in the table below are sorted and displayed according to K_{s20}^{corr} brightness, as derived by means of the *iPSF-Fitting* procedure (cf. Table 5.9 on page 147).

WKK* ident.	$R_{r_{14}^{circ}}$ [mag]	$K_{r_{14}^{circ}}$ [mag]	$(R_c - K_s)^{r_{14}^{circ}\dagger}$ [mag]
6269	12.295	9.079	3.216
6318	12.816	9.512	3.304
6204	12.927	9.718	3.209
6116	13.179	9.886	3.294
5987	13.319	10.113	3.206
6019	13.150	10.010	3.140
5972	13.285	10.071	3.213
5920	13.449	10.217	3.233
6360	13.242	10.152	3.090
6600	13.653	10.377	3.276
6183	13.509	10.490	3.020
6180	13.666	10.483	3.183
6250	13.742	10.541	3.200
6679	13.616	10.695	2.920
6221	13.949	10.906	3.043
6242	14.025	10.785	3.240
6431	13.817	10.740	3.077
6383	14.118	11.042	3.076
6342	14.042	10.965	3.077
6012	14.142	10.901	3.241

Table 5.5: (continued) Corrected integrated magnitudes and colours for the circular apertures obtained with the phot task.

WKK* ident.	$R_{r_{14}^{circ}}$ [mag]	$K_{r_{14}^{circ}}$ [mag]	$(R_c - K_s)^{r_{14}^{circ}}$† [mag]
6235	14.187	11.000	3.186
6555	14.212	10.994	3.217
6282	14.308	11.248	3.060
6229	14.635	11.564	3.071
6075	14.718	n.a.	n.a.
6198	14.574	11.726	2.848
6047	14.599	11.584	3.015
6477	14.491	11.811	2.680
6473	14.874	11.879	2.995
6233	14.820	11.778	3.042
6615	14.665	11.843	2.822
6620	15.627	12.942	2.685

*Taken from Woudt (1998).

†See Section 4.8 on page 114.

Table 5.6: Corrected integrated magnitudes and colours for the effective K_s band radius $r_{e,Ks}$ obtained by applying the *iPSF-Fitting* procedure. For these magnitudes, all except the extinction correction of the photometric corrections described in Section 4.9 on page 116 have been applied. The data in the table below are sorted and displayed according to K_{s20}^{corr} brightness, as derived by means of the *iPSF-Fitting* procedure (cf. Table 5.9 on page 147).

WKK* ident.	obs. field.†	WFI CCD‡	$R_{r_{e,Ks}}$ [mag]	$K_{r_{e,Ks}}$ [mag]	$(R_c - K_s)^{r_e^{Ks}}$§ [mag]
6269	01	52	11.737	8.629	3.108
	01	55	11.897		3.268
6318	01	51	12.342	9.108	3.234
6204	01	54	12.659	9.444	3.215
6116	03	56	13.622	10.289	3.333
5987	03	53	13.223	10.052	3.172
	11	50	13.241		3.190
6019	04	53	13.967	10.543	3.423
	04	52	13.767		3.223
5972	03	53	13.629	10.395	3.234
	11	50	13.714		3.319
5920	11	51	13.662	10.399	3.262
6360	01	57	13.919	10.719	3.201
	01	56	13.950		3.232
6600	07	50	13.824	10.475	3.349
6183	03	57	13.845	10.895	2.950
	01	53	14.021		3.126
6180	04	50	13.816	10.790	3.027
	01	54	13.849		3.060
6250	01	55	13.838	10.620	3.217
6679	16	52	14.125	11.236	2.889
6221	02	54	13.790	10.679	3.111
6242	01	52	14.299	11.131	3.168
	01	55	14.475		3.344
6431	06	53	14.399	11.321	3.078

Table 5.6: (continued) Corrected integrated magnitudes and colours for the effective K_s band radius $r_{e,Ks}$.

WKK* ident.	obs. field.†	WFI CCD‡	$R_{r_{e,Ks}}$ [mag]	$K_{r_{e,Ks}}$ [mag]	$(R_c - K_s)^{r_e^{Ks}}$§ [mag]
6383	01	50	14.348	11.194	3.154
6342	01	56	14.689	11.477	3.213
6012	04	54	14.300	11.163	3.137
6235	05	52	14.416	11.524	2.893
	05	53	14.595		3.072
	01	55	14.594		3.071
6555	06	51	14.662	11.481	3.181
6282	01	55	14.761	11.503	3.258
6229	01	53	16.493	13.115	3.378
6075	09	56	n.a.	n.a.	n.a.
	03	51	n.a.		n.a.
6198	05	54	14.843	11.967	2.876
6047	04	52	15.014	12.123	2.892
	03	55	15.147		3.025
6477	06	52	15.354	12.466	2.889
6473	18	55	15.715	12.609	3.106
6233	01	52	15.717	12.561	3.156
	01	54	15.922		3.361
	01	53	15.888		3.327
6615	06	57	15.579	12.801	2.777
	15	50	15.701		2.899
6620	06	57	18.184	15.248	2.936
	16	54	17.982		2.734

*Taken from Woudt (1998).

†As defined by Dr. Woudt (priv. comm.).

‡Extracted from the FITS header.

§See Section 4.8 on page 114.

Table 5.7: The *GALFIT* software was used to derive various parameters, some of which are shown here. These data would be useful for further analysis, e.g. for determining a Fundamental Plane. However, this additional analysis is not part of this dissertation and the data is only shown for reasons of completeness. The photometric corrections described in Section 4.9 on page 116 have not yet been applied. The data in the table below are sorted and displayed according to K_{s20}^{corr} brightness, as derived by means of the *iPSF-Fitting* procedure (cf. Table 5.9 on page 147).

WKK* ident.	obs. field.†	WFI CCD‡	R_c^{total} [mag]	$r_{e,Rc}^{GALFIT}$ [arcsec]	Sèrsic index $n_{s,Rc}$	K_s^{total} [mag]	$r_{e,Ks}^{GALFIT}$ [arcsec]	Sèrsic index $n_{s,Ks}$
6269	01	52	10.81	42.89	4.32	8.21	18.65	3.19
	01	55	11.11	35.93	4.04			
6318	01	51	11.51	33.69	3.07	8.51	22.16	2.98
6204	01	54	11.82	36.98	7.59	8.97	18.13	6.53
6116	03	56	12.01	32.66	6.61	9.07	17.19	6.44
5987	03	53	12.63	14.41	4.54	8.75	43.57	6.43
	11	50	12.65	14.32	4.59			
6019	04	53	12.78	13.62	3.83	9.32	15.92	5.77
	04	52	12.65	11.44	3.60			
5972	03	53	12.43	20.79	5.10	9.27	18.14	5.73

Table 5.7: (continued) Various parameters derived with the *GALFIT* software. No photometric corrections have been applied yet.

WKK* ident.	obs. field.†	WFI CCD‡	R_c^{total} [mag]	$r_{e,Rc}^{GALFIT}$ [arcsec]	Sèrsic index $n_{s,Rc}$	K_s^{total} [mag]	$r_{e,Ks}^{GALFIT}$ [arcsec]	Sèrsic index $n_{s,Ks}$
	11	50	12.54	20.12	5.03			
5920	11	51	12.43	27.72	6.20	9.07	30.44	6.98
6360	01	57	12.92	6.88	3.76	9.75	7.05	5.18
	01	56	12.96	6.75	3.92			
6600	07	50	13.28	8.42	4.73	9.93	7.61	6.23
6183	03	57	12.83	11.85	5.04	9.90	11.03	5.07
	01	53	12.95	13.14	5.15			
6180	04	50	12.46	28.07	5.32	9.78	15.28	4.75
	01	54	12.64	22.40	4.96			
6250	01	55	13.43	9.30	4.32	10.15	8.83	4.63
6679	16	52	13.20	9.12	4.92	10.11	11.84	5.89
6221	02	54	13.66	10.37	2.27	10.15	15.85	3.17
6242	01	52	13.90	4.07	2.99	10.66	3.90	4.18
	01	55	14.11	3.80	2.30			
6431	06	53	13.50	7.04	5.13	10.36	8.51	6.77
6383	01	50	13.94	6.89	2.61	10.66	7.73	2.81
6342	01	56	13.96	4.25	3.03	10.75	4.01	3.92

Table 5.7: (continued) Various parameters derived with the *GALFIT* software. No photometric corrections have been applied yet.

WKK* ident.	obs. field.†	WFI CCD‡	R_c^{total} [mag]	$r_{e,Rc}^{GALFIT}$ [arcsec]	Sèrsic index $n_{s,Rc}$	K_s^{total} [mag]	$r_{e,Ks}^{GALFIT}$ [arcsec]	Sèrsic index $n_{s,Ks}$
6012	04	54	13.91	6.52	4.19	10.85	5.05	3.97
6235	05	52	13.40	9.93	3.69	10.23	16.97	5.60
	05	53	13.56	10.20	3.79			
	01	55	13.60	9.54	3.69			
6555	06	51	13.87	8.40	4.41	10.44	13.06	6.46
6282	01	55	14.12	5.10	4.50	10.79	5.79	7.43
6229	01	53	14.72	2.41	1.84	11.50	2.24	2.35
6075	09	56	14.75	3.84	2.87			
	03	51	14.84	3.86	2.72			
6198	05	54	14.20	8.62	3.02	11.17	10.24	3.68
6047	04	52	14.48	5.29	2.96	11.44	5.72	4.03
	03	55	14.51	6.16	3.33			
6477	06	52	14.35	4.55	3.41	11.39	5.35	4.42
6473	18	55	14.84	3.24	3.10	11.29	6.99	6.34
6233	01	52	14.56	4.18	4.31	11.48	3.90	6.26
	01	54	14.82	3.67	3.32			
	01	53	14.79	3.80	4.24			

Table 5.7: (continued) Various parameters derived with the *GALFIT* software. No photometric corrections have been applied yet.

WKK* ident.	obs. field.†	WFI CCD‡	R_c^{total} [mag]	$r_{e,Rc}^{GALFIT}$ [arcsec]	Sèrsic index $n_{s,Rc}$	K_s^{total} [mag]	$r_{e,Ks}^{GALFIT}$ [arcsec]	Sèrsic index $n_{s,Ks}$
6615	06	57	14.21	7.57	4.94	11.30	9.81	7.63
	15	50	14.26	8.75	5.91			
6620	06	57	15.63	4.84	1.76	12.84	3.95	1.39
	16	54	15.78	4.49	1.73			

*Taken from Woudt (1998).

†As defined by Dr. Woudt (priv. comm.).

‡Extracted from the FITS header.

Table 5.8: Derived ellipticities and position angles for the galaxy sample. The data in the table below are sorted and displayed according to photometrically corrected K_{s20}^{corr} brightness, as derived by means of the *iPSF-Fitting* procedure (cf. Table 5.9 on page 147).

WKK* ident.	obs. field.†	WFI CCD‡	ellip. R_c§	ellip. K_s§	P.A. R_c§ [°]	P.A. K_s§ [°]	gal. type¶ class.
6269	01	# 52	0.20	0.20	−50	−50	E2 (cD)
	01	# 55	0.20		−50		E2 (cD)
6318	01	# 51	0.25	0.25	−40	−30	E3
6204	01	# 54	0.30	0.20	70	60	SO
6116	03	# 56	0.05	0.05	40	30	E0
5987	03	# 53	0.05	0.05	45	70	E0
	11	# 50	0.05		60		E0
6019	04	# 53	0.35	0.30	−50	−50	SO
	04	# 52	0.50		−50		SO
5972	03	# 53	0.30	0.30	45	45	E3
	11	# 50	0.30		45		E3
5920	11	# 51	0.10	0.15	0	5	E1
6360	01	# 57	0.20	0.20	−10	−10	E2
	01	# 56	0.20		−10		E2

Table 5.8: (continued) Derived ellipticities and position angles for the galaxy sample.

WKK* ident.	obs. field.†	WFI CCD‡	ellip. R_c§	ellip. K_s§	P.A. R_c§ [°]	P.A. K_s§ [°]	gal. type¶ class.
6600	07	# 50	0.20	0.05	−60	0	E1
6183	03	# 57	0.15	0.20	40	30	E2
	01	# 53	0.15		40		E2
6180	04	# 50	0.10	0.05	−70	−70	E0
	01	# 54	0.05		−80		E0
6250	01	# 55	0.55	0.35	25	30	SO
6679	16	# 52	0.10	0.10	−40	−50	E1
6221	02	# 54	0.20	0.20	−60	−50	E2
6242	01	# 52	0.40	0.30	−60	−60	SO
	01	# 55	0.30		−60		SO
6431	06	# 53	0.25	0.20	30	30	E2
6383	01	# 50	0.40	0.35	70	70	E4
6342	01	# 56	0.25	0.15	−20	−20	E2
6012	04	# 54	0.20	0.20	10	10	SO
6235	05	# 52	0.10	0.10	−20	−10	E1
	01	# 55	0.10		−20		E1
	05	# 53	0.10		−20		E1

Table 5.8: (continued) Derived ellipticities and position angles for the galaxy sample.

WKK* ident.	obs. field.†	WFI CCD‡	ellip. R_c§	ellip. K_s§	P.A. R_c§ [°]	P.A. K_s§ [°]	gal. type¶ class.
6555	06	# 51	0.35	0.10	−20	−20	SO
6282	01	# 55	0.10	0.10	0	40	E1
6229	01	# 53	0.15	0.15	−20	−20	E2
6075	09	# 56	0.40	n.a.	−80	n.a.	SO
	03	# 51	0.40		−80		SO
6198	05	# 54	0.05	0.05	80	90	E0
6047	04	# 52	0.15	0.10	−70	−50	E1
	03	# 55	0.15		−60		E1
6477	06	# 52	0.10	0.10	−60	−70	E1
6473	18	# 55	0.40	0.40	−50	−50	SO
6233	01	# 52	0.25	0.20	−50	−50	E3
	01	# 54	0.25		−50		E3
	01	# 53	0.25		−50		E3
6615	06	# 57	0.05	0.10	−20	−60	E0
	15	# 50	0.05		−50		E0
6620	06	# 57	0.55	0.50	30	30	SO
	16	# 54	0.55		30		SO

*Taken from Woudt (1998).

†As defined by Dr. Woudt (priv. comm.).

‡Extracted from the FITS header.

§Extracted from the plots as shown in Part II of this dissertation. Only a rough value could be estimated, since the ellipticities as well as the position angle parameters were often kept variable during the isophote fitting. For instance, deriving the values was often based on sections where the position angle stayed roughly constant when observed radially outward. Furthermore, the numbers given here for the position angles were adjusted to a coordinate system where 0° would point northwards and 90° points to the east (i.e. increasing counter-clockwise) and the semi-major axis would be the pointer. Compare also with the images given for each galaxy in Part II of this dissertation, where northwards and westwards are at the top and the right side, respectively. This adjustment was necessary, because orientation of the images was only adopted to the same coordinate system after the isophote fitting had been conducted already. Furthermore, for the plotting, the angles were sometimes rotated by 180°.

¶Determined from the stated ellipticities and by visually inspecting each galaxy.

Table 5.9: Photometrically corrected magnitudes as derived by means of the *iPSF-Fitting* procedure. For these magnitudes, the photometric corrections described in Section 4.9 on page 116 have been applied. The extinction correction was taken from Schlegel et al. (1998) and the k and evolutionary corrections from Poggianti (1997). The data are sorted and displayed according to K_{s20}^{corr} brightness.

WKK* ident.	obs. field.†	WFI CCD‡	R_{c23}^{corr} [mag]	$R_{r_{Ks20}}^{corr}$ § [mag]	K_{s20}^{corr} [mag]	$R_{r_e,Ks}^{corr}$ ¶ [mag]	$K_{r_e,Ks}^{corr}$ ¶ [mag]
6269	01	52	10.822	10.882	8.208	11.216	8.557
	01	55	10.960	10.966		11.376	
6318	01	51	11.327	11.402	8.759	11.741	9.025
6204	01	54	11.933	11.873	9.144	12.086	9.365
6116	03	56	12.209	12.273	9.647	13.041	10.209
5987	03	53	12.362	12.332	9.724	12.552	9.960
	11	50	12.393	12.604		12.570	
6019	04	53	12.500	12.532	9.801	13.377	10.462
	04	52	12.278	12.376		13.177	
5972	03	53	12.219	12.319	9.802	12.946	10.301
	11	50	12.331	12.409		13.031	
5920	11	51	12.413	12.437	9.901	12.903	10.295
6360	01	57	12.522	12.584	10.039	13.378	10.645
	01	56	12.600	12.627		13.409	
6600	07	50	12.973	12.984	10.177	13.247	10.396
6183	03	57	12.655	12.688	10.252	13.311	10.822
	01	53	12.848	12.856		13.487	
6180	04	50	12.618	12.786	10.351	13.248	10.712
	01	54	12.715	12.830		13.281	
6250	01	55	13.127	13.146	10.443	13.269	10.542
6679	16	52	12.922	12.997	10.631	13.489	11.149
6221	02	54	13.354	13.316	10.692	13.219	10.601
6242	01	52	13.461	13.435	10.753	13.769	11.058
	01	55	13.611	13.590		13.945	
6431	06	53	13.164	13.208	10.755	13.760	11.233
6383	01	50	13.512	13.462	10.813	13.753	11.112

Table 5.9: (continued) Photometrically corrected magnitudes as derived by means of the *iPSF-Fitting* procedure.

WKK* ident.	obs. field.†	WFI CCD‡	R_{c23}^{corr} [mag]	$R_{r_{Ks20}}^{corr}$ § [mag]	K_{s20}^{corr} [mag]	$R_{r_{e,Ks}}^{corr}$ ¶ [mag]	$K_{r_{e,Ks}}^{corr}$ ¶ [mag]
6342	01	56	13.549	13.540	10.867	14.159	11.404
6012	04	54	13.444	13.413	10.923	13.600	11.067
6235	05	52	13.150	13.240	10.981	13.820	11.442
	05	53	13.403	13.437		13.999	
	01	55	13.362	13.434		13.998	
6555	06	51	13.624	13.619	11.004	14.082	11.401
6282	01	55	13.845	13.845	11.106	14.237	11.431
6229	01	53	14.176	14.171	11.477	15.951	13.041
6075	09	56	14.255	n.a.	n.a.	n.a.	n.a.
	03	51	14.348	n.a.		n.a.	
6198	05	54	14.116	14.164	11.708	14.360	11.901
6047	04	52	14.103	14.118	11.716	14.424	12.042
	03	55	14.215	14.220		14.557	
6477	06	52	13.942	13.986	11.722	14.725	12.380
6473	18	55	14.379	14.342	11.730	15.136	12.530
6233	01	52	14.266	14.289	11.742	15.183	12.488
	01	54	14.441	14.459		15.388	
	01	53	14.486	14.483		15.354	
6615	06	57	14.176	14.291	12.029	15.064	12.730
	15	50	14.330	14.427		15.186	
6620	06	57	15.265	15.300	12.859	17.650	15.175
	16	54	15.409	15.443		17.448	

*Taken from Woudt (1998).

†As defined by Dr. Woudt (priv. comm.).

‡Extracted from the FITS header.

§See Section 4.8 on page 114.

¶See Section 4.6 on page 110.

5.2 Galactic Colour Excess

The observation of cluster galaxies in more than one waveband not only provides information about the galaxy, but also about the environment in which the galaxy resides, and even about the observation itself. The colour, i.e. the difference in brightness or intensity of two observations in different wavebands, can be used to measure the absorption of intermediate matter that obscures some of the light coming from the galaxy. Since this is an effect that varies with the energy of the emitted photons, the different intensities measured in two wavebands can offer insight into the amount of foreground matter. The difference of the measured fluxes of two similar objects, with one being obscured by intervening matter, is called the colour excess and is often referred to as reddening, since in general the absorption and scattering of light is stronger for shorter wavelengths.

Measuring different intensities for different wavebands can also offer insight about the kind of matter that may lie in the line of sight, e.g. by looking at absorption and emission lines. This is one of the main applications of spectra, i.e. observations over a broad waveband, so to say, rather than a narrow observation through a filter. These filters are especially designed to be only transparent to a particular kind of light, usually within a short range of photon energy. In this dissertation, the Cousins R_c band in the optical and the K_s band filter in the near infrared were used.

One can, however, only deduce correct information about the intervening matter if the emitted spectral energy distribution is known, at least for the photon energies that one intends to analyse. This is not a trivial task, not even for elliptical galaxies. The appearance of early-type galaxies can generally be modelled easily by representing them with a series of elliptical isophotes. Thus, establishing the amount of light received from an early-type galaxy in a particular waveband can be relatively effortless. In the case of spiral or irregular galaxies, this is much harder. There are, however, difficulties in determining how much light may be obscured by foreground matter.

The easiest way around this appears to be by looking at a set of elliptical

Figure 5.1: A view of the part of the Galaxy behind which the Great Attractor is suspected to lie. Clearly visible in the foreground is the band of stars, dust and gas that obscures the extragalactic sky. The investigated area is indicated by the arrow. The Galactic centre would be further to the left, just outside the borders of the image. This optical composite image was provided by Dr. Mellinger (see *http://home.arcor-online.de/axel.mellinger/* and Mellinger (2000)). The width of this image corresponds to about 70 degrees.

galaxies for which one assumes little or no intervening matter in the line of sight. Although it is not known what the amount of intergalactic extinction may be, which is caused by potentially existing intergalactic matter, it is generally assumed that one can find these galaxies, when looking at the part of the visible sky that lies far away from the Galactic Plane. Thus, a possible source for these galaxies could be the Coma cluster.

Nevertheless, another difficulty arises when looking at a series of early-type galaxies. The galaxies evolve, and they do this not only with time, and therefore with distance, but also depending on their size and the environment they inhabit (Sparkle and Gallagher, 2000). One can apply photometric corrections to account for the development of the galaxy over time, e.g. by

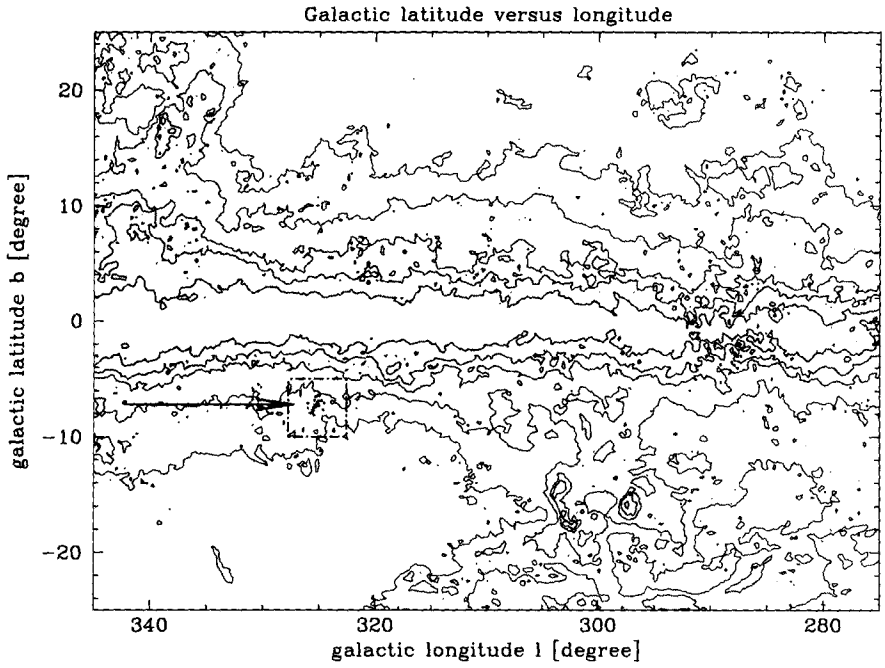

Figure 5.2: A DIRBE/IRAS dust contour plot of the Norma cluster region. The plot shows a similar part of the sky as Figure 5.1 on page 150. The shown contours are for the colour excess $E(R_c - K_s)$ of 0.4, 0.7, 1.4, 2.1 and 4.1 magnitudes, from brighter to darker lines, respectively. The rectangle indicates the size of the contour plot shown in Figure 5.3 on page 152. The positions of the investigated galaxies are indicated.

assuming a particular composition of stars (cf. Section 4.9 on page 116). However, the change of $(R_c - K_s)$ colours with size and environment, e.g. in the case of central rich cluster member or an outlying field galaxy, is not yet well known and needs some further analyses (Haines et al., 2006).

To further complicate things, elliptical galaxies often tend to show colour gradients, when the surface brightness profile is observed radially outwards. The centres are usually redder than the outer parts (Tamura and Ohta, 2004). This effect becomes more prominent for observations in the longer wavelengths, as is the case for this study. The reason for the existence of this

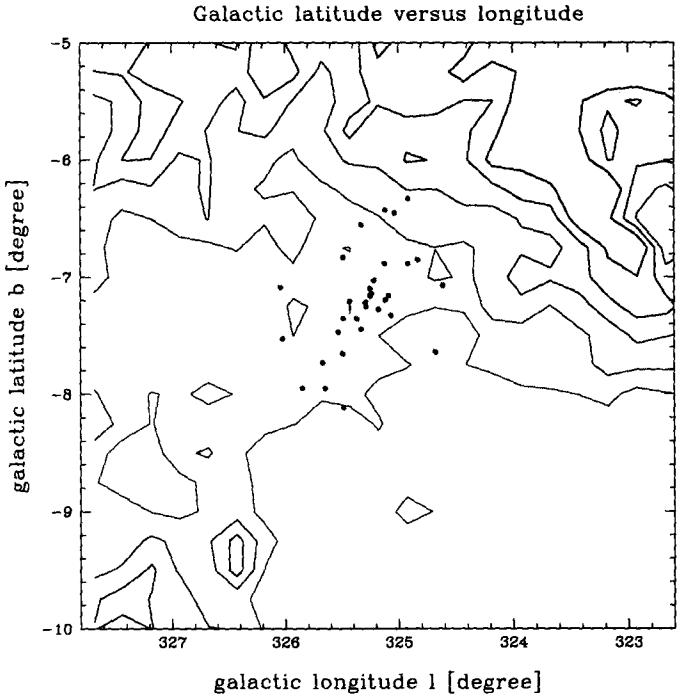

Figure 5.3: A DIRBE/IRAS dust contour plot of the Norma cluster region. The shown contours are for the colour excess $E(R_c - K_s)$ of 0.5, 0.6, 0.7, 0.8 and 0.9 magnitudes, from brighter to darker lines, respectively. The positions of the investigated galaxies are indicated. Compare also with Figure 5.2 on page 151 and the galaxy position plots of the final galaxy set as shown in Figure 2.1 on page 33 in Section 2.1.

gradient is still much debated, but the general consensus seems to be that it is caused by metallicity effects. It is further found that these gradients are dependent on the size of the galaxy (Tamura and Ohta, 2004) and they seem to be less steep for galaxies found in denser regions, like rich galaxy clusters, which is probably due the more frequently occurring galaxy mergers (Barbera et al., 2005). The colour gradient also complicates things, as proper comparisons between different data sets can only be made for similar ranges in radii for which the intensities have been determined.

In this section, the data from the Norma cluster are compared with

the data from the Coma cluster, which was generously made available by Dr. Lucey[1]. The tabulated data can be found in Appendix A.8 in Table A.10 on page 233. The photometrically corrected data, according to the corrections outlined in Section 4.9 on page 116, can be found in Table A.11 on page 241. More details about this data will be published elsewhere (Dr. Lucey, priv. comm.). The here chosen $(R_c - K_s)$ colours are ideally suited to determining the colour excess, since they are largely independent of the shape of the assumed extinction curve. Magnitudes for the Coma cluster were obtained with a fixed circular aperture with a radius of 10 arcsec, unlike the magnitudes originally obtained in this dissertation by means of elliptical apertures and varying radii. The resulting deviations in colours can be seen in Figures 5.4 and 5.5 on pages 155 and 156, respectively. The slope of the $(R_c - K_s)$ colours versus velocity dispersion σ_0 deviates slightly for the different data sets. Despite these deviations, the data could be used to estimate the Galactic foreground extinction. Nevertheless, circular aperture photometry was obtained subsequently, as described in Section 4.3 on page 95. The comparison of this data with the Coma data can be seen in Figure 5.6 on page 157.

Two functions were fitted to each data set, using the *Gnuplot* implementation of the nonlinear least-squares Marquardt-Levenberg algorithm. Note that errors in the abscissae were not taken into account, as they were an order of magnitude smaller than the corresponding errors in the ordinate. The fitted functions are

$$g(\log(\sigma_0)) = a \cdot \log(\sigma_0) + b \tag{5.1}$$

and

$$h(\log(\sigma_0)) = c\,. \tag{5.2}$$

The fitted $g(\log(\sigma_0))$ functions are indicated in the plots. For the fitting parameters a, b and c, the resulting values are given in Table 5.10 on page 158.

[1]Department of Physics, University of Durham, United Kingdom, see *http://www.dur.ac.uk/john.lucey/*

All obtained colours given in the table are for the Norma cluster, except where stated. For the fitting, the Norma cluster data was averaged over the two or three values that were obtained for some galaxies from the different WFI-CCDs (cf. Section 4.4 on page 95). Similarly, multiple measurements for the Coma cluster galaxies were averaged (cf. Appendix A.8, Tables A.10 and A.11 on pages 233 and 241, respectively).

For the Norma cluster, two fits of Equation 5.2 were conducted. The first was done for the Norma cluster corrected according to the DIRBE/IRAS extinction maps, as derived by Schlegel et al. (1998), and the second one was done without applying the correction. A comparison of these constant fits for Norma and Coma gives a first estimate of the colour excess. Comparing the colours from Coma cluster with the ones obtained when applying the extinction corrected Norma cluster, results in mean offsets of -0.011 ± 0.028 mag, -0.066 ± 0.032 mag and -0.011 ± 0.031 mag when the $(R_c - K_s)^{r_{Ks20}}$, the $(R_c - K_s)^{r_e^{Ks}}$ and the $(R_c - K_s)^{r_{14}^{circ}}$ colours are subtracted from the $(R_c - K_s)^{r_{10}^{circ}}$ colours from the Coma data, respectively. This seems to suggests a slight underestimation of the extinction in the DIRBE/IRAS dust maps.

To get a more meaningful comparison, however, four fits of Equation 5.1 were obtained for each set of data. The first two involved fitting both parameters a and b, and the second two involved keeping the slope a fixed to the value obtained for the Coma cluster, i.e. $a = 0.536$ mag/dex. For each of these two sets, one fit was obtained with regard to the data corrected according to the DIRBE/IRAS extinction maps, and the other fit was done without applying this correction. This linear fitting enables one to compare the data sets more accurately than does the constant fit with Equation 5.2, due to the connection of galaxy colours with galaxy size.

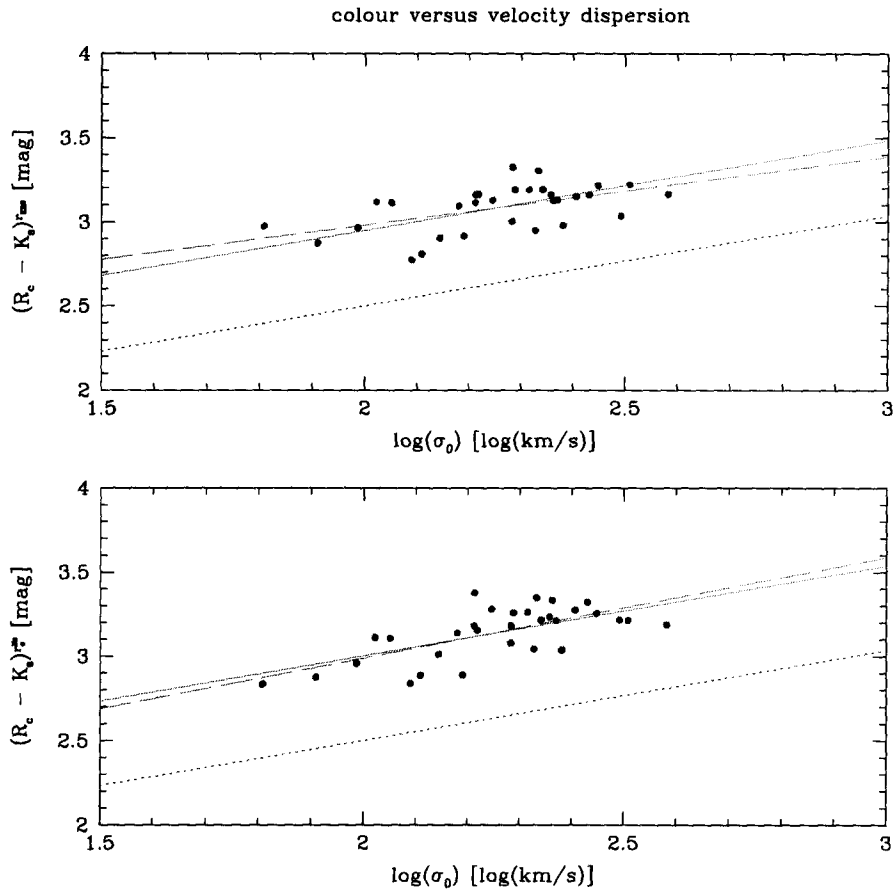

Figure 5.4: The $(R_c - K_s)^{r_{Ks20}}$ (top) and the $(R_c - K_s)^{r_e^{Ks}}$ (bottom) colours are plotted versus the central velocity dispersion σ_0. A dependency of colour with respect to central velocity dispersion, i.e. galaxy size, can be observed. The dashed lines indicate the fits of the data with Equation 5.1 and the solid lines refer to the fit of Equation 5.1 with constant slope a = 0.536, as derived for the Coma cluster data (generously provided by Dr. Lucey). The dotted lines show how the Coma cluster data fit Equation 5.1, using a circular aperture radius of 10 arcsec. See text and Table 5.10 for more detailed information.

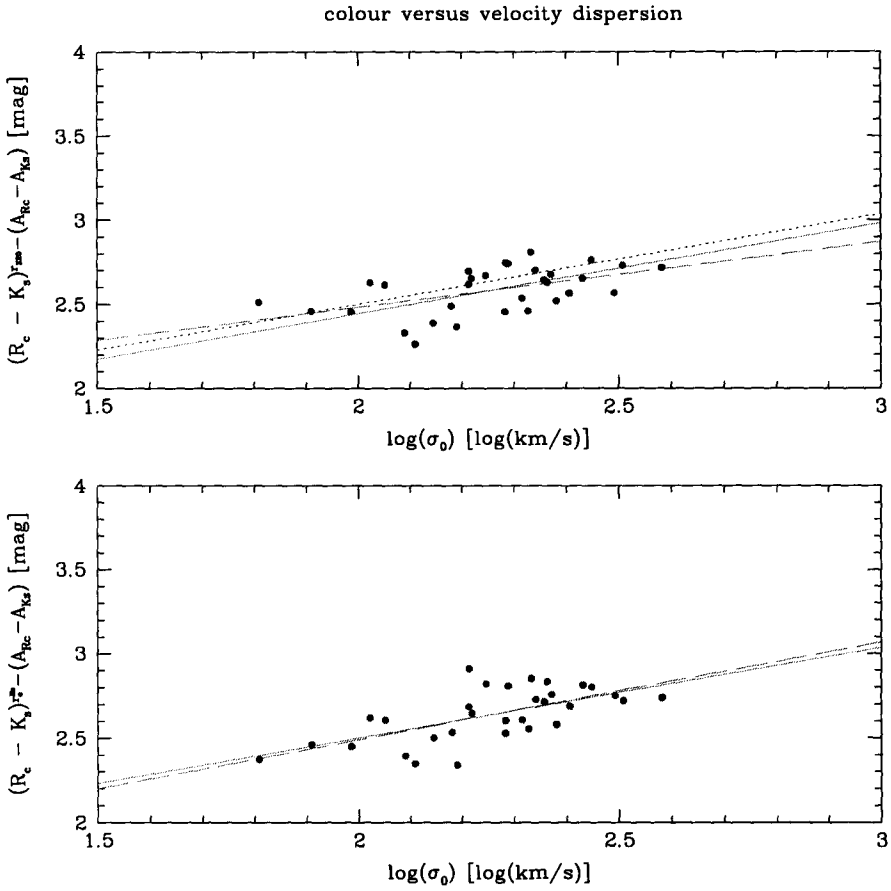

Figure 5.5: Similar plot as Figure 5.4, but with the colours corrected for the Galactic extinction as determined by the DIRBE/IRAS dust maps (Schlegel et al., 1998). The $(R_c - K_s)^{r_{Ks20}} - (A_{Rc} - A_{Ks})$ (top) and the $(R_c - K_s)^{r_e^{Ks}} - (A_{Rc} - A_{Ks})$ (bottom) colours are plotted versus the central velocity dispersion σ_0. The dashed lines indicate the fits of the data with Equation 5.1. The solid lines refer to the fit of Equation 5.1 with constant slope a = 0.536, as derived for the Coma cluster data (generously provided by Dr. Lucey). The dotted lines show how the Coma cluster data fit Equation 5.1, using a circular aperture radius of 10 arcsec, which is not necessarily comparable to the other two fits. See text and Table 5.10 for more detailed information.

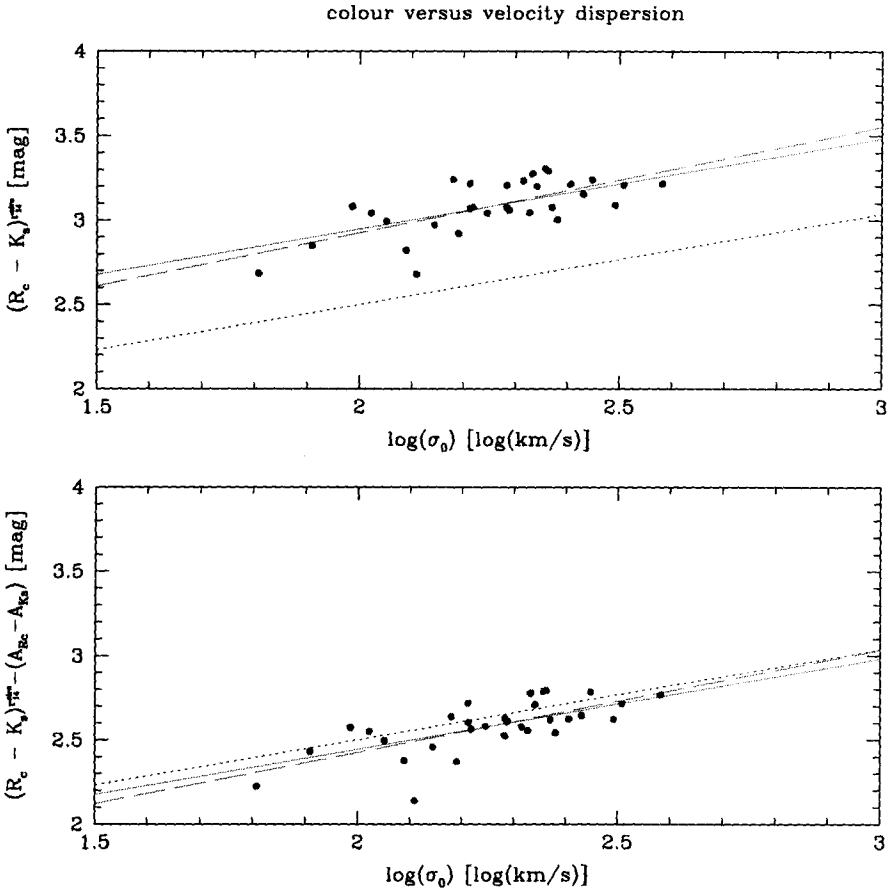

Figure 5.6: The $(R_c - K_s)^{r^{circ}_{14}}$ (top) and the $(R_c - K_s)^{r^{circ}_{14}} - (A_{Rc} - A_{Ks})$ (bottom) colours are plotted versus the central velocity dispersion σ_0 for circular aperture photometry, using a aperture radius of 14 arcsec. A dependency of colour with respect to central velocity dispersion, i.e. galaxy size, can be observed. The dashed lines indicate the fits of the data with Equation 5.1. The solid lines refer to the fit of Equation 5.1 with constant slope a = 0.536, as derived for the Coma cluster data (generously provided by Dr. Lucey). The dotted lines show how the Coma cluster data fit Equation 5.1, using a circular aperture radius of 10 arcsec. See text and Table 5.10 for more detailed information.

Table 5.10: Results from fitting of the colour versus the velocity dispersion σ_0 for the different colours obtained for the Norma and the Coma cluster. The fitted functions are given in Equations 5.1 and 5.2 on page 153 using the fitting parameters a, b and c. Numbers in brackets were kept fixed during the fit. Here, $\sigma_{\rm fit}$ is the derived root mean square of the residuals. A_{Rc} and A_{Ks} were taken from Schlegel et al. (1998). The number of galaxies used for the fitting are 31 for the Norma cluster and 73 for the Coma cluster.

fitted colour	a [mag/dex]	b [mag]	c [mag]	$\sigma_{\rm fit}$ g(log(σ_0))	$\sigma_{\rm fit}$ h(log(σ_0))
$(R_c - K_s)^{r_{Ks20}}$	0.408 ± 0.121	2.164 ± 0.273	3.084 ± 0.025	0.118	0.137
$(R_c - K_s)^{r_{Ks20}} - (A_{Rc} - A_{Ks})$	0.387 ± 0.123	1.708 ± 0.279	2.581 ± 0.025	0.121	0.137
$(R_c - K_s)^{r_{Ks20}}$	(0.536)	1.875 ± 0.021		0.119	
$(R_c - K_s)^{r_{Ks20}} - (A_{Rc} - A_{Ks})$	(0.536)	1.372 ± 0.022		0.122	
$(R_c - K_s)^{r_e^{Ks}}$	0.600 ± 0.120	1.788 ± 0.271	3.140 ± 0.028	0.117	0.157
$(R_c - K_s)^{r_e^{Ks}} - (A_{Rc} - A_{Ks})$	0.579 ± 0.126	1.331 ± 0.286	2.636 ± 0.029	0.124	0.160
$(R_c - K_s)^{r_e^{Ks}}$	(0.536)	1.930 ± 0.021		0.116	
$(R_c - K_s)^{r_e^{Ks}} - (A_{Rc} - A_{Ks})$	(0.536)	1.427 ± 0.022		0.122	

Table 5.10: (continued) Results from fitting of the colour versus the velocity dispersion σ_0 for the different colours obtained for the Norma and the Coma cluster.

fitted colour	a [mag/dex]	b [mag]	c [mag]	$\sigma_{\rm fit}$ g($\log(\sigma_0)$)	$\sigma_{\rm fit}$ h($\log(\sigma_0)$)
$(R_c - K_s)^{r_{14}^{circ}}$	0.630 ± 0.124	1.664 ± 0.281	3.084 ± 0.029	0.121	0.164
$(R_c - K_s)^{r_{14}^{circ}} - (A_{Rc} - A_{Ks})$	0.609 ± 0.116	1.207 ± 0.263	2.581 ± 0.028	0.114	0.156
$(R_c - K_s)^{r_{14}^{circ}}$	(0.536)	1.875 ± 0.022		0.121	
$(R_c - K_s)^{r_{14}^{circ}} - (A_{Rc} - A_{Ks})$	(0.536)	1.371 ± 0.020		0.113	
$(R_c - K_s)^{r_{10}^{circ}}_{Coma}$	0.536 ± 0.063	1.427 ± 0.134	2.570 ± 0.013	0.080	0.114
$(R_c - K_s)^{r_{10}^{circ}}_{Coma}$	(0.536)	1.427 ± 0.009		0.080	

The obtained offsets b for variable slopes a from Equation 5.1 on page 153 are -0.281 ± 0.310 mag, 0.096 ± 0.316 mag and 0.220 ± 0.295 mag for the $(R_c - K_s)^{r_{Ks20}}$, the $(R_c - K_s)^{r_e^{Ks}}$ and the $(R_c - K_s)^{r_{14}^{circ}}$ colours, respectively. The values scatter around zero and agree within the relatively large errors. However, with a fixed slope of a = 0.536 mag/dex, as obtained for the Coma data, the offsets are found to be 0.055 ± 0.024 mag, 0.000 ± 0.024 mag and 0.056 ± 0.022 mag for the $(R_c - K_s)^{r_{Ks20}}$, the $(R_c - K_s)^{r_e^{Ks}}$ and the $(R_c - K_s)^{r_{14}^{circ}}$ colours, respectively. In general, the circular aperture data is considered to be the most reliable for this comparison, as they were determined in a similar manner to the Coma cluster data. Therefore, a slight overestimation of the Galactic extinction by the use of the DIRBE/IRAS dust maps seems evident.

This result is supported by similar research that was conducted elsewhere (Arce and Goodman, 1999; Dutra et al., 2002; Nagayama et al., 2004). Arce and Goodman (1999), for instance, used four different methods to study the extinction towards the Taurus dark cloud complex. Their results suggest that the DIRBE/IRAS dust maps overestimate the reddening by a factor of 1.3 to 1.5 for regions with $E(B-V) > 0.15$ ($A_V > 0.5$ mag). The Norma cluster lies in a region of $E(B-V) \geq 0.2$ and the here measured average overestimation is by a factor of about 1.13 ± 0.09 (using the circular aperture colours). Similarly, Nagayama et al. (2004) were using $J - K_s$ colours of foreground giant stars to determine their extinction A_{Ks}, which they then extrapolated throughout the Galaxy. They found an overestimation of 0.4 mag of the A_{Ks} extinction by the DIRBE/IRAS dust maps, compared to their findings. Though, they did this study for a region at a Galactic latitude of $b = 1.73°$, i.e. for much higher extinction than what can be found in the Norma cluster region. Having said that, a previous attempt at determining the extinction in the Norma cluster region by Woudt (1998), using $(B_J - R_c)$ colours and Mg_2 spectral indices, found that the DIRBE/IRAS dust maps underestimate the Galactic reddening. Woudt (1998) was looking at a much

larger area of the sky, using a 18 early-type galaxies. His data[2] suggests that the DIRBE/IRAS dust maps are by 0.04 ± 0.04 mag too low. However, due to the expected fluctuations in the foreground extinction, the data obtained here seems more reliable for the comparably smaller area that was investigated. This is furthermore the case, because the here used $(R_c - K_s)$ colours are not particularly sensitive to the assumed extinction law, contrary to the $(B_J - R_c)$ colours used by Woudt (1998). Thus, the found overestimation of the Galactic reddening by the DIRBE/IRAS dust maps is most likely authentic.

However, one should note that the R_c is very broad and the reddening law used by Schlegel et al. (1998) and in this dissertation is founded upon broad-band photometry (Cardelli et al., 1989). Now, Bessel (1990) has stated that the effective wavelength shifts significantly with spectral type and Fitzpatrick (1999) has indicated that the R_c band is where monochromatic and broad-band reddening laws differ significantly, primarily because of the sensitivity of the band to effective wavelength shifts. Furthermore, the ratio of total to selective extinction used by Schlegel et al. (1998) for elliptical galaxies is too high (Dr. McCall, priv. comm.). In general, research on extinction with the DIRBE/IRAS dust maps heavily relies on the reddening law and the ratio on total to selective extinction that were assumed and differences can emerge by making different choices in this regard.

In addition to this, studies of stars in the Milky Way, such as the one of Nagayama et al. (2004), are most likely underestimating reddening toward galaxies. This is because stars usually can't be observed far enough out. Thus any colour excess measured this way ends up being a lower limit only (Dr. McCall, priv. comm.).

For the $(R_c - K_s)^{r_{Ks20}}$ and the $(R_c - K_s)^{r_e^{Ks}}$ colours, another effect may be visible. It can be seen in Table 5.10, that the standard deviation σ_{fit} of the fitting residuals has slightly increased for the Norma cluster data after the extinction correction has been applied. Although this increase seems not

[2]See Table 4.5 in Woudt (1998).

significant, it may be an indication for a variation of foreground extinction on smaller scales compared to the DIRBE/IRAS dust maps.

In view of these findings, Equation 5.1 was used in connection with the values for a and b that were determined from the Coma cluster data. The colour excess $E(R_c - K_s) = A_{Rc} - A_{Ks}$ and the extinction corrected colours $(R_c - K_s)_0 = (R_c - K_s)^{r_{14}^{circ}} - (A_{Rc} - A_{Ks})$ were calculated for all 31 galaxies in the set and are shown in Table 5.11 on page 164. However, the slope of the relation found for the Coma cluster is slightly different to the one found for the Norma cluster, though the difference is not very large and well within the errors. Also, the slope determined for the Norma cluster is very dependent on a few galaxies at low and high velocity dispersion σ_0. Nevertheless, it could cause small deviations of the colours obtained here, compared to the real colours. If found verifiable, the difference in the slope is most likely caused by the different environment in which the galaxies evolve (Barbera et al., 2005). For the circular aperture data, a larger slope was obtained for the Norma cluster than for the Coma cluster. This would indicate a less dense environment, i.e. that the Coma cluster may be higher in richness than the Norma cluster.

In Figure 5.7 on page 163, the here obtained colour excess $E(R_c - K_s)$ is compared to the colour excess obtained from the DIRBE/IRAS dust maps. The mentioned overestimation of the reddening can clearly be seen. Moreover, one can make out a patchiness in the distribution of galaxies. This is probably due to the low spatial resolution of the DIRBE/IRAS dust maps, compared to the actual size of fluctuations in the foreground matter. For a few galaxies, like WKK 6477 and WKK 6679, a strong deviation from the mean can be seen. These galaxies all lie in the WFI observing fields 06 and 16 (compare with Figure 2.4 on page 41). Assuming the correctness of these observations, it can be deduced that in this area, about one degree southeast of the adopted centre of the Norma cluster, the reddening seems much lower than suggested by the DIRBE/IRAS dust maps.

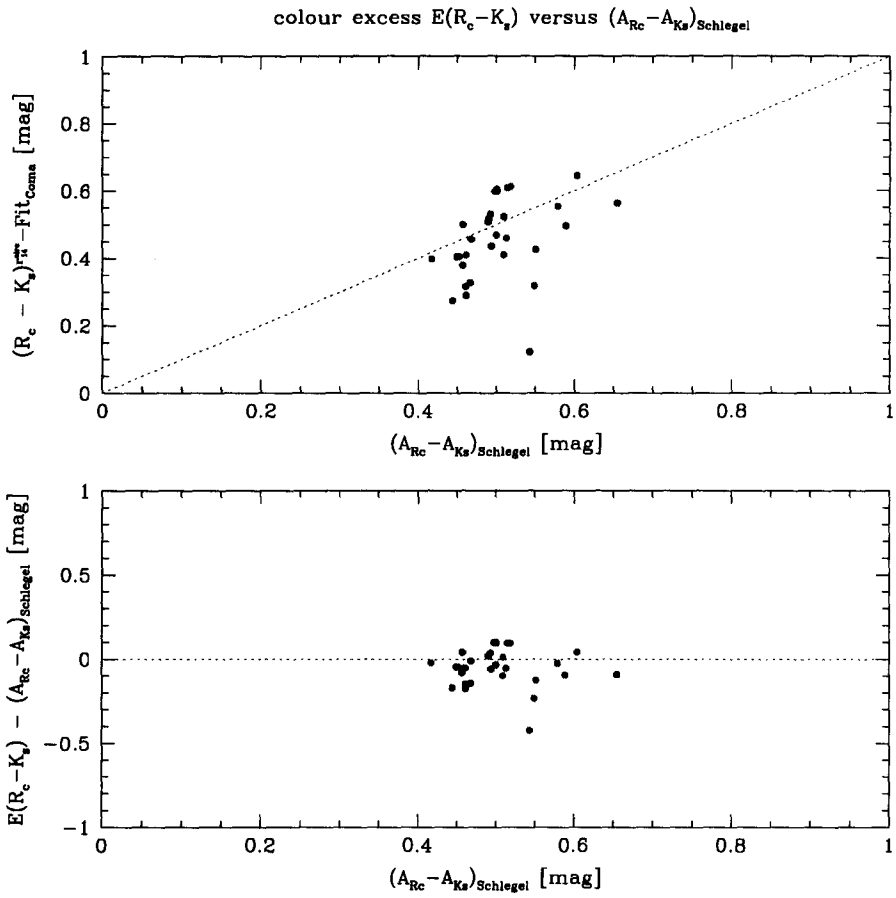

Figure 5.7: The $(R_c - K_s)^{r_{14}^{circ}}$ minus the fitted Equation 5.1 for the Coma data (generously provided by Dr. Lucey) is plotted in the top panel versus $(A_{Rc} - A_{Ks})$ from Schlegel et al. (1998). The differences between the colour excess $E(R_c - K_s)$ determined here and the $(A_{Rc} - A_{Ks})$ from Schlegel et al. (1998) versus the $(A_{Rc} - A_{Ks})$ from Schlegel et al. (1998) is shown in the bottom panel. See text for more detailed information.

Table 5.11: The colour excess and the extinction corrected integrated magnitudes and colours for the circular aperture photometry. The average was used if more than one measurement was available from the R_c band data analysis. For these magnitudes, all except the extinction correction of the photometric corrections described in Section 4.9 on page 116 have been applied. Subsequently the extinction correction obtained from external Coma data was applied, resulting in the colour excess and colour for each galaxy. The data are sorted and displayed according to K_{s20}^{corr} brightness, as derived by means of the *iPSF-Fitting* procedure (cf. Table 5.9 on page 147).

WKK* ident.	$E(R_c - K_s)$ [mag]	$(R_c - K_s)_0$ [mag]
6269	0.404	2.812
6318	0.612	2.692
6204	0.436	2.773
6116	0.599	2.695
5987	0.554	2.652
6019	0.409	2.731
5972	0.495	2.718
5920	0.563	2.669
6360	0.327	2.764
6600	0.598	2.678
6183	0.316	2.704
6180	0.508	2.675
6250	0.517	2.683
6679	0.318	2.602
6221	0.531	2.512
6242	0.500	2.740

Table 5.11: (continued) The colour excess and the extinction corrected integrated magnitudes and colours for the circular aperture photometry.

WKK* ident.	$E(R_c - K_s)$ [mag]	$(R_c - K_s)_0$ [mag]
6431	0.425	2.652
6383	0.459	2.617
6342	0.378	2.699
6012	0.645	2.596
6235	0.609	2.577
6555	0.604	2.614
6282	0.405	2.654
6229	0.456	2.614
6075	n.a.	n.a.
6198	0.397	2.451
6047	0.523	2.492
6477	0.121	2.559
6473	0.468	2.528
6233	0.410	2.632
6615	0.274	2.548
6620	0.289	2.397

*Taken from Woudt (1998).

Chapter 6

Discussion and Conclusion

This chapter discusses the findings of this study. An overview of the results is given and these are put into perspective and related to ongoing research. Furthermore, recommendations are given with regard to the practical and theoretical steps that can be taken when conducting future research in response to the outcome of this dissertation, with specific reference to the Norma cluster.

Analysing the Norma cluster region is certainly one of the most interesting subjects in the study of large-scale dynamics of galaxies. This region of the local universe is particularly interesting, because it is considered to lie close to the position of the Great Attractor, with the Norma cluster possibly playing a central role in this structure. The massive Norma cluster is most likely part of a much larger overdensity of galaxies, called the Norma Supercluster. Thus, investigating this part of the sky can offer important insights into the nearby large-scale structures in the universe. It will also hint at the possible upper limit of the sizes of large-scale structures, and is therefore important in developing cosmological models. Furthermore, the nearby position of the cluster – closer to the Milky Way than the rich Coma cluster – makes it an ideal candidate for studying galaxies in a dense cluster environment.

Studying the Norma cluster is especially interesting because of something that is generally considered a disadvantage; its position close to the Galactic

Plane forces the observer to take the foreground Milky Way into account. The observations of extragalactic objects behind our Galaxy are affected by the gas and dust in the foreground. This causes the light of the observed galaxies in the Norma cluster to be dimmed considerably. Thus, locating and analysing these galaxies is more complicated than would be the case for galaxy clusters at latitudes far away from the Milky Way. Similarly, the large number of stars that are often seen in front of a galaxy substantially influences the determination of surface brightness profiles. Both of these effects can make it impossible to determine the brightness and spectral energy distribution of a galaxy. One can partly overcome the effect of the extinction by conducting observations at longer wavelengths. However, this introduces a selection effect towards early-type galaxies, since the amount of light emitted in these wavebands is far less for the other galaxy types. Additionally, the heavy star-crowding becomes a limiting factor for observations very close to the Galactic Plane.

In this study, both above mentioned effects were investigated by looking at galaxies in the Norma cluster region. A series of different methods on how to derive accurate galaxy luminosities were developed and investigated to account particularly for the heavy star crowding (cf. Chapter 3 on page 47). Three different and often applied procedures were redefined, and the results obtained with each method were then compared. The first approach is based on the k-sigma-clipping, as implemented in the *IRAF* `ellipse` software package. A second attempt rests on applying a pixel-mask for the parts of an image that could influence the galaxy brightness profile. The last technique simulates the stars in the image by means of point spread functions to thereafter subtract these artificial stars from the original. The methods were called *σ-Clipping*, *Star-Masking* and *iPSF-Fitting*, respectively.

It was found that the *σ-Clipping* method is biased towards brighter magnitudes. This is expected, as this mechanism only clips out intensities several sigma higher than the average intensity of an isophote. Thus, the low-intensity wings of the point spread function of stars can influence the results.

In contrast, the *Star-Masking* method appears to offer quite reasonable results. However, the best results were obtained when applying the *iPSF-Fitting* method. The disadvantage of this method is, admittedly, the large effort that is involved in obtaining reasonable results, compared to the other two procedures. It is therefore recommended that the *Star-Masking* procedure could be used when much data has to be analysed in a limited amount of time. Nevertheless, this technique will certainly become increasingly imprecise the more parts of the galaxies will be masked out, for example, for very high numbers of foreground stars, as would be the case in a band of a few degrees of latitude, centred on the Milky Way. In such a case, and if very accurate photometry is needed, the *iPSF-Fitting* method seems to be more appropriate. Another situation could be the analysis of images where galaxies lie close together or even partly in front of each other. Determining reasonable values for properties such as the brightness of these galaxies can still be achieved, when using the *iPSF-Fitting* method (cf. Appendix A.4 on page 213).

The extinction in the central area of the Norma cluster was furthermore investigated (cf. Section 5.2 on page 149), and the analysis for the wavebands used in this dissertation (R_c and K_s) was found to be nontrivial. Accurate determination of $(R_c - K_s)$ colours depends on series of conditions applied to the data. Hence, a comparison with external data is difficult. The obtained results seem to suggest that the extinction maps by Schlegel et al. (1998) are reasonably good for the central Norma cluster area, except for a slight overestimation of the Galactic reddening of about a factor of 1.13 ± 0.09. Although this result may have been influenced by incompatible parameters when comparing data from different sources, like the radius for which the colours are determined, the overestimation seems nevertheless probable. Moreover, this result is in agreement with the research conducted elsewhere. Assuming the correctness of these maps for this part of the sky is not indisputable, since the DIRBE/IRAS dust maps were calibrated with data far away from the Galactic Plane. An overestimation of the extinction in these maps for

lower latitudes has been suggested before. Furthermore, due to the relatively low resolution compared to the patchiness of the dust and gas layer, the DIRBE/IRAS dust maps are considered to be accurate only when one looks at a large enough area in the sky.

The colour gradients across the radial profiles of the galaxies were confirmed, too, generally showing that galaxies tend to be redder in their centres. This is presumably an effect due to rising metallicities towards the centre of the galaxies, indicating different star populations. Dust and gas in the galaxy might also contribute to the observed effect. Another confirmed finding is that larger elliptical galaxies tend to be redder than smaller ones. Again, the exact relation is dependent on the defined set of parameters, but the trend is nevertheless notable.

The Norma cluster and its nearby large-scale structures are being closely investigated nowadays. The research of this area has a series of objectives. One is the creation of a 'complete' galaxy catalogue in several different wavebands and thus the ability to derive the luminosity function of the cluster for each of these bands. Moreover, the study of colour gradients for sets of cluster galaxies, but also for individual galaxies would be an interesting field of study, especially since the Norma cluster is a relatively close and rich cluster. However, an appropriate treatment of the foreground stars, as described in this study, is essential to obtain satisfying results. Another important goal is a redshift independent estimation of the distance of the Norma cluster. As an initial basis for such an estimate, the effective magnitudes and radii, and total magnitudes that were obtained in this dissertation could be used (cf. Sections 4.6 and 4.7 on pages 110 and 113, respectively, and Tables 5.3 and 5.7 on pages 129 and 139, respectively. Further studies in this direction could be founded on the results obtained earlier in this dissertation.

The most imminent steps from here are to automate the developed *Star-Masking* and *iPSF-Fitting* techniques as far as possible. Although much input is required from the user, some parts of the workflow could be combined into *IRAF* scripts. This seems especially important for the *iPSF-Fitting*

method. Furthermore, one should attempt to build an extended version of *iPSF-Fitting*, which could allow for the subtraction of stars in an image, thereby revealing the objects that were hidden behind the stars. Software like *SExtractor* could then be used to identify and catalogue these objects Bertin and Arnouts (1996). Another task that it is worth looking into, is to determine the Fundamental Plane of the Norma cluster. As mentioned before, the effective radii and magnitudes for about 30 galaxies have already been computed in this dissertation. Consequently, deriving a Fundamental Plane in the R_c and K_s bands is a small step from here. Finally, the complete Norma cluster region should be investigated more closely. In fact, this is very much in the works at the moment, e.g. by collecting more information about the numbers, positions and redshift distances of the galaxies in this region, which is soon to be published in an extended galaxy catalogue.

Bibliography

G. O. Abell et al. A Catalog of Rich Clusters of Galaxies. *Astrophysical Journal Supplement Series*, 70:1, 1989.

H. G. Arce and A. A. Goodman. Measuring Galactic Extinction: A Test. *Astrophysical Journal*, 512:L135–L138, 1999.

D. Baade. *Wide Field Imager User Manual.* European Southern Observatory, Garching, GER, 1.0.4 edition, May 1999. http://www.ls.eso.org/.

F. La Barbera et al. Color Gradients in Early-Type Galaxies: Dependence on Environment and Redshift, 2005. astro-ph/0504626.

R. Bender et al. Dynamically hot galaxies. ii global stellar populations. *Astrophysical Journal*, 411:153–169, 1993.

E. Bertin and S. Arnouts. SExtractor: Software for source extraction. *Astronomy and Astrophysics Supplement Series*, 117:393–404, 1996.

E. Bertschinger and A. Dekel. Recovering the full Velocity and Density Fields from Large-Scale Redshift-Distance Samples. *Astrophysical Journal*, 336: 5, 1989.

M. S. Bessel. UBVRI Passbands. *Publications of the Astronomical Society of the Pacific*, 102:1181–1199, 1990.

E. Böhm-Vitense. Extragalactic Nebulae Close to the Galactic Plane. *Publications of the Astronomical Society of the Pacific*, 68:430, 1956.

H. Böhringer et al. Abell 3627: A Nearby, X-Ray Bright, and Massive Galaxy Cluster. *Astrophysical Journal*, 467:168, 1996.

H. Böhringer et al. The ROSAT-ESO Flux Limited X-ray (REFLEX) Galaxy cluster survey. V. The cluster catalogue. *Astronomy and Astrophysics*, 425: 367–383, 2004.

D. Burstein. Line-of-Sight Reddening Predictions: Zero Points, Accuracies, the Interstellar Medium, and the Stellar Populations of Elliptical Galaxies. *Astronomical Journal*, 126:1849–1860, 2003.

D. Burstein. Using Galaxies to Determine Reddenings in the Zone of Avoidance. In A. P. Fairall and P. A. Woudt, editors, *Nearby Large-Scale Structures and the Zone of Avoidance*, volume 329 of *ASP Conference Series*, page 3, 2005.

D. Burstein and C. Heiles. Reddenings derived from HI and galaxy counts: accuracy and maps. *Astronomical Journal*, 87:1165, 1982.

D. Burstein et al. Reddenings derived from HI and galaxy counts: accuracy and maps. *Astrophysical Journal Supplement Series*, 64:601–642, 1987.

I. Busko. Error Estimation in Elliptical Isophote Fitting. In G. H. Jacoby and J. Barnes, editors, *Proceedings of the Fifth Astronomical Data Analysis Software and Systems Conference, Tucson*, volume 101 of *A.S.P. Conference Series*, pages 139–142, 1996.

R. J. Buta and M. L. McCall. The IC 342/Maffei Group Revealed. *Astrophysical Journal Supplement Series*, 124:33, 1999.

N. Caldwell et al. Star formation in early-type galaxies in the Coma cluster. *Astronomical Journal*, 106:473–492, 1993.

L. M. Cameron. The influence of aborption on galaxy diameters and magnitudes. *Astronomy and Astrophysics*, 233:16–20, 1990.

N. Caon, M. Capaccioli, and M. D'Onofrio. On the Shape of the Light Profiles of Early Type Galaxies. *Monthly Notices of the Royal Astronomical Society*, 265:1013, 1993.

J. A. Cardelli et al. The relationship between infrared, optical, and ultraviolet extinction. *Astrophysical Journal*, 345:245–256, 1989.

F. Casoli et al. A ˆ12ˆCO(1-0) survey of spiral galaxies in the region of the Coma supercluster. *Astronomy and Astrophysics Supplement Series*, 116: 193–202, 1996.

M. Colless et al. The 2dF Galaxy Redshift Survey: spectra and redshifts. *Monthly Notices of the Royal Astronomical Society*, 328:1039–1063, 2001.

R. M. Cutri et al. 2MASS All-Sky Catalog of Point Sources (Cutri+ 2003). *VizieR Online Data Catalog*, 2246, 2003.

T. M. Dame et al. A composite CO Survey of the entire Milky Way. *Astrophysical Journal*, 322:706, 1987.

Lindsey E. Davis. *A Reference Guide to the IRAF/DAOPHOT Package.* National Optical Astronomy Observatories, Tucson, USA, January 1994. http://iraf.naoo.edu/.

G. de Vaucouleur. Recherches sur les Nebuleuses Extragalactiques. *Ann. Astrophys.*, 11:247, 1948.

G. de Vaucouleur. General Physical Properties of External Galaxies. *Hand. Phys.*, 53:311, 1959.

G. de Vaucouleur et al. *Third Reference Catalogue of Bright Galaxies.* Volume 1-3, XII, 2069 pp. 7 figs.. Springer-Verlag Berlin Heidelberg New York, 1991.

A. Dekel. Dynamics of Cosmic Flows. *Annual Review of Astronomy and Astrophysics*, 32:371, 1994.

S. Djorgovski and M. Davis. Fundamental properties of elliptical galaxies. *Astrophysical Journal*, 313:59–68, February 1987.

A. Dressler. The Supergalactic Plane Redshift Survey - A Candidate for the Great Attractor. *Astrophysical Journal*, 329:519, 1988.

A. Dressler. *Voyage to the Great Attractor.* Random House Value Publishing, 1997.

A. Dressler et al. Spectroscopy and Photometry of Elliptical Galaxies - A Large-Scale Streaming Motion in the Local Universe. *Astrophysical Journal*, 313:L37–L42, 1987.

M. Drinkwater, D. G. Barnes, and S. L. Ellison. Using the Cosmos / UKST Southern Sky Object Catalogue. *Publications of the Astronomical Society of Australia*, 12:248, 1995.

A. M. Dunn and R. Laflamme. The Least-Action Method, Cold Dark Matter, and Omega. *Astrophysical Journal*, 443:L1, 1995.

C. M. Dutra, B. X. Santiago, and E. Bica. Low-Extinction Windows in the inner Galactic Bulge. *Astronomy and Astrophysics*, 381:219, 2002.

H. Ebeling, C. R. Mullis, and B. R. Tully. Closing the gap: an X-ray selected sample of clusters of galaxies behind the Galactic plane. *Bulletin of the American Astronomical Society*, 31:699, 1999.

H. Ebeling, C. R. Mullis, and R. B. Tully. CIZA - The First Systematic X-Ray Search for Clusters of Galaxies Behind the Milky Way. In *ASP Conf. Ser. 218: Mapping the Hidden Universe: The Universe behind the Mily Way - The Universe in HI*, page 79, 2000.

H. Ebeling, C. R. Mullis, and R. B. Tully. A Systematic X-Ray Search for Clusters of Galaxies behind the Milky Way. *Astrophysical Journal*, 580: 774–788, 2002.

H. Ebeling et al. The ROSAT Brightest Cluster Sample - I. The compilation of the sample and the cluster log N-log S distribution. *Monthly Notices of the Royal Astronomical Society*, 301:881–914, 1998.

H. Ebeling et al. CIZA: X-ray Selected Galaxy Clusters as Tracers of Large-Scale Structure and Streaming Motions behind the Galactic Plane. In A. P. Fairall and P. A. Woudt, editors, *Nearby Large-Scale Structures and the Zone of Avoidance*, volume 329 of *ASP Conference Series*, page 83, 2005.

A. C. Edge et al. An X-Ray Flux-Limited Sample of Clusters of Galaxies - Evidence for Evolution of the Luminosity Function. *Monthly Notices of the Royal Astronomical Society*, 245:559, 1990.

N. Epchtein, editor. *The impact of near-infrared sky surveys on galactic and extragalactic astronomy*, 1998.

N. Epchtein et al. The Deep Near-Infrared Southern Sky Survey (DENIS). *The Messenger*, 87:27–34, 1997.

P. Erdogdu et al. The 2dF Galaxy Redshift Survey: Wiener reconstruction of the cosmic web. *Monthly Notices of the Royal Astronomical Society*, 352:939–960, 2004.

S. M. Faber and R. E. Jackson. Velocity Dispersions and Mass-to-Light Ratios for Elliptical Galaxies. *Astrophysical Journal*, 204:668–683, 1976.

A. C. Fabian. X-Ray Observations in the Zone of Avoidance. In *ASP Conf. Ser. 67: Unveiling Large-Scale Structures Behind the Milky Way*, page 73, 1994.

A. P. Fairall. *Large-Scale Structures in the Universe.* John Wiley & Sons Ltd, 1998. ISBN 0-47196-253-8.

A. P. Fairall and P. A. Woudt, editors. *Nearby Large-Scale Structures and the Zone of Avoidance*, volume 329 of *ASP Conference Series*, 2005. ISBN 1-58381-192-3.

A. P. Fairall et al. Visualisations of Nearby Large-Scale Structures. In A. P. Fairall and P. A. Woudt, editors, *Nearby Large-Scale Structures and the Zone of Avoidance*, volume 329 of *ASP Conference Series*, page 225, 2005a.

A. P. Fairall et al. Percolation Properties of Nearby Large-Scale Structures: Every Galaxy has a Neighbour. In A. P. Fairall and P. A. Woudt, editors, *Nearby Large-Scale Structures and the Zone of Avoidance*, volume 329 of *ASP Conference Series*, page 229, 2005b.

K. B. Fisher et al. The IRAS 1.2 Jy Survey: Redshift Data. *Astrophysical Journal Supplement Series*, 100:69, 1995.

E. L. Fitzpatrick. Correcting for the Effects of Interstellar Extinction. *Publications of the Astronomical Society of the Pacific*, 111:63–75, 1999.

R. Giovanelli and M. P. Haynes. The Lynx-Ursa Major Supercluster. *Astronomical Journal*, 87:1355, 1982.

R. A. González et al. Total Opacity of Local Group Galaxies and Large Scale Structure behind the Galactic Bulge. In A. P. Fairall and P. A. Woudt, editors, *Nearby Large-Scale Structures and the Zone of Avoidance*, volume 329 of *ASP Conference Series*, page 103, 2005.

C. P. Haines et al. Shapley Optical Survey II: The Effect of Environment on the Colour-Magnitude Relation and Galaxy Colours. *Monthly Notices of the Royal Astronomical Society*, 376:55–66, 2006.

D. Hartmannn and W. B. Burton. *Atlas of Galactic Neutral Hydrogen.* Cambridge University Press, 1997.

P. A. Henning, R. C. Kraan-Korteweg, and L. Staveley-Smith. The HI Parkes Deep Zone of Avoidance Survey. In A. P. Fairall and P. A. Woudt, editors, *Nearby Large-Scale Structures and the Zone of Avoidance*, volume 329 of *ASP Conference Series*, page 199, 2005.

P. A. Henning et al. Galaxies discovered behind the Milky Way by the Dwingeloo Obscured Galaxies Survey. *Astronomical Journal*, 115:584, 1998.

P. A. Henning et al. The HI Parkes Zone of Avoidance Shallow Survey. *Publications of the Astronomical Society of Australia*, 16:35–7, April 1999.

P. A. Henning et al. HI-bright Galaxies in the Southern Zone of Avoidance. *Astronomical Journal*, 119:2686–2698, 2000.

J. F. W. Herschel. *Outlines of Astronomy.* Longmans, Green and Co., 5th edition edition, 1858.

J. F. W. Herschel. General Catalogue of Nebulae. Philosophial Transactions, 1864.

Y. Hoffman. Wiener Reconstruction of the Large-Scale Structure in the Zone of Avoidance. In R. C. Kraan-Korteweg C. Balkowski, editor, *Unveiling Large-Scale Structures behind the Milky Way*, volume 67 of *ASP Conference Series*, page 185, 1994.

Y. Hoffman. Reconstruction of the Zone of Avoidance. In H. Andernach R. C. Kraan-Korteweg, P.A. Henning, editor, *Mapping the Hidden Universe: The Universe Behind the Milky Way - The Universe in HI*, ASP Conference Series, 2000.

B. Hogg. The 2MASS Fundamental Plane of Nearby Elliptical Galaxies. M.sc. dissertation, University of Durham, 2001.

S. B. Howell. Two-Dimensional Aperture Photometry: Signal-to-Noise Ratio of Point-Source Observations and Optimal Data-Extraction Techniques. *Publications of the Astronomical Society of the Pacific*, 101:616–612, 1989.

E. P. Hubble. Cepheids in Spiral Nebulae. *The Observatory*, 48:139–142, 1925.

E. P. Hubble. A Relation between Distance and Radial Velocity among Extra-Galactic Nebulae. *Proceedings of the National Academy of Science*, 15:168–173, 1929.

E. P. Hubble. *The Realm of the Universe.* Yale University Press, 1936.

J. Huchra et al. The 2MASS Redshift Survey and Low Galactic Latitude Large-Scale Structure. In A. P. Fairall and P. A. Woudt, editors, *Nearby Large-Scale Structures and the Zone of Avoidance*, volume 329 of *ASP Conference Series*, page 11, 2005.

M. J. Hudson. Optical Galaxies within 8000 km s^{-1} - I. The Density Field. *Monthly Notices of the Royal Astronomical Society*, 265:43, 1993a.

M. J. Hudson. Optical Galaxies within 8000 km s^{-1} - II. The Peculiar Velocity of the Local Group. *Monthly Notices of the Royal Astronomical Society*, 265:72, 1993b.

M. J. Hudson. A test for large-scale systematic errors in maps of galactic reddening. *Publications of the Astronomical Society of the Pacific*, 111: 57–62, 1999.

K. Jahoda and R. F. Mushotzky. A search for X-ray emission associated with the great attractor. *Astrophysical Journal*, 346:638–647, 1989.

T. H. Jarrett et al. 2MASS Extended Source Catalog: Overview and Algorithms. *Astronomical Journal*, 119:2498–2531, 2000.

R. Jedrzejewski. CCD Surface Photometry of Elliptical Galaxies. I - Observations, Reduction and Results. *Monthly Notices of the Royal Astronomical Society*, 226:747, 1987.

M. Joeveer and J. Einasto. Has the Universe the Cell Structure? In M. Longair and J. Einasto, editors, *The Large-Scale Structure of the Universe*, volume 79 of *International Astonomical Union Symposium*, page 241, 1978.

D. H. Jones et al. The 6dF Galaxy Survey: samples, observational techniques and the first data release. *Monthly Notices of the Royal Astronomical Society*, 355:747–763, 2004.

D. H. Jones et al. The 6dF Galaxy Survey: First Data Release. In A. P. Fairall and P. A. Woudt, editors, *Nearby Large-Scale Structures and the Zone of Avoidance*, volume 329 of *ASP Conference Series*, page 11, 2005.

H. Jones and F. Valdes. *Handling ESO WFI Data with IRAF*. European Southern Observatory, Garching, GER, June 2000. http://www.ls.eso.org/.

I. Jørgensen, M. Franx, and P. Kjærgaard. CCD Surface Photopmetry for E and S0 Galaxies in the Coma Cluster. *Astronomy and Astrophysics Supplement Series*, 95:489–534, 1992.

W. A. Joye and E. Mandel. New Features of SAOImage DS9. In *ASP Conf. Ser. 295: Astronomical Data Analysis Software and Systems XII*, pages 489–+, 2003.

S. J. Juraszek et al. A Blind HI Survey for Galaxies in the Zone of Avoidance, 308 deg$_j$=L$_j$=332. *Astronomical Journal*, 119:1627–1637, 2000.

F. D. Kahn and L. Woltjer. Intergalactic Matter and the Galaxy. *Astrophysical Journal*, 130:705, 1959.

I. Kant. *Allgemeine Naturgeschichte und Theorie des Himmels*. Zeitz, Bei W. Webel, 1798. Neue aufl., 1798.

F. J. Kerr and P. A. Henning. Searching at 21 centimeters for galaxies behind the Milky Way. *Astrophysical Journal*, 320:L99–L103, 1987.

F. J. Kerr et al. Fully sampled neutral hydrogen survey of the Southern Milky Way. *Astronomy and Astrophysics Supplement Series*, 66:373, 1986.

D. D. Kocevski et al. The Dipole Anisotropy of the First All-Sky X-ray Cluster Sample. In A. P. Fairall and P. A. Woudt, editors, *Nearby Large-Scale Structures and the Zone of Avoidance*, volume 329 of *ASP Conference Series*, page 199, 2005.

A. Kogut et al. Dipole Anisotropy in the COBE Differential Microwave Radiometers First-Year Sky Maps. *Astrophysical Journal*, 419:1, 1993.

T. Kolatt et al. Large-Scale Mass Distribution behind the Galactic Plane. *Monthly Notices of the Royal Astronomical Society*, 275:797, 1995.

R. C. Kraan-Korteweg. Cosmological Structures behind the Milky Way. In S. Röser, editor, *From Cosmological Structures to the Milky Way*, volume 18 of *Reviews in Modern Astronomy*, page 48, 2005.

R. C. Kraan-Korteweg and T. Jarrett. The Zone of Avoidance: Optical Compared to Near-Infrared Searches. In A. P. Fairall and P. A. Woudt, editors, *Nearby Large-Scale Structures and the Zone of Avoidance*, volume 329 of *ASP Conference Series*, page 119, 2005.

R. C. Kraan-Korteweg and O. Lahav. The universe behind the milky way. *Astronomy and Astrophysics Review*, 10:211–261, 2000.

R. C. Kraan-Korteweg and P. A. Woudt. Prominent Overdensity in the Southern Milky Way. In M. Lachieze-Rey F. Bouchet, editor, *9th IAP Astrophysics Meeting on "Cosmic Velocity Fields"*, page 557, 1993.

R. C. Kraan-Korteweg and P. A. Woudt. Overview of uncovered and suspected large-scale structures behind the Milky Way. *Publications of the Astronomical Society of Australia*, 16:53–9, 1999.

R. C. Kraan-Korteweg, A. P. Fairall, and C. Balkowski. Extragalactic Large-scale structures behind the southern Milky Way.I. Redshifts obtained at the SAAO in the Hydra/Antlia extension. *Astronomy and Astrophysics*, 297:617, 1995.

R. C. Kraan-Korteweg, B. Koribalski, and S. Juraszek. Galaxies Behind the Deepest Extinction Layer of the Southern Milky Way. In *Looking Deep in the Southern Sky*, page 23, 1999.

R. C. Kraan-Korteweg et al. Discovery of a Nearby Spiral Galaxy behind the Milky Way. *Nature*, 372:77, 1994.

R. C. Kraan-Korteweg et al. A Nearby Massive Galaxy Cluster behind the Milky Way. *Nature*, 379:519, 1996.

R. C. Kraan-Korteweg et al. Large-Scale Structures Behind the Milky way from Near-Ir Surveys. In *ASSL Vol. 230: The Impact of Near-Infrared Sky Surveys on Galactic and Extragalactic Astronomy*, page 209, 1998.

R. C. Kraan-Korteweg et al. A 2 x 2 Degree I-band Survey around PKS 1343-601. In A. P. Fairall and P. A. Woudt, editors, *Nearby Large-Scale Structures and the Zone of Avoidance*, volume 329 of *ASP Conference Series*, page 119, 2005.

O. Lahav. Wiener Reconstruction of All-Sky Spherical Harmonic Maps of the Large-Scale Structure. In R. C. Kraan-Korteweg C. Balkowski, editor, *Unveiling Large-Scale Structures behind the Milky Way*, volume 67 of *ASP Conference Series*, page 171, 1994.

O. Lahav. Quantifying the Cosmic Web in the New Era of Redshift Surveys. In A. P. Fairall and P. A. Woudt, editors, *Nearby Large-Scale Structures and the Zone of Avoidance*, volume 329 of *ASP Conference Series*, page 3, 2005.

A. U. Landolt. UBVRI photometric standard stars in the magnitude range 11.5-16.0 around the celestial equator. *Astronomical Journal*, 104:340–371, 1992.

G. Lewis and M. Irwin. The Unix APM Sky Catalogues. *Spectrum, Newsletter of the Royal Observatories*, 12:22, 1996.

I. J. Lewis et al. The Anglo-Australian Observatory 2dF facility. *Monthly Notices of the Royal Astronomical Society*, 333:279–299, 2002.

N. Y. Lu et al. Identifying galaxies in the zone of avoidance. *Astrophysical Journal*, 357:388–407, 1990.

R. H. Lupton and P. Monger. *The SM Reference Manual*, 1997. http://www.astro.princeton.edu/~rhl/sm/sm.html.

D. Lynden-Bell. The Ursa Minor Dwarf Galaxy is a Member of the Magellanic Stream. *Observatory*, 102:7, 1982.

D. Lynden-Bell. Ω on the Scale of 3Mm/s. In T. Shanks et al., editors, *Observational Test of Cosmological Inflation*, page 337, 1991.

D. Lynden-Bell et al. Spectroscopy and Photometry of Elliptical Galaxies. V - Galaxy Streaming toward the new Supergalactic Center. *Astrophysical Journal*, 326:19–49, 1988.

G. A. Mamon. How Well should the DENIS Survey Probe through the Galactic Plane? In *ASP Conf. Ser. 67: Unveiling Large-Scale Structures Behind the Milky Way*, page 53, 1994.

G. A. Mamon. The Wide-Field DENIS Near-IR Imaging Survey and 6dF Redshift and Peculiar Velocity Surveys. In *Wide Field Surveys in Cosmology, 14th IAP meeting held May 26-30, 1998, Paris. Publisher: Editions Frontieres. ISBN: 2-8 6332-241-9, p. 323.*, page 323, 1998.

R. O. Marzke et al. Large-Scale Structure at Low Galactic Latitude. *Astronomical Journal*, 112:1803, 1996.

Phillip Massey and Lindsey E. Davis. *A User's Guide to Stellar CCD Photometry with IRAF*. National Optical Astronomy Observatories, April 1992. http://iraf.naoo.edu/.

J. S. Mathis. Interstellar Dust and Extinction. *Annual Review of Astronomy and Astrophysics*, 28:37, 1990.

W. B. McAdam. The core jet and relic radiation in the radio source 1343 - 601. *Publications of the Astronomical Society of Australia*, 9:255, 1991.

M. L. McCall. H II Regions, Extinction, and IC 342 - A new View of the Galactic Neighborhood. *Astronomical Journal*, 97:1341, 1989.

M. L. McCall and M.-H. Armour. Extinction of Galaxies by the Milky Way: Bringing R Out of Obscurity. In H. Andernach R. C. Kraan-Korteweg, P.A. Henning, editor, *Mapping the Hidden Universe: The Universe Behind the Milky Way - The Universe in HI*, ASP Conference Series, 2000.

A. Mellinger. Die Milchstraße im Computer. *Sterne und Weltraum*, 39:174, 2000.

C. Messier. Catalog of Nebulae and Star Clusters. Connoissance des Temps for 1784, 1781.

E. J. A. Meurs, H. M. Adorf, and R. T. Harmon. Mapping the extragalactic sky with IRAS PSC data. In *Astronomy from Large Databases*, pages 49–53, 1988.

S. A. W. Moore et al. Stellar populations in early-type Coma cluster galaxies - I. The data. *Monthly Notices of the Royal Astronomical Society*, 336:382–408, 2002.

K. R. Müller et al. Fundamental plane distances to early-type field galaxies in the South Equatorial Strip. I. The spectroscopic data. *Astronomy and Astrophysics Supplement Series*, 140:327–344, 1999.

C. R. Mullis et al. XMM-Newton Observations of CIZAJ1324.7-5736 A Massive, Newly Discovered Galaxy Cluster in the Great Attractor Region. In A. P. Fairall and P. A. Woudt, editors, *Nearby Large-Scale Structures and the Zone of Avoidance*, volume 329 of *ASP Conference Series*, page 183, 2005.

T. Nagayama et al. A deep near-infrared survey around the giant radio galaxy PKS 1343-601. *Monthly Notices of the Royal Astronomical Society*, 354:980–990, 2004.

T. Nagayama et al. Deep Near-Infrared Survey of PKS 1343-601 and CIZAJ1324.7-5736. In A. P. Fairall and P. A. Woudt, editors, *Nearby Large-Scale Structures and the Zone of Avoidance*, volume 329 of *ASP Conference Series*, page 177, 2005.

A. Naim. The Application of Artificial Neural Networks to Astronomical Classification. *Bulletin of the American Astronomical Society*, 27:1416, 1995.

F. Ochsenbein, P. Bauer, and J. Marcout. The VizieR database of astronomical catalogues. *Astronomy and Astrophysics Supplement Series*, 143: 23–32, 2000.

P. J. E. Peebles. The Gravitational Instability Picture and the Formation of the Local Group. *Astrophysical Journal*, 362:1, 1990.

C. Y. Peng et al. Detailed Structural Decomposition of Galaxy Images. *Astronomical Journal*, 124:266–293, 2002.

S. E. Persson et al. A New System of Faint Near-Infrared Standard Stars. *Astronomical Journal*, 116:2475–2488, 1998.

B. M Poggianti. K and evolutionary corrections from UV to IR. *Astronomy and Astrophysics Supplement Series*, 122:399–407, 1997.

R. A. Proctor. *The Universe of Stars*. Longmans, Green and Co., 1878.

K. Rines et al. Infrared Mass-to-Light Profile throughout the Infall Region of the Coma Cluster. *Astrophysical Journal*, 561:L41–L44, 2001.

M. Rowan-Robinson et al. The IRAS PSCz dipole. *Monthly Notices of the Royal Astronomical Society*, 314:375–397, 2000.

M. Rowin-Robinson et al. A Sparse-Sampled Redshift Survey of IRAS Galaxies - Part One - The Convergence of the IRAS Dipole and the Origin of Our Motion with Respect to the Microwave Background. *Monthly Notices of the Royal Astronomical Society*, 247:1, 1990.

V. C. Rubin and W. K. J. Ford. Rotation of the Andromeda Nebula from a Spectroscopic Survey of Emission Regions. *Astrophysical Journal*, 159: 379, 1970.

M. Saito et al. InterStellar-Cloud Formation in the Extended Envelopes of Blue Compact Dwarf Galaxies. In H. Andernach R. C. Kraan-Korteweg, P.A. Henning, editor, *Mapping the Hidden Universe: The Universe Behind the Milky Way - The Universe in HI*, ASP Conference Series, 2000.

W. Saunders et al. The Density Field of the Local Universe. *Nature*, 349:32, 1991.

W. Saunders et al. The Behind The Plane Survey. In *Mapping the Hidden Universe: The Universe Behind the Milky Way - The Universe in HI*, page 153, 2000a.

W. Saunders et al. The PSCz catalogue. *Monthly Notices of the Royal Astronomical Society*, 317:55–63, 2000b.

D. J. Schlegel et al. Maps of dust infrared emission for use in estimation of reddening and cosmic microwave background radiation foregrounds. *Astrophysical Journal*, 500:525, 1998.

I. Schmoldt et al. Likelihood analysis of the Local Group acceleration. *Monthly Notices of the Royal Astronomical Society*, 304:893–905, 1999.

A. Schröder, R. C. Kraan-Korteweg, and G. A. Mamon. Near-Infrared Determination of Large-Scale Structures in the Zone of Avoidance. In *ASP Conf. Ser. 151: Cosmic Microwave Background and Large Scale Structure of the Universe*, page 99, 1998.

A. Schröder et al. DENIS Galaxies in the Zone of Avoidance. In *Extragalactic Astronomy in the Infrared*, page 381, 1997.

A. Schröder et al. DENIS Detections of Highly Obscured Galaxies in the Area around PKS 1343 601. In A. P. Fairall and P. A. Woudt, editors, *Nearby Large-Scale Structures and the Zone of Avoidance*, volume 329 of *ASP Conference Series*, page 177, 2005.

J. Sèrsic. Atlas de Galaxias Australes Córdoba: Obs. Astronómico, 1968.

H. Shapley. A First Search for a Metagalactic Gradieni. *Harvard College Observatory Bulletin*, 894:5–13, 1934.

A. Shuttle, editor. *Philosophy for Africa.* Marquette University Press, 1995. ISBN 08-7462-6080.

Y. Sigad et al. IRAS versus POTENT Density Fields on Large Scales: Biasing Parameter and Omega. *Astrophysical Journal*, 495:516, 1998.

M. Skrutskie. The Two Micron all Sky Survey (2MASS): Status Report November 1997. In *ASSL Vol. 230: The Impact of Near-Infrared Sky Surveys on Galactic and Extragalactic Astronomy*, pages 11–+, 1998.

M. F. Skrutskie et al. The Two Micron All Sky Survey (2MASS): Overview and Status. In *ASSL Vol. 210: The Impact of Large Scale Near-IR Sky Surveys*, page 25, 1997.

R. J. Smith et al. Streaming motions of galaxy clusters within 12000km/s - I. New spectroscopic data. *Monthly Notices of the Royal Astronomical Society*, 313:469–490, 2000.

R. J. Smith et al. NOAO Fundamental Plane Survey. I. Survey Design, Redshifts, and Velocity Dispersion Data. *Astronomical Journal*, 128:1558–1569, 2004.

L. S. Sparkle and J. S. Gallagher, editors. *Galaxies in the Universe - An Introduction.* Cambridge University Press, 2000. ISBN 0-521-59740-4.

L. Staveley-Smith et al. The Parkes 21 cm Multibeam Receiver. *Publications of the Astronomical Society of Australia*, 13:243–248, November 1996.

L. Staveley-Smith et al. New H I-detected Galaxies in the Zone of Avoidance. *Astronomical Journal*, 116:2717–2727, 1998.

P. B. Stetson. On the Growth-Curve Method for Calibrating Stellar Photometry with CCDs. *Publications of the Astronomical Society of the Pacific*, 102:932–948, 1990.

M. A. Strauss et al. A redshift survey of IRAS galaxies. VII - The infrared and redshift data for the 1.936 Jansky sample. *Astrophysical Journal Supplement Series*, 83:29–63, 1992.

T. Takata, T. Yamada, and M. Saito. A Systematic Search for IRAS Galaxies behind the Milky Way. *Astrophysical Journal*, 457:693, 1996.

N. Tamura and K. Ohta. Radial Variation of Optical and Near-Infrared Colours in Luminous Early-Type Galaxies in A2199. *Monthly Notices of the Royal Astronomical Society*, 355:617–629, 2004.

T. Tamura et al. ASCA Observations of a Nearby and Massive Galaxy Cluster Abell 3627. *Publications of the Astronomical Society of Japan*, 50: 195–201, 1998.

M. Tashiro et al. Evidence of Energy Nonequipartition between Particles and Fields in Lobes of the Radio Galaxy PKS 1343-601 (Centaurus B). *Astrophysical Journal*, 499:713, May 1998.

S. Temporin et al. Gauging Dust Straight through the Milky Way: First Results of Photometry of Galaxies in the ZOA. In H. Andernach R. C. Kraan-Korteweg, P.A. Henning, editor, *Mapping the Hidden Universe: The Universe Behind the Milky Way - The Universe in HI*, ASP Conference Series, 2000.

D. Tody. The IRAF Data Reduction and Analysis System. In D. L. Crawford, editor, *Instrumentation in astronomy VI; Proceedings of the Meeting, Tucson, AZ, Mar. 4-8, 1986. Part 2 (A87-36376 15-35). Bellingham, WA, Society of Photo-Optical Instrumentation Engineers, 1986, p. 733.*, volume 627, page 733, 1986.

D. Tody. IRAF in the Nineties. In J. Barnes R. J. Hanisch, R. J. V. Brissenden, editor, *Astronomical Data Analysis Software and Systems II*, volume 52 of *ASPCS*, page 173, 1993.

J. L. Tonry et al. The Surface Brightness Fluctuation Survey of Galaxy Distances. II. Local and Large-Scale Flows. *Astrophysical Journal*, 530: 625–651, 2000.

R. B. Tully and J. R. Fisher. A new Method of Determining Distances to Galaxies. *Astronomy and Astrophysics*, 54:661–673, 1977.

M. J. Valtonen et al. A Revised History of the Local Group and a Generalized Method of Timing. *Astronomical Journal*, 105:886, 1993.

W. Voges et al. The ROSAT all-sky survey bright source catalogue. *Astronomy and Astrophysics*, 349:389–405, 1999.

R. Weinberger. Galaxies near the Northern Galactic Plane. *Astronomy and Astrophysics Supplement Series*, 40:123–127, 1980.

R. M. West and M. Tarenghi. The optical counterpart of the strong southern radio source PKS 1343-601 (13S6A). *Astronomy and Astrophysics*, 223: 61–65, 1989.

P. A. Woudt. *Large Scale Structures behind the Southern Milky Way.* Ph.D. Dissertation, University of Cape Town, June 1998.

P. A. Woudt and R. C. Kraan-Korteweg. Large-Scale Structures Behind the Southern Milky Way in the Great Attractor Region. In *ASP Conf. Ser.*

218: Mapping the Hidden Universe: The Universe behind the Mily Way - The Universe in HI, page 193, 2000.

P. A. Woudt, R. C. Kraan-Korteweg, and A. P. Fairall. Extragalactic large-scale structures behind the southern Milky Way. III. Redshifts obtained at the SAAO in the Great Attractor region. *Astronomy and Astrophysics*, 352:39–48, 1999.

P. A. Woudt, R. C. Kraan-Korteweg, and A. P. Fairall. The Core of the Great Attractor. In *ASP Conf. Ser. 201: Cosmic Flows Workshop*, page 88, 2000a.

P. A. Woudt, R. C. Kraan-Korteweg, and A. P. Fairall. The Core of the Great Attractor Unveiled. In *ASP Conf. Ser. 218: Mapping the Hidden Universe: The Universe behind the Mily Way - The Universe in HI*, page 203, 2000b.

P. A. Woudt et al. Peculiar Velocities in the Zone of Avoidance: Determining the Distance to the Norma cluster. In A. P. Fairall and P. A. Woudt, editors, *Nearby Large-Scale Structures and the Zone of Avoidance*, volume 329 of *ASP Conference Series*, page 147, 2005.

T. Yamada et al. A Search for IRAS Galaxies behind the Southern Milky Way. *Astrophysical Journal Supplement Series*, 89:57–84, 1993.

S. Zaroubi. Reconstructing the ZOA from Galaxy Peculiar Velocities. In H. Andernach R. C. Kraan-Korteweg, P. A. Henning, editor, *Mapping the Hidden Universe: The Universe Behind the Milky Way - The Universe in HI*, ASP Conference Series, 2000.

Appendix A

Tables, Plots and Images

A.1 Data Set Tables

WKK	Remark	WKK	Remark	WKK	Remark
5703	No σ_{2dF}[a]	6080	No σ_{2dF}	6512	No σ_{2dF}
5727	No σ_{2dF}	6146	No σ_{2dF}	6575	No σ_{2dF}
5742	No σ_{2dF}	6190	No σ_{2dF}	6580	No σ_{2dF}
5764	No σ_{2dF}	6201	No σ_{2dF}	6586	No σ_{2dF}
5798	No σ_{2dF}	6212	No σ_{2dF}	6724	No σ_{2dF}
5836	No σ_{2dF}	6252	No R_c band[b]	6765	No σ_{2dF}
5868	No σ_{2dF}	6298	No σ_{2dF}	6772	No σ_{2dF}
5919	No σ_{2dF}	6305	2 galaxies[c]	6808	No σ_{2dF}
5974	No σ_{2dF}	6312	No σ_{2dF}	6821	No σ_{2dF}
5975	No K_s band[d]	6313	No σ_{2dF}	6870	No σ_{2dF}
5986	No σ_{2dF}	6329	No σ_{2dF}		

[a]For this galaxy, no velocity dispersion was available from the 2dF-survey.
[b]The R_c band exposures were badly combined, Section 2.4 on page 39.
[c]Two elliptical galaxies on top of each other.
[d]The K_s band exposure shows a non-elliptical galaxy.

Table A.1: Excluded early-type galaxies from the initial galaxy set.

Table A.2: Collected information for the final galaxy set.

WKK* ident.	R.A.† [h m s]	Dec.† [° ′ ″]	gal. l† [°]	gal. b† [°]	B_J* [mag]	gal. type* class.
5920	16 07 52.68	−60 31 12.6	324.913	−6.329	14.9	E/S0
5972	16 09 16.07	−60 31 50.8	325.032	−6.453	14.8	E
5987	16 09 36.97	−60 27 20.7	325.115	−6.427	15.2	E
6012	16 10 12.15	−61 16 01.0	324.610	−7.069	15.8	E/S0
6019	16 10 17.09	−60 57 32.3	324.830	−6.851	15.1	E/S0
6047	16 10 58.93	−60 55 24.9	324.916	−6.883	16.6	E/S0
6075	16 11 32.69	−60 24 15.9	325.325	−6.553	16.7	E/S0
6116	16 12 11.55	−60 46 59.9	325.121	−6.882	14.6	E
6180	16 13 32.14	−61 00 22.6	325.085	−7.157	15.2	E/S0
6183	16 13 32.94	−60 49 23.6	325.214	−7.026	15.6	E
6198	16 13 53.04	−61 38 09.5	324.675	−7.639	16.1	E
6204	16 13 56.20	−61 00 41.1	325.117	−7.194	14.9	L
6221	16 14 02.87	−60 29 40.8	325.488	−6.831	15.6	E/S0
6229	16 14 10.42	−60 51 01.1	325.250	−7.098	16.6	E
6233	16 14 18.05	−60 53 26.0	325.234	−7.138	17.1	E
6235	16 14 22.62	−61 08 38.0	325.063	−7.326	15.6	E
6242	16 14 30.54	−60 53 46.0	325.248	−7.159	16.4	E/S0
6250	16 14 45.23	−61 01 50.6	325.175	−7.277	15.7	L

Table A.2: (continued) Collected information for final galaxy set.

WKK* ident.	R.A.† [h m s]	Dec.† [° ′ ″]	gal. l† [°]	gal. b† [°]	B_J* [mag]	gal. type* class.
6269	16 15 03.85	−60 54 26.1	325.289	−7.214	13.5	cD
6282	16 15 15.43	−60 56 15.3	325.285	−7.252	15.9	E
6318	16 15 50.16	−60 48 11.0	325.430	−7.205	13.2	E
6342	16 16 18.93	−60 57 23.6	325.364	−7.355	16.3	E/S0
6360	16 16 36.97	−61 02 45.6	325.327	−7.445	15.3	E
6383	16 17 00.36	−60 52 24.5	325.483	−7.355	15.9	L
6431	16 17 57.30	−60 55 22.9	325.531	−7.471	15.7	E/S0
6473	16 18 41.39	−60 17 37.8	326.042	−7.088	17.0	E
6477	16 18 48.60	−61 04 47.8	325.493	−7.656	16.5	E
6555	16 20 15.08	−61 00 44.9	325.666	−7.731	16.3	E/S0
6600	16 21 06.13	−60 37 08.5	326.022	−7.529	15.1	E/S0
6615	16 21 26.83	−61 24 42.5	325.481	−8.114	16.9	E/S0
6620	16 21 26.87	−61 11 06.2	325.645	−7.956	17.3	E/S0
6679	16 22 34.86	−61 02 13.9	325.848	−7.950	15.9	E

*Taken from Woudt (1998).

†Taken from the NASA/IPAC Extragalactic Database (NED); *http://nedwww.ipac.caltech.edu/.*

Table A.3: An overview of the data extracted from the optical observations related to the galaxy set described in Section 2.1 on page 31. The number of each observation field was defined by Dr. Woudt (priv. comm.) while the CCD number and the observing date were extracted from the FITS file header. The exposure time and airmass stated were calculated from FITS header information, and the FWHM was obtained with the IRAF task `imexamine`. For each galaxy, the sky brightness μ_{Rc}^{sky} was calculated as described in Section 4.1 on page 86. For observation fields that included more than one object, the calculated mean of the determined sky brightness is shown in the table.

WKK* ident.	obs. field.†	WFI CCD‡	obs. date‡	exp. time‡ [s]	airmass‡	FWHM§ [pixel]	FWHM§ [arcsec]	σ_{bg}§ [counts]	μ_{Rc}^{sky}¶ [mag/arcsec^2]
5920	11	# 51	18 May 1999	179.9188	1.3423	3.80	0.904	8.0	20.143
5972	03	# 53	18 May 1999	179.9189	1.3020	3.25	0.773	9.5	20.497
	11	# 50	18 May 1999	179.9188	1.3423	3.73	0.888	8.7	20.143
5987	03	# 53	18 May 1999	179.9189	1.3020	3.27	0.778	7.0	20.497
	11	# 50	18 May 1999	179.9188	1.3423	3.82	0.909	8.2	20.143
6012	04	# 54	18 May 1999	179.9116	1.2605	3.38	0.804	8.2	20.588

Table A.3: (continued) Observations with the WFI.

WKK* ident.	obs. field.†	WFI CCD‡	obs. date‡	exp. time‡ [s]	airmass‡	FWHM§ [pixel]	FWHM§ [arcsec]	σ_{bg}§ [counts]	μ_{Rc}^{sky}¶ [mag/arcsec^2]
6019	04	# 52	18 May 1999	179.9116	1.2605	3.28	0.781	10.6	20.588
	04	# 53	18 May 1999	179.9116	1.2605	3.36	0.800	10.3	20.588
6047	03	# 55	18 May 1999	179.9189	1.3020	4.01	0.954	9.7	20.497
	04	# 52	18 May 1999	179.9116	1.2605	3.33	0.793	7.3	20.588
6075	03	# 51	18 May 1999	179.9189	1.3020	3.50	0.833	13.2	20.497
	09	# 56	18 May 1999	179.9187	1.7350	4.44	1.057	10.5	20,014
6116	03	# 56	18 May 1999	179.9191	1.5335	3.35	0.797	6.1	20.497
6180	01	# 54	18 May 1999	179.9191	1.5335	3.07	0.731	8.7	20.311
	04	# 50	18 May 1999	179.9116	1.2605	3.30	0.785	7.2	20.588
6183	01	# 53	18 May 1999	179.9191	1.5335	3.23	0.769	7.2	20.311
	03	# 57	18 May 1999	179.9189	1.3020	3.41	0.812	8.1	20.497
6198	05	# 54	18 May 1999	179.9188	1.2394	3.55	0.845	6.9	20.642
6204	01	# 54	18 May 1999	179.9191	1.5335	2.99	0.690	6.6	20.311
6221	02	# 54	18 May 1999	179.9189	1.1721	3.22	0.766	6.7	20.610
6229	01	# 53	18 May 1999	179.9191	1.5335	3.17	0.754	8.8	20.311
6233	01	# 52	18 May 1999	179.9191	1.5335	3.26	0.776	11.8	20.311
	01	# 53	18 May 1999	179.9191	1.5335	3.19	0.759	11.3	20.311
	01	# 54	18 May 1999	179.9191	1.5335	3.92	0.933	14.5	20.311

Table A.3: (continued) Observations with the WFI.

WKK* ident.	obs. field.†	WFI CCD‡	obs. date‡	exp. time‡ [s]	airmass‡	FWHM§ [pixel]	FWHM§ [arcsec]	σ_{bg}§ [counts]	μ_{Rc}^{sky}¶ [mag/arcsec^2]
6235	01	# 55	18 May 1999	179.9191	1.5335	3.26	0.776	11.4	20.311
	05	# 52	18 May 1999	179.9188	1.2394	3.36	0.800	12.5	20.642
	05	# 53	18 May 1999	179.9188	1.2394	3.33	0.793	10.5	20.642
6242	01	# 52	18 May 1999	179.9191	1.5335	3.33	0.793	12.0	20.311
	01	# 55	18 May 1999	179.9191	1.5335	3.90	0.928	12.7	20.311
6250	01	# 55	18 May 1999	179.9191	1.5335	2.96	0.704	6.9	20.311
6269	01	# 52	18 May 1999	179.9191	1.5335	3.55	0.845	10.4	20.311
	01	# 55	18 May 1999	179.9191	1.5335	4.14	0.985	9.7	20.311
6282	01	# 55	18 May 1999	179.9191	1.5335	3.28	0.781	8.5	20.311
6318	01	# 51	18 May 1999	179.9191	1.5335	3.06	0.728	8.7	20.311
6342	01	# 52	18 May 1999	179.9191	1.5335	3.33	0.793	12.0	20.311
	01	# 56	18 May 1999	179.9191	1.5335	3.36	0.800	7.4	20.311
6360	01	# 56	18 May 1999	179.9191	1.5335	3.03	0.721	9.2	20.311
	01	# 57	18 May 1999	179.9191	1.5335	3.14	0.747	9.8	20.311
6383	01	# 50	18 May 1999	179.9191	1.5335	3.53	0.840	8.4	20.311
6431	06	# 53	18 May 1999	179.9188	1.2169	3.90	0.928	6.4	20.661
6473	18	# 55	19 May 1999	179.9187	1.1772	4.11	0.978	6.6	20.605
6477	06	# 52	18 May 1999	179.9188	1.2169	3.43	0.816	6.2	20.661

Table A.3: (continued) Observations with the WFI.

WKK* ident.	obs. field.†	WFI CCD‡	obs. date‡	exp. time‡ [s]	airmass‡	FWHM§ [pixel]	FWHM§ [arcsec]	σ_{bg}§ [counts]	μ_{Rc}^{sky}¶ [mag/arcsec^2]
6555	06	# 51	18 May 1999	179.9188	1.2169	3.41	0.812	6.6	20.661
6600	07	# 50	18 May 1999	179.9188	1.1887	3.10	0.738	6.5	20,657
6615	06	# 57	18 May 1999	179.9188	1.2169	4.38	1.042	10.0	20.661
	15	# 50	19 May 1999	179.9188	1.2431	3.48	0.828	7.0	20.558
6620	06	# 57	18 May 1999	179.9188	1.2169	3.58	0.852	6.0	20.661
	16	# 54	19 May 1999	179.9187	1.1948	3.39	0.807	6.1	20.589
6679	16	# 52	19 May 1999	179.9187	1.1948	3.36	0.800	6.8	20.589

*Taken from Woudt (1998).

†As defined by Dr. Woudt (priv. comm.).

‡Extracted and calculated from the FITS header.

§Extracted in pixels with the IRAF task `imexamine`.

¶Derived from the data, see Section 4.1 on page 86. For observation fields that included more than one object, the calculated mean is shown.

Table A.4: An overview of the data extracted from the near infrared observations related to the galaxy set described in Section 2.1 on page 31. The observing date was extracted from the FITS file header. The total exposure time is 300 seconds for each combined image and the airmass stated was calculated from FITS header information. The FWHM was obtained with the IRAF task `imexamine`. For each galaxy, the sky brightness μ_{Ks}^{sky} was calculated as described in Section 4.1 on page 86.

WKK* ident.	obs. date†	airmass†	FWHM‡ [pixel]	FWHM‡ [arcsec]	σ_{bg}‡ [counts]	μ_{Ks}^{sky}¶ [mag/arcsec^2]
5920	11 June 2000	1.229	3.25	0.943	6.7	12.895
5972	10 June 2000	1.322	3.66	1.061	7.9	12.838
5987	11 June 2000	1.213	3.37	0.977	7.4	12.879
6012	10 June 2000	1.281	3.73	1.082	6.4	12.902
6019	11 June 2000	1.205	3.30	0.957	6.7	12.851
6047	10 June 2000	1.254	3.46	1.003	6.4	12.910
6116	10 June 2000	1.233	3.71	1.076	4.5	12.934
6180	10 June 2000	1.219	3.89	1.128	5.9	12.893
6183	11 June 2000	1.178	3.22	0.934	6.5	12.840
6198	11 June 2000	1.195	3.56	1.032	7.2	12.845
6204	10 June 2000	1.178	2.54	0.737	6.3	13.026
6221	10 June 2000	1.178	3.65	1.059	4.2	13.018
6229	11 June 2000	1.222	2.90	0.841	5.3	12.893
6233	11 June 2000	1.817	3.38	0.980	6.7	12.571
6235	10 June 2000	1.195	3.77	1.073	6.3	13.020
6242	10 June 2000	1.230	3.47	1.006	5.6	12.959
6250	11 June 2000	1.277	3.26	0.945	5.7	12.816
6269	10 June 2000	1.250	3.77	1.073	6.2	12.920
6282	11 June 2000	1.306	3.21	0.931	7.0	12.791
6318	11 June 2000	1.369	3.10	0.899	5.8	12.768
6342	10 June 2000	1.331	3.58	1.038	5.5	12.887

Table A.4: (continued) Observations with SOFI.

WKK* ident.	obs. date†	airmass†	FWHM‡ [pixel]	FWHM‡ [arcsec]	σ_{bg}‡ [counts]	μ_{Ks}^{sky}¶ [mag/arcsec^2]
6360	11 June 2000	1.447	3.71	1.076	6.3	12.762
6383	11 June 2000	1.495	3.25	0.943	5.6	12.723
6431	10 June 2000	1.362	3.97	1.151	6.1	12.854
6473	11 June 2000	1.548	3.43	0.995	7.0	12.703
6477	10 June 2000	1.401	4.08	1.183	5.8	12.835
6555	10 June 2000	1.446	3.48	1.009	7.0	12.797
6600	10 June 2000	1.818	4.97	1.441	9.1	12.543
6615	11 June 2000	2.379	4.39	1.273	7.7	12.295
6620	11 June 2000	1.976	3.61	1.047	7.9	12.486
6679	10 June 2000	1.905	4.75	1.378	7.9	12.533

*Taken from Woudt (1998).

†Extracted from the FITS header.

‡Extracted with the IRAF task `imexamine`.

§Derived from the data, see Section 4.1 on page 86.

Table A.5: (continued) Data obtained with 2dF.

WKK* ident.	v_{hel}† (cz) [km/s]	v_{hel}^{err}† [km/s]	σ_0† [km/s]	σ_0^{err}† [km/s]
6600	5042	14.3	215.2	6.6
6615	4170	13.8	122.9	6.5
6620	6250	8.7	64.2	10.9
6679	4642	16.5	155.0	5.5

*Taken from Woudt (1998).

†From Dr. Lucey (priv. comm.).

A.2 R_c Standard Star Solution Plots

This section contains plots for the WFI-CCDs #52 to #57, showing the residuals (function – fit) from the standard star solution described in Section 2.5 on page 41. The plots for the WFI-CCDs #50 and #51 can be found on page 45.

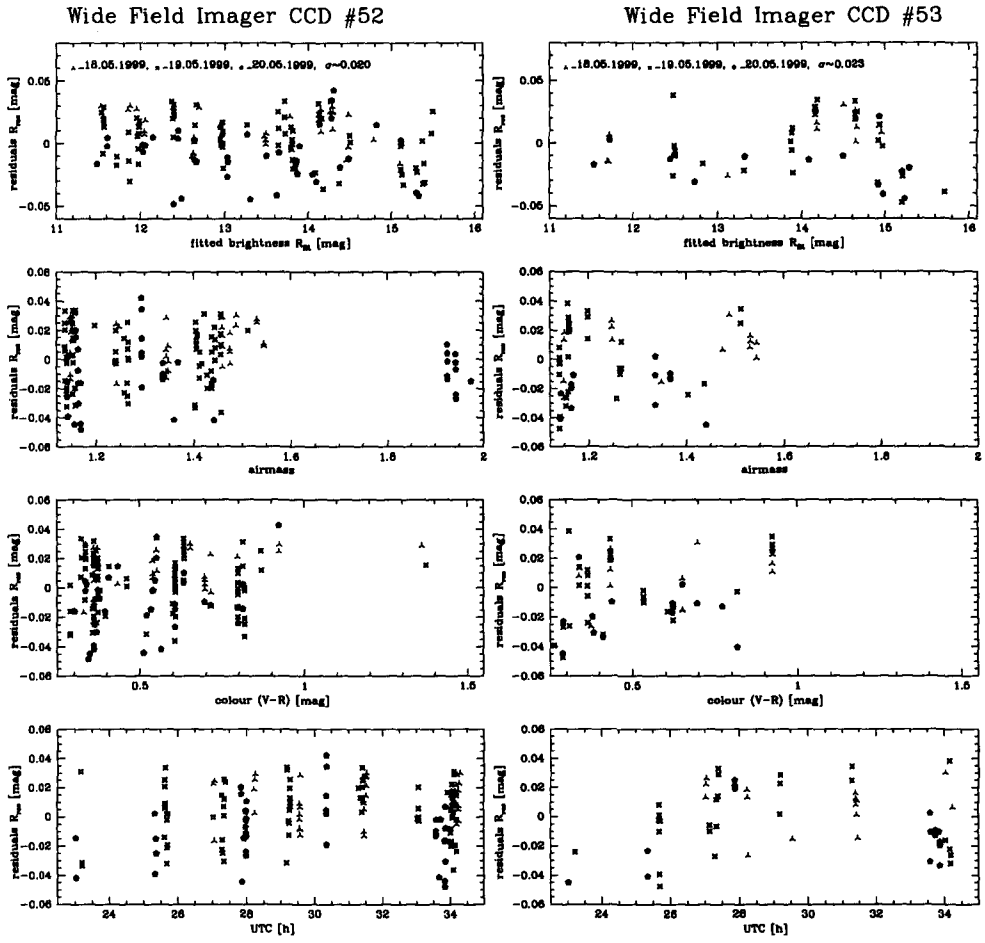

Figure A.1: Residuals (function − fit) from the R_c standard star solution for the WFI CCDs #52 and #53 as described in Section 2.5 on page 41. The residuals are shown for different standard star brightness, airmass at time of observation, colour of the standard star and observation time. The slight shift that can be seen for each day is due to the data being fitted for each night, while for the resulting function the coefficients c_{r1} and c_{r3} were averaged over all days, as described in Section 2.5 on page 41.

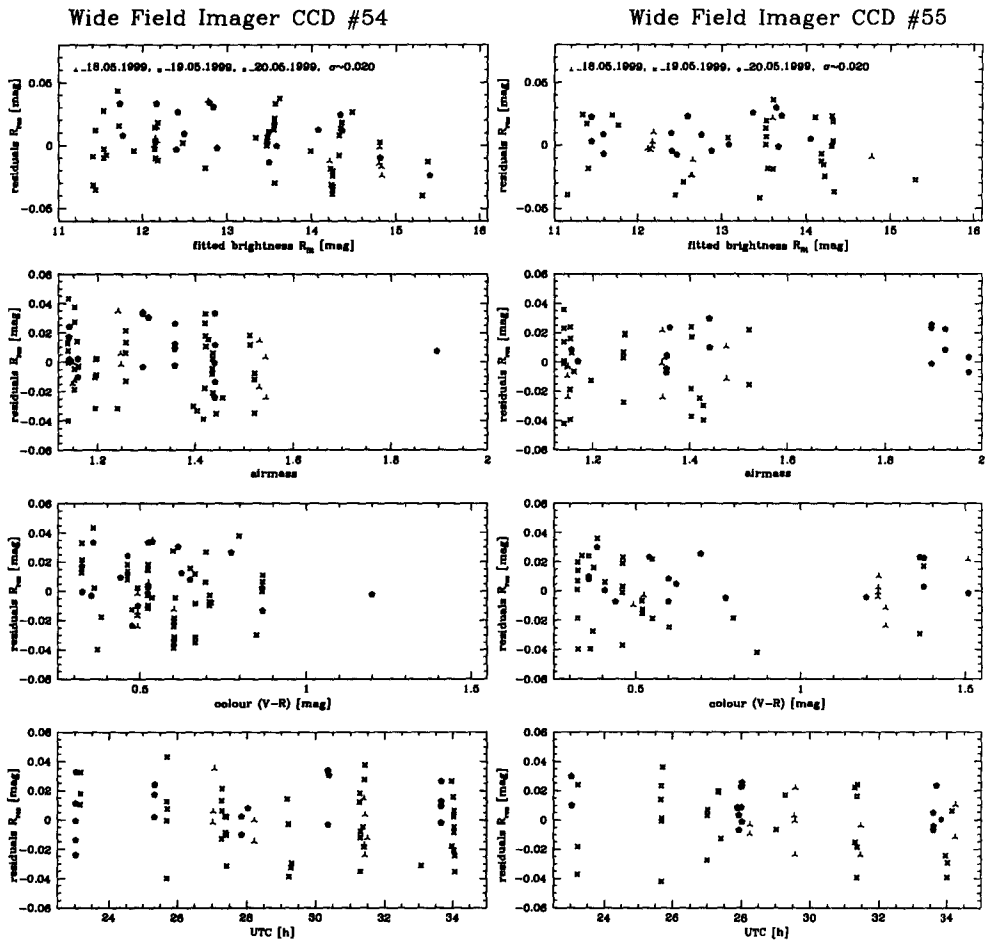

Figure A.2: Residuals (function − fit) from the R_c standard star solution for the WFI CCDs #54 and #55 as described in Section 2.5 on page 41. The residuals are shown for different standard star brightness, airmass at time of observation, colour of the standard star and observation time. The slight shift that can be seen for each day is due to the data being fitted for each night, while for the resulting function the coefficients c_{r1} and c_{r3} were averaged over all days, as described in Section 2.5 on page 41.

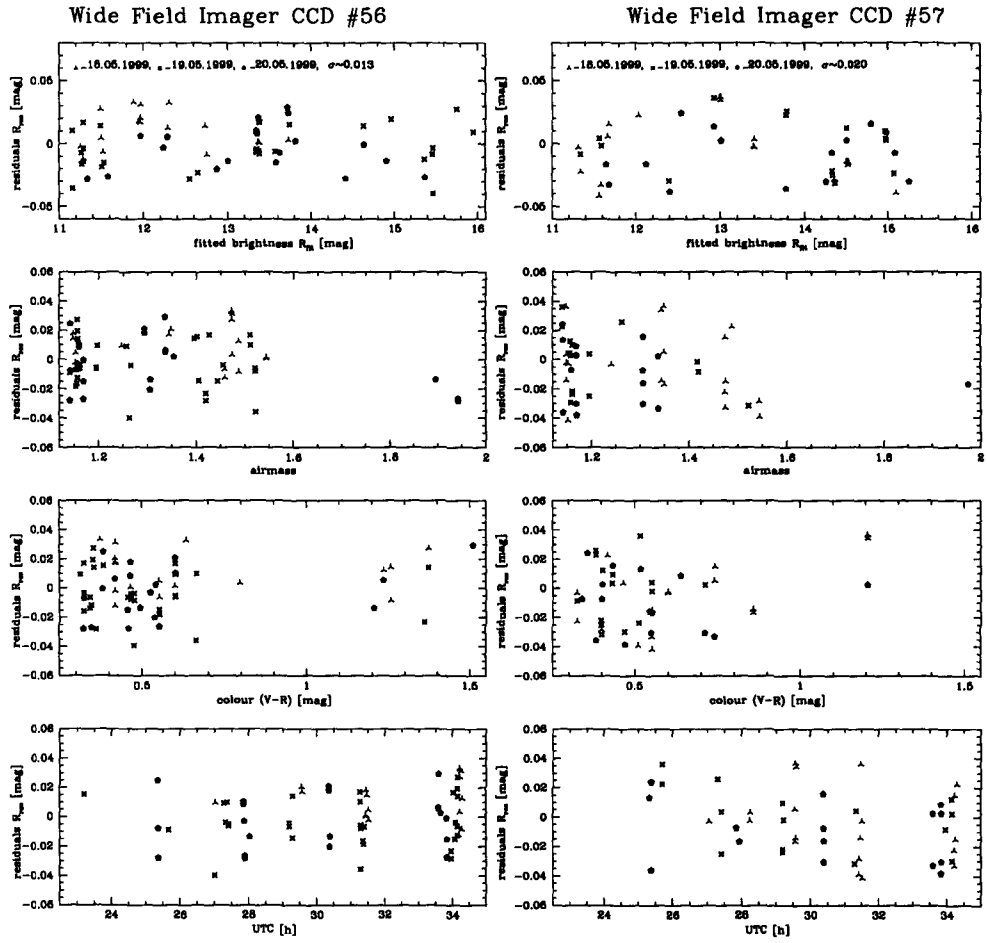

Figure A.3: Residuals (function − fit) from the R_c standard star solution for the WFI CCDs #56 and #57 as described in Section 2.5 on page 41. The residuals are shown for different standard star brightness, airmass at time of observation, colour of the standard star and observation time. The slight shift that can be seen for each day is due to the data being fitted for each night, while for the resulting function the coefficients c_{r1} and c_{r3} were averaged over all days, as described in Section 2.5 on page 41.

A.3 Background-Fitting Plots

The background-fitting results mentioned in Section 4.1 on page 86 are shown in this section. The outer parts of the galaxy profiles are shown as well as the two functions that fitted the profile best.

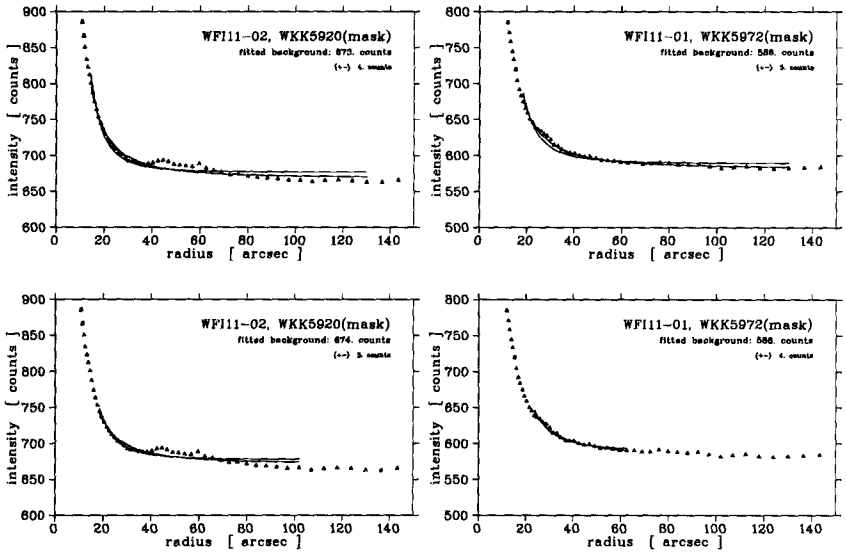

Figure A.4: Galaxies WKK 5920 and WKK 5972, WFI background-fits as described in Section 4.1 on page 86.

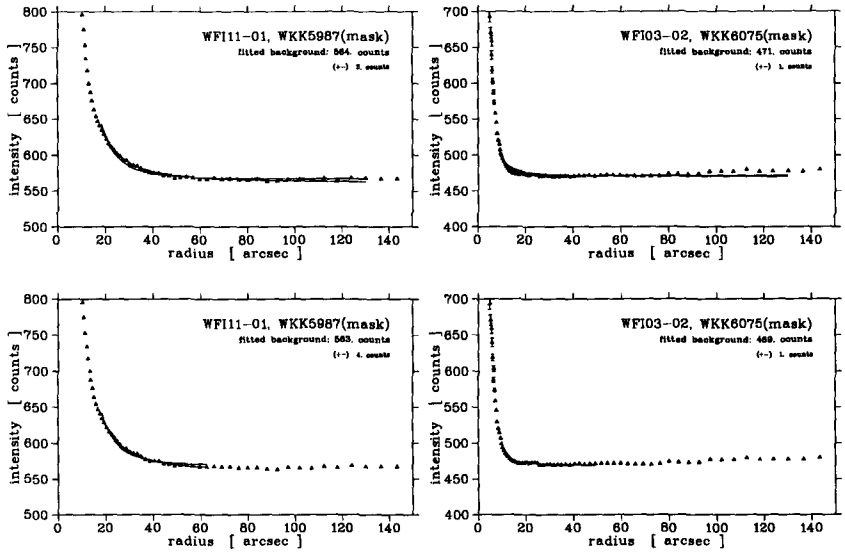

Figure A.5: Galaxies WKK 5987 and WKK 6075, WFI background-fits as described in Section 4.1 on page 86.

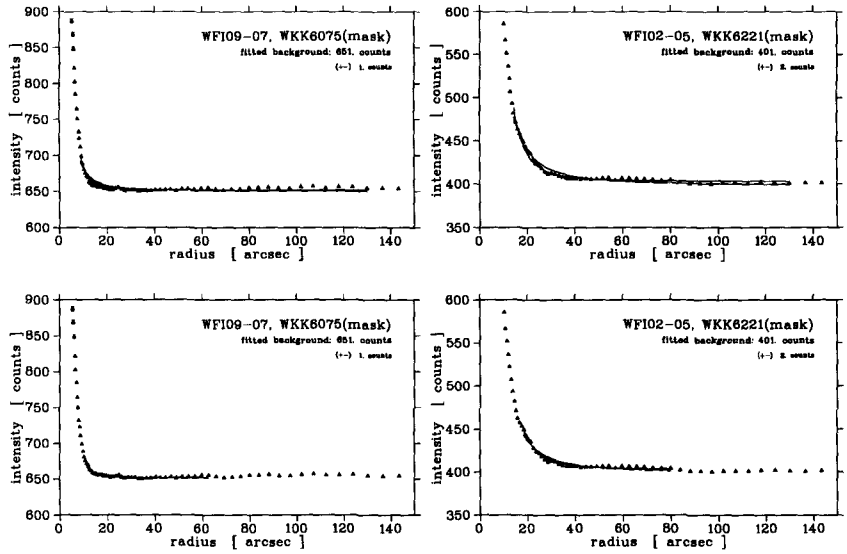

Figure A.6: Galaxies WKK 6075 and WKK 6221, WFI background-fits as described in Section 4.1 on page 86.

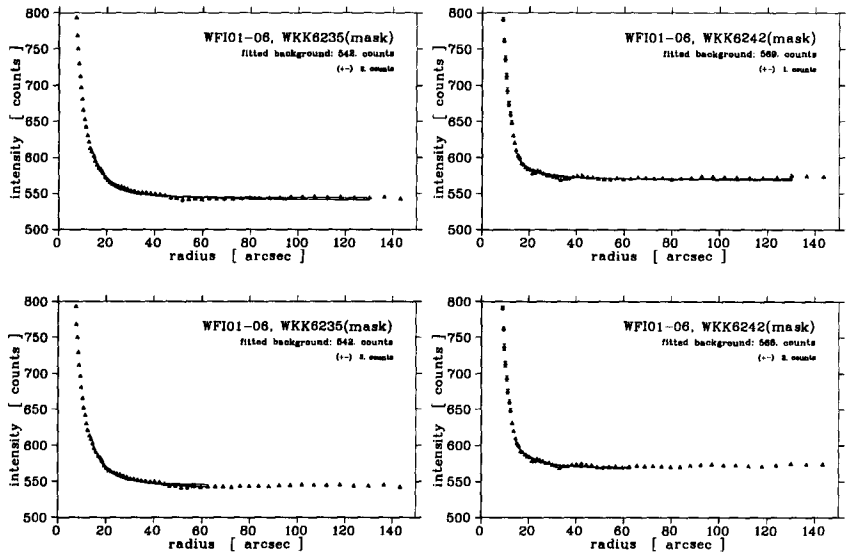

Figure A.7: Galaxies WKK 6235 and WKK 6242, WFI background-fits as described in Section 4.1 on page 86.

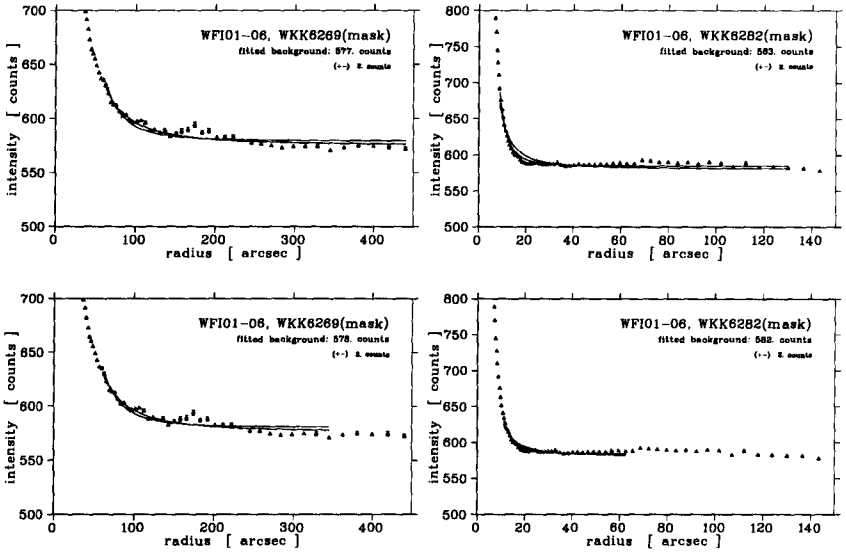

Figure A.8: Galaxies WKK 6269 and WKK 6282, WFI background-fits as described in Section 4.1 on page 86.

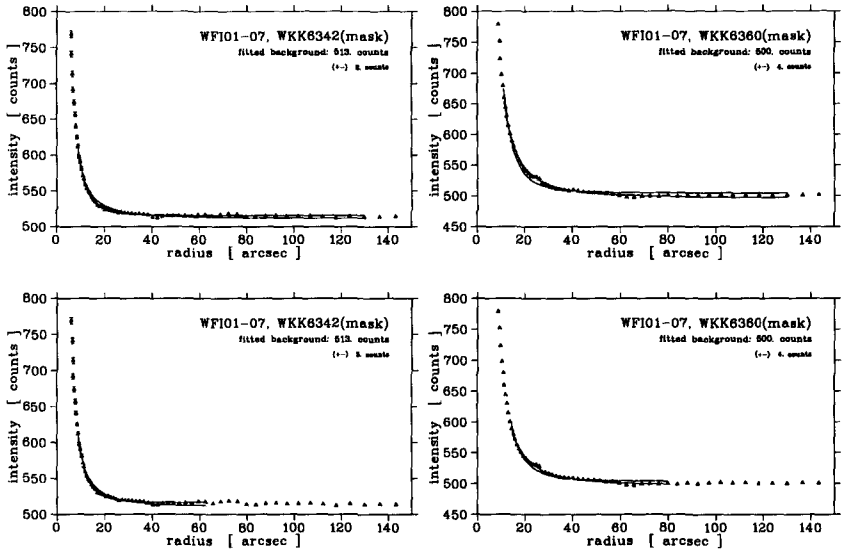

Figure A.9: Galaxies WKK 6342 and WKK 6360, WFI background-fits as described in Section 4.1 on page 86.

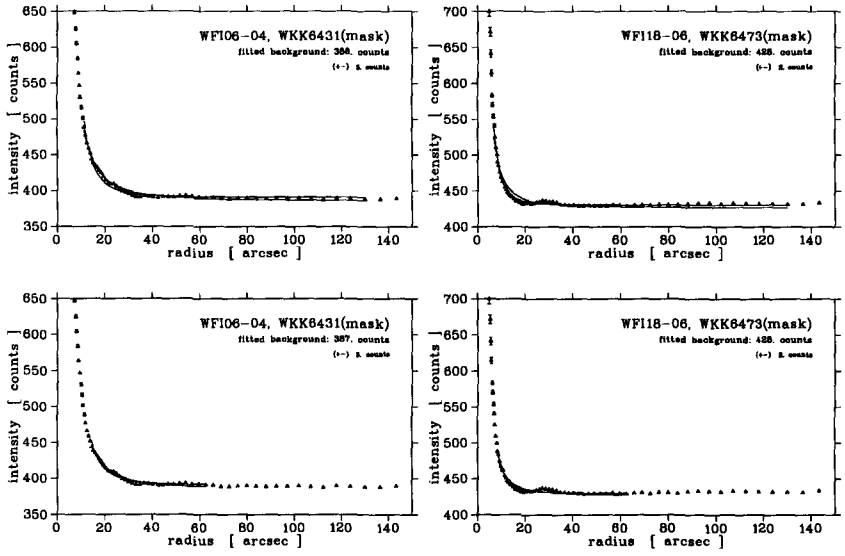

Figure A.10: Galaxies WKK 6431 and WKK 6473, WFI background-fits as described in Section 4.1 on page 86.

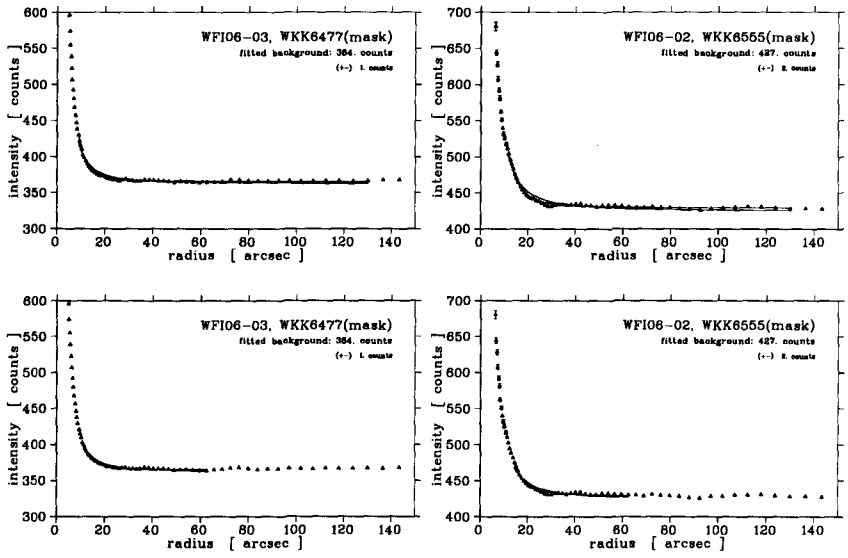

Figure A.11: Galaxies WKK 6477 and WKK 6555, WFI background-fits as described in Section 4.1 on page 86.

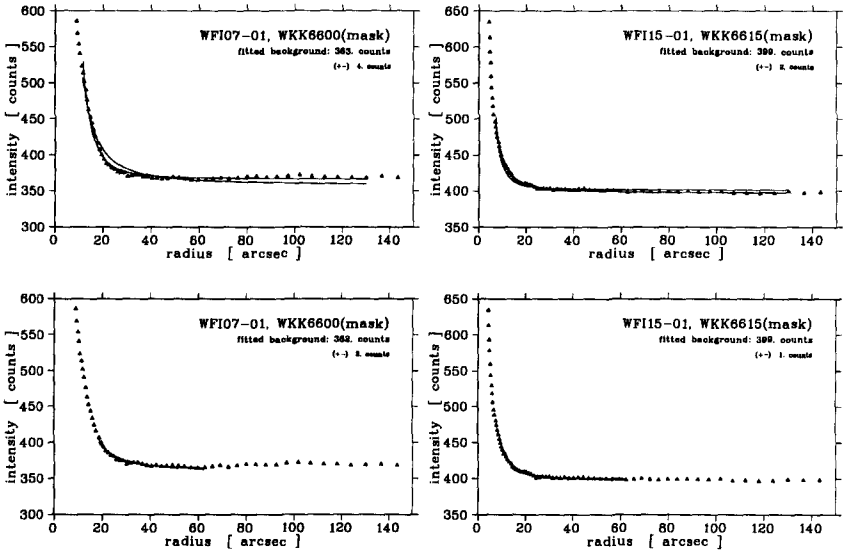

Figure A.12: Galaxies WKK 6600 and WKK 6615, WFI background-fits as described in Section 4.1 on page 86.

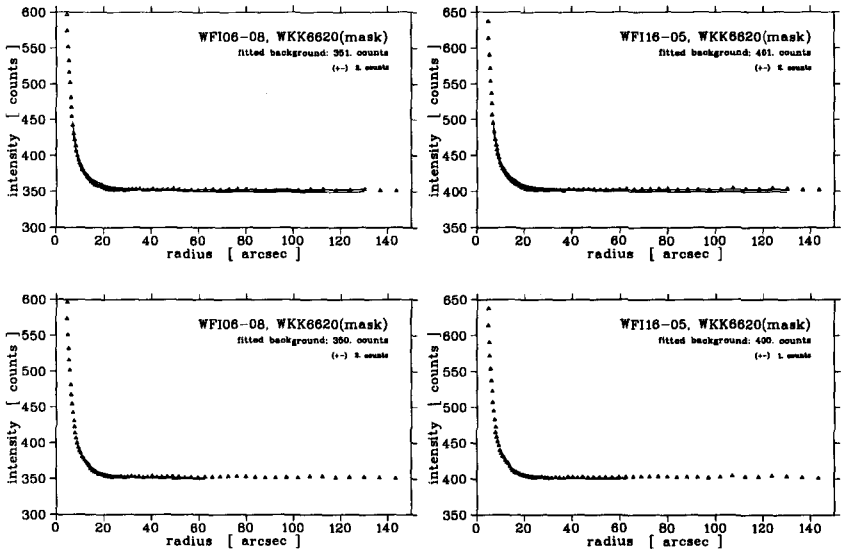

Figure A.13: Galaxy WKK 6620, WFI background-fits as described in Section 4.1 on page 86.

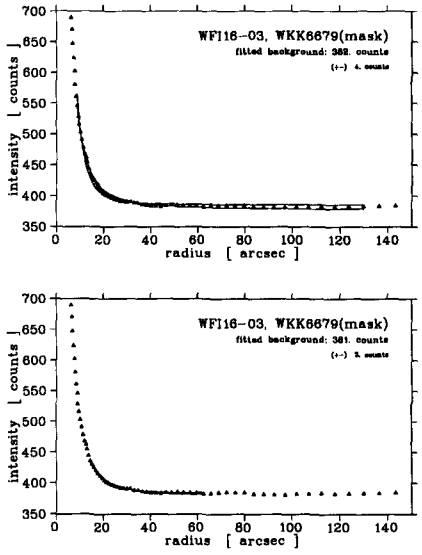

Figure A.14: Galaxy WKK 6679, WFI background-fit as described in Section 4.1 on page 86.

A.4 WKK 6305a and 6305b

The *iPSF-Fitting* analysis of the two galaxies WKK 6305a and 6305b is not finished yet. However, the images in this section give a brief outlook on the capabilities of the developed *iPSF-Fitting* procedure. Although both galaxies basically lie on top of each other, it was possible to derive models for each of the two galaxies. The two models were subtracted in an alternating interactive manner to obtain good models for both galaxies. The results of this effort is not shown in this dissertation, since the analysis is not finished yet (cf. Section 6 on page 170).

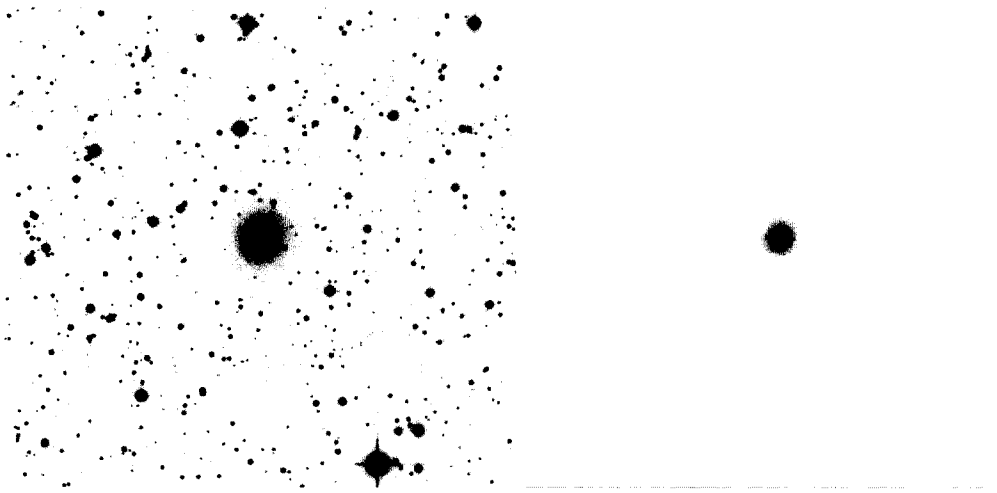

Figure A.15: The absolute worst case that was processed so far was an image with two elliptical galaxies (WKK 6305a, 6305b) on top of each other. On the left, the original R_c image and the model of the larger galaxy WKK 6305a on the right.

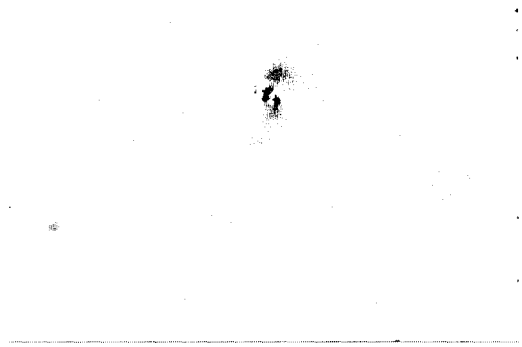

Figure A.16: The two galaxy models were subtracted in an alternating interactive manner to obtain good models for both galaxies. The results of this effort is not shown in this dissertation, since the analysis is not finished yet. On the left, the model of the smaller galaxy WKK 6305b and the final image with stars and both galaxies subtracted on the right.

A.5 *Star-Masking* and *PSF-Fitting* Plots

This section contains the *SM* plots of the ellipticity and position angle of the galaxies as well as their isophotal and integrated magnitudes. These plots resulted from applying the masking and PSF-fitting data reduction methods as described in sections 3.3 and 3.2 on pages 62 and 53, respectively. The reader is referred to Part II of this dissertation for comparison with the results obtained with the σ-clipping and improved PSF-fitting methods described in sections 3.1 and 3.4 on pages 49 and 65, respectively. Note that in most of these plots shown here, the surface brightness seems to level off for large radii and the integrated brightness doesn't reach an asymptote. This seems to be a result of the rather bad background determination that was described in Section 4.1 on page 86.

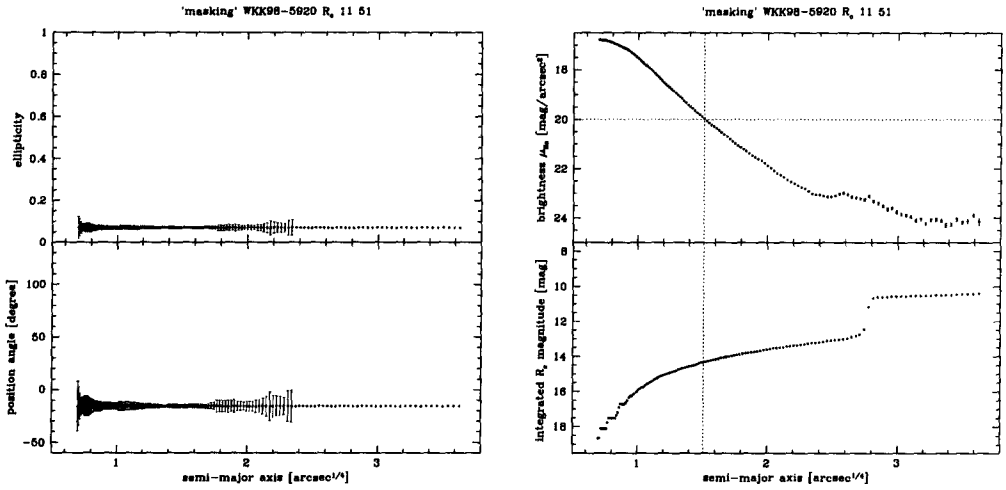

Figure A.17: Galaxy WKK 5920, ellipticity and position angle as well as isophotal and integrated magnitude plots using the masking data reduction method as described in Section 3.3 on page 62.

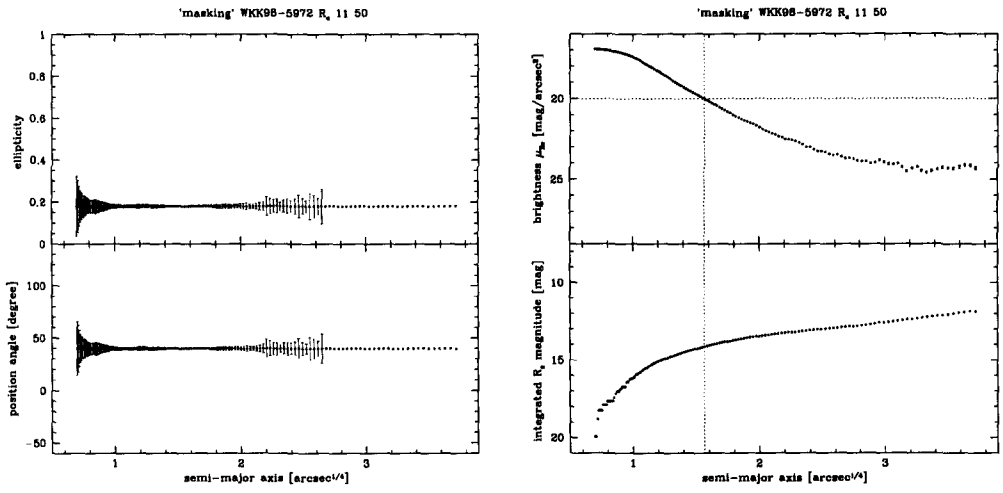

Figure A.18: As Figure A.17 on page 215, but now for galaxy WKK 5972.

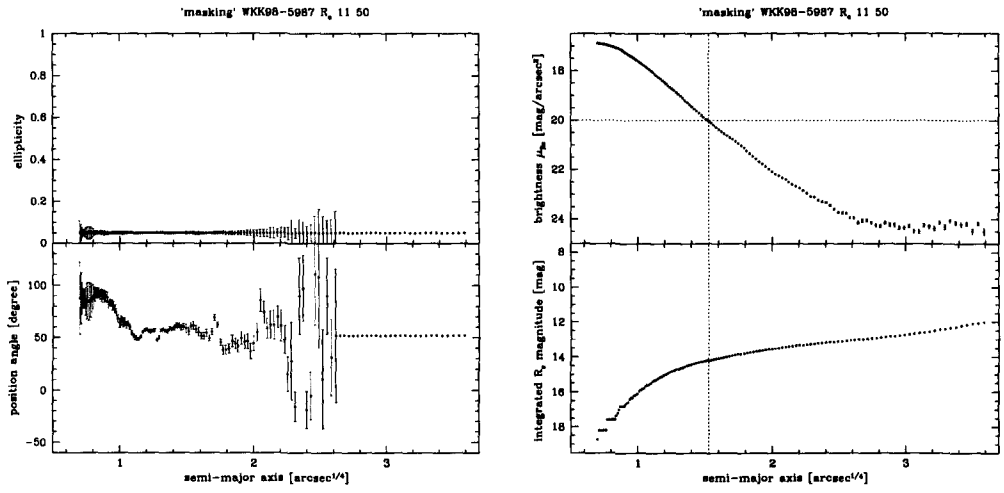

Figure A.19: As Figure A.17 on page 215, but now for galaxy WKK 5987.

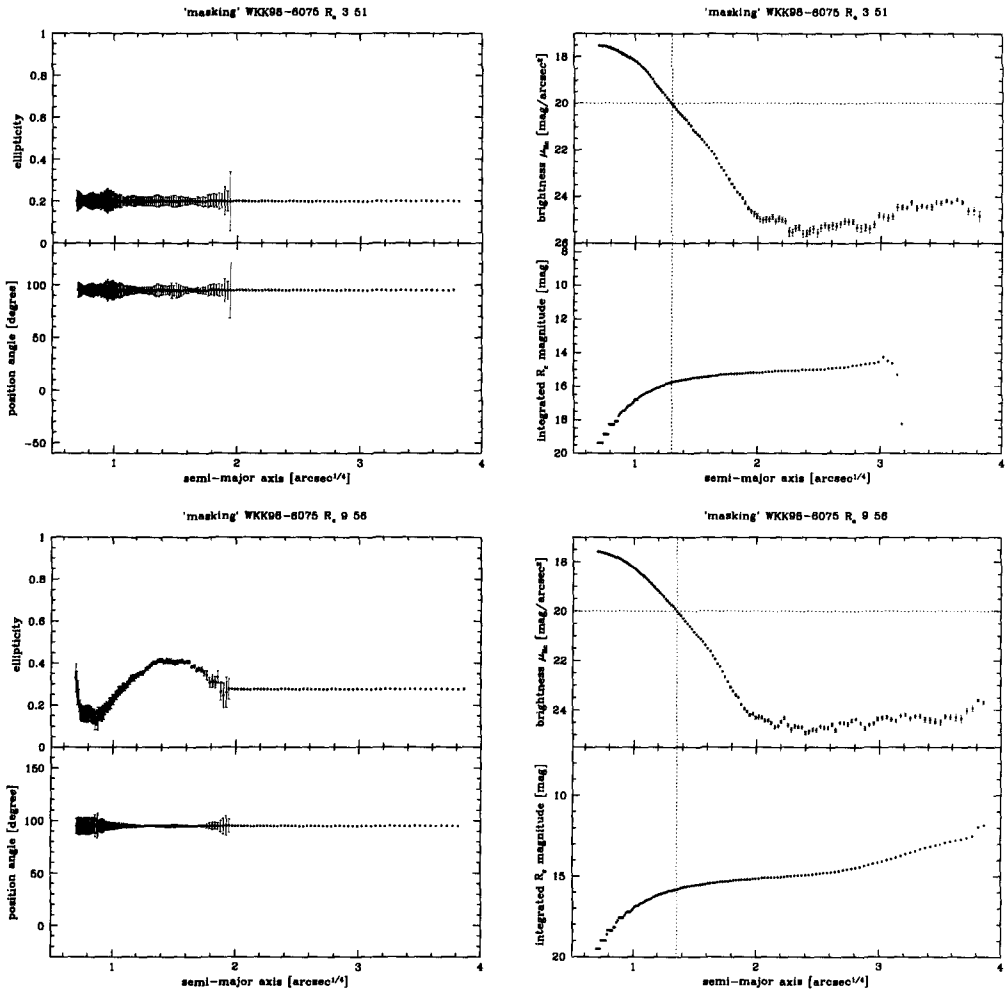

Figure A.20: As Figure A.17 on page 215, but now for galaxy WKK 6075.

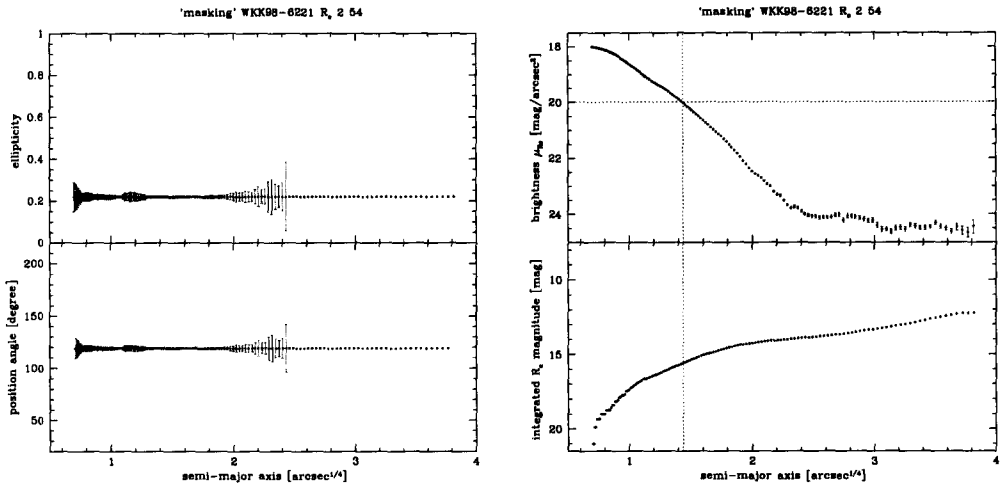

Figure A.21: As Figure A.17 on page 215, but now for galaxy WKK 6221.

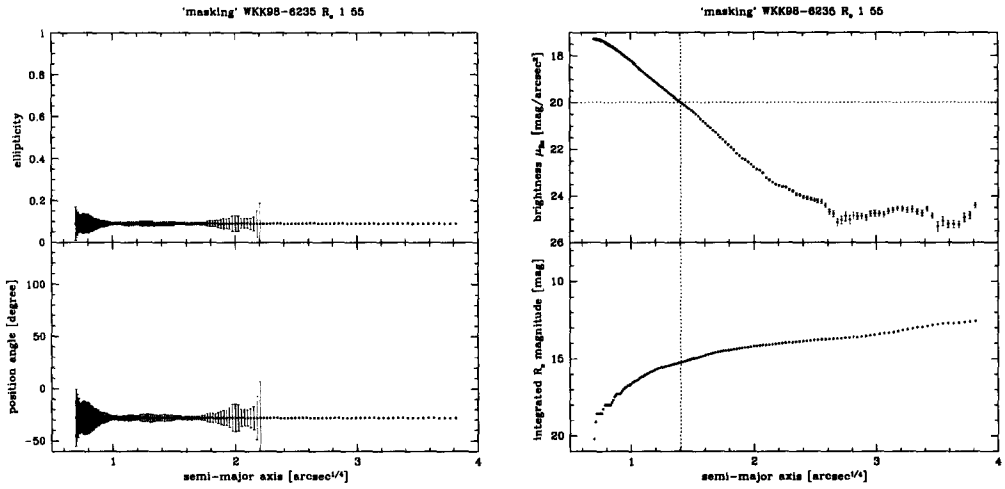

Figure A.22: As Figure A.17 on page 215, but now for galaxy WKK 6235.

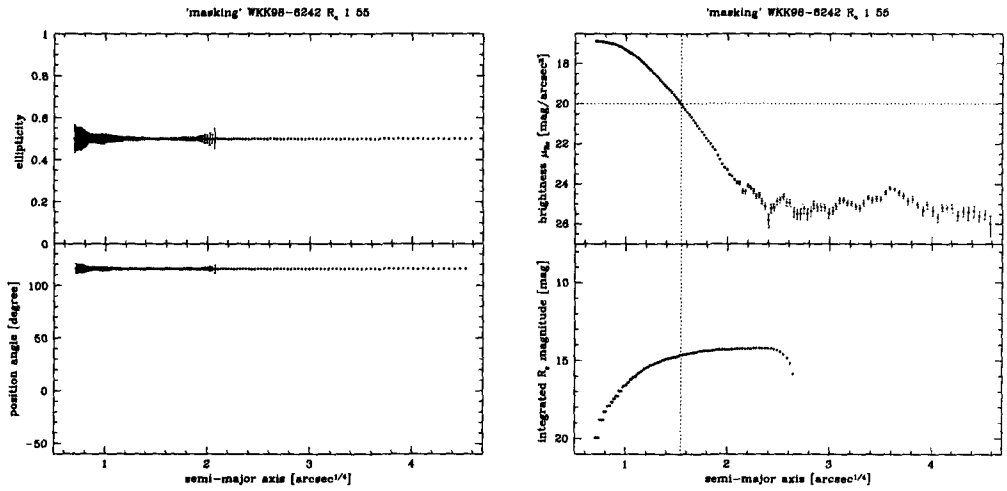

Figure A.23: As Figure A.17 on page 215, but now for galaxy WKK 6242.

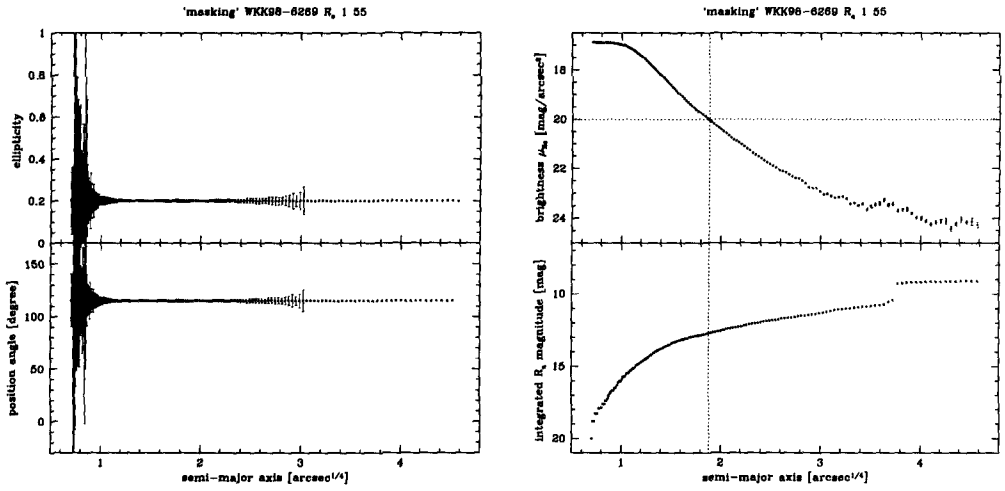

Figure A.24: As Figure A.17 on page 215, but now for galaxy WKK 6269.

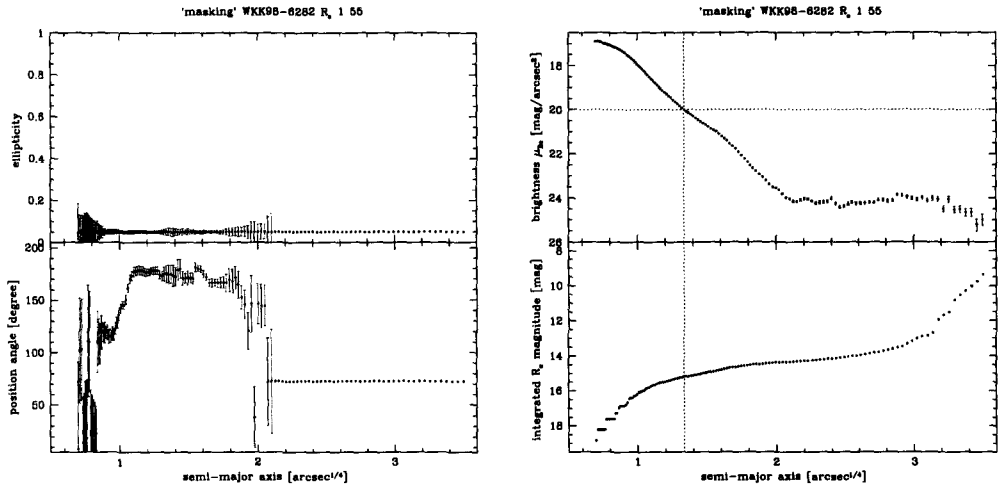

Figure A.25: As Figure A.17 on page 215, but now for galaxy WKK 6282.

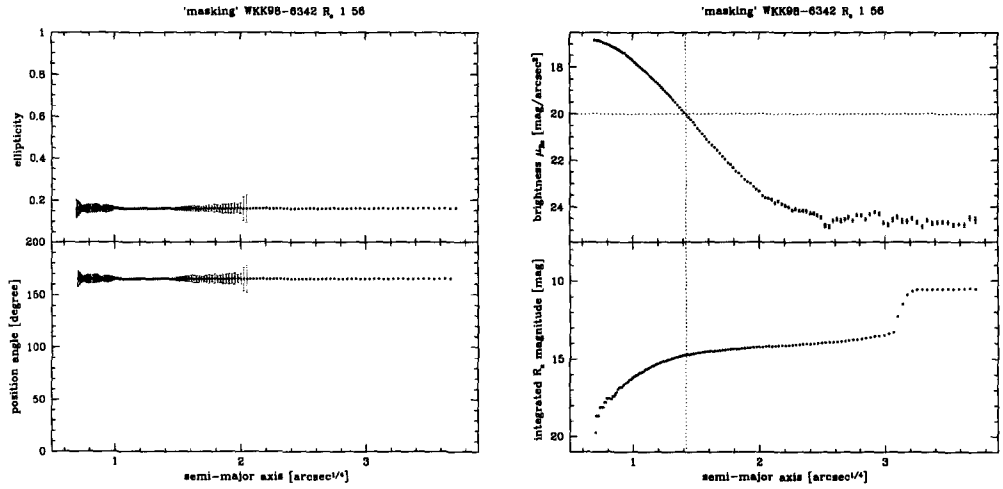

Figure A.26: As Figure A.17 on page 215, but now for galaxy WKK 6342.

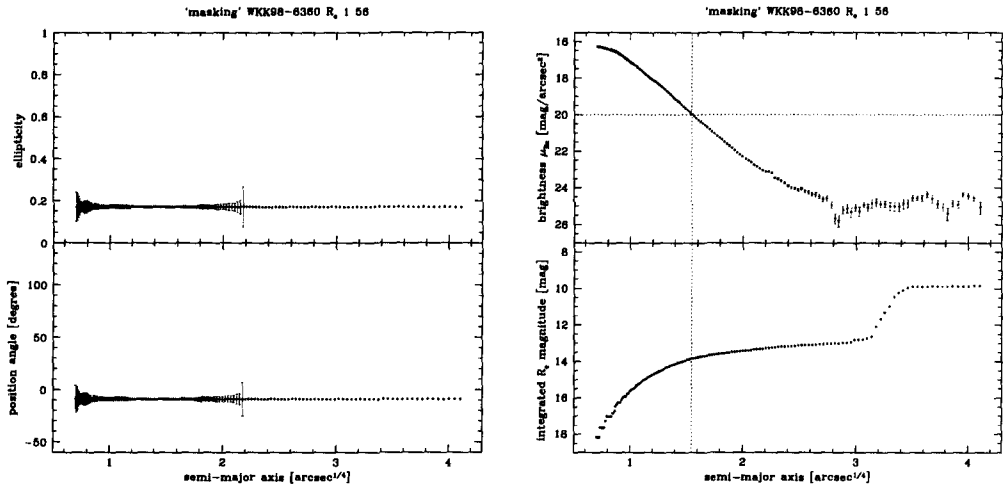

Figure A.27: As Figure A.17 on page 215, but now for galaxy WKK 6360.

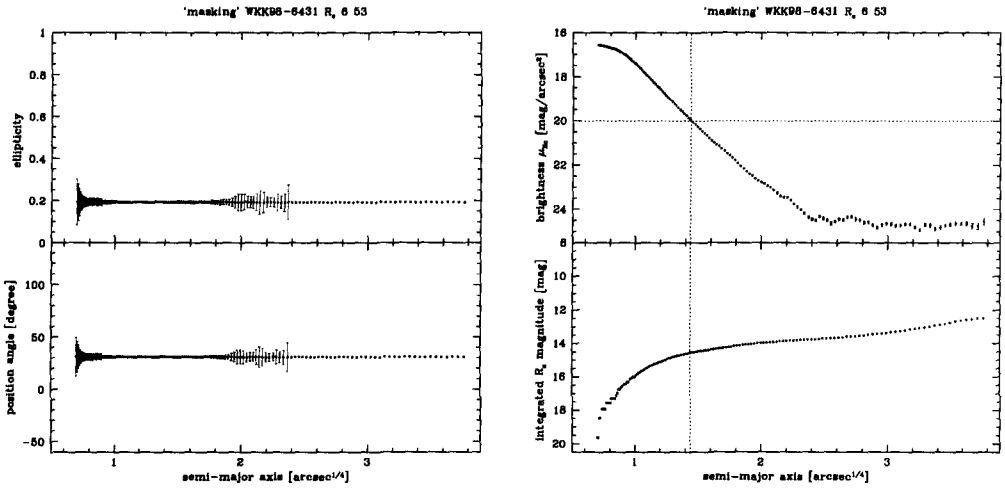

Figure A.28: As Figure A.17 on page 215, but now for galaxy WKK 6431.

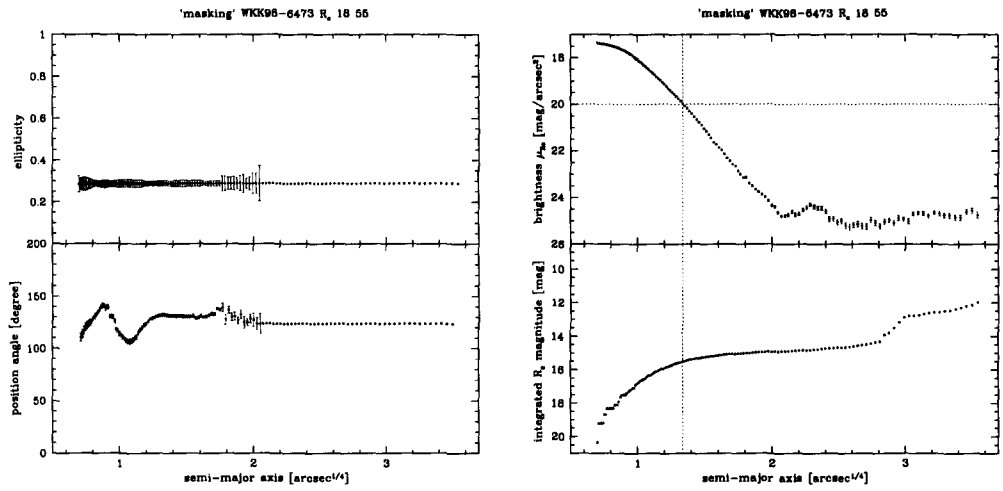

Figure A.29: As Figure A.17 on page 215, but now for galaxy WKK 6473.

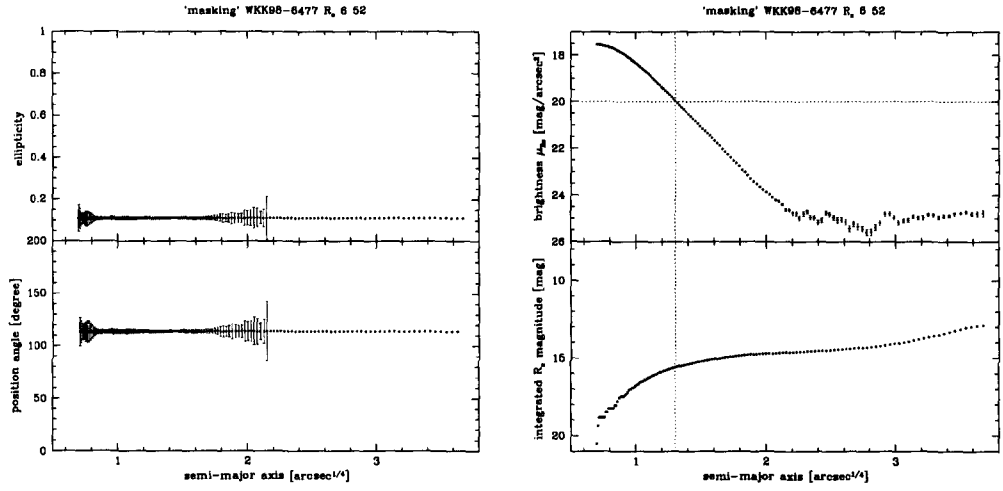

Figure A.30: As Figure A.17 on page 215, but now for galaxy WKK 6477.

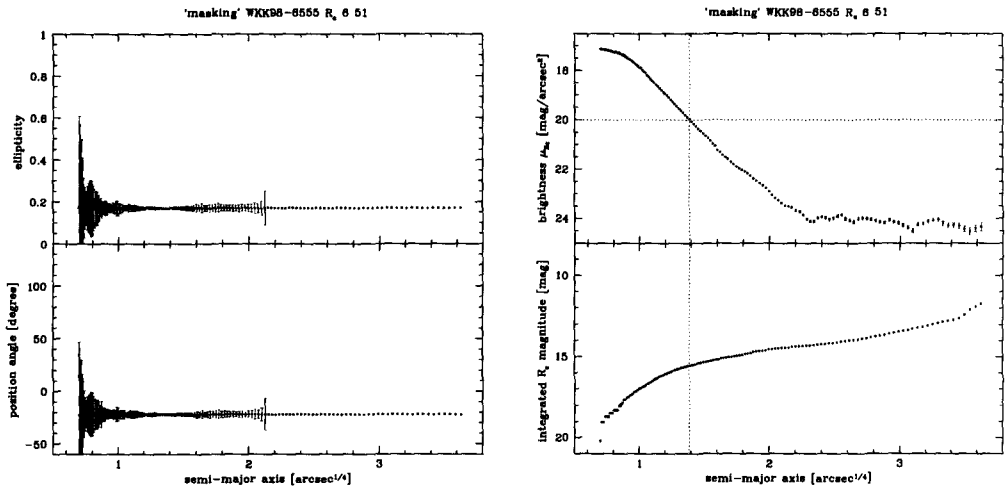

Figure A.31: As Figure A.17 on page 215, but now for galaxy WKK 6555.

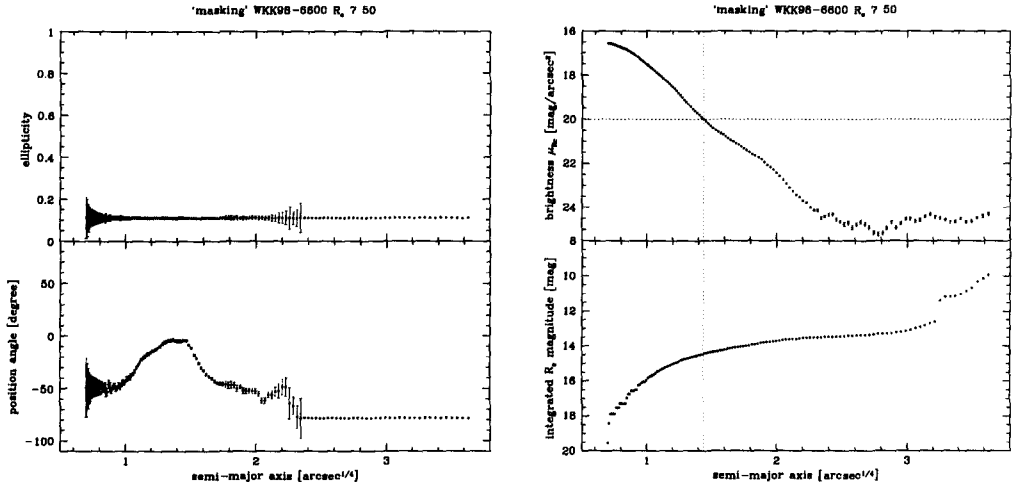

Figure A.32: As Figure A.17 on page 215, but now for galaxy WKK 6600.

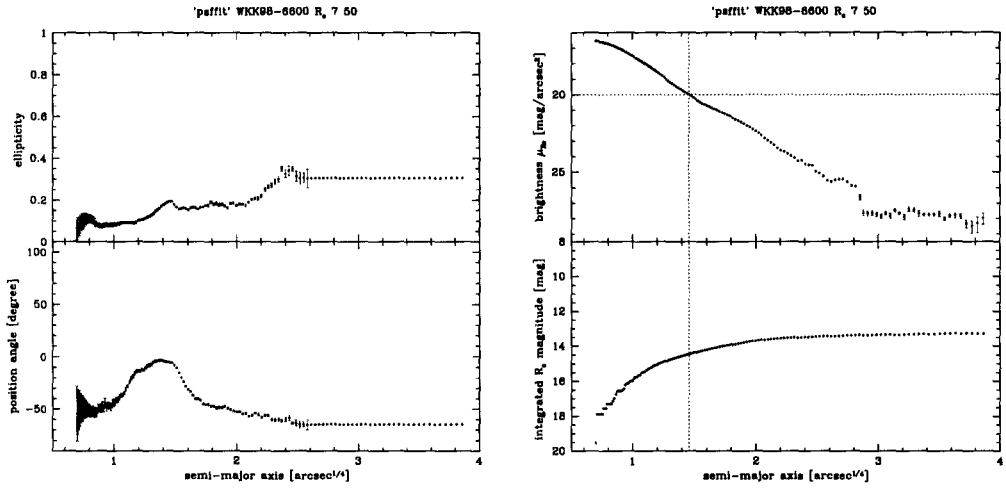

Figure A.33: As Figure A.17 on page 215, but now for galaxy WKK 6600.

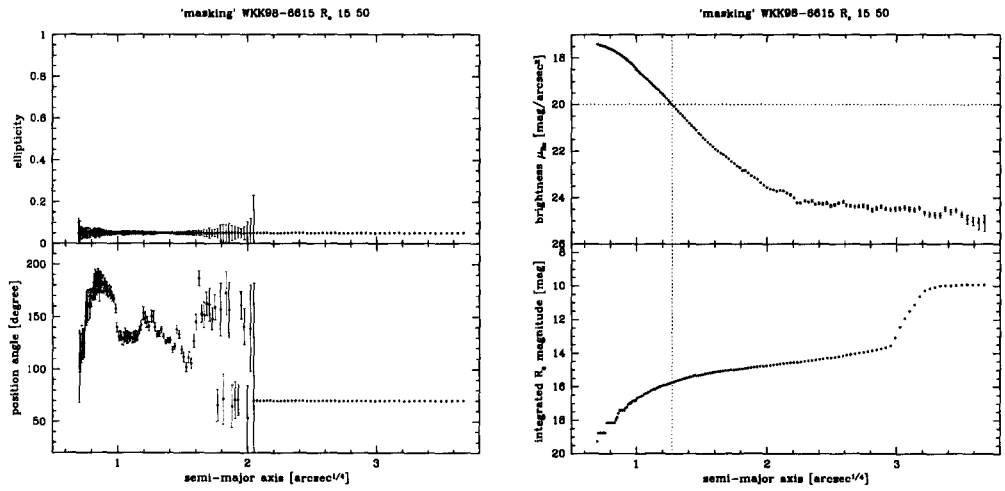

Figure A.34: As Figure A.17 on page 215, but now for galaxy WKK 6615.

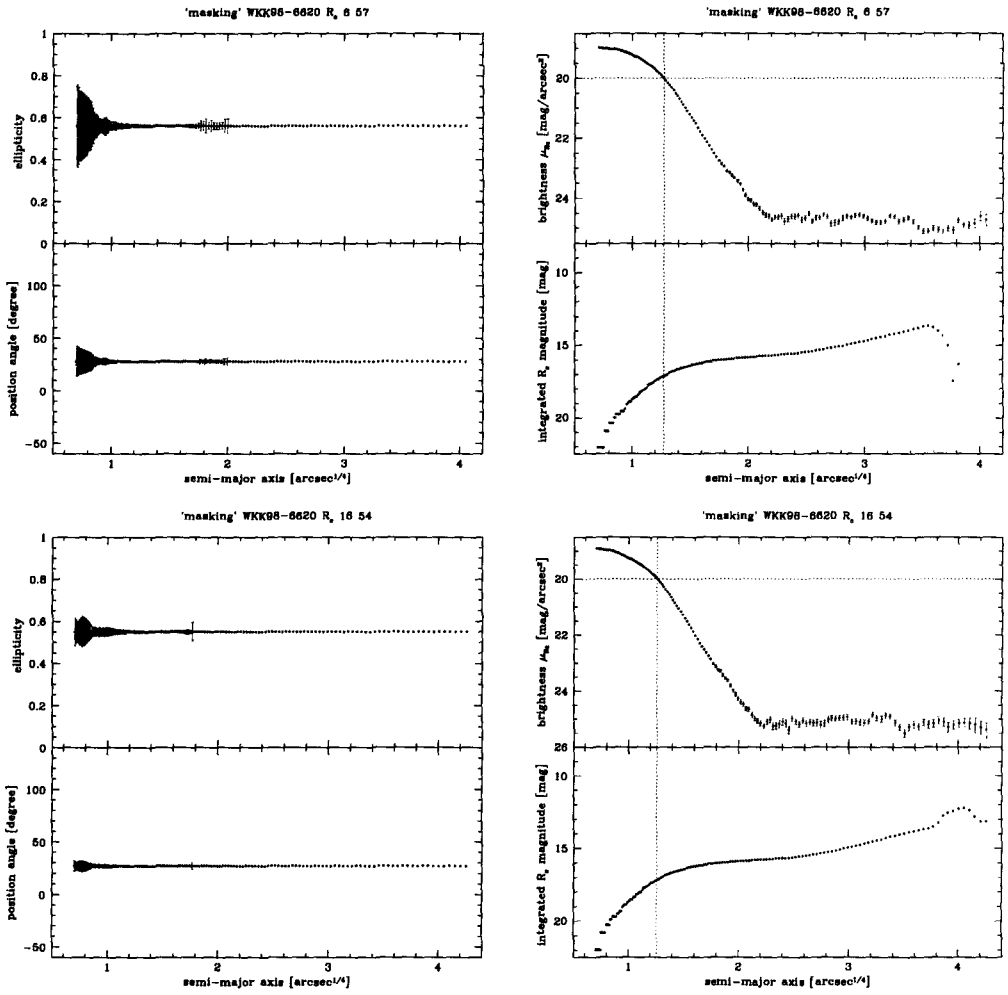

Figure A.35: As Figure A.17 on page 215, but now for galaxy WKK 6620.

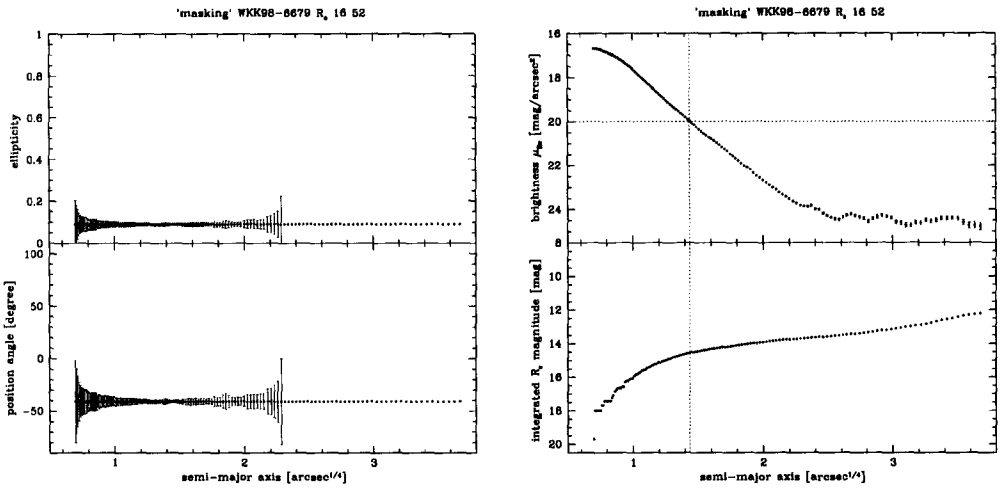

Figure A.36: As Figure A.17 on page 215, but now for galaxy WKK 6679.

A.6 Results from the *PSF-Fitting* and *Star-Masking* procedures

The results mentioned in this section are only mentioned for completeness. They are used only for a comparison of the different methods used to separate the galaxies from the foreground starfield. No further analysis was applied to this data. See Chapter 3 on page 47 and part III of this dissertation for more information on the different procedures. The main results from the *σ-Clipping* and *iPSF-Fitting* used for the analysis are presented in Section 5.1 on page 121.

As mentioned earlier, the data from the *PSF-Fitting* and *Star-Masking* procedures were incomplete due to an unfortunate data loss that occurred. The remaining data for the *Star-Masking* are shown in Table A.6 on page 227. Only one set of results is available for the *PSF-Fitting* method. This one set is shown in Table A.7 on page 228.

Table A.6: Magnitudes and radii from applying the *Star-Masking* procedure. For these magnitudes, the photometric corrections described in Section 4.9 on page 116 have not been applied. The data are sorted and displayed according to photometrically corrected K_{s20}^{corr} brightness, as derived with the *iPSF-Fitting* procedure (cf. Table 5.9 on page 147).

WKK* ident.	obs. field.†	WFI CCD‡	R_{c23} [mag]	r_{Rc23}§ [arcsec]
6269	01	# 55	11.234	88.021
5987	11	# 50	13.285	25.995
5972	11	# 50	13.085	33.178
5920	11	# 51	13.233	30.085
6360	01	# 56	13.270	22.461
6600	07	# 50	13.624	19.411
6679	16	# 52	13.853	18.467

Table A.6: (continued) Magnitudes and radii from applying the *Star-Masking* procedure.

WKK* ident.	obs. field.†	WFI CCD‡	R_{c23} [mag]	r_{Rc23}§ [arcsec]
6221	02	# 54	14.084	21.368
6242	01	# 52	14.259	14.459
6431	06	# 53	13.934	18.467
6342	01	# 56	14.281	13.789
6235	01	# 55	14.130	18.467
6555	06	# 51	14.538	16.749
6282	01	# 55	14.452	13.115
6075	09	# 56	15.228	10.289
6075	03	# 51	15.271	8.895
6477	06	# 52	14.820	11.338
6473	18	# 55	15.032	9.793
6615	15	# 50	14.852	12.492
6620	06	# 57	15.990	10.289
6620	16	# 54	16.045	9.793

*Taken from Woudt (1998).

†As defined by Dr. Woudt (priv. comm.).

‡Extracted from the FITS header.

§Stated as semi-major axis length

Table A.7: Magnitudes and radii from applying the *PSF-Fitting* procedure. For these magnitudes, the photometric corrections described in Section 4.9 on page 116 have not been applied yet.

WKK* ident.	obs. field.†	WFI CCD‡	R_{c23} [mag]	r_{Rc23}§ [arcsec]
6600	07	# 50	13.610	19.411

*Taken from Woudt (1998).

†As defined by Dr. Woudt (priv. comm.).

‡Extracted from the FITS header.

§Stated as semi-major axis length

A.7 Tabulated External Data for Comparison

Table A.8: Magnitudes and radii from 2MASS. The data were taken from the *NASA/IPAC Extragalactic Database* (NED), in which the extinction corrections given are calculated according to the method described in the Appendix of Schlegel et al. (1998). The data are sorted and displayed according to photometrically corrected K_{s20}^{corr} brightness, as derived with the *iPSF-Fitting* procedure (cf. Table 5.9 on page 147).

WKK* ident.	K_{s20} [mag]	K_{s20}^{err} [mag]	r_{Ks20} [arcsec]
6269	8.339	0.026	55.0
6318	8.612	0.036	55.4
6204	9.512	0.034	32.7
6116	9.638	0.040	29.9
5987	n.a.	n.a.	n.a.
6019	9.782	0.034	32.0
5972	9.854	0.041	27.8
5920	9.964	0.045	25.9
6360	10.079	0.037	22.7
6600	10.297	0.044	20.8
6183	10.366	0.049	20.1
6180	10.352	0.055	21.7
6250	10.604	0.045	19.1

Table A.8: (continued) Magnitudes and radii from *2MASS*.

WKK* ident.	K_{s20} [mag]	K_{s20}^{err} [mag]	r_{Ks20} [arcsec]
6679	10.649	0.067	19.2
6221	10.887	0.071	22.3
6242	n.a.	n.a.	n.a.
6431	10.963	0.045	12.1
6383	11.002	0.062	17.9
6342	10.819	0.045	15.1
6012	11.162	0.060	13.8
6235	11.101	0.073	15.8
6555	11.072	0.062	18.4
6282	11.164	0.056	12.2
6229	11.641	0.051	7.6
6075	11.841	0.071	10.0
6198	11.853	0.082	10.7
6047	12.126	0.100	11.3
6477	12.027	0.068	8.5
6473	12.053	0.065	8.4
6233	11.978	0.067	7.9
6615	12.308	0.076	9.6
6620	13.046	0.099	6.4

*Taken from Woudt (1998).

Table A.9: Extinction and colour excess from Schlegel et al. (1998). The data were taken from the *NASA/IPAC Extragalactic Database* (NED) and are sorted and displayed according to photometrically corrected K_{s20}^{corr} brightness, as derived with the *iPSF-Fitting* procedure (cf. Table 5.9 on page 147).

WKK* ident.	E(B − V) [mag]	A_B [mag]	A_{Rc} [mag]	A_{Ks} [mag]	$(A_{Rc} - A_{Ks})$ [mag]
6269	0.195	0.842	0.521	0.072	0.449
6318	0.225	0.971	0.601	0.083	0.518
6204	0.214	0.924	0.573	0.079	0.494
6116	0.217	0.938	0.581	0.080	0.501
5987	0.251	1.083	0.671	0.092	0.579
6019	0.221	0.953	0.590	0.081	0.509
5972	0.255	1.102	0.683	0.094	0.589
5920	0.284	1.226	0.759	0.104	0.655
6360	0.202	0.873	0.541	0.074	0.467
6600	0.216	0.932	0.577	0.079	0.498
6183	0.200	0.861	0.534	0.073	0.461
6180	0.212	0.916	0.568	0.078	0.490
6250	0.213	0.919	0.569	0.078	0.491
6679	0.238	1.027	0.636	0.087	0.549
6221	0.214	0.922	0.571	0.078	0.493
6242	0.198	0.856	0.530	0.073	0.457
6431	0.239	1.032	0.639	0.088	0.551
6383	0.223	0.961	0.595	0.082	0.513
6342	0.198	0.855	0.530	0.073	0.457
6012	0.262	1.130	0.700	0.096	0.604
6235	0.223	0.962	0.596	0.082	0.514
6555	0.217	0.937	0.580	0.080	0.500
6282	0.196	0.846	0.524	0.072	0.452
6229	0.203	0.874	0.542	0.074	0.468

Table A.9: (continued) Extinction and colour excess from Schlegel et al. (1998).

WKK* ident.	E(B − V) [mag]	A_B [mag]	A_{Rc} [mag]	A_{Ks} [mag]	$(A_{Rc} - A_{Ks})$ [mag]
6075	0.234	1.012	0.627	0.086	0.541
6198	0.181	0.779	0.483	0.066	0.417
6047	0.221	0.953	0.590	0.081	0.509
6477	0.235	1.016	0.629	0.086	0.543
6473	0.216	0.934	0.579	0.079	0.500
6233	0.200	0.863	0.534	0.073	0.461
6615	0.193	0.831	0.515	0.071	0.444
6620	0.200	0.862	0.534	0.073	0.461

*Taken from Woudt (1998).

A.8 Data for early-type galaxies in the Coma cluster

The data shown here was generously made available by Dr. Lucey[1]. More details about this data will be published elsewhere (Dr. Lucey, priv. comm.). In this dissertation it is used to determine a relationship for extinction free $(R_c - K_s)$ colours with respect to velocity dispersion, i.e. galaxy size. This made it possible, for instance, to estimate the colour excess for the central region of the Norma cluster. For further details see Section 5.2 on page 149.

[1]Department of Physics, University of Durham, United Kingdom, see *http://www.dur.ac.uk/john.lucey/*

Table A.10: Information about R_c and K_s magnitudes and velocity dispersion σ_0 of 73 early-type Coma cluster galaxies. The data shown here was generously made available by Dr. Lucey and more details about this data will be published elsewhere (Dr. Lucey, priv. comm.). A circular aperture with a radius of ten arcsec was applied to obtain the given magnitudes. None of the corrections described in Section 4.9 on page 116 have been applied yet. For the corrected data, see Table A.11 on page 241. For further details on how this data was used in this dissertation, see Section 5.2 on page 149.

2MASS ident.	$\log(\sigma_0)$ [log(km/s)]	FWHM [arcsec]	R_c [mag]	R_c^{err} [mag]	K_s [mag]	K_s^{err} [mag]	gal. type class.
2MASXJ13003251+2745576	1.926	1.34	15.877	0.004	13.362	0.056	S0/a
2MASXJ12591348+2746289	2.107	1.51	15.014	0.002	12.428	0.028	S0
		1.52	15.023	0.002			
2MASXJ13010925+2749052	2.133	1.29	15.339	0.002	12.861	0.036	E
2MASXJ13005921+2753592	2.127	1.19	14.867	0.001	12.273	0.021	S0/a
		1.29	14.921	0.001			
		1.43	14.878	0.001			
		1.48	14.892	0.001			
2MASXJ12594610+2751257	2.079	1.43	15.088	0.002	12.448	0.027	S0

Table A.10: (continued) Information about R_c and K_s magnitudes and velocity dispersion σ_0 of 73 early-type Coma cluster galaxies.

2MASS ident.	log(σ_0) [log(km/s)]	FWHM [arcsec]	R_c [mag]	R_c^{err} [mag]	K_s [mag]	K_s^{err} [mag]	gal. type class.
		1.51	15.061	0.002			
2MASXJ12594007+2751177	1.885	1.41	15.954	0.004	13.368	0.062	S0
2MASXJ12593079+2753028	2.364	1.23	14.375	0.001	11.617	0.013	S0/a
		1.44	14.369	0.001			
2MASXJ12593789+2754267	2.264	1.19	14.735	0.001	12.005	0.018	S0
		1.44	14.761	0.001			
2MASXJ12592333+2754418	2.302	1.35	14.182	0.001	11.468	0.011	E
		1.44	14.206	0.001			
2MASXJ12592265+2753488	2.079	1.37	15.252	0.002	12.753	0.036	S0
		1.44	15.267	0.002			
2MASXJ12592016+2753098	1.851	1.22	15.479	0.003	12.898	0.040	E
		1.25	15.485	0.002			
		1.37	15.477	0.003			
		1.44	15.498	0.003			
		1.59	15.504	0.003			
		1.65	15.513	0.003			

Table A.10: (continued) Information about R_c and K_s magnitudes and velocity dispersion σ_0 of 73 early-type Coma cluster galaxies.

2MASS ident.	$\log(\sigma_0)$ [log(km/s)]	FWHM [arcsec]	R_c [mag]	R_c^{err} [mag]	K_s [mag]	K_s^{err} [mag]	gal. type class.
2MASXJ12590459+2754389	2.046	1.21	15.454	0.002	13.020	0.047	S0
		1.52	15.505	0.003			
2MASXJ12590791+2751179	2.244	1.51	14.811	0.001	11.936	0.018	S0
2MASXJ12575059+2752454	2.074	1.34	15.516	0.002	12.882	0.038	S0/E
2MASXJ12574803+2752584	2.184	1.34	14.848	0.001	12.221	0.021	S0
2MASXJ13004285+2757476	2.096	1.20	15.186	0.001	12.592	0.028	SB0
2MASXJ13004737+2755196	1.946	1.18	15.533	0.002	12.984	0.041	S0/a
2MASXJ13003975+2755256	2.242	1.24	14.570	0.001	11.905	0.015	E
2MASXJ13002798+2757216	2.158	1.16	15.260	0.002	12.648	0.030	S0
		1.38	15.262	0.002			
2MASXJ13001768+2757192	2.315	1.15	14.142	0.001	11.344	0.009	E
2MASXJ13001655+2758032	1.932	1.15	15.210	0.002	12.655	0.031	S0
2MASXJ12595670+2755483	1.999	1.14	15.667	0.003	13.103	0.046	SB0
		1.31	15.663	0.002			
2MASXJ12594438+2754447	2.234	1.16	14.531	0.001	11.893	0.017	E
		1.44	14.597	0.001			

Table A.10: (continued) Information about R_c and K_s magnitudes and velocity dispersion σ_0 of 73 early-type Coma cluster galaxies.

2MASS ident.	$\log(\sigma_0)$ [log(km/s)]	FWHM [arcsec]	R_c [mag]	R_c^{err} [mag]	K_s [mag]	K_s^{err} [mag]	gal. type class.
2MASXJ12594234+2755287	2.211	1.19	15.214	0.002	12.655	0.033	E
2MASXJ12594423+2757307	1.946	1.19	15.646	0.003	13.176	0.053	S0
2MASXJ12592529+2758048	1.983	1.26	15.659	0.003	13.076	0.049	S0
2MASXJ12591525+2758147	2.356	1.22	14.423	0.001	11.670	0.014	E
		1.51	14.421	0.001			
2MASXJ12590006+2758029	1.974	1.22	15.833	0.003	13.322	0.062	E
2MASXJ12585523+2757529	2.226	1.23	15.201	0.002	12.640	0.033	E
2MASXJ12582185+2758037	2.259	1.44	14.410	0.001	11.677	0.013	E/S0
2MASXJ13012713+2759566	2.204	1.14	15.484	0.002	12.771	0.034	E
2MASXJ13005445+2800271	2.347	1.23	14.351	0.001	11.586	0.012	E
2MASXJ13004277+2758166	2.238	1.20	14.449	0.001	11.704	0.013	S0/a
2MASXJ13004081+2759476	2.111	1.23	15.067	0.001	12.464	0.025	S0
2MASXJ13002835+2758206	2.003	1.16	15.479	0.002	12.932	0.039	S0
		1.38	15.487	0.002			
2MASXJ13000643+2800142	2.074	1.18	15.151	0.002	12.553	0.028	E
2MASXJ12594681+2758252	2.142	1.19	14.986	0.002	12.316	0.023	SB0

Table A.10: (continued) Information about R_c and K_s magnitudes and velocity dispersion σ_0 of 73 early-type Coma cluster galaxies.

2MASS ident.	$\log(\sigma_0)$ [log(km/s)]	FWHM [arcsec]	R_c [mag]	R_c^{err} [mag]	K_s [mag]	K_s^{err} [mag]	gal. type class.
		1.49	14.987	0.001			
2MASXJ12593827+2759137	1.757	1.19	16.080	0.004	13.640	0.081	S0
2MASXJ12593276+2759008	2.244	1.23	14.649	0.001	12.009	0.018	S0
2MASXJ12592657+2759548	1.950	1.23	15.807	0.006	13.280	0.058	E/S0
2MASXJ12592544+2758238	2.103	1.26	15.368	0.002	12.802	0.038	S0
2MASXJ12592136+2758248	1.768	1.33	16.295	0.005	13.923	0.105	S0
2MASXJ12591312+2758369	2.310	1.22	14.212	0.001	11.547	0.012	E
		1.51	14.216	0.001			
2MASXJ12590603+2759479	2.172	1.22	14.769	0.001	12.101	0.021	SB0
2MASXJ12583023+2800527	2.276	1.34	14.446	0.001	11.744	0.014	E
		1.47	14.459	0.001			
2MASXJ13005158+2802341	2.363	1.24	14.185	0.001	11.398	0.010	S0/E
		1.27	14.178	0.001			
2MASXJ13004867+2805266	2.334	1.31	14.203	0.001	11.451	0.010	E
2MASXJ13002215+2802495	2.007	1.20	14.967	0.001	12.306	0.022	SB0
		1.24	14.941	0.001			

Table A.10: (continued) Information about R_c and K_s magnitudes and velocity dispersion σ_0 of 73 early-type Coma cluster galaxies.

2MASS ident.	log(σ_0) [log(km/s)]	FWHM [arcsec]	R_c [mag]	R_c^{err} [mag]	K_s [mag]	K_s^{err} [mag]	gal. type class.
		1.25	14.969	0.001			
		1.44	14.946	0.001			
		1.48	14.941	0.001			
		1.48	14.948	0.001			
2MASXJ13001702+2803502	2.058	1.23	15.423	0.002	12.788	0.035	S0
2MASXJ13001475+2802282	2.211	1.19	14.849	0.001	12.101	0.019	E
		1.22	14.849	0.001			
2MASXJ13001286+2804322	2.093	1.23	15.174	0.002	12.545	0.028	S0
2MASXJ13000803+2804422	2.271	1.23	14.642	0.001	11.914	0.016	E
2MASXJ12595601+2802052	2.222	1.15	14.579	0.001	11.861	0.015	S0
		1.22	14.565	0.001			
		1.26	14.568	0.001			
		1.30	14.571	0.001			
2MASXJ12593141+2802478	2.127	1.23	14.927	0.002	12.315	0.024	S0
		1.27	14.942	0.002			
2MASXJ12592846+2805078	1.800	1.28	16.010	0.003	13.626	0.080	S0

Table A.10: (continued) Information about R_c and K_s magnitudes and velocity dispersion σ_0 of 73 early-type Coma cluster galaxies.

2MASS ident.	log(σ_0) [log(km/s)]	FWHM [arcsec]	R_c [mag]	R_c^{err} [mag]	K_s [mag]	K_s^{err} [mag]	gal. type class.
2MASXJ12591985+2805038	2.402	1.26	13.850	0.001	11.115	0.008	S0
		1.33	13.835	0.000			
2MASXJ12591389+2804349	2.151	1.25	15.396	0.002	12.979	0.046	S0
		1.37	15.390	0.003			
2MASXJ12585077+2805019	2.087	1.33	15.297	0.002	12.725	0.036	S0
2MASXJ12583190+2802587	2.070	1.35	15.574	0.002	13.080	0.046	S0
		1.60	15.571	0.002			
2MASXJ13004459+2806026	1.979	1.28	15.472	0.002	12.920	0.038	S0
2MASXJ13003552+2808466	1.965	1.30	15.258	0.002	12.730	0.032	S0
2MASXJ12595511+2807422	2.068	1.32	15.317	0.002	12.739	0.033	E
		1.36	15.313	0.002			
2MASXJ12590392+2807249	2.423	1.30	13.983	0.001	11.151	0.009	E
2MASXJ12585341+2807339	2.105	1.29	15.361	0.002	12.790	0.037	E
2MASXJ12583636+2806497	2.244	1.36	14.518	0.001	11.837	0.015	S0/a
		1.55	14.521	0.001			
2MASXJ12582169+2808557	2.111	1.29	15.011	0.001	12.376	0.024	S0

Table A.10: (continued) Information about R_c and K_s magnitudes and velocity dispersion σ_0 of 73 early-type Coma cluster galaxies.

2MASS ident.	$\log(\sigma_0)$ [log(km/s)]	FWHM [arcsec]	R_c [mag]	R_c^{err} [mag]	K_s [mag]	K_s^{err} [mag]	gal. type class.
2MASXJ12581504+2807327	2.274	1.28	14.650	0.001	11.983	0.017	S0
2MASXJ13004875+2809296	2.171	1.28	14.639	0.001	11.894	0.015	SBb
2MASXJ13000909+2810132	2.178	1.23	15.038	0.001	12.356	0.023	E
2MASXJ12574866+2810494	2.163	1.39	14.850	0.001	12.202	0.020	Ep
		1.71	14.828	0.013			
2MASXJ12572841+2810348	2.081	1.49	15.197	0.002	12.462	0.026	S0
		1.75	15.188	0.018			
2MASXJ12590180+2813309	2.272	1.65	14.480	0.002	11.638	0.013	S0/a
2MASXJ12580552+2814335	2.029	1.67	14.810	0.013	11.834	0.015	Scd

Table A.11: R_c^{corr} and K_s^{corr} magnitudes and $(R_c - K_s)^{corr}$ colours for the Coma cluster data shown in Table A.10 on page 233. Except the extinction correction, all of the corrections described in Section 4.9 on page 116 have been applied. For the redshift $\overline{z}_{cluster}$ of the Coma cluster, the average redshift $\overline{z}_{Coma} = 0.0227$ of all the shown galaxies was used. For the multiple R_c band measurements shown in Table A.10 on page 233, the mean value was calculated and used.

2MASS ident.	R_c^{corr} [mag]	K_s^{corr} [mag]	$(R_c - K_s)^{corr}$ [mag]	redshift† (z) [ ]	redshift source ref.
2MASXJ13003251+2745576	15.782	13.330	2.452	0.022339	Smith et al. (2004)
2MASXJ12591348+2746289	14.923	12.397	2.527	0.022846	Smith et al. (2004)
2MASXJ13010925+2749052	15.247	12.825	2.422	0.019897	Smith et al. (2000)
2MASXJ13005921+2753592	14.794	12.242	2.552	0.023003	Smith et al. (2004)
2MASXJ12594610+2751257	14.974	12.423	2.552	0.027075	Smith et al. (2004)
2MASXJ12594007+2751177	15.870	13.321	2.548	0.012742	Smith et al. (2004)
2MASXJ12593079+2753028	14.284	11.575	2.709	0.015861	Smith et al. (2000)
2MASXJ12593789+2754267	14.648	11.980	2.669	0.026835	Smith et al. (2000)
2MASXJ12592333+2754418	14.099	11.437	2.662	0.022879	Smith et al. (2004)
2MASXJ12592265+2753488	15.170	12.713	2.457	0.017155	Smith et al. (2004)
2MASXJ12592016+2753098	15.399	12.865	2.534	0.021725	Smith et al. (2004)

Table A.11: (continued) R_c^{corr} and K_s^{corr} magnitudes and $(R_c - K_s)^{corr}$ colours for the Coma cluster data shown in Table A.10 on page 233.

2MASS ident.	R_c^{corr} [mag]	K_s^{corr} [mag]	$(R_c - K_s)^{corr}$ [mag]	redshift† (z) [ ]	redshift source ref.
2MASXJ12590459+2754389	15.386	12.986	2.399	0.021455	Smith et al. (2004)
2MASXJ12590791+2751179	14.716	11.903	2.813	0.022089	Smith et al. (2004)
2MASXJ12575059+2752454	15.420	12.851	2.569	0.023176	Moore et al. (2002)
2MASXJ12574803+2752584	14.756	12.185	2.571	0.019697	Smith et al. (2004)
2MASXJ13004285+2757476	15.085	12.568	2.517	0.027906	Caldwell et al. (1993)
2MASXJ13004737+2755196	15.431	12.961	2.470	0.028653	Smith et al. (2004)
2MASXJ13003975+2755256	14.472	11.877	2.595	0.025087	Smith et al. (2000)
2MASXJ13002798+2757216	15.165	12.617	2.547	0.023456	Smith et al. (2004)
2MASXJ13001768+2757192	14.046	11.313	2.734	0.023026	Smith et al. (2004)
2MASXJ13001655+2758032	15.123	12.612	2.510	0.015457	Caldwell et al. (1993)
2MASXJ12595670+2755483	15.566	13.076	2.490	0.025801	Smith et al. (2004)0
2MASXJ12594438+2754447	14.469	11.861	2.608	0.022402	Smith et al. (2004)
2MASXJ12594234+2755287	15.118	12.624	2.495	0.023016	Müller et al. (1999)
2MASXJ12594423+2757307	15.550	13.145	2.405	0.023166	Smith et al. (2004)
2MASXJ12592529+2758048	15.561	13.049	2.512	0.025678	Moore et al. (2002)
2MASXJ12591525+2758147	14.334	11.629	2.705	0.016208	Müller et al. (1999)

Table A.11: (continued) R_c^{corr} and K_s^{corr} magnitudes and $(R_c - K_s)^{corr}$ colours for the Coma cluster data shown in Table A.10 on page 233.

2MASS ident.	R_c^{corr} [mag]	K_s^{corr} [mag]	$(R_c - K_s)^{corr}$ [mag]	redshift† (z) [ ]	redshift source ref.
2MASXJ12590006+2758029	15.732	13.298	2.434	0.027783	Smith et al. (2000)
2MASXJ12585523+2757529	15.110	12.603	2.507	0.019016	Smith et al. (2000)
2MASXJ12582185+2758037	14.318	11.641	2.676	0.020087	Smith et al. (2004)
2MASXJ13012713+2759566	15.386	12.743	2.642	0.025434	Smith et al. (2004)
2MASXJ13005445+2800271	14.262	11.545	2.717	0.016658	Moore et al. (2002)
2MASXJ13004277+2758166	14.355	11.670	2.685	0.021321	Smith et al. (2004)
2MASXJ13004081+2759476	14.971	12.434	2.537	0.023723	Smith et al. (2000)
2MASXJ13002835+2758206	15.384	12.905	2.480	0.025728	Smith et al. (2004)
2MASXJ13000643+2800142	15.054	12.524	2.530	0.024243	Smith et al. (2000)
2MASXJ12594681+2758252	14.882	12.298	2.584	0.031532	Smith et al. (2004)
2MASXJ12593827+2759137	15.985	13.608	2.376	0.022792	Moore et al. (2002)
2MASXJ12593276+2759008	14.557	11.972	2.585	0.019407	Moore et al. (2002)
2MASXJ12592657+2759548	15.712	13.248	2.464	0.022295	Smith et al. (2000)
2MASXJ12592544+2758238	15.275	12.767	2.508	0.020454	Smith et al. (2004)
2MASXJ12592136+2758248	16.203	13.888	2.315	0.020207	Moore et al. (2002)
2MASXJ12591312+2758369	14.119	11.515	2.603	0.022796	Smith et al. (2004)

Table A.11: (continued) R_c^{corr} and K_s^{corr} magnitudes and $(R_c - K_s)^{corr}$ colours for the Coma cluster data shown in Table A.10 on page 233.

2MASS ident.	R_c^{corr} [mag]	K_s^{corr} [mag]	$(R_c - K_s)^{corr}$ [mag]	redshift† (z) [ ]	redshift source ref.
2MASXJ12590603+2759479	14.671	12.074	2.597	0.025611	Smith et al. (2000)
2MASXJ12583023+2800527	14.356	11.714	2.642	0.023890	Smith et al. (2004)
2MASXJ13005158+2802341	14.079	11.376	2.703	0.029160	Smith et al. (2004)
2MASXJ13004867+2805266	14.107	11.420	2.687	0.023149	Smith et al. (2000)
2MASXJ13002215+2802495	14.852	12.281	2.570	0.027346	Smith et al. (2004)
2MASXJ13001702+2803502	15.330	12.753	2.577	0.020521	Smith et al. (2004)
2MASXJ13001475+2802282	14.758	12.064	2.694	0.019137	Smith et al. (2000)
2MASXJ13001286+2804322	15.076	12.517	2.559	0.025037	Smith et al. (2004)
2MASXJ13000803+2804422	14.545	11.885	2.660	0.024243	Smith et al. (2000)
2MASXJ12595601+2802052	14.470	11.836	2.634	0.027289	Smith et al. (2004)
2MASXJ12593141+2802478	14.839	12.284	2.554	0.023279	Smith et al. (2004)
2MASXJ12592846+2805078	15.926	13.579	2.347	0.012409	Smith et al. (2004)
2MASXJ12591985+2805038	13.755	11.073	2.682	0.015677	Smith et al. (2004)
2MASXJ12591389+2804349	15.294	12.952	2.342	0.026091	Smith et al. (2004)
2MASXJ12585077+2805019	15.204	12.690	2.515	0.020357	Smith et al. (2004)
2MASXJ12583190+2802587	15.481	13.043	2.438	0.019046	Smith et al. (2004)

Table A.11: (continued) R_c^{corr} and K_s^{corr} magnitudes and $(R_c - K_s)^{corr}$ colours for the Coma cluster data shown in Table A.10 on page 233.

2MASS ident.	R_c^{corr} [mag]	K_s^{corr} [mag]	$(R_c - K_s)^{corr}$ [mag]	redshift† (z) [ ]	redshift source ref.
2MASXJ13004459+2806026	15.377	12.887	2.490	0.022069	Smith et al. (2004)
2MASXJ13003552+2808466	15.168	12.692	2.476	0.018216	Smith et al. (2004)
2MASXJ12595511+2807422	15.217	12.711	2.506	0.025277	Smith et al. (2004)
2MASXJ12590392+2807249	13.883	11.125	2.758	0.026618	Müller et al. (1999)
2MASXJ12585341+2807339	15.265	12.759	2.506	0.023349	Smith et al. (2004)
2MASXJ12583636+2806497	14.424	11.806	2.619	0.022826	Smith et al. (2004)
2MASXJ12582169+2808557	14.912	12.350	2.562	0.026372	Smith et al. (2004)
2MASXJ12581504+2807327	14.552	11.955	2.597	0.025011	Smith et al. (2004)
2MASXJ13004875+2809296	14.547	11.858	2.689	0.019610	Casoli et al. (1996)
2MASXJ13000909+2810132	14.943	12.324	2.619	0.022619	Smith et al. (2000)
2MASXJ12574866+2810494	14.742	12.173	2.570	0.024140	Smith et al. (2000)
2MASXJ12572841+2810348	15.092	12.437	2.655	0.027292	Rines et al. (2001)
2MASXJ12590180+2813309	14.380	11.612	2.768	0.026742	Smith et al. (2004)
2MASXJ12580552+2814335	14.714	11.804	2.910	0.023513	de Vaucouleur et al. (1991)

†Taken from the NASA/IPAC Extragalactic Database (NED); *http://nedwww.ipac.caltech.edu/.*

Appendix B

Selection of Utilised Abbreviations

Table B.1: Abbreviations used in this dissertation.

Abbreviation	Description
AAO	Anglo-Australian Observatory
ACO	Abell, Corwin and Olowin
ADU	Analog-to-Digital Unit
BTP	Behind The Plane
CIZA	Clusters in the Zone of Avoidance
DENIS	Deep Near Infrared Survey
DIRBE	Diffuse Infra-Red Background Experiment
ESO	European Southern Observatory
ESO/SRC	ESO / United Kingdom Science Research Council
FWHM	Full Width at Half the Maximum
IRAF	Image Reduction and Analysis Facility
IRAS	Infrared Astronomical Satellite
IRAS PSC	Infrared Astronomical Satellite Point Source Catalogue
IRAS PSCz	IRAS PSC Redshift Survey
ISAAC	Infrared Spectrometer and Array Camera

Table B.1: (continued) Abbreviations used in this dissertation.

Abbreviation	Description
POSS	Palomar Observatory Sky Survey
PSC	Point Source Catalogue
PSF	Point Spread Function
REFLEX	ROSAT-ESO Flux Limited X-ray
RON	Readout Noise
ROSAT	Roentgen Satellite
ROSAT BSC	Roentgen Satellite Bright Source Catalogue
6dF	Six degree Field facility
SOFI	Son of ISAAC
2dF	Two degree Field facility
2dFGRS	2dF Galaxy Redshift Survey
2MASS	Two Micron All Sky Survey
WFI	Wide Field Imager

Appendix C

Changes made in this Dissertation

This chapter only applies at a later stage.

Appendix D

Vita

Karsten Markus was born in Thuine, Germany, on August 10th, 1974, as the son of Rudolf Bernhard Markus and Elisabeth Johanna Markus (neé Bonnekessen). After leaving the grammar schools Johanneum and Geor-

Figure D.1: The author, Karsten Markus

gianum in Lingen/Ems, Germany, he participated in the compulsory army service at the Luftlandebrigade 31 (paratroops) in Wildeshausen and Oldenburg, Germany. In 1995 he entered the Ruperto Carola in Heidelberg, Germany, where he obtained his Vordiplom in 1998. The following year, he entered the University of Cape Town, South Africa, and obtained a B.Sc. Hons. in Theoretical Physics and Astrophysics the same year. He has since been a part-time graduate student at the Department of Astronomy of the University of Cape Town and carried out observational work at observatories in France, Germany and South Africa.

Appendix E

Availability

A copy of this dissertation or a corrected version thereof should be available on the World Wide Web: http://www.karstenmarkus.de/publications/

Appendix F

Contact Details

Karsten Markus

Department of Astronomy
University of Cape Town
Rondebosch, Cape Town 7701
Republic of South Africa

Email: contact@karstenmarkus.de
WWW: karstenmarkus.de

In Memoriam

Helmut Tieke

02. March 1941 – 19. December 2005

This is in memory of my beloved uncle and friend, Helmut Tieke. His kindness and persistently positive attitude has left a deep impression on me.

I am sad and angry that you should have left this world for good, but I am contented in thinking that your life was a prosperous one. You have left all of us in a good spirit, despite our momentary grief about you leaving us.

Photometry of Elliptical Galaxies in Crowded Starfields

[Part II / III: Galaxy Catalogue]

KARSTEN MARKUS

Department of Astronomy

University of Cape Town

Republic of South Africa

Cape Town & Berlin

01.12.2006

In Memoriam

Anna Markus

neé Brinker

18. August 1913 – 08. November 2006

This is in memory of my grandmother. She survived two world wars and saw many friends leave this world before her. However, she also saw her family prosper and the growing-up of her great-grandchildren.

I remember you as a vivid person and I am thankful for your permanent support to the whole family, despite all the shortcomings that you encountered. You have done well, and I am proud to be your descendant.

Abstract

Observations of nearby large-scale structures in the Zone of Avoidance have revealed a number of important findings. Amongst these were large-scale structures like the Norma cluster and the surmised Norma Supercluster. However, various difficulties arise when extragalactic objects are investigated close to the band of stars, dust and gas that form the Milky Way. The most severe of these problems, star crowding and Galactic extinction, are analysed in this study. Stars superimposed on a galaxy can cause significant deviations in the established surface brightness profiles of these galaxies. Furthermore, the light received from these galaxies is reduced by the increasing amount of dust and gas in the line of sight towards lower Galactic latitudes. In this study, a set of thirty elliptical galaxies in the central Norma cluster region was analysed by means of high quality optical and near infrared observational data. It is found that the determination and application of a pixel mask for interfering parts in the image offers sufficiently good results for moderate numbers of foreground stars and with relatively little effort. For heavy star crowding and awkwardly positioned stars or even other galaxies close to the investigated galaxy, a more accurate method was developed: the stars were modelled with a point spread function and thereafter subtracted. Subsequently, the $(\mathrm{R_c} - \mathrm{K_s})$ colour (which is relatively insensitive to the choice of Galactic reddening law) and the colour excess were obtained. These were then compared with the most commonly used measure of extinction, the DIRBE/IRAS dust maps. The latter are, however, poorly calibrated at low Galactic latitude and are believed to overestimate the Galactic extinction at lower latitudes. The results obtained here do in fact show that the DIRBE/IRAS dust maps already slightly overestimate the Galactic extinction at the position of the central Norma cluster region.

Dedication

This thesis is dedicated to my parents,

ELISABETH JOHANNA MARKUS
– neé Bonnekessen –

and

RUDOLF BERNHARD MARKUS.

This thesis is also dedicated to the approximately 7 million South Africans who are expected to die within the next 10 years due to HIV and AIDS.

May the loss of wisdom and culture due to their deaths bring new thoughts and insights to the following generations.

Acknowledgments

Ubuntu ungamntu ngabanye abantu. [1]

There are innumerable people that – in one way or another – had influence on the positive outcome of my studies, and this dissertation in particular. Unfortunately, I will have to limit this little demonstration of gratitude to the most immediate supporters.

Professor Anthony – Tony – Patrick Fairall and Dr. Patrick Alan Woudt from the Astronomy Department at the University of Cape Town (UCT) will be the first ones to be mentioned. Both took very good care of me – against all odds. Tony, thanks a lot for being open to listening to me and for not getting tired of dealing with the various problems that occurred on and on. I also would like to emphasize that I have very much enjoyed your very good skills of 'explaining the local universe' and your interest in good quality education. Meeting you has left a deep impression on me. Patrick, the same holds for you. If it wasn't about your abilities to multitask and to turn problems into opportunities, the whole department would come to stand still. I will always be grateful to both of you for being your student and I am looking forward to working together with you in the future.

I would also like to mention Dr. Anja Schröder, who was a visiting astronomer at the UCT Astronomy Department in 2001. She may not have realised, but in her very kind way, she made me feel good about the things I was working on.

[1] Xhosa proverb: Ubuntu ungamntu ngabanye abantu – A person is only a person through other people; meaning that to develop as persons, we need to be empowered by others (Shuttle, 1995)

Meeting her has certainly put scientific work into a new perspective for me – Thank you!

Dr. Wolfgang Hasse from the Wilhelm-Foerster-Observatory (WFO) in Berlin, Germany, introduced me to quite a different scientific philosophy. Not only did I benefit from his theoretical knowledge, but also from his kind offer to join his working group at the WFO. Being a theoretical cosmologist, he showed great interest in my work and the discussions with him not seldomly opened my eyes as to where I was standing – literally. For this, a big "Danke!".

The most important person in my life, however, has been my friend and wife, Wilnelia Edith Adams. She was and still is the most valuable source of inspiration I have. Meeting her at UCT was a lucky chance in my life and I am happy that she offered me the opportunity of getting to know her better. Wilnelia, you may not be aware of this, but I do not regret a minute of the time I spent with you, be it in good or in bad times!

In terms of non-scientific support, I would first like to thank my family, and in particular my parents, Rudolf Markus and Elisabeth Markus. They never stopped believing in me and they supported me as much as they could. I will never forget this and I am proud to be your son!

Moreover, many friends and colleagues have been very encouraging in various ways. I will briefly mention a few representative names here, but the list is obviously incomplete. May those who are not mentioned forgive me for not doing so. I certainly should have mentioned you!

Joan **A**dams	Olivia Adams	Robert Adams
Rory Adams	William Adams	Wilnelia Adams
Marguerite Armstrong		
Frank **B**eier	Daniel Bendix	Andrea Bierau
Herrmann Bonnekessen	Franz Bonnekessen	Hannah Bohle
Stefan Bubenzer	Prof. Buffler	
Michelle **C**luver	Lisa Crause	
Britta **D**eutsch	Hans-Joachim Döbler	
Prof. **F**airall	Prof. Feast	Julia Frantz
Jörn **G**reving		
Katrin **H**ammerstein	Dr. Hasse	Björn Heggemann
Dr. Hempel	Ulrike Hentschel	Frank Hermes
Prof. Hunklinger		
Lesley **J**ennings	Birgit Joest	
Robert **K**astl	Volker Kathöfer	Dr. Kirstein
Thorsten Koch	Andreas Köster	Prof. Kraan-Korteweg
Katya Kumkova-Wolpert		
Regine **L**ord		
Anna **M**arkus	Elisabeth Markus	Oliver Markus
Rudolf Markus	Tanja Markus	Johannes Meier
Sabine Morgner		
Dr. **N**ickel	Sandra Nikolic	Prof. Nordmeier
Mark **P**ollmeier	Mellanie Pollmeier	Retha Pretorius
Tobias **R**odäbel		
Prof. **S**ahm	Katrin Sailer	Christian Schäfers
Christine Siewert	Dr. Schreiber	Dr. Schröder
Ralf Staudemeyer		
Helmut **T**hieke	Mia Thieke	Prof. Thomsen
Prof. **U**lmschneider		
Prof. **W**arner	Kerstin Wagner	Florian Weißbach
Dr. Woudt		

Utilised Data Sources

ArXiv e-print service:

See *http://lanl.arxiv.org/*.

Astrophysics Data System:

See *http://adswww.harvard.edu/*.

Coma cluster data:

Generously supplied by Dr. J. Lucey, Department of Physics, *University of Durham*, United Kingdom, see *http://www.dur.ac.uk/john.lucey/*.

Near infrared Norma cluster data:

Data obtained with *European Southern Observatory* facilities and generously supplied by Dr. A. C. Schröder, Department of Physics & Astronomy, *University of Leicester*, United Kingdom.

Milky Way image:

Generously supplied by Dr. A. Mellinger, see Mellinger (2000) and *http://home.arcor-online.de/axel.mellinger/*.

NED database:

NASA/IPAC Extragalactic Database, see *http://nedwww.ipac.caltech.edu/*.

Optical Norma cluster data:

Data obtained with *European Southern Observatory* facilities and generously supplied by Dr. P. A. Woudt, Astronomy Department, *University of Cape Town*, Republic of South Africa, see *http://mensa.ast.uct.ac.za/~pwoudt/*.

Redshift data:

Obtained with the *Anglo Australian Observatory 2dF* instrument and generously supplied by Dr. J. Lucey, Department of Physics, *University of Durham*, United Kingdom, see *http://www.dur.ac.uk/john.lucey/*.

SIMBAD database:

This research has made use of the *SIMBAD* database, operated at the *Centre de Données astronomiques de Strasbourg*, France, see *http://simbad.u-strasbg.fr/*.

ViZieR service:

This research has made use of the *ViZieR* service, operated at the *Centre de Données astronomiques de Strasbourg*, France,
see Ochsenbein et al. (2000) and *http://vizier.u-strasbg.fr/*.

Utilised Software

GALFIT software:

See *http://zwicky.as.arizona.edu/~cyp/work/galfit/galfit.html* and Peng et al. (2002).

GNUPlot software:

See *http://www.gnuplot.info/*.

Hierarch28 software:

Provided by the *European Southern Observatory*, see *http://archive.eso.org/saft/*.

IRAF software:

IRAF is distributed by the *National Optical Astronomy Observatories*, which are operated by the *Association of Universities for Research in Astronomy, Inc.*, under cooperative agreement with the *National Science Foundation*. See *http://iraf.noao.edu/* and Tody (1986, 1993).

Killall software:

I kindly acknowledge Prof. McCall for the use of the *Killall* software,
also see Buta and McCall (1999).

Mac OS:

Developed by *Apple Computer, Inc.*, see *http://www.apple.com/*.

Physica software:

Provided by the *TRIUMPH Computing Services Group*,
see *http://www.triumf.ca/physica/html/homepage.html*.

RedHat Linux :

Provided by *Red Hat, Inc.*, See *http://www.redhat.com/*.

SAOImage DS9 software:

This research has made use of *SAOImage DS9*, developed by *Smithsonian Astrophysical Observatory*, see *http://hea-www.harvard.edu/RD/ds9/* and Joye and Mandel (2003).

SkyCat software:

Provided by the *European Southern Observatory*, see *http://archive.eso.org/skycat/*.

SM software:

Previously known as *SuperMongo*, see *http://www.astro.princeton.edu/~rhl/sm/* and Lupton and Monger (1997).

STSDAS & TABLES packages:

Products of the *Space Telescope Science Institute*, which is operated by *Association of Universities for Research in Astronomy, Inc.*, for *NASA*,
see *http://www.stsci.edu/resources/software_hardware/*.

Contents

List of Tables

List of Figures

Chapter 1

Introduction

This is the second part of three parts in which this dissertation is divided into. However, similar to Part III, this part is considered to be only an attachment to the first part, which contains all details about the subject, data, analysis, results and the discussion. The third part contains more detailed information about how the data was processed and gives instructions on how to repeat similar investigations. However, part of the results consist of plots and images of the galaxies which were investigated. These are not necessary for following the analysis and results shown in part one, but they nonetheless offer information about the analysis that was applied to the data and even give more details about the galaxies that were processed. These 'peripheral' results are what can be seen in this part of the dissertation.

The 'Galaxy Catalogue', as this part is called, gives all surface brightness plots, plots of colour and fitted de Vaucouleur $r^{1/4}$ profiles and images of the galaxies before and after the *iPSF-Fitting* procedure was applied. The information is given for each galaxy that was investigated and the galaxies are sorted by their identification code as defined by Woudt (1998). For more information, e.g. on the data analysis, the reader is referred to Part I and III of this dissertation.

In the images shown for each galaxy, northwards and westwards are at the top and the right side, respectively. The orientation may deviate from the

position angles shown in the corresponding plots, since the orientation of the images was only adopted to the same coordinate system after the isophote fitting had been conducted already. Furthermore, for the plotting, the angles were sometimes rotated by 180°.

Chapter 2

Galaxy WKK 5920

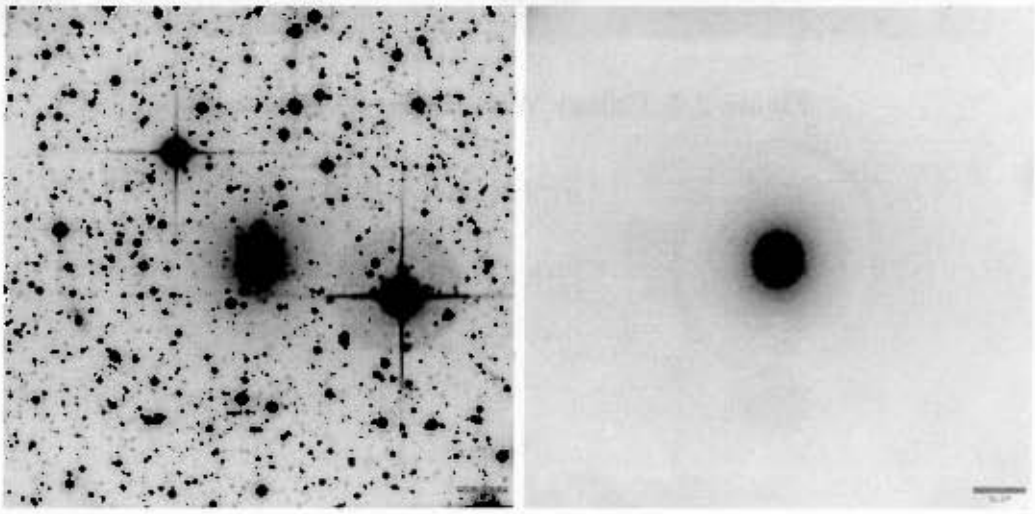

Figure 2.1: Galaxy WKK 5920. R_c band images, field 11. WFI CCD #51.

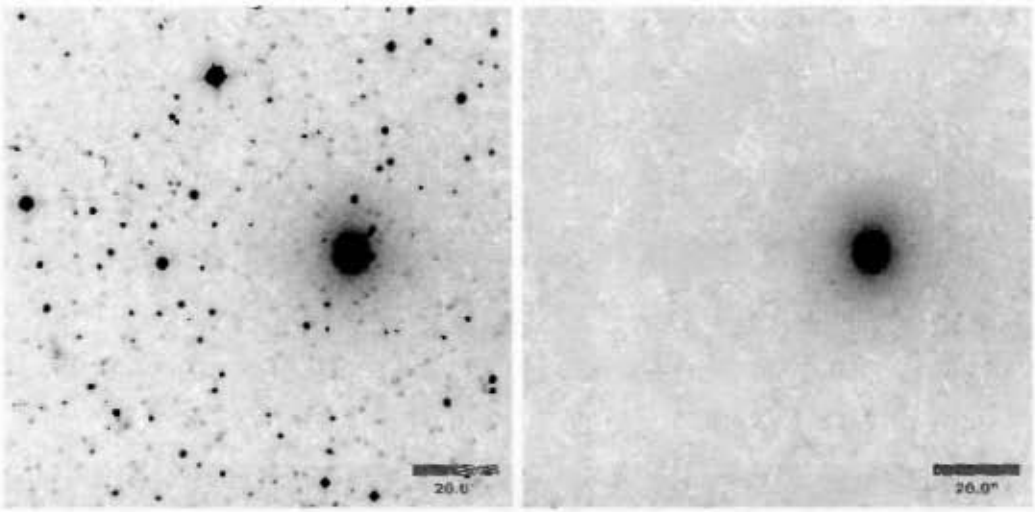

Figure 2.2: Galaxy WKK 5920, K_s band images.

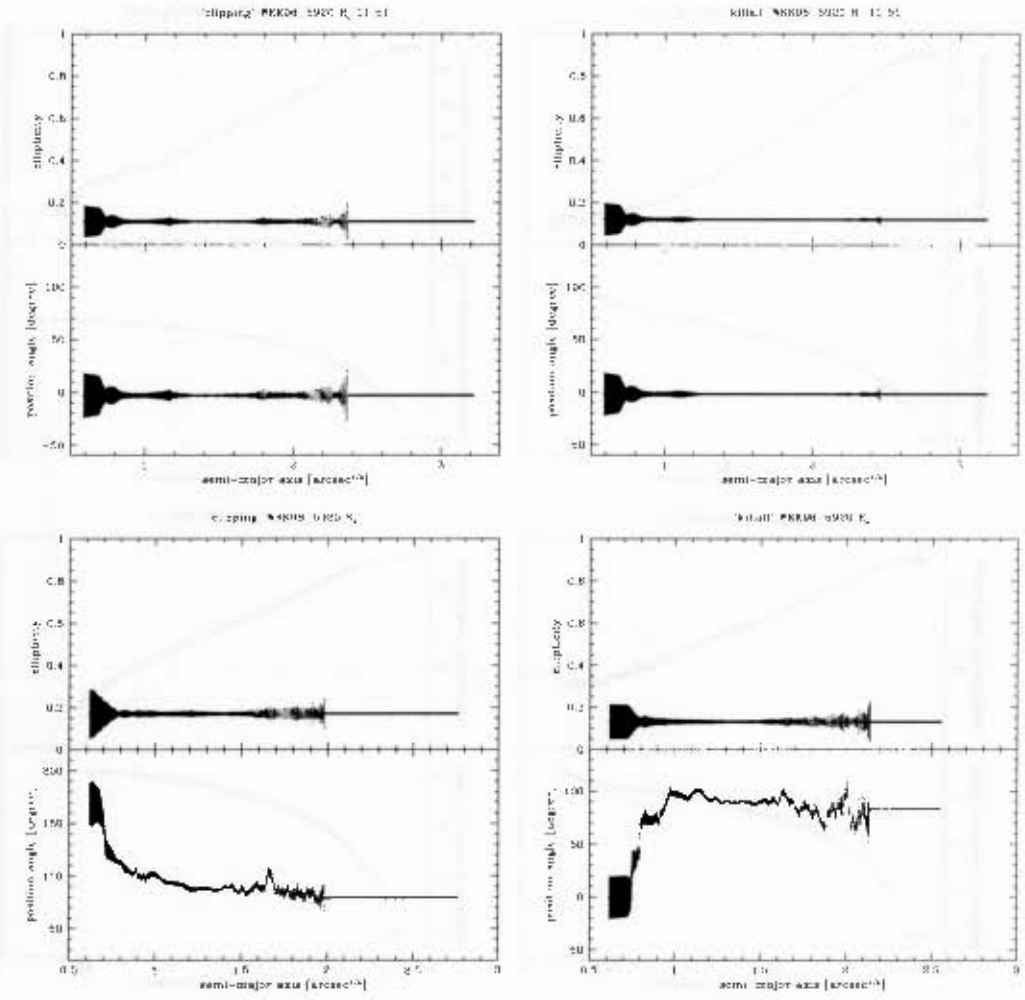

Figure 2.3: Galaxy WKK 5920, ellipticity and position angle plots.

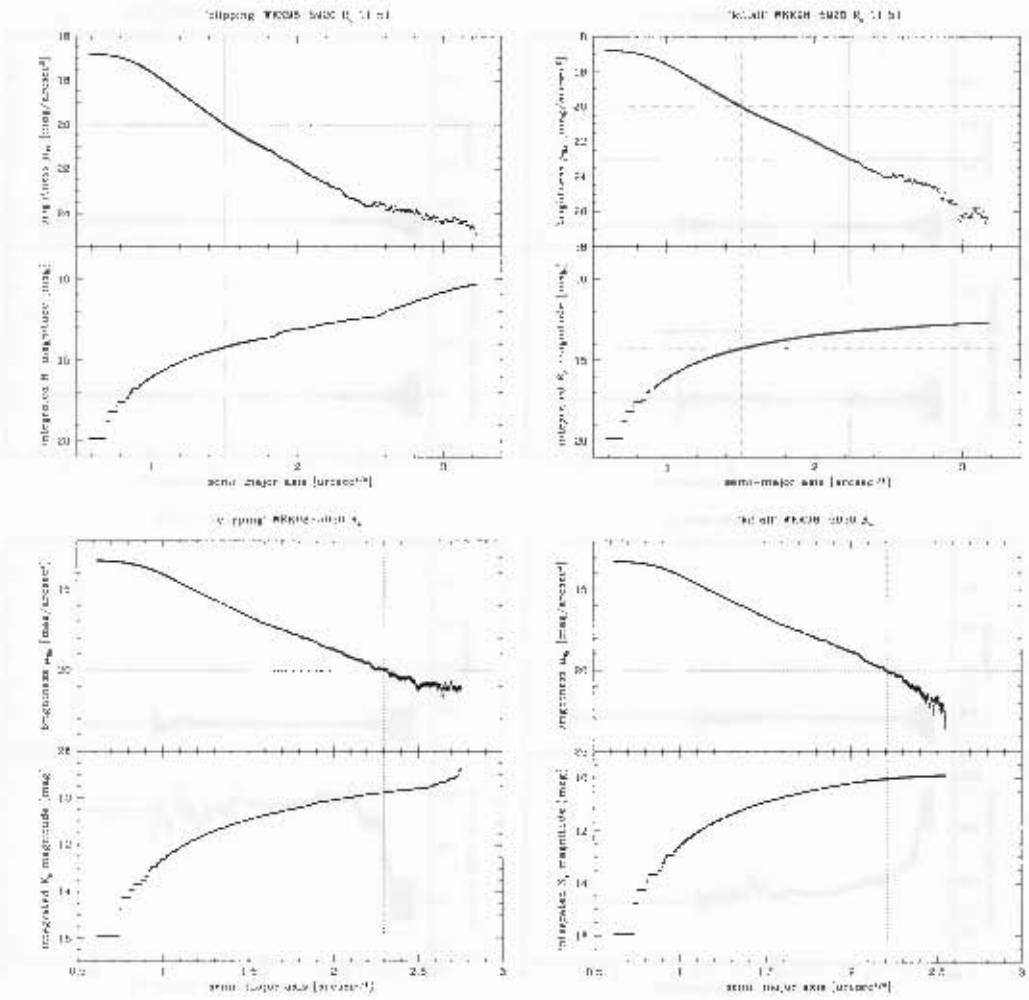

Figure 2.4: Galaxy WKK 5920. isophotal and integrated magnitude plot.

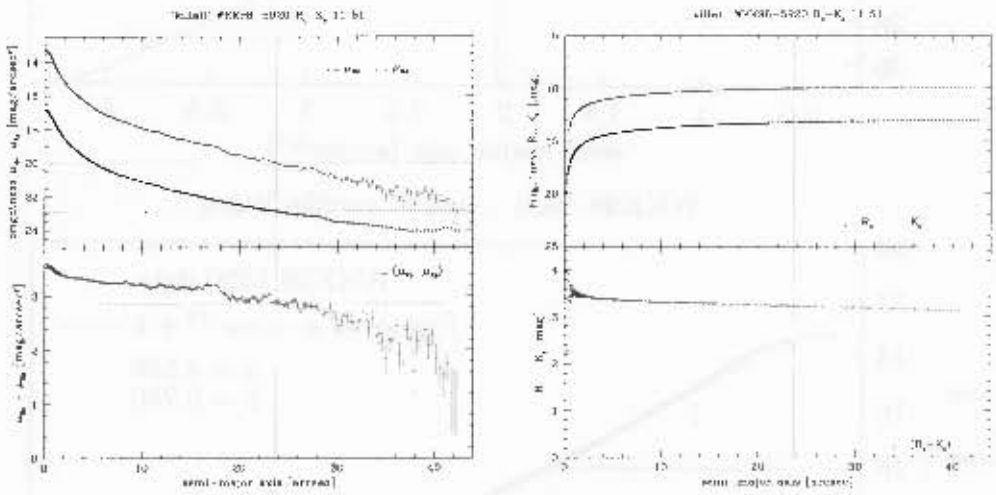

Figure 2.5: Galaxy WKK 5920. $(\mu_{R_c} - \mu_{K_s})$ and $(R_c - K_s)$ magnitude plots.

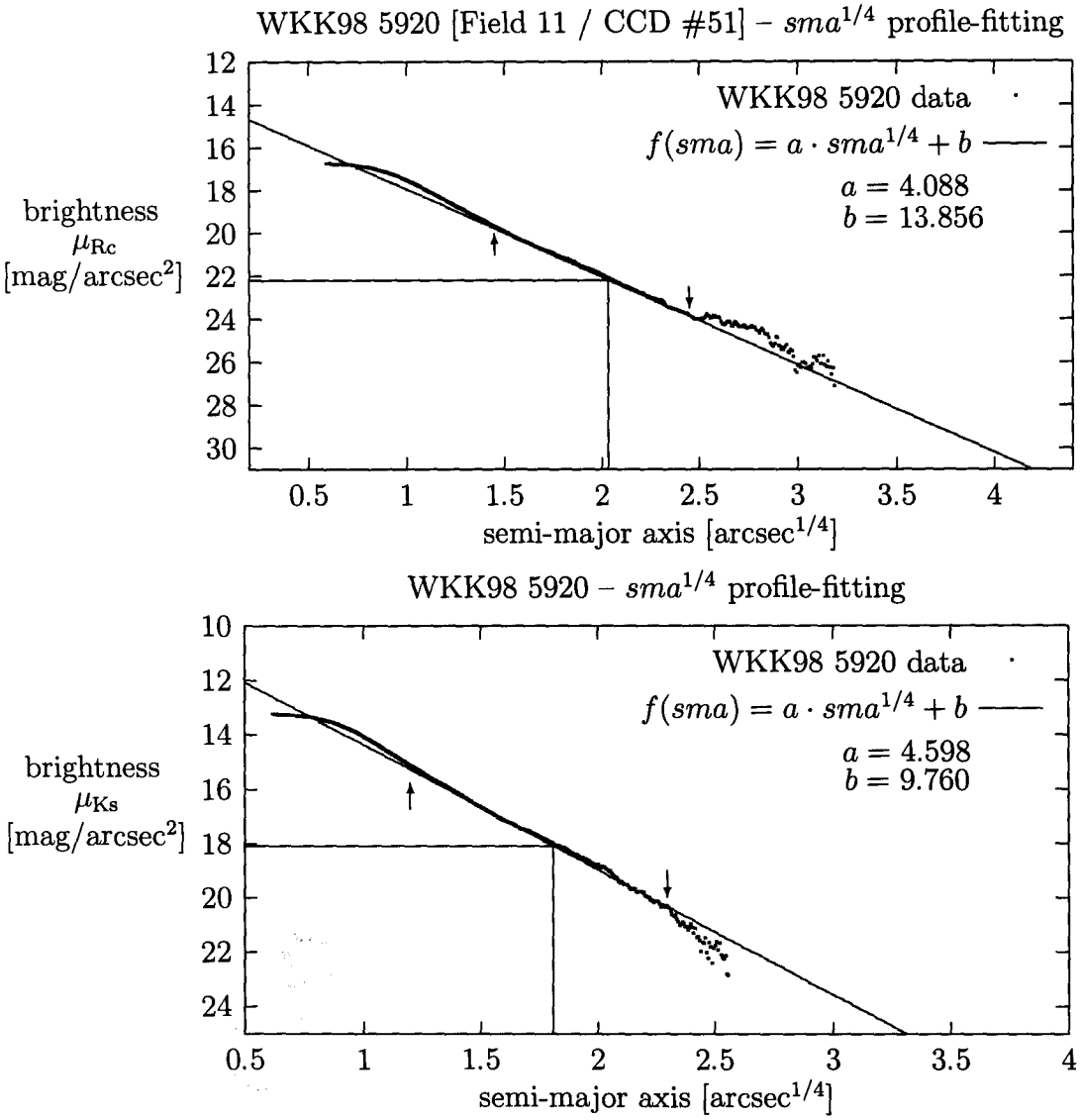

Figure 2.6: Galaxy WKK 5920, plots of brightness (μ_{R_c} and μ_{K_s}) versus semi-major axis sma$^{1/4}$ to demonstrate the profile-fitting. The arrows point to the upper and lower limit of the data set that was used for the fit. The resulting effective (half-light) radius $r_e^{1/4}$ and effective (half-light) surface brightness μ_e are indicated by straight lines.

Chapter 3

Galaxy WKK 5972

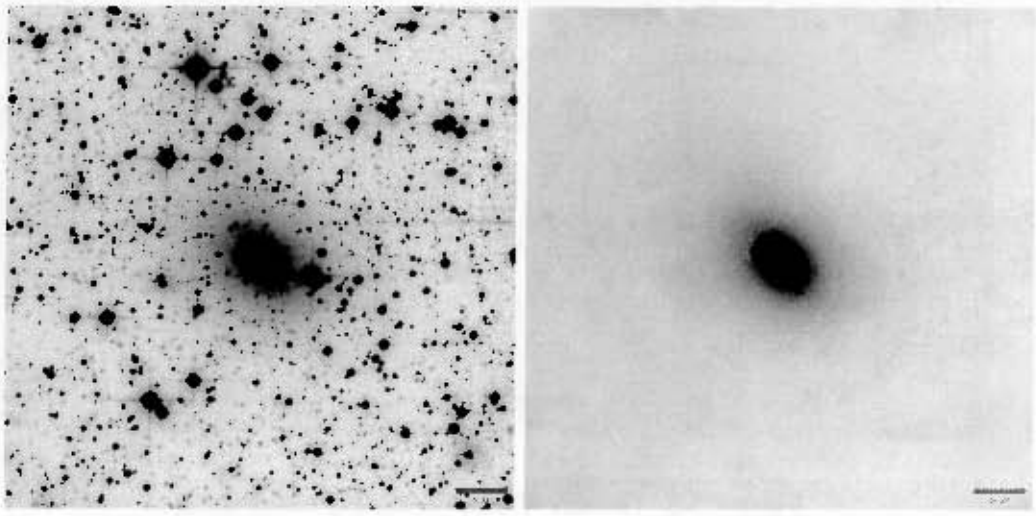

Figure 3.1: Galaxy WKK 5972, R_c band images, field 03, WFI CCD #53

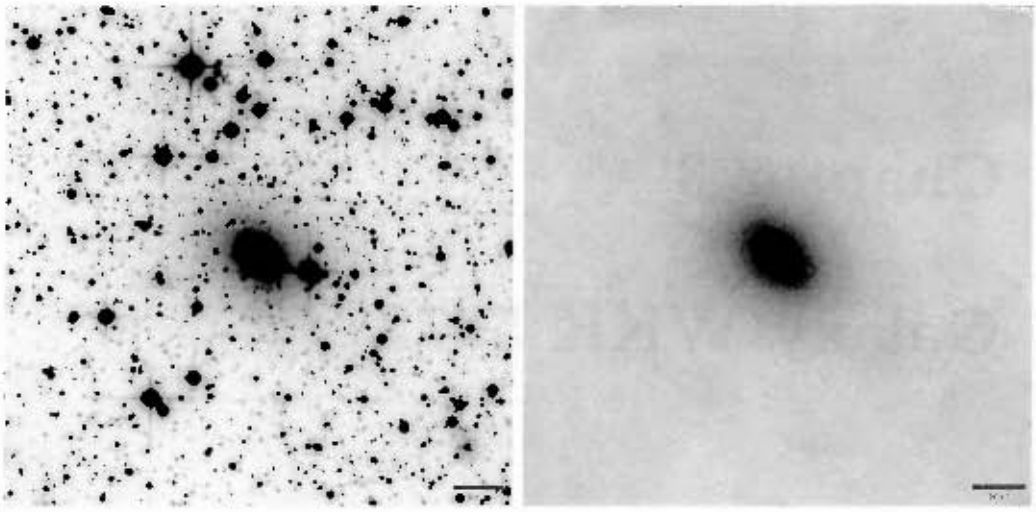

Figure 3.2: Galaxy WKK 5972, R_c band images, field 11, WFI CCD #50

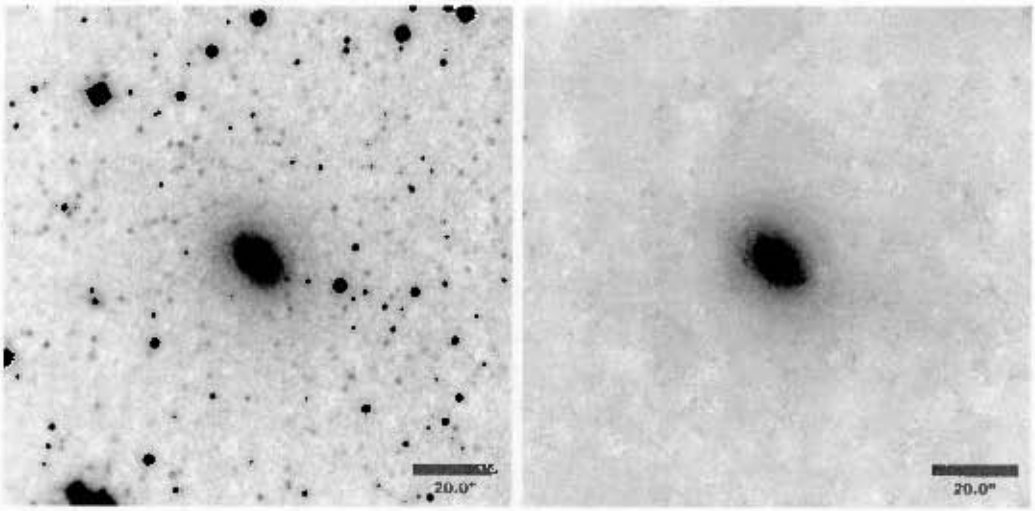

Figure 3.3: Galaxy WKK 5972, K_s band images

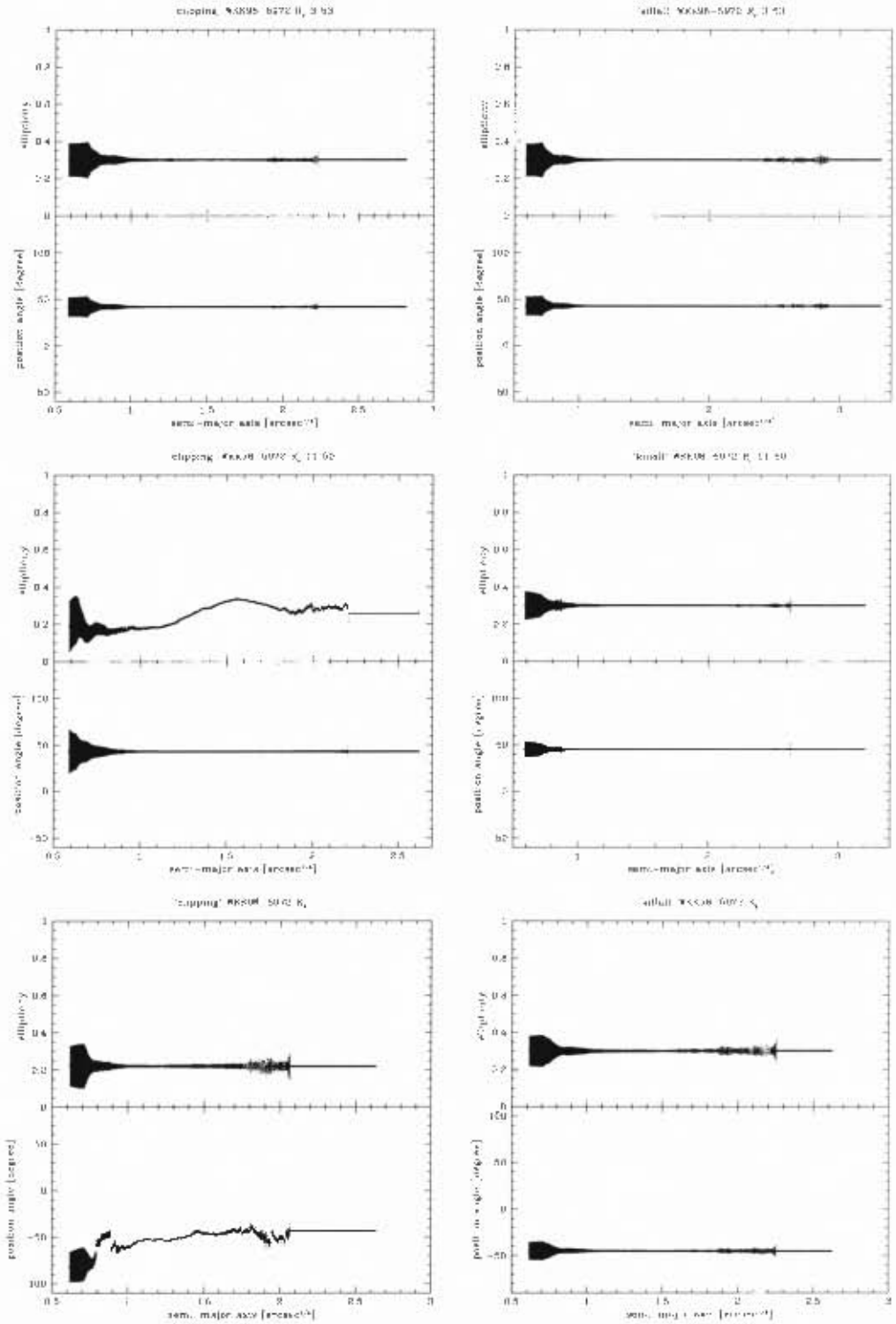

Figure 3.4: Galaxy WKK 5972, ellipticity and position angle plots

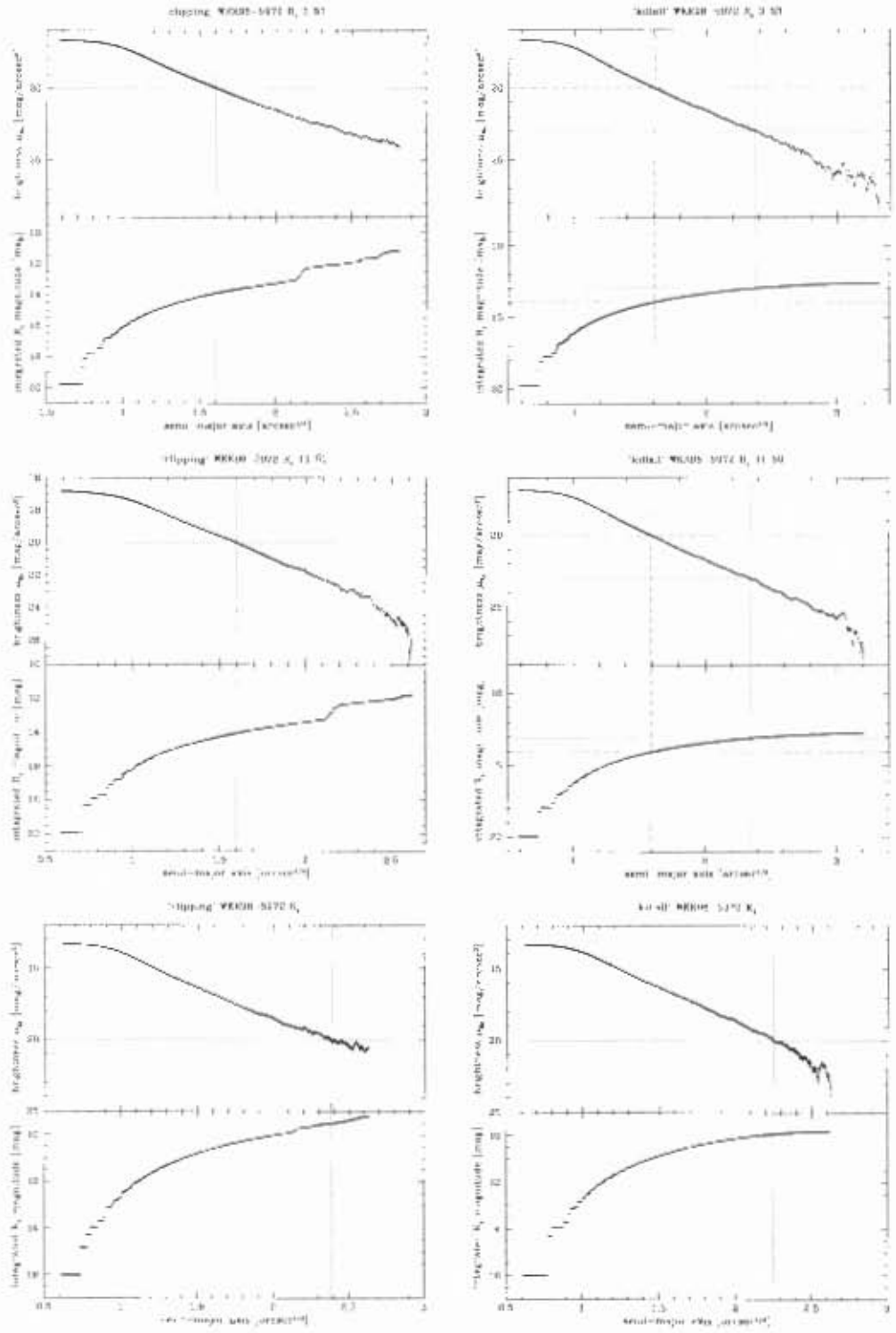

Figure 3.5: Galaxy WKK 5972, isophotal and integrated magnitude plots

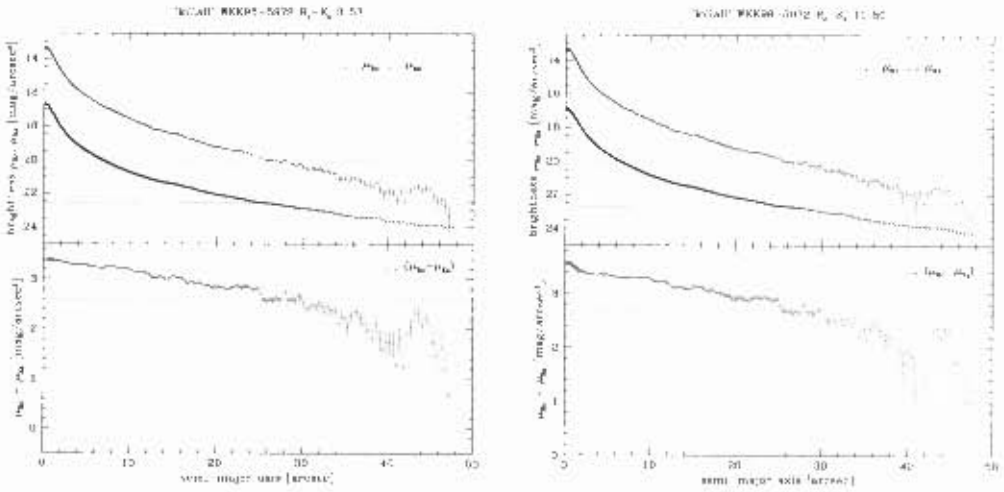

Figure 3.6: Galaxy WKK 5972, $(\mu_{R_c} - \mu_{K_s})$ magnitude plots

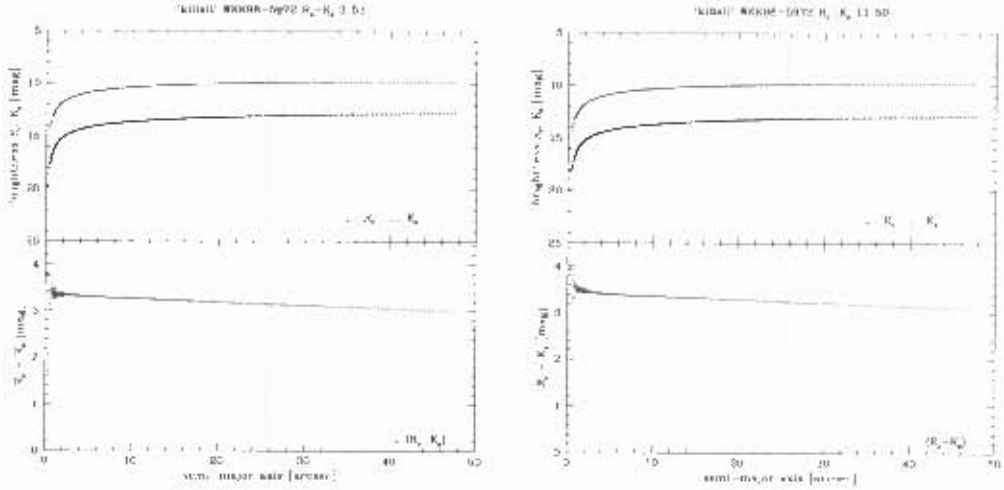

Figure 3.7: Galaxy WKK 5972, $(R_c - K_s)$ magnitude plots

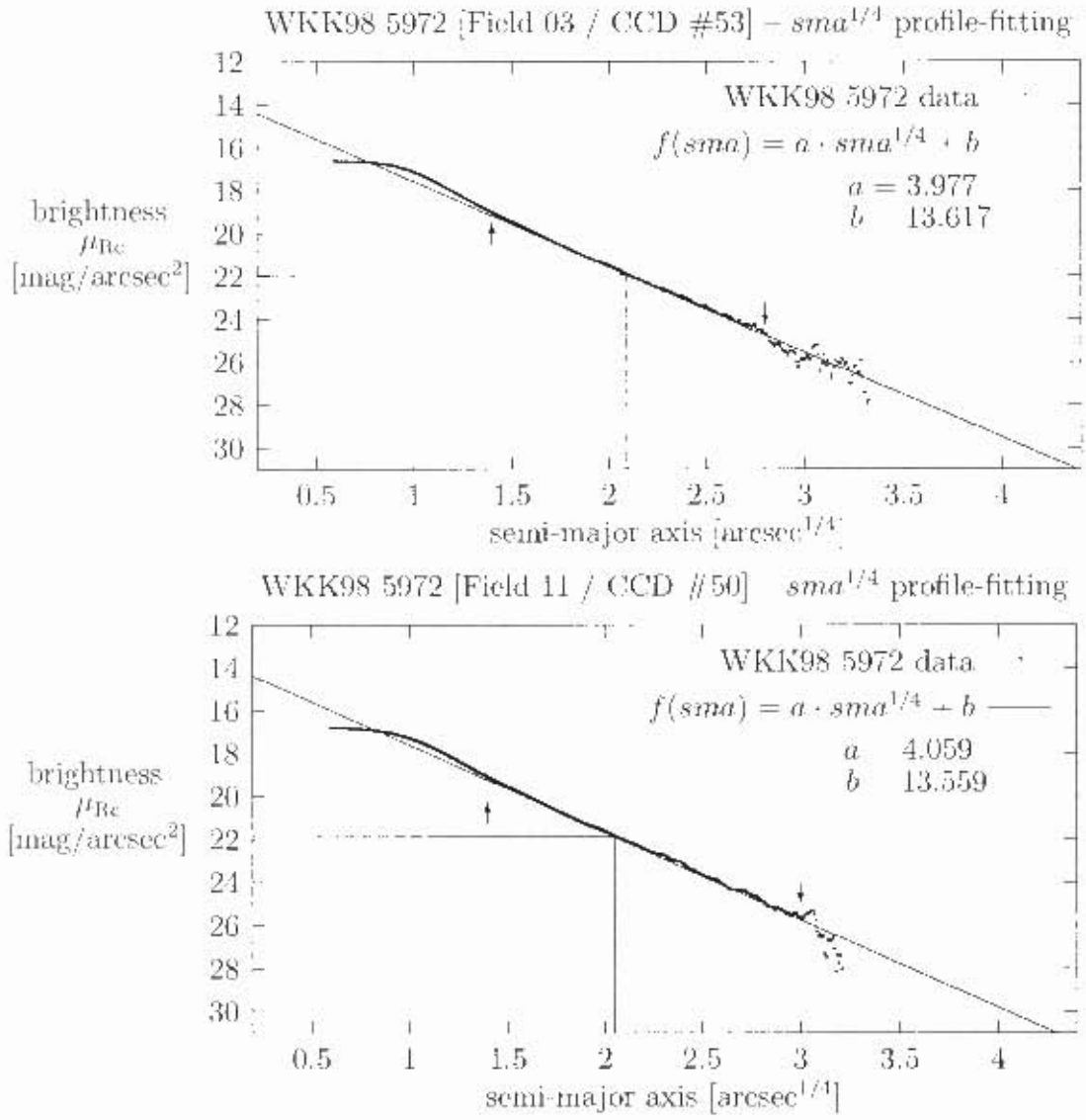

Figure 3.8: Galaxy WKK 5972, plots of brightness μ_{R_c} versus semi major axis $sma^{1/4}$ to demonstrate the profile-fitting. The arrows point to the upper and lower limit of the data set that was used for the fit. The resulting effective (half-light) radius $r_e^{1/4}$ and effective (half-light) surface brightness μ_e are indicated by straight lines.

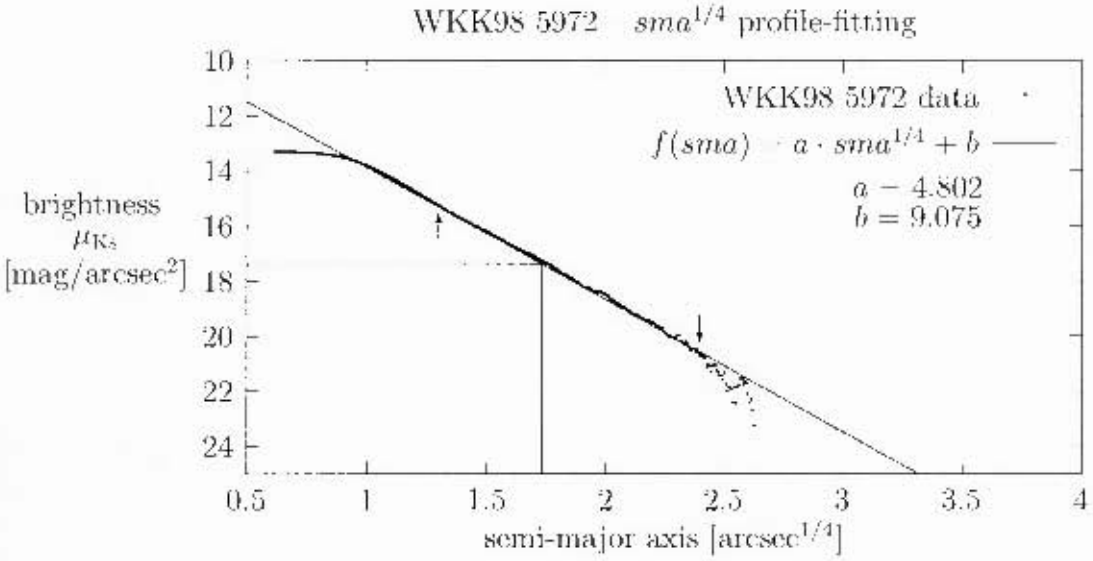

Figure 3.9: Galaxy WKK 5972, plot of brightness μ_{K_s} versus semi-major axis $sma^{1/4}$ to demonstrate the profile-fitting. The arrows point to the upper and lower limit of the data set that was used for the fit. The resulting effective (half-light) radius $r_e^{1/4}$ and effective (half-light) surface brightness μ_e are indicated by straight lines.

Chapter 4

Galaxy WKK 5987

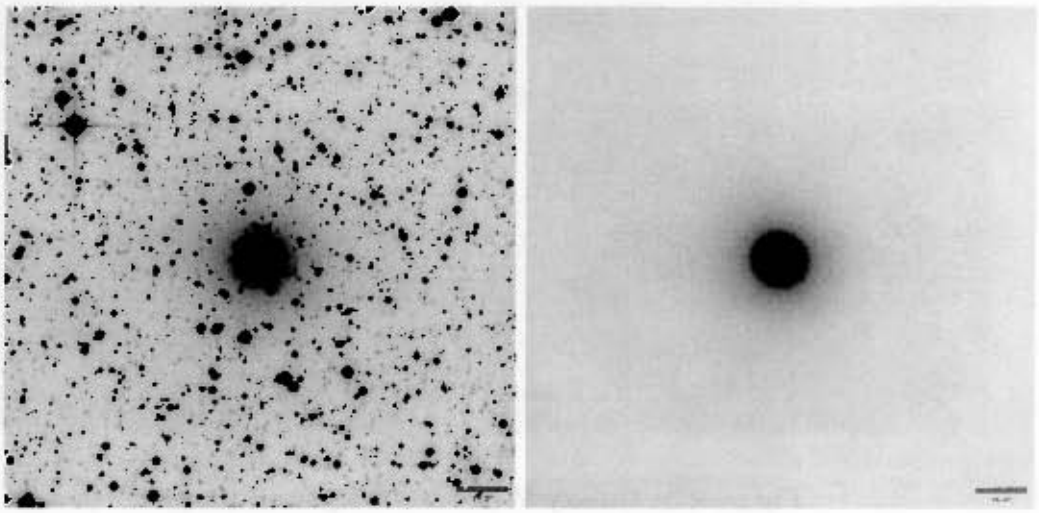

Figure 4.1: Galaxy WKK 5987, R_c band images, field 03, WF1 CCD #53

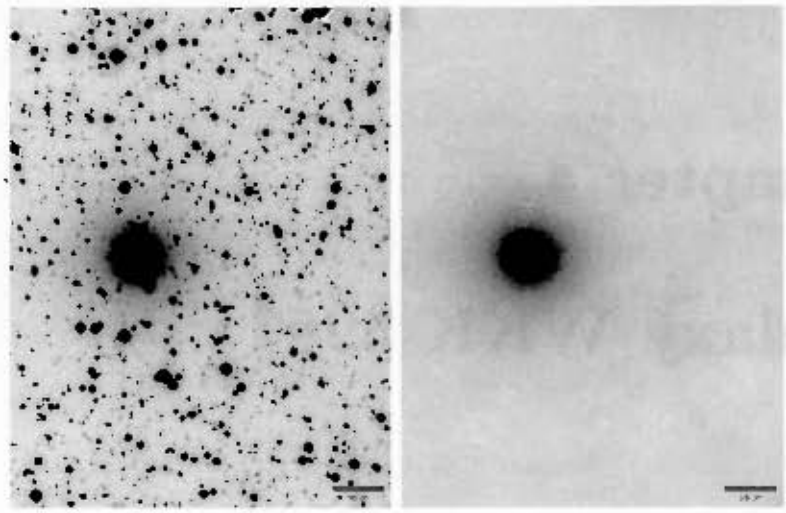

Figure 4.2: Galaxy WKK 5987, R_c band images, field 11, WFI CCD #50

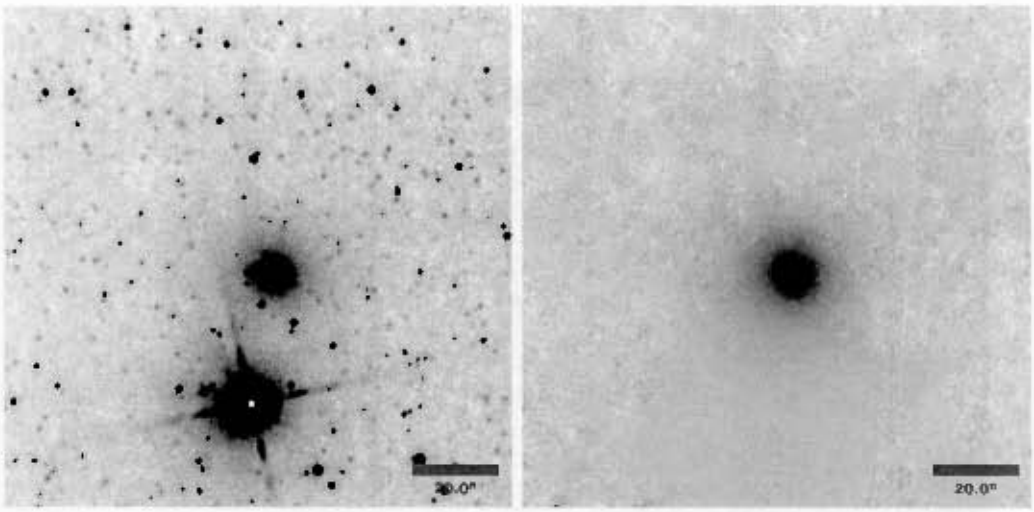

Figure 4.3: Galaxy WKK 5987, K_s band images

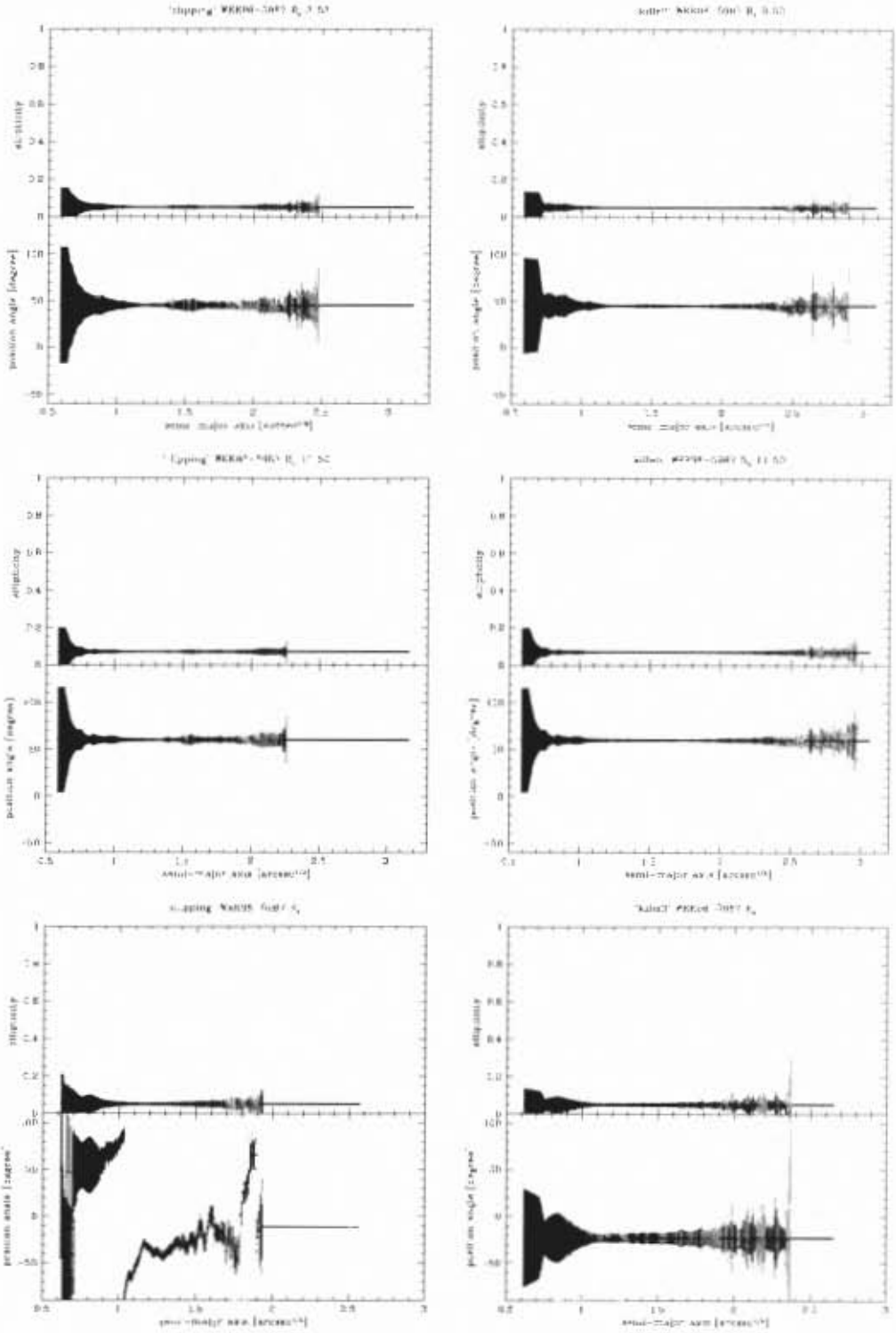

Figure 4.4: Galaxy WKK 5987, ellipticity and position angle plots

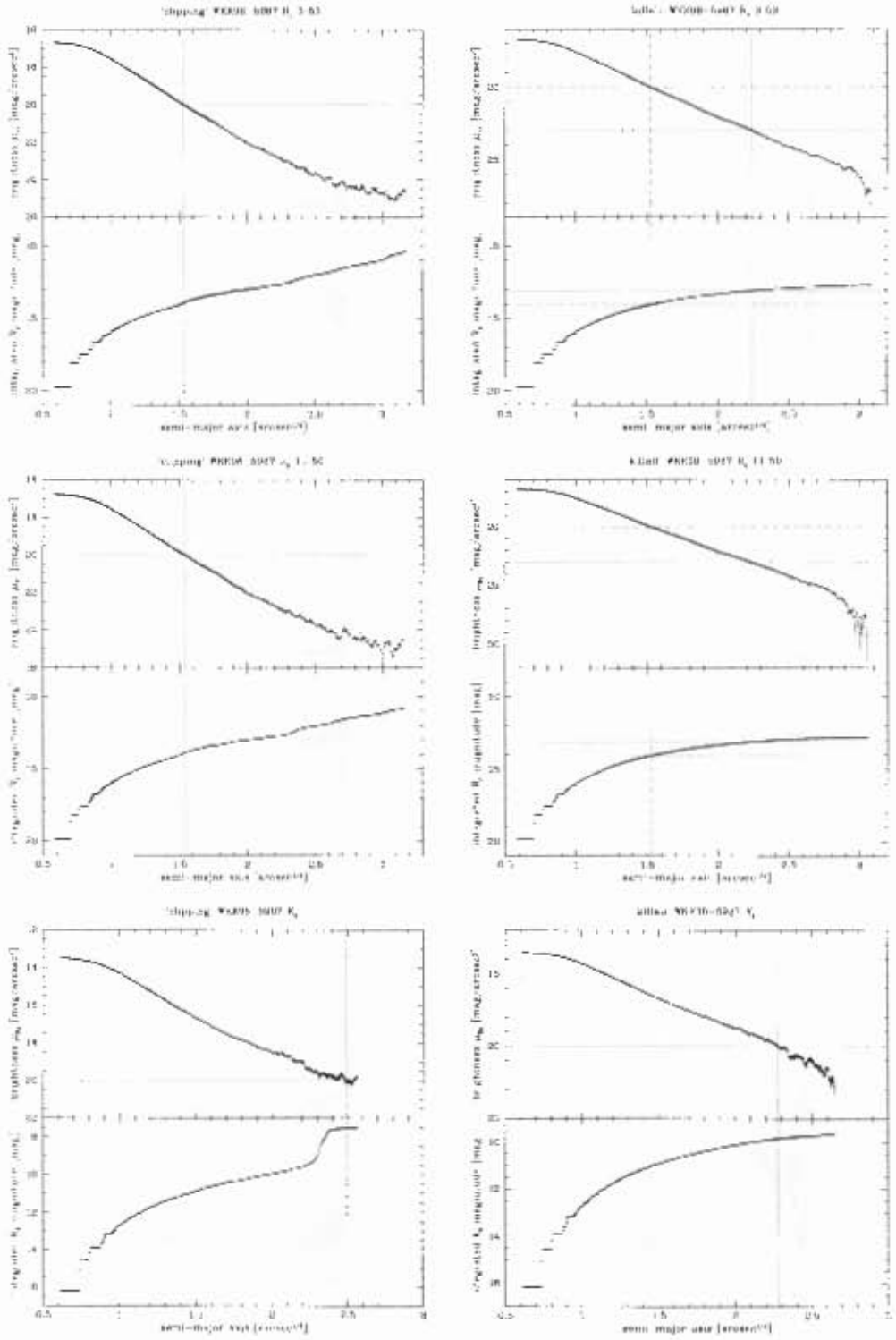

Figure 4.5: Galaxy WKK 5987, isophotal and integrated magnitude plots

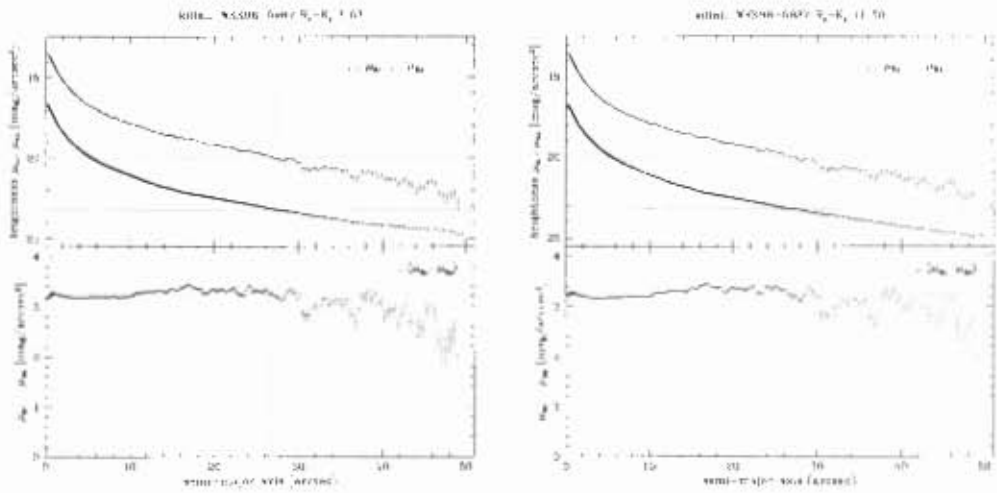

Figure 4.6: Galaxy WKK 5987, (μ_{R_e} μ_{K_s}) magnitude plots

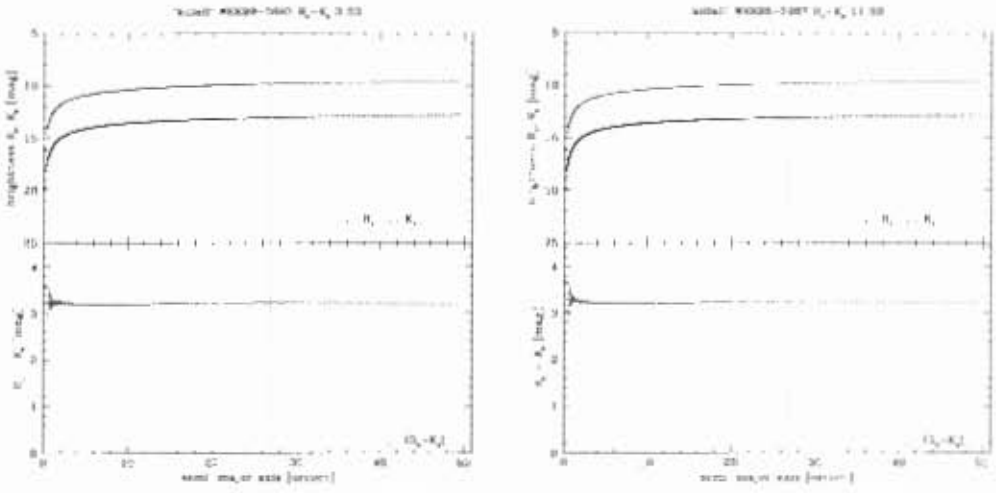

Figure 4.7: Galaxy WKK 5987, ($R_e - K_s$) magnitude plots

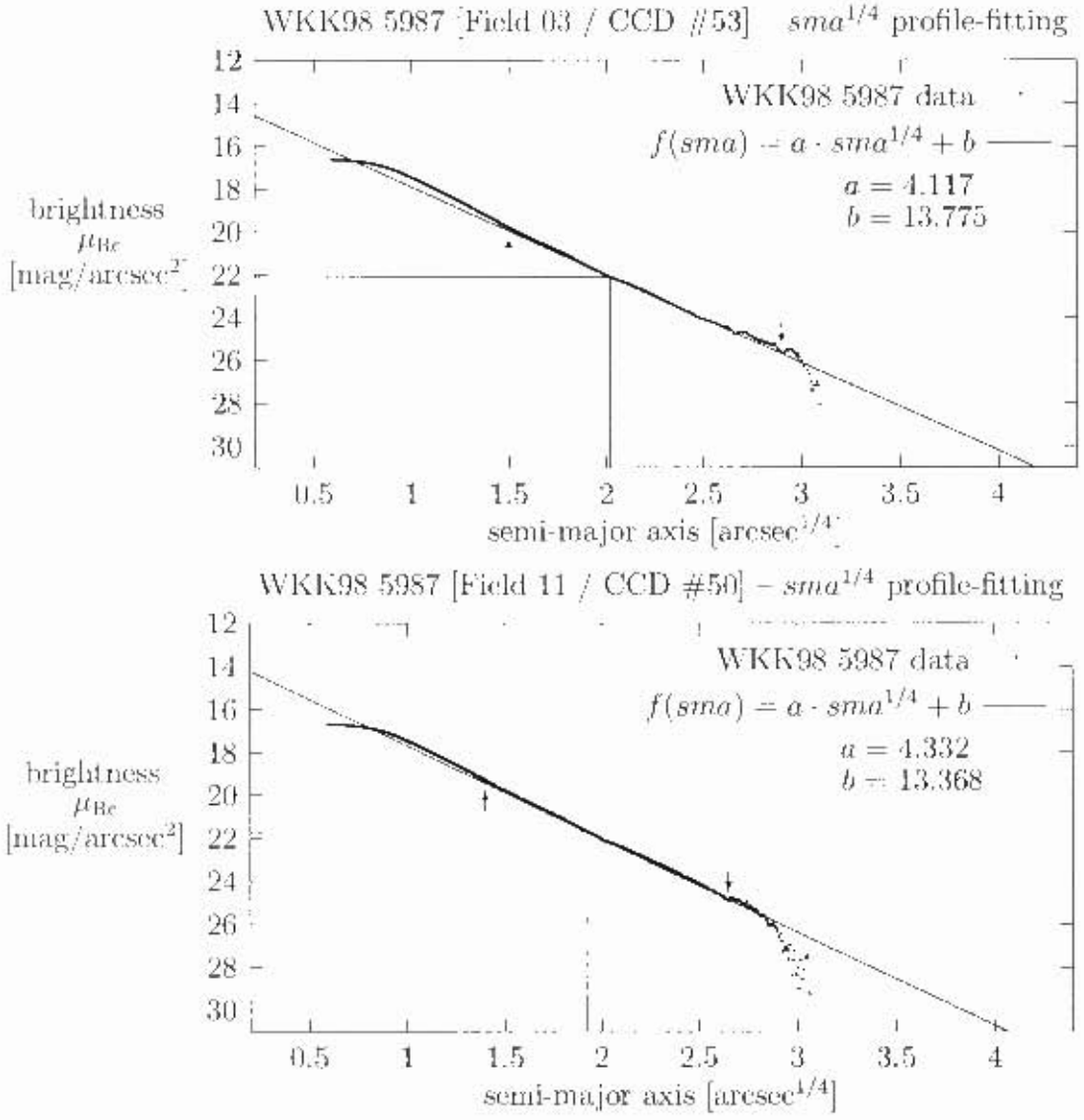

Figure 4.8: Galaxy WKK 5987, plots of brightness μ_{R_c} versus semi-major axis $sma^{1/4}$ to demonstrate the profile-fitting. The arrows point to the upper and lower limit of the data set that was used for the fit. The resulting effective (half-light) radius $r_e^{1/4}$ and effective (half-light) surface brightness μ_e are indicated by straight lines.

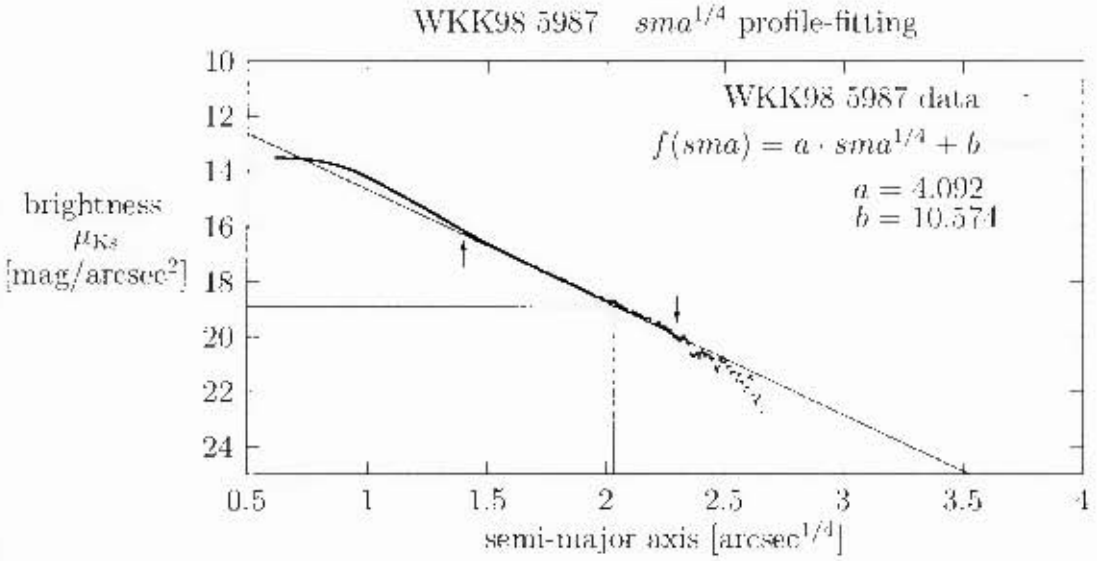

Figure 4.9: Galaxy WKK 5987, plot of brightness μ_{K_s} versus semi-major axis $\mathrm{sma}^{1/4}$ to demonstrate the profile-fitting. The arrows point to the upper and lower limit of the data set that was used for the fit. The resulting effective (half-light) radius $r_e^{1/4}$ and effective (half-light) surface brightness μ_e are indicated by straight lines.

Chapter 5

Galaxy WKK 6012

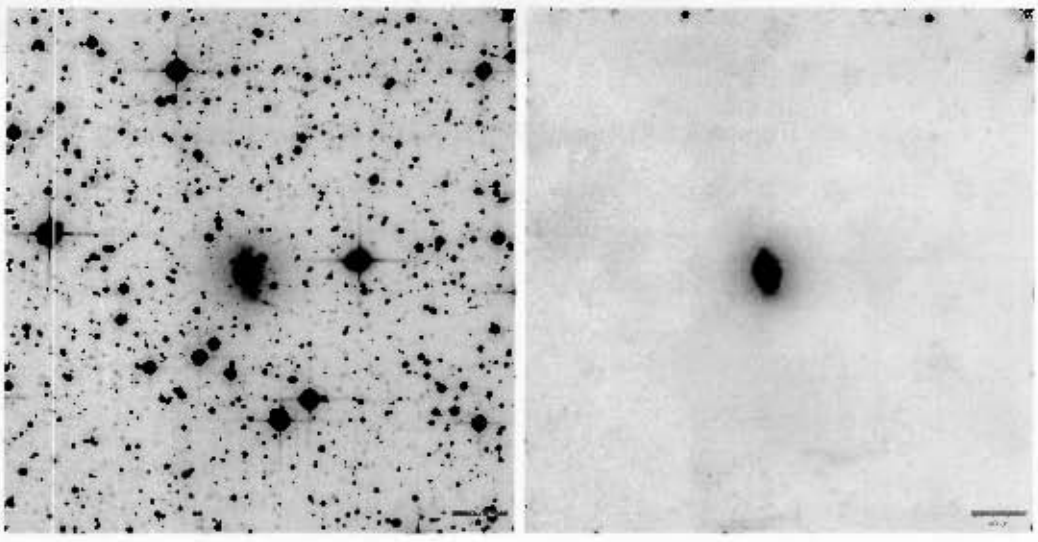

Figure 5.1: Galaxy WKK 6012, R_c band images, field 04, WFI CCD #54

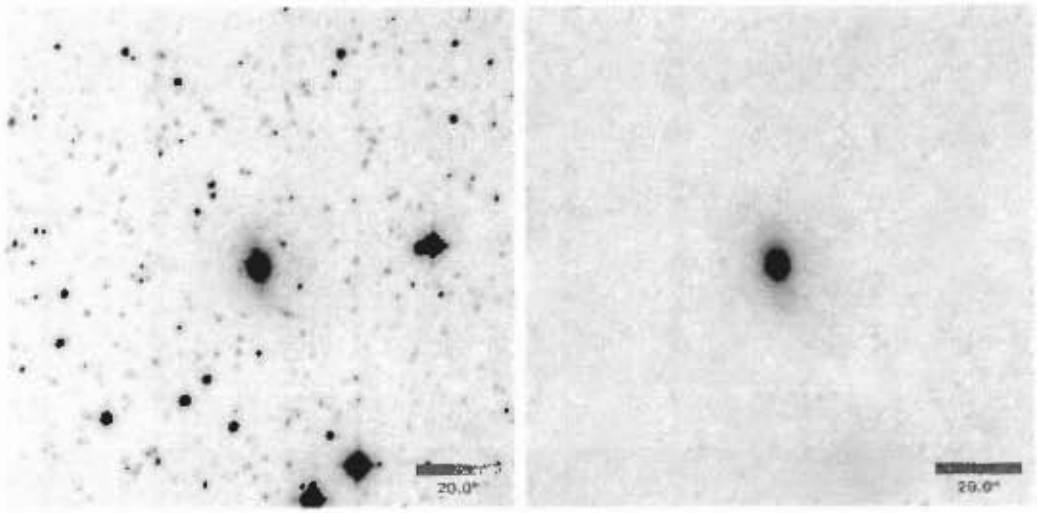

Figure 5.2: Galaxy WKK 6012. K_s band images

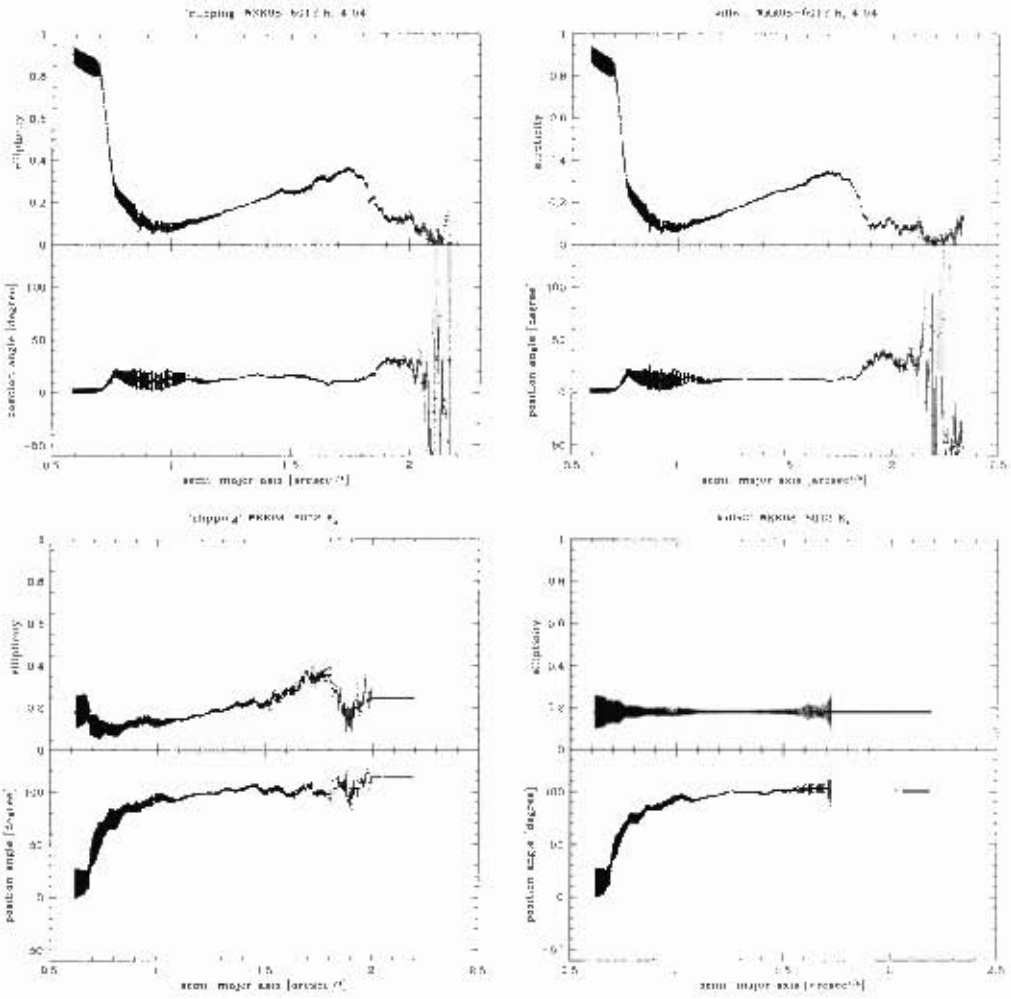

Figure 5.3: Galaxy WKK 6012, ellipticity and position angle plots

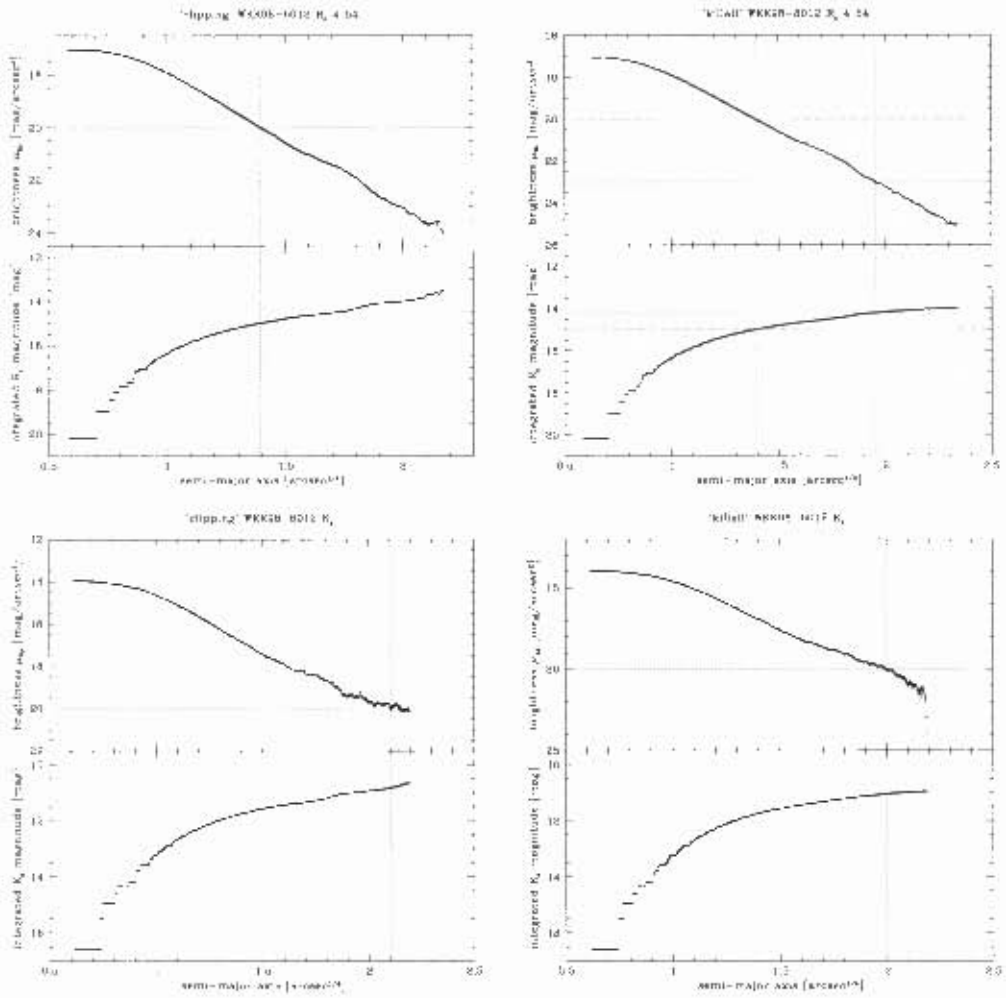

Figure 5.4: Galaxy WKK 6012, isophotal and integrated magnitude plots

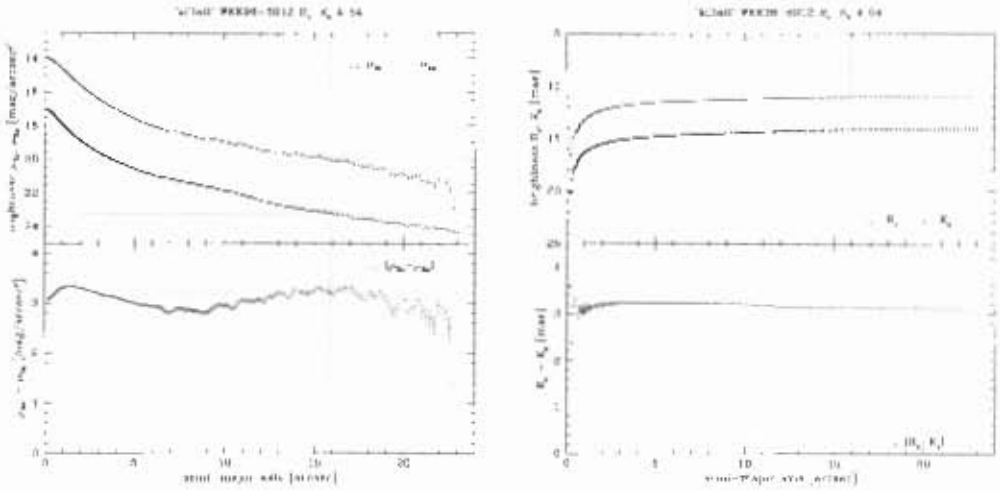

Figure 5.5: Galaxy WKK 6012, ($\mu_{R_c} - \mu_{K_s}$) and (R_c K_s) magnitude plots

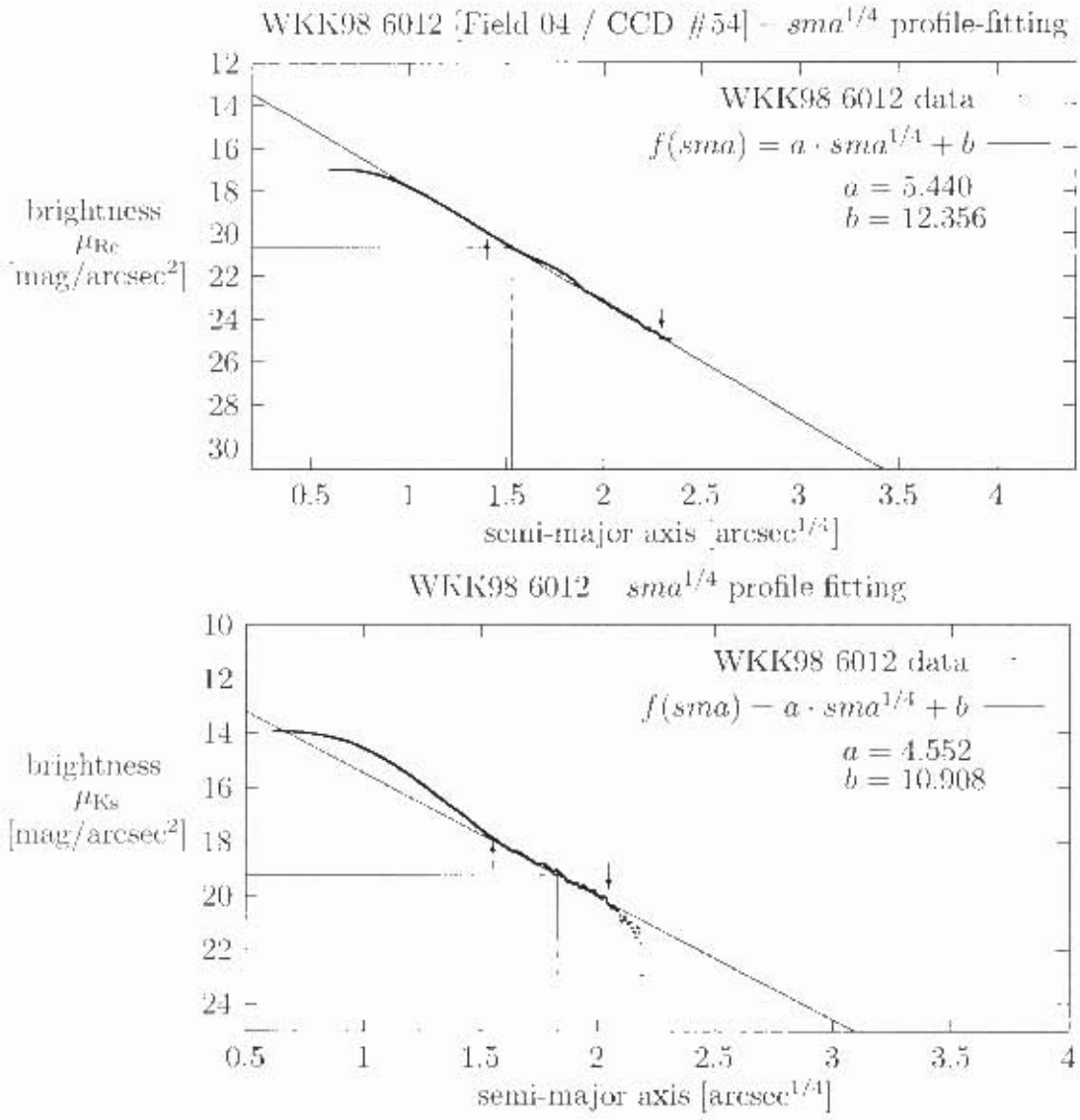

Figure 5.6: Galaxy WKK 6012, plots of brightness (μ_{R_c} and μ_{K_s}) versus semi-major axis $sma^{1/4}$ to demonstrate the profile-fitting. The arrows point to the upper and lower limit of the data set that was used for the fit. The resulting effective (half-light) radius $r_e^{1/4}$ and effective (half-light) surface brightness μ_e are indicated by straight lines.

Chapter 6

Galaxy WKK 6019

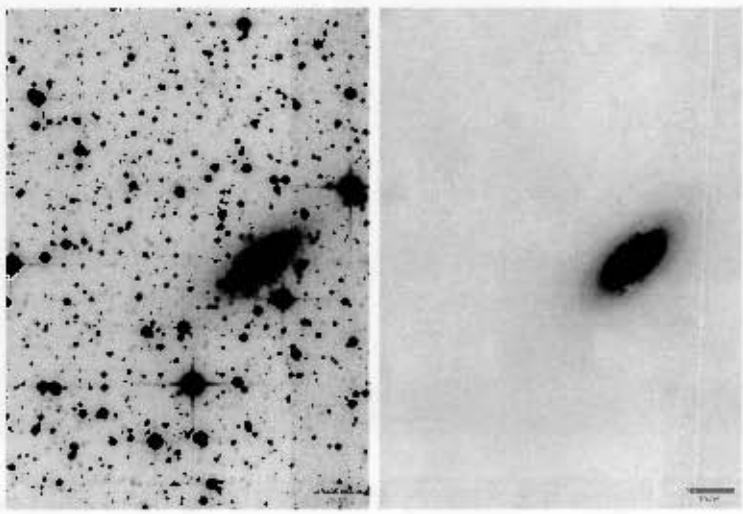

Figure 6.1: Galaxy WKK 6019, R_c band images, field 04, WFI CCD #52

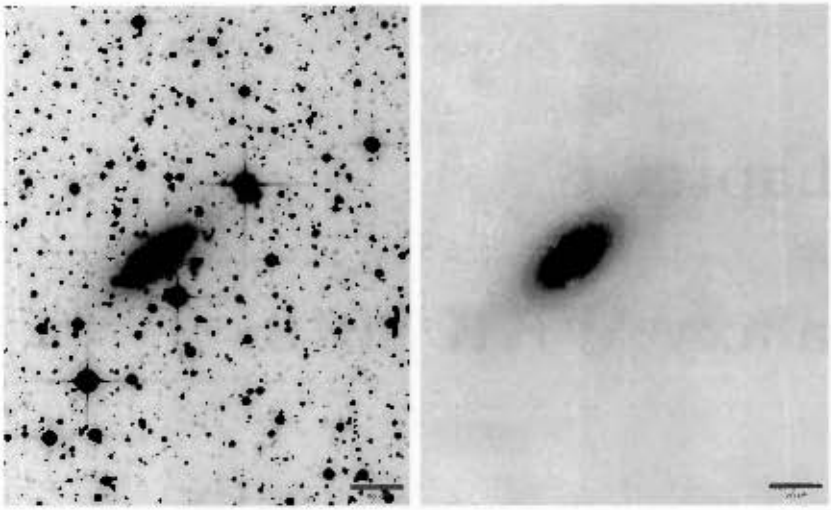

Figure 6.2: Galaxy WKK 6019, R_c band images, field 04, WFI CCD #53

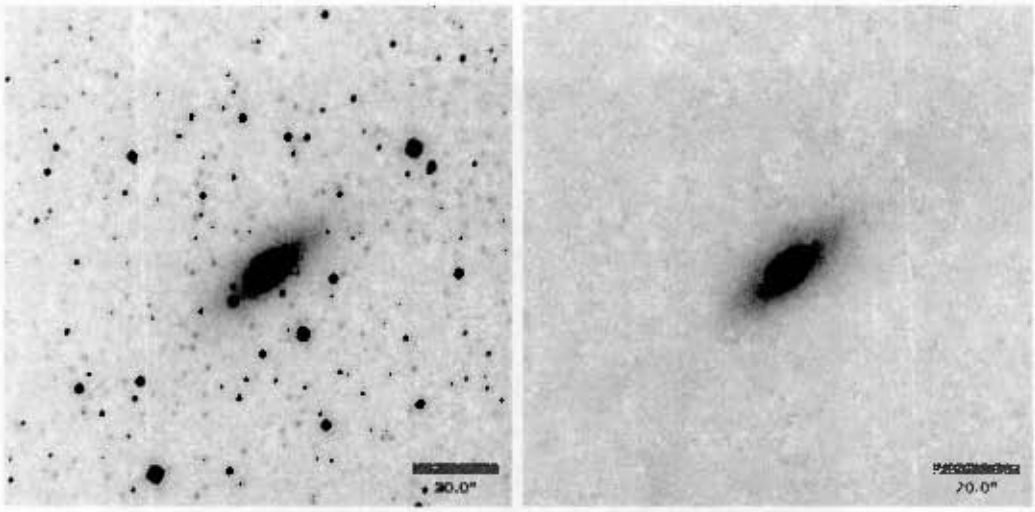

Figure 6.3: Galaxy WKK 6019, K_s band images

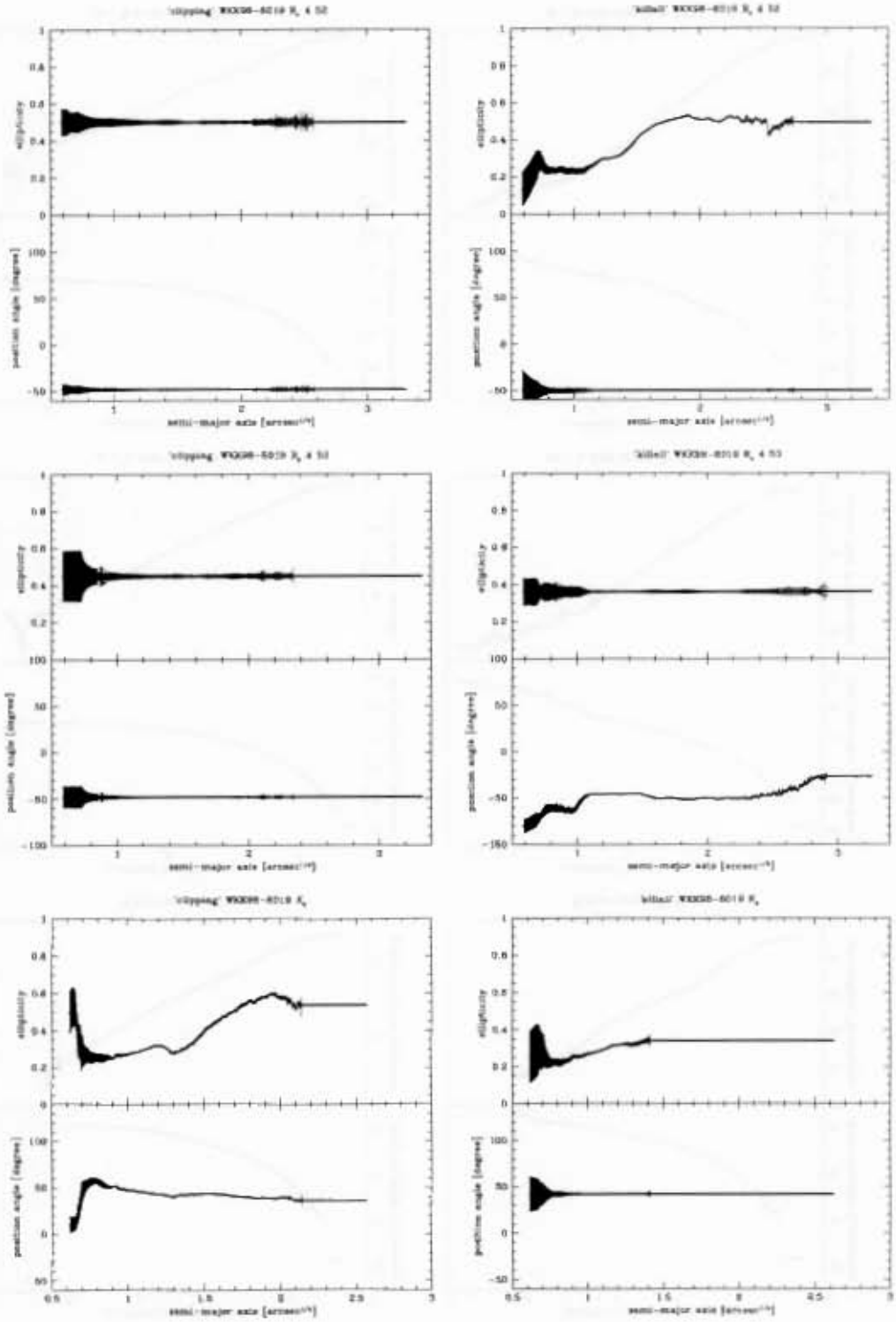

Figure 6.4: Galaxy WKK 6019, ellipticity and position angle plots

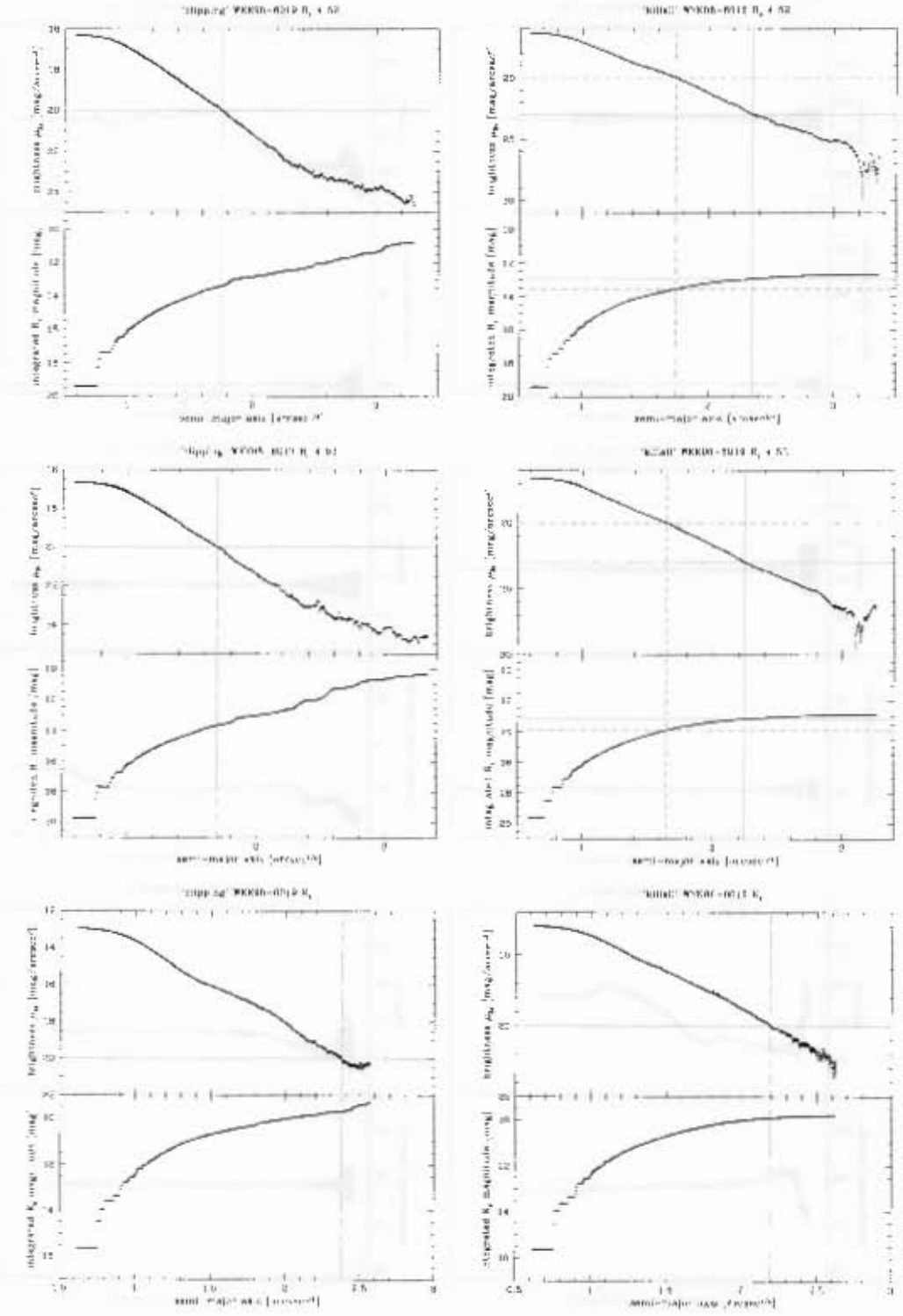

Figure 6.5: Galaxy WKK 6019, isophotal and integrated magnitude plots

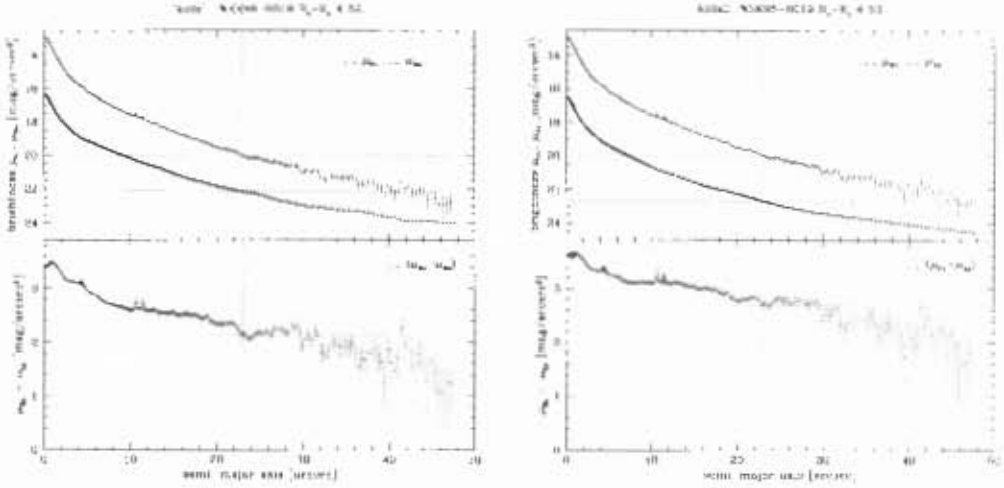

Figure 6.6: Galaxy WKK 6019. $(\mu_{R_e} - \mu_{K_s})$ magnitude plots

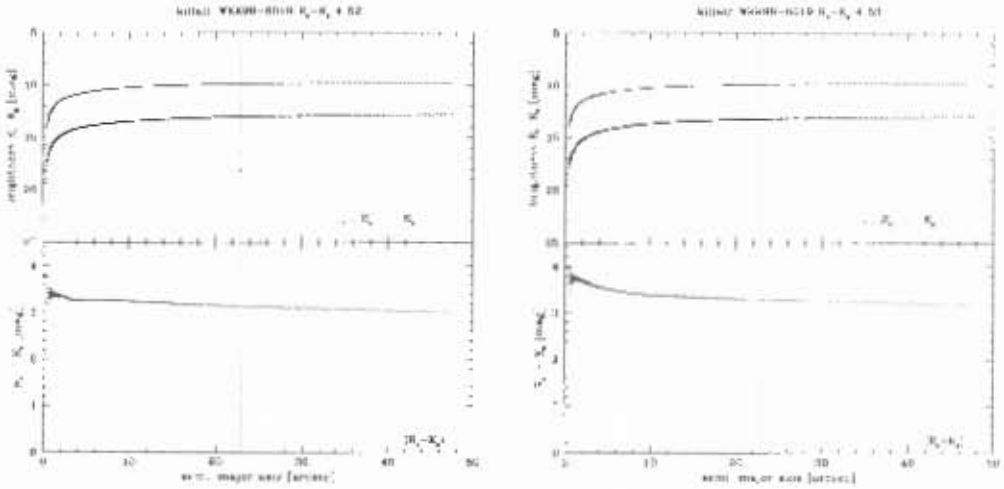

Figure 6.7: Galaxy WKK 6019. $(R_e - K_s)$ magnitude plots

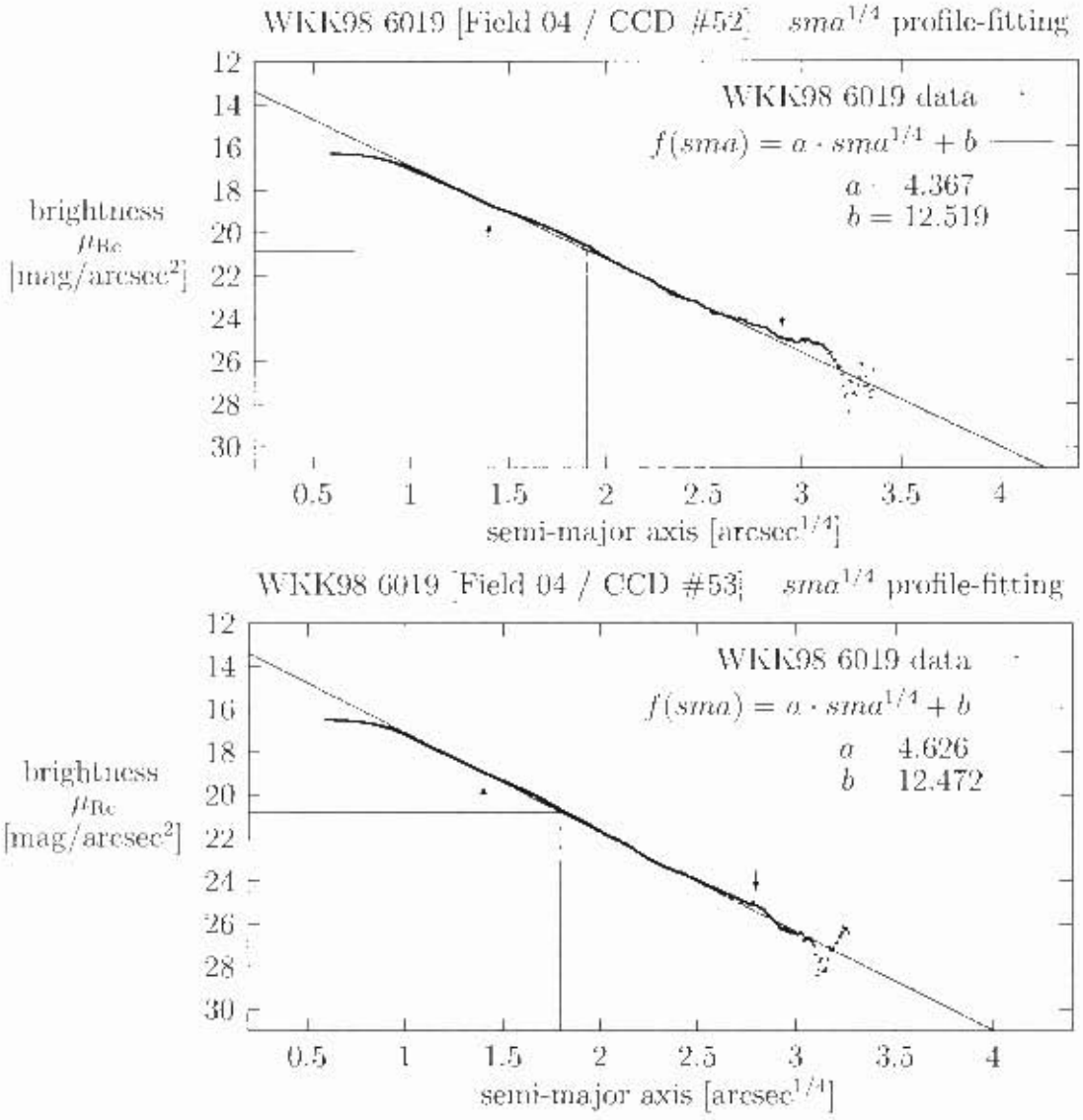

Figure 6.8: Galaxy WKK 6019, plots of brightness μ_{R_c} versus semi-major axis $sma^{1/4}$ to demonstrate the profile-fitting. The arrows point to the upper and lower limit of the data set that was used for the fit. The resulting effective (half-light) radius $r_e^{1/4}$ and effective (half-light) surface brightness μ_e are indicated by straight lines.

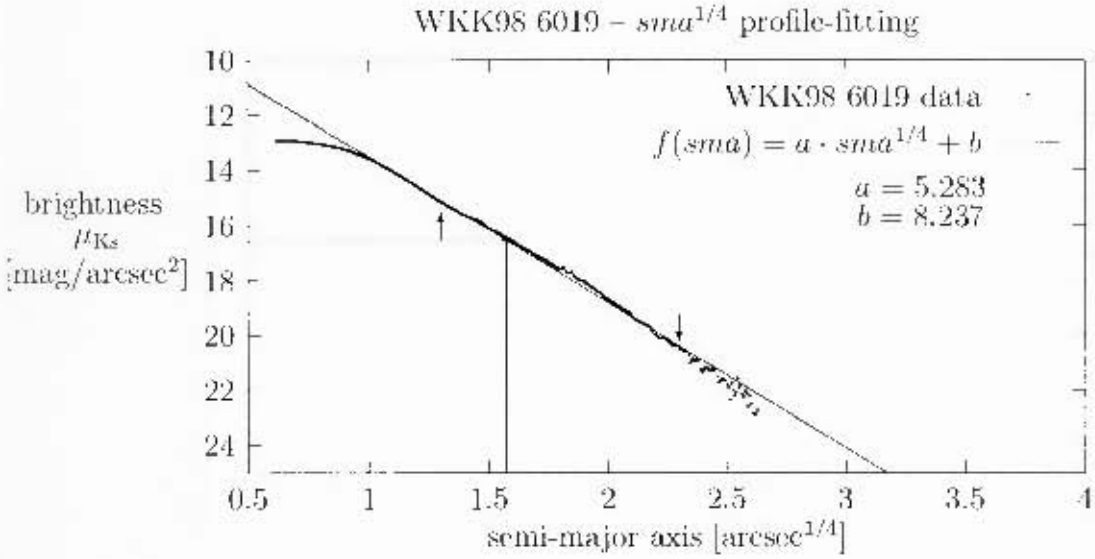

Figure 6.9: Galaxy WKK 6019, plot of brightness μ_{K_s} versus semi-major axis $sma^{1/4}$ to demonstrate the profile-fitting. The arrows point to the upper and lower limit of the data set that was used for the fit. The resulting effective (half-light) radius $r_e^{1/4}$ and effective (half-light) surface brightness μ_e are indicated by straight lines.

Chapter 7

Galaxy WKK 6047

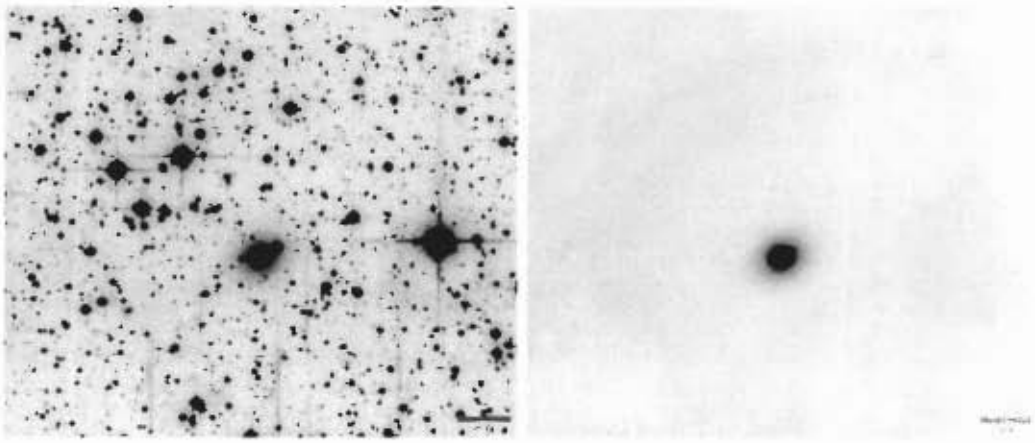

Figure 7.1: Galaxy WKK 6047, R_c band images, field 03, WFI CCD #55

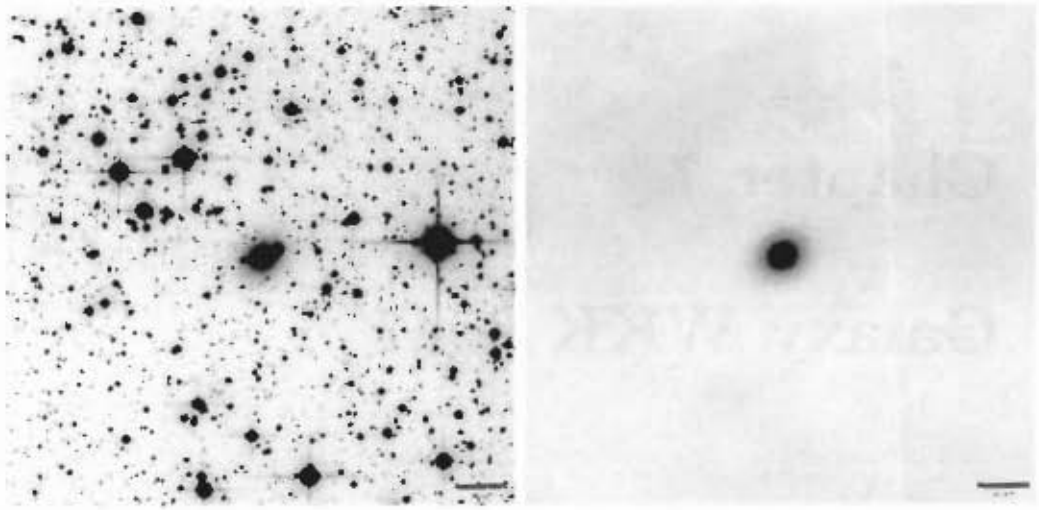

Figure 7.2: Galaxy WKK 6047, R_c band images, field 04, WFI CCD #52

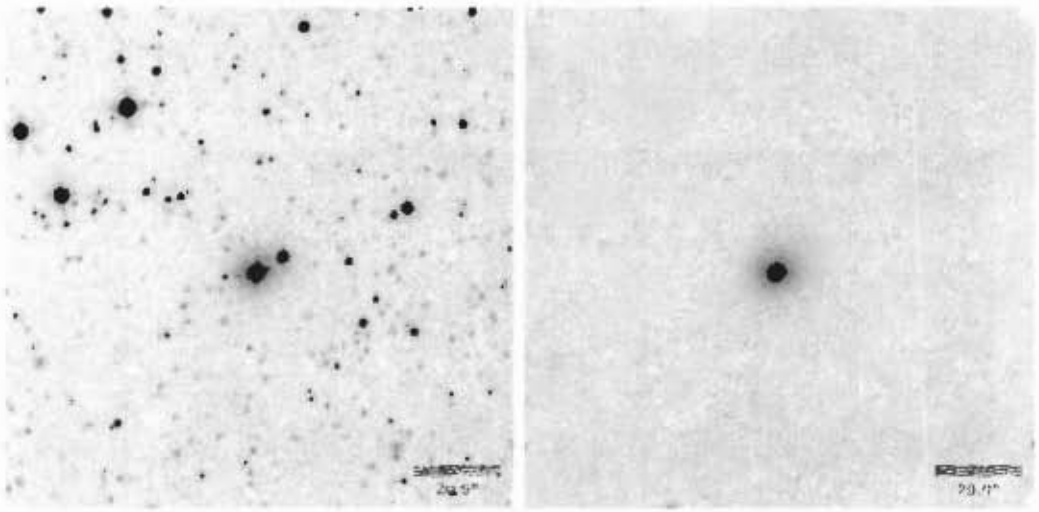

Figure 7.3: Galaxy WKK 6047, K_s band images

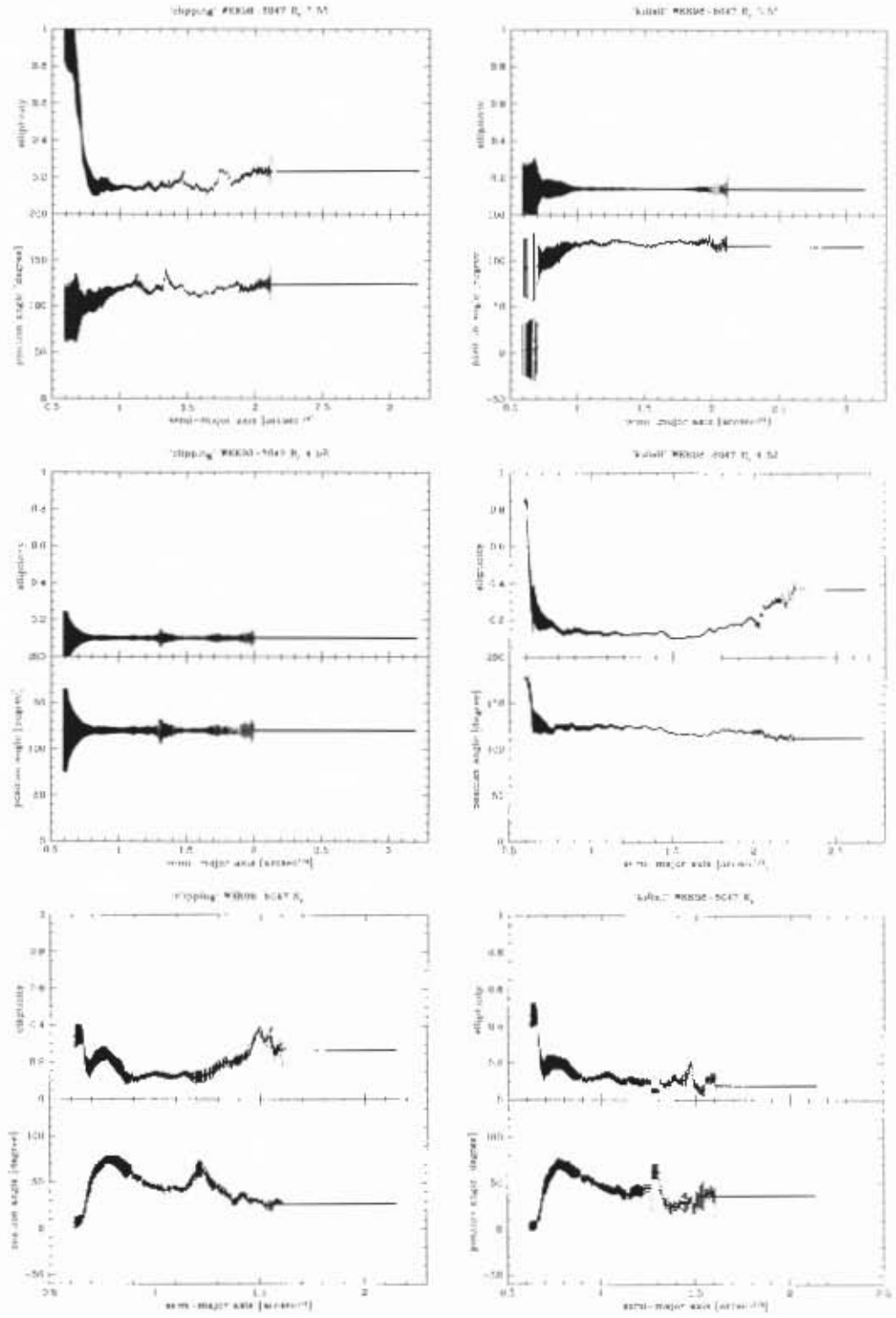

Figure 7.4: Galaxy WKK 6047, ellipticity and position angle plots

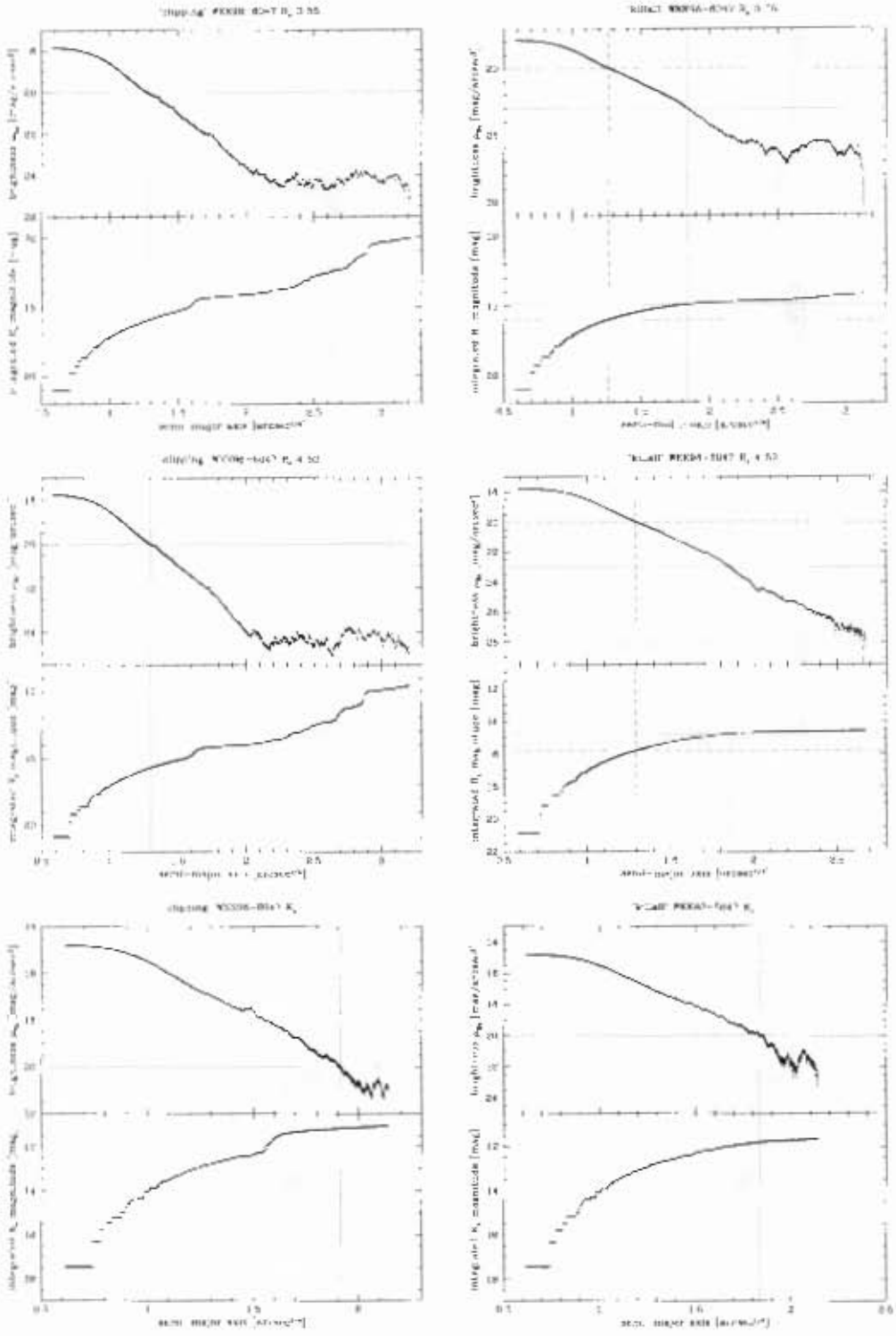

Figure 7.5: Galaxy WKK 6047, isophotal and integrated magnitude plots

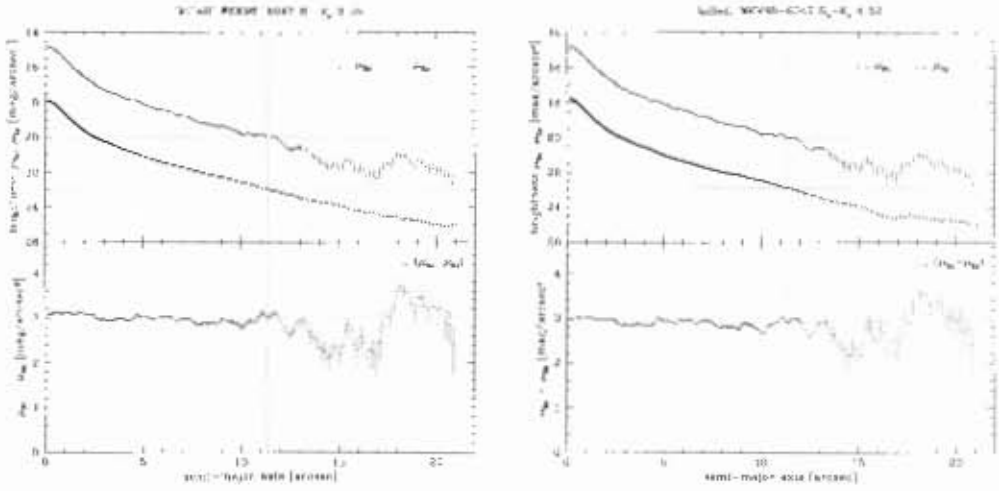

Figure 7.6: Galaxy WKK 6047, ($u_{R_c} - u_{K_s}$) magnitude plots

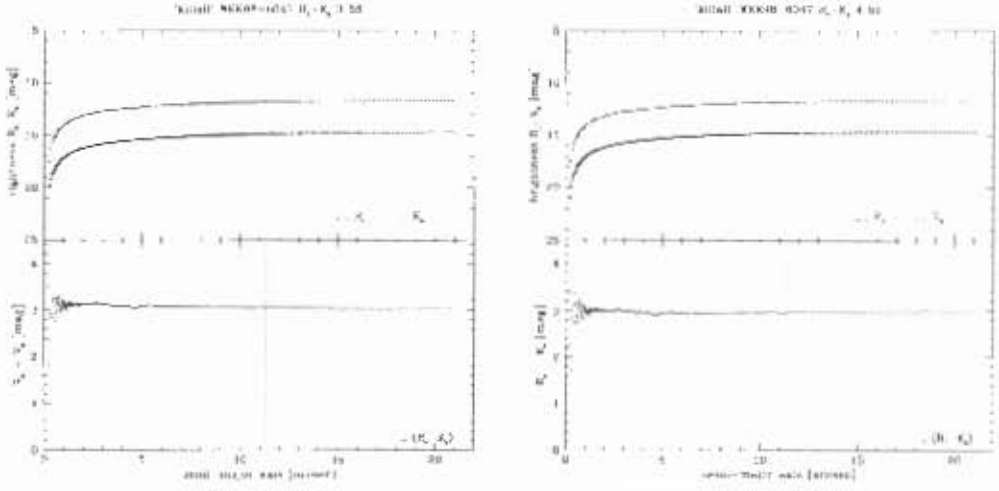

Figure 7.7: Galaxy WKK 6047, ($R_c - K_s$) magnitude plots

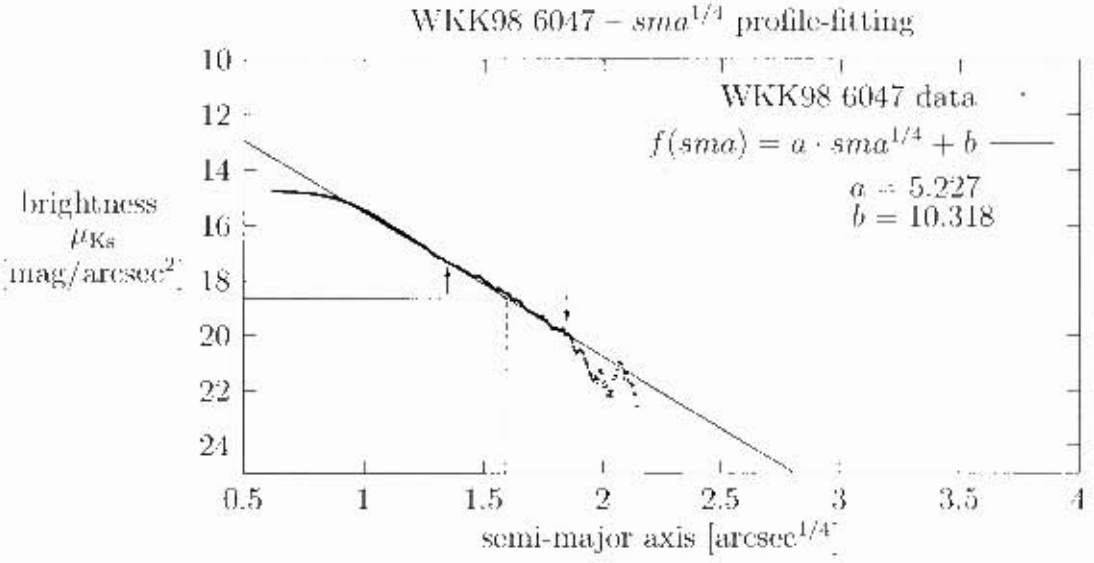

Figure 7.9: Galaxy WKK 6047, plot of brightness μ_{K_s} versus semi-major axis $sma^{1/4}$ to demonstrate the profile-fitting. The arrows point to the upper and lower limit of the data set that was used for the fit. The resulting effective (half-light) radius $r_e^{1/4}$ and effective (half-light) surface brightness μ_e are indicated by straight lines.

Chapter 8

Galaxy WKK 6075

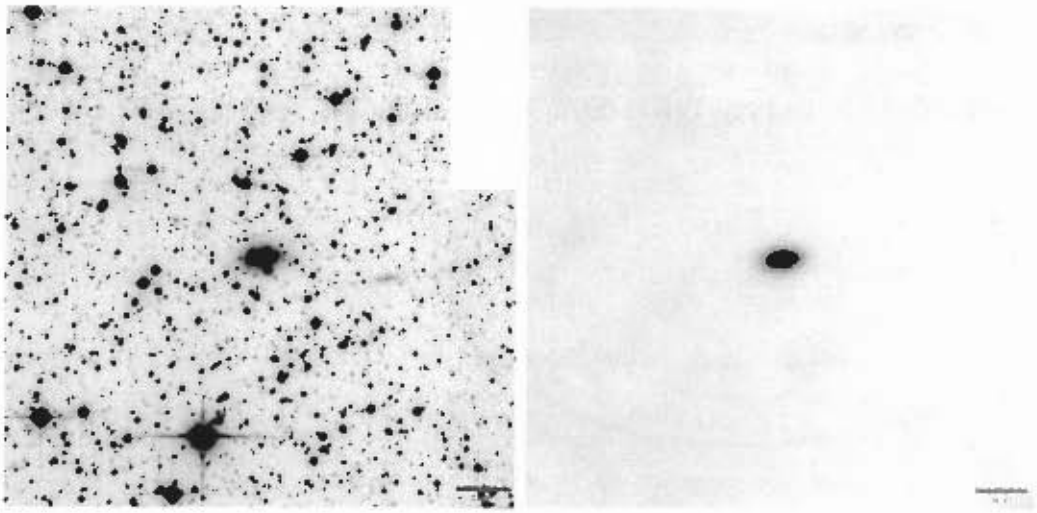

Figure 8.1: Galaxy WKK 6075, R_c band images, field 03, WF1 CCD #51

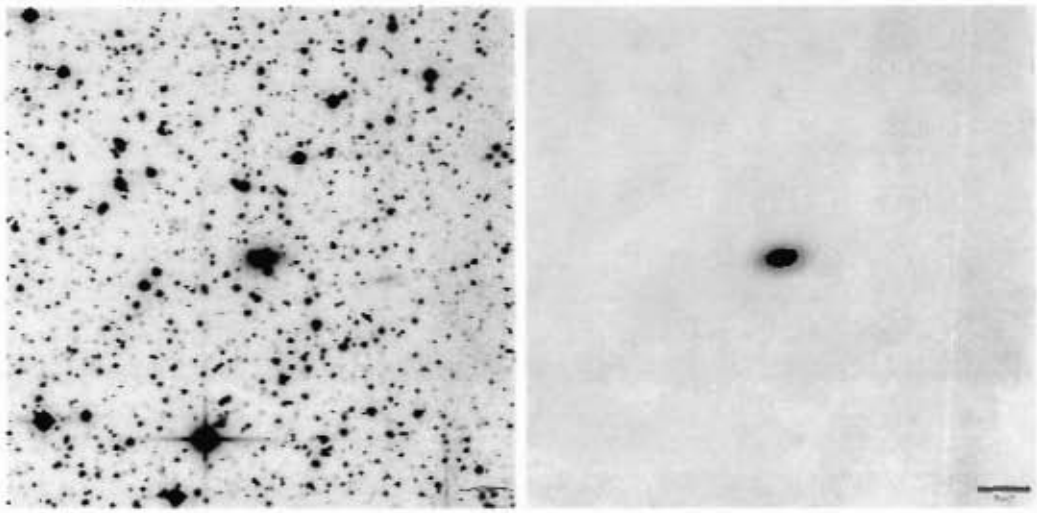

Figure 8.2: Galaxy WKK 6075, R_c band images, field 09, WFI CCD #56

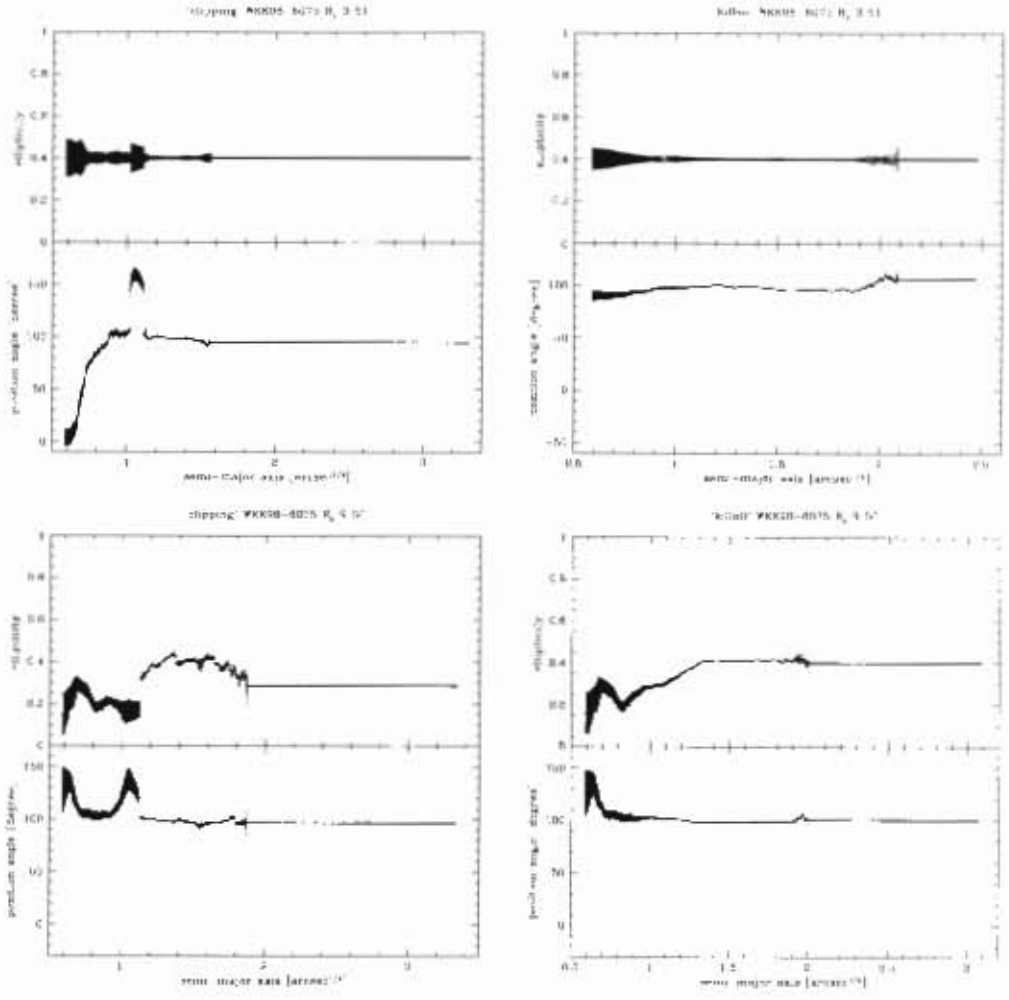

Figure 8.3: Galaxy WKK 6075, ellipticity and position angle plots

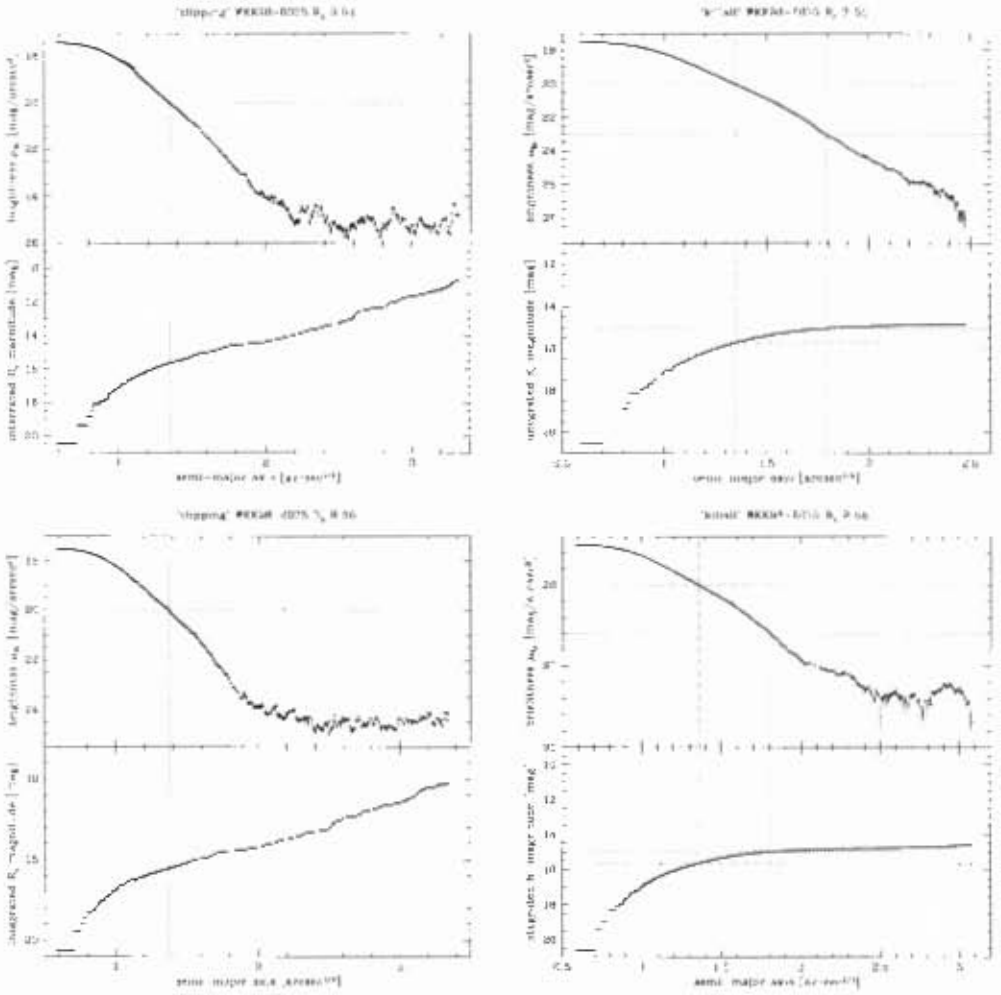

Figure 8.4: Galaxy WKK 6075, isophotal and integrated magnitude plots

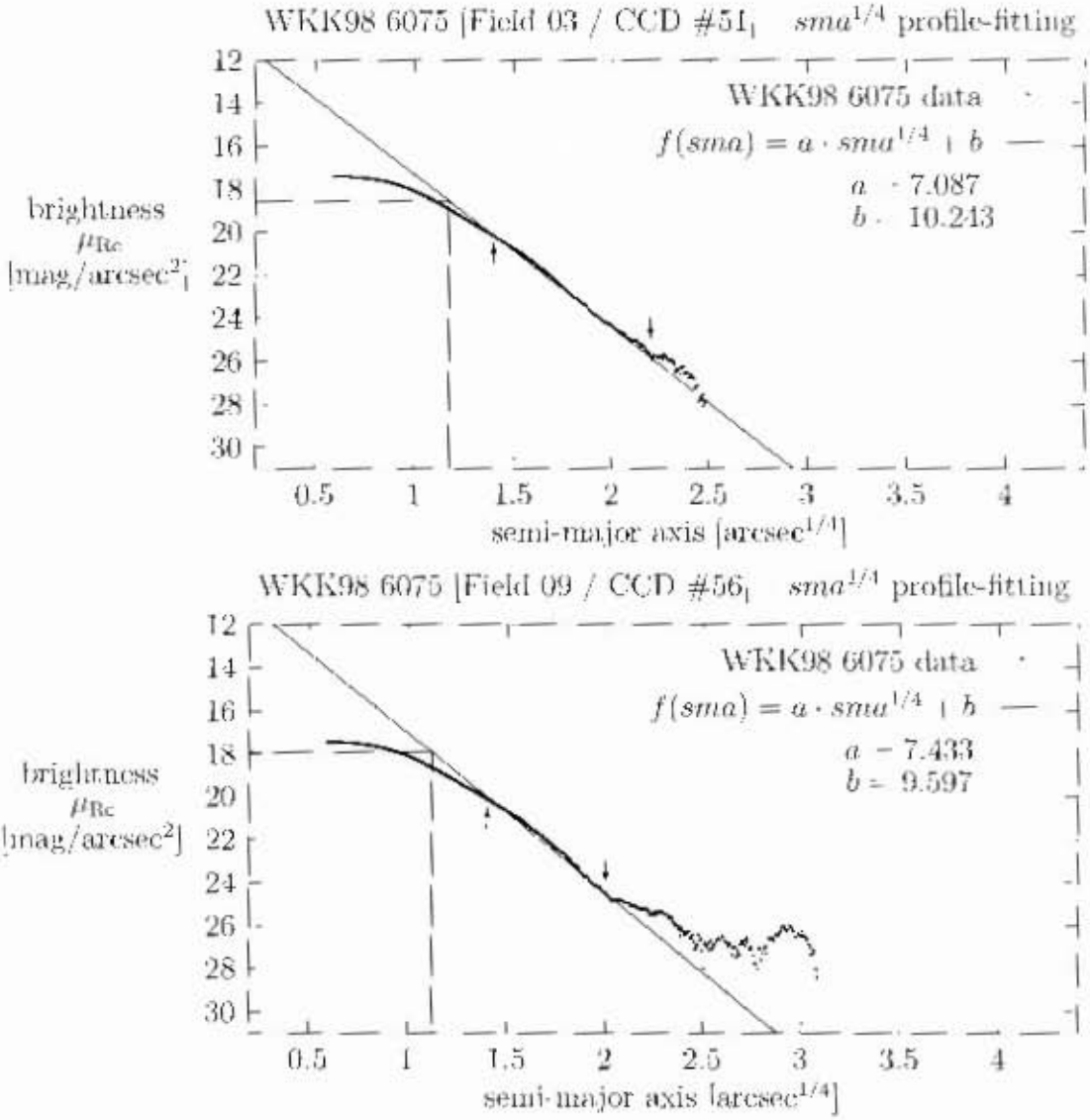

Figure 8.5: Galaxy WKK 6075, plots of brightness μ_{Rc} versus semi-major axis $sma^{1/4}$ to demonstrate the profile fitting. The arrows point to the upper and lower limit of the data set that was used for the fit. The resulting effective (half-light) radius $r_e^{1/4}$ and effective (half-light) surface brightness μ_e are indicated by straight lines.

Chapter 9

Galaxy WKK 6116

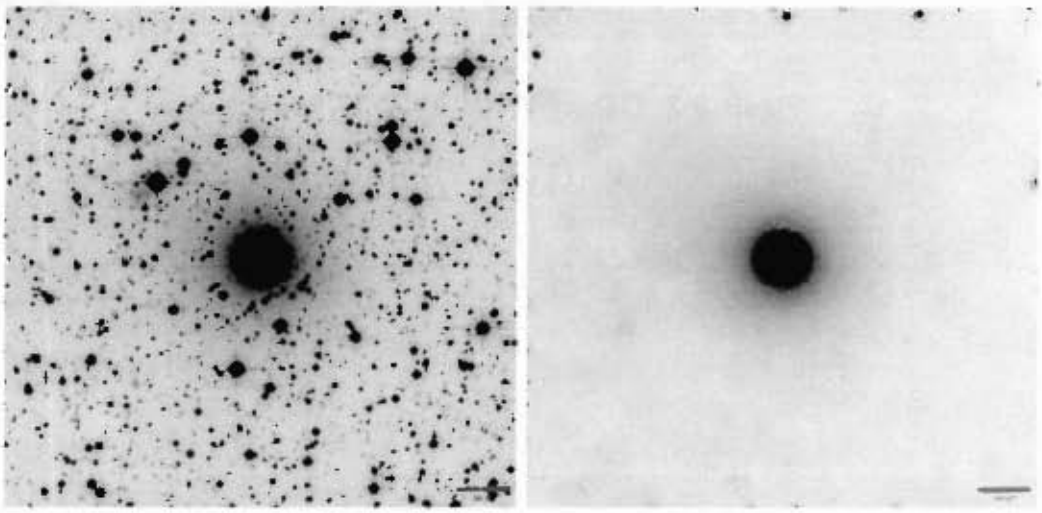

Figure 9.1: Galaxy WKK 6116, R_c band images, field 03, WFI CCD #56

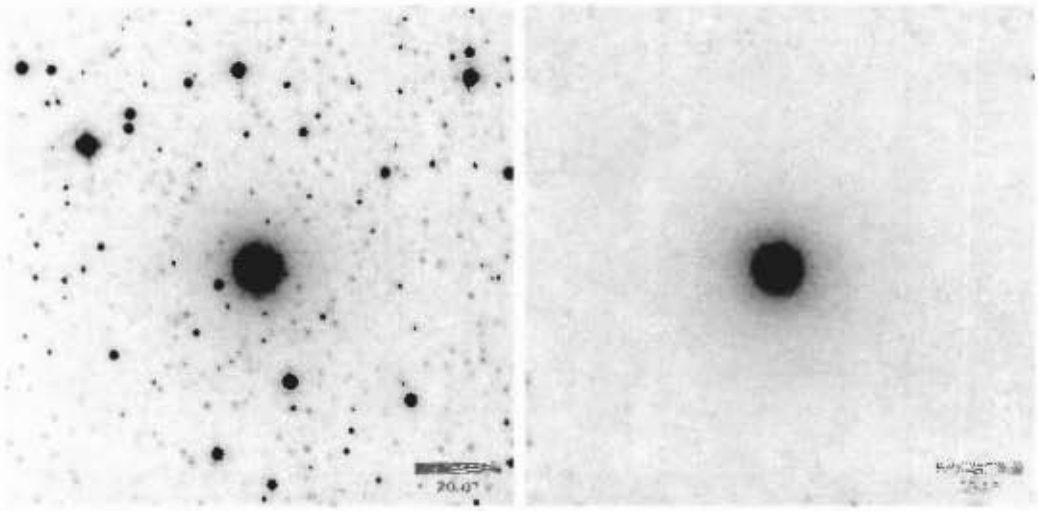

Figure 9.2: Galaxy WKK 6116, K_s band images

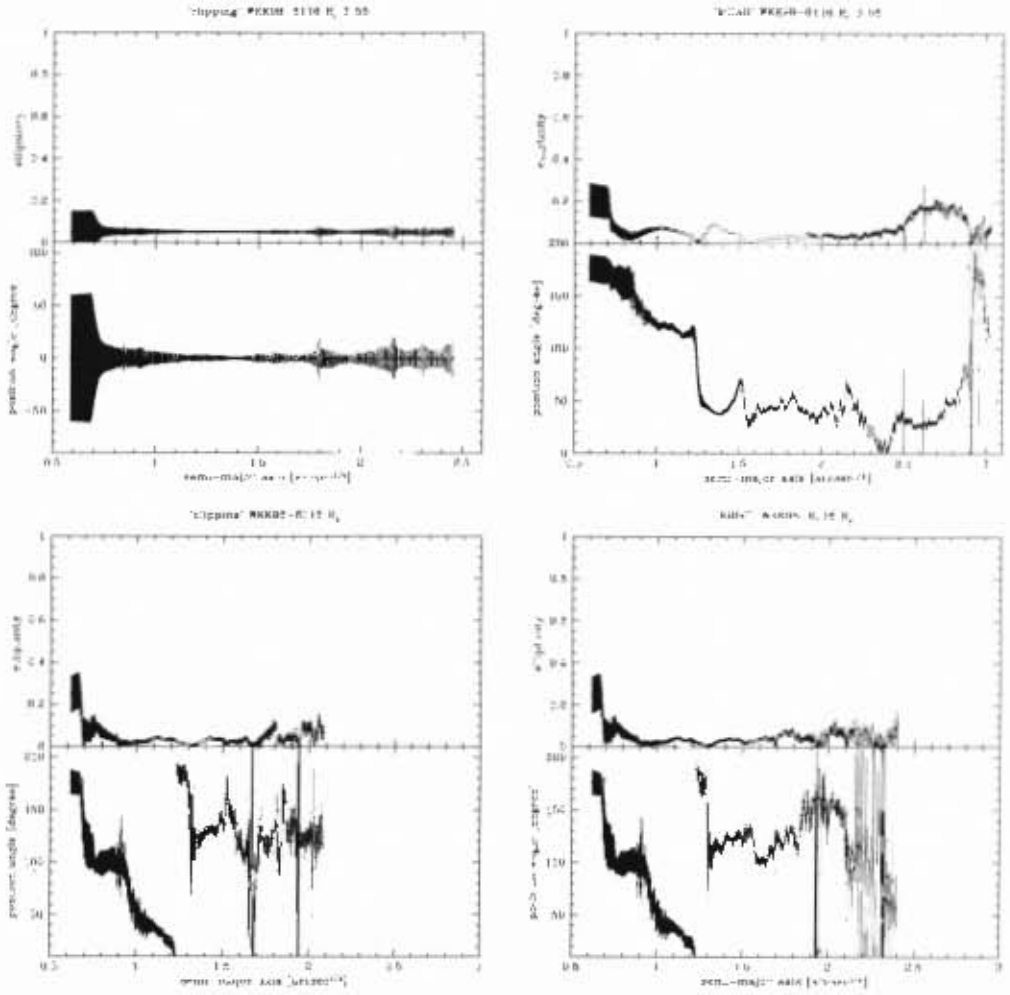

Figure 9.3: Galaxy WKK 6116, ellipticity and position angle plots

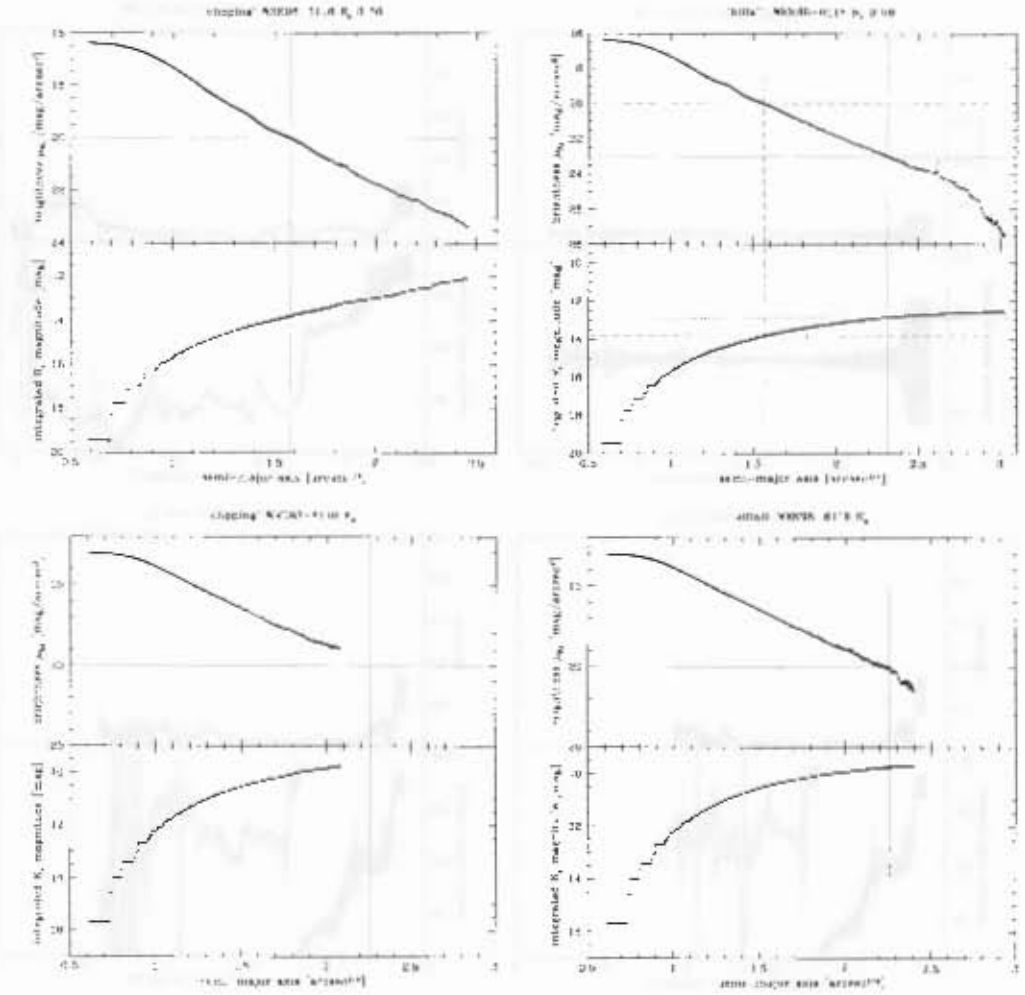

Figure 9.4: Galaxy WKK 6116, isophotal and integrated magnitude plots

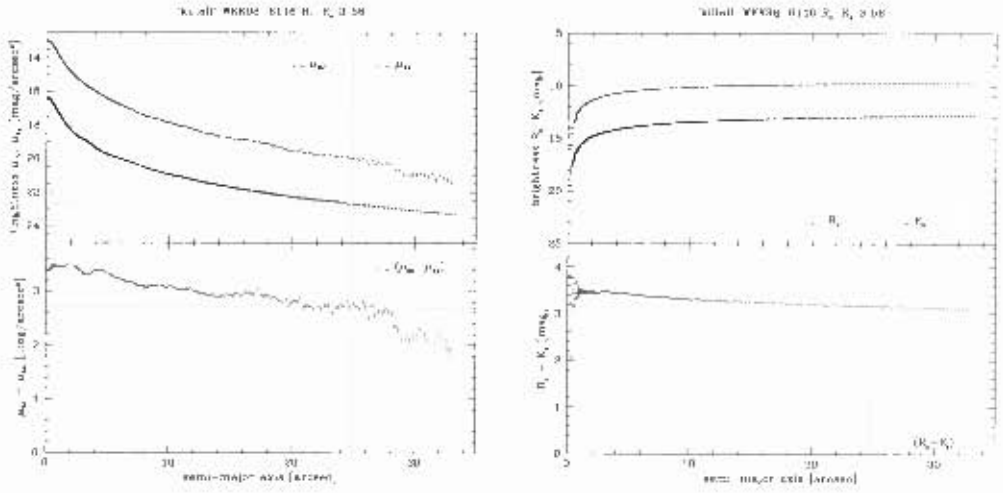

Figure 9.5: Galaxy WKK 6116. (u_{R_c} u_{K_s}) and ($R_c - K_s$) magnitude plots

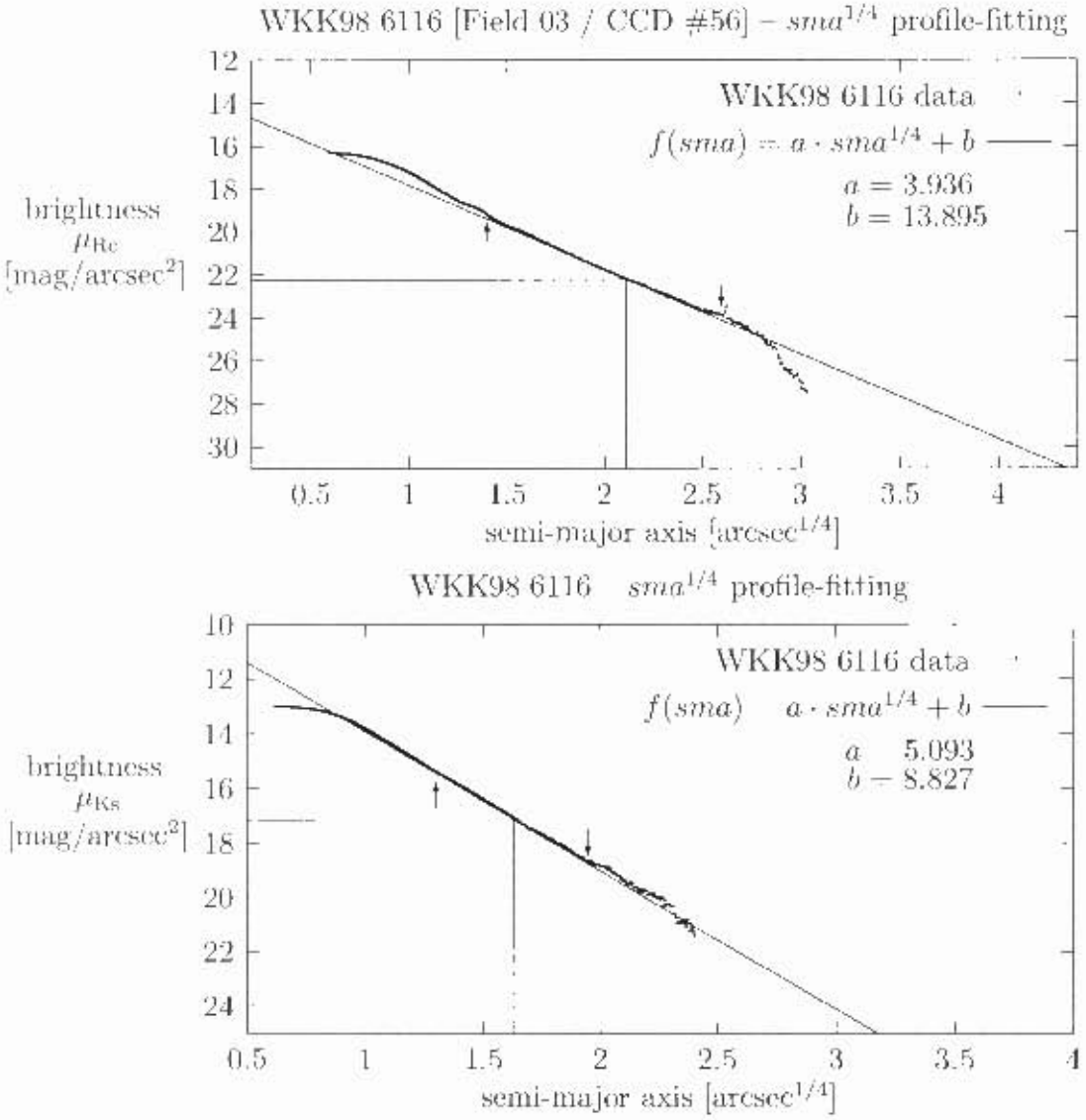

Figure 9.6: Galaxy WKK 6116, plots of brightness (μ_{R_c} and μ_{K_s}) versus semi-major axis sma$^{1/4}$ to demonstrate the profile-fitting. The arrows point to the upper and lower limit of the data set that was used for the fit. The resulting effective (half-light) radius $r_e^{1/4}$ and effective (half light) surface brightness μ_e are indicated by straight lines.

Chapter 10

Galaxy WKK 6180

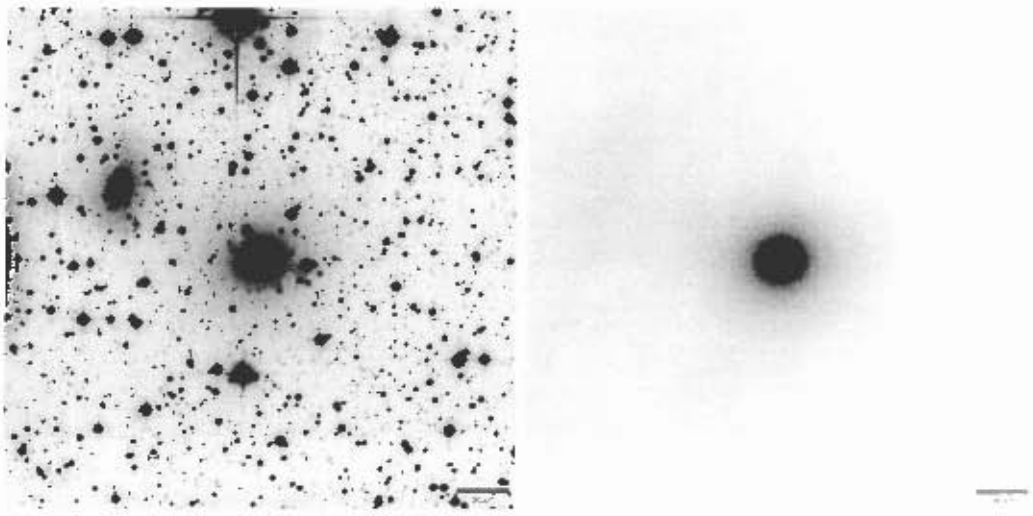

Figure 10.1: Galaxy WKK 6180, R_c band images, field 01, WFI CCD #54

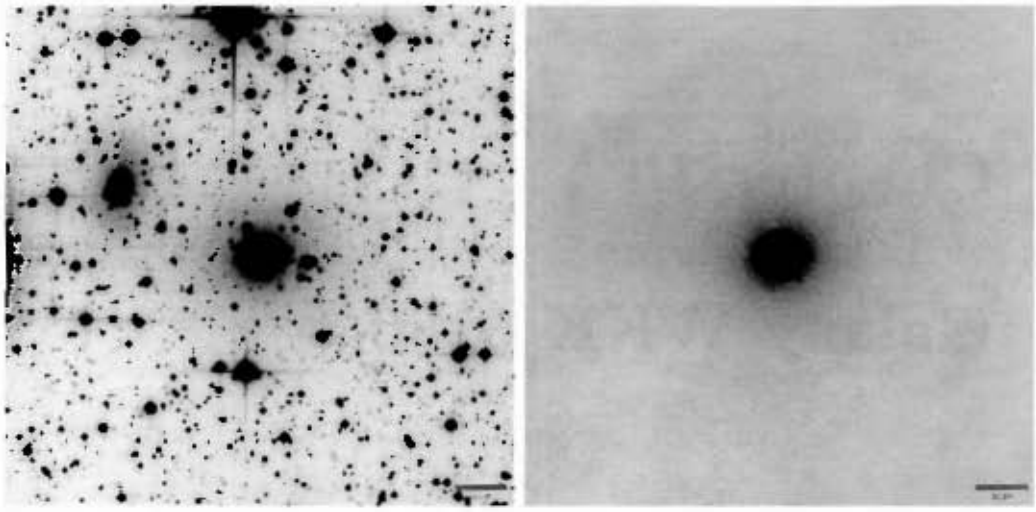

Figure 10.2: Galaxy WKK 6180. R_c band images, field 04, WF1 CCD #50

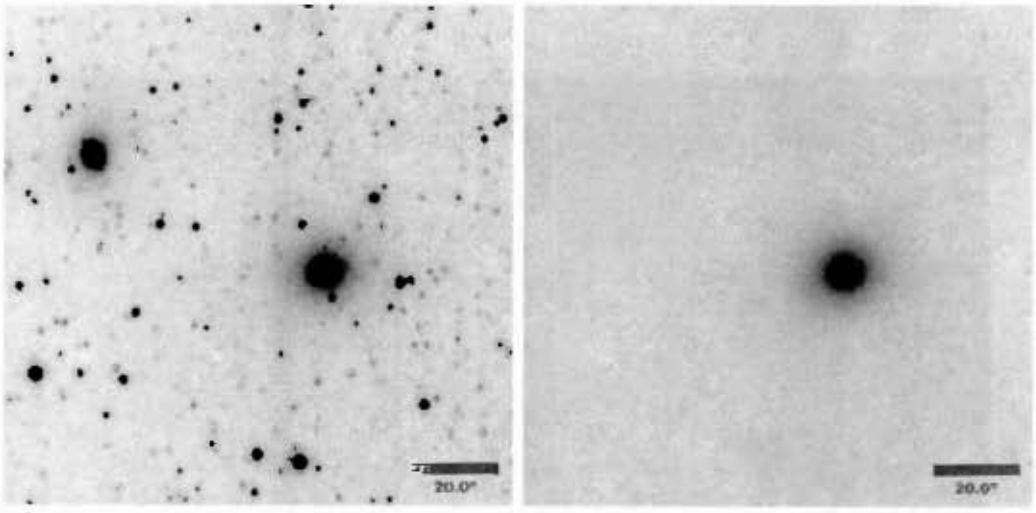

Figure 10.3: Galaxy WKK 6180. K_s band images

Chapter 10

Galaxy WKK 6180

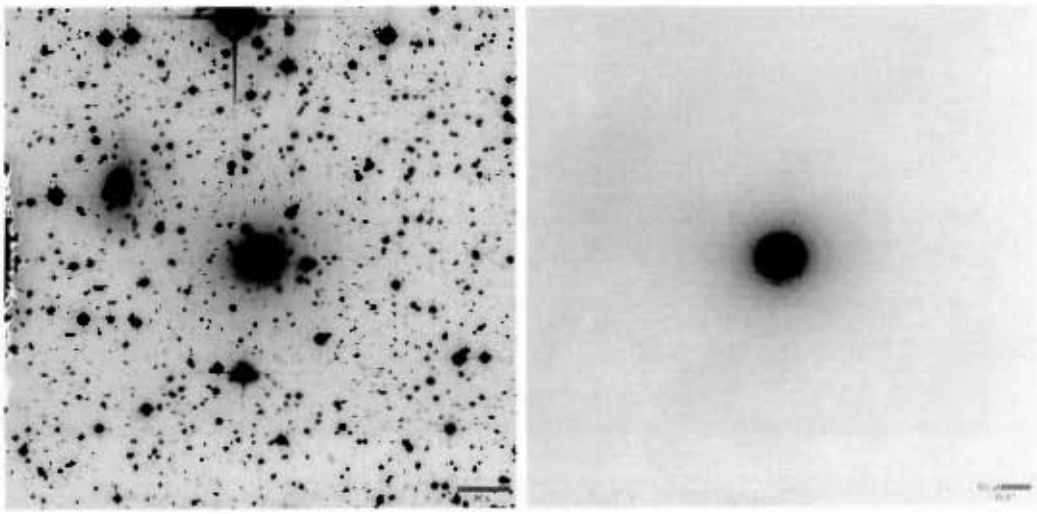

Figure 10.1: Galaxy WKK 6180, R_c band images, field 01, WF1 CCD #54

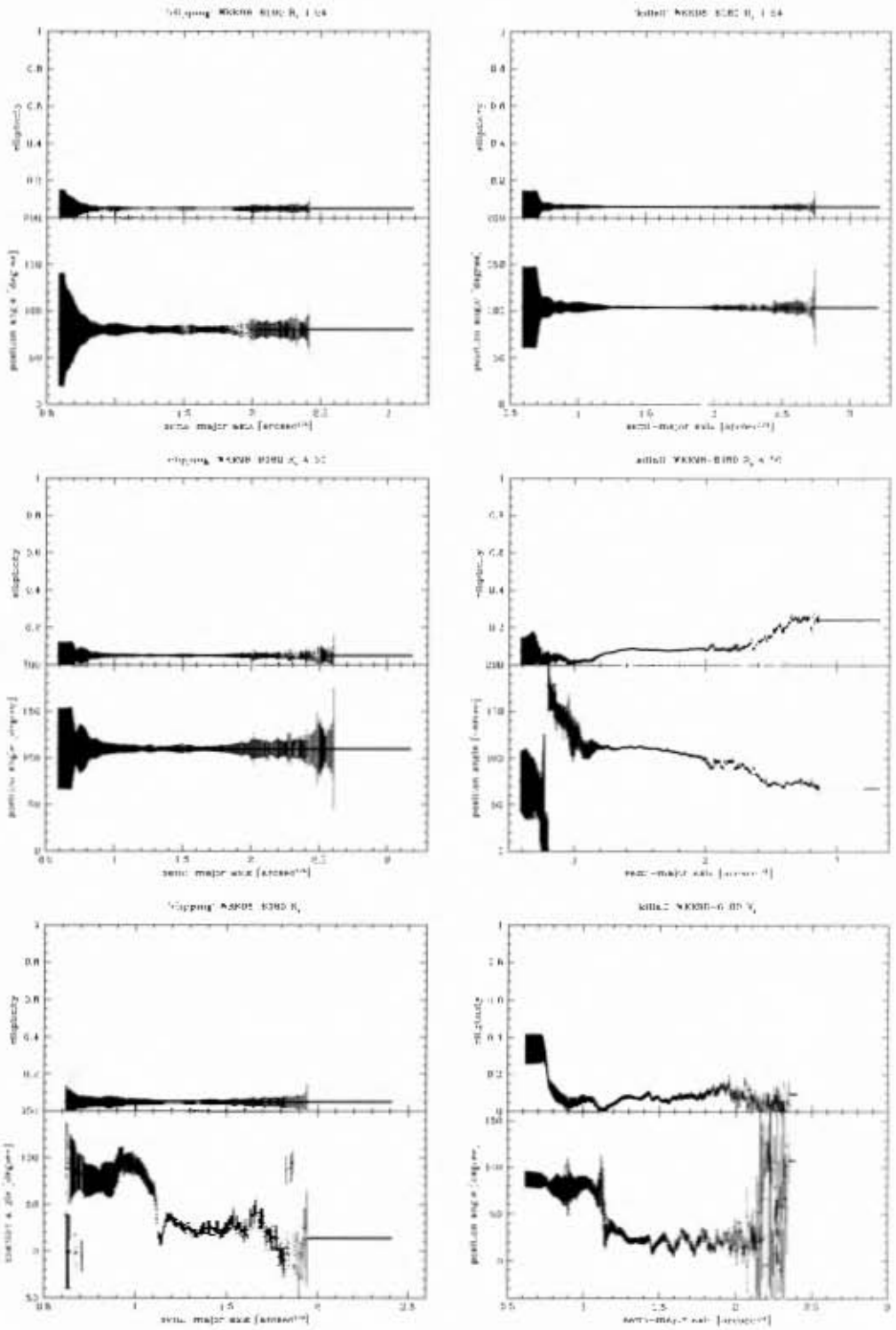

Figure 10.4: Galaxy WKK 6180, ellipticity and position angle plots

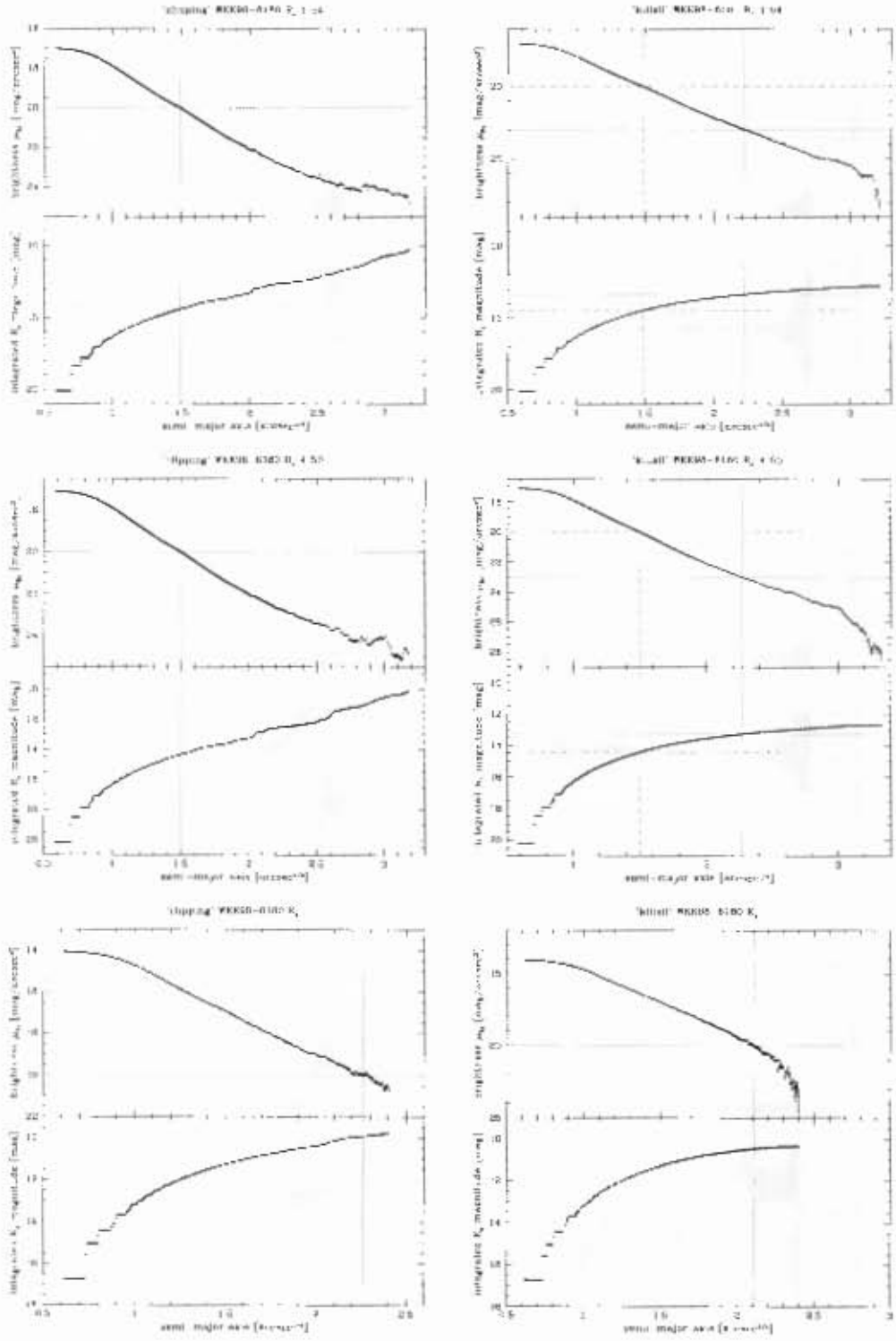

Figure 10.5: Galaxy WKK 6180, isophotal and integrated magnitude plots

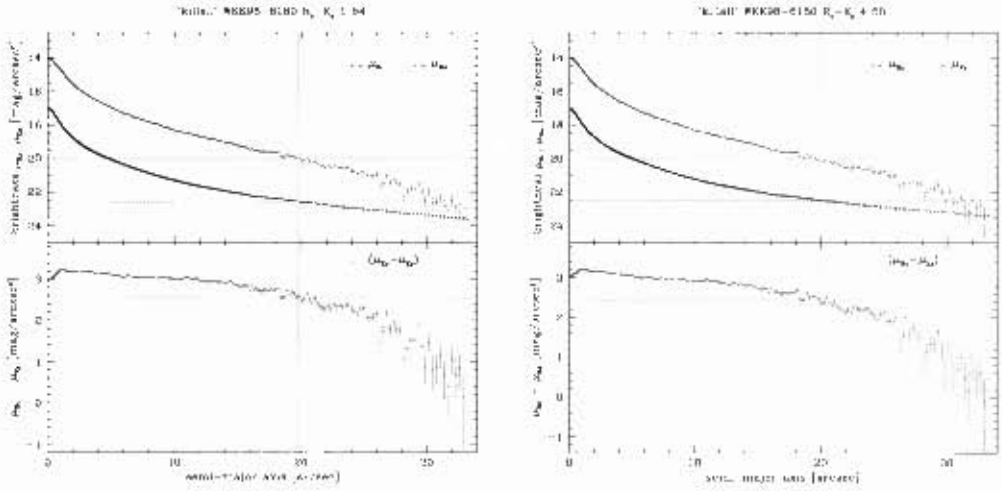

Figure 10.6: Galaxy WKK 6180, (μ_{R_c} μ_{K_s}) magnitude plots

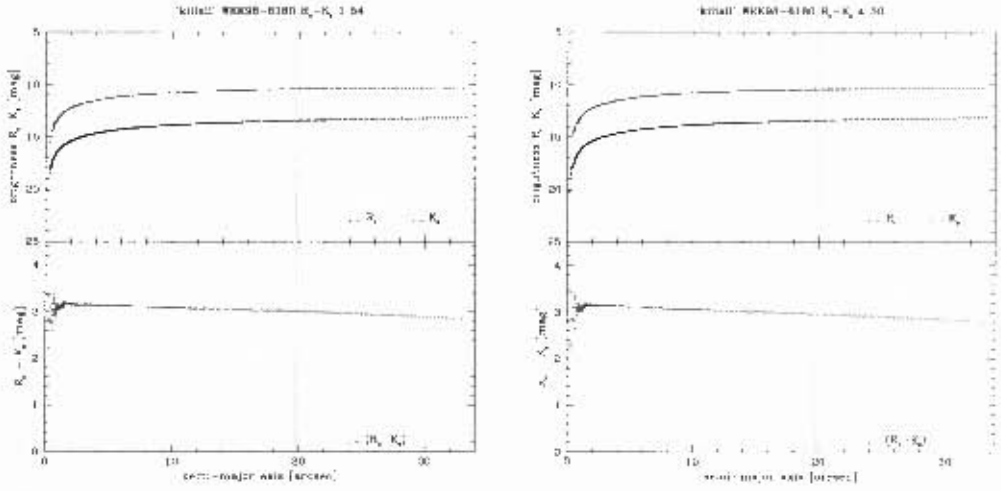

Figure 10.7: Galaxy WKK 6180, ($R_c - K_s$) magnitude plots

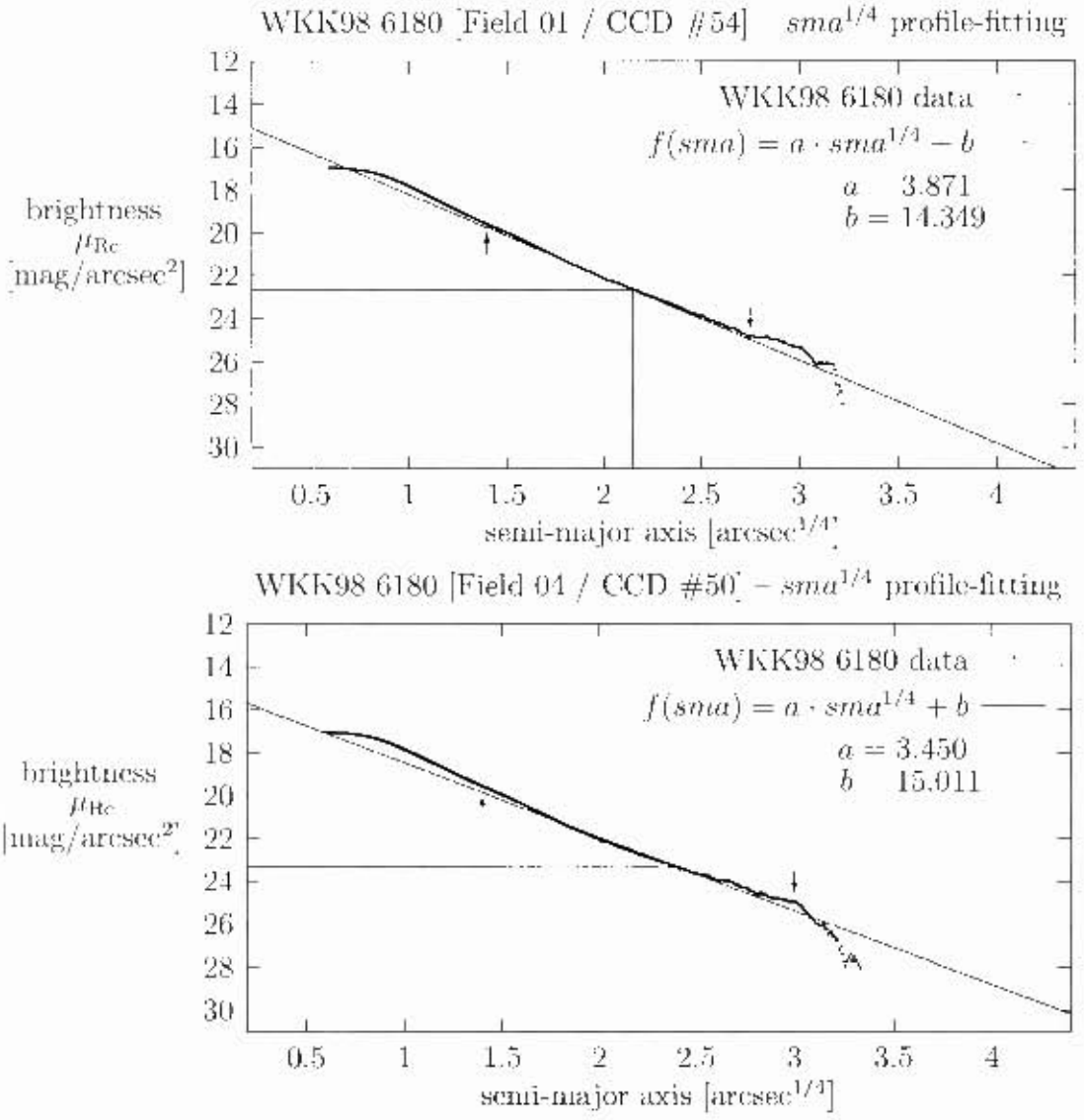

Figure 10.8: Galaxy WKK 6180, plots of brightness u_{R_c} versus semi-major axis $sma^{1/4}$ to demonstrate the profile-fitting. The arrows point to the upper and lower limit of the data set that was used for the fit. The resulting effective (half-light) radius $r_e^{1/4}$ and effective (half-light) surface brightness μ_e are indicated by straight lines.

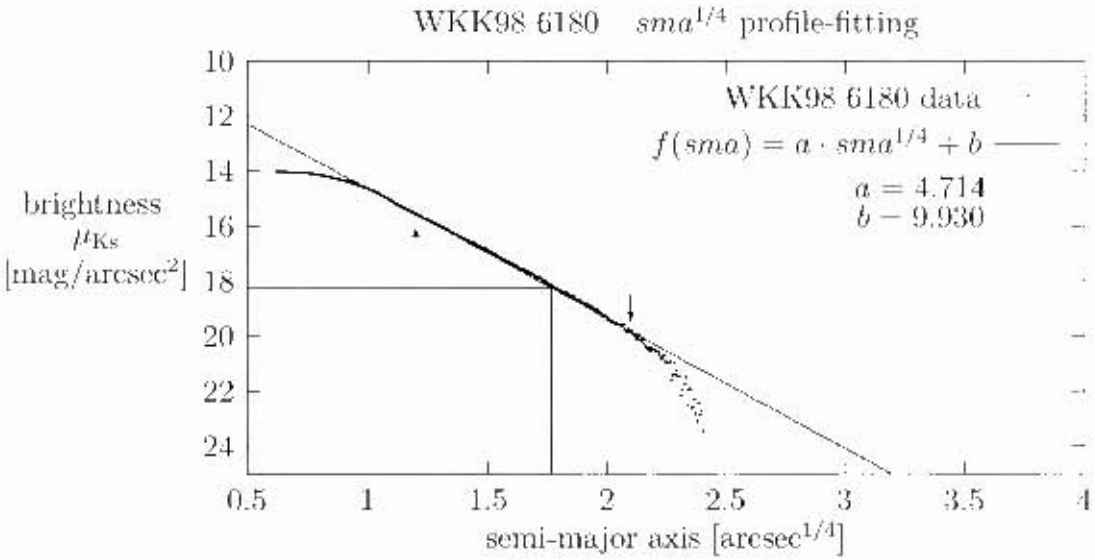

Figure 10.9: Galaxy WKK 6180, plot of brightness μ_{K_s} versus semi-major axis $sma^{1/4}$ to demonstrate the profile-fitting. The arrows point to the upper and lower limit of the data set that was used for the fit. The resulting effective (half-light) radius $r_e^{1/4}$ and effective (half-light) surface brightness μ_e are indicated by straight lines.

Chapter 11

Galaxy WKK 6183

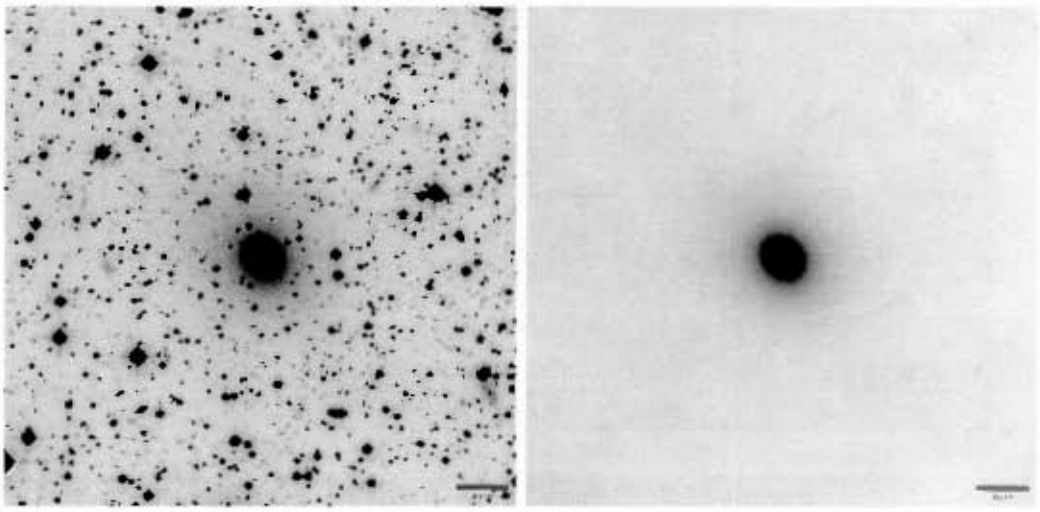

Figure 11.1: Galaxy WKK 6183, R_c band images, field 01, WFI CCD #53

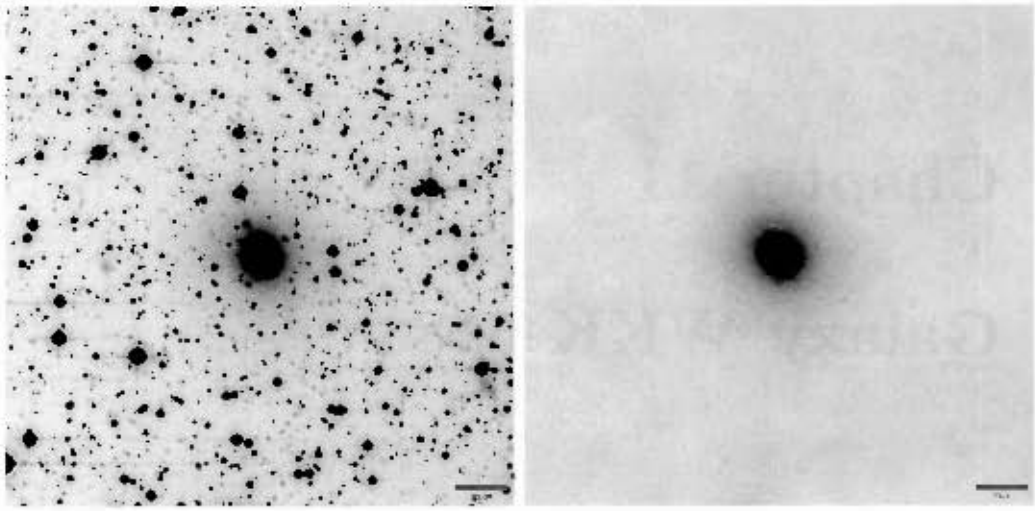

Figure 11.2: Galaxy WKK 6183, R_c band images, field 03, WFI CCD #57

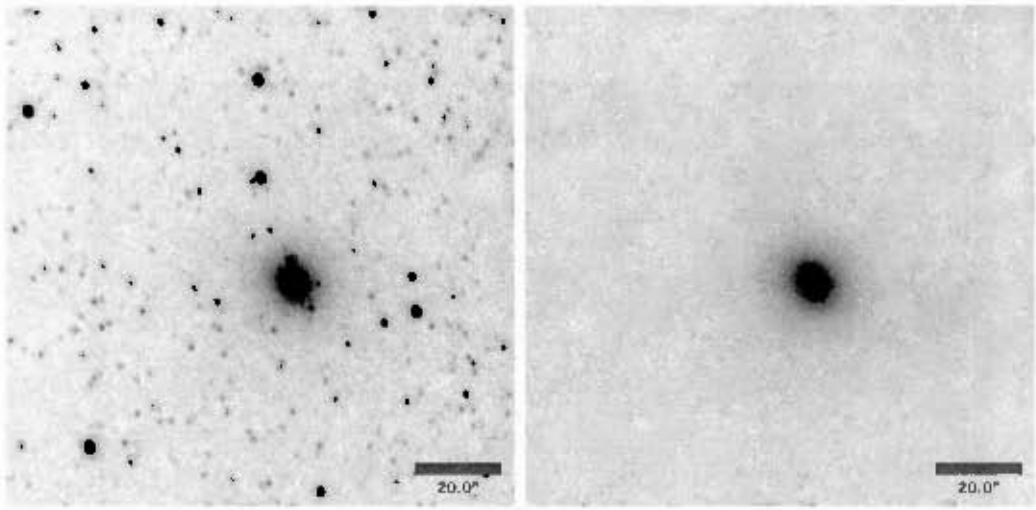

Figure 11.3: Galaxy WKK 6183, K_s band images

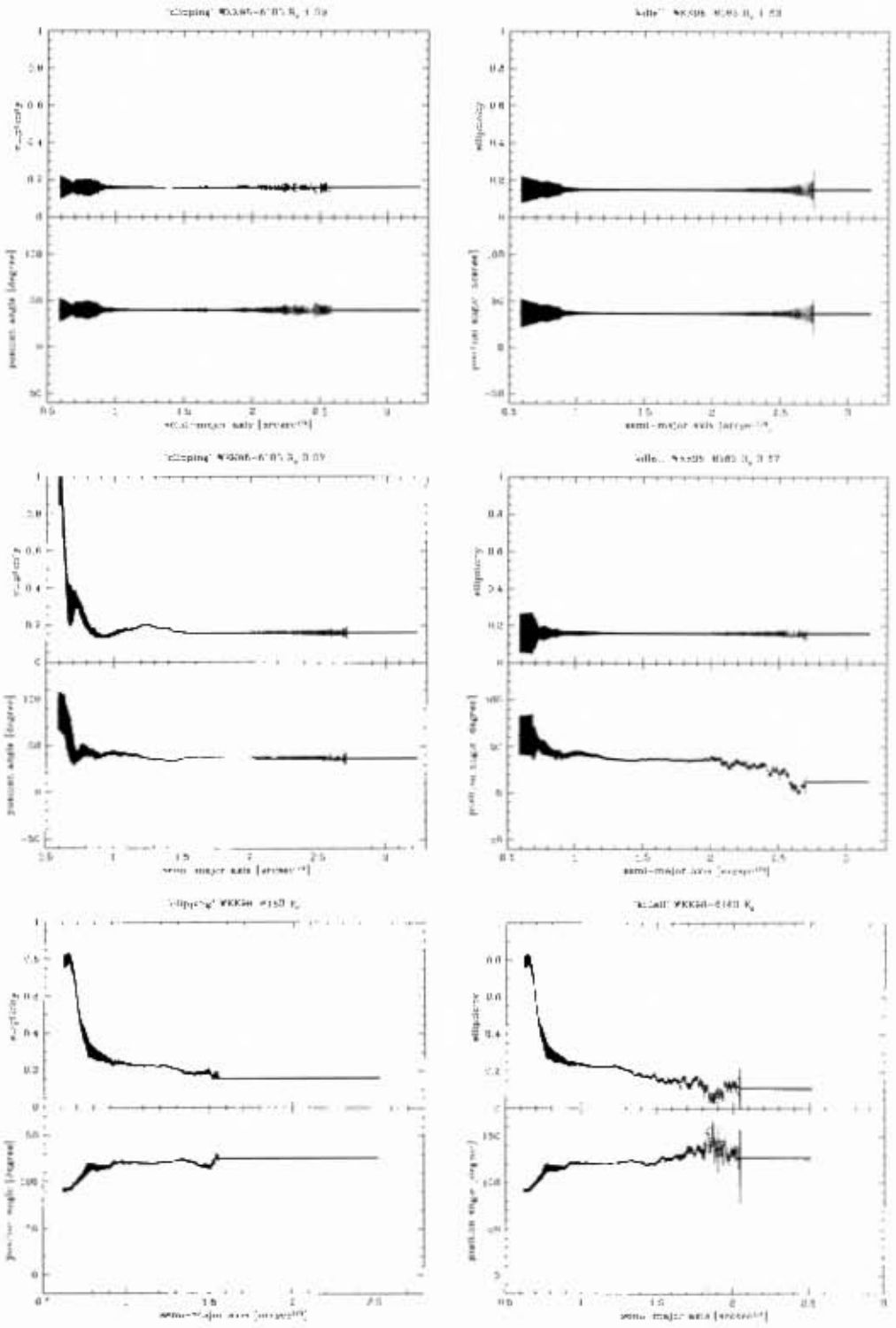

Figure 11.4: Galaxy WKK 6183, ellipticity and position angle plots

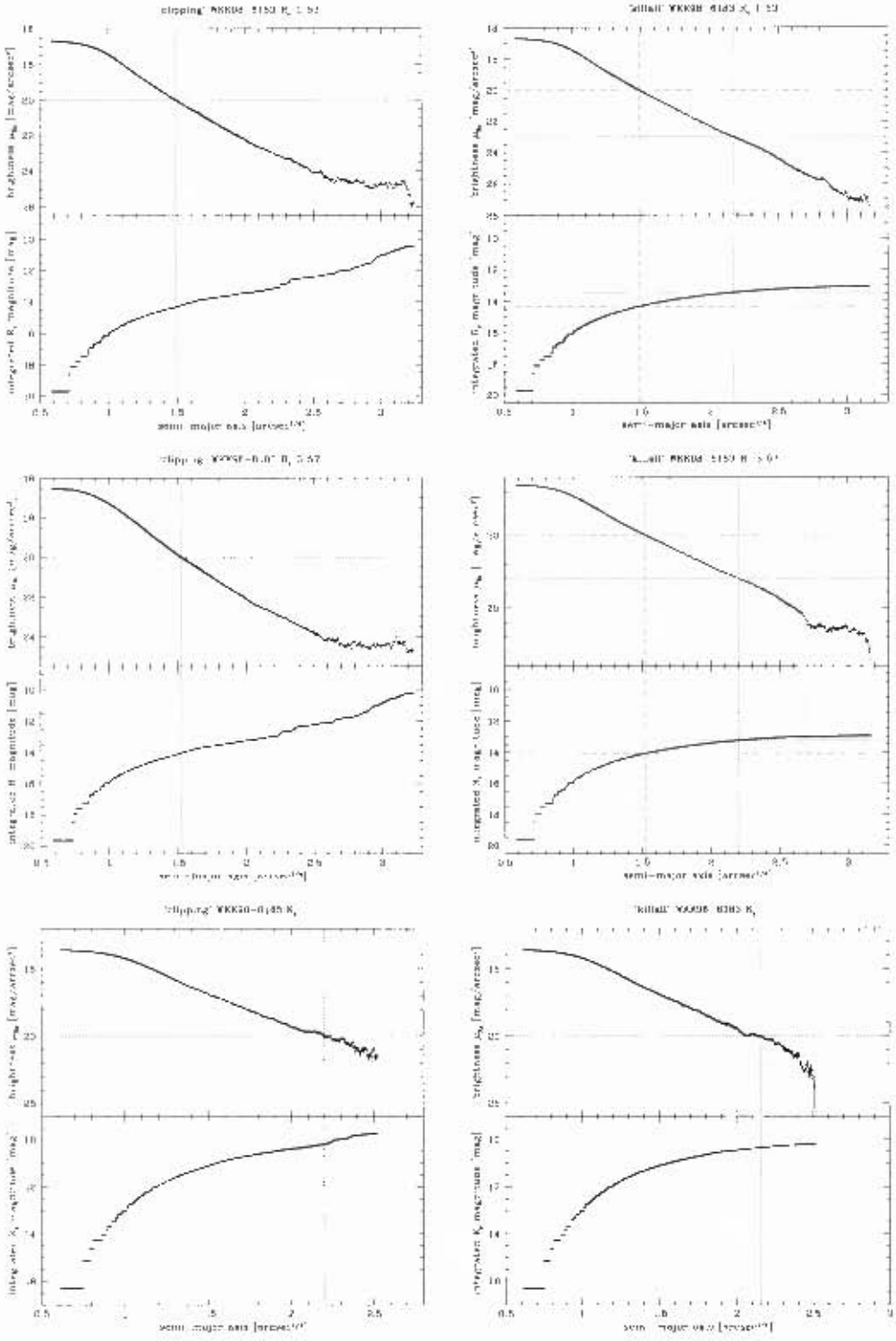

Figure 11.5: Galaxy WKK 6183, isophotal and integrated magnitude plots

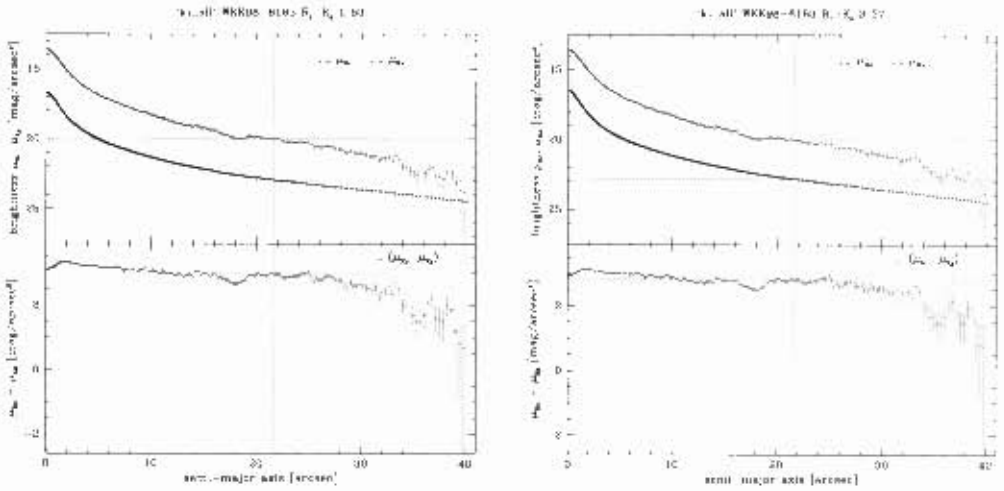

Figure 11.6: Galaxy WKK 6183, $(\mu_{R_c} - \mu_{K_s})$ magnitude plots

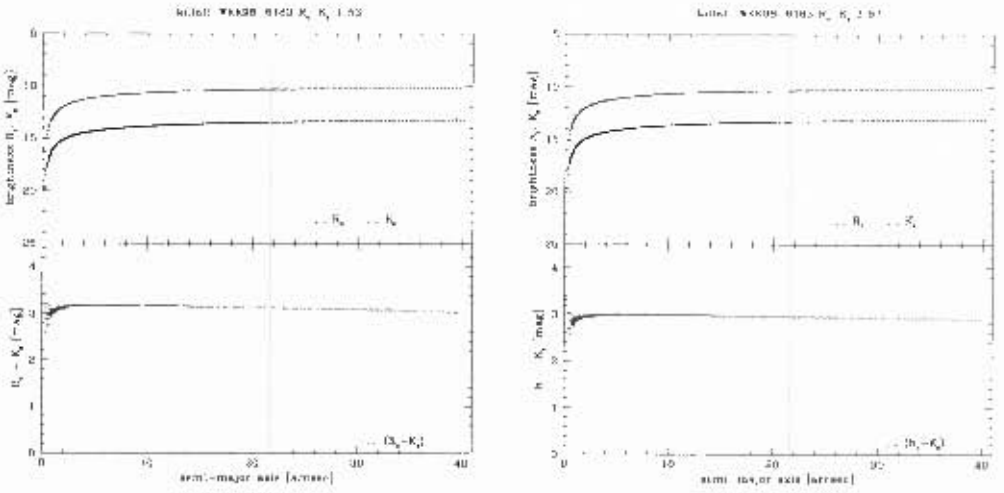

Figure 11.7: Galaxy WKK 6183, $(R_c - K_s)$ magnitude plots

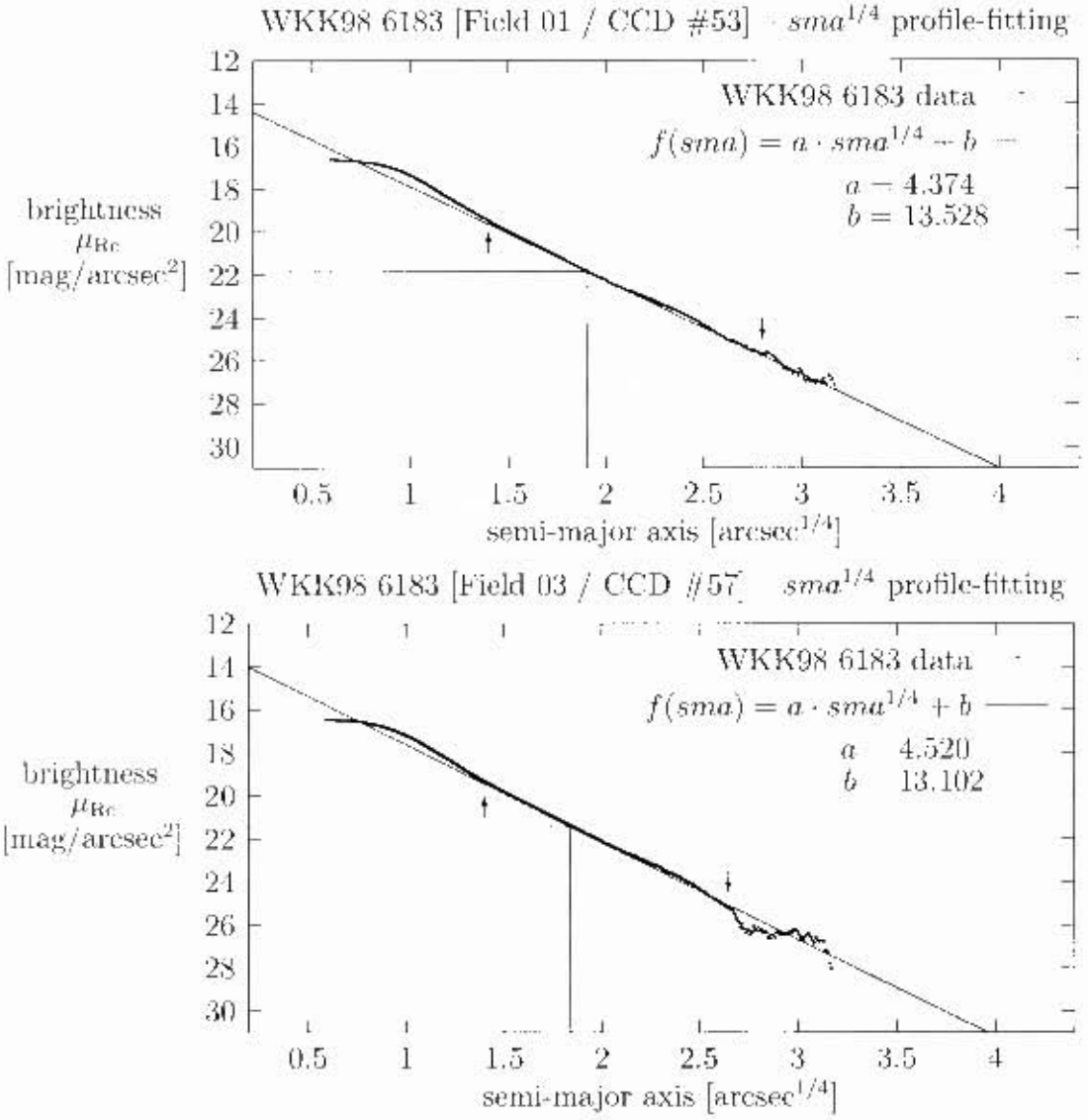

Figure 11.8: Galaxy WKK 6183, plots of brightness μ_{R_c} versus semi-major axis $sma^{1/4}$ to demonstrate the profile-fitting. The arrows point to the upper and lower limit of the data set that was used for the fit. The resulting effective (half-light) radius $r_e^{1/4}$ and effective (half-light) surface brightness μ_e are indicated by straight lines.

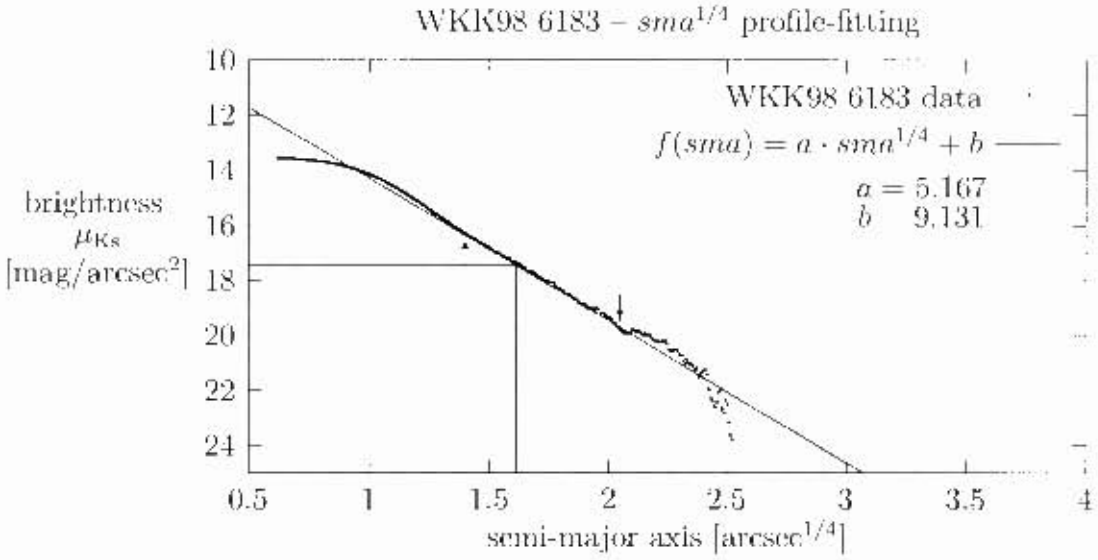

Figure 11.9: Galaxy WKK 6183, plot of brightness μ_{K_s} versus semi-major axis sma$^{1/4}$ to demonstrate the profile-fitting. The arrows point to the upper and lower limit of the data set that was used for the fit. The resulting effective (half-light) radius $r_e^{1/4}$ and effective (half-light) surface brightness μ_e are indicated by straight lines.

Chapter 12

Galaxy WKK 6198

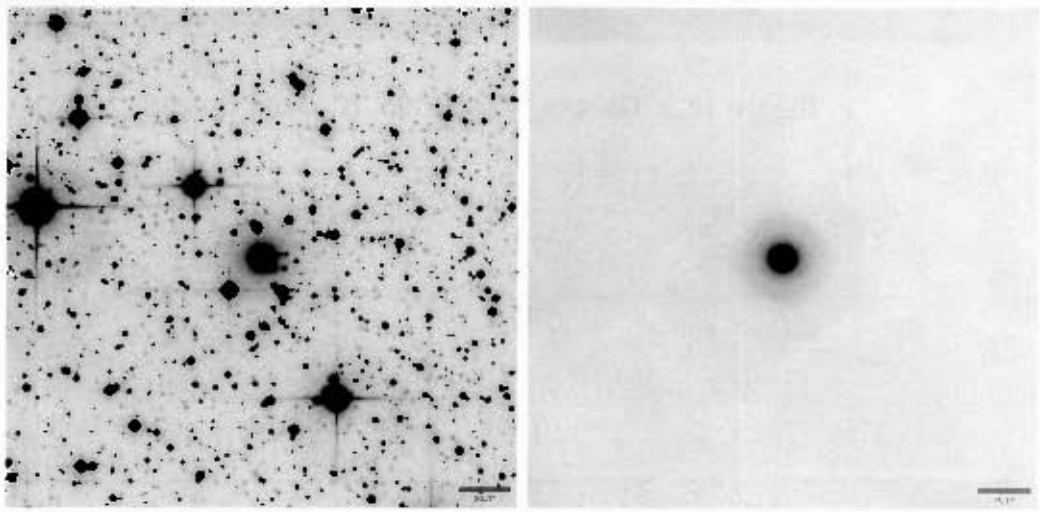

Figure 12.1: Galaxy WKK 6198, R_c band images, field 05, WFI CCD #54

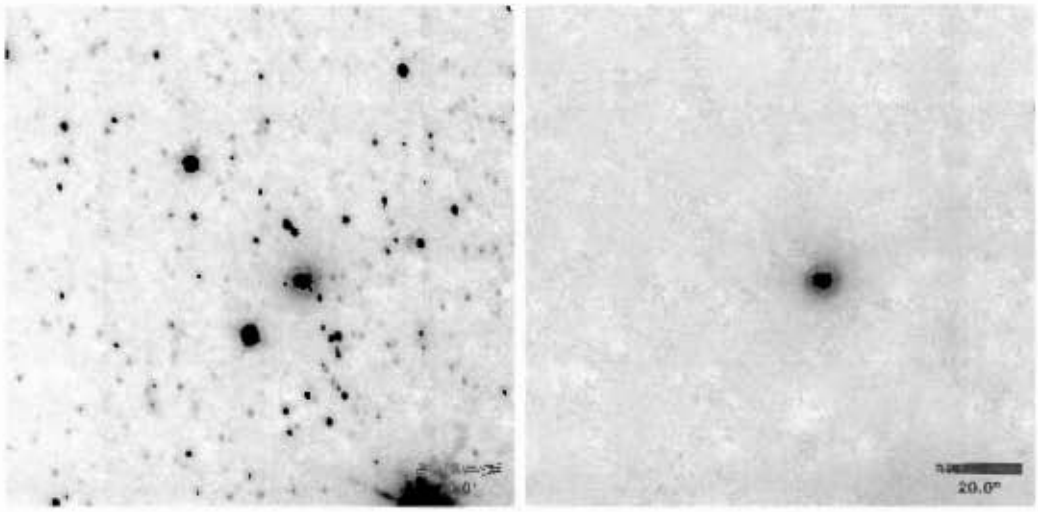

Figure 12.2: Galaxy WKK 6198, K_s band images

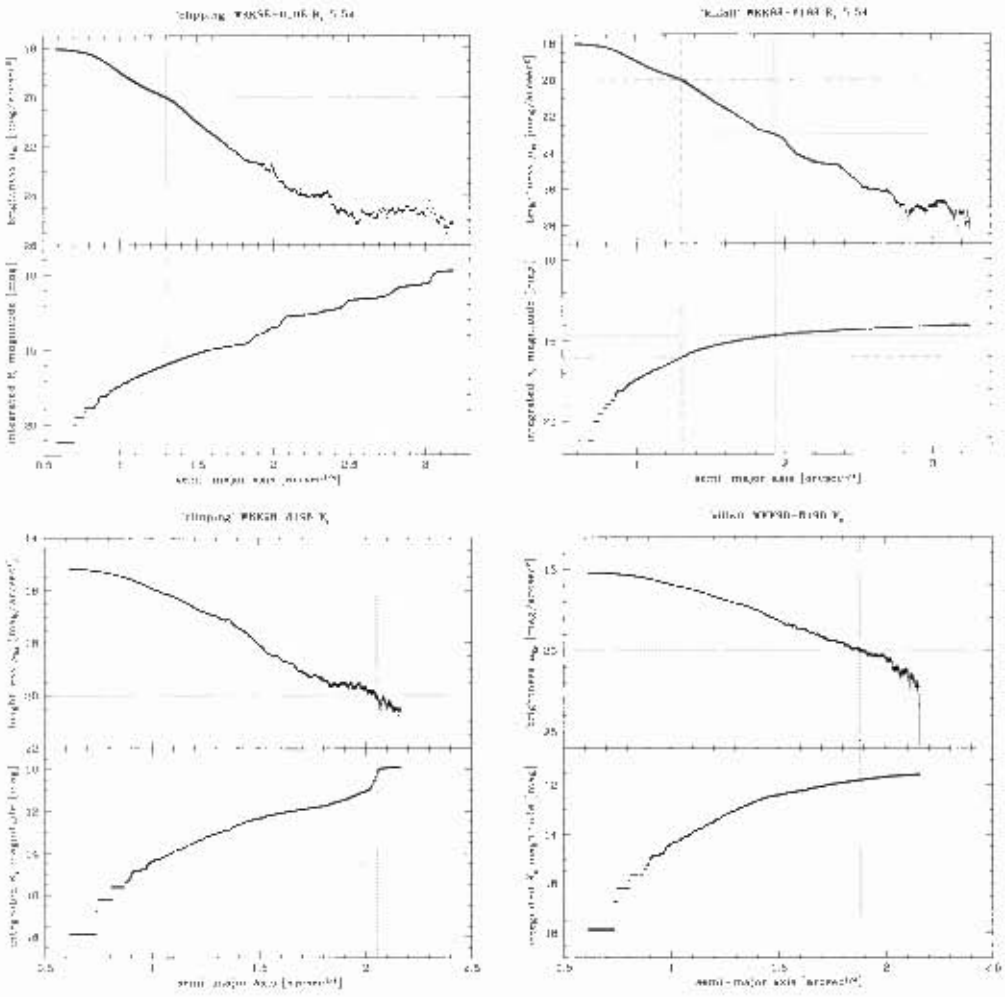

Figure 12.4: Galaxy WKK 6198, isophotal and integrated magnitude plots

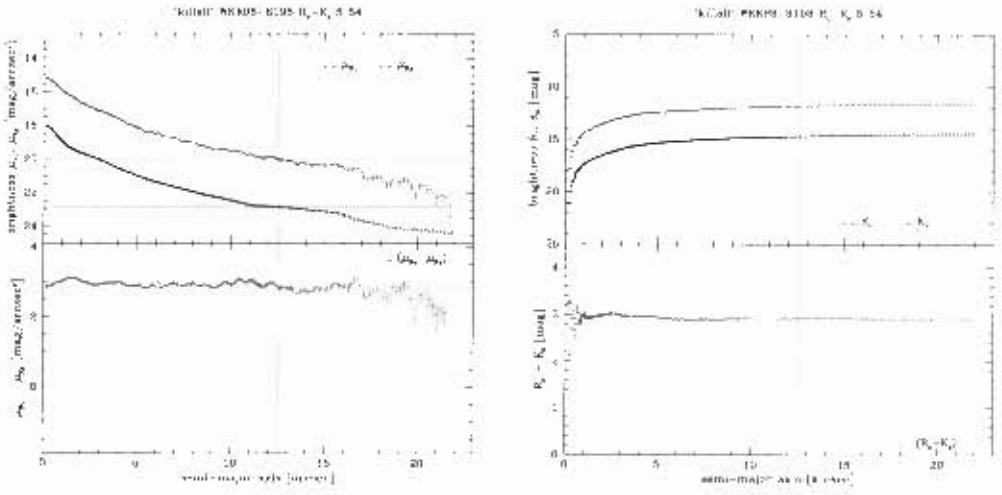

Figure 12 5: Galaxy WKK 6198, $(u_{R_c} - \mu_{K_s})$ and $(R_c - K_s)$ magnitude plots

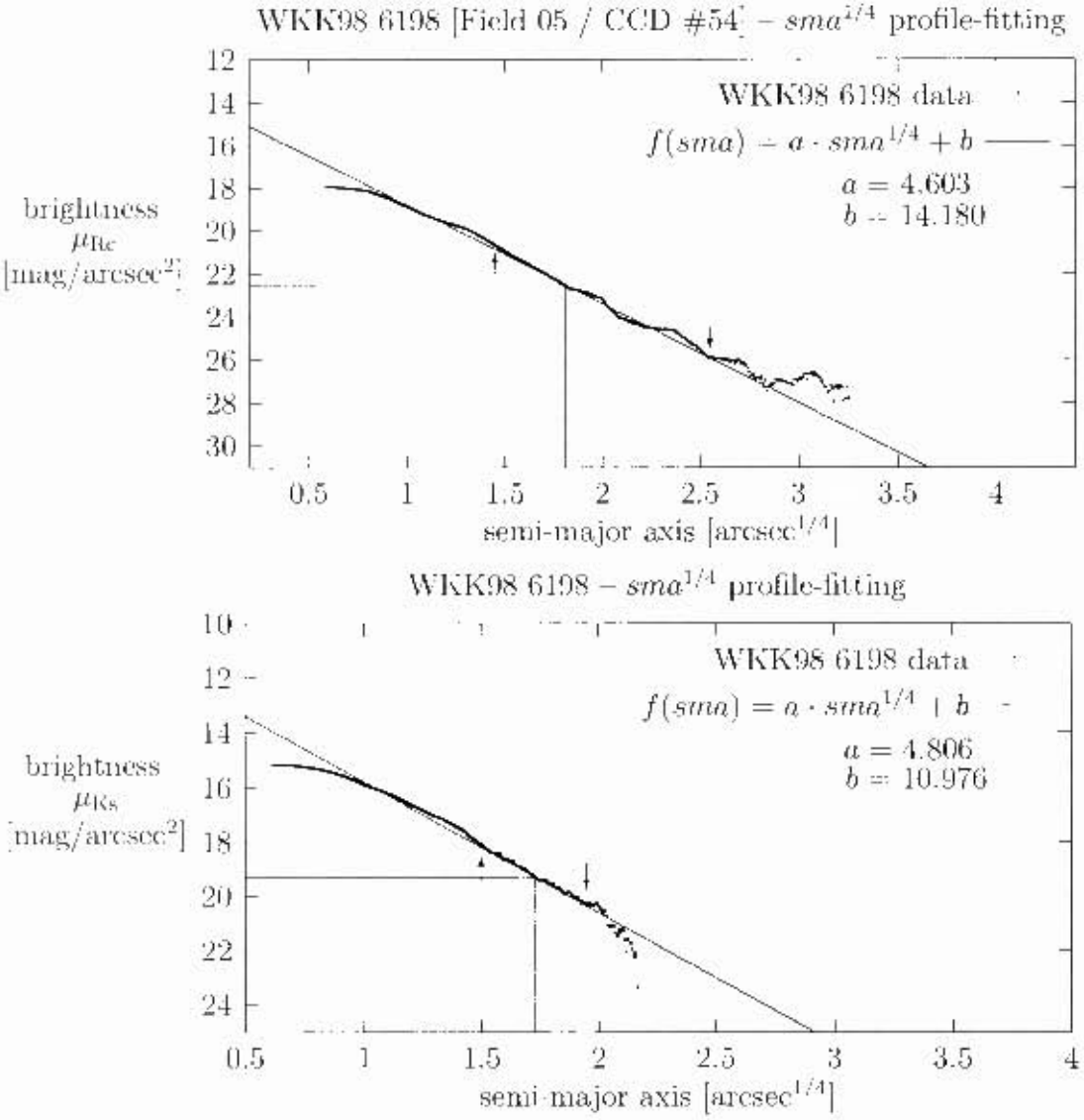

Figure 12.6: Galaxy WKK 6198, plots of brightness (μ_{R_c} and μ_{K_s}) versus semi-major axis $sma^{1/4}$ to demonstrate the profile-fitting. The arrows point to the upper and lower limit of the data set that was used for the fit. The resulting effective (half-light) radius $r_e^{1/4}$ and effective (half-light) surface brightness μ_e are indicated by straight lines.

Chapter 13

Galaxy WKK 6204

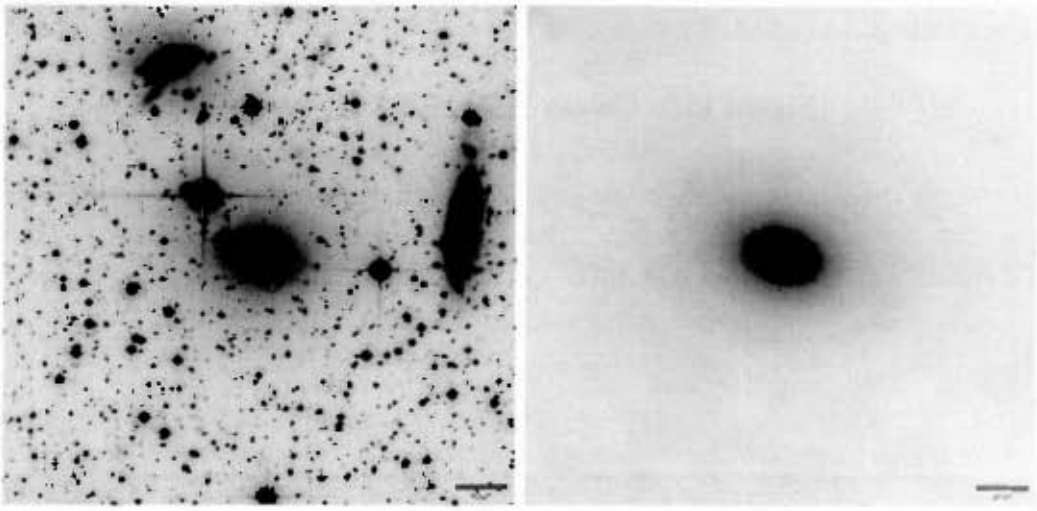

Figure 13.1: Galaxy WKK 6204, R_c band images, field 01, WFI CCD #54

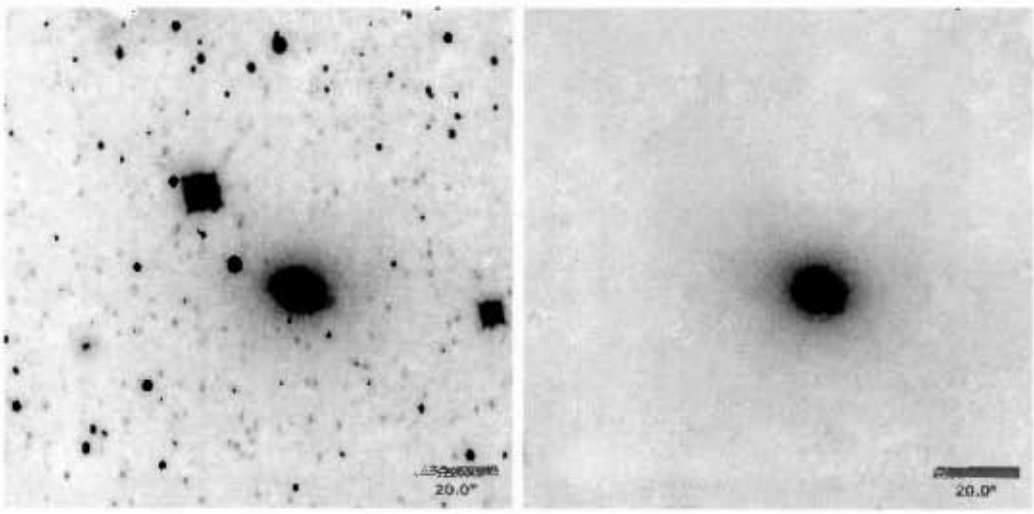

Figure 13.2: Galaxy WKK 6204, K_s band images

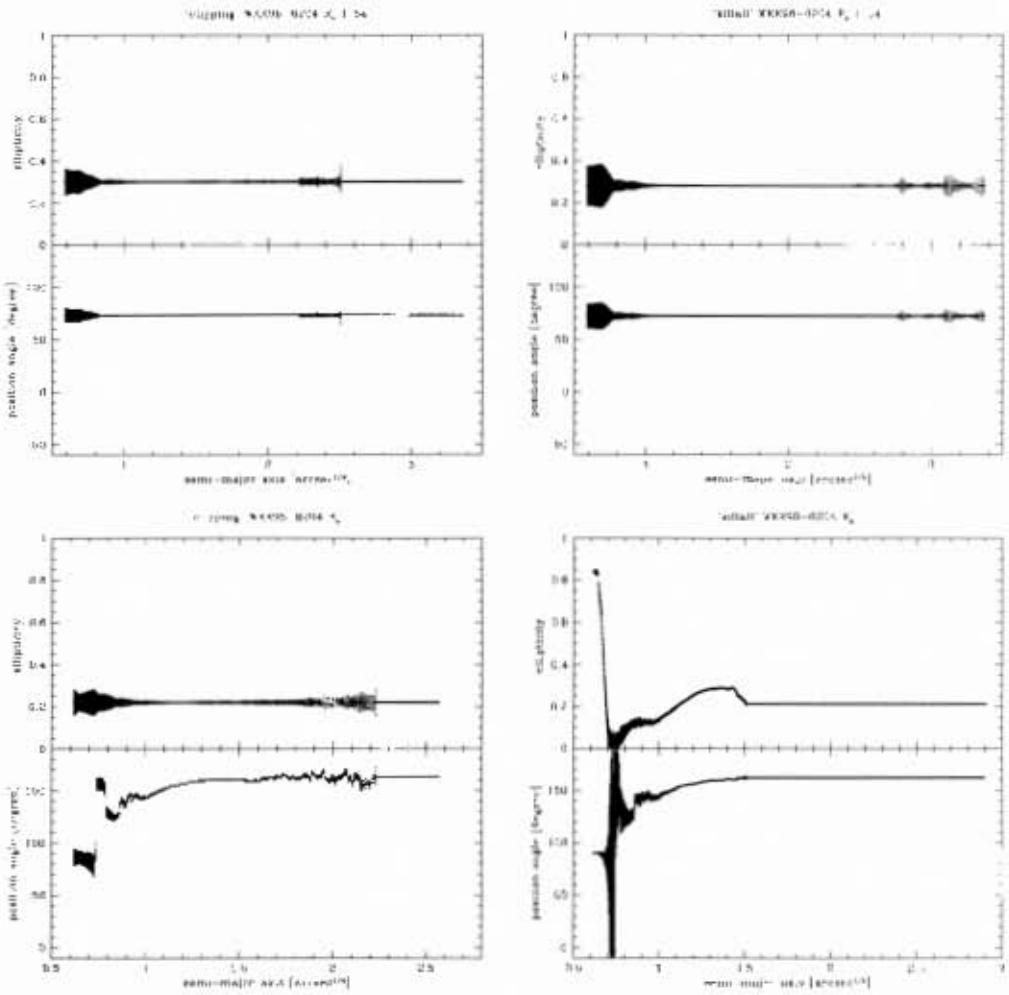

Figure 13.3: Galaxy WKK 6204, ellipticity and position angle plots

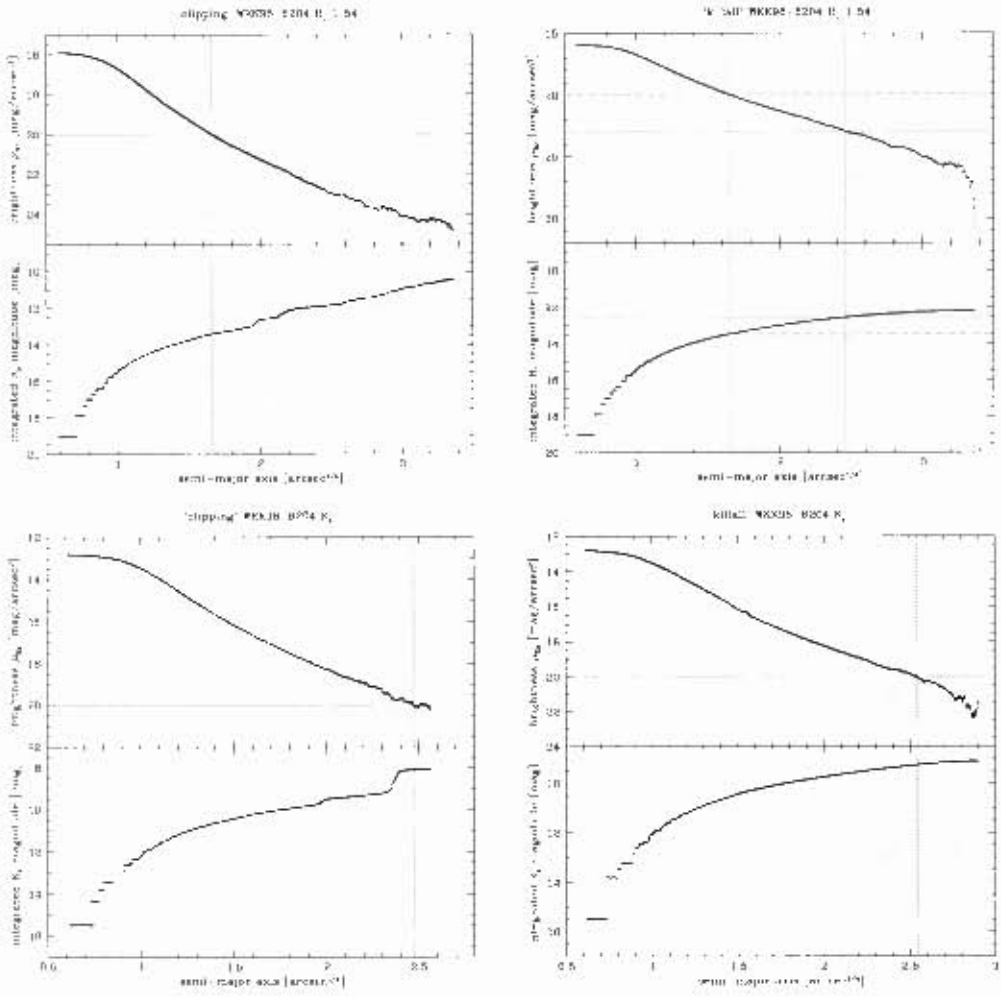

Figure 13.4: Galaxy WKK 6204, isophotal and integrated magnitude plots

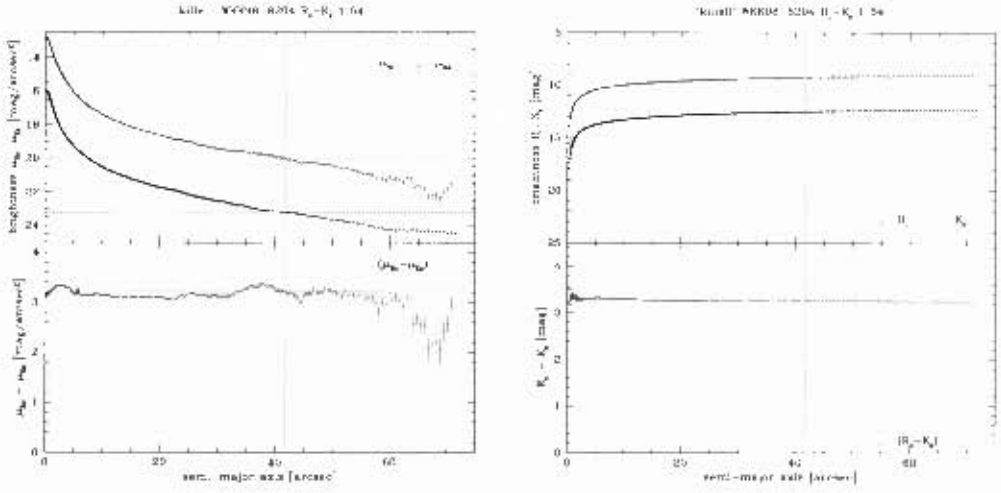

Figure 13.5: Galaxy WKK 6204, $(\mu_{R_c} - \mu_{K_s})$ and $(R_c - K_s)$ magnitude plots

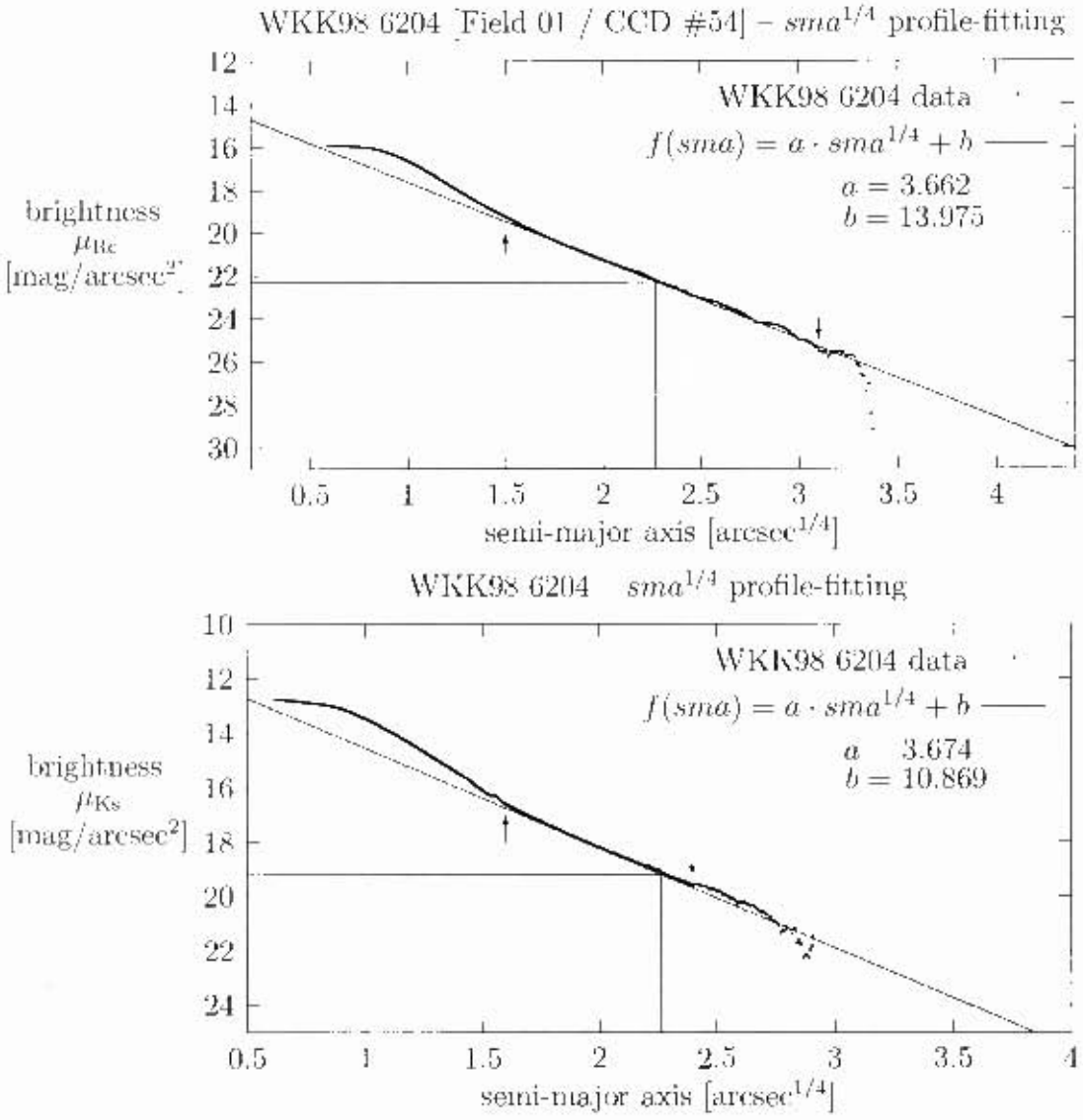

Figure 13.6: Galaxy WKK 6204, plots of brightness (μ_{R_c} and μ_{K_s}) versus semi-major axis $sma^{1/4}$ to demonstrate the profile-fitting. The arrows point to the upper and lower limit of the data set that was used for the fit. The resulting effective (half-light) radius $r_e^{1/4}$ and effective (half-light) surface brightness μ_e are indicated by straight lines.

Chapter 14

Galaxy WKK 6221

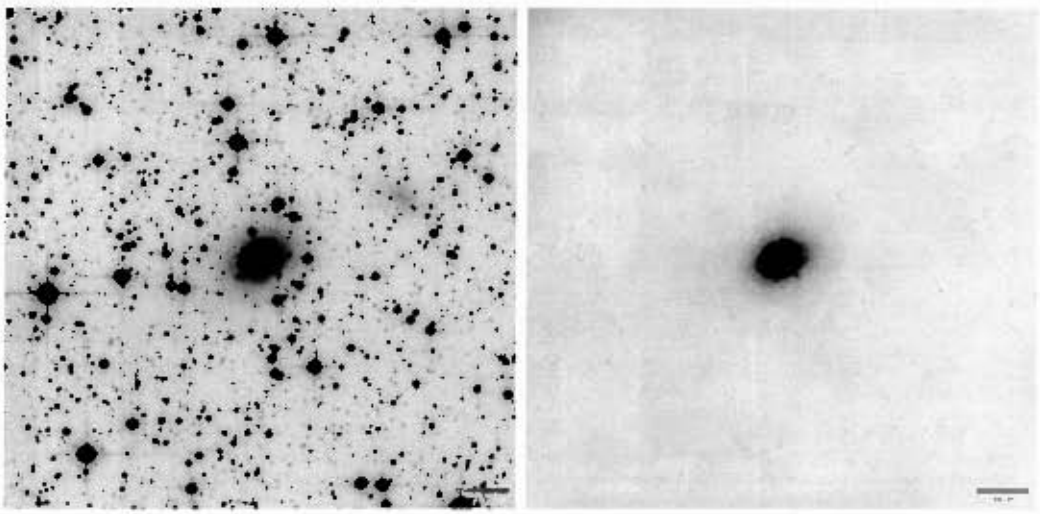

Figure 14.1: Galaxy WKK 6221, R_c band images, field 02, WFI CCD #54

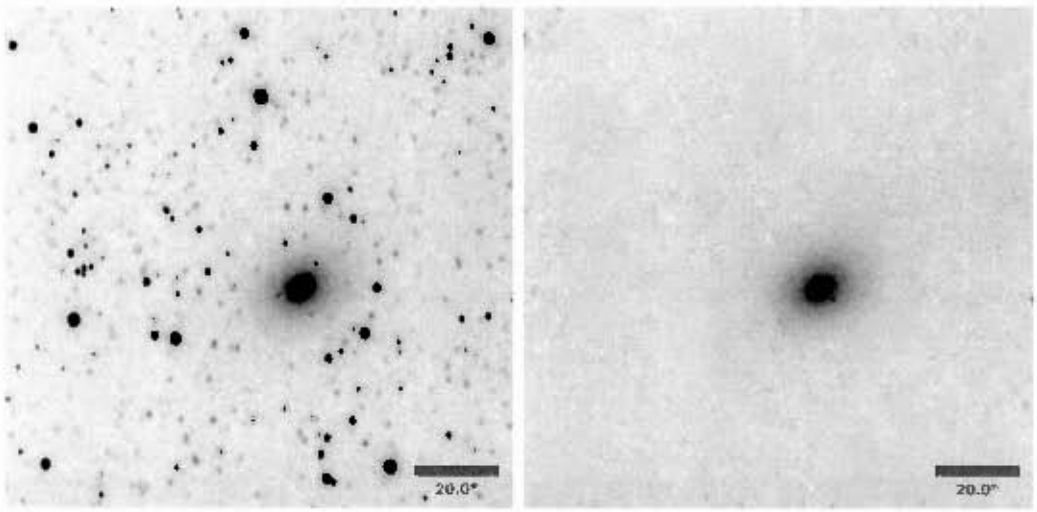

Figure 14.2: Galaxy WKK 6221, K_s band images

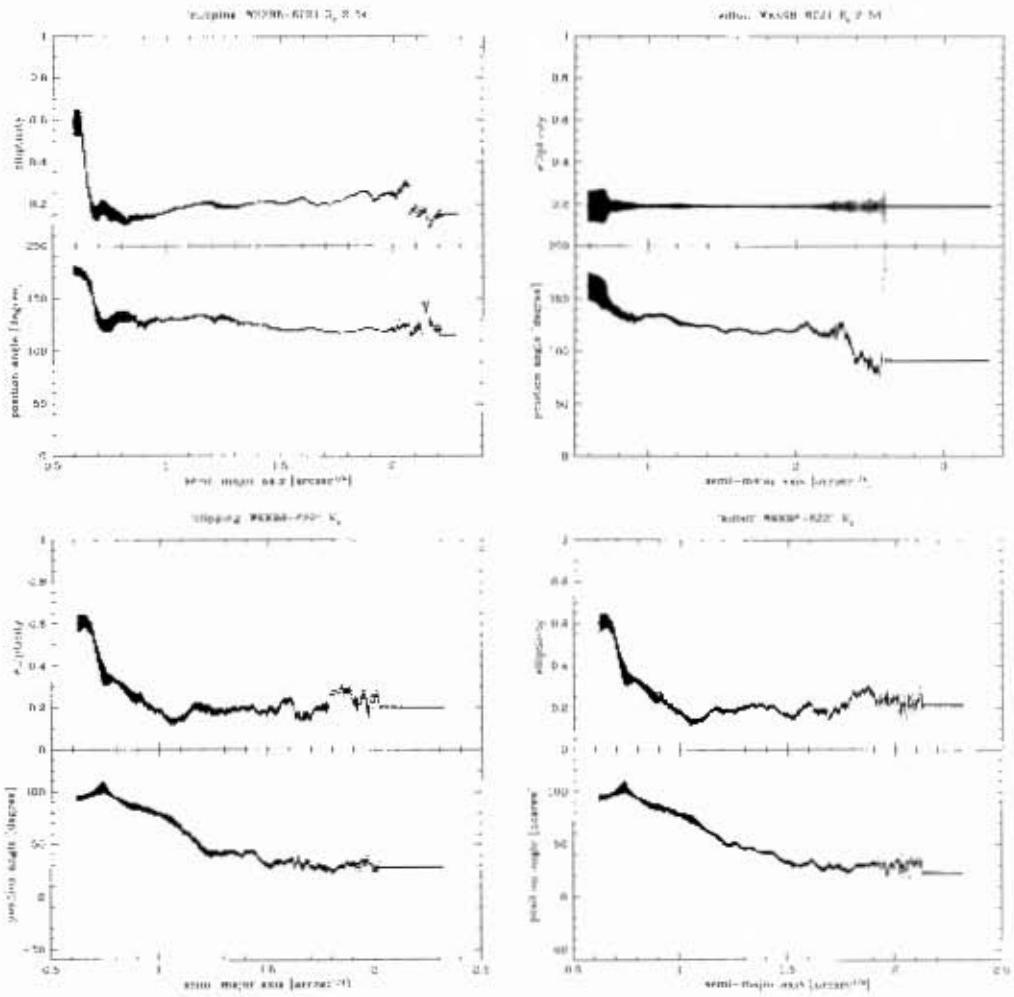

Figure 14.3: Galaxy WKK 6221, ellipticity and position angle plots

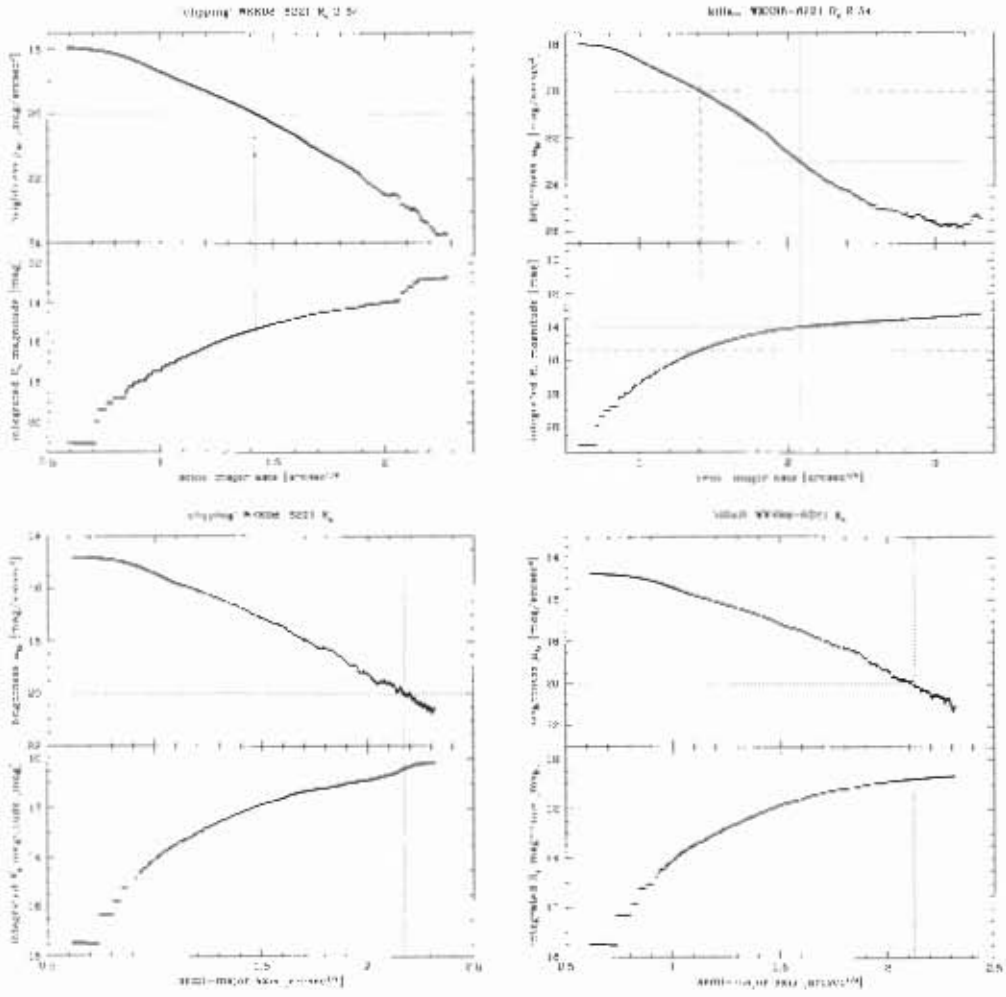

Figure 14.4: Galaxy WKK 6221, isophotal and integrated magnitude plots

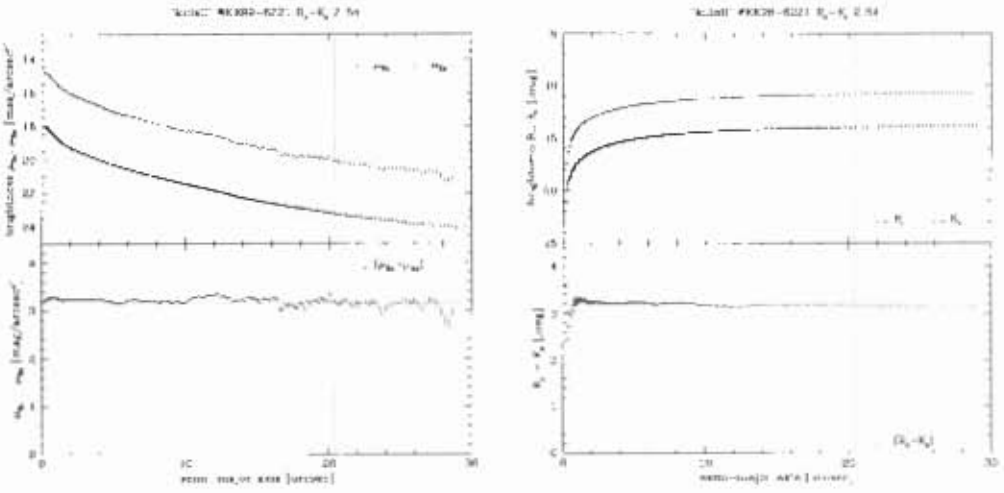

Figure 14.5: Galaxy WKK 6221, $(\mu_{R_c} - \mu_{K_s})$ and $(R_c - K_s)$ magnitude plots

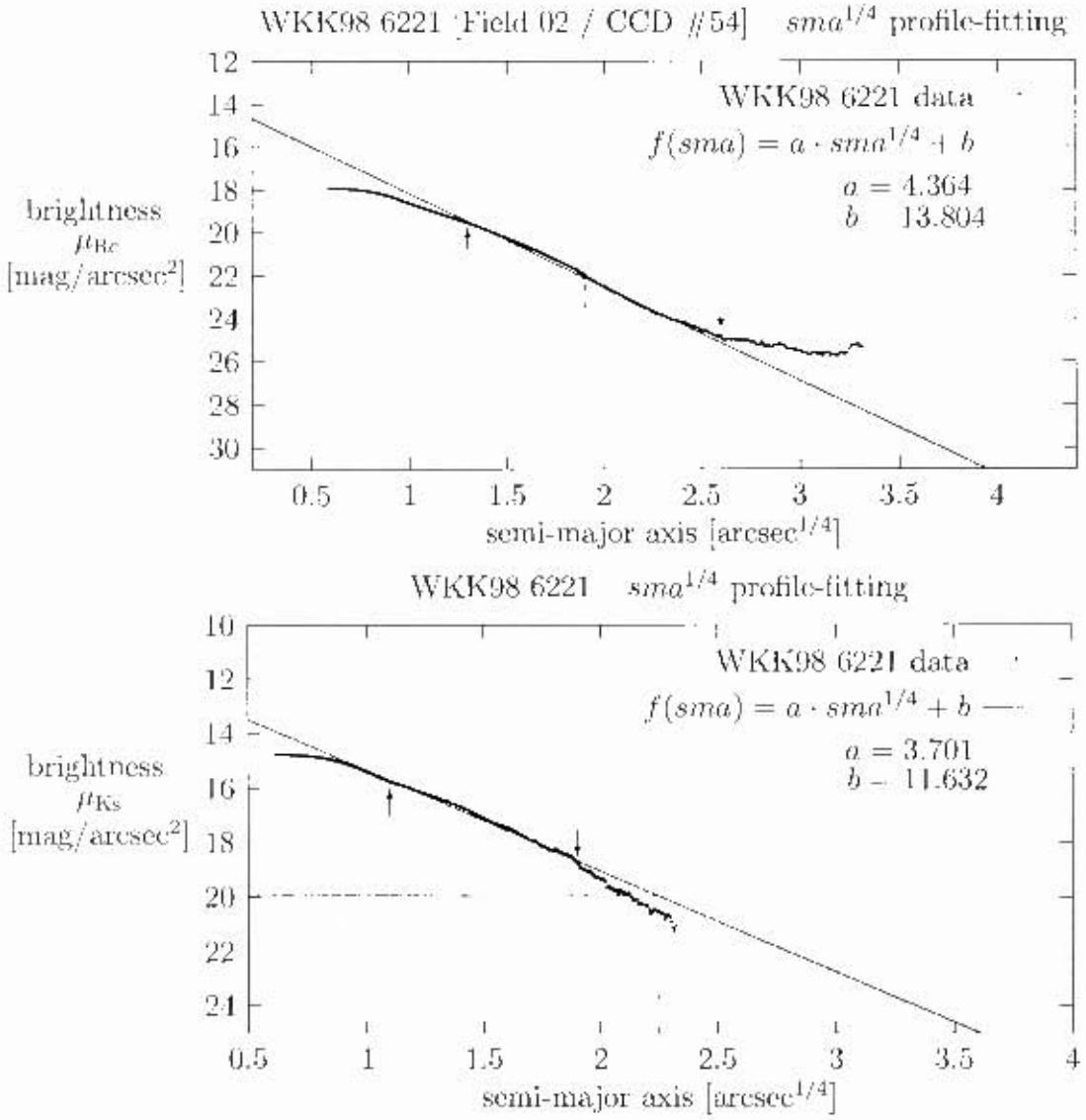

Figure 14.6: Galaxy WKK 6221, plots of brightness (μ_{R_c} and μ_{K_s}) versus semi-major axis sma$^{1/4}$ to demonstrate the profile-fitting. The arrows point to the upper and lower limit of the data set that was used for the fit. The resulting effective (half-light) radius $r_e^{1/4}$ and effective (half-light) surface brightness μ_e are indicated by straight lines.

Chapter 15

Galaxy WKK 6229

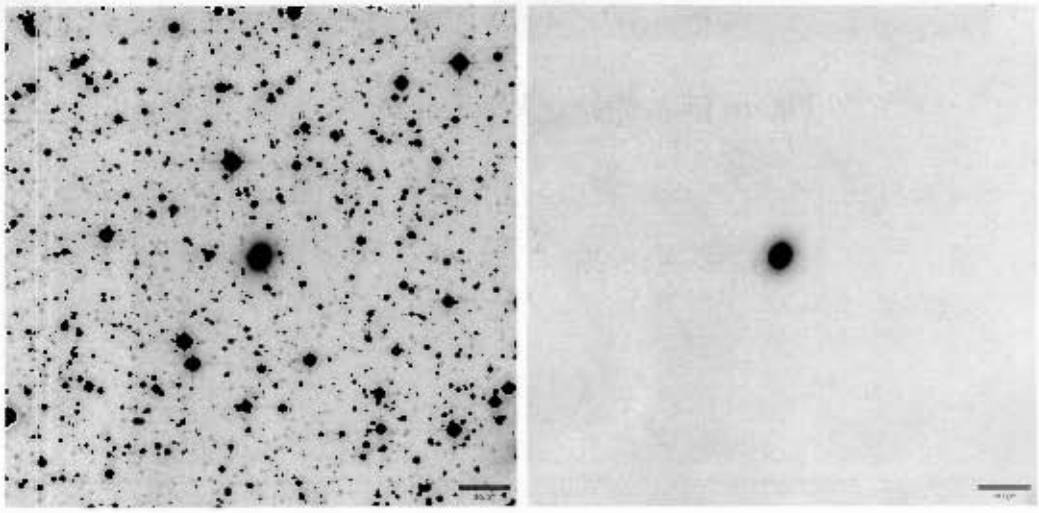

Figure 15.1: Galaxy WKK 6229, R_c band images, field 01, WFI CCD #53

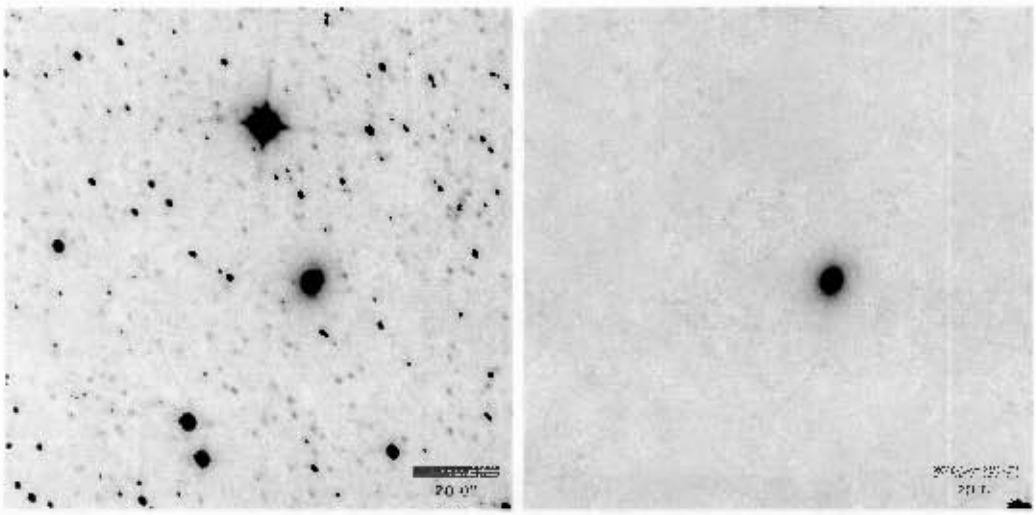

Figure 15.2: Galaxy WKK 6229, K_s band images

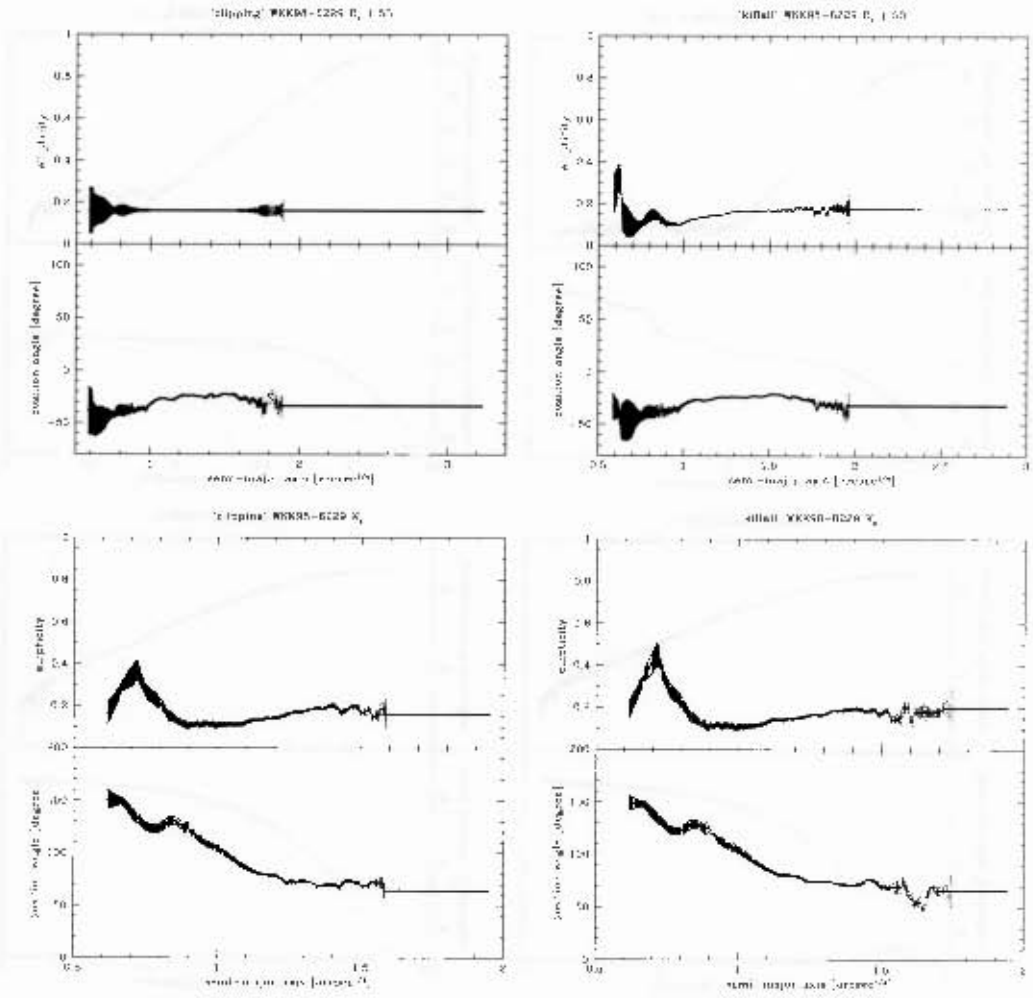

Figure 15.3: Galaxy WKK 6229, ellipticity and position angle plots

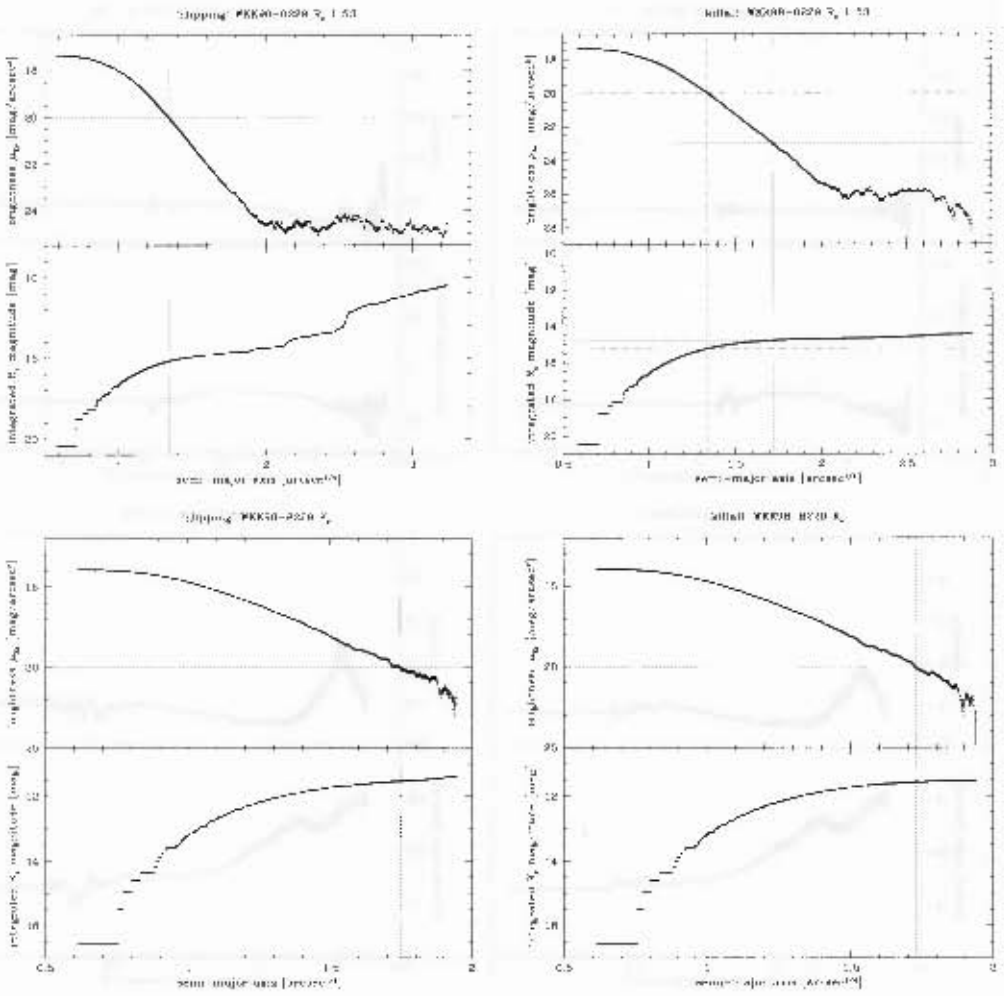

Figure 15.4: Galaxy WKK 6229, isophotal and integrated magnitude plots

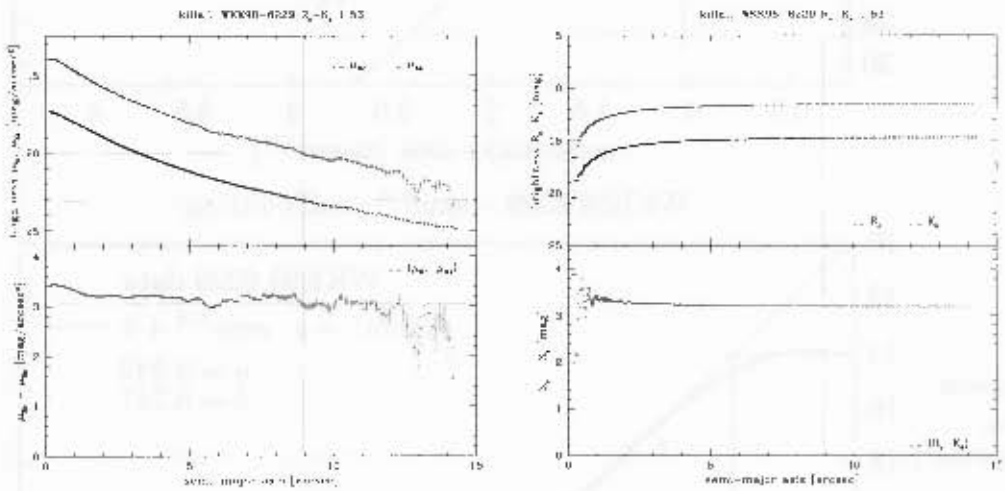

Figure 15.5: Galaxy WKK 6229, $(\mu_{R_c} - \mu_{K_s})$ and $(R_c - K_s)$ magnitude plots

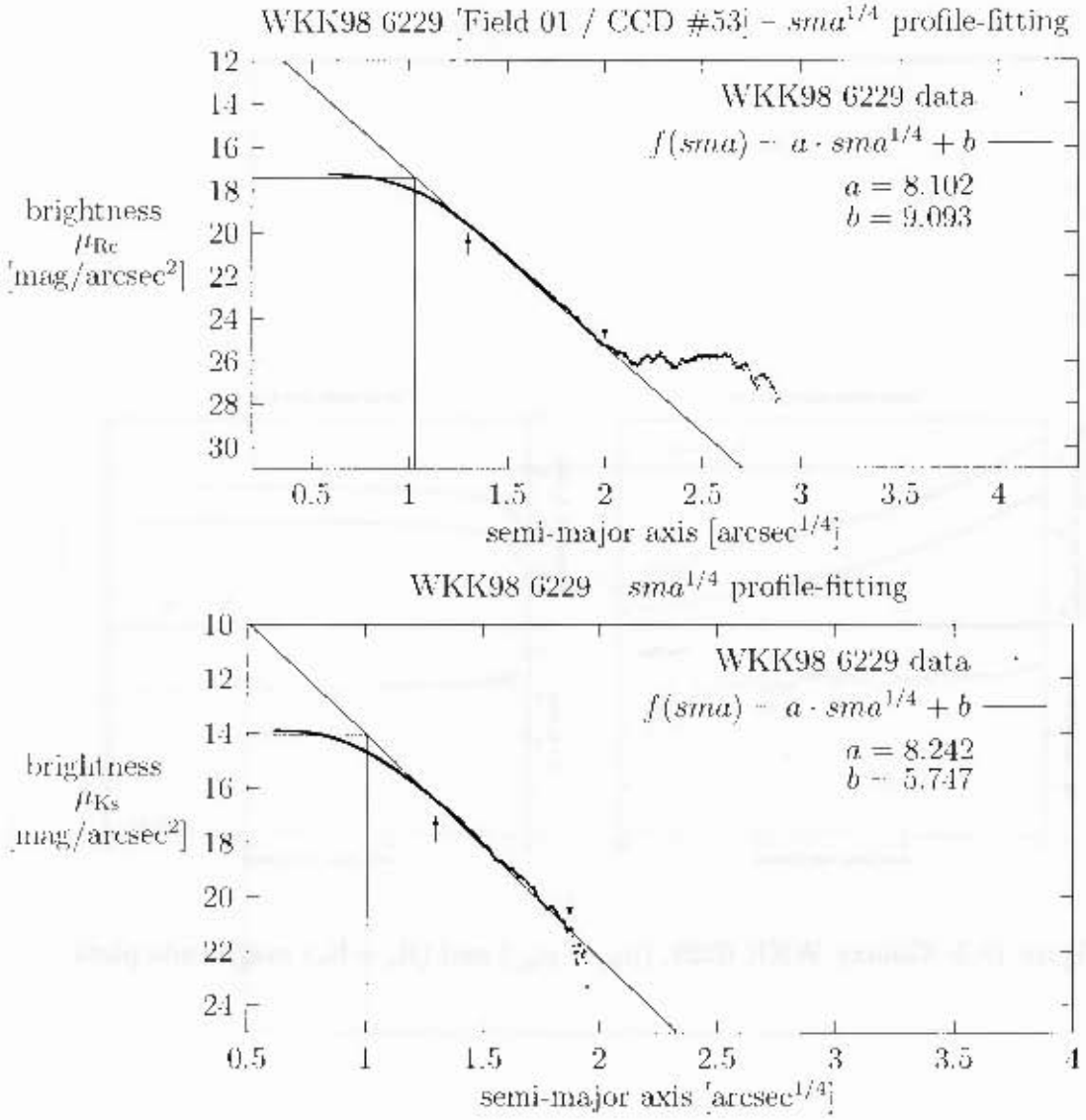

Figure 15.6: Galaxy WKK 6229, plots of brightness (μ_{R_c} and μ_{K_s}) versus semi-major axis sma$^{1/4}$ to demonstrate the profile-fitting. The arrows point to the upper and lower limit of the data set that was used for the fit. The resulting effective (half-light) radius $r_e^{1/4}$ and effective (half-light) surface brightness μ_e are indicated by straight lines.

Chapter 16

Galaxy WKK 6233

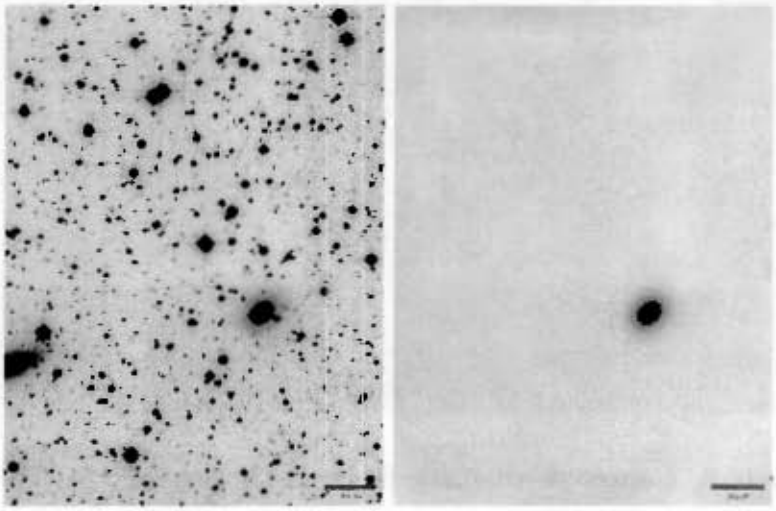

Figure 16.1: Galaxy WKK 6233, R_c band images, field 01, WFI CCD #52

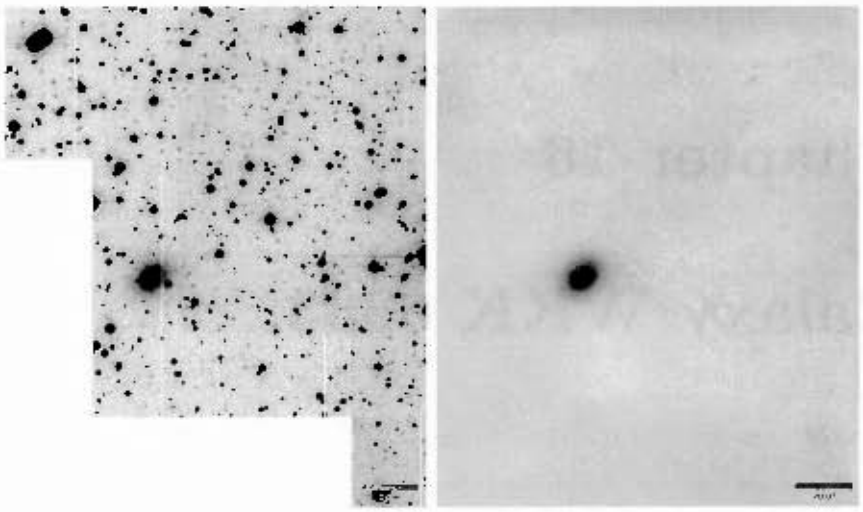

Figure 16.2: Galaxy WKK 6233, R_c band images, field 01, WFI CCD #53

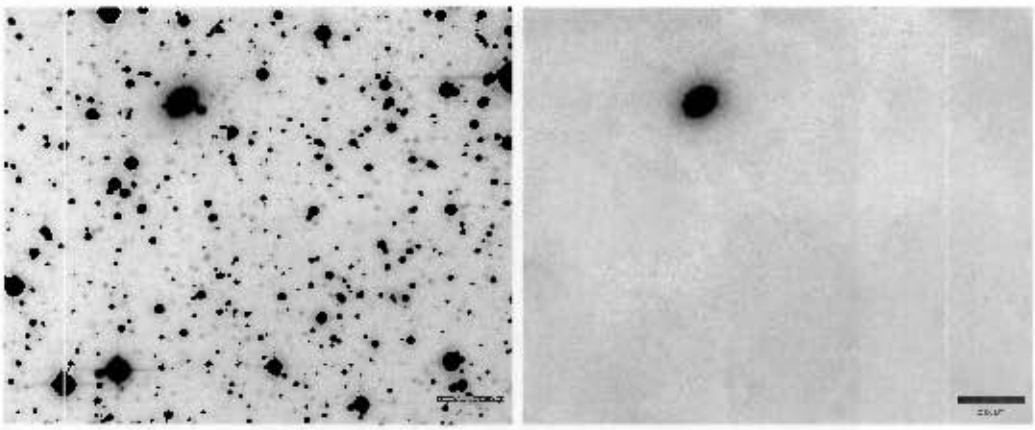

Figure 16.3: Galaxy WKK 6233, R_c band images, field 01, WFI CCD #54

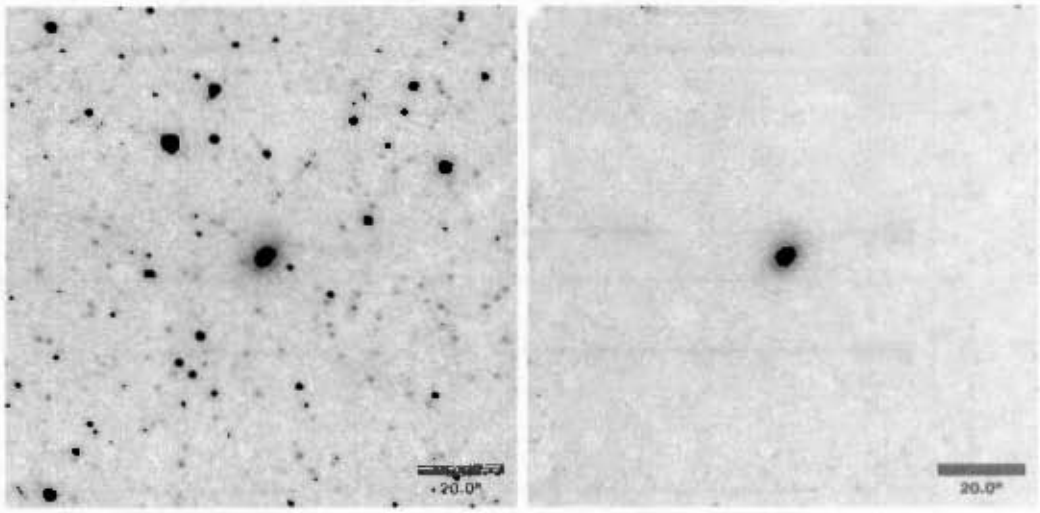

Figure 16.4: Galaxy WKK 6233, K, band images

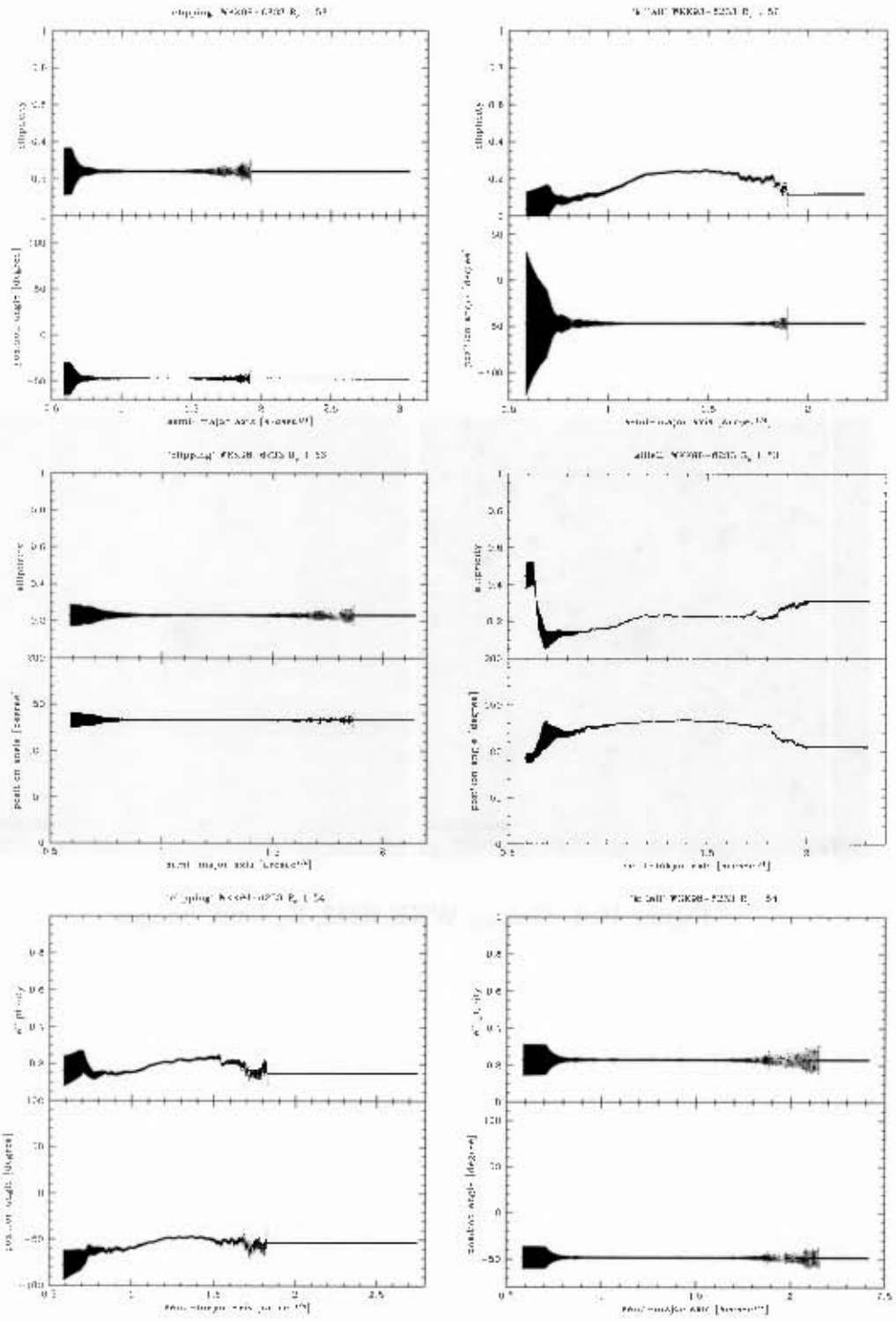

Figure 16.5: Galaxy WKK 6233, ellipticity and position angle plots, R_c band

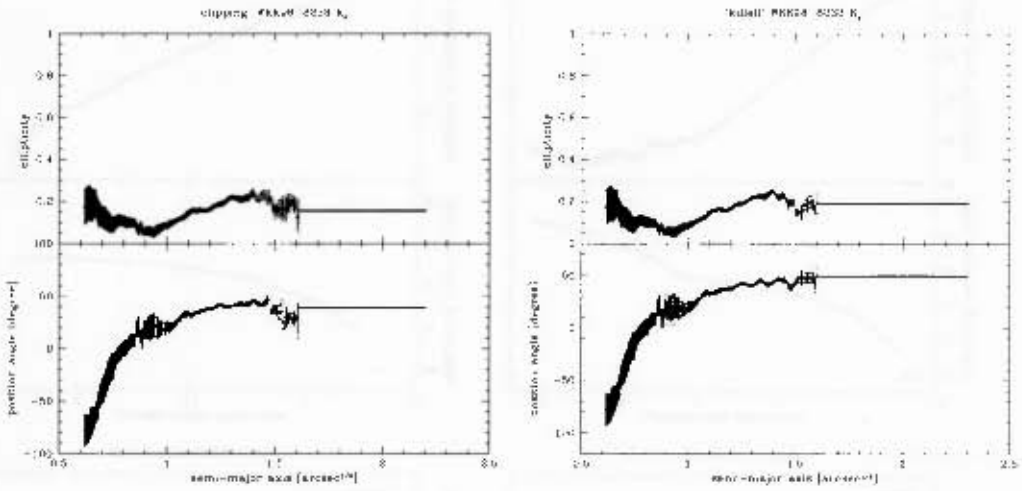

Figure 16.6: Galaxy WKK 6233, ellipticity and position angle plots, K_s band

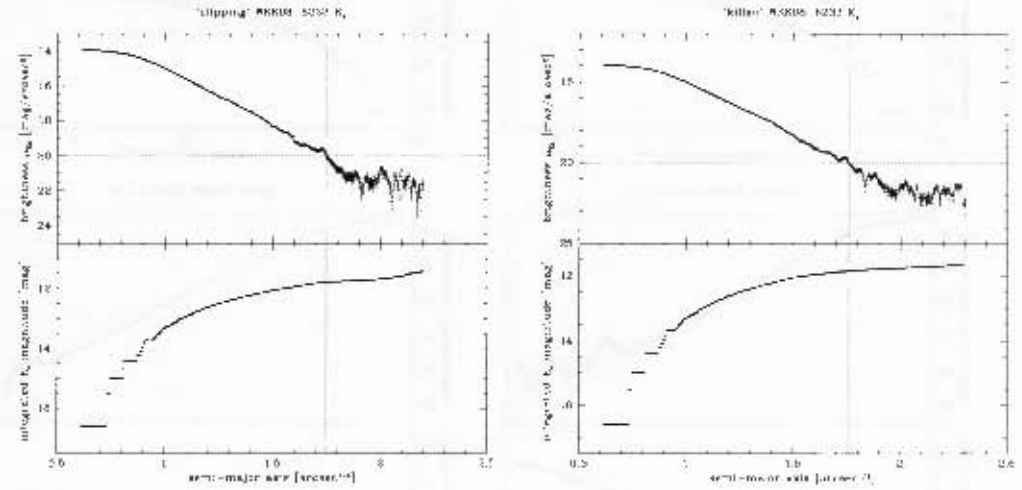

Figure 16.7: Galaxy WKK 6233, isophotal and integrated magnitude plots, K_s band

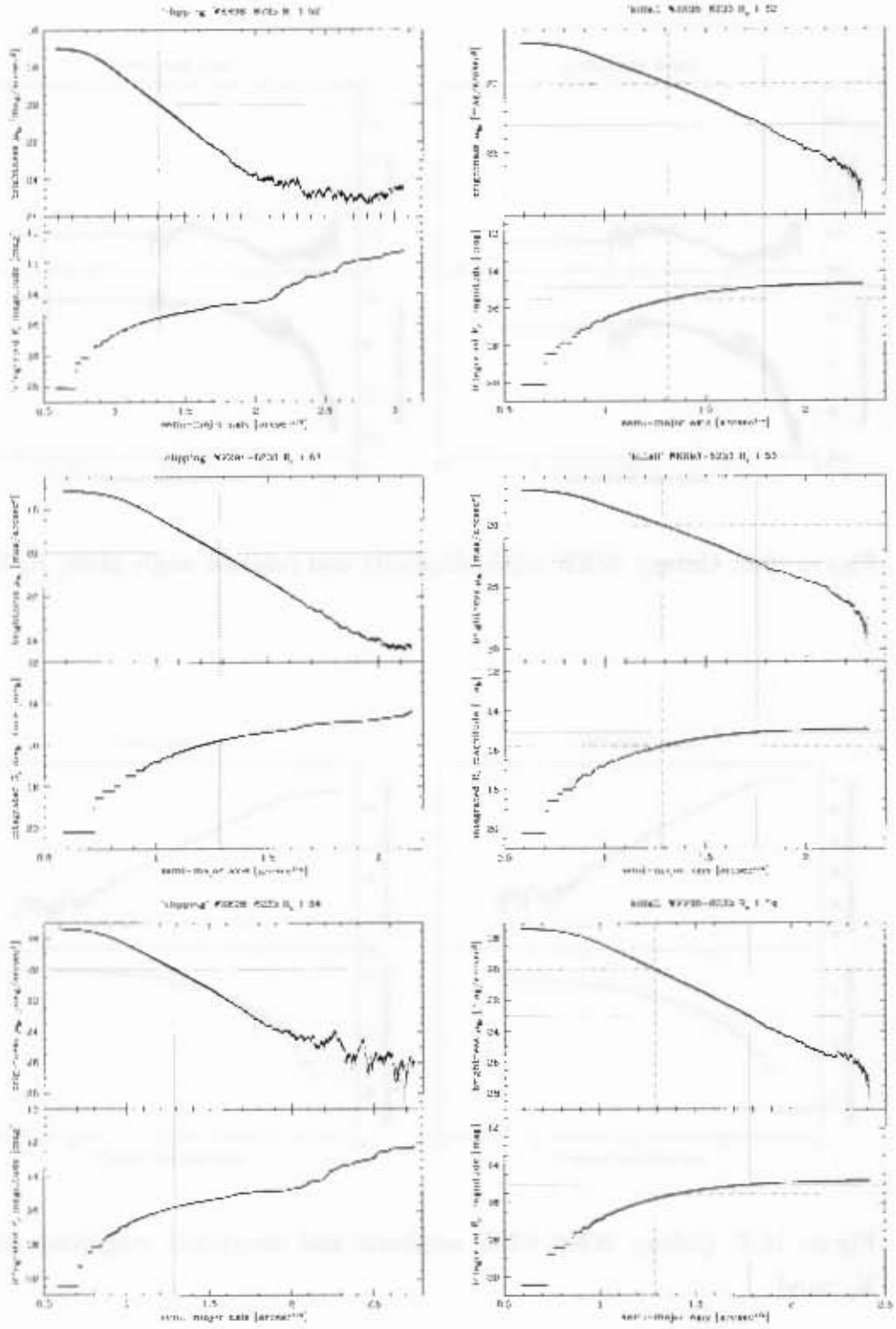

Figure 16.8: Galaxy WKK 6233, isophotal and integrated magnitude plots, R_c band

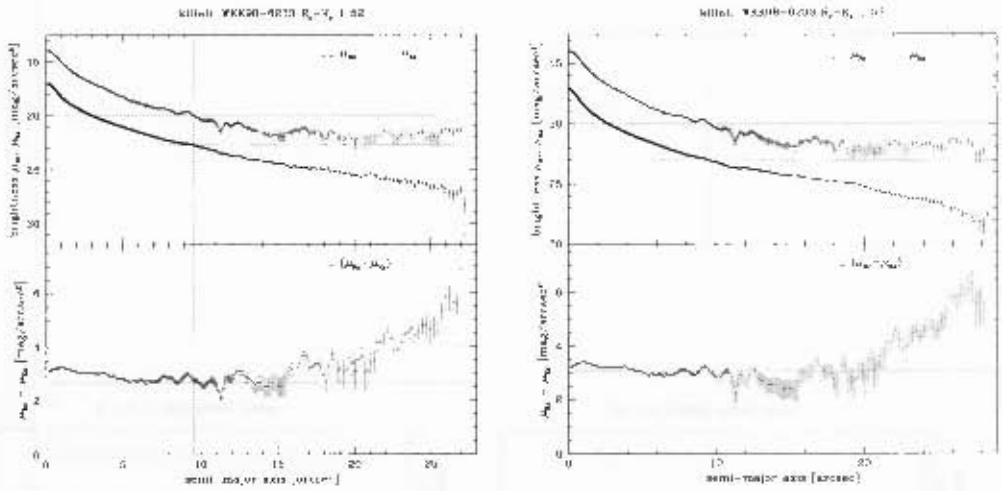

Figure 16.9: Galaxy WKK 6233, $(\mu_{R_c} - \mu_{K_s})$ magnitude plots

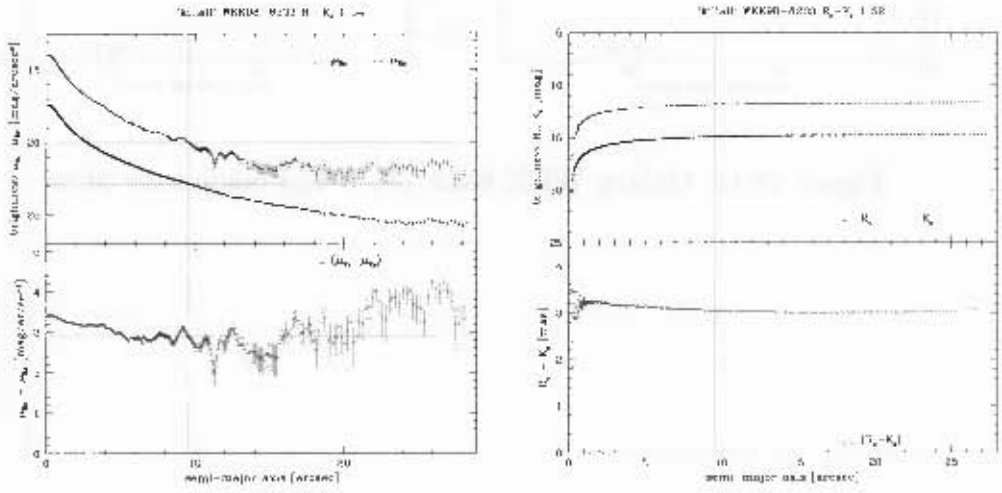

Figure 16.10: Galaxy WKK 6233, $(\mu_{R_c} - \mu_{K_s})$ and $(R_c - K_s)$ magnitude plots

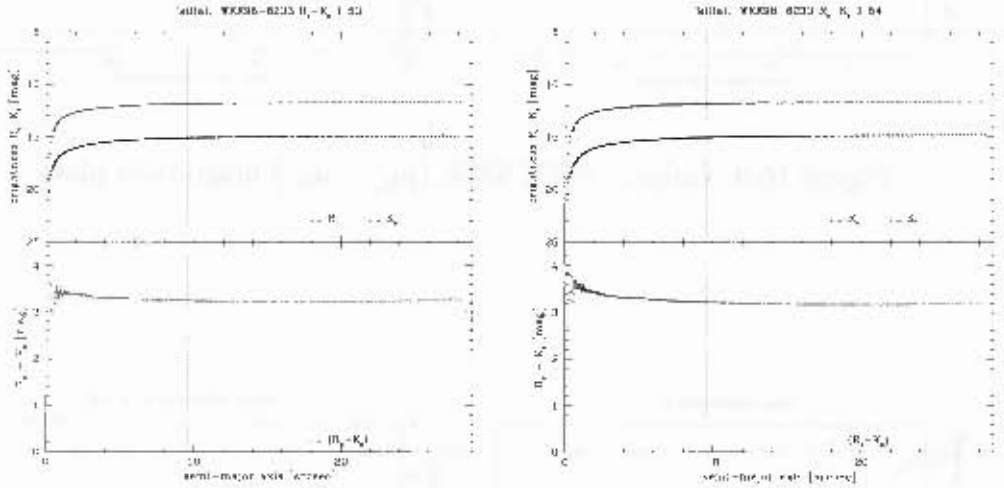

Figure 16.11: Galaxy WKK 6233, (R_c K_s) magnitude plots

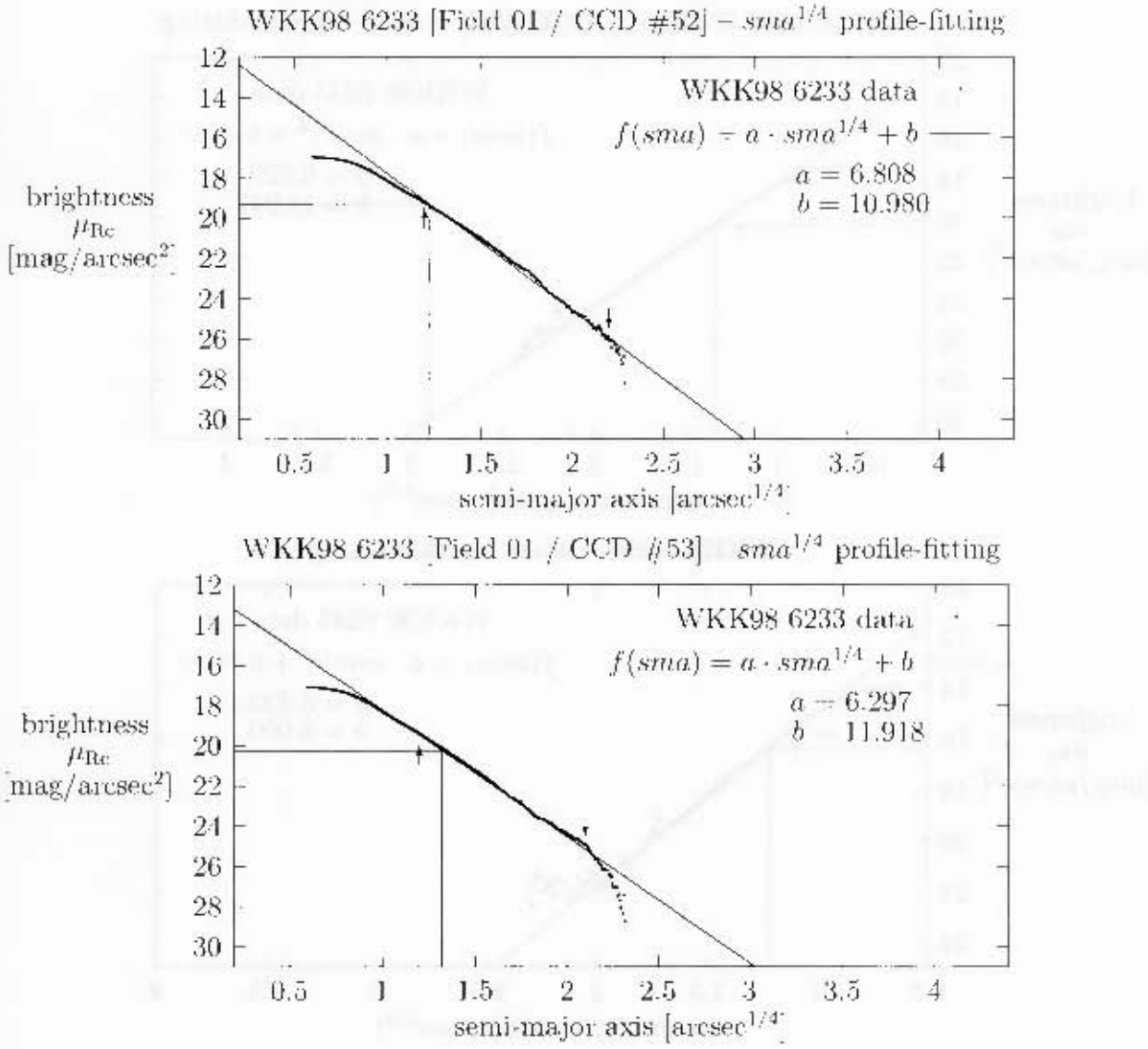

Figure 16.12: Galaxy WKK 6233, plots of brightness μ_{R_c} versus semi-major axis $sma^{1/4}$ to demonstrate the profile-fitting. The arrows point to the upper and lower limit of the data set that was used for the fit. The resulting effective (half-light) radius $r_e^{1/4}$ and effective (half-light) surface brightness μ_e are indicated by straight lines.

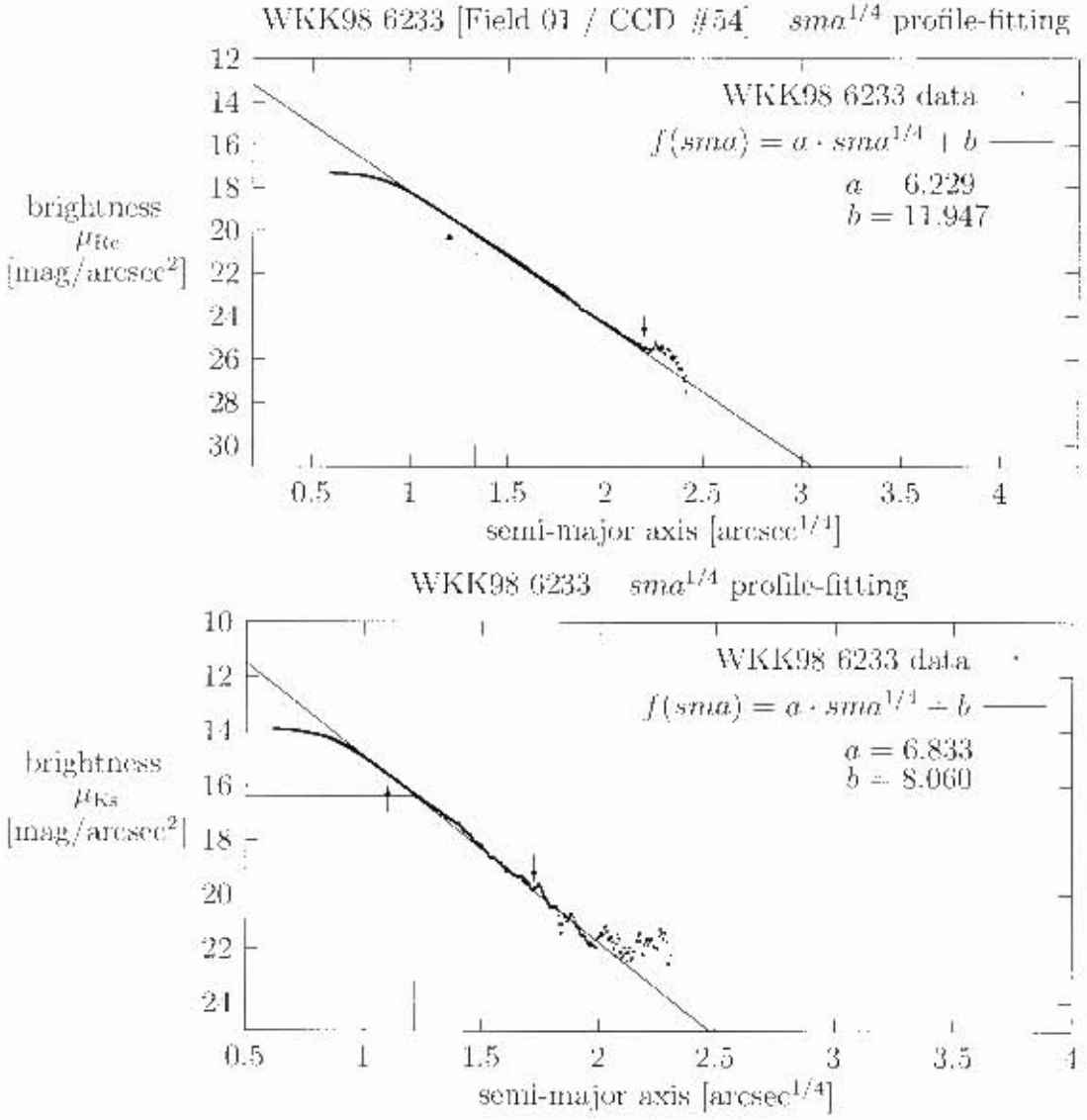

Figure 16.13: Galaxy WKK 6233, plots of brightness (μ_{R_c} and μ_{K_s}) versus semi-major axis sma$^{1/4}$ to demonstrate the profile-fitting. The arrows point to the upper and lower limit of the data set that was used for the fit. The resulting effective (half-light) radius $r_e^{1/4}$ and effective (half-light) surface brightness μ_e are indicated by straight lines.

Chapter 17

Galaxy WKK 6235

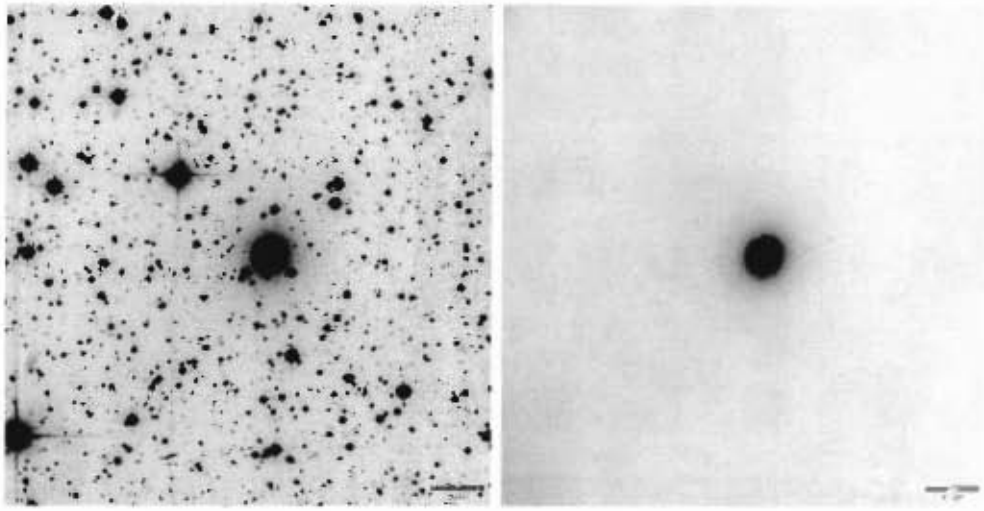

Figure 17.1: Galaxy WKK 6235, R_c band images, field 01, WFI CCD #55

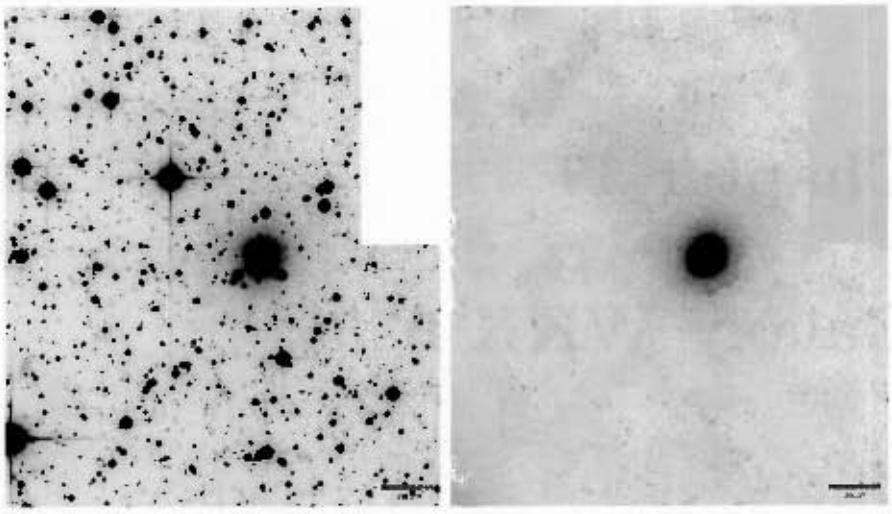

Figure 17.2: Galaxy WKK 6235, R_c band images, field 05, WFI CCD #52

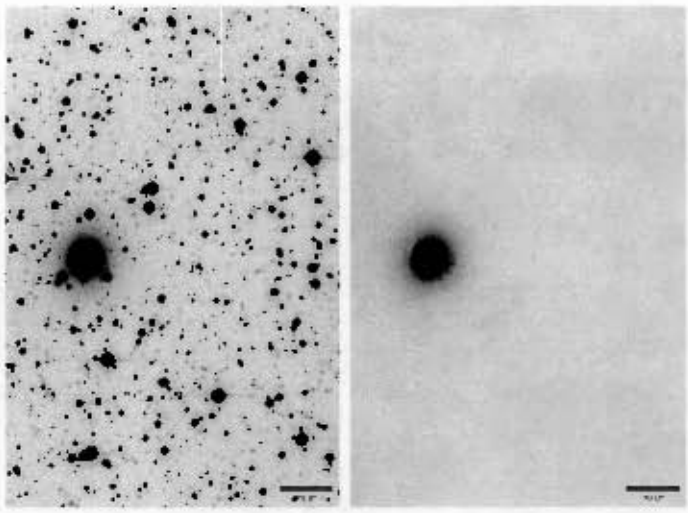

Figure 17.3: Galaxy WKK 6235, R_c band images, field 05, WFI CCD #53

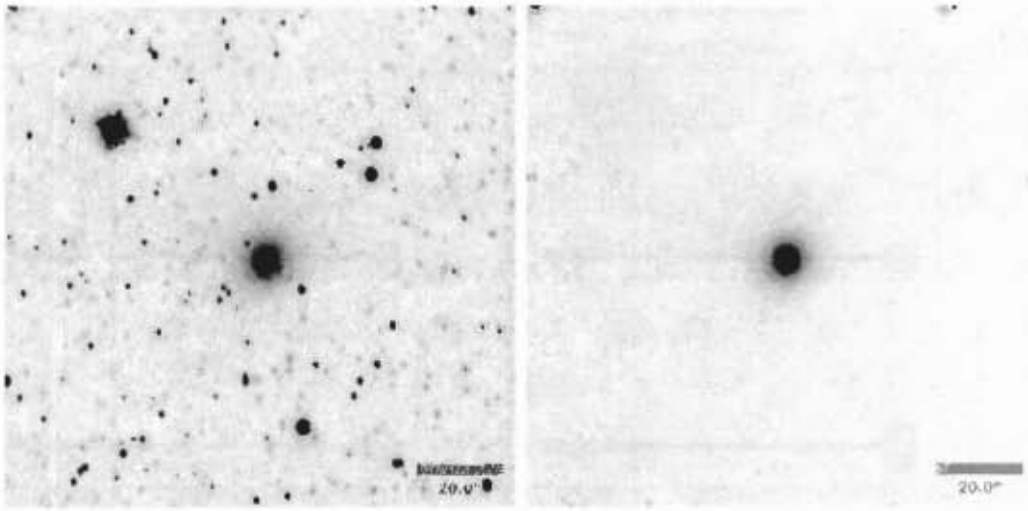

Figure 17.4: Galaxy WKK 6235, K_s band images

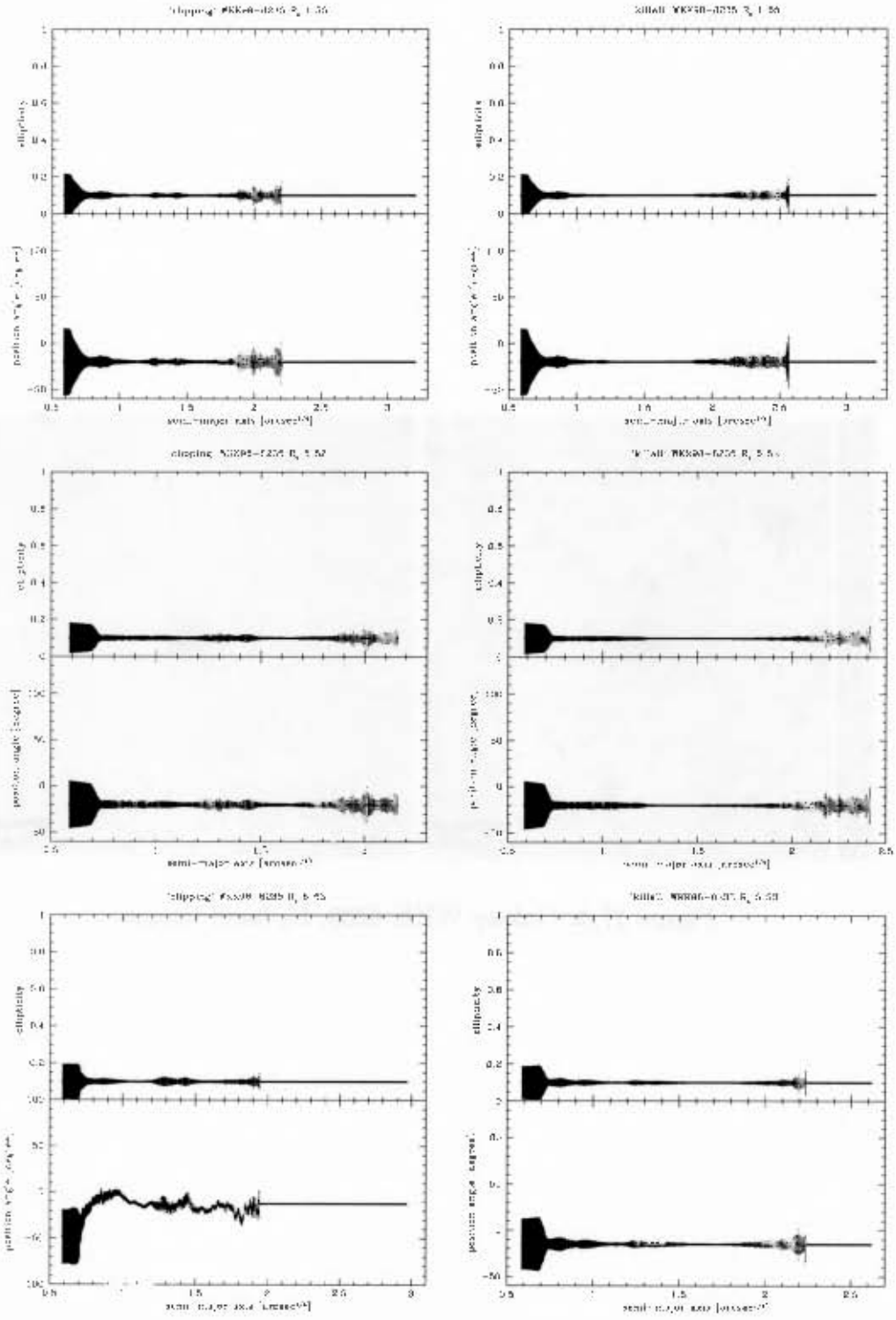

Figure 17.5: Galaxy WKK 6235, ellipticity and position angle plots, R_c band

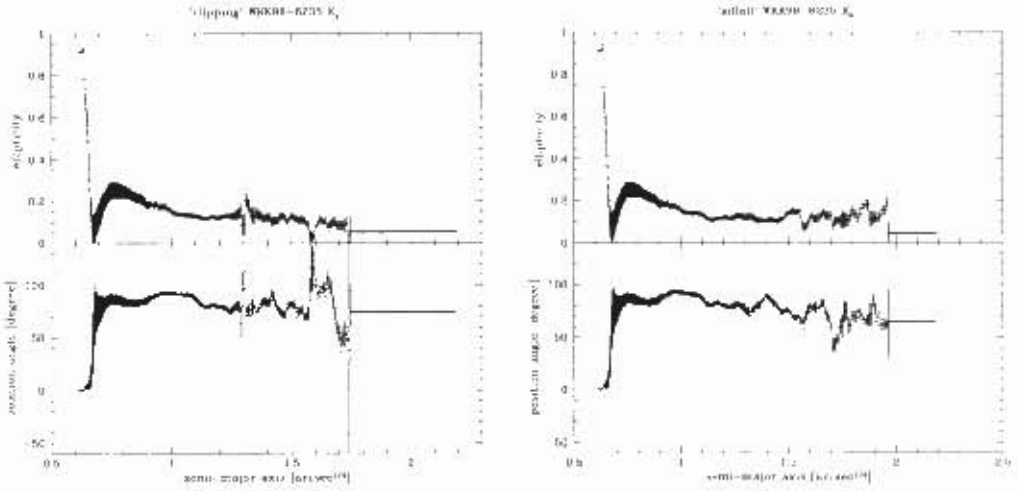

Figure 17.6: Galaxy WKK 6235, ellipticity and position angle plots, K_s band

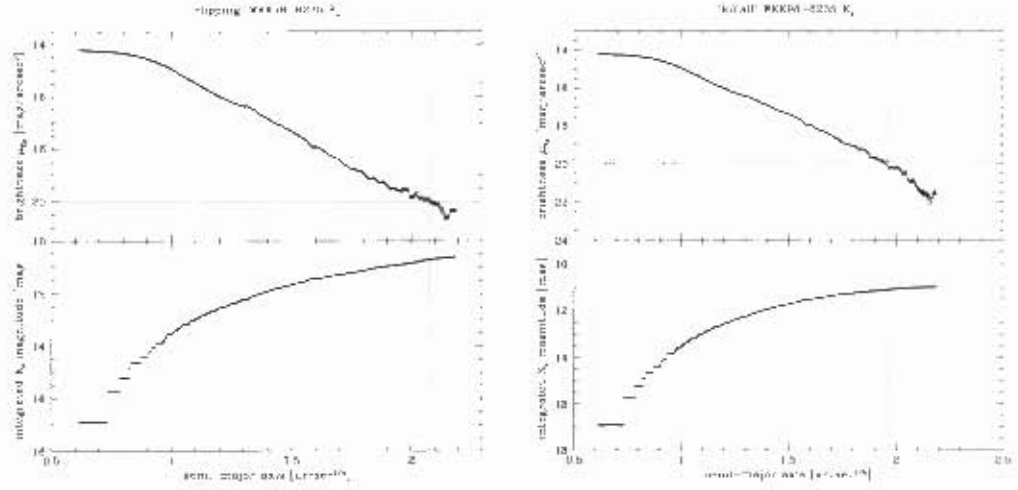

Figure 17.7: Galaxy WKK 6235, isophotal and integrated magnitude plots, K_s band

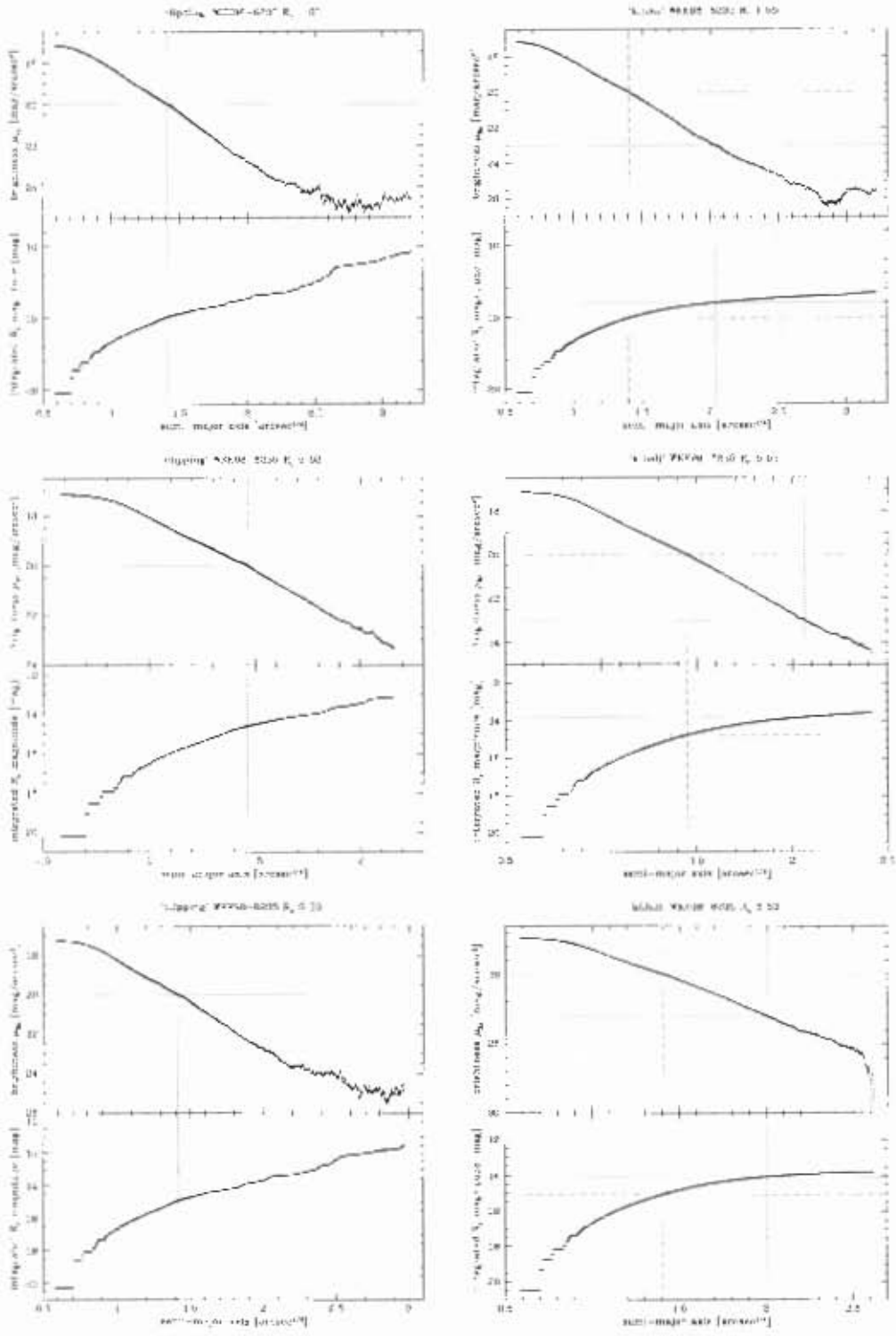

Figure 17.8: Galaxy WKK 6235, isophotal and integrated magnitude plots, R_c band

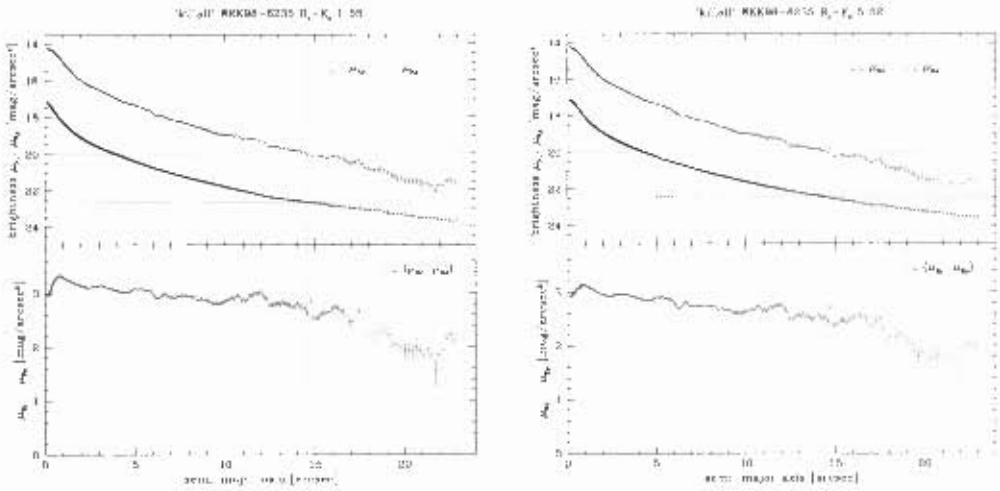

Figure 17.9: Galaxy WKK 6235, $(\mu_{R_c} - \mu_{K_s})$ magnitude plots

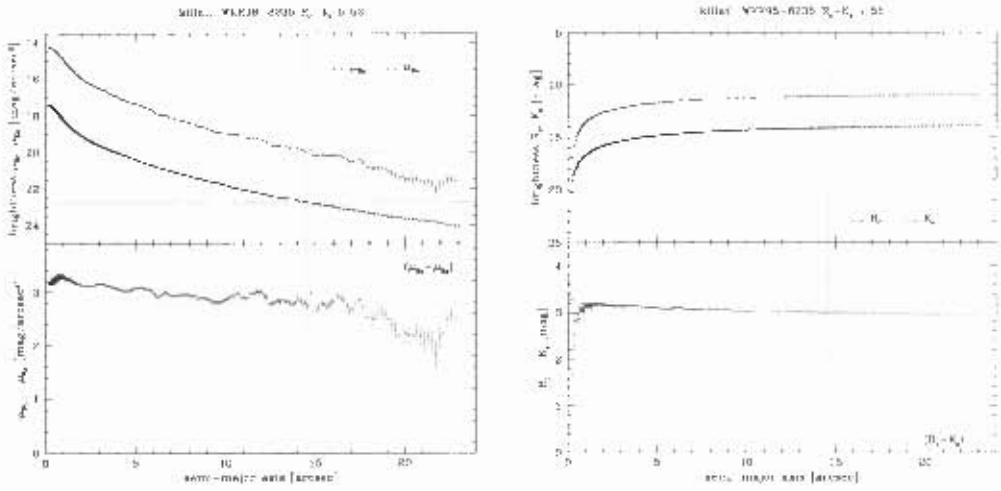

Figure 17.10: Galaxy WKK 6235, $(\mu_{R_c} - \mu_{K_s})$ and $(R_c \quad K_s)$ magnitude plots

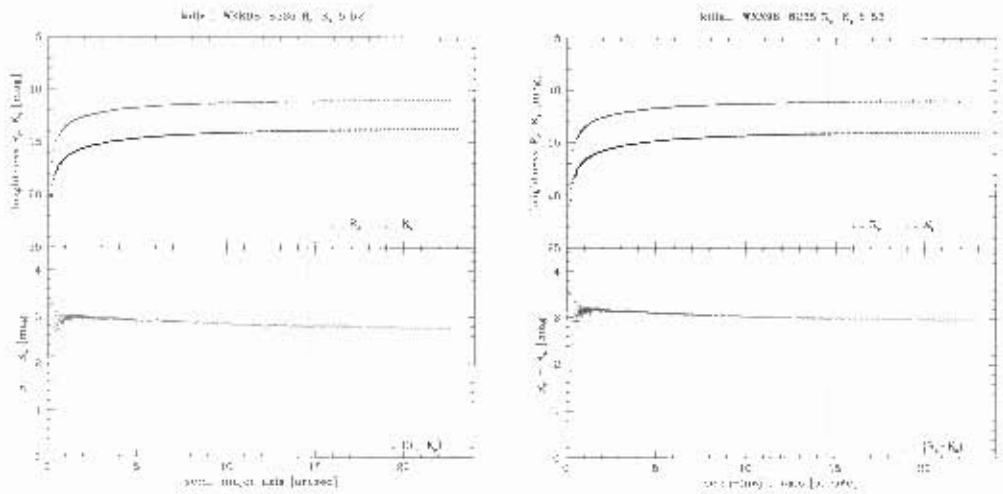

Figure 17.11: Galaxy WKK 6235, (R_c K_s) magnitude plots

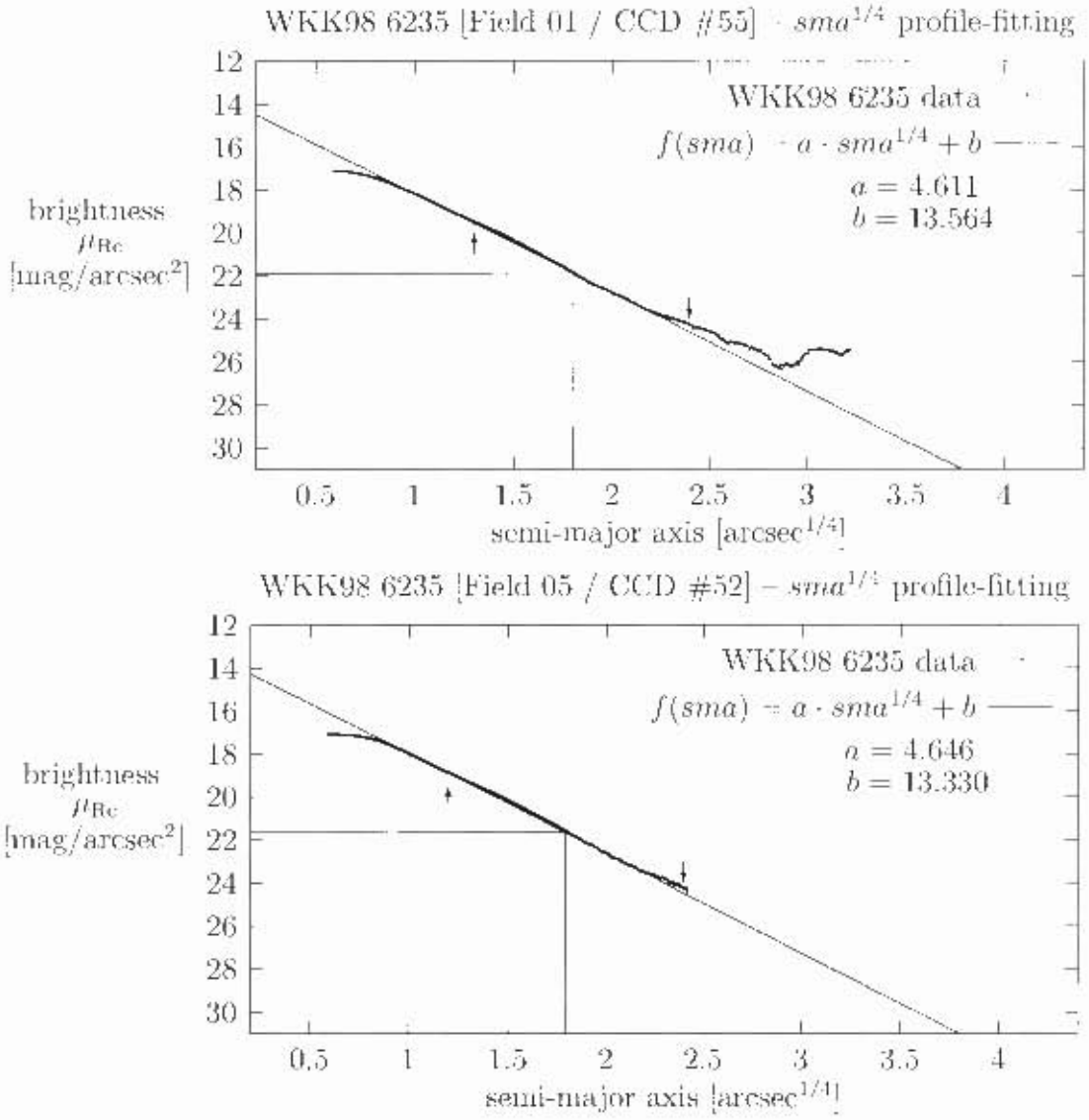

Figure 17.12: Galaxy WKK 6235, plots of brightness μ_{R_c} versus semi-major axis $sma^{1/4}$ to demonstrate the profile-fitting. The arrows point to the upper and lower limit of the data set that was used for the fit. The resulting effective (half-light) radius $r_e^{1/4}$ and effective (half-light) surface brightness μ_e are indicated by straight lines.

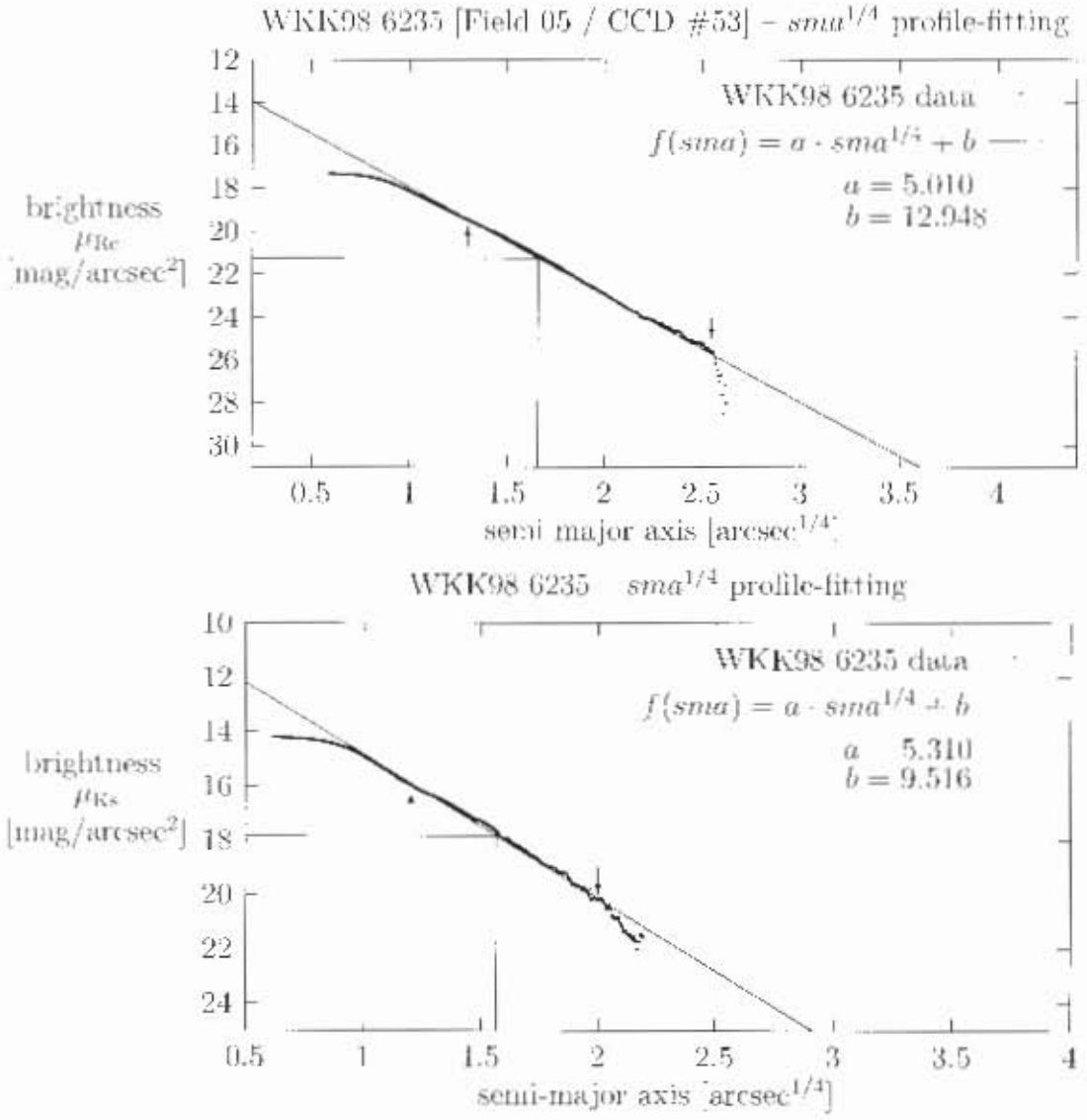

Figure 17.13: Galaxy WKK 6235, plots of brightness (μ_{R_c} and μ_{K_s}) versus semi-major axis $sma^{1/4}$ to demonstrate the profile fitting. The arrows point to the upper and lower limit of the data set that was used for the fit. The resulting effective (half-light) radius $r_e^{1/4}$ and effective (half-light) surface brightness μ_e are indicated by straight lines.

Chapter 18

Galaxy WKK 6242

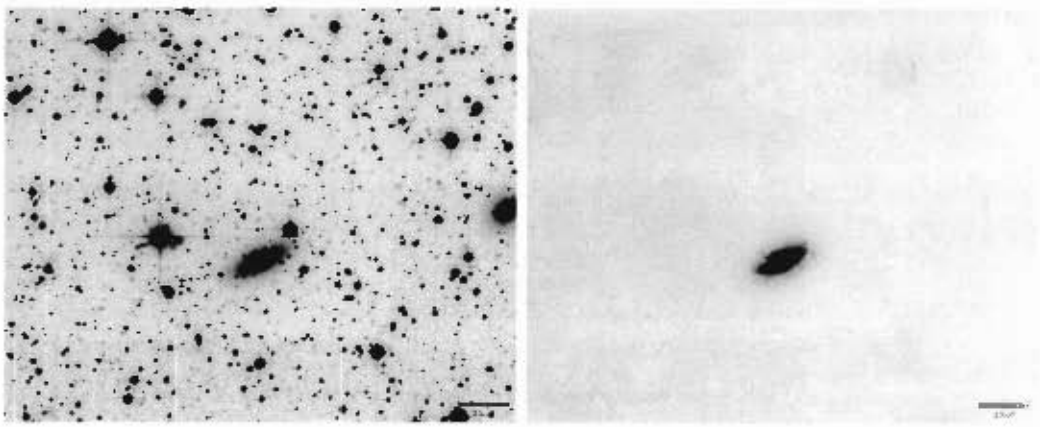

Figure 18.1: Galaxy WKK 6242, R_c band images, field 01, WFI CCD #52

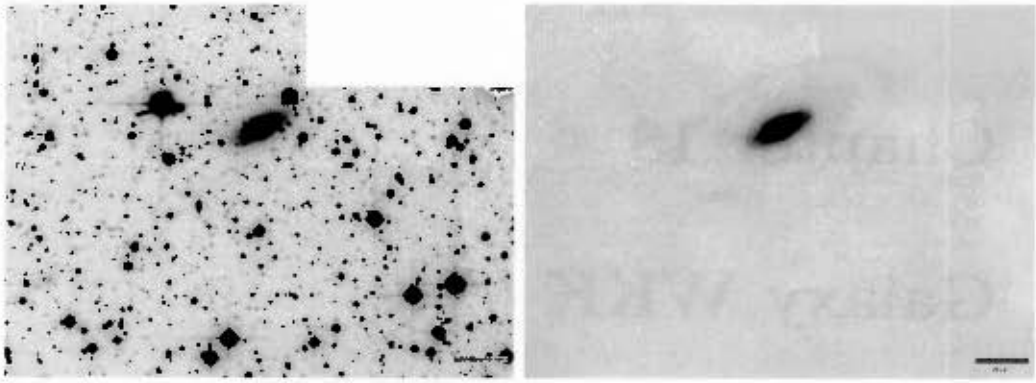

Figure 18.2: Galaxy WKK 6242, R_c band images, field 01, WFI CCD #55

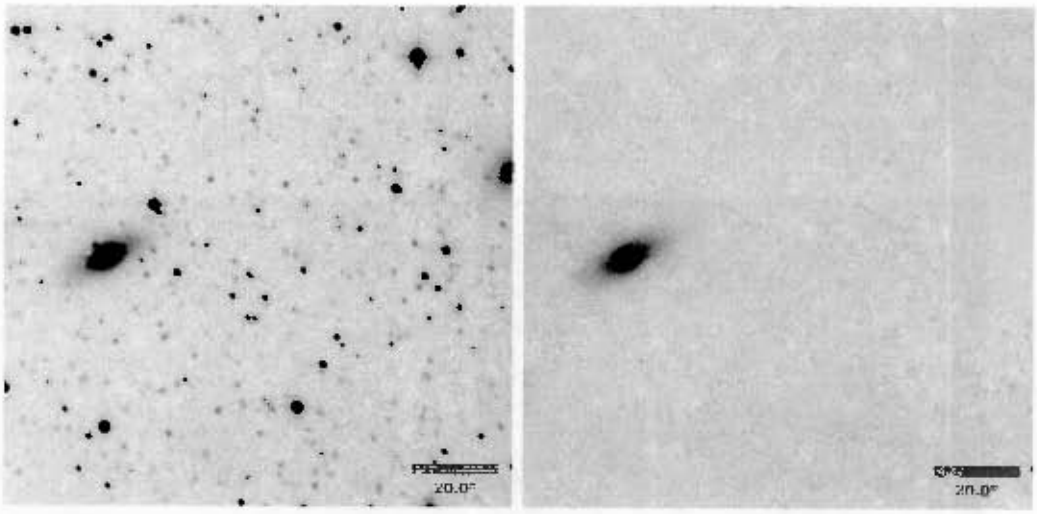

Figure 18.3: Galaxy WKK 6242, K_s band images

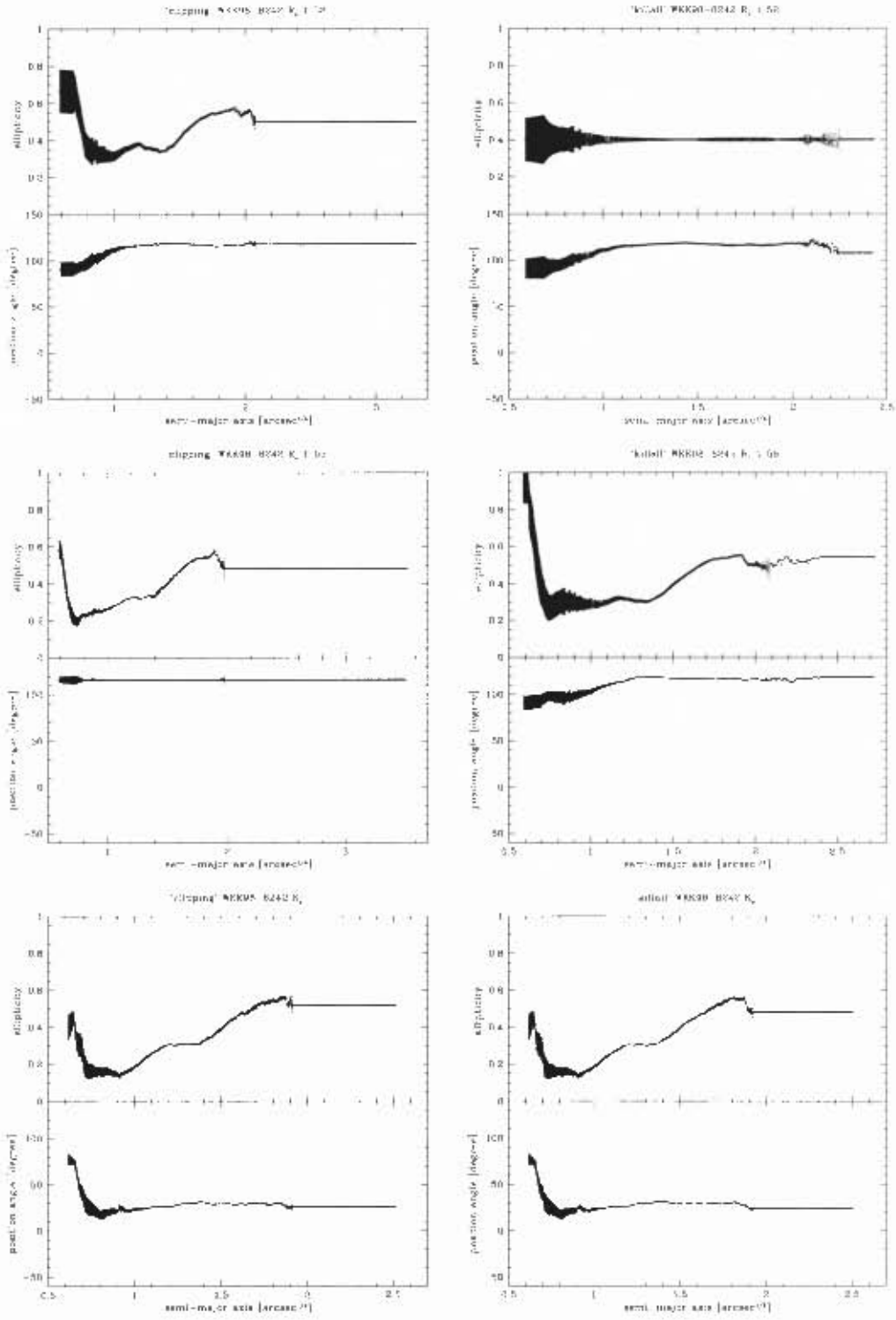

Figure 18.4: Galaxy WKK 6242, ellipticity and position angle plots

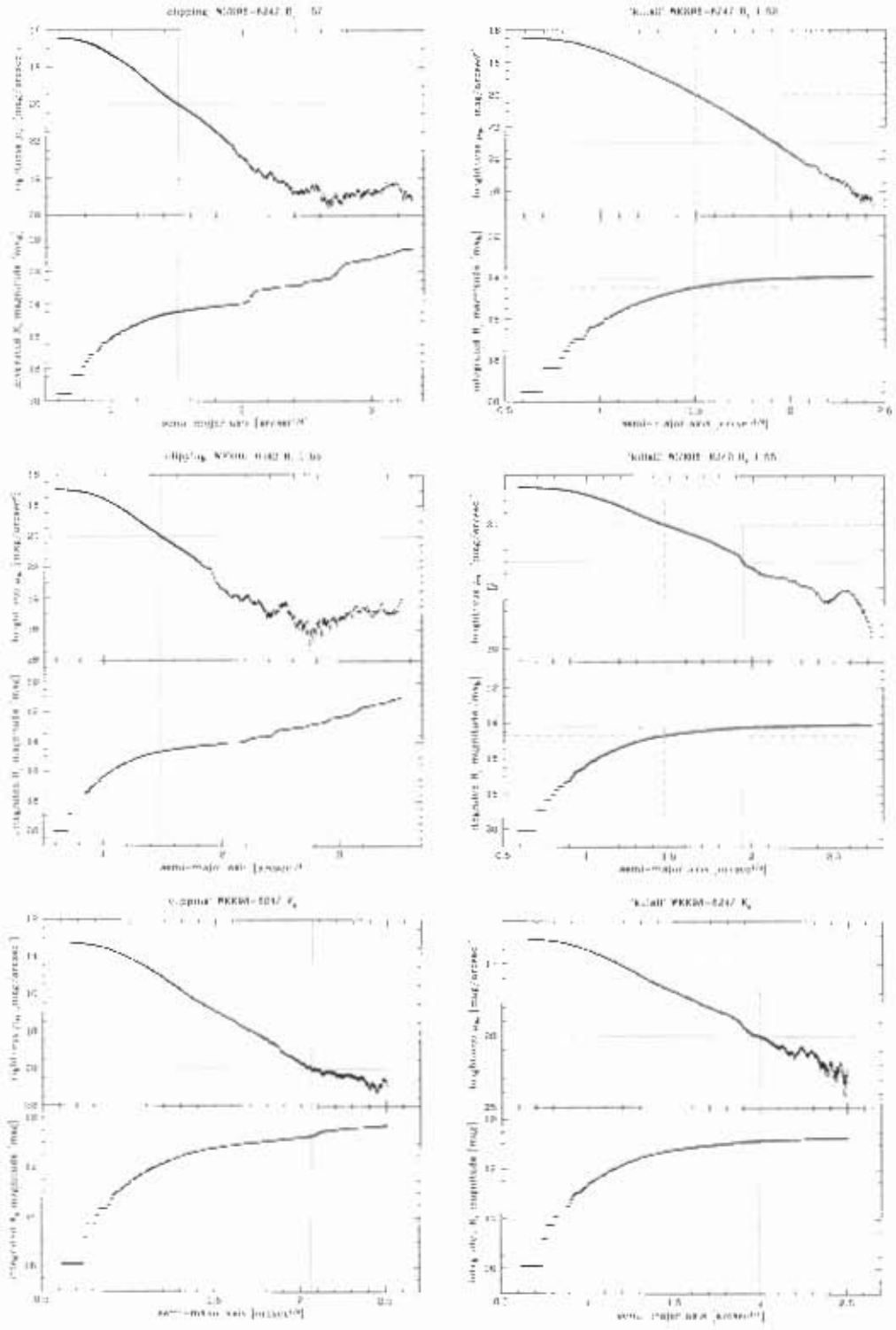

Figure 18.5: Galaxy WKK 6242, isophotal and integrated magnitude plots

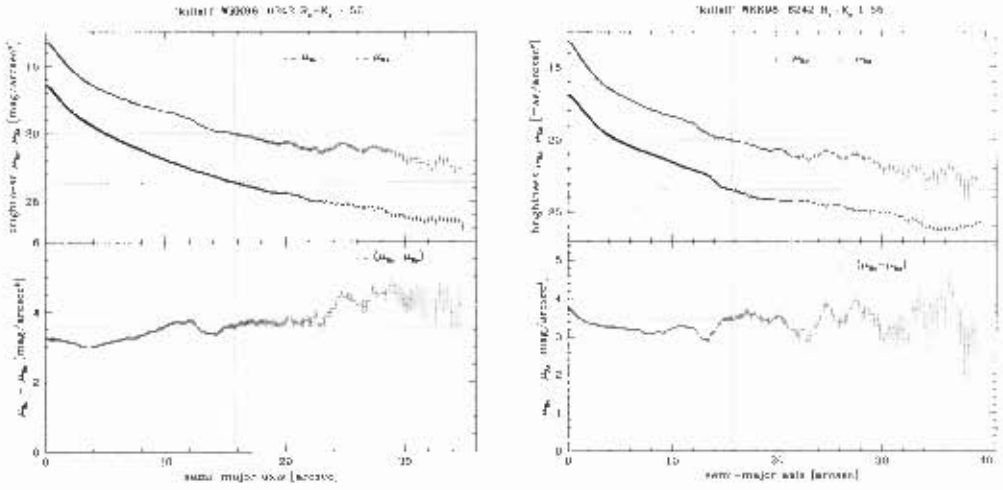

Figure 18.6: Galaxy WKK 6242, ($\mu_{R_c} - \mu_{K_s}$) magnitude plots

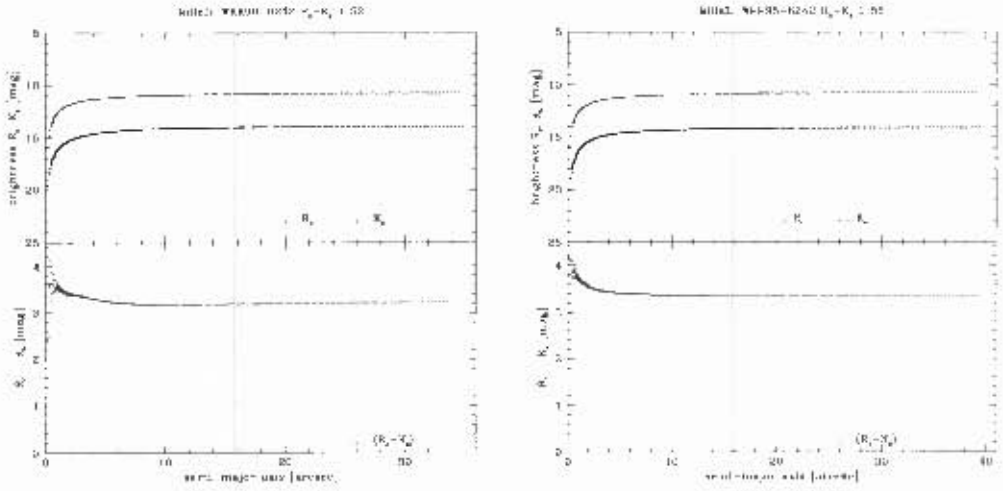

Figure 18.7: Galaxy WKK 6242, (R_c K_s) magnitude plots

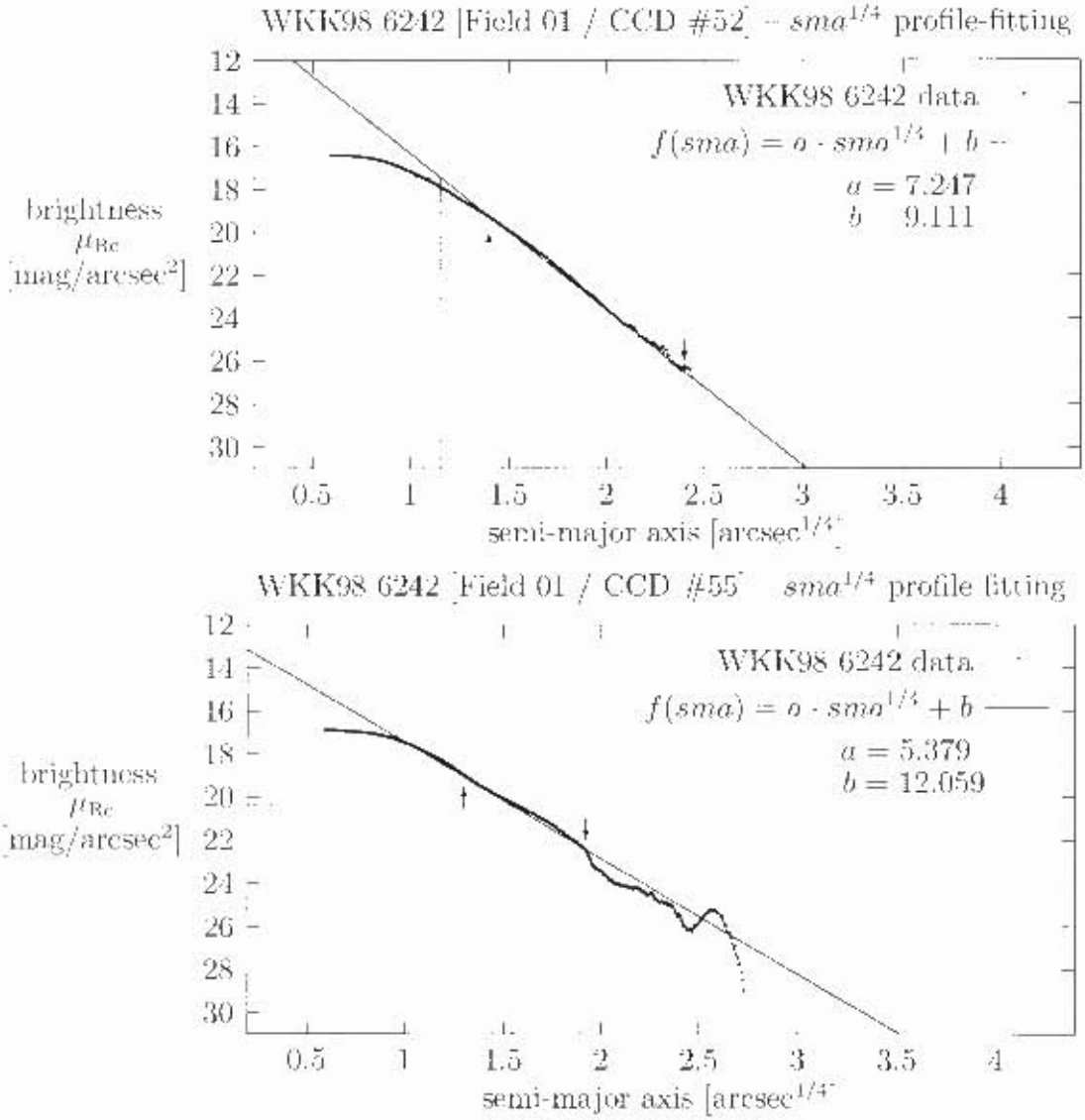

Figure 18.8: Galaxy WKK 6242, plots of brightness μ_{R_c} versus semi-major axis $sma^{1/4}$ to demonstrate the profile-fitting. The arrows point to the upper and lower limit of the data set that was used for the fit. The resulting effective (half light) radius $r_e^{1/4}$ and effective (half-light) surface brightness μ_e are indicated by straight lines.

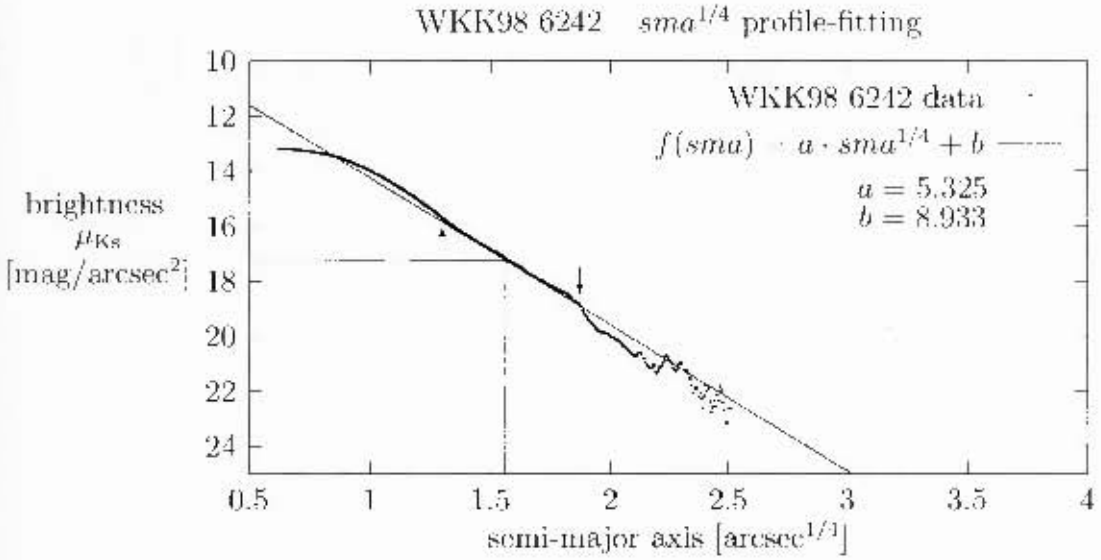

Figure 18.9: Galaxy WKK 6242, plot of brightness μ_{K_s} versus semi-major axis $sma^{1/4}$ to demonstrate the profile-fitting. The arrows point to the upper and lower limit of the data set that was used for the fit. The resulting effective (half-light) radius $r_e^{1/4}$ and effective (half-light) surface brightness μ_e are indicated by straight lines.

Chapter 19

Galaxy WKK 6250

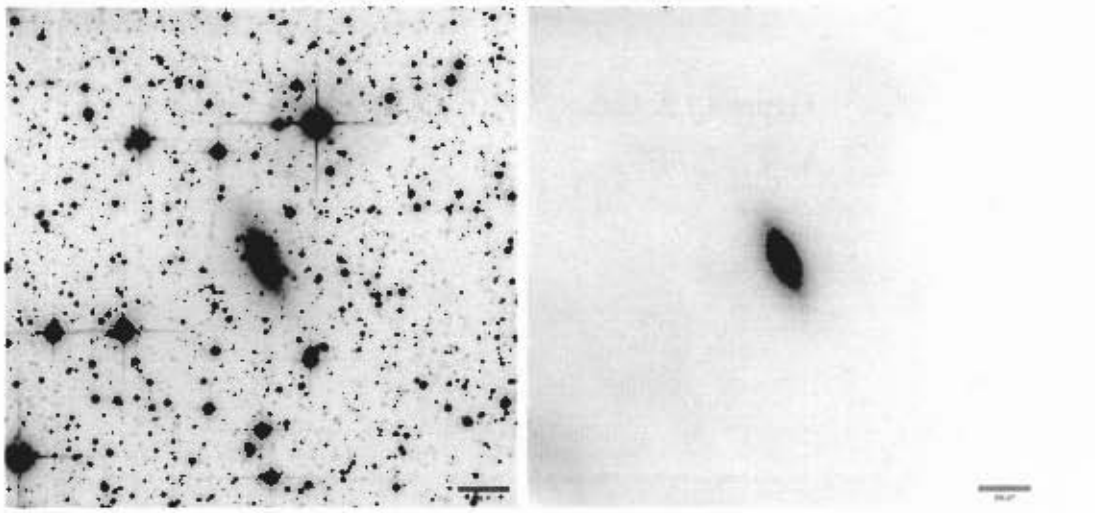

Figure 19.1: Galaxy WKK 6250, R_c band images, field 01, WF1 CCD #55

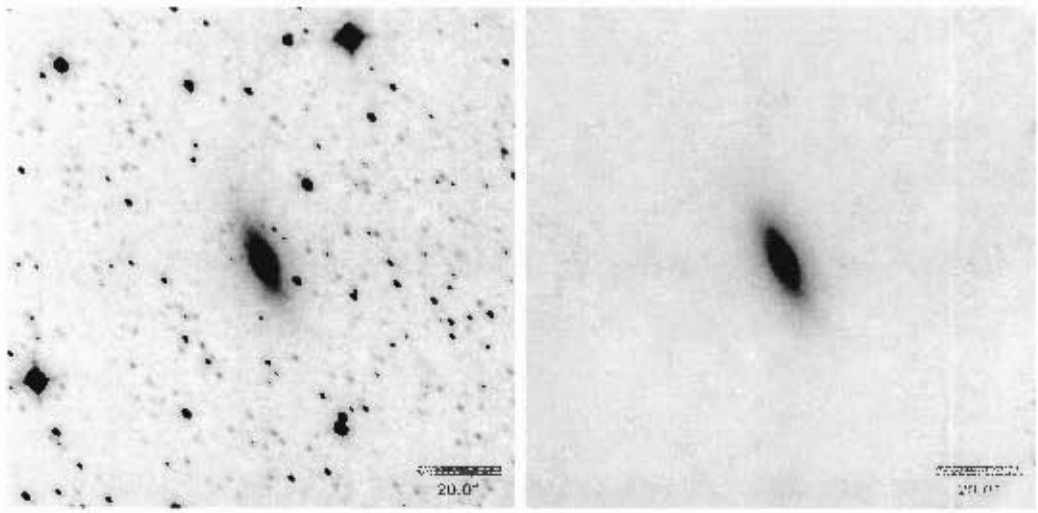

Figure 19.2: Galaxy WKK 6250, K_s band images

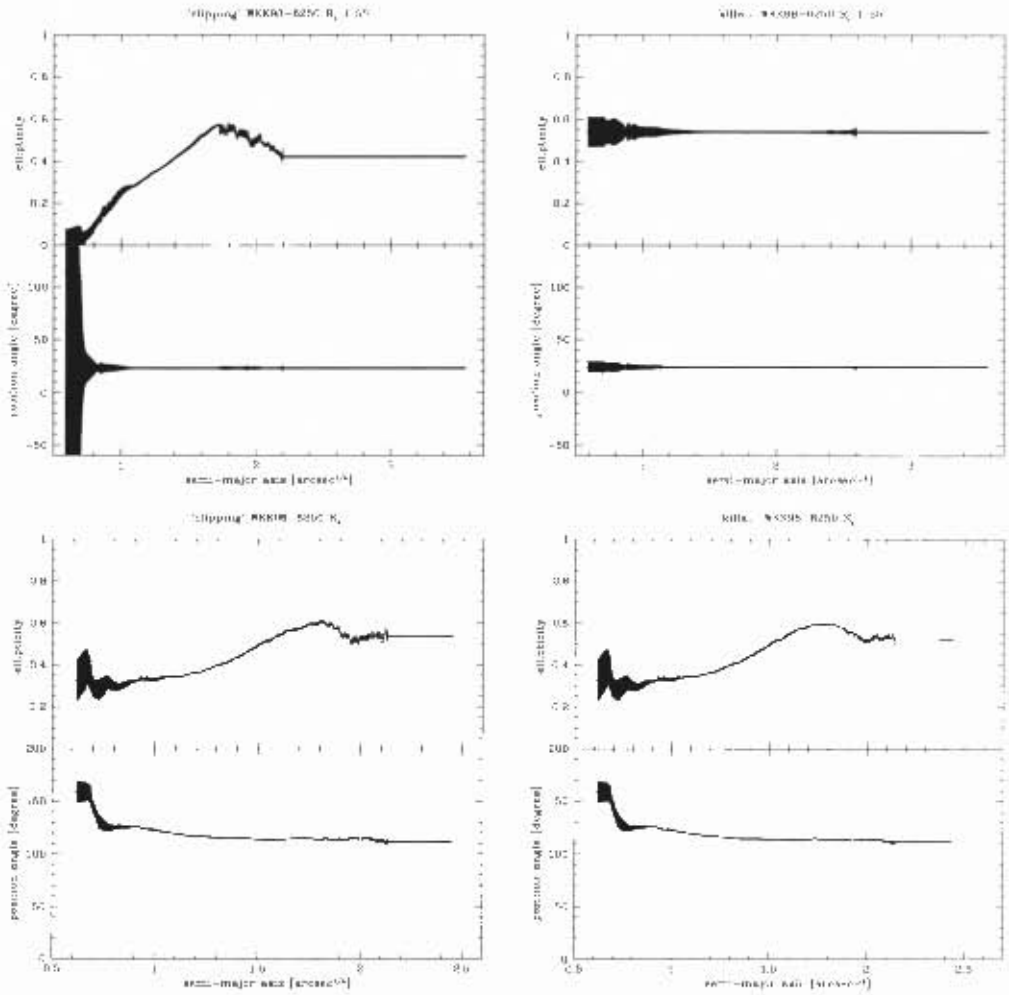

Figure 19.3: Galaxy WKK 6250, ellipticity and position angle plots

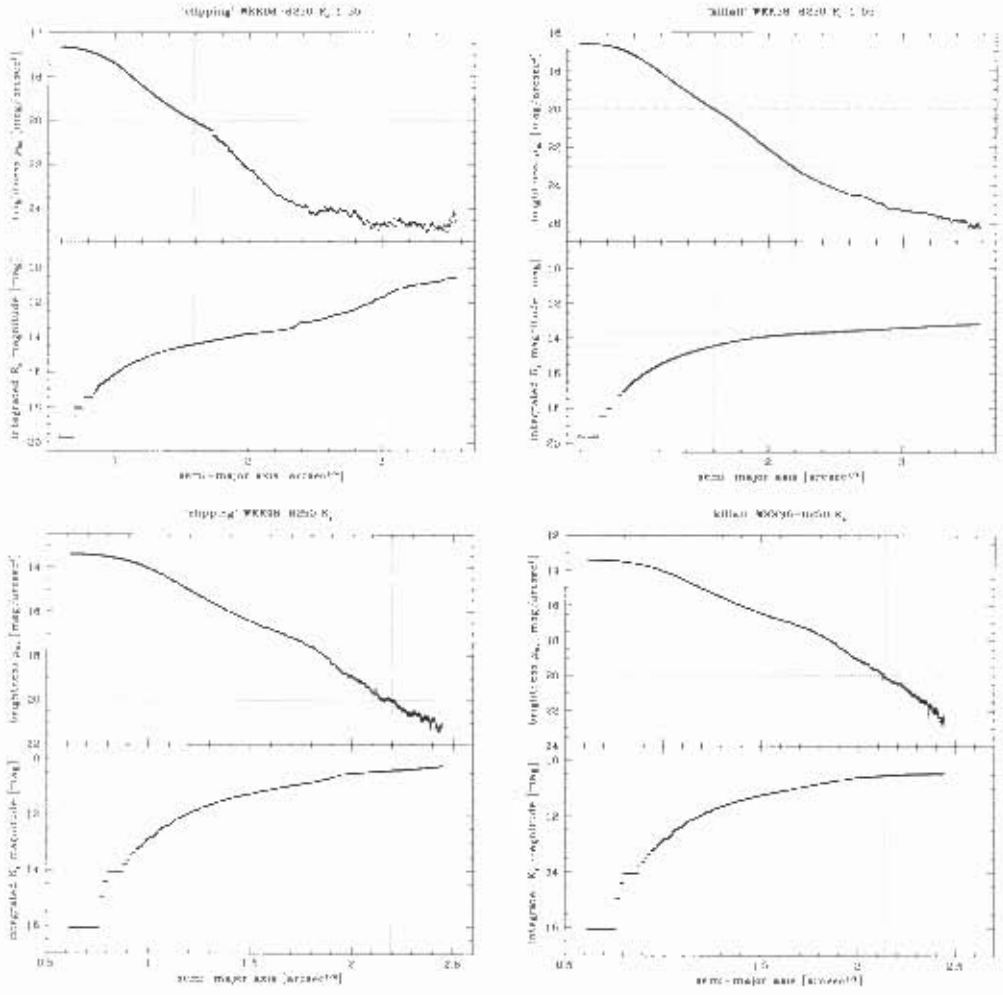

Figure 19.4: Galaxy WKK 6250, isophotal and integrated magnitude plots

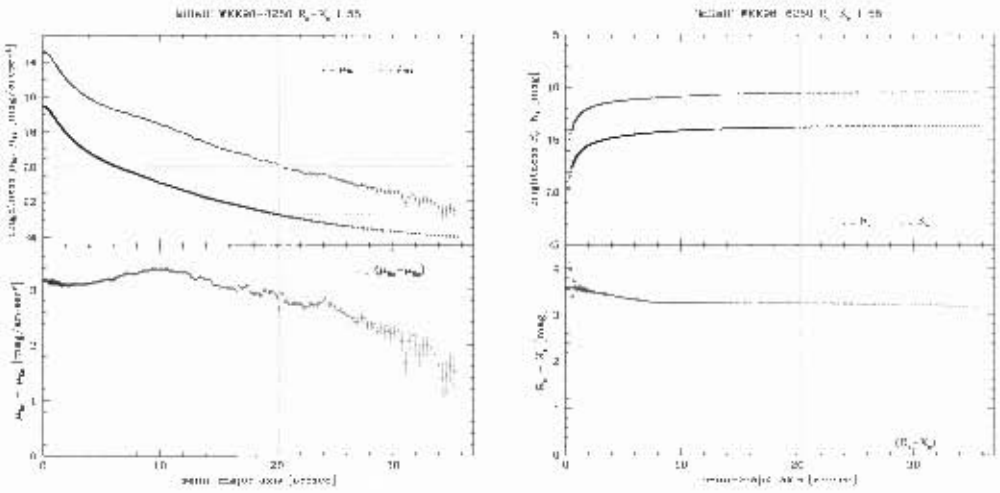

Figure 19.5: Galaxy WKK 6250. (μ_{R_c} - μ_{K_s}) and (R_c K_s) magnitude plots

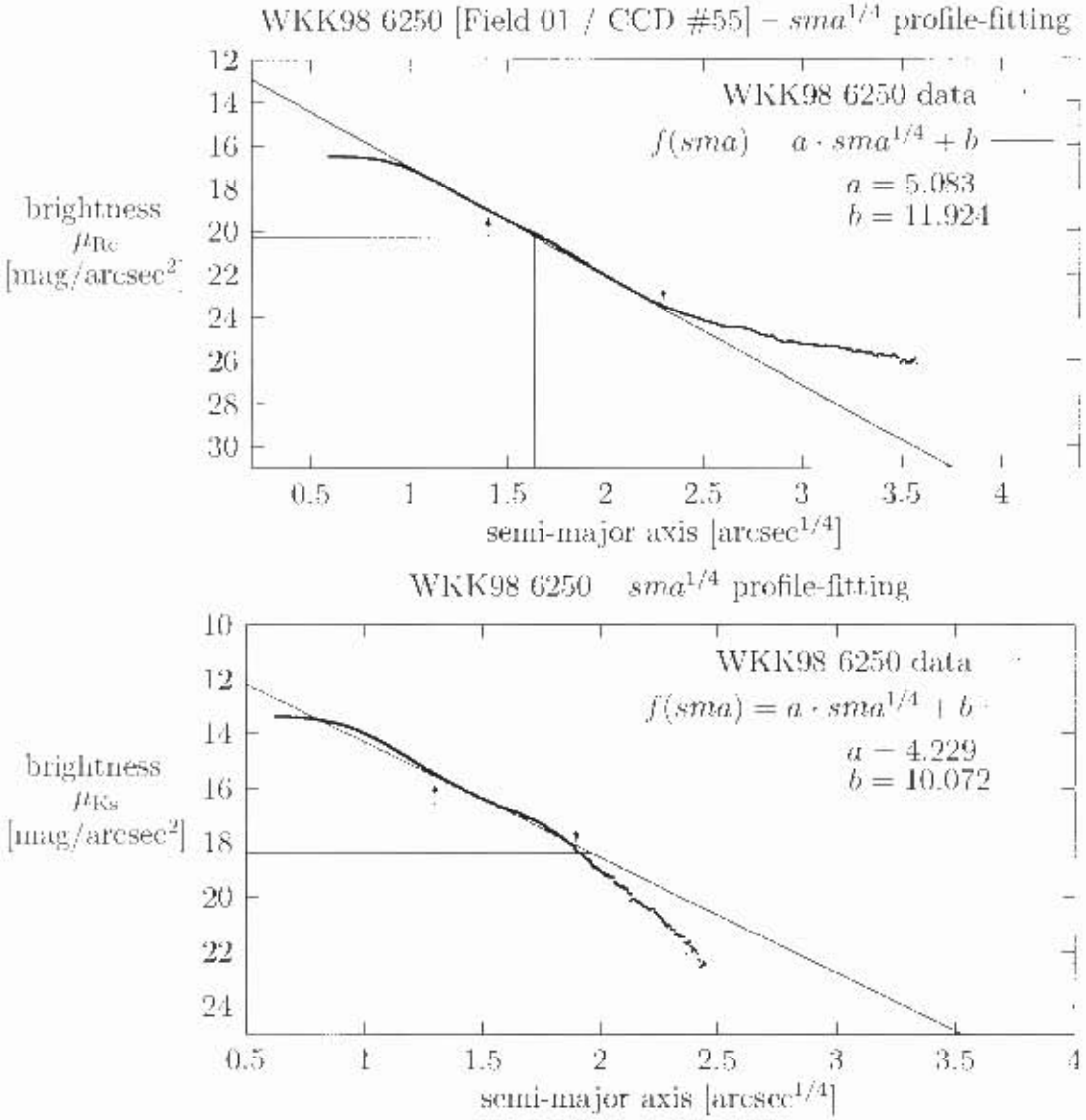

Figure 19.6: Galaxy WKK 6250, plots of brightness (μ_{R_c} and μ_{K_s}) versus semi-major axis sma$^{1/4}$ to demonstrate the profile-fitting. The arrows point to the upper and lower limit of the data set that was used for the fit. The resulting effective (half-light) radius $r_e^{1/4}$ and effective (half light) surface brightness μ_e are indicated by straight lines.

Chapter 20

Galaxy WKK 6269

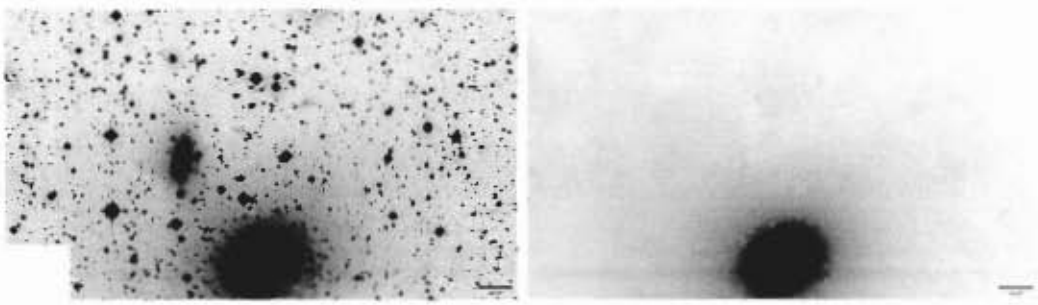

Figure 20.1: Galaxy WKK 6269, R_c band images, field 01, WFI CCD #52

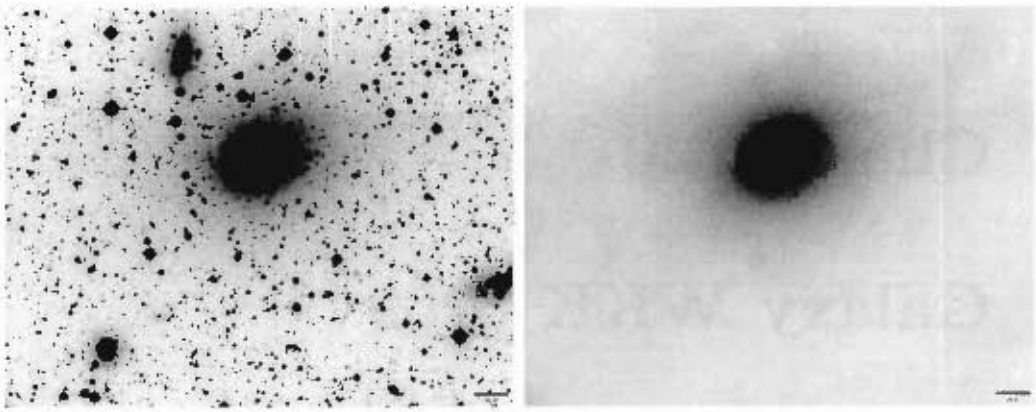

Figure 20.2: Galaxy WKK 6269, R_c band images, field 01, WFI CCD #55

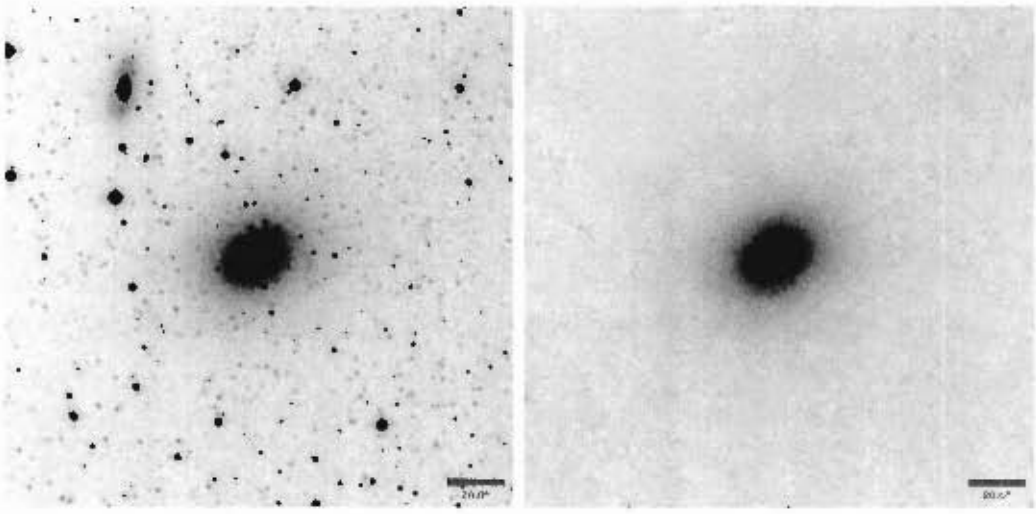

Figure 20.3: Galaxy WKK 6269, K_s band images

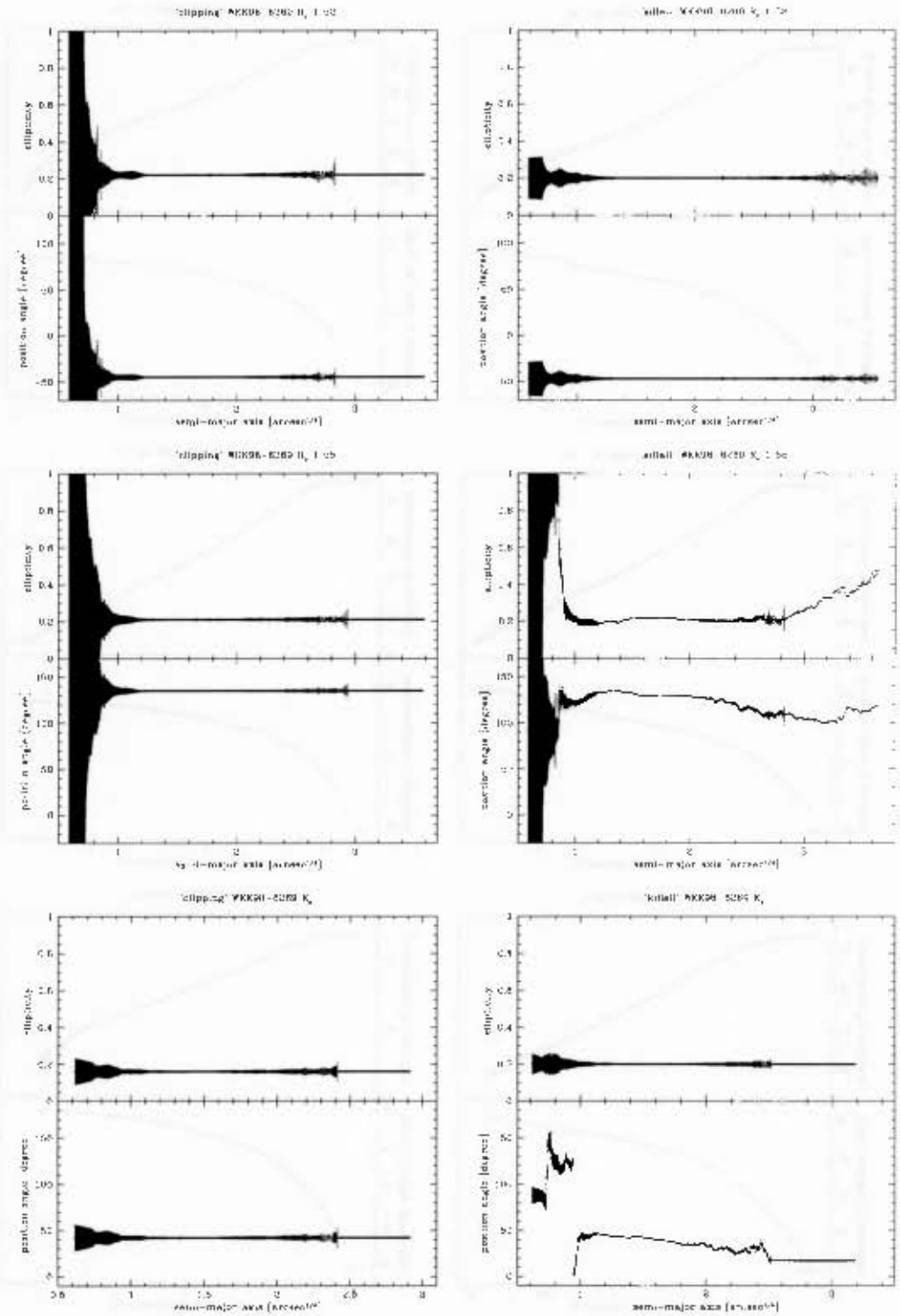

Figure 20.4: Galaxy WKK 6269, ellipticity and position angle plots

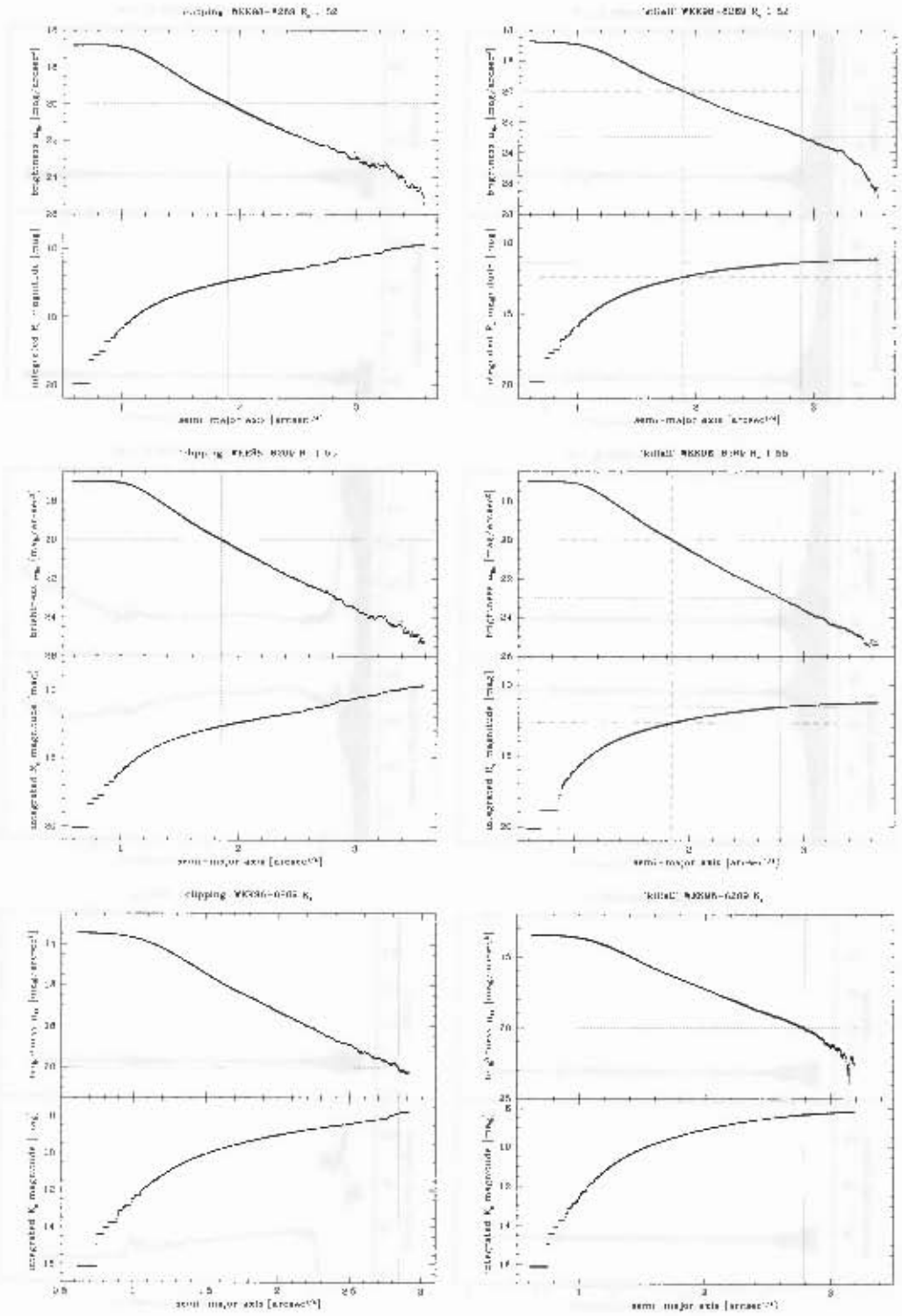

Figure 20.5: Galaxy WKK 6269, isophotal and integrated magnitude plots

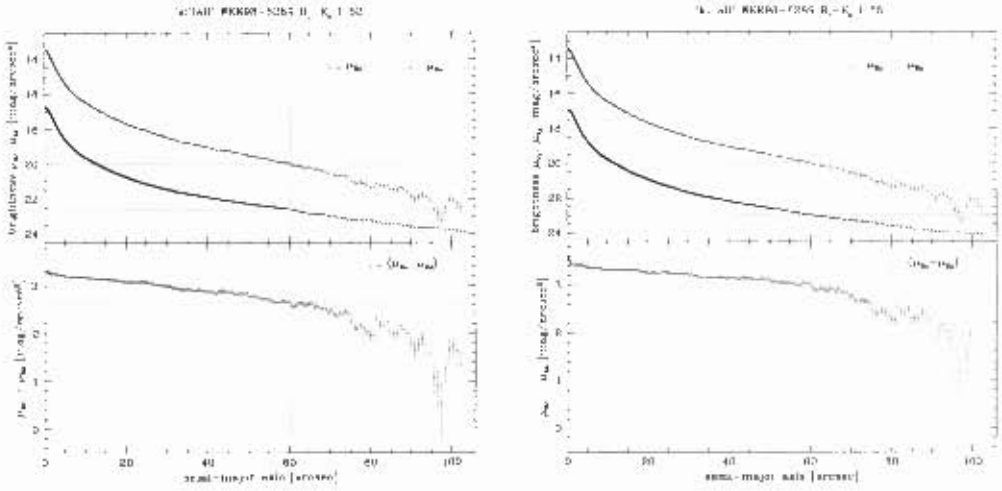

Figure 20.6: Galaxy WKK 6269, $(\mu_{R_c} - \mu_{K_s})$ magnitude plots

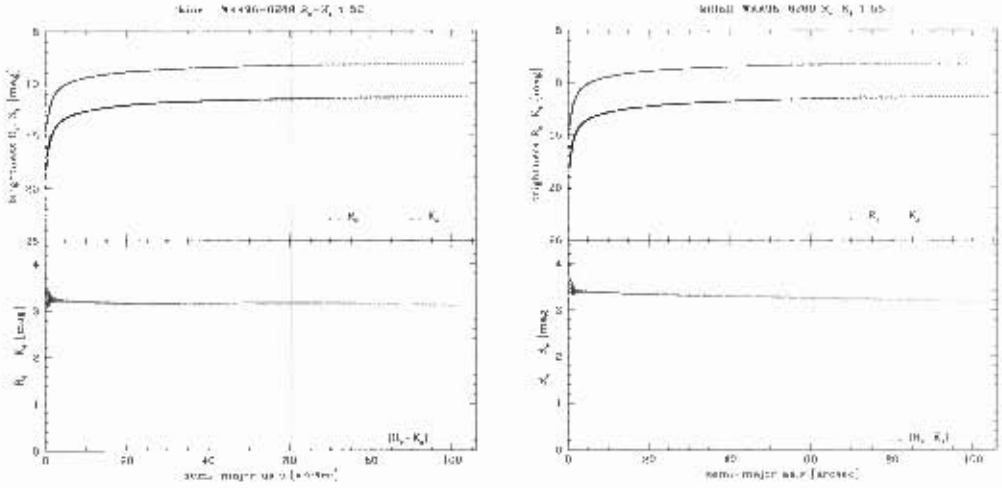

Figure 20.7: Galaxy WKK 6269, $(R_c - K_s)$ magnitude plots

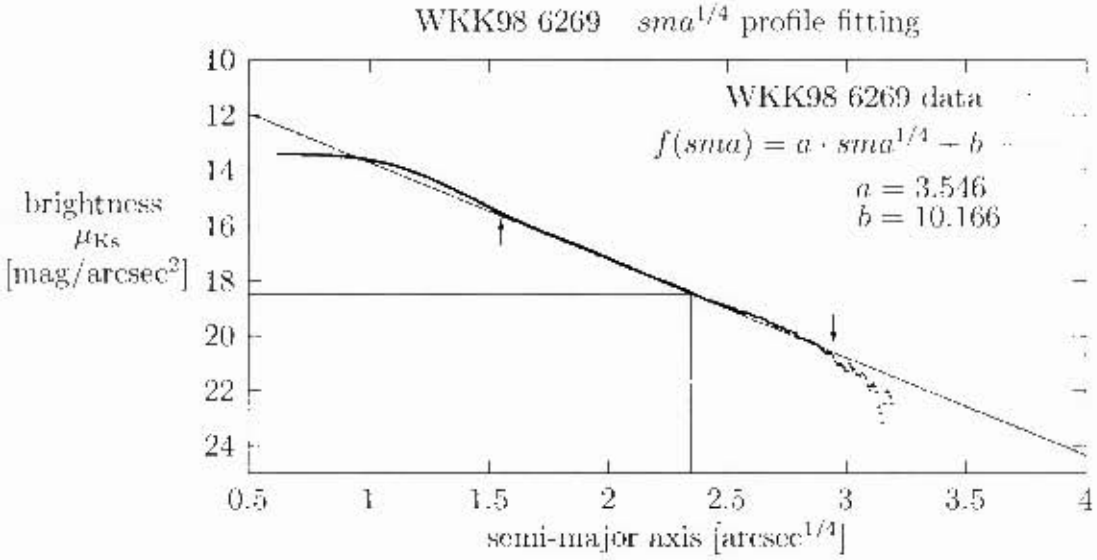

Figure 20.9: Galaxy WKK 6269, plot of brightness μ_{K_s} versus semi-major axis $\mathrm{sma}^{1/4}$ to demonstrate the profile-fitting. The arrows point to the upper and lower limit of the data set that was used for the fit. The resulting effective (half-light) radius $r_e^{1/4}$ and effective (half-light) surface brightness μ_e are indicated by straight lines.

Chapter 21

Galaxy WKK 6282

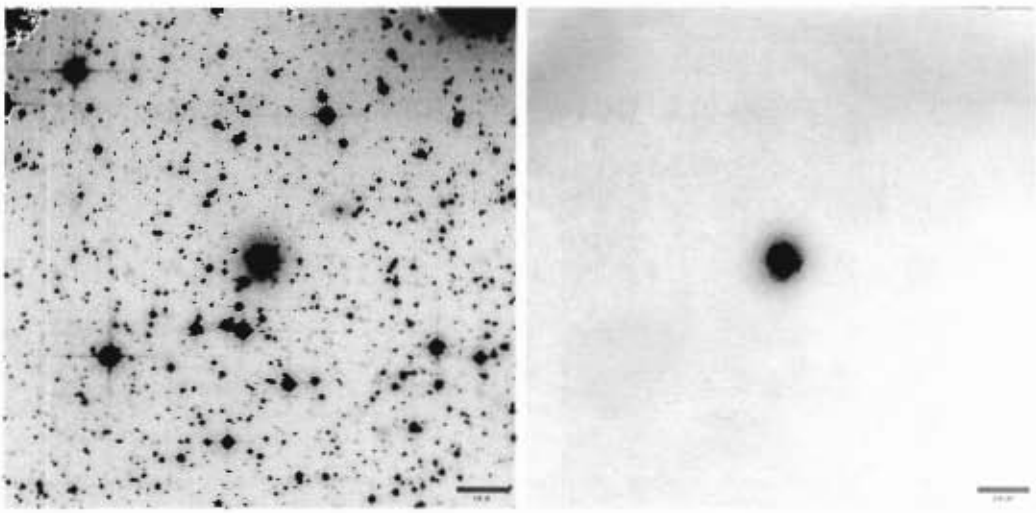

Figure 21.1: Galaxy WKK 6282, R_c band images, field 01, WFI CCD #55

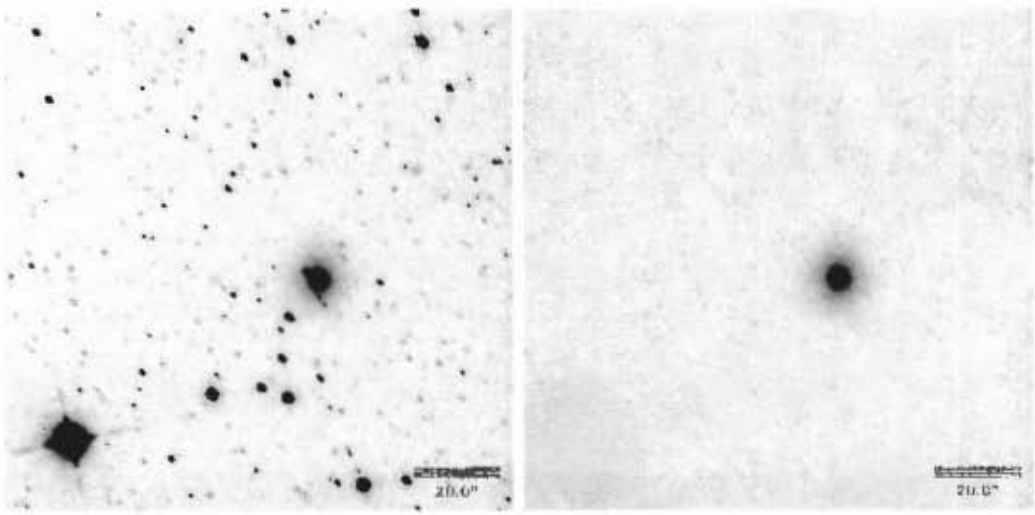

Figure 21.2: Galaxy WKK 6282, K_s band images

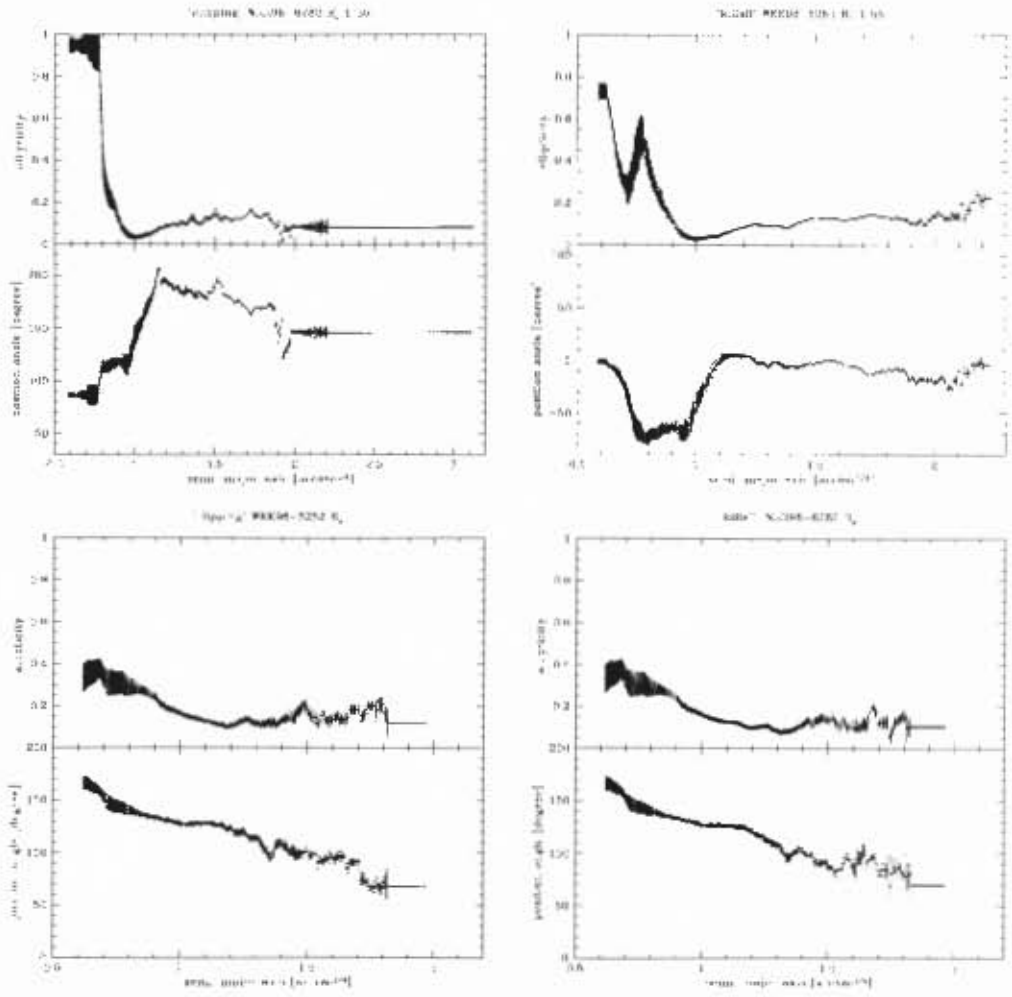

Figure 21.3: Galaxy WKK 6282, ellipticity and position angle plots

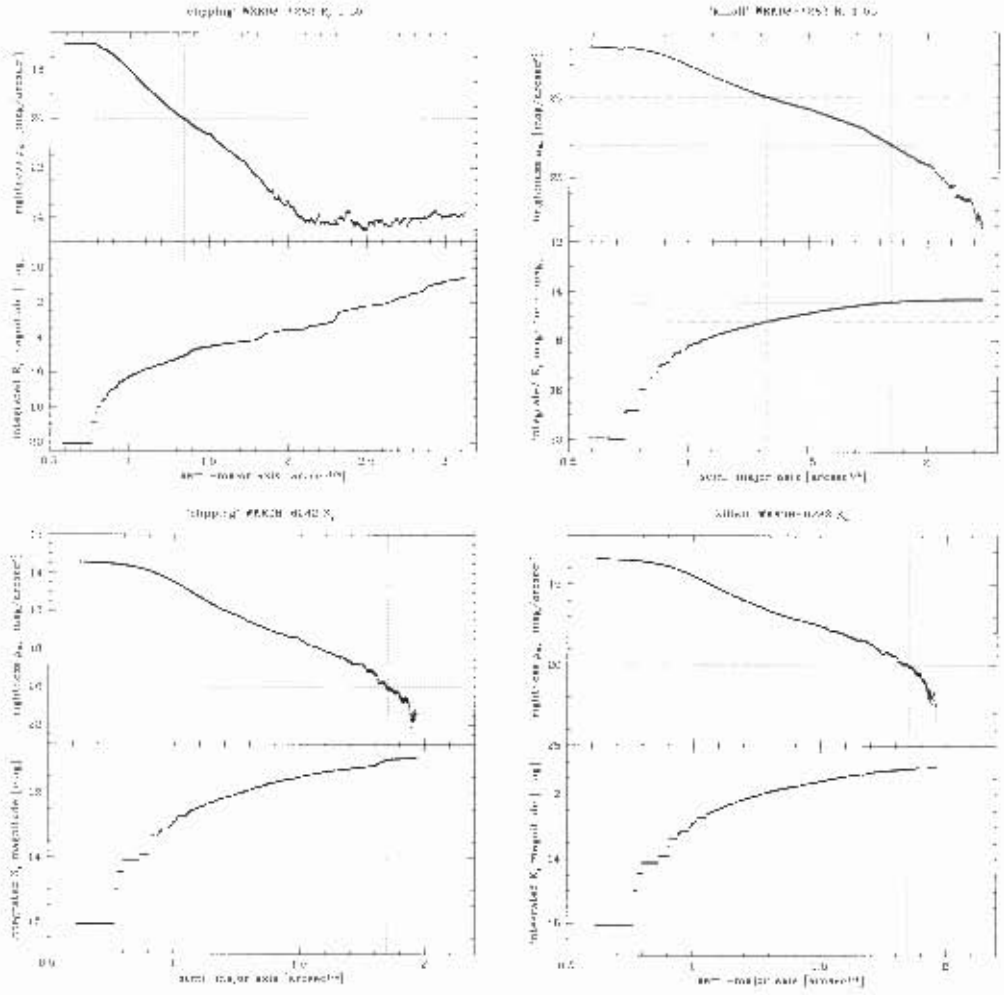

Figure 21.4: Galaxy WKK 6282, isophotal and integrated magnitude plots

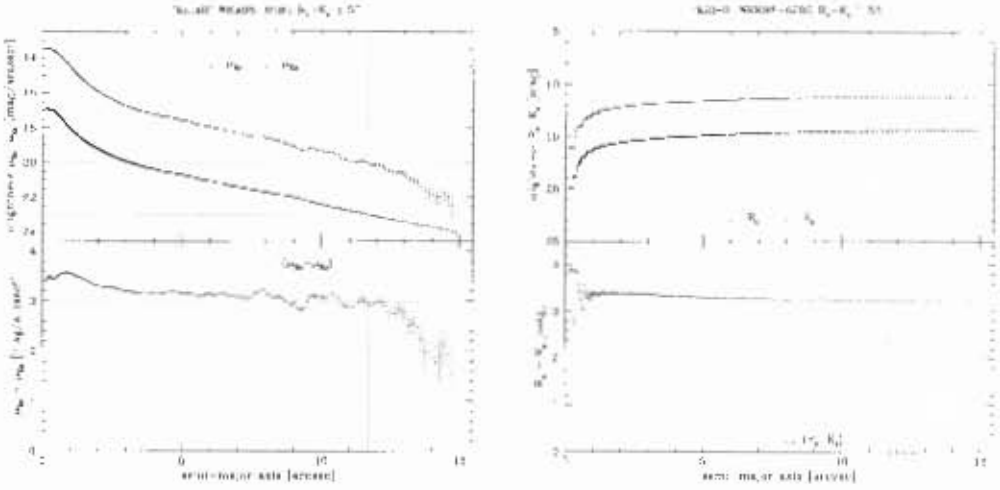

Figure 21.5: Galaxy WKK 6282, (μ_{R_c} μ_{K_s}) and ($R_c - K_s$) magnitude plots

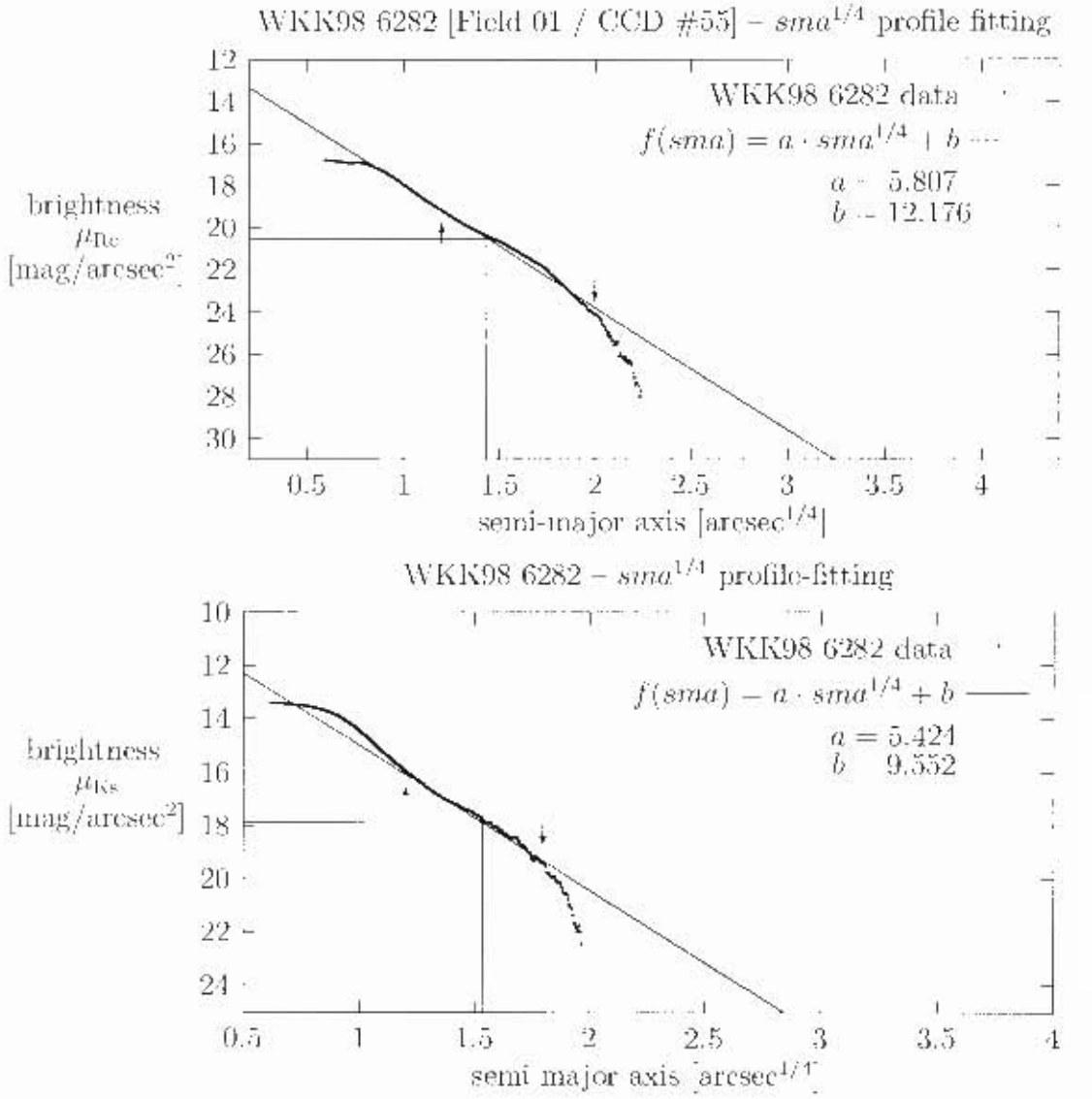

Figure 21.6: Galaxy WKK 6282, plots of brightness (μ_{R_c} and $\mu_{I_{KC}}$) versus semi-major axis sma$^{1/4}$ to demonstrate the profile-fitting. The arrows point to the upper and lower limit of the data set that was used for the fit. The resulting effective (half light) radius $r_e^{1/4}$ and effective (half-light) surface brightness μ_e are indicated by straight lines.

Chapter 22

Galaxy WKK 6318

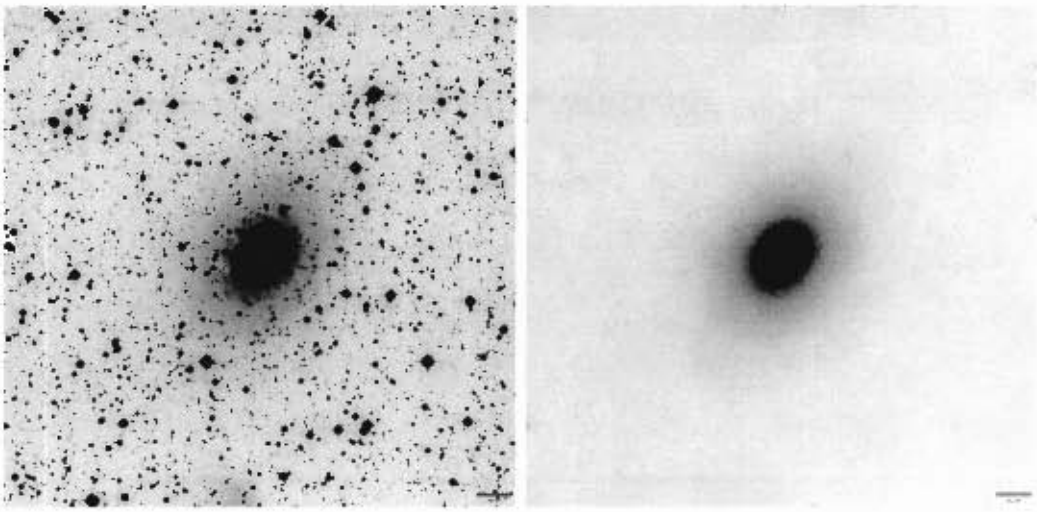

Figure 22.1: Galaxy WKK 6318, R_c band images, field 01, WFI CCD #51

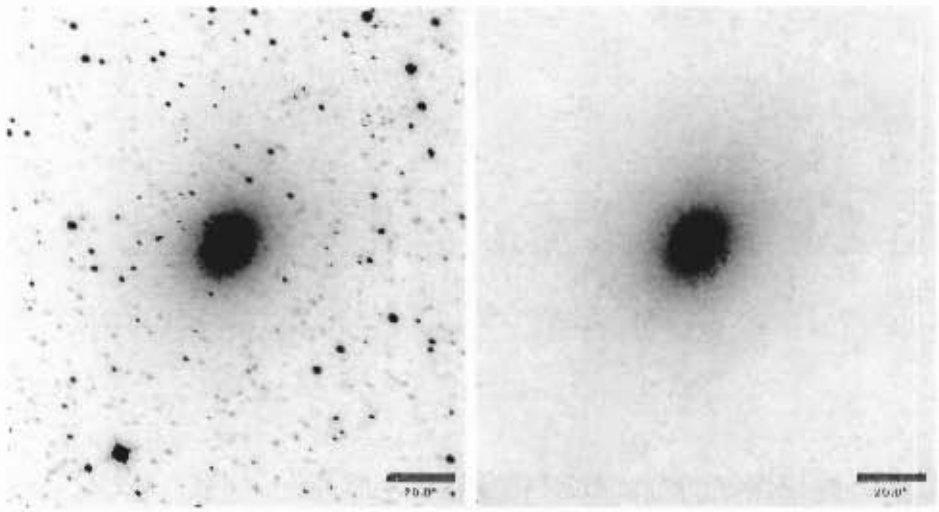

Figure 22.2: Galaxy WKK 6318, K_s band images

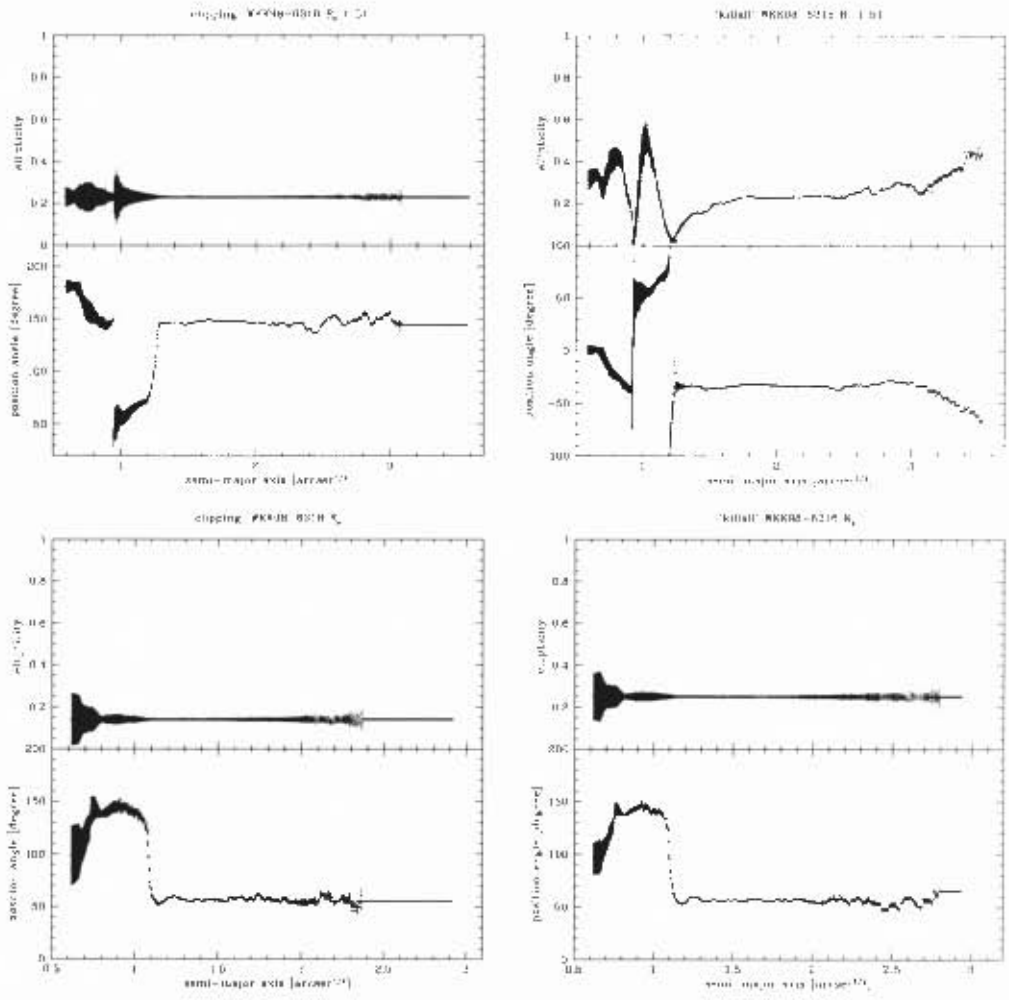

Figure 22.3: Galaxy WKK 6318, ellipticity and position angle plots

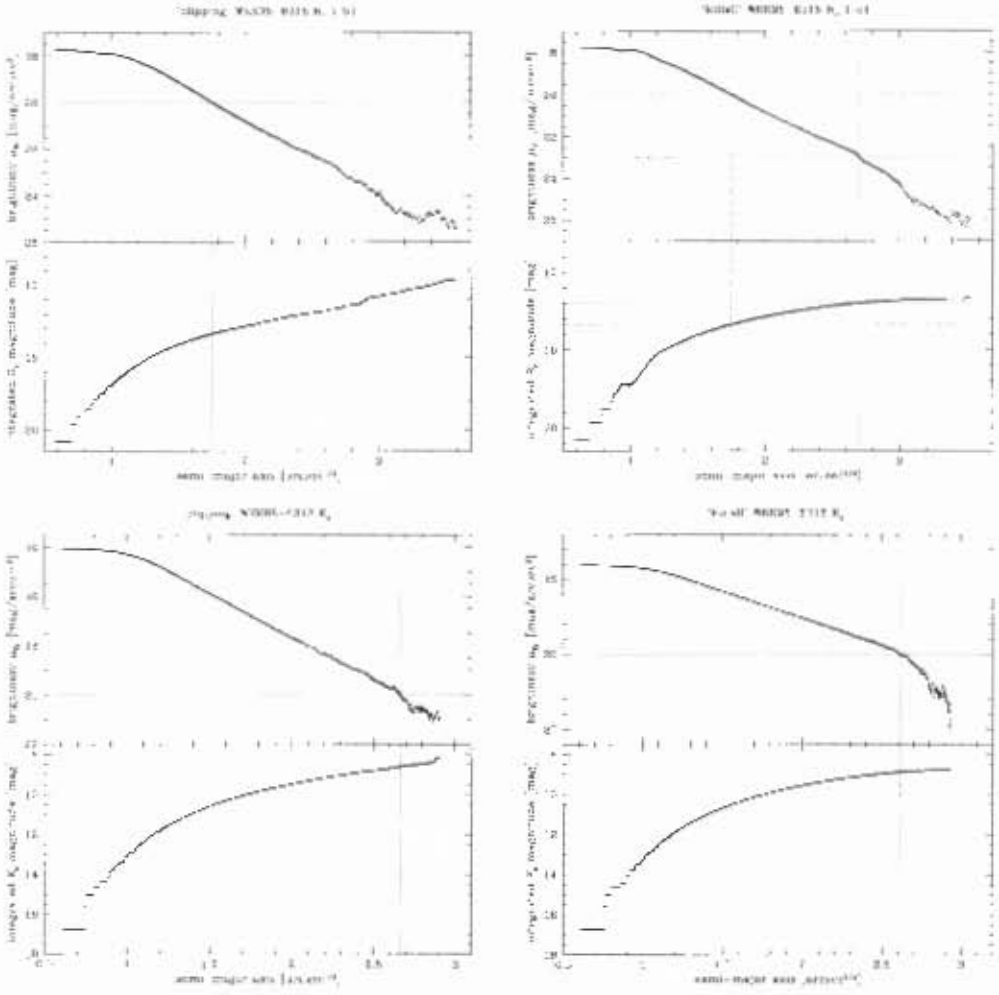

Figure 22.4: Galaxy WKK 6318, isophotal and integrated magnitude plots

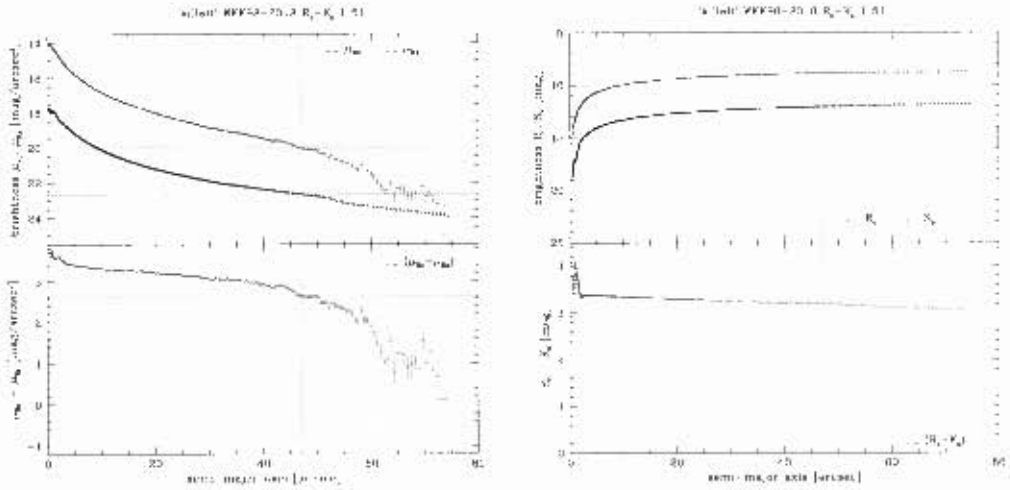

Figure 22.5: Galaxy WKK 6318, $(\mu_{R_c} - \mu_{K_s})$ and $(R_c - K_s)$ magnitude plots

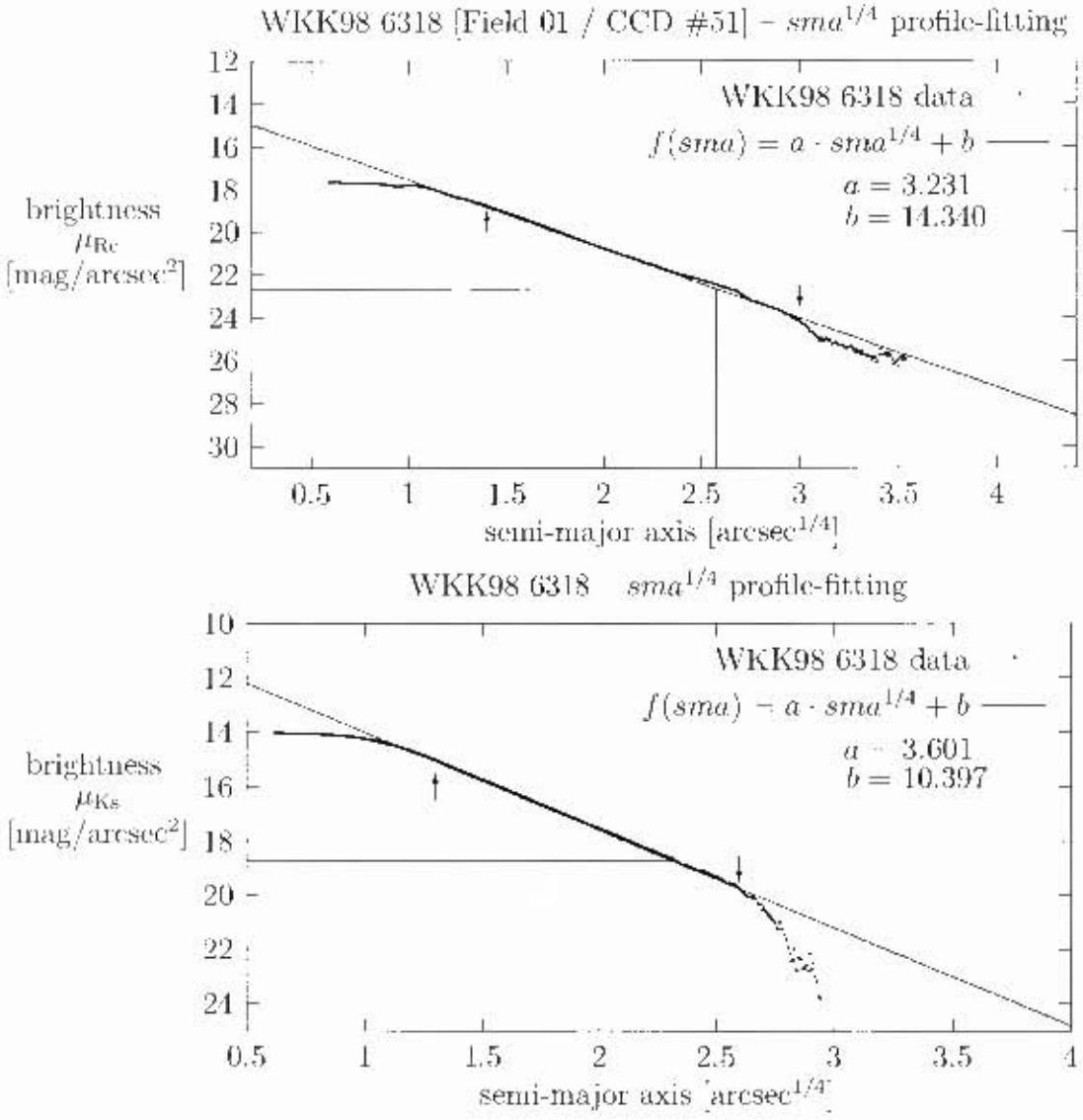

Figure 22.6: Galaxy WKK 6318, plots of brightness (μ_{R_c} and μ_{K_s}) versus semi-major axis sma$^{1/4}$ to demonstrate the profile-fitting. The arrows point to the upper and lower limit of the data set that was used for the fit. The resulting effective (half-light) radius $r_e^{1/4}$ and effective (half-light) surface brightness μ_e are indicated by straight lines.

Chapter 23

Galaxy WKK 6342

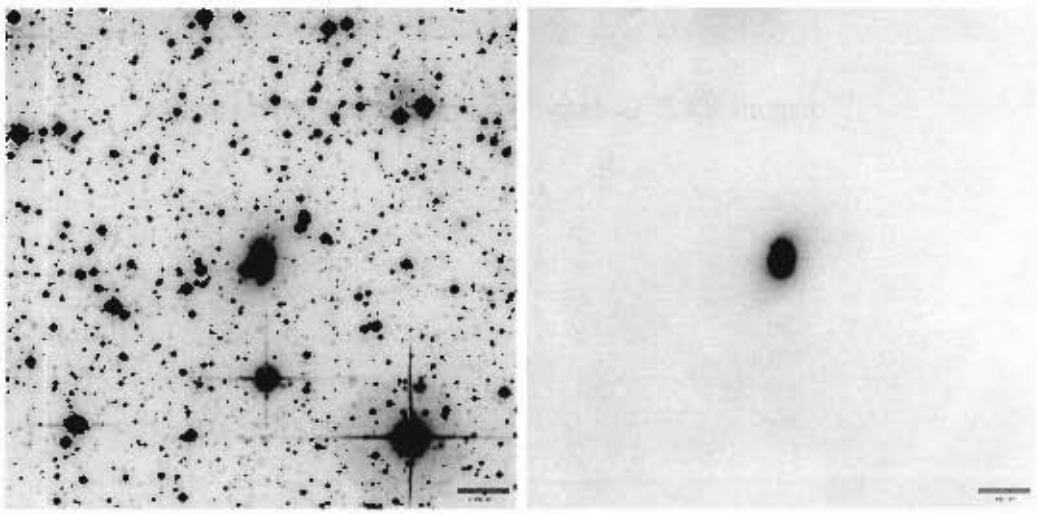

Figure 23.1: Galaxy WKK 6342, R_c band images, field 01, WF1 CCD #56

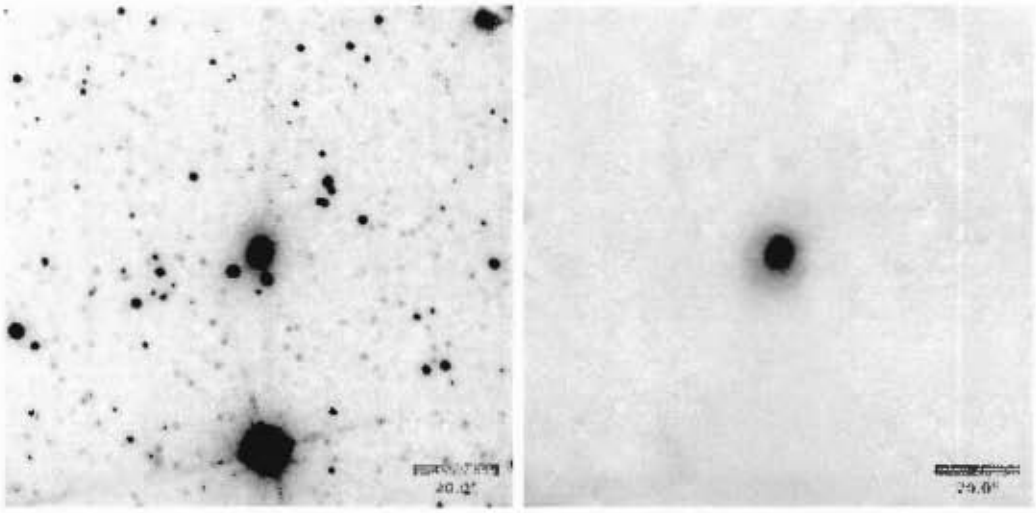

Figure 23.2: Galaxy WKK 6342, K_s band images

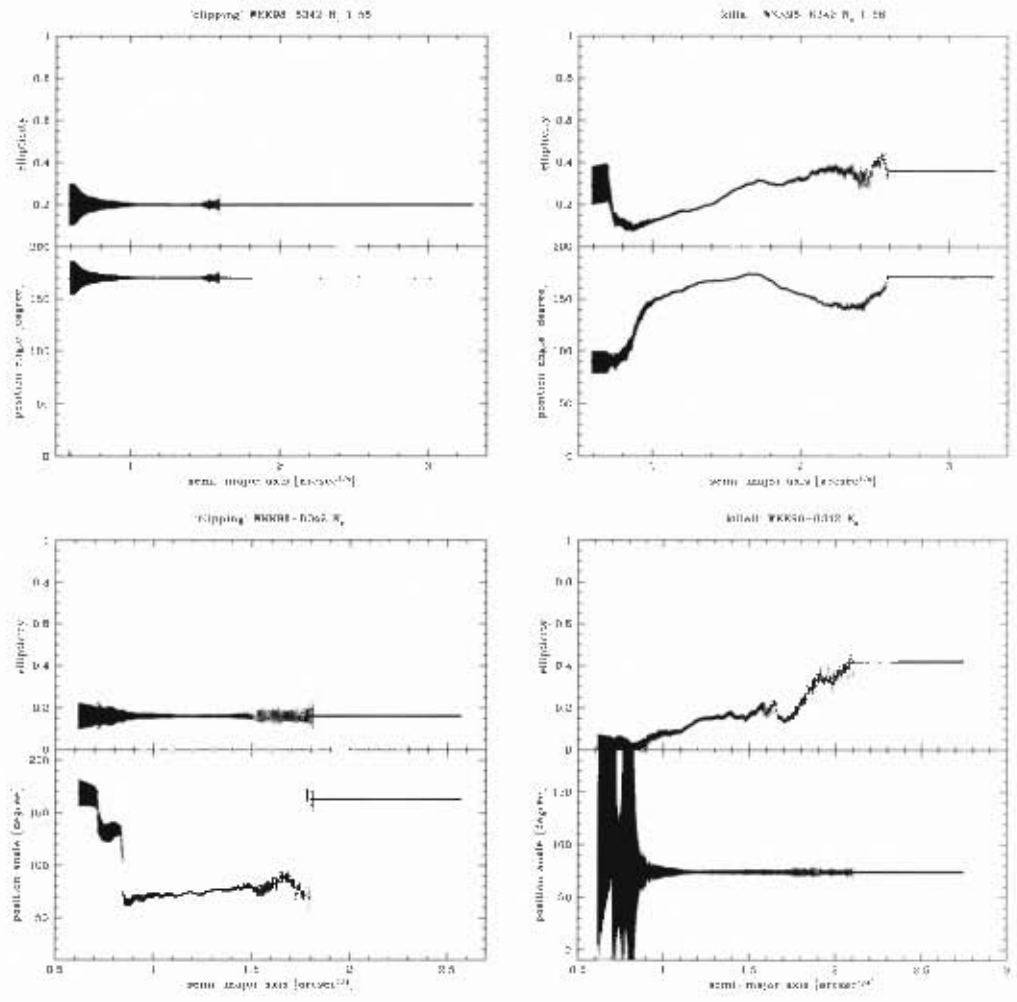

Figure 23.3: Galaxy WKK 6342, ellipticity and position angle plots

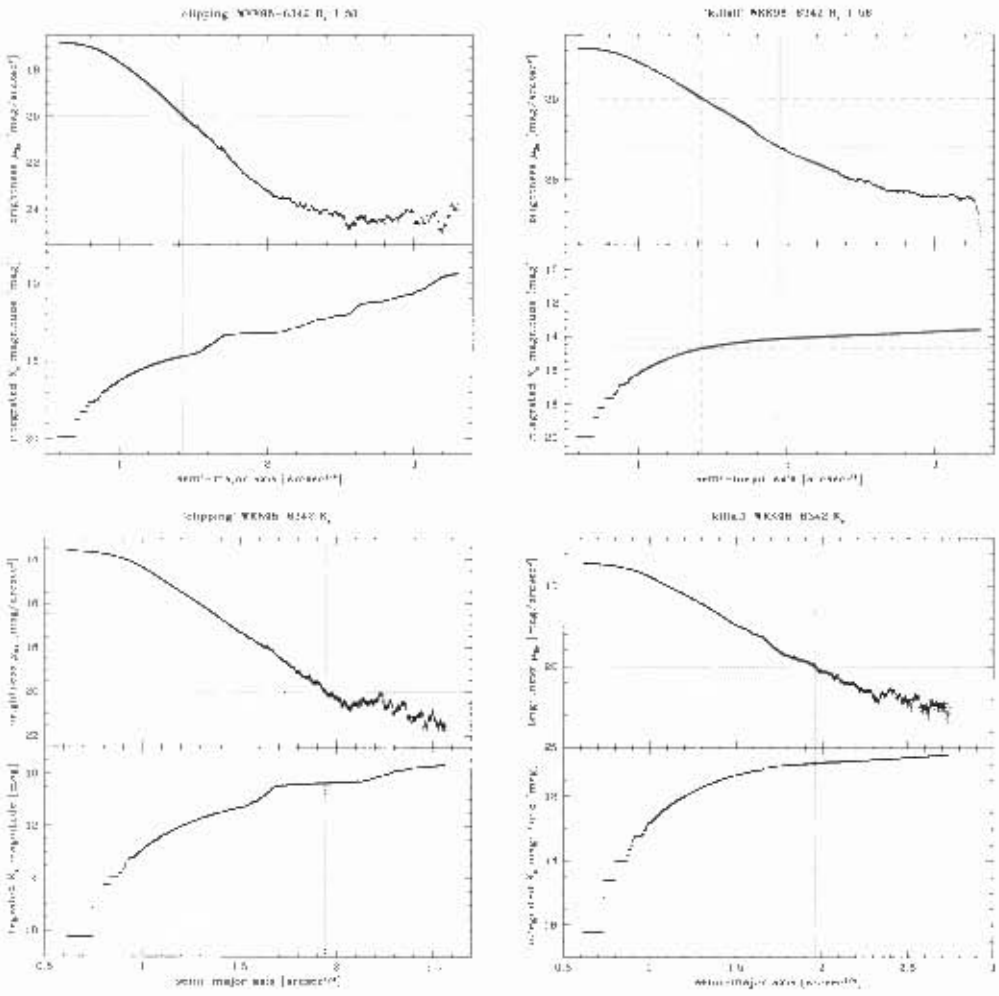

Figure 23.4: Galaxy WKK 6342, isophotal and integrated magnitude plots

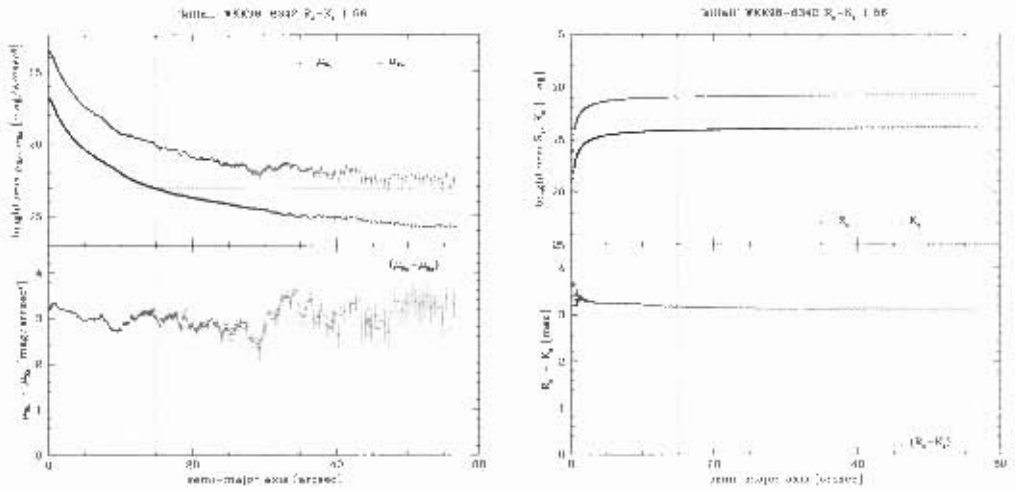

Figure 23.5: Galaxy WKK 6342, $(\mu_{R_c} - \mu_{K_s})$ and $(R_c - K_s)$ magnitude plots

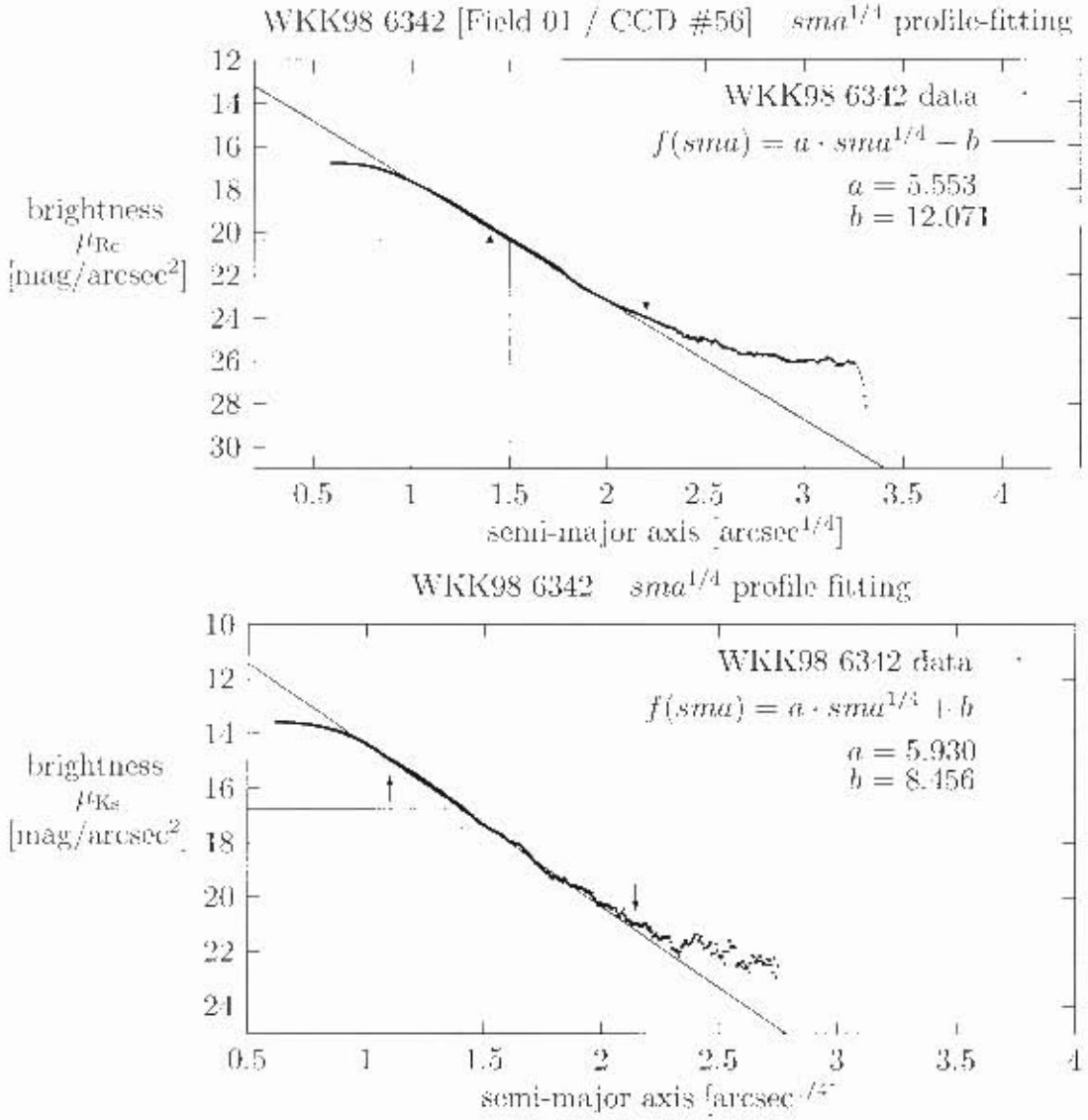

Figure 23.6: Galaxy WKK 6342, plots of brightness (μ_{R_c} and μ_{K_s}) versus semi-major axis sma$^{1/4}$ to demonstrate the profile-fitting. The arrows point to the upper and lower limit of the data set that was used for the fit. The resulting effective (half-light) radius $r_e^{1/4}$ and effective (half-light) surface brightness μ_e are indicated by straight lines.

Chapter 24

Galaxy WKK 6360

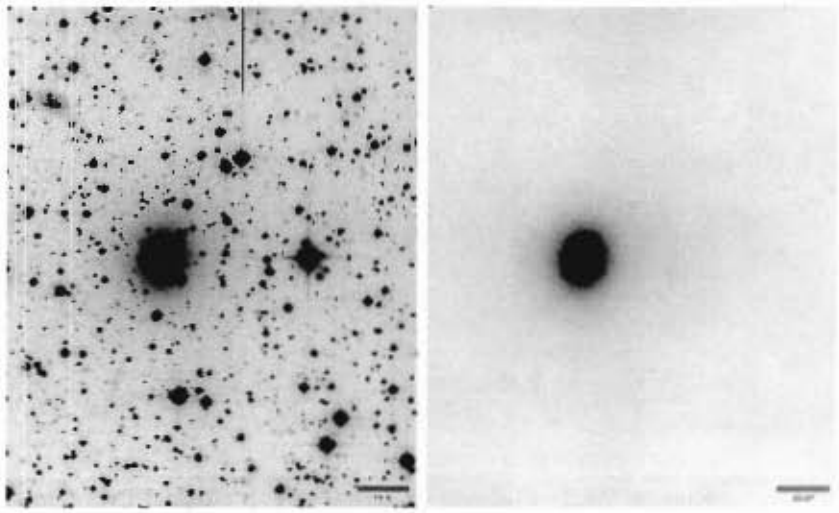

Figure 24.1: Galaxy WKK 6360, R_c band images, field 01, WFI CCD #56

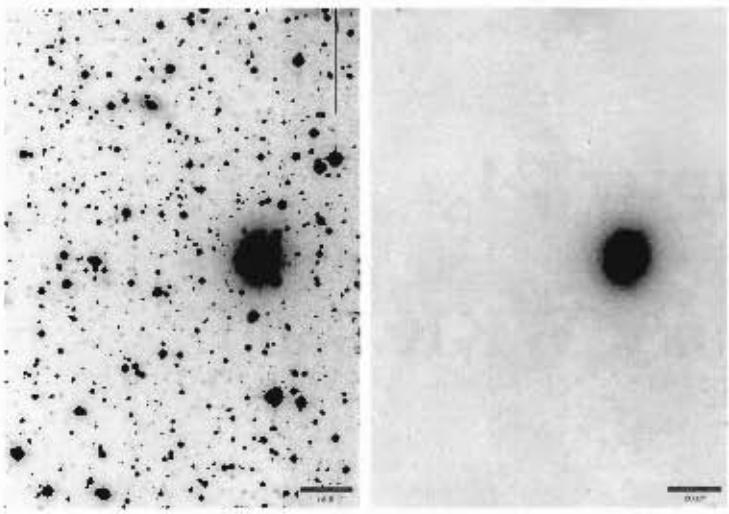

Figure 24.2: Galaxy WKK 6360, R_c band images, field 01, WFI CCD #57

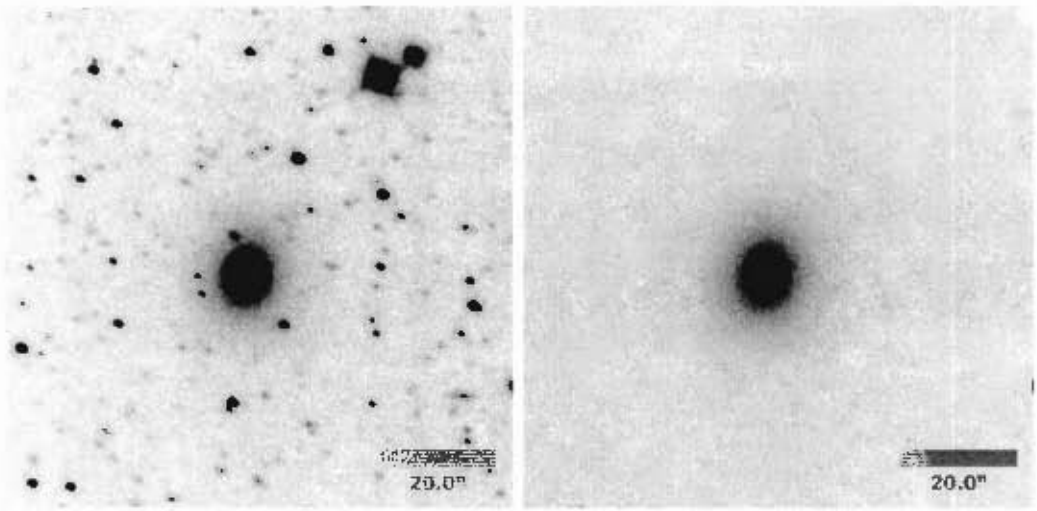

Figure 24.3: Galaxy WKK 6360, K_s band images

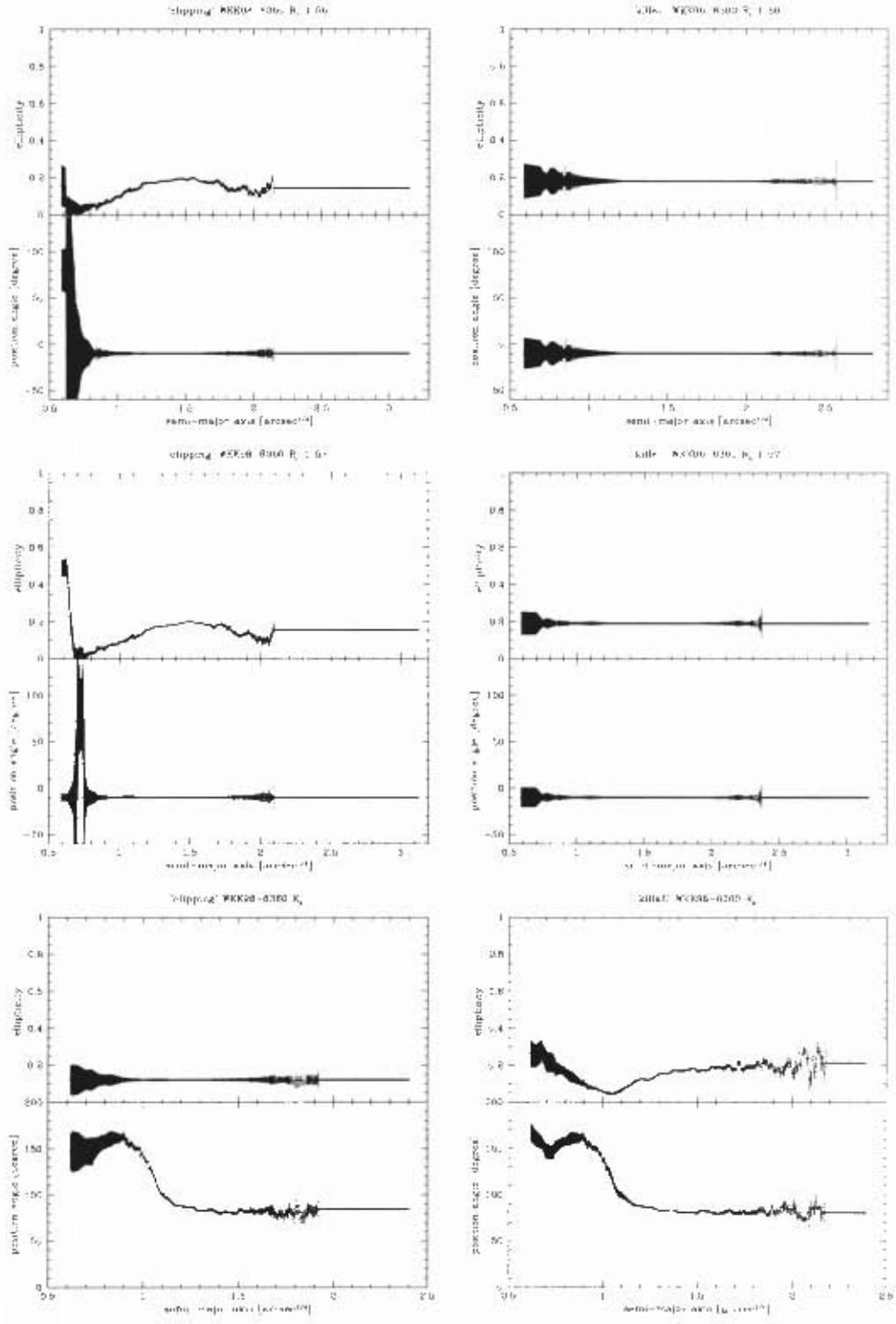

Figure 24.4: Galaxy WKK 6360, ellipticity and position angle plots

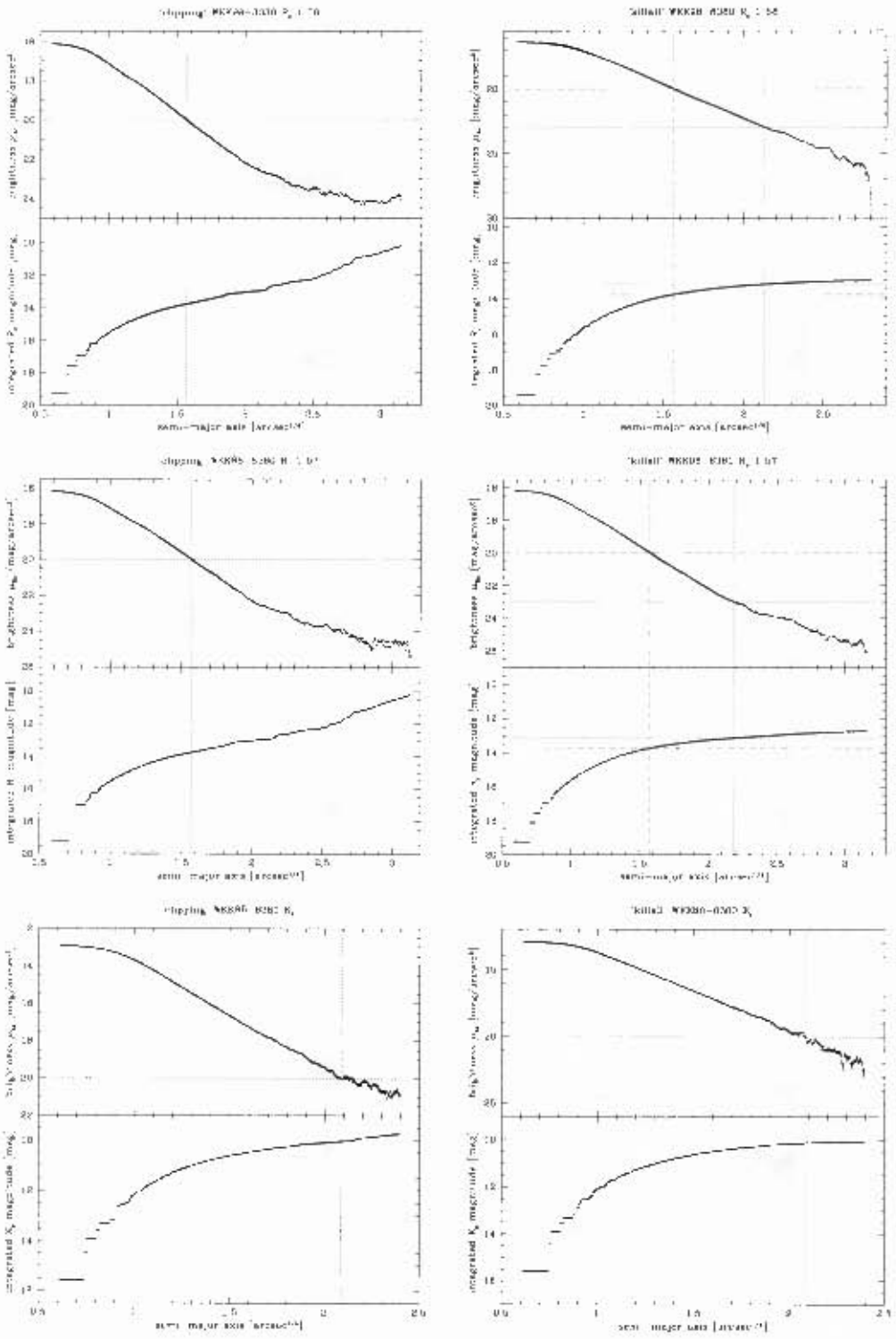

Figure 24.5: Galaxy WKK 6360, isophotal and integrated magnitude plots

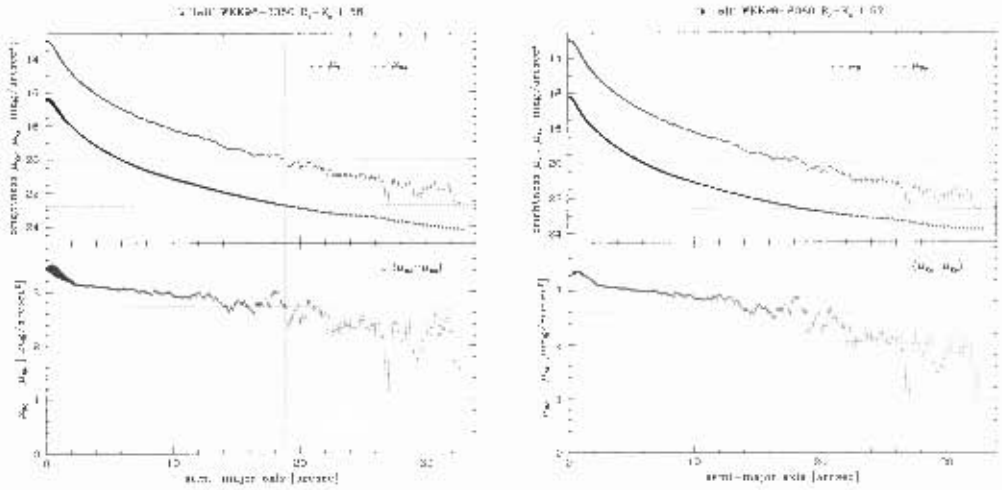

Figure 24.6: Galaxy WKK 6360. $(\mu_{R_c} - \mu_{K_s})$ magnitude plots

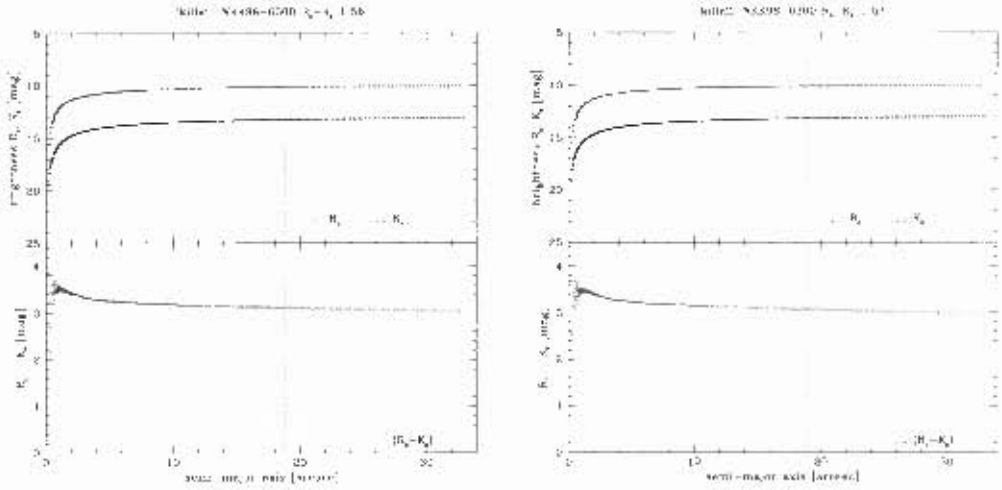

Figure 24.7: Galaxy WKK 6360. $(R_c - K_s)$ magnitude plots

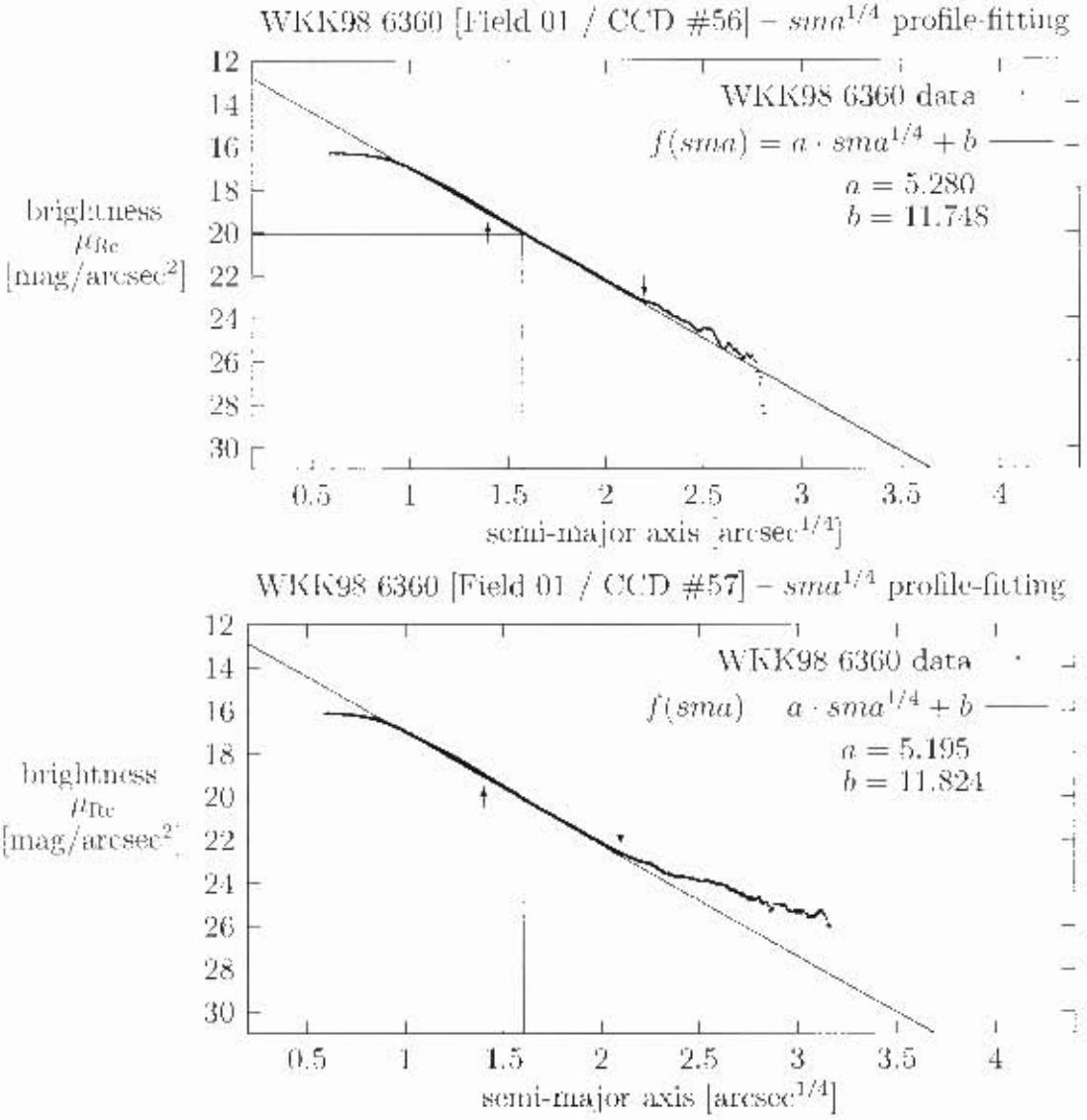

Figure 24.8: Galaxy WKK 6360, plots of brightness μ_{I_c} versus semi-major axis $sma^{1/4}$ to demonstrate the profile-fitting. The arrows point to the upper and lower limit of the data set that was used for the fit. The resulting effective (half-light) radius $r_e^{1/4}$ and effective (half-light) surface brightness μ_e are indicated by straight lines.

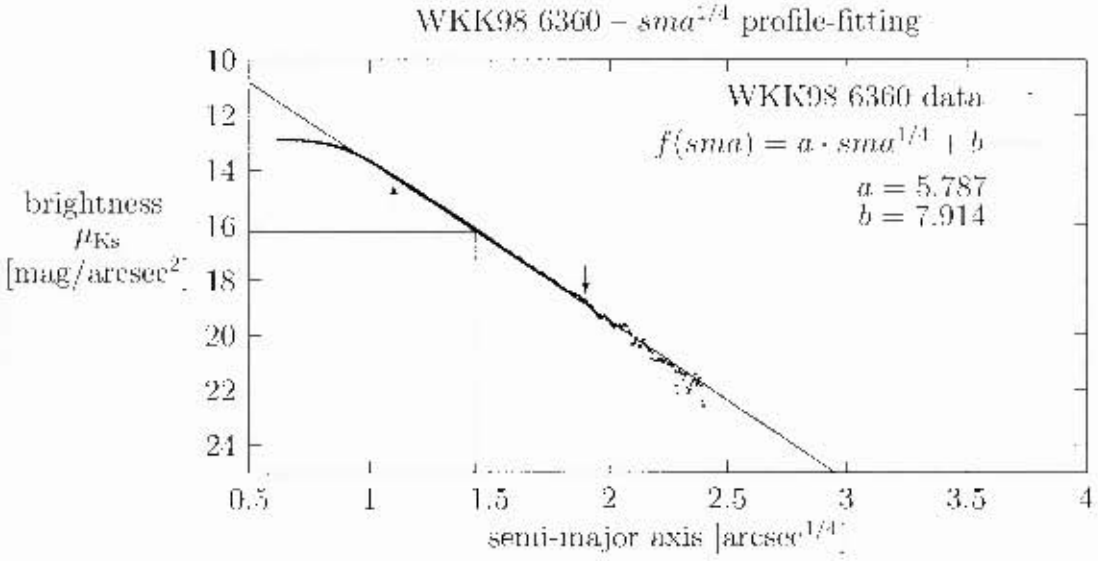

Figure 24.9: Galaxy WKK 6360, plot of brightness μ_{K_s} versus semi-major axis $sma^{1/4}$ to demonstrate the profile-fitting. The arrows point to the upper and lower limit of the data set that was used for the fit. The resulting effective (half-light) radius $r_e^{1/4}$ and effective (half-light) surface brightness μ_e are indicated by straight lines.

Chapter 25

Galaxy WKK 6383

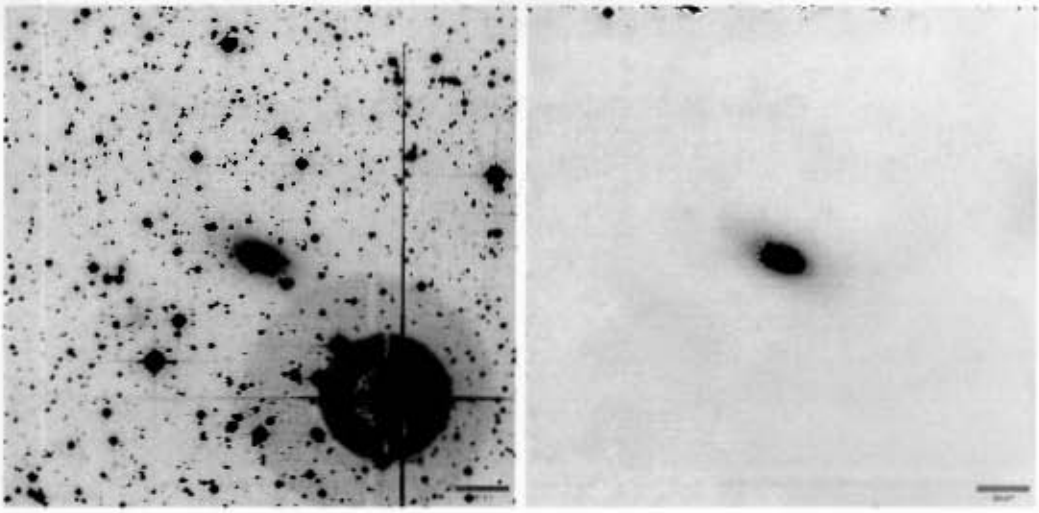

Figure 25.1: Galaxy WKK 6383, R_c band images, field 01. WFI CCD #50

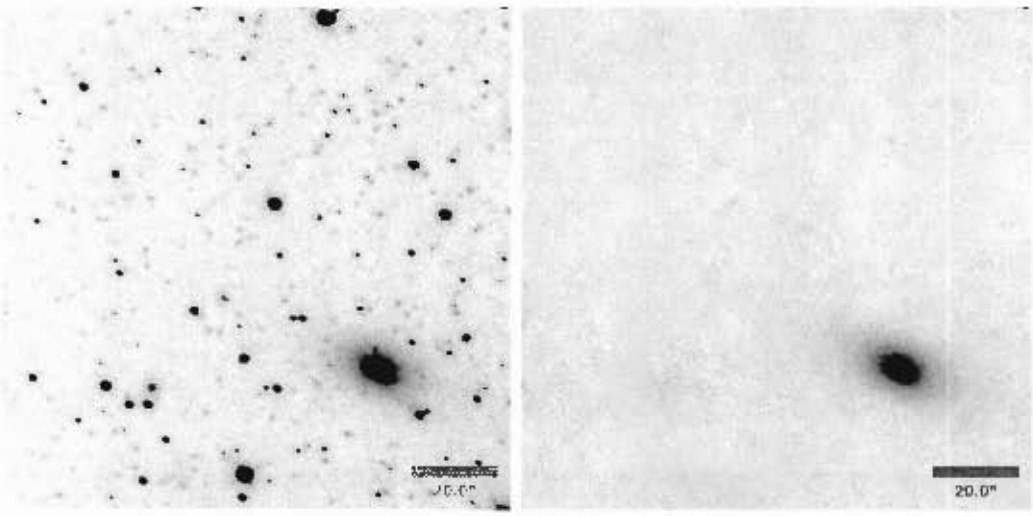

Figure 25.2: Galaxy WKK 6383, K_s band images

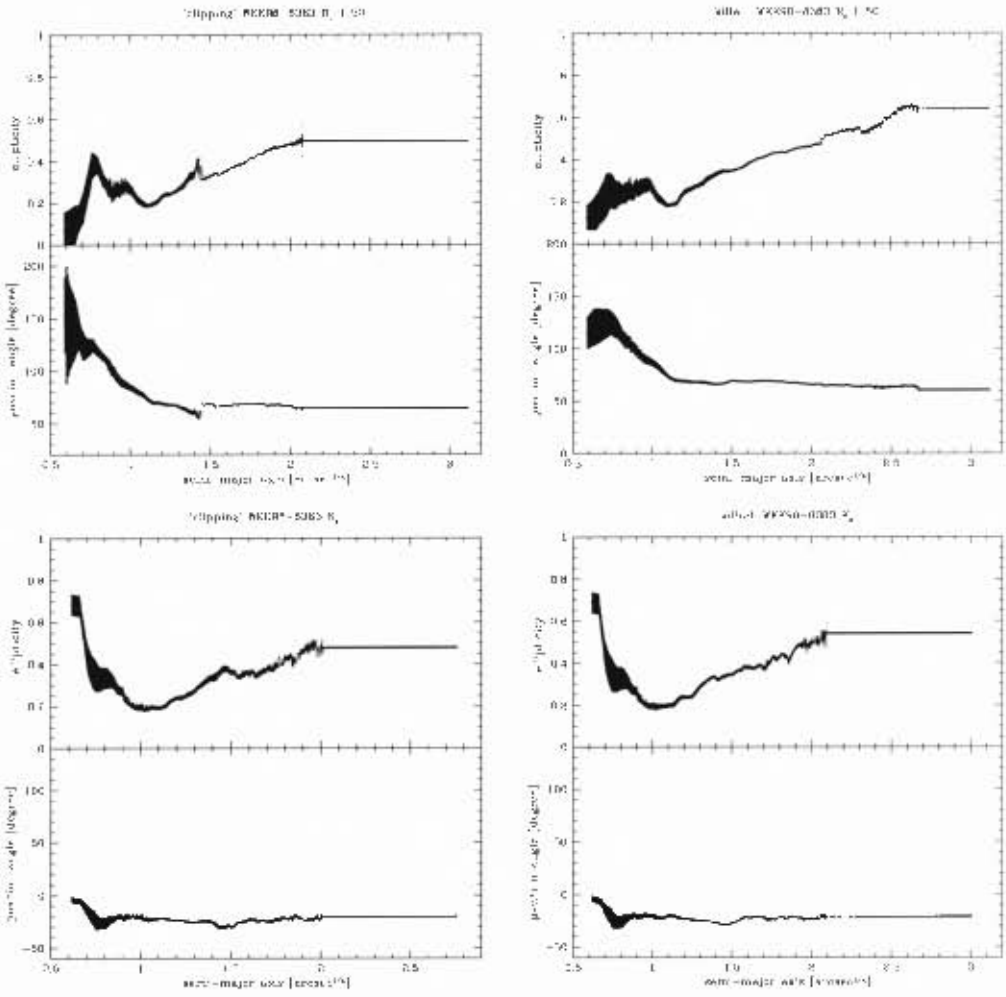

Figure 25.3: Galaxy WKK 6383, ellipticity and position angle plots

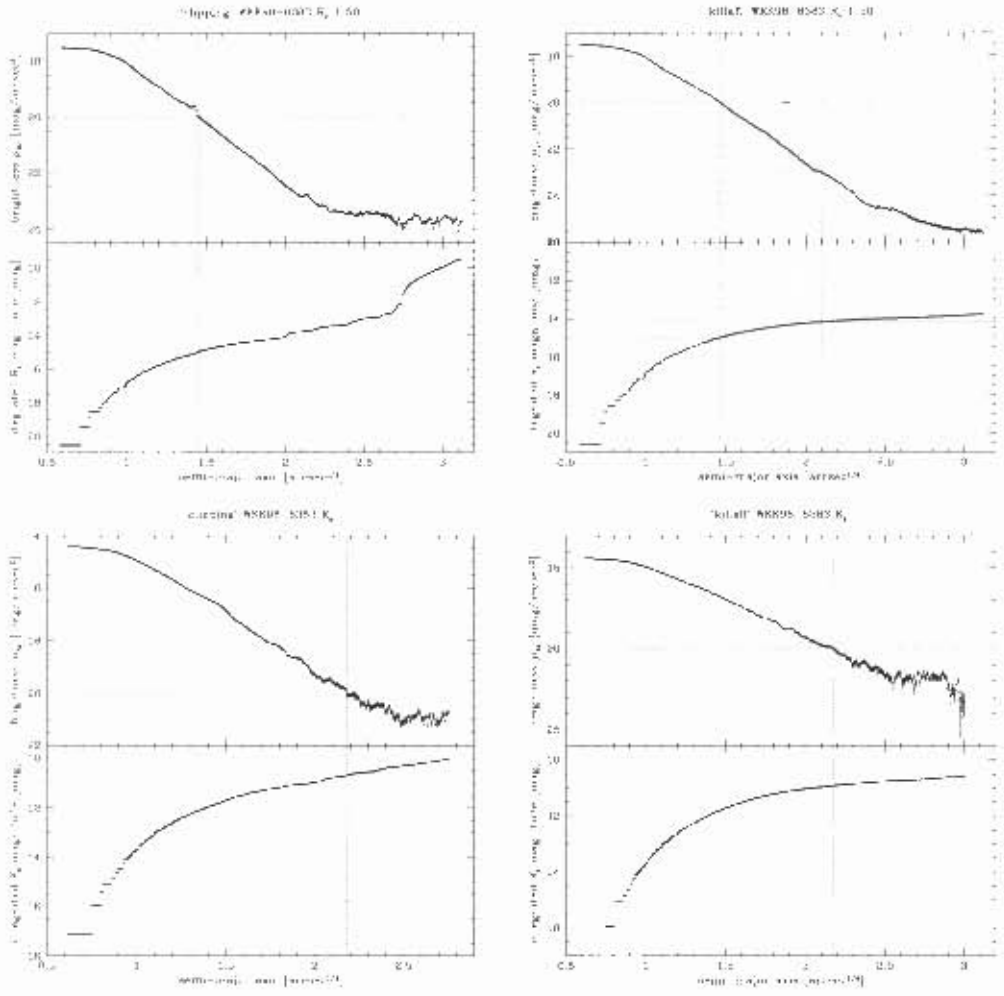

Figure 25.4: Galaxy WKK 6383, isophotal and integrated magnitude plots

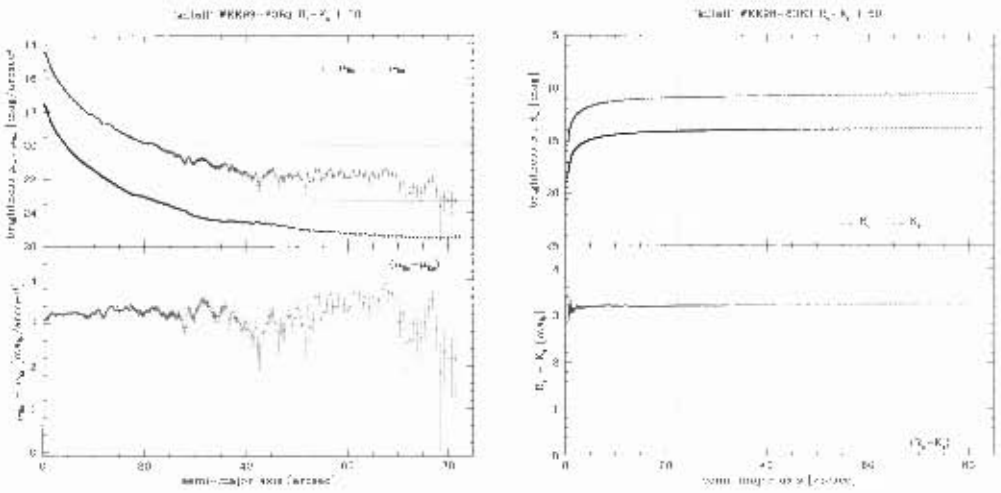

Figure 25.5: Galaxy WKK 6383, $(\mu_{R_c} - \mu_{K_s})$ and $(R_c - K_s)$ magnitude plots

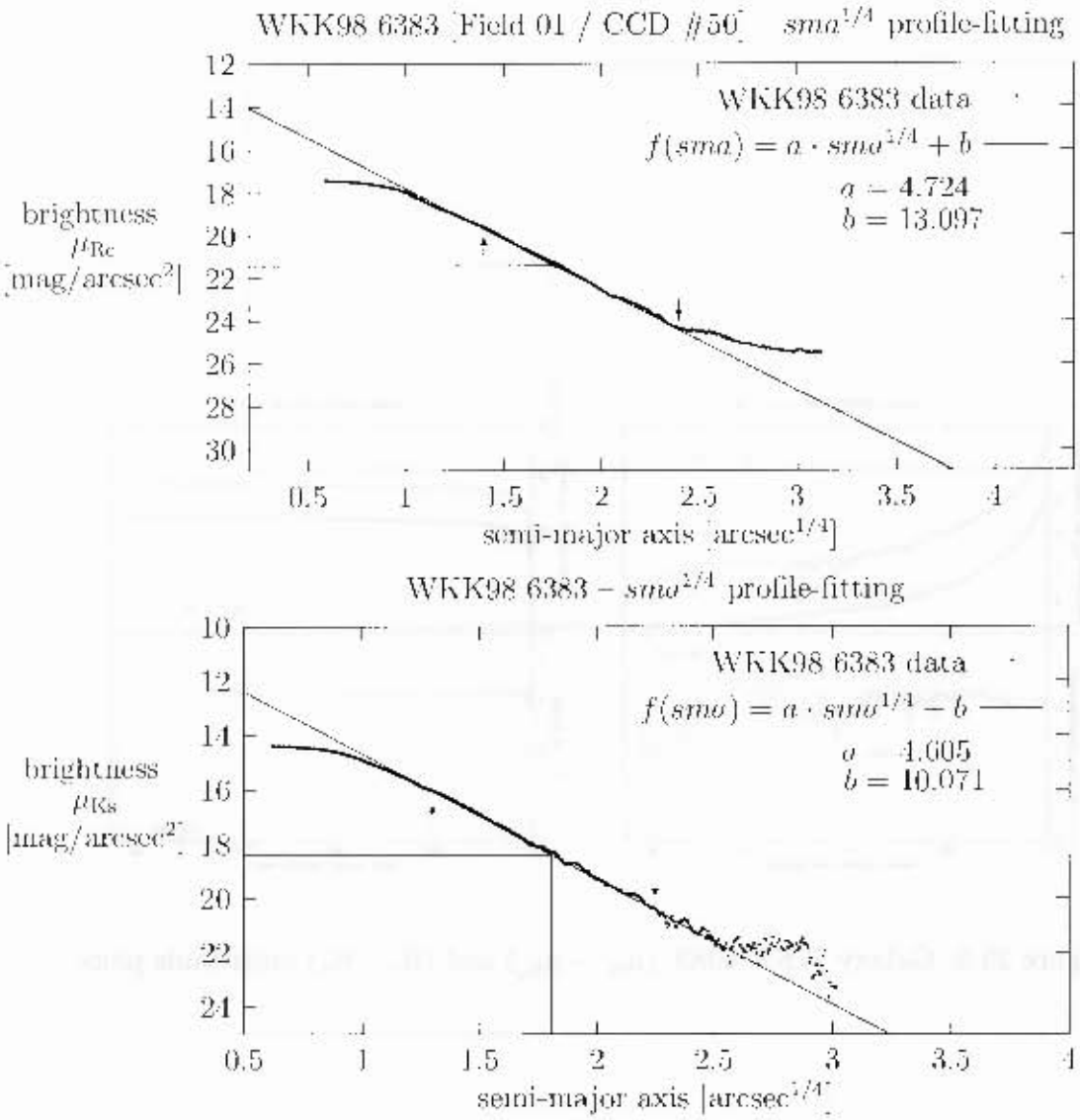

Figure 25.6: Galaxy WKK 6383, plots of brightness (μ_{R_c} and μ_{K_s}) versus semi-major axis sma$^{1/4}$ to demonstrate the profile-fitting. The arrows point to the upper and lower limit of the data set that was used for the fit. The resulting effective (half-light) radius $r_e^{1/4}$ and effective (half light) surface brightness μ_e are indicated by straight lines.

Chapter 26

Galaxy WKK 6431

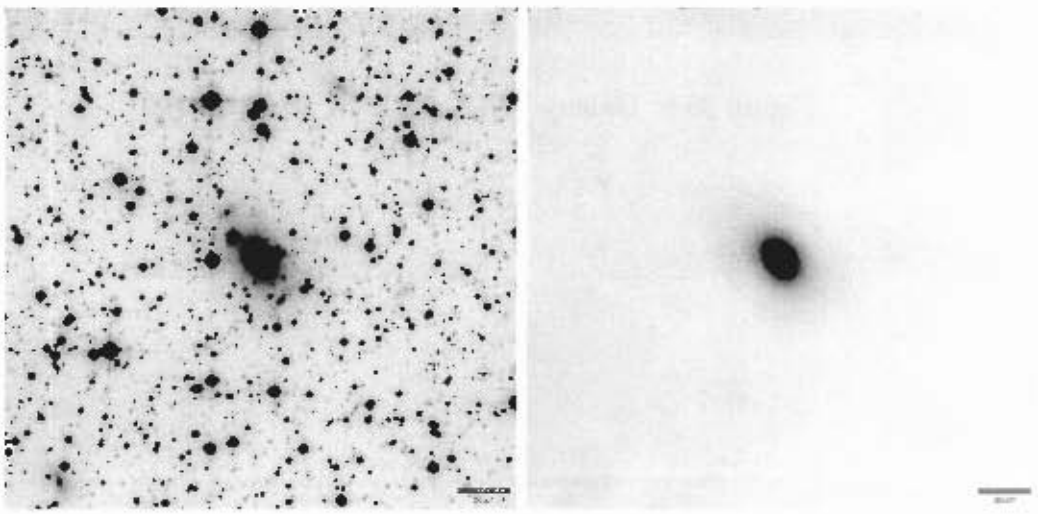

Figure 26.1: Galaxy WKK 6431, R_c band images, field 06, WFI CCD #53

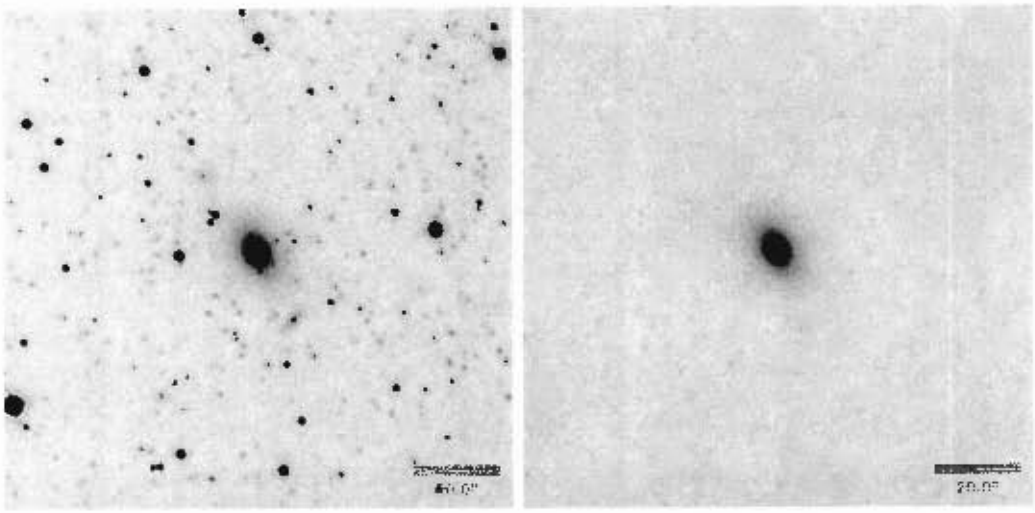

Figure 26.2: Galaxy WKK 6431, K_s band images

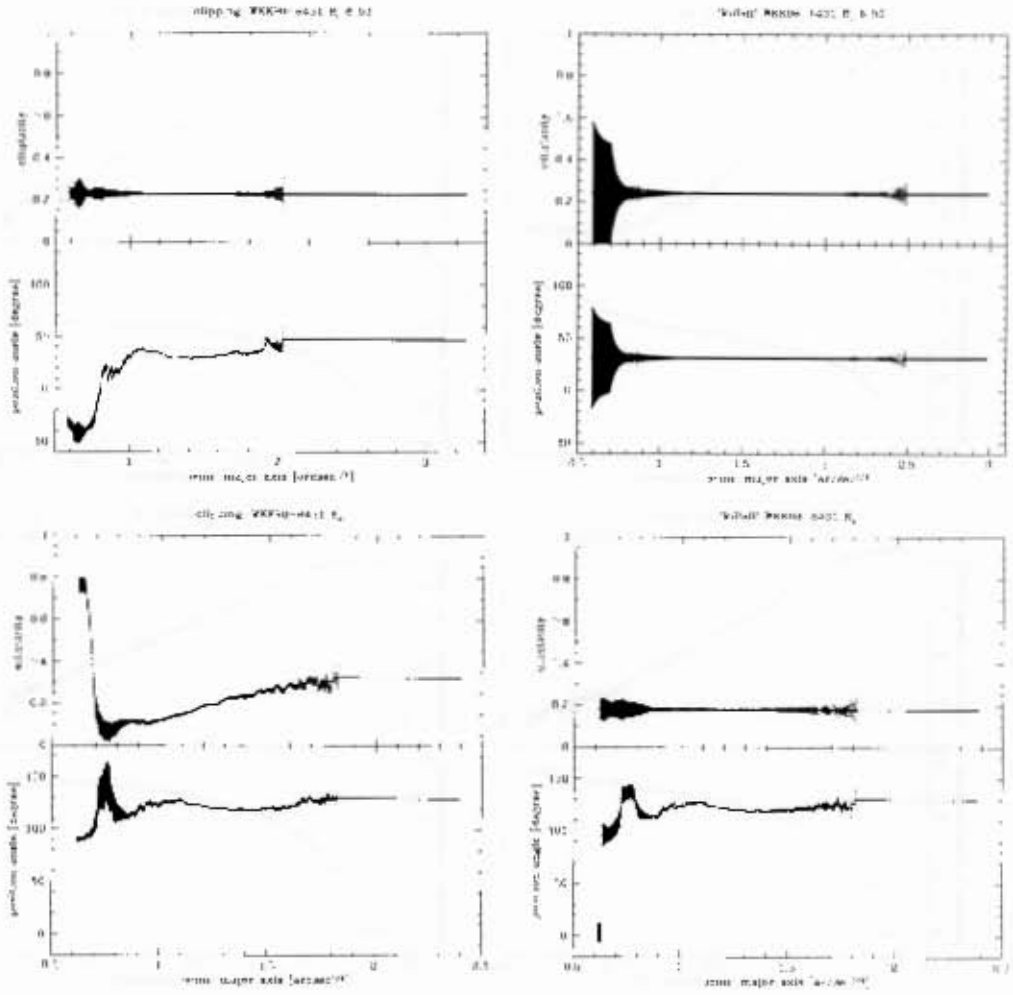

Figure 26.3: Galaxy WKK 6431, ellipticity and position angle plots

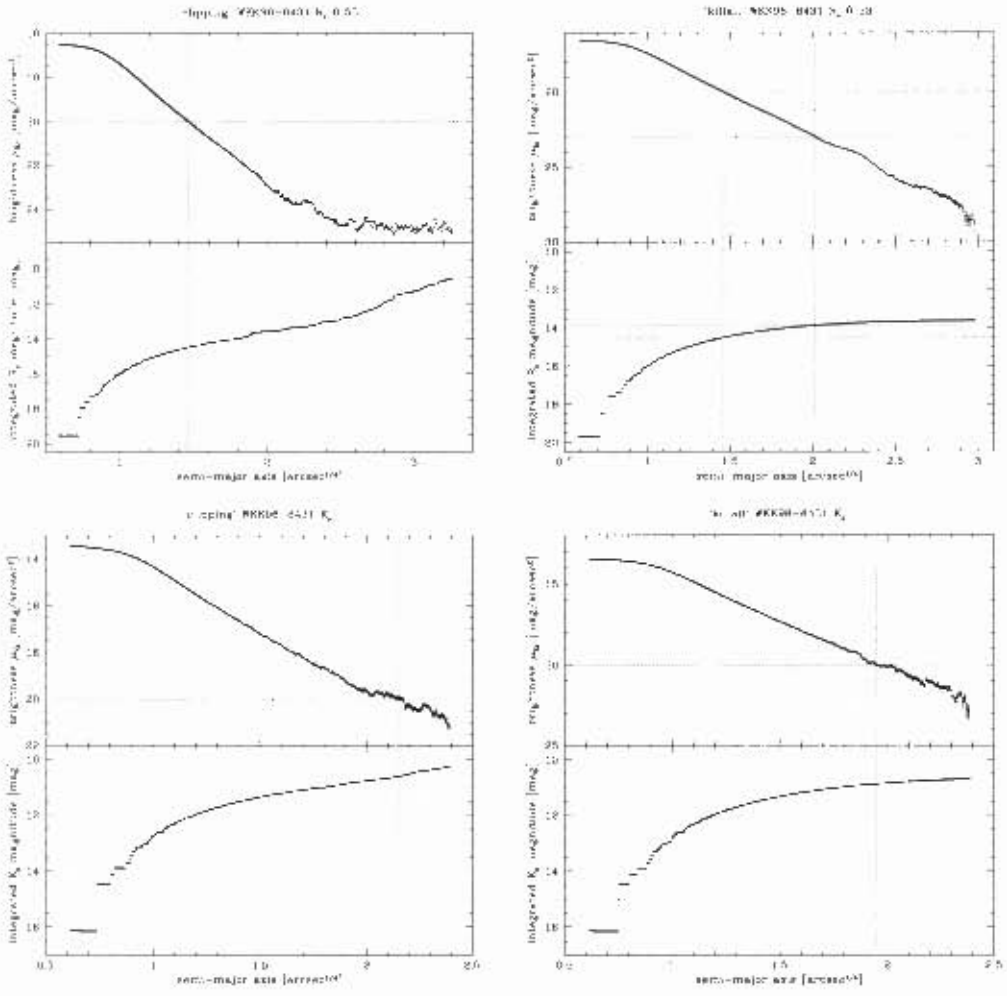

Figure 26.4: Galaxy WKK 6431, isophotal and integrated magnitude plots

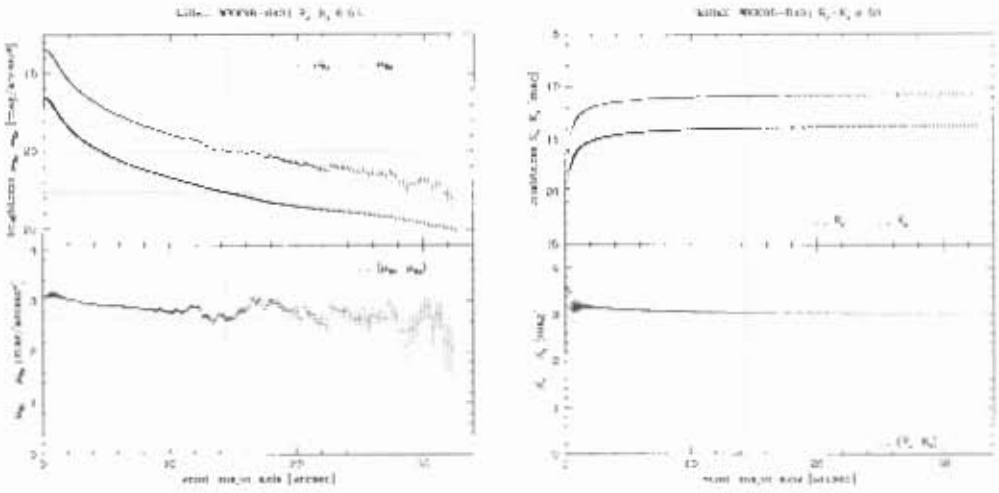

Figure 26.5: Galaxy WKK 6431, (μ_{R_c} μ_{K_s}) and ($R_c - K_s$) magnitude plots

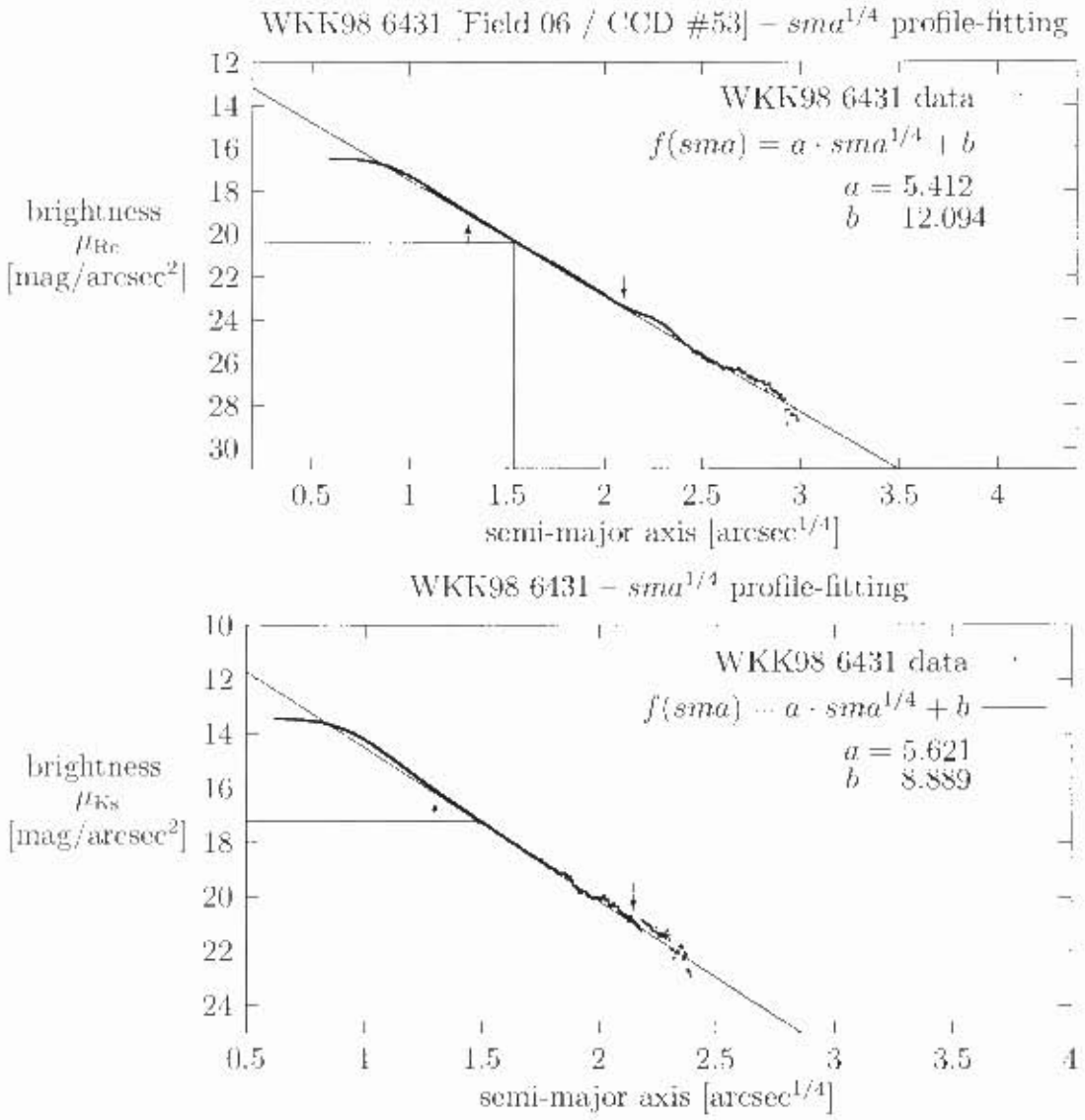

Figure 26.6: Galaxy WKK 6431, plots of brightness (μ_{R_c} and μ_{K_s}) versus semi-major axis sma$^{1/4}$ to demonstrate the profile-fitting. The arrows point to the upper and lower limit of the data set that was used for the fit. The resulting effective (half-light) radius $r_e^{1/4}$ and effective (half-light) surface brightness μ_e are indicated by straight lines.

Chapter 27

Galaxy WKK 6473

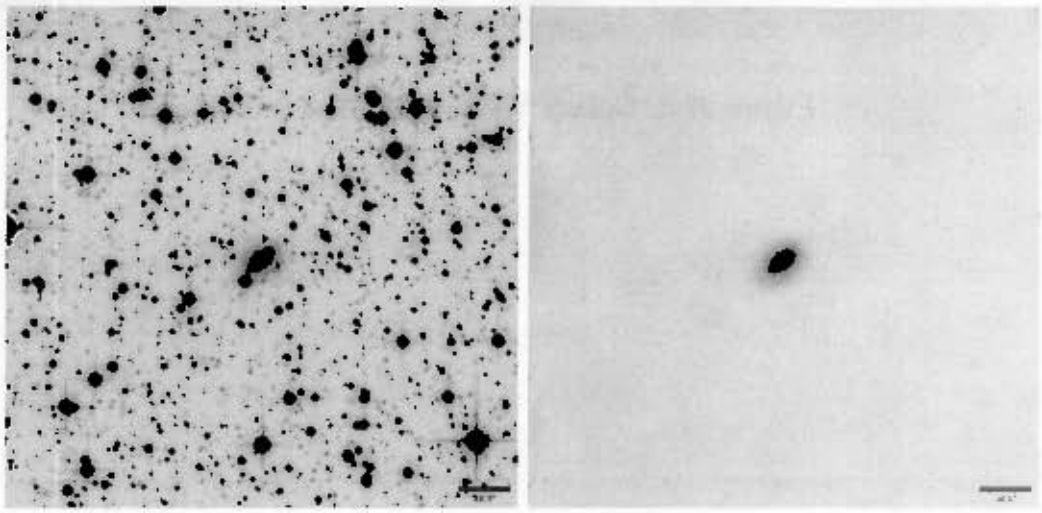

Figure 27.1: Galaxy WKK 6473, R_c band images, field 18, WFI CCD #55

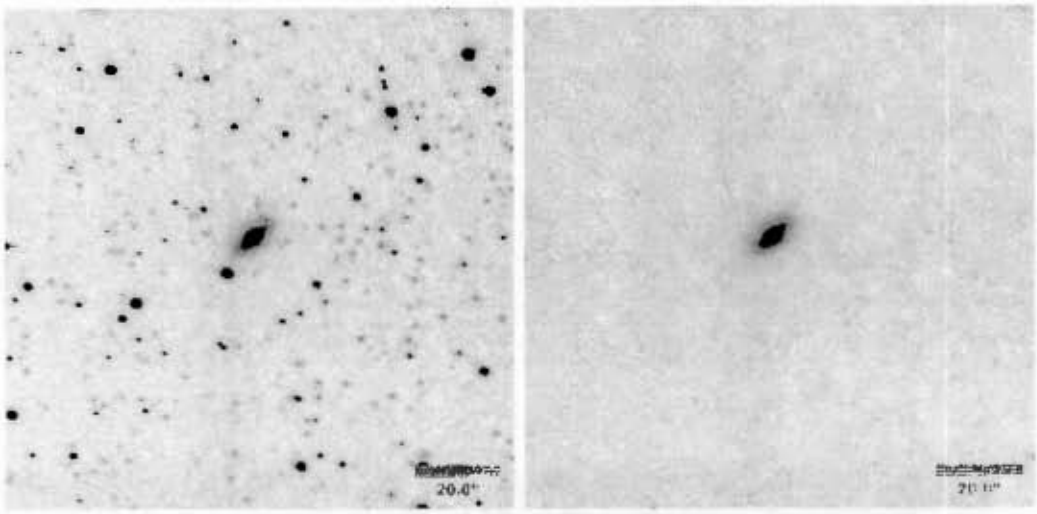

Figure 27.2: Galaxy WKK 6473, K_s band images

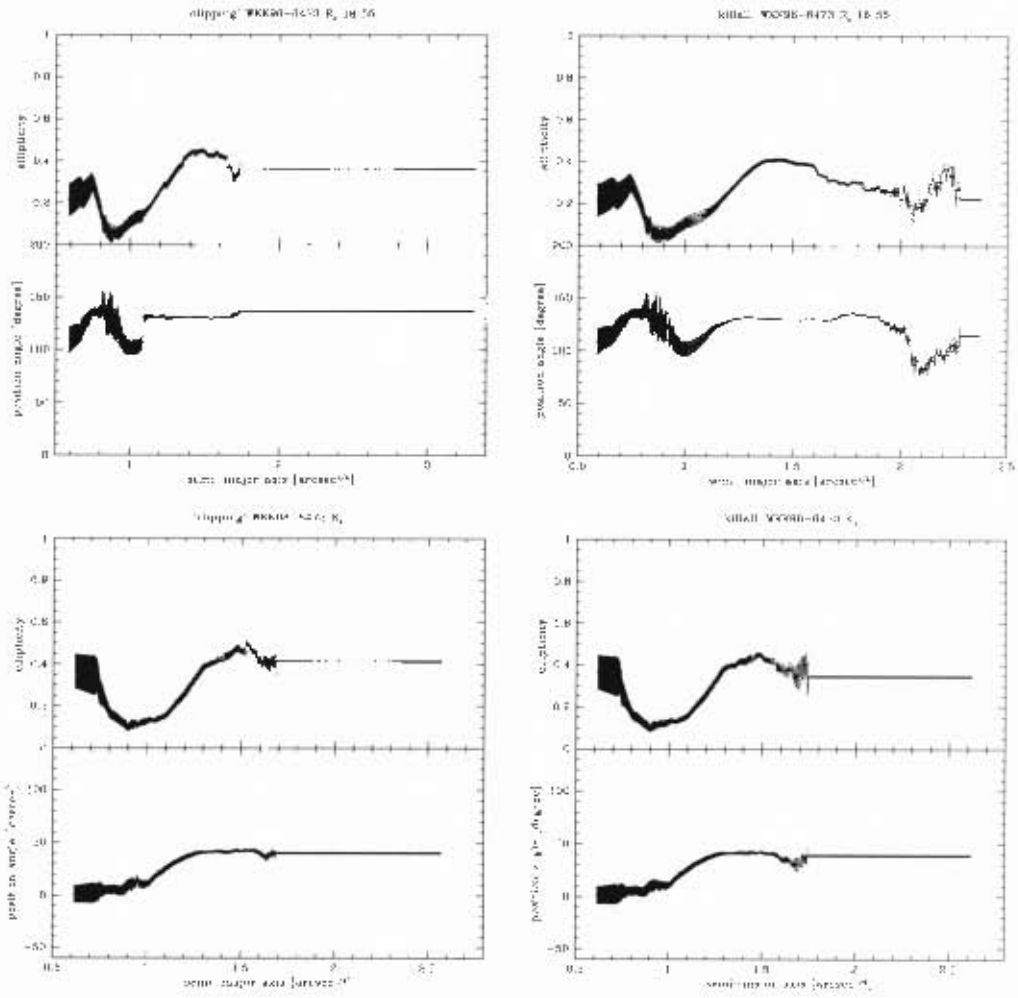

Figure 27.3: Galaxy WKK 6473, ellipticity and position angle plots

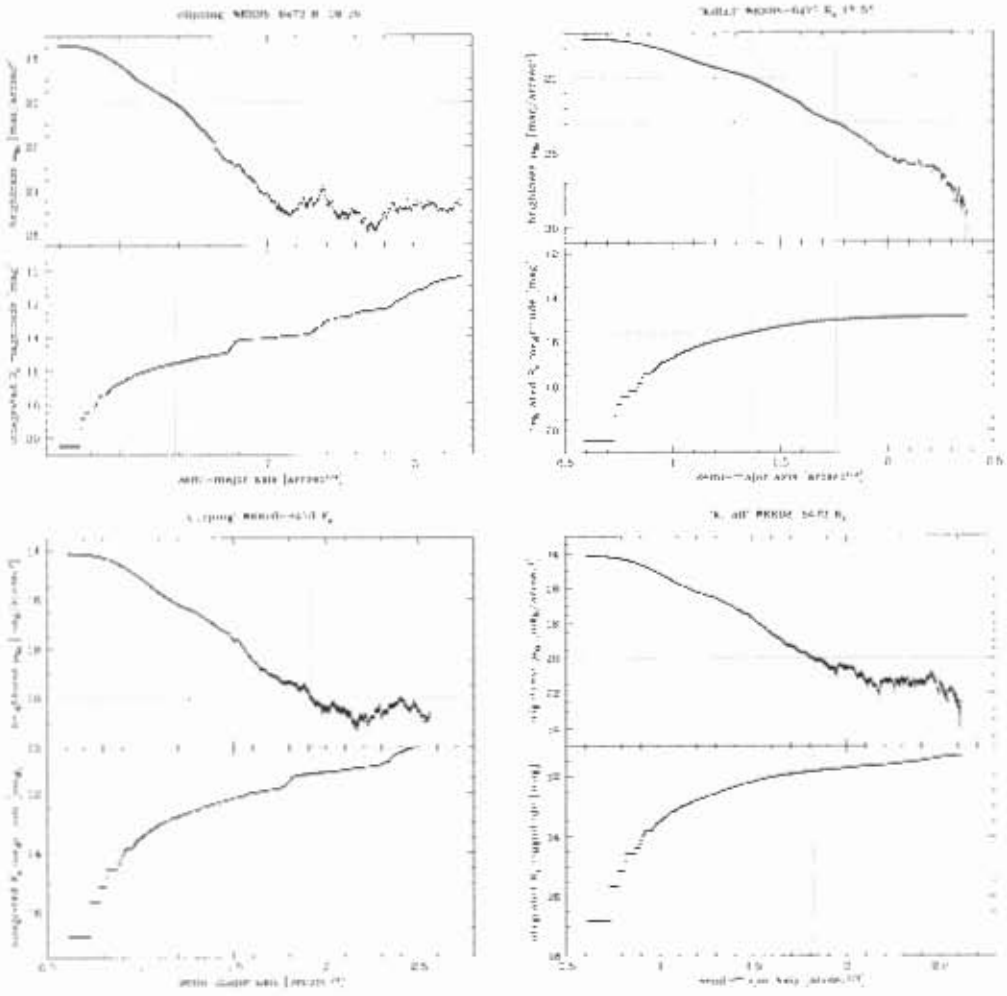

Figure 27.4: Galaxy WKK 6173, isophotal and integrated magnitude plots

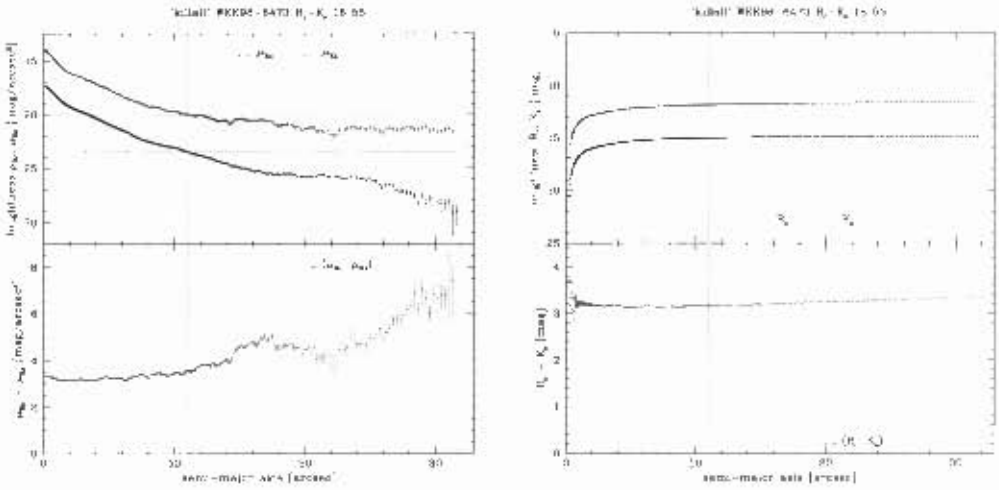

Figure 27.5: Galaxy WKK 6473, $(\mu_{R_c} - \mu_{K_s})$ and $(R_c - K_s)$ magnitude plots

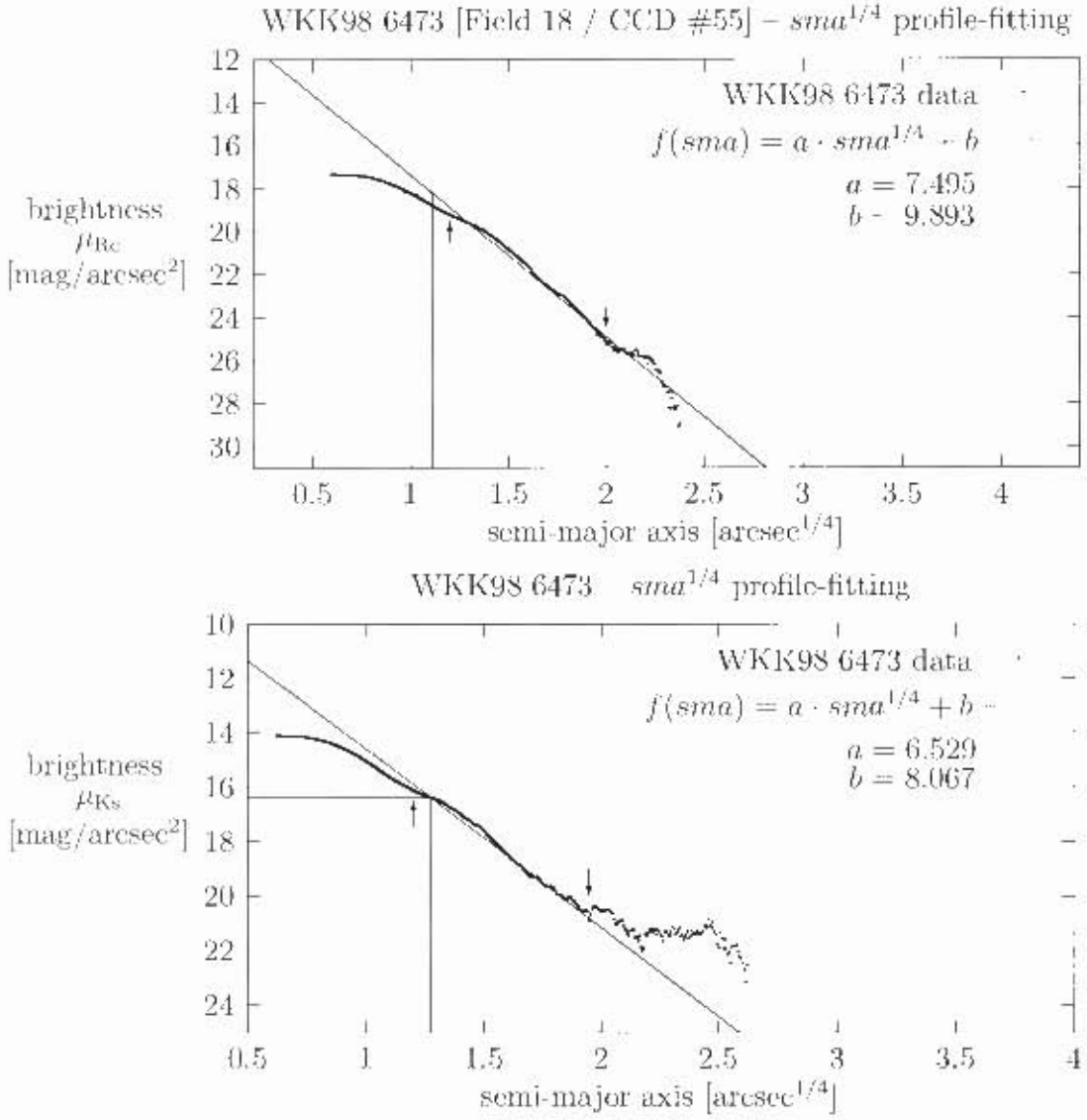

Figure 27.6: Galaxy WKK 6473, plots of brightness (μ_{R_c} and μ_{K_s}) versus semi-major axis sma$^{1/4}$ to demonstrate the profile-fitting. The arrows point to the upper and lower limit of the data set that was used for the fit. The resulting effective (half-light) radius $r_e^{1/4}$ and effective (half-light) surface brightness μ_e are indicated by straight lines.

Chapter 28

Galaxy WKK 6477

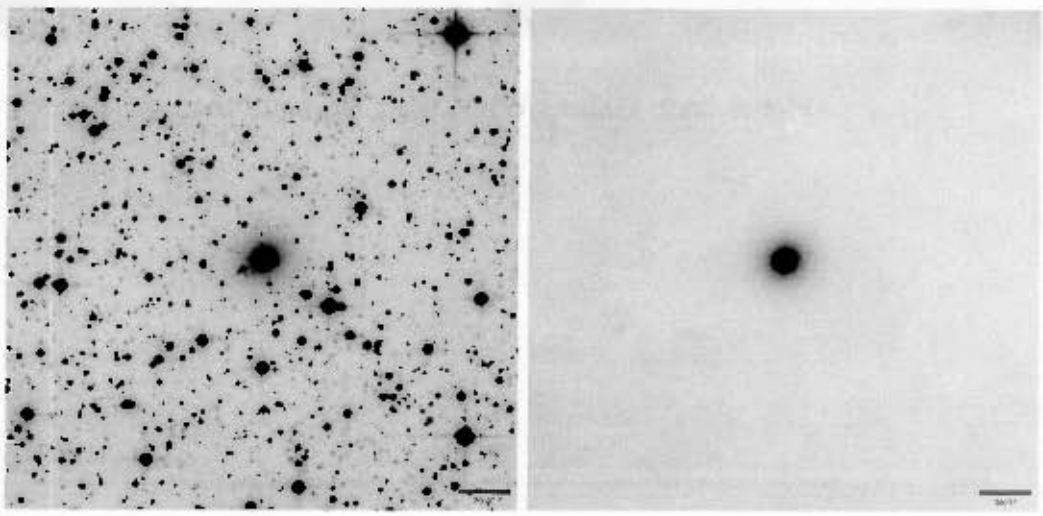

Figure 28.1: Galaxy WKK 6477, R_c band images, field 06, WFI CCD #52

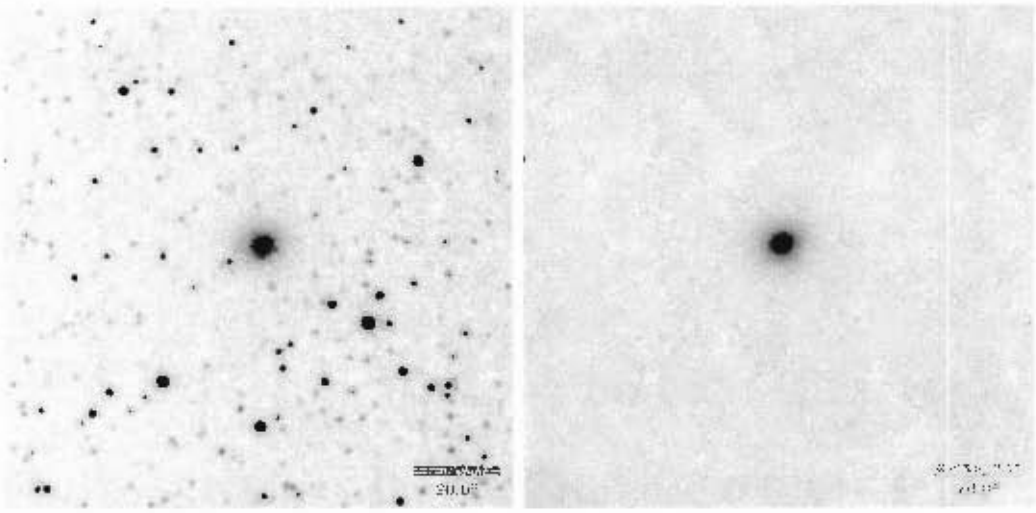

Figure 28.2: Galaxy WKK 6477, K_s band images

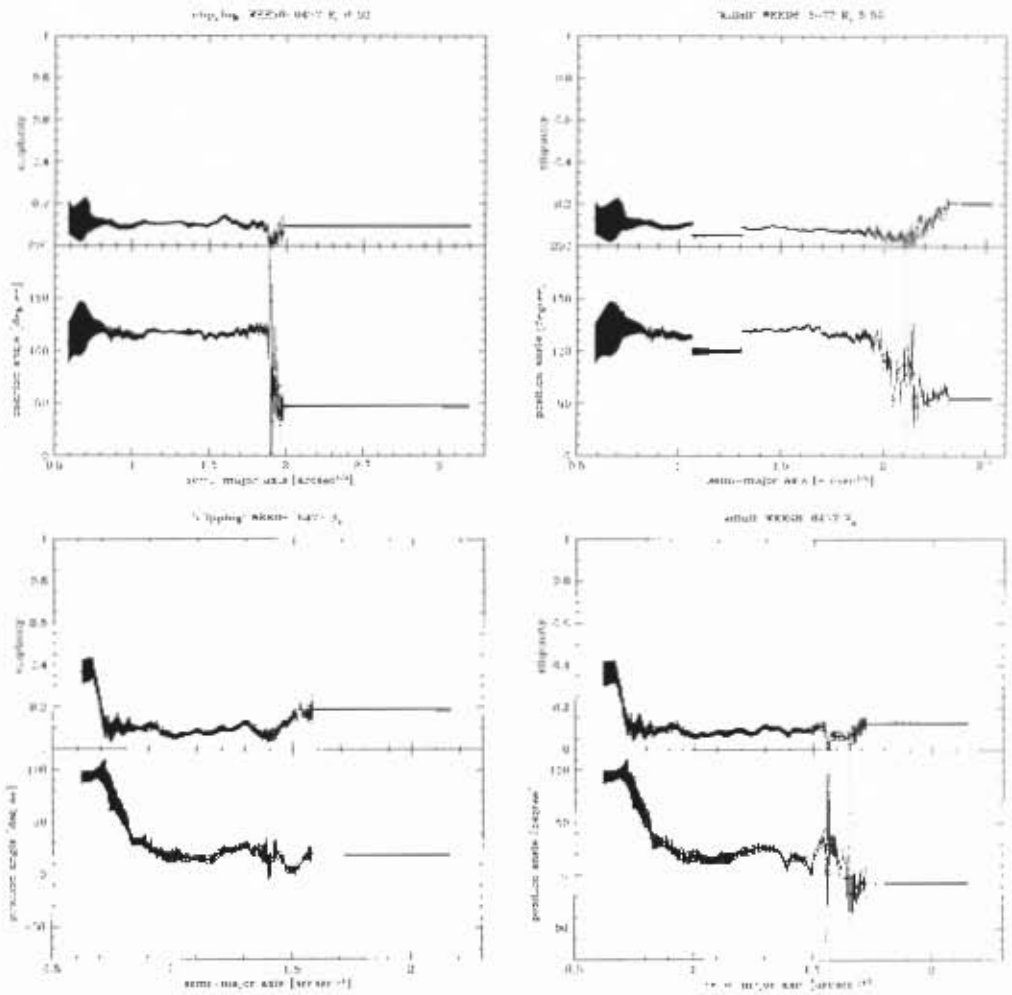

Figure 28.3: Galaxy WKK 6177, ellipticity and position angle plots

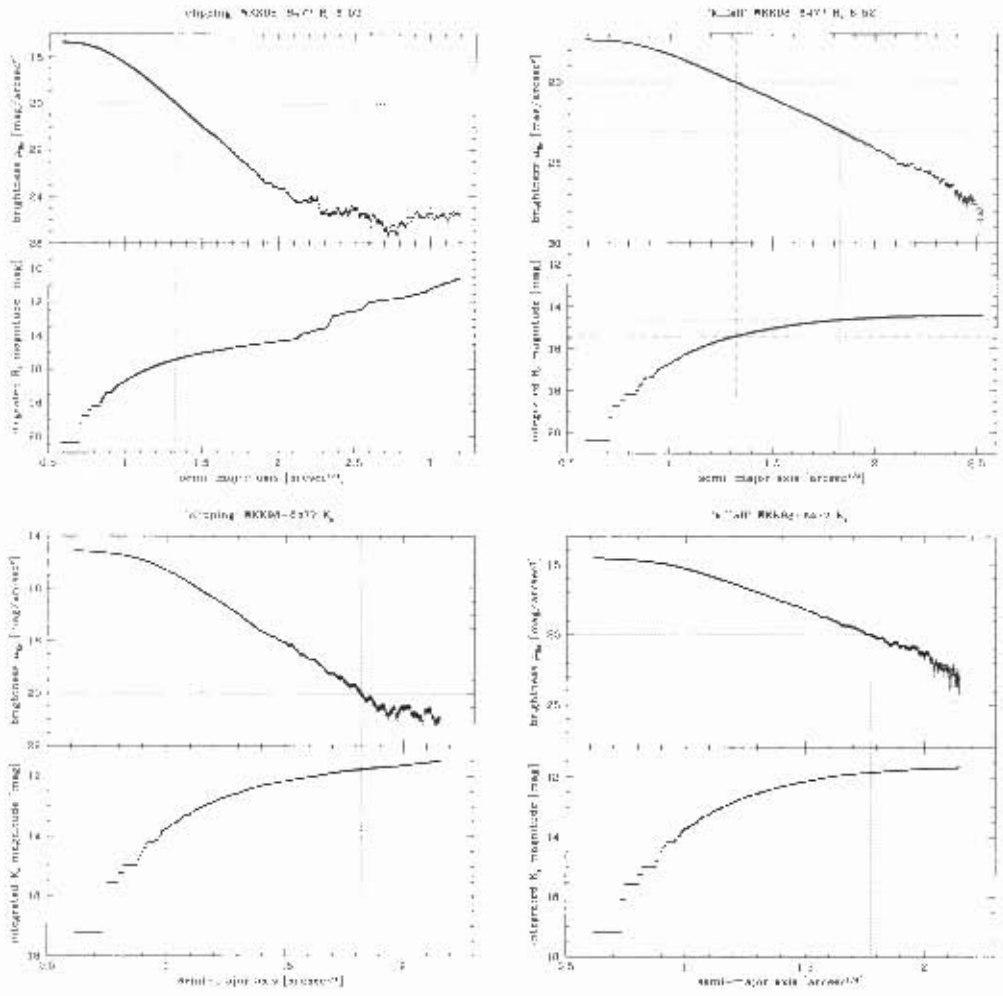

Figure 28.4: Galaxy WKK 6477, isophotal and integrated magnitude plots

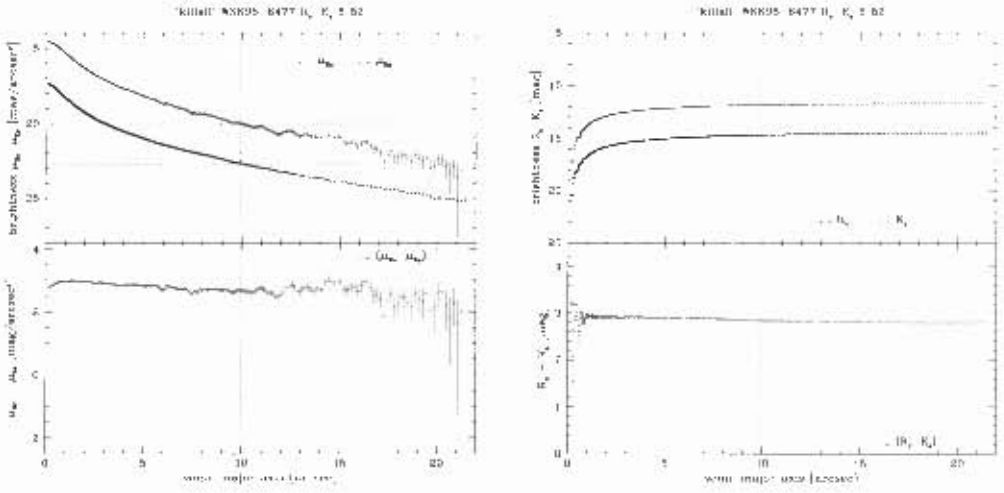

Figure 28.5: Galaxy WKK 6477, (u_{R_c} − μ_{K_s}) and (R_c − K_s) magnitude plots

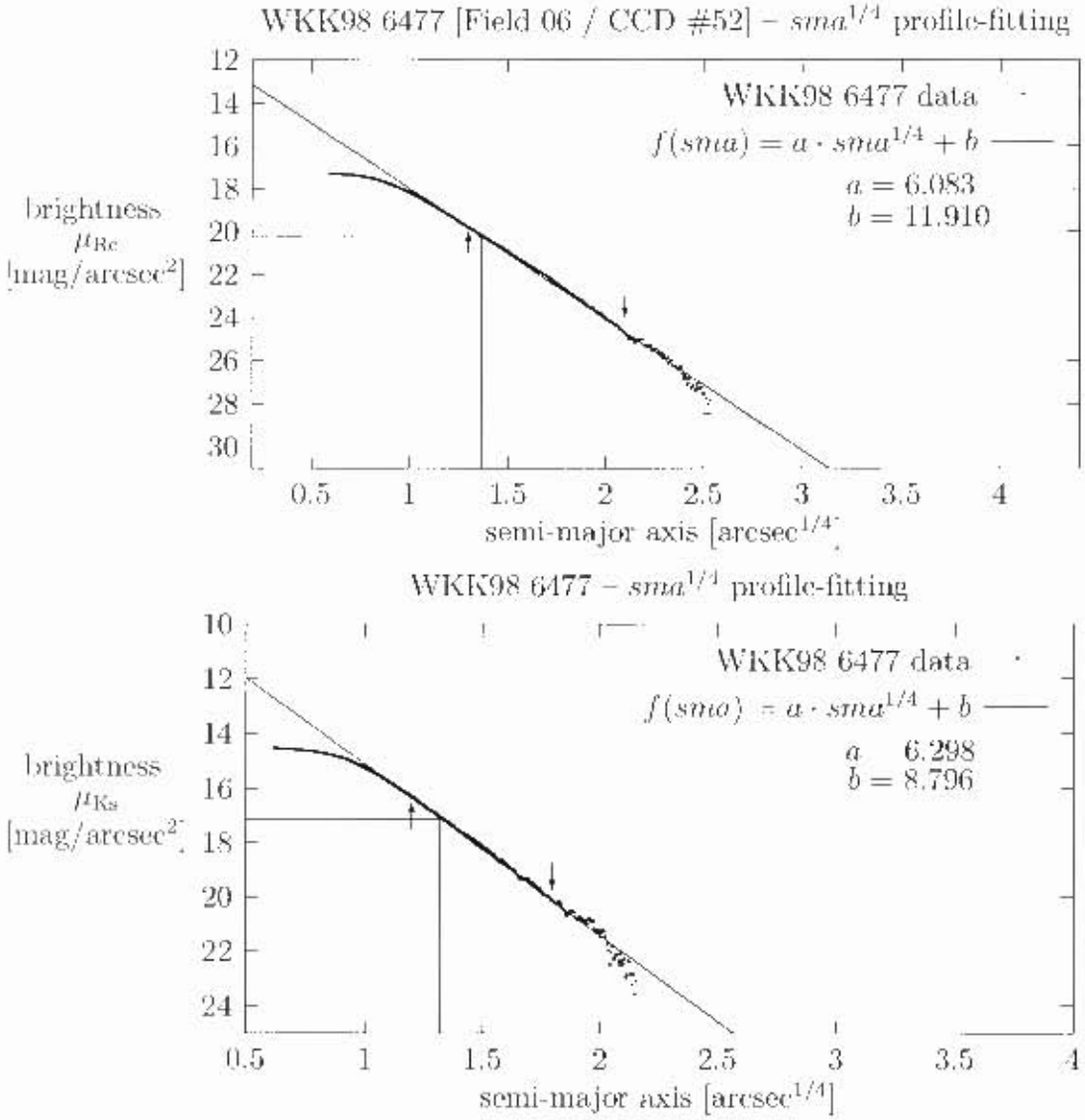

Figure 28.6: Galaxy WKK 6477, plots of brightness (μ_{R_c} and μ_{K_s}) versus semi-major axis sma$^{1/4}$ to demonstrate the profile-fitting. The arrows point to the upper and lower limit of the data set that was used for the fit. The resulting effective (half-light) radius $r_e^{1/4}$ and effective (half-light) surface brightness μ_e are indicated by straight lines.

Chapter 29

Galaxy WKK 6555

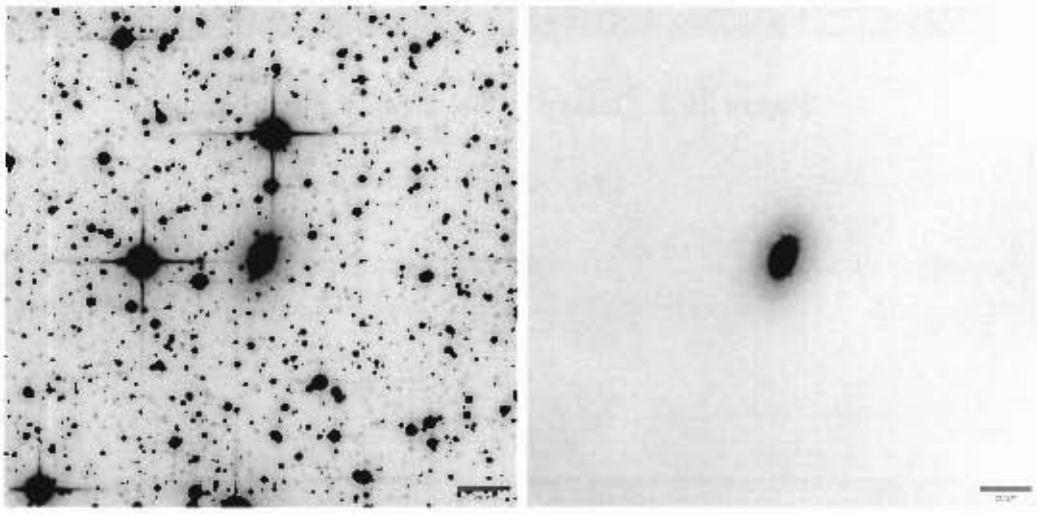

Figure 29.1: Galaxy WKK 6555, R_c band images, field 06, WFI CCD #51

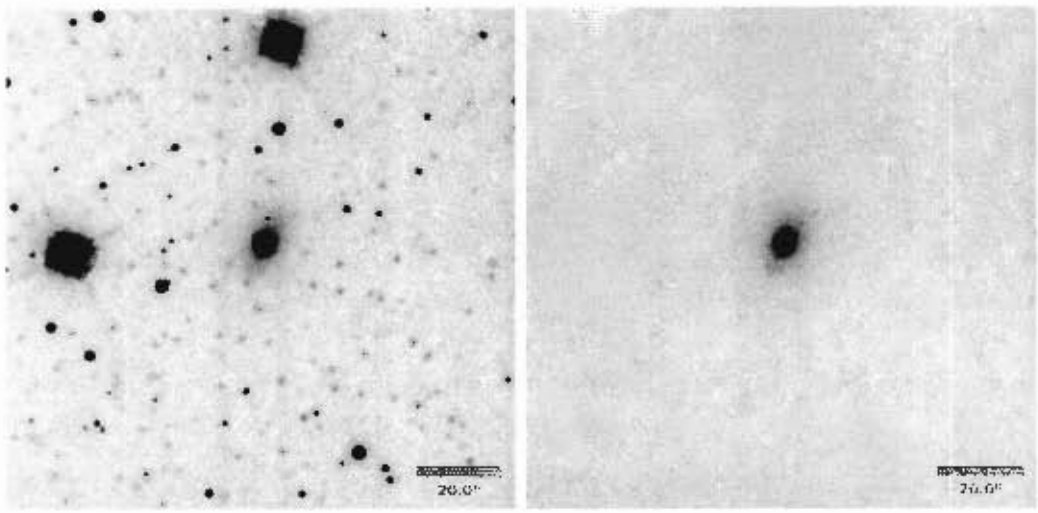

Figure 29.2: Galaxy WKK 6555, K_s band images

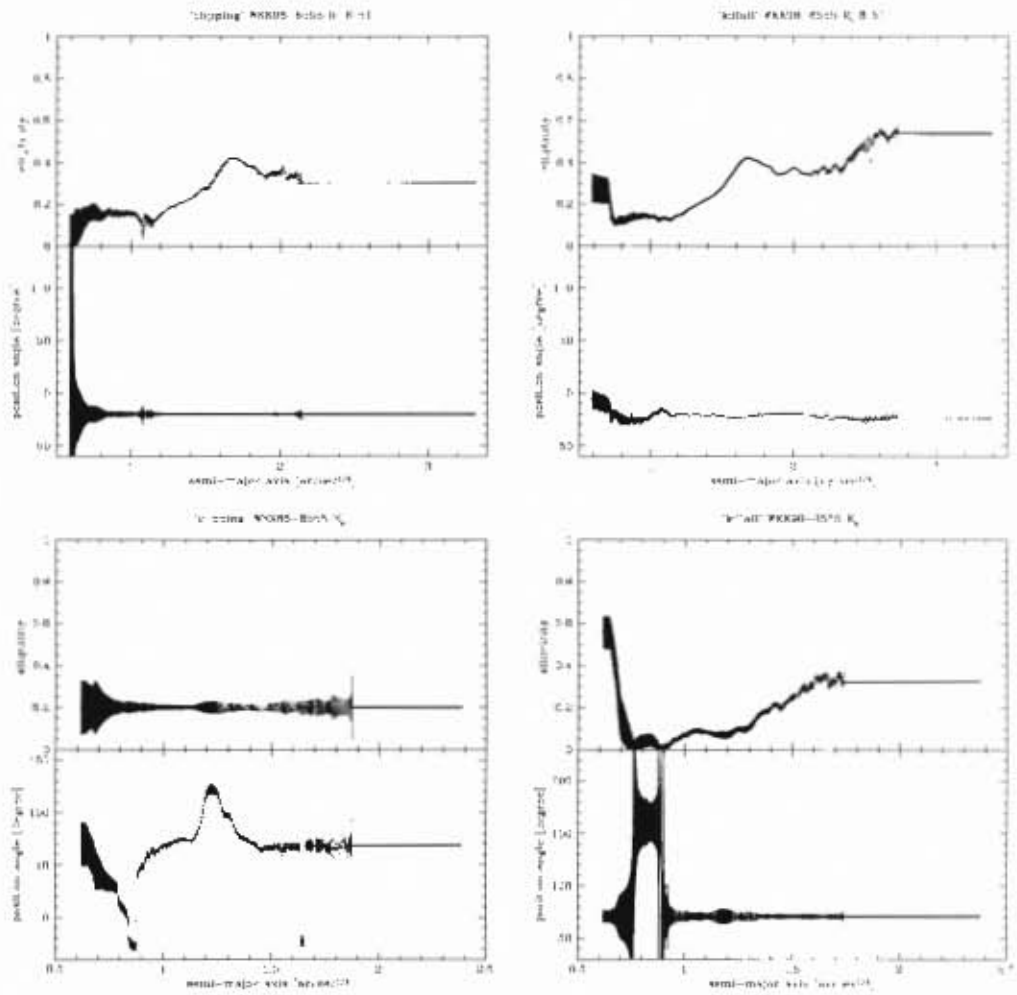

Figure 29.3: Galaxy WKK 6555, ellipticity and position angle plots

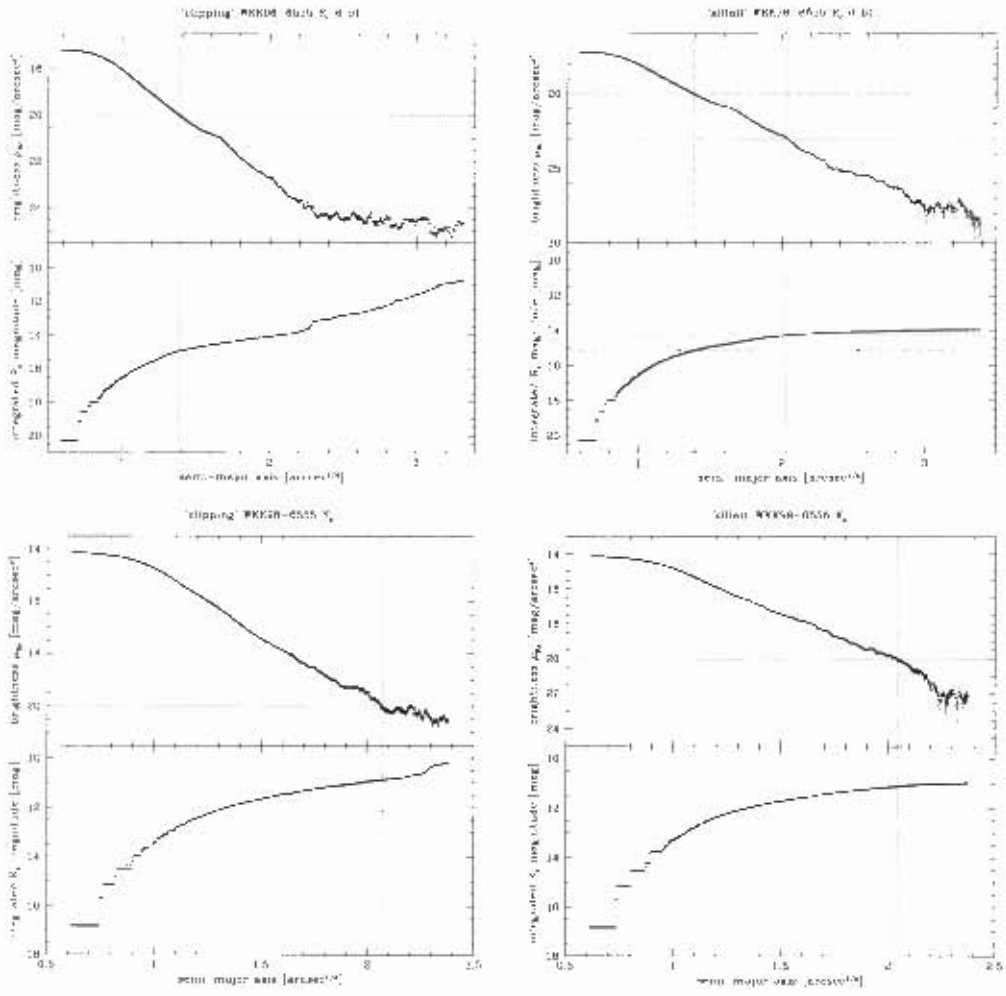

Figure 29.4: Galaxy WKK 6555, isophotal and integrated magnitude plots

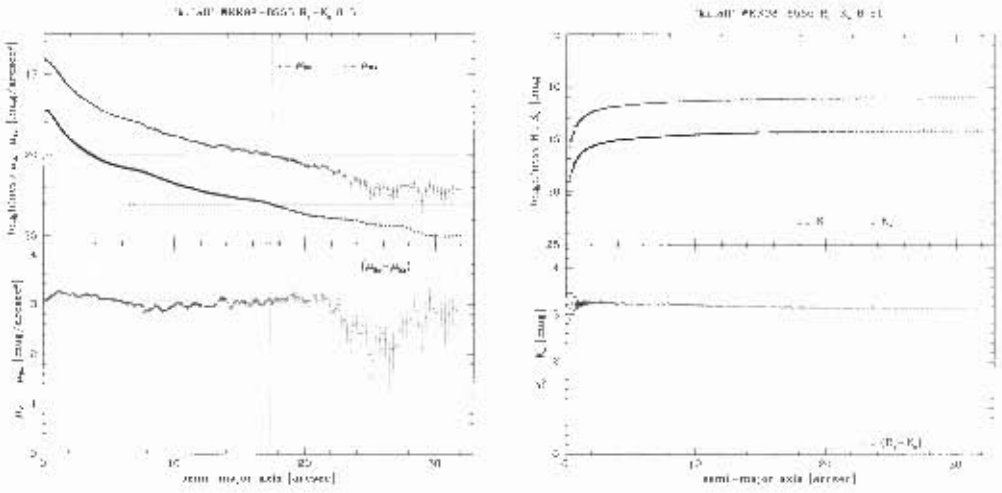

Figure 29.5: Galaxy WKK 6555: $(\mu_{R_c} - \mu_{K_s})$ and $(R_c - K_s)$ magnitude plots

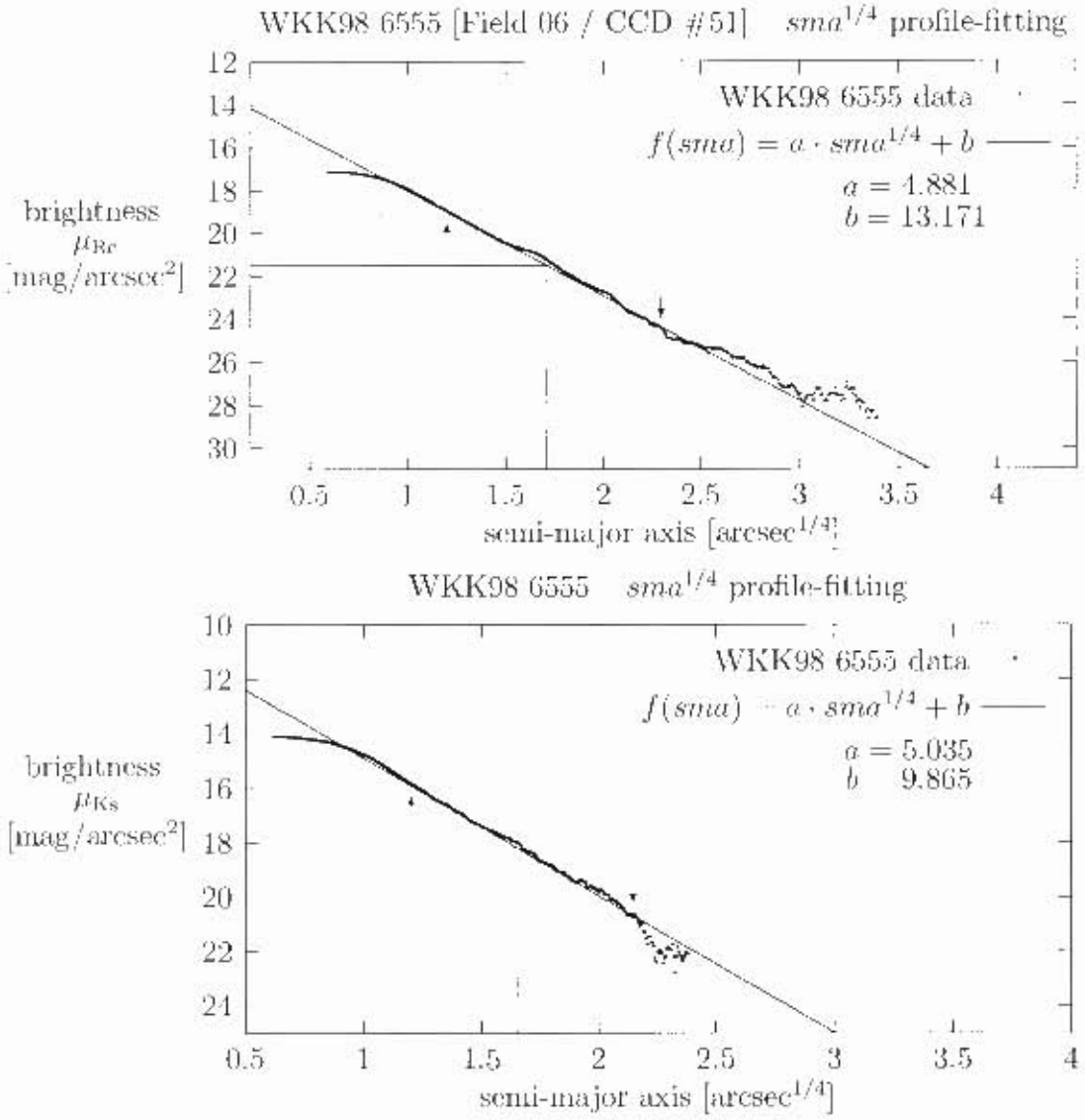

Figure 29.6: Galaxy WKK 6555, plots of brightness (μ_{R_c} and μ_{K_s}) versus semi-major axis $sma^{1/4}$ to demonstrate the profile-fitting. The arrows point to the upper and lower limit of the data set that was used for the fit. The resulting effective (half-light) radius $r_e^{1/4}$ and effective (half-light) surface brightness μ_e are indicated by straight lines.

Chapter 30

Galaxy WKK 6600

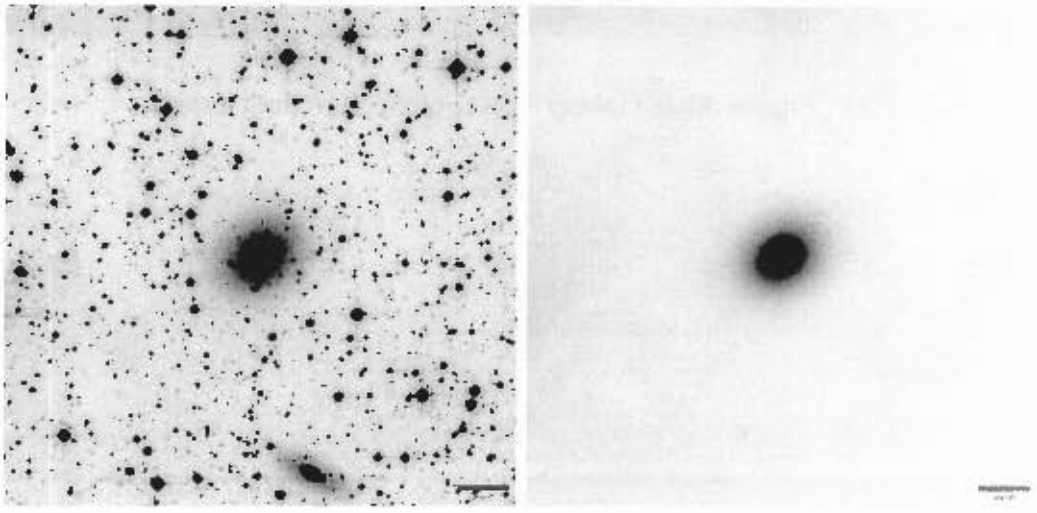

Figure 30.1: Galaxy WKK 6600, R_c band images, field 07, WFI CCD #50

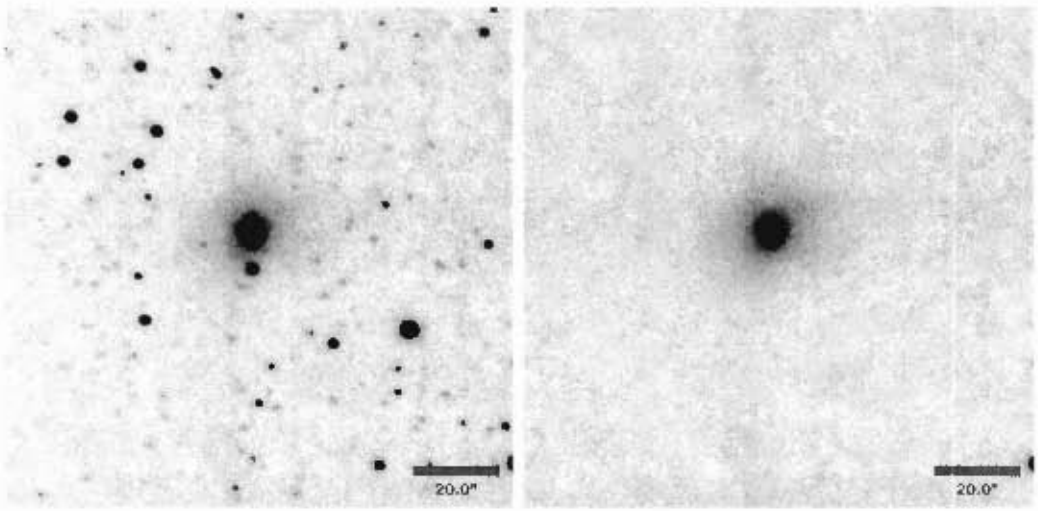

Figure 30.2: Galaxy WKK 6600, K_s band images

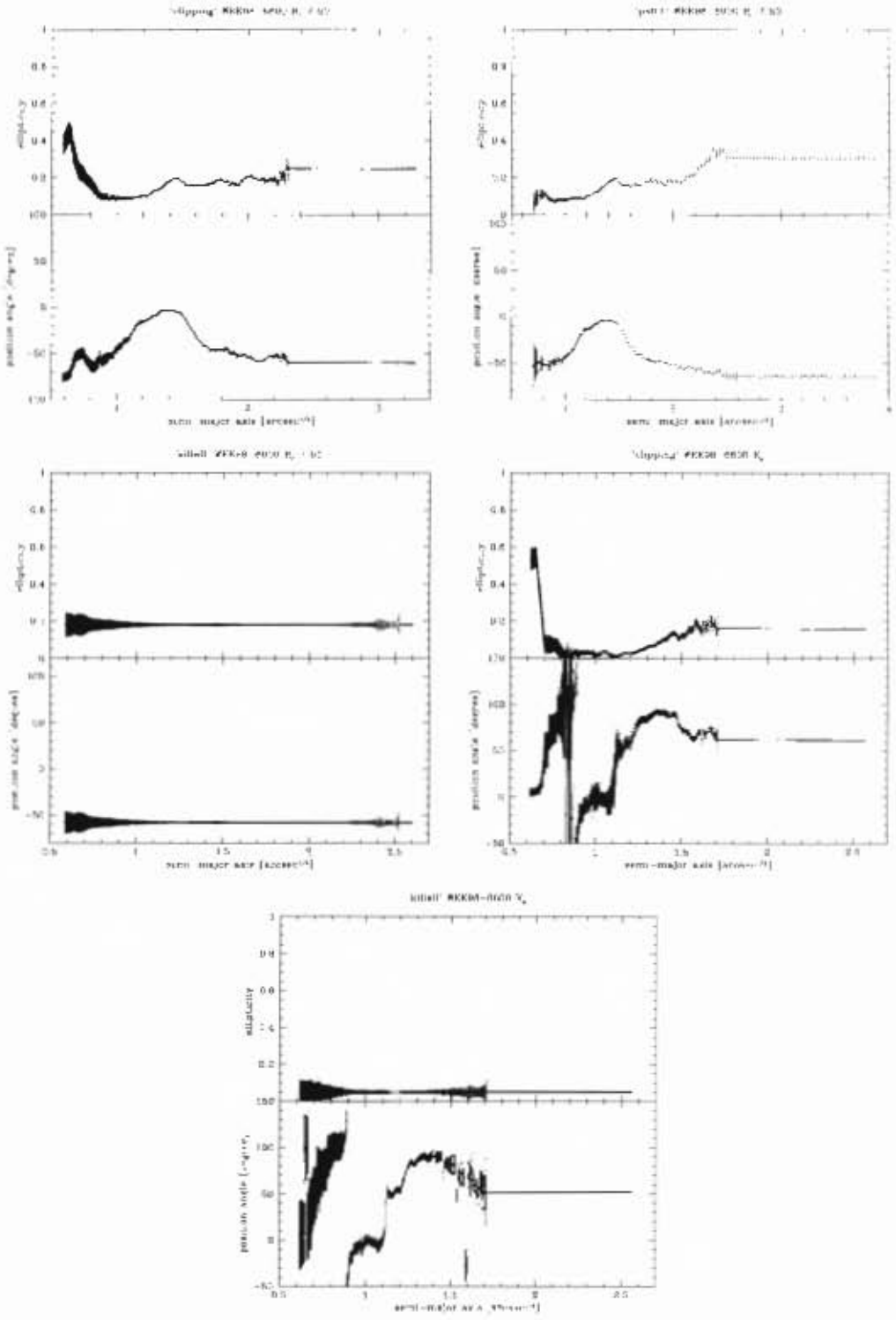

Figure 30.3: Galaxy WKK 6600, ellipticity and position angle plots

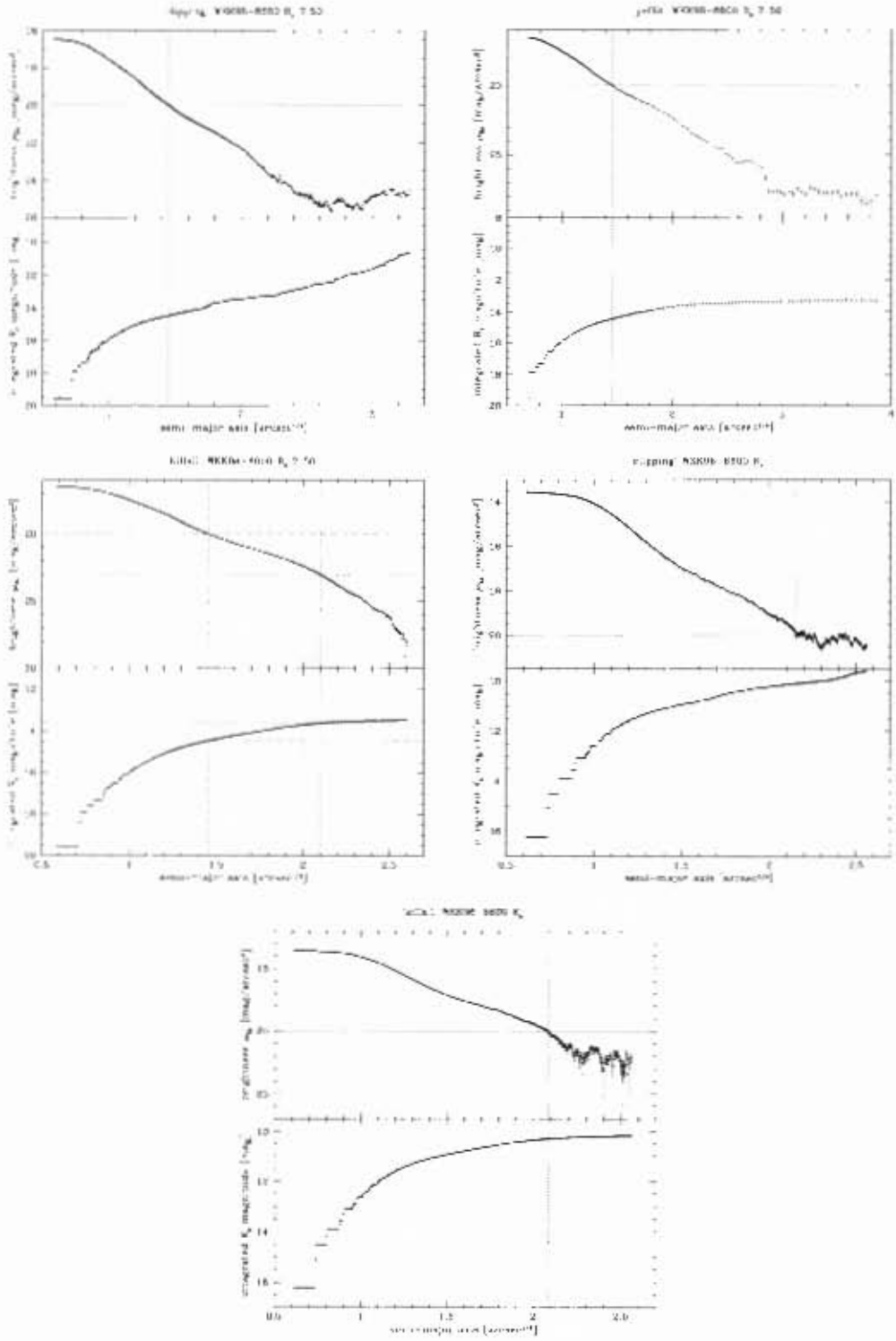

Figure 30.4: Galaxy WKK 6600, isophotal and integrated magnitude plots

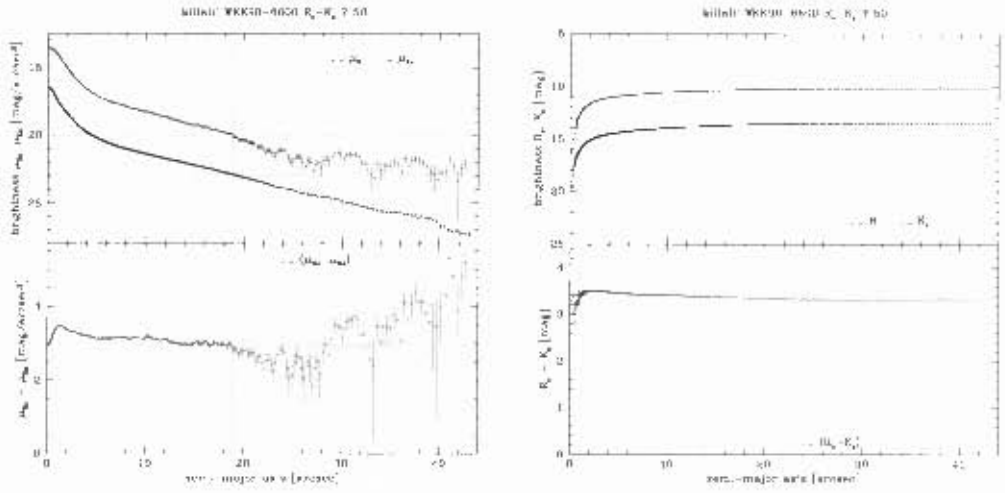

Figure 30.5: Galaxy WKK 6600, $(\mu_{R_c} - \mu_{K_s})$ and $(R_c - K_s)$ magnitude plots

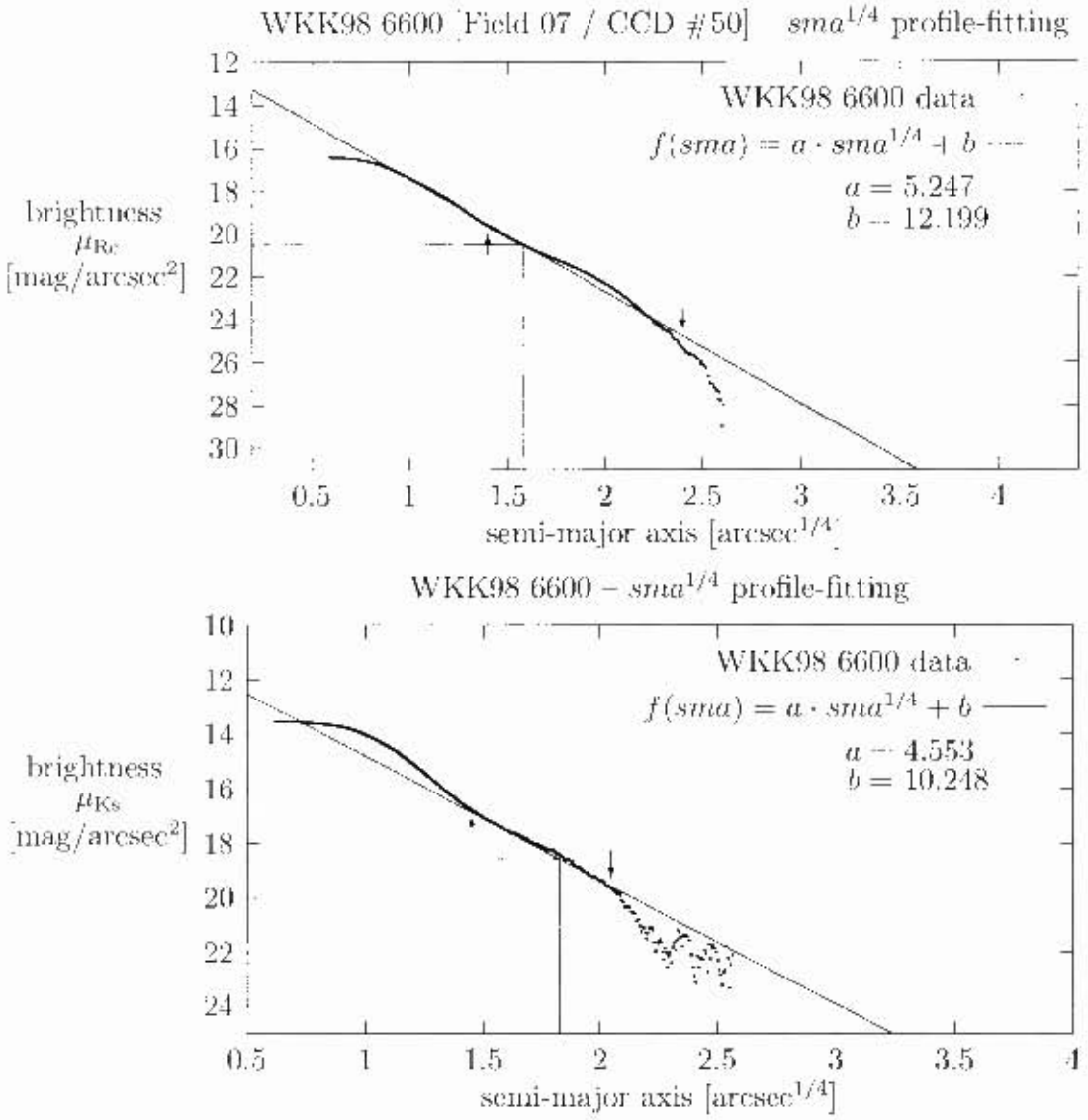

Figure 30.6: Galaxy WKK 6600, plots of brightness (μ_{R_c} and μ_{K_s}) versus semi-major axis sma$^{1/4}$ to demonstrate the profile-fitting. The arrows point to the upper and lower limit of the data set that was used for the fit. The resulting effective (half-light) radius $r_e^{1/4}$ and effective (half-light) surface brightness μ_e are indicated by straight lines.

Chapter 31

Galaxy WKK 6615

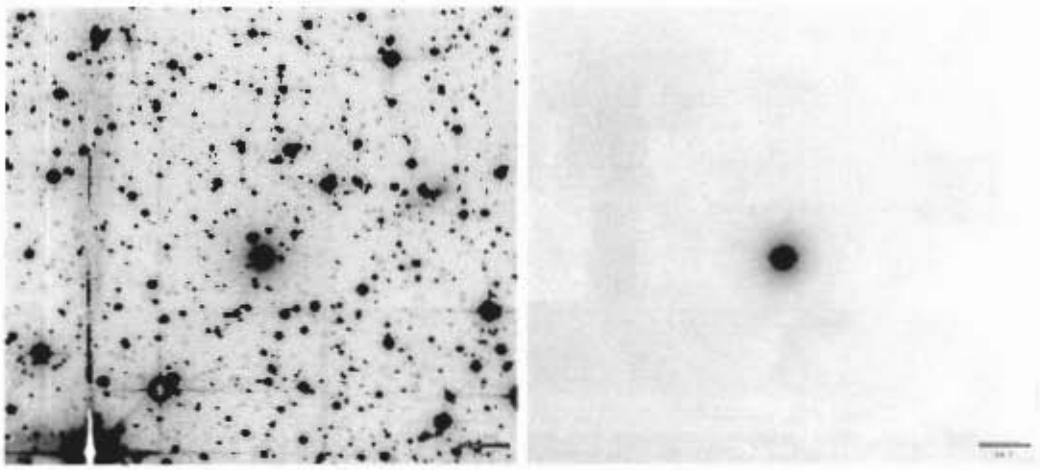

Figure 31.1: Galaxy WKK 6615, R_c band images, field 06, WFI CCD #57

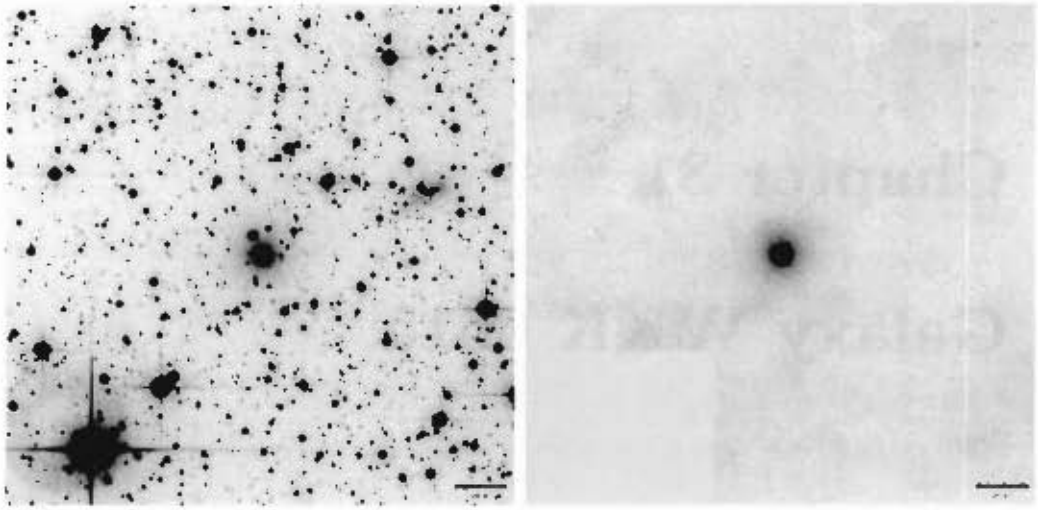

Figure 31.2: Galaxy WKK 6615, R_c band images, field 15, WFI CCD #50

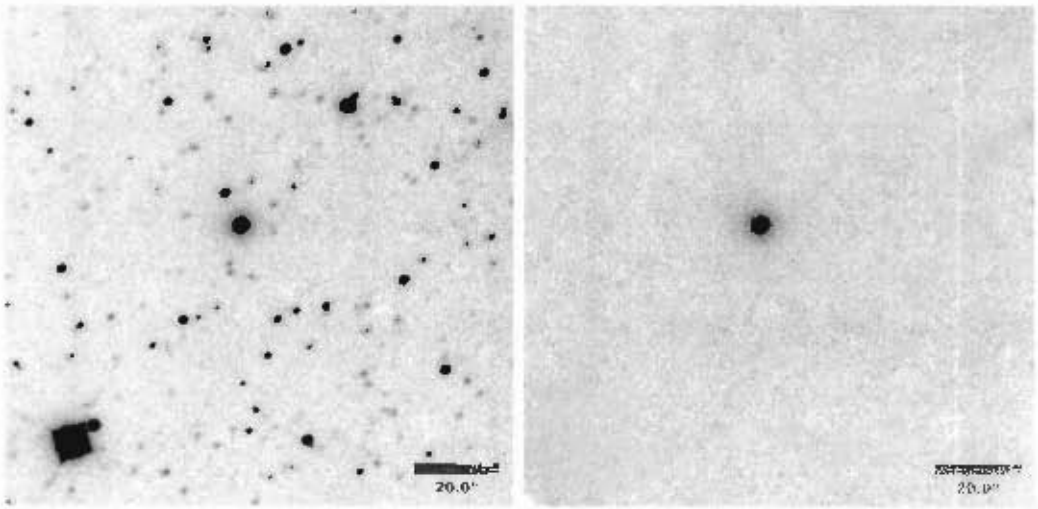

Figure 31.3: Galaxy WKK 6615, K_s band images

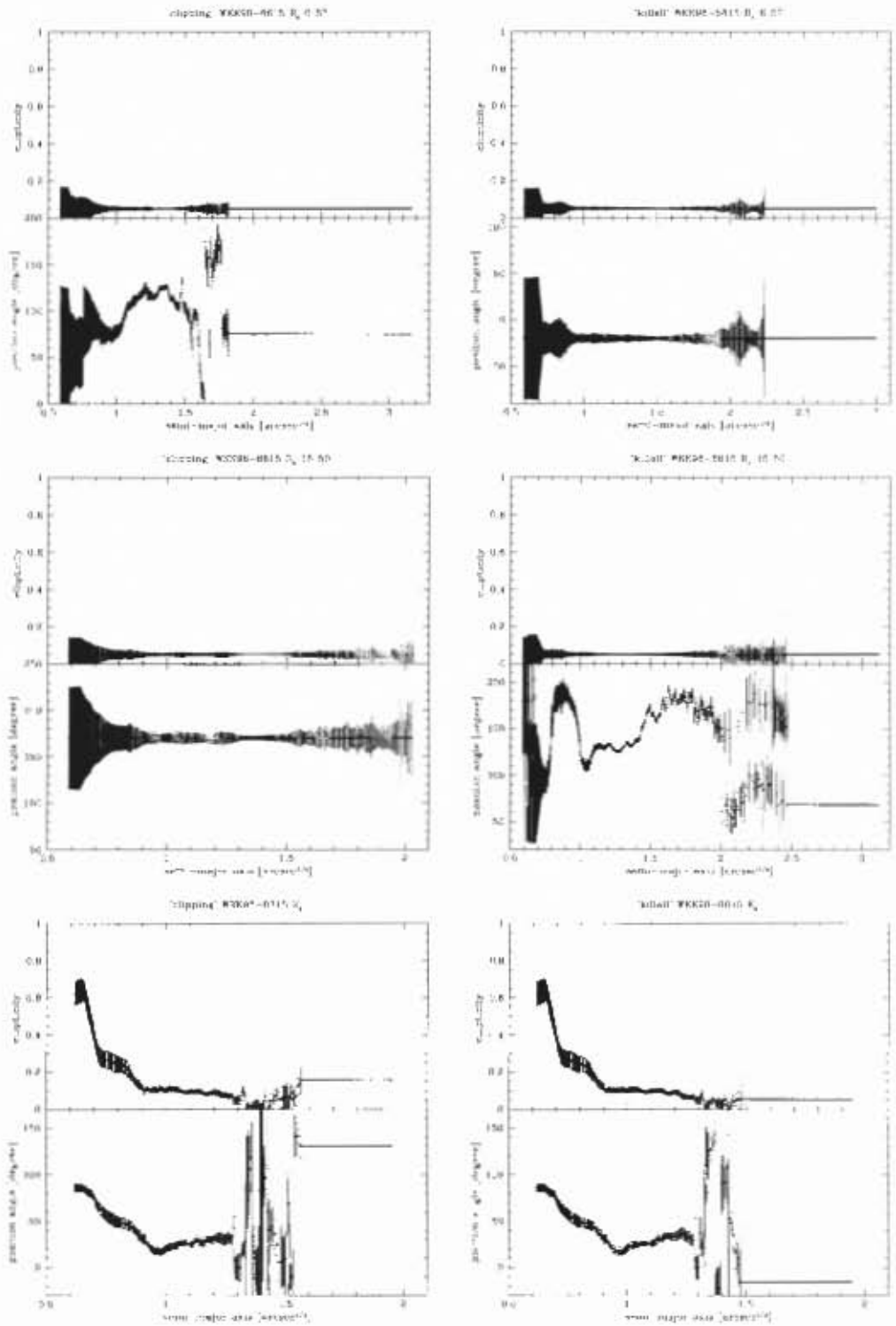

Figure 31.4: Galaxy WKK 6615, ellipticity and position angle plots

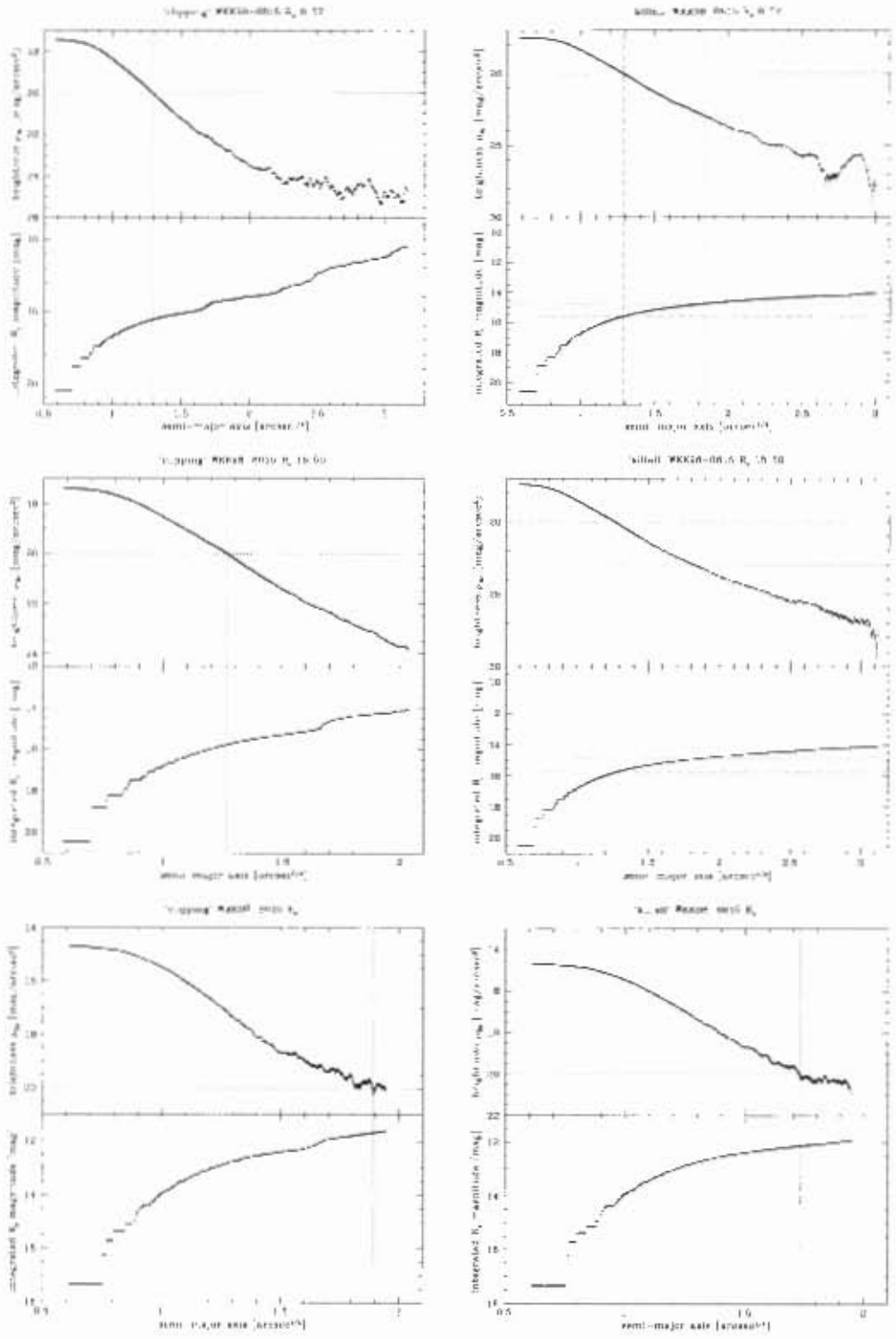

Figure 31.5: Galaxy WKK 6615, isophotal and integrated magnitude plots

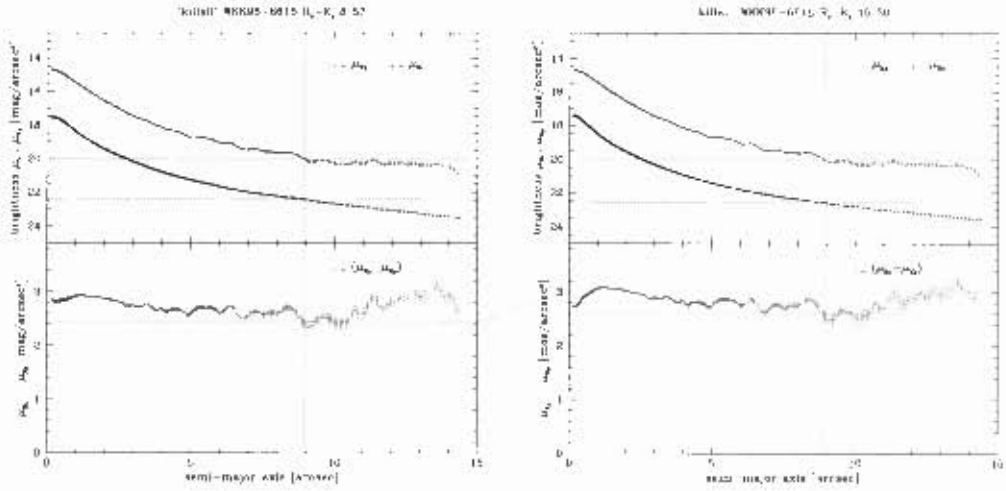

Figure 31.6: Galaxy WKK 6615. $(\mu_{R_c} - \mu_{K_s})$ magnitude plots

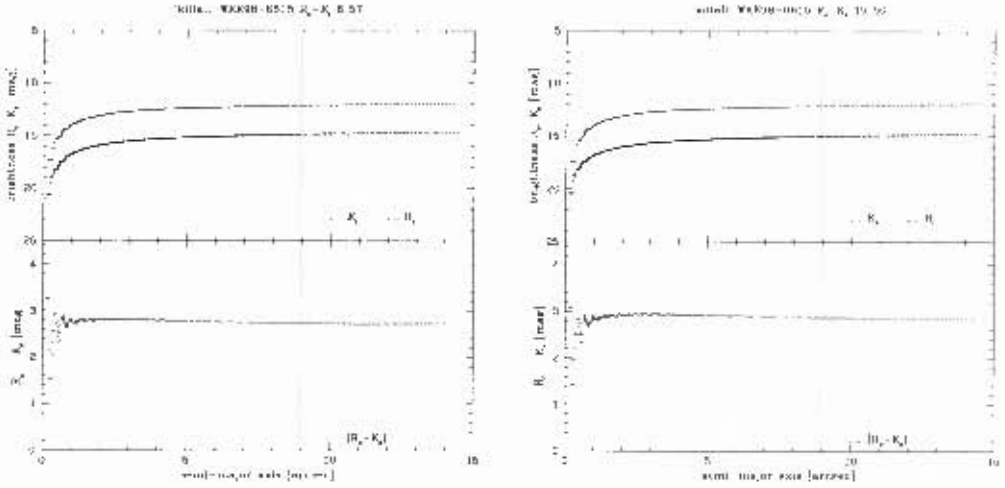

Figure 31.7: Galaxy WKK 6615, $(R_c - K_s)$ magnitude plots

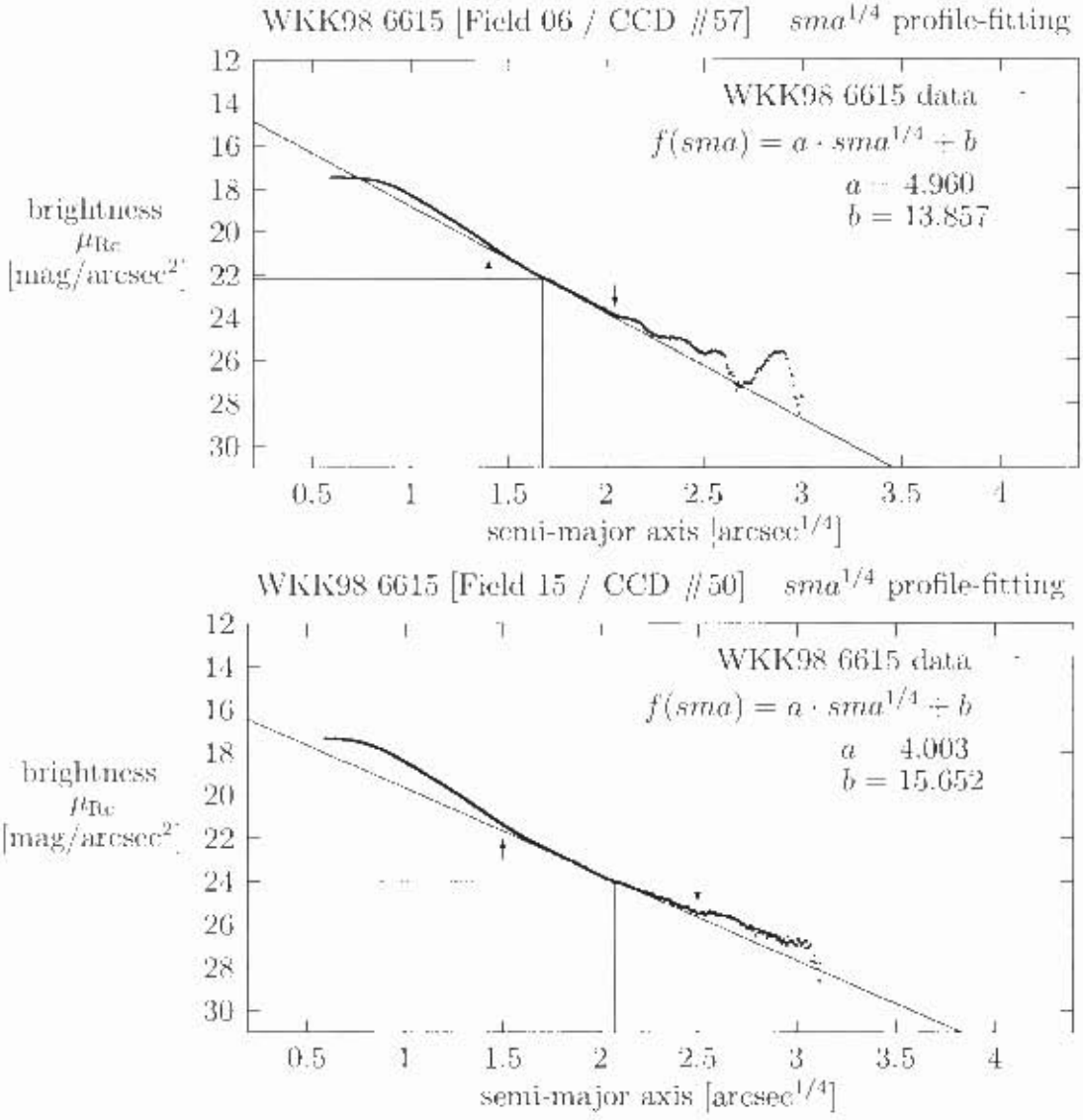

Figure 31.8: Galaxy WKK 6615, plots of brightness μ_{R_c} versus semi-major axis $sma^{1/4}$ to demonstrate the profile-fitting. The arrows point to the upper and lower limit of the data set that was used for the fit. The resulting effective (half-light) radius $r_e^{1/4}$ and effective (half-light) surface brightness μ_e are indicated by straight lines.

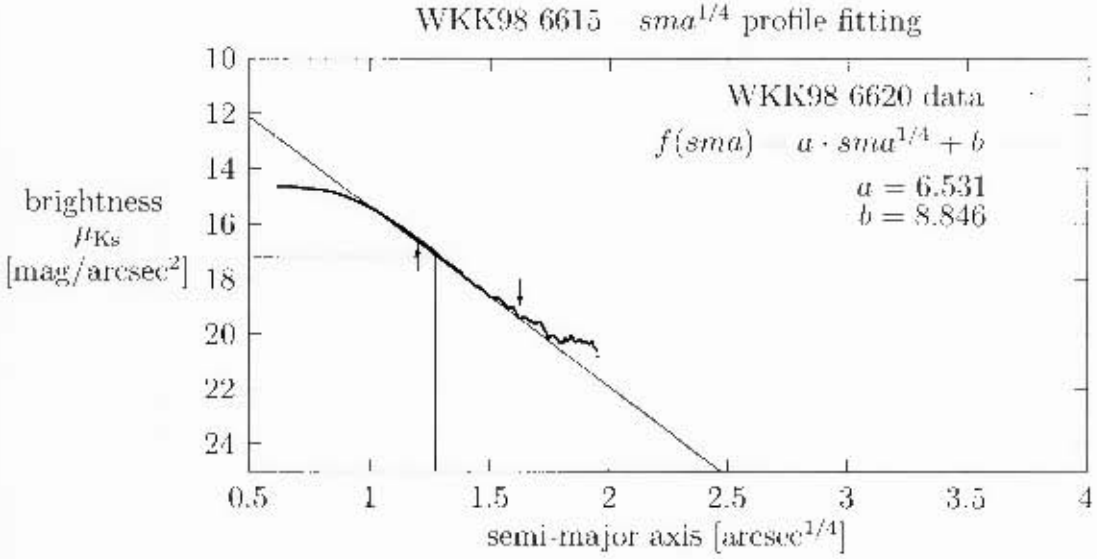

Figure 31.9: Galaxy WKK 6615, plot of brightness μ_{K_s} versus semi-major axis $sma^{1/4}$ to demonstrate the profile-fitting. The arrows point to the upper and lower limit of the data set that was used for the fit. The resulting effective (half-light) radius $r_e^{1/4}$ and effective (half-light) surface brightness μ_e are indicated by straight lines.

Chapter 32

Galaxy WKK 6620

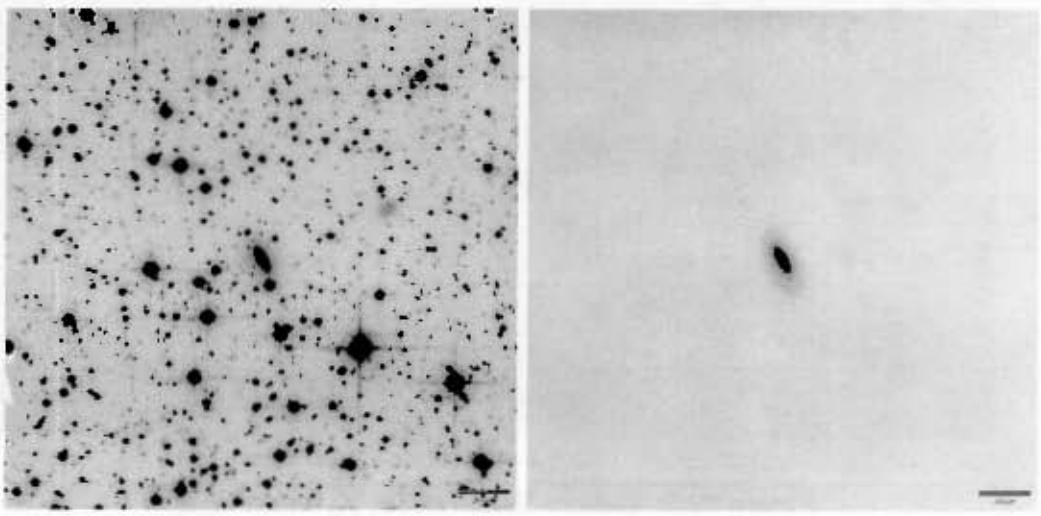

Figure 32.1: Galaxy WKK 6620. R_c band images, field 06, WFI CCD #57

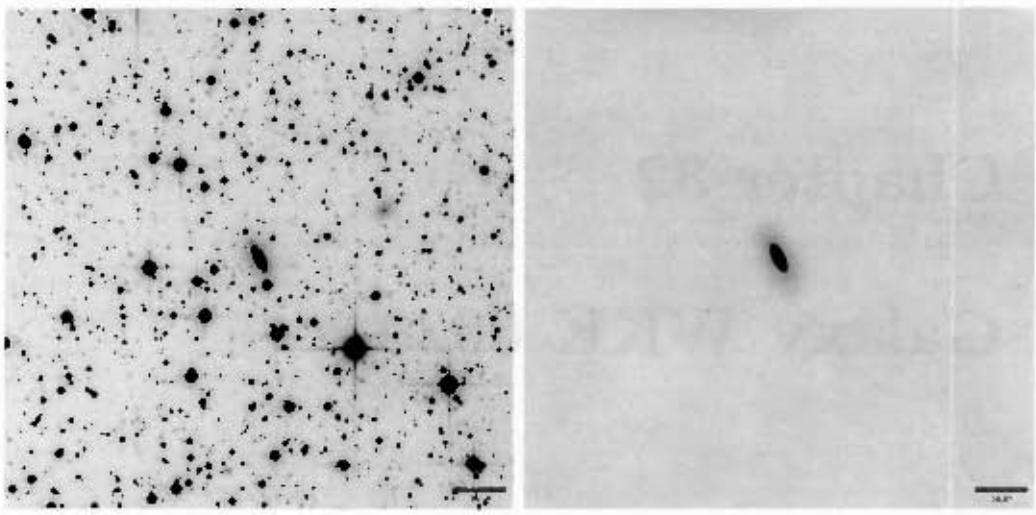

Figure 32.2: Galaxy WKK 6620, R_c band images, field 16, WFI CCD #54

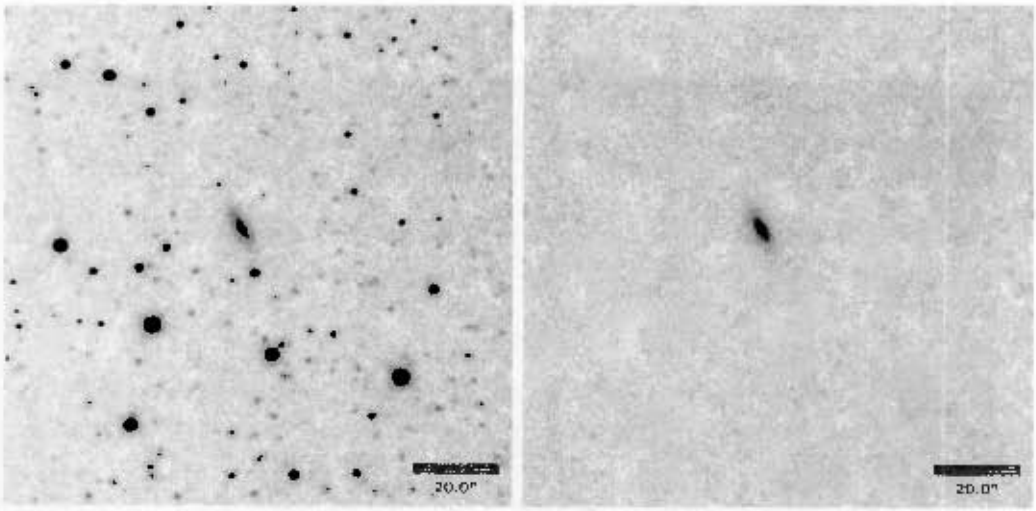

Figure 32.3: Galaxy WKK 6620, K_s band images

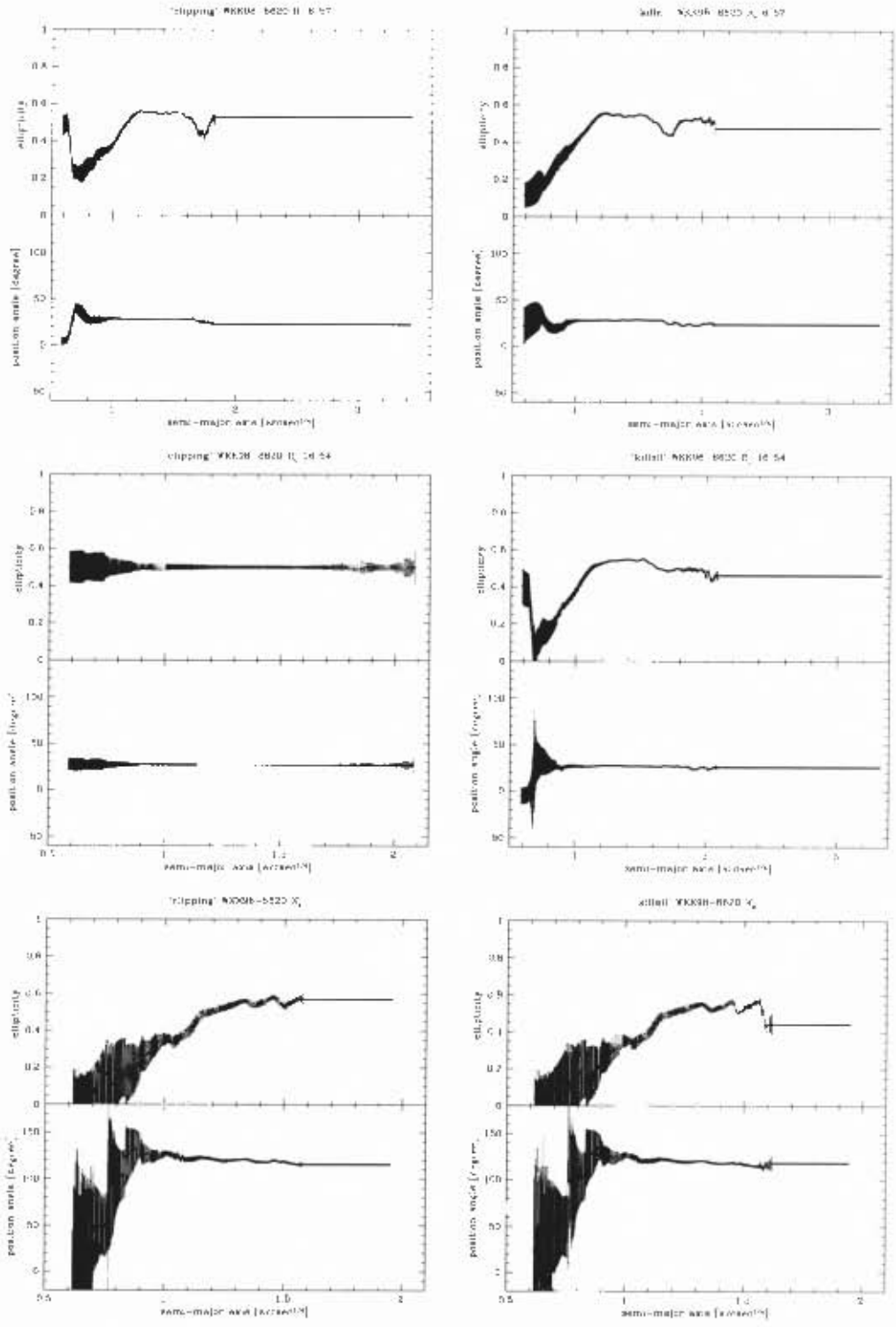

Figure 32.4: Galaxy WKK 6620, ellipticity and position angle plots

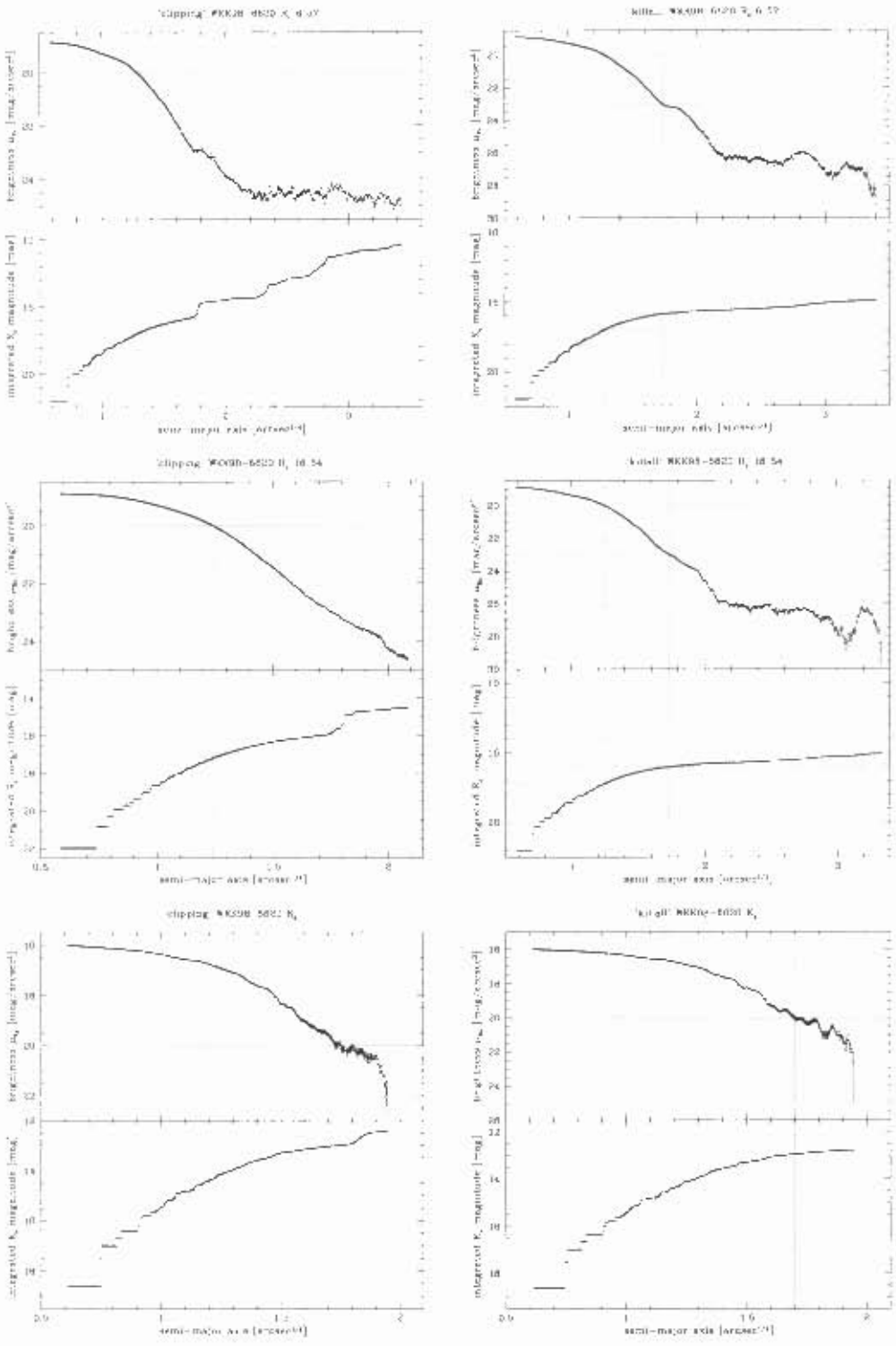

Figure 32 5: Galaxy WKK 6620, isophotal and integrated magnitude plots

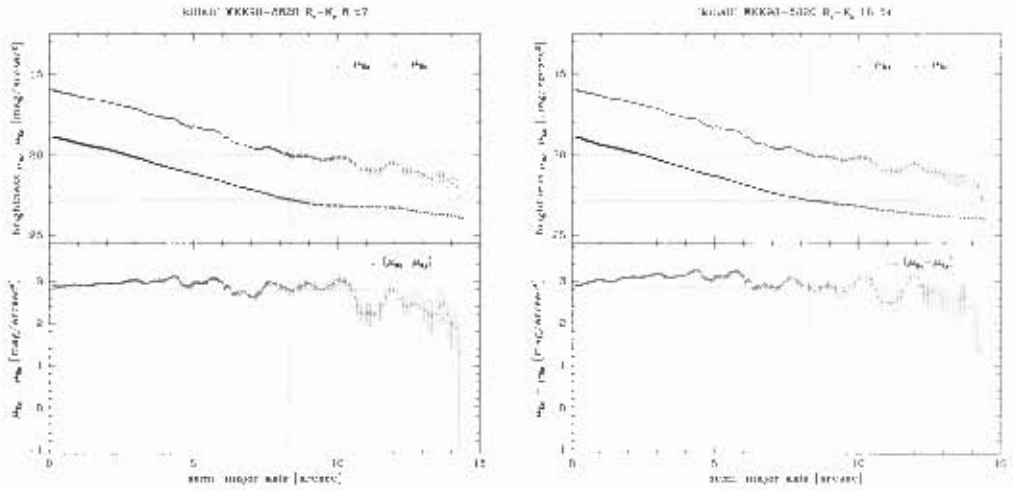

Figure 32.6: Galaxy WKK 6620. $(\mu_{R_c} - \mu_{K_s})$ magnitude plots

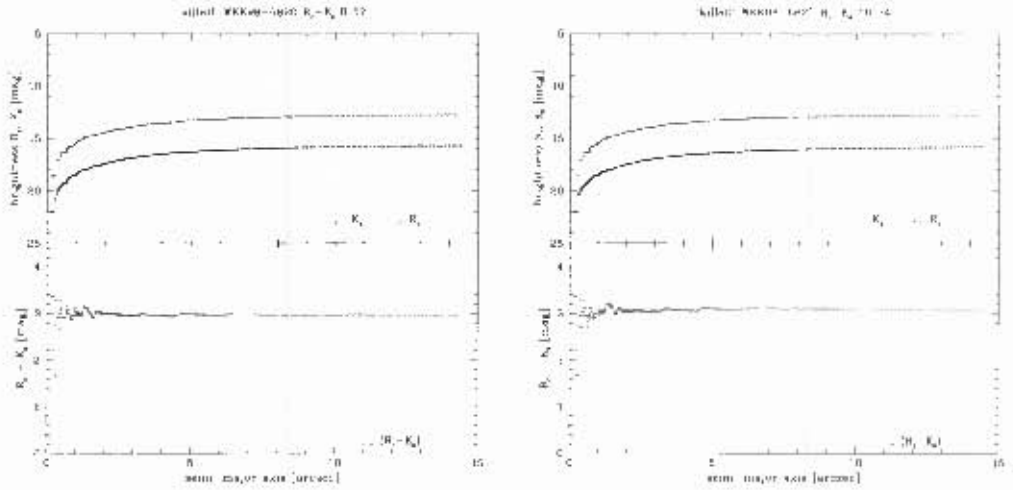

Figure 32.7: Galaxy WKK 6620. $(R_c - K_s)$ magnitude plots

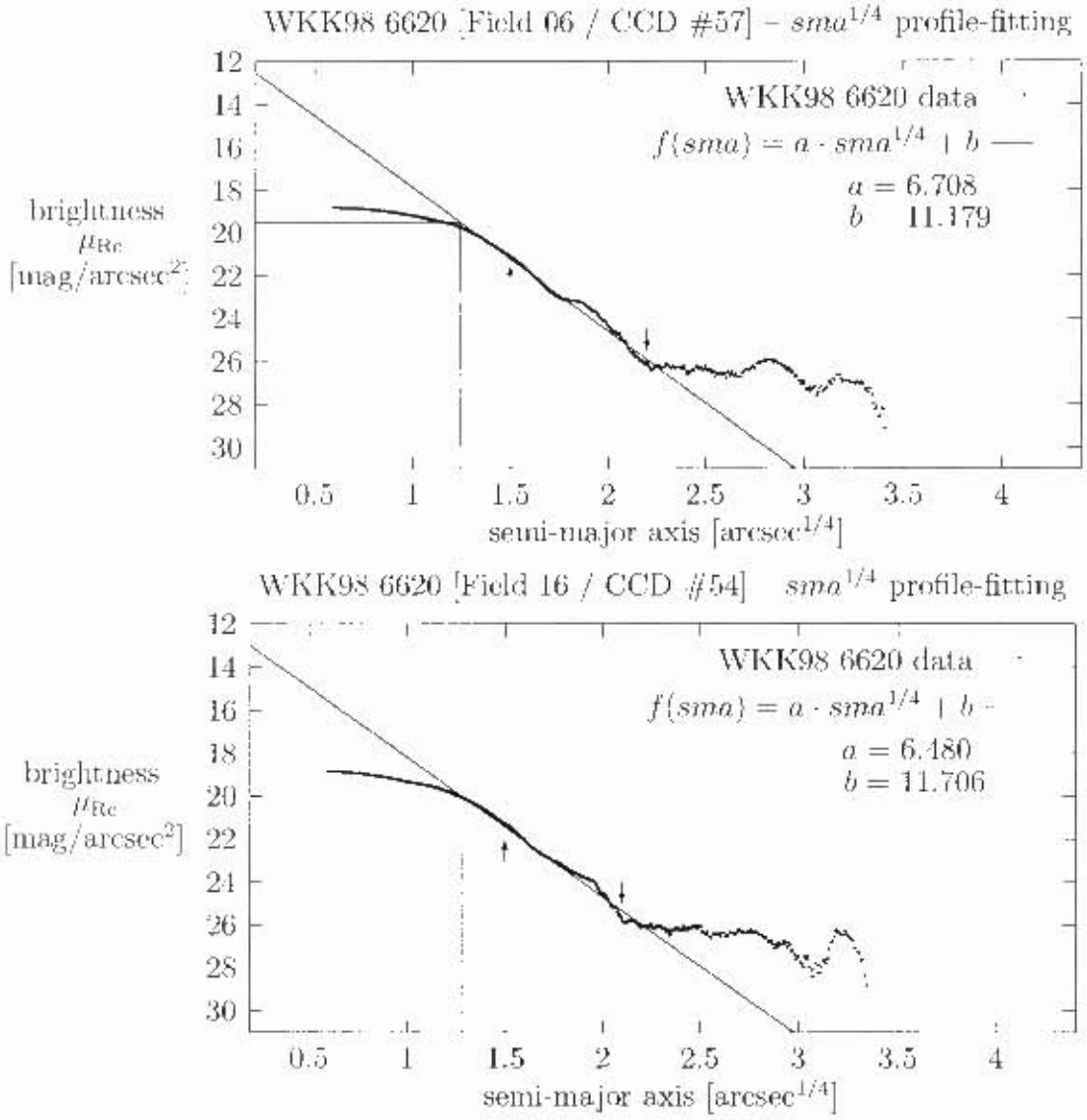

Figure 32.8: Galaxy WKK 6620, plots of brightness μ_{R_c} versus semi-major axis $sma^{1/4}$ to demonstrate the profile-fitting. The arrows point to the upper and lower limit of the data set that was used for the fit. The resulting effective (half-light) radius $r_e^{1/4}$ and effective (half-light) surface brightness μ_e are indicated by straight lines.

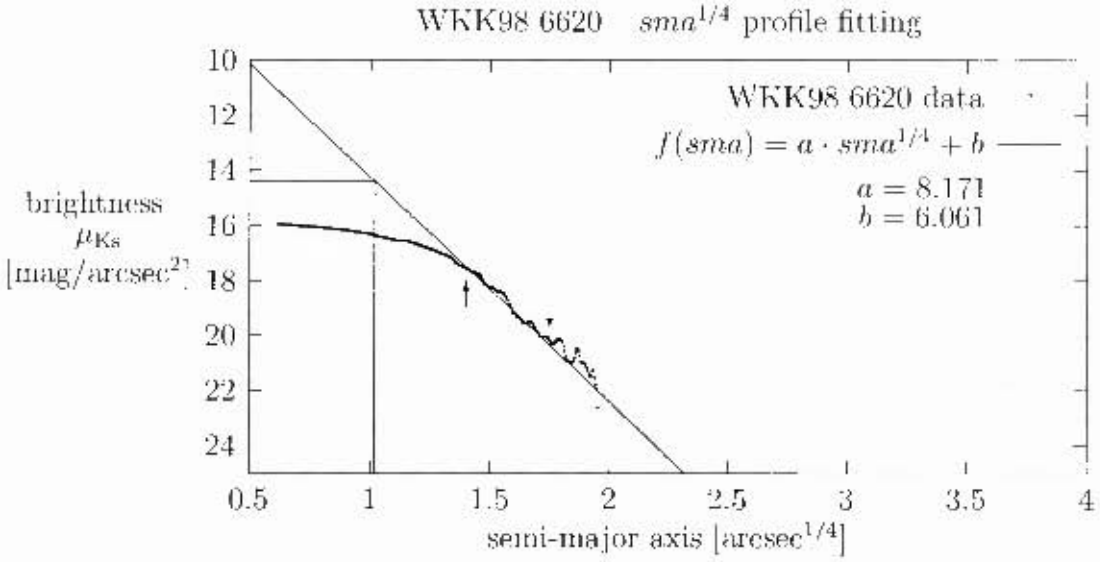

Figure 32.9: Galaxy WKK 6620, plot of brightness μ_{K_s} versus semi-major axis $\mathrm{sma}^{1/4}$ to demonstrate the profile-fitting. The arrows point to the upper and lower limit of the data set that was used for the fit. The resulting effective (half-light) radius $r_e^{1/4}$ and effective (half-light) surface brightness μ_e are indicated by straight lines.

Chapter 33

Galaxy WKK 6679

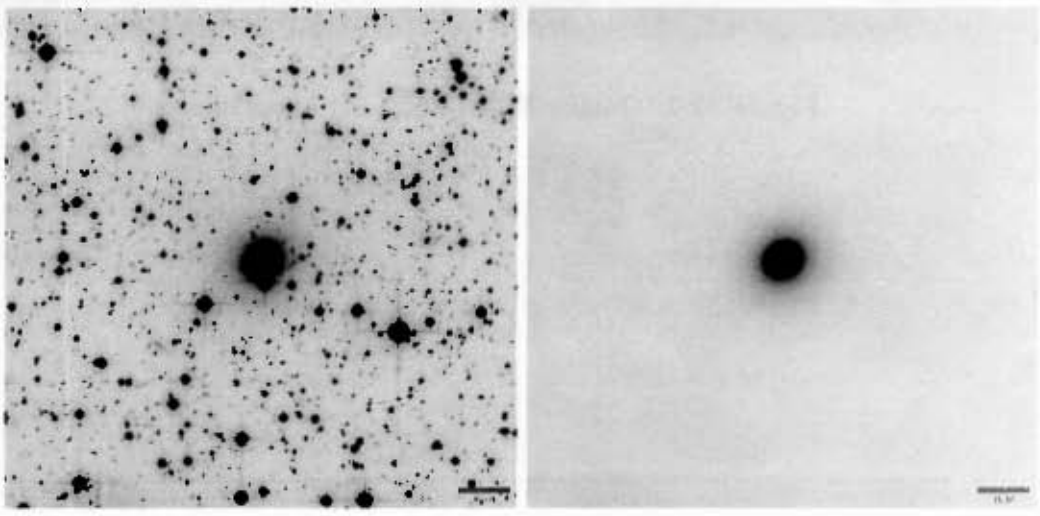

Figure 33.1: Galaxy WKK 6679, R_c band images, field 03, WFI CCD #53

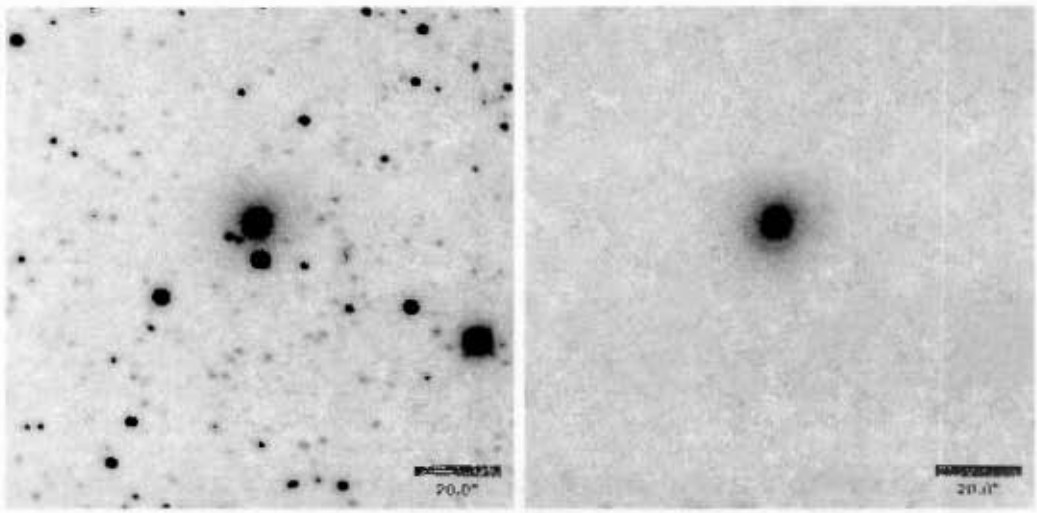

Figure 33.2: Galaxy WKK 6679, K_s band images

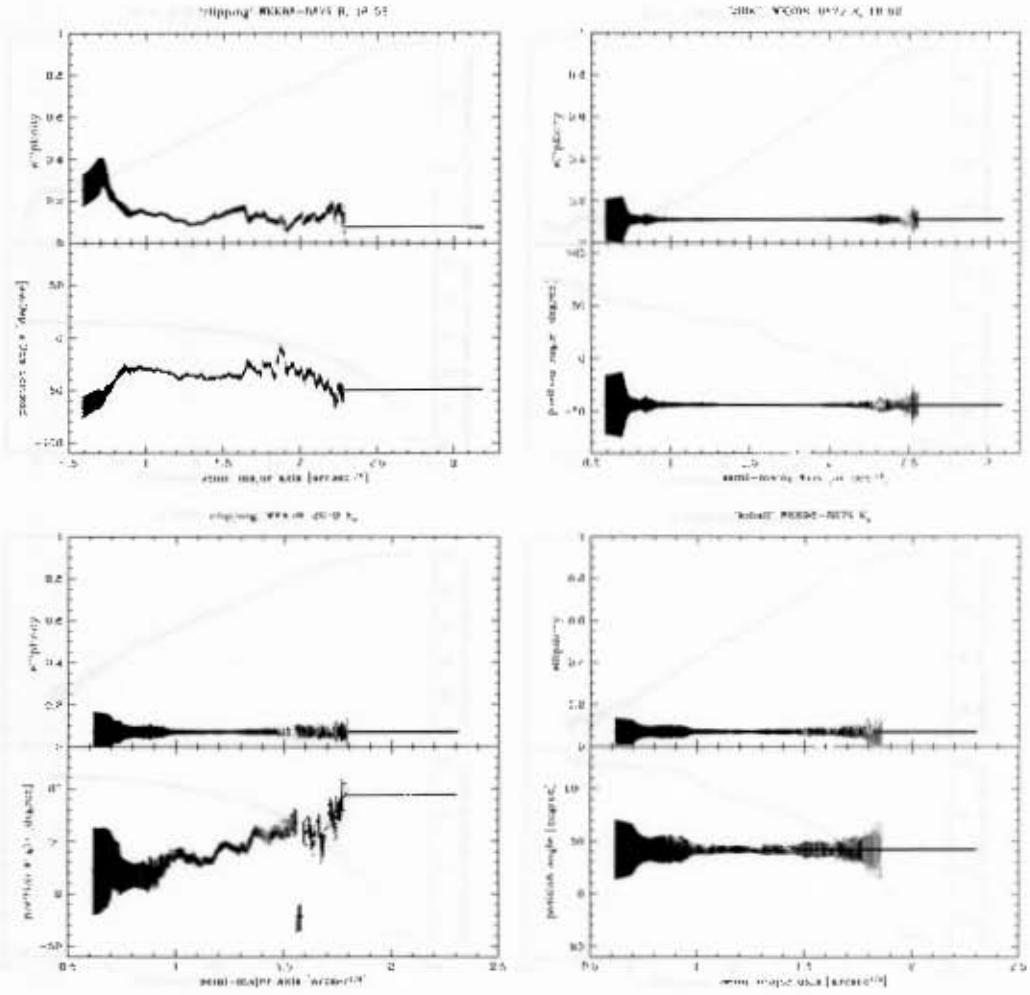

Figure 33.3: Galaxy WKK 6679, ellipticity and position angle plots

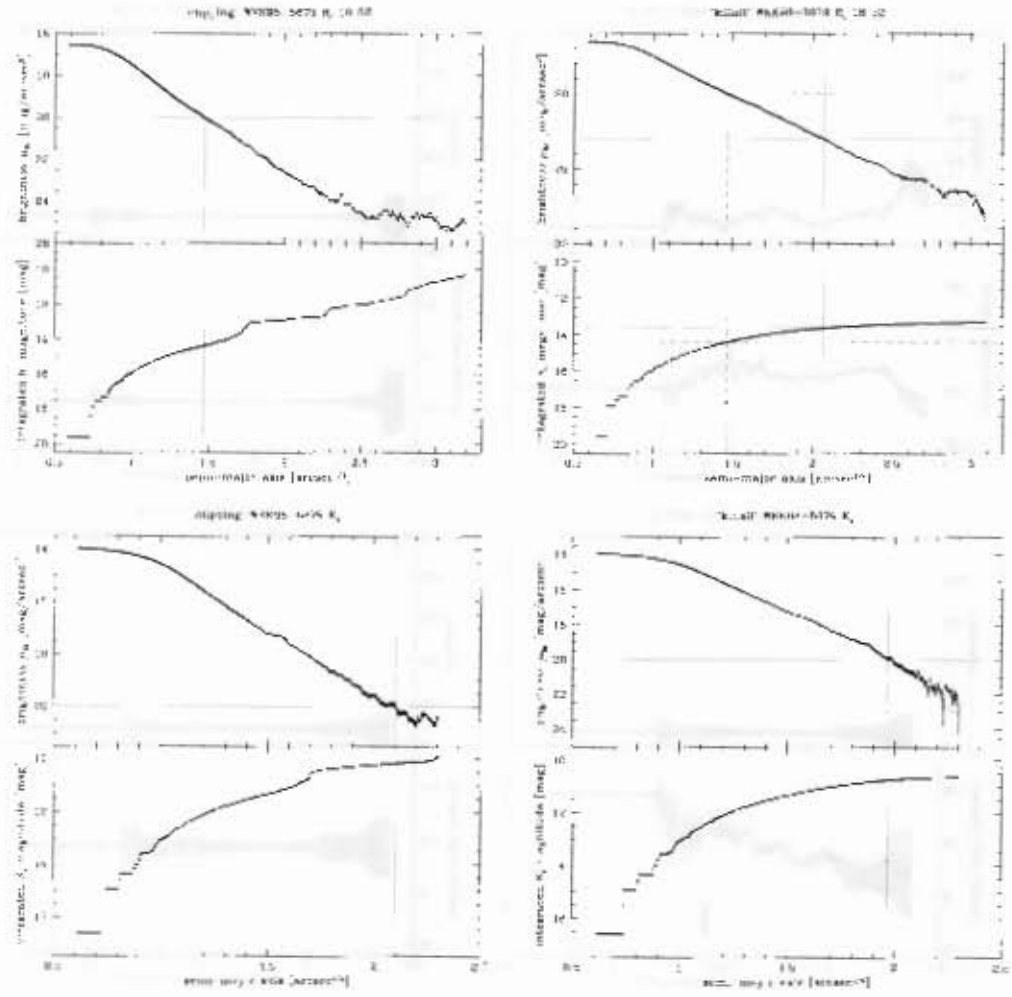

Figure 33.4: Galaxy WKK 6679, isophotal and integrated magnitude plots

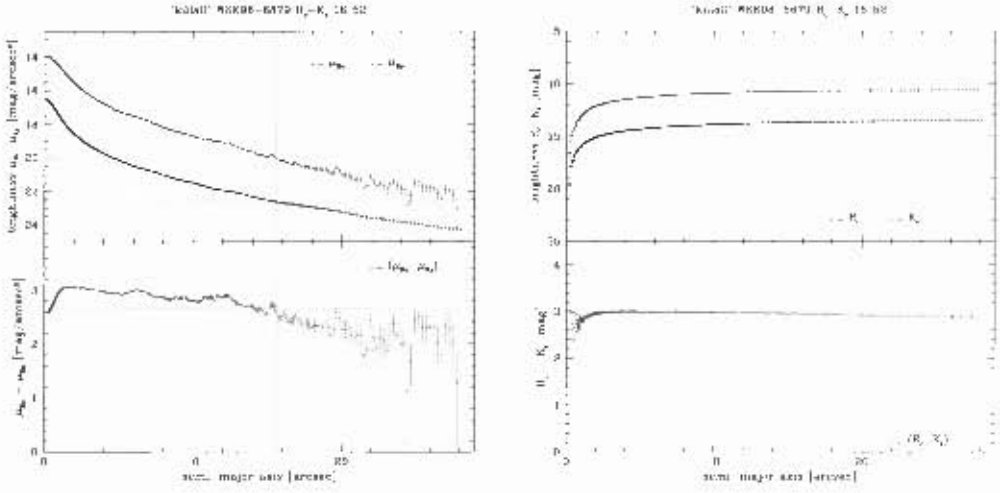

Figure 33.5: Galaxy WKK 6679, $(\mu_{H_c} - u_{K_c})$ and $(R_c - K_s)$ magnitude plots

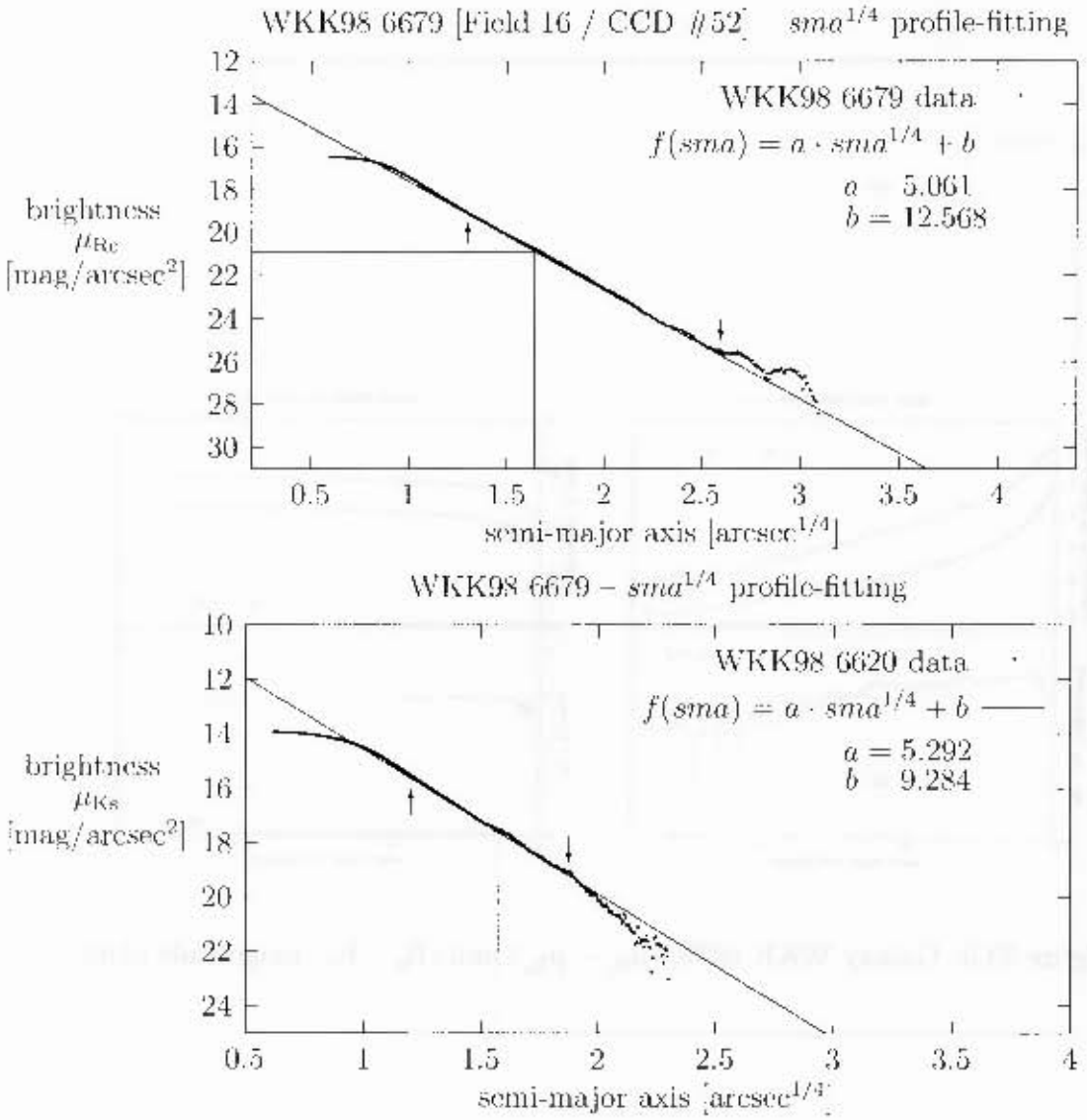

Figure 33.6: Galaxy WKK 6679, plots of brightness (μ_{R_c} and μ_{K_s}) versus semi-major axis sma$^{1/4}$ to demonstrate the profile-fitting. The arrows point to the upper and lower limit of the data set that was used for the fit. The resulting effective (half-light) radius $r_e^{1/4}$ and effective (half-light) surface brightness μ_e are indicated by straight lines.

Bibliography

R. J. Buta and M. L. McCall. The IC 342/Maffei Group Revealed. *Astrophysical Journal Supplement Series*, 124:33, 1999.

W. A. Joye and E. Mandel. New Features of SAOImage DS9. In *ASP Conf. Ser. 295: Astronomical Data Analysis Software and Systems XII*, pages 489–+, 2003.

R. H. Lupton and P. Monger. *The SM Reference Manual*, 1997. http://www.astro.princeton.edu/~rhl/sm/sm.html.

A. Mellinger. Die Milchstraße im Computer. *Sterne und Weltraum*, 39:174, 2000.

F. Ochsenbein, P. Bauer, and J. Marcout. The VizieR database of astronomical catalogues. *Astronomy and Astrophysics Supplement Series*, 143: 23–32, 2000.

C. Y. Peng et al. Detailed Structural Decomposition of Galaxy Images. *Astronomical Journal*, 124:266–293, 2002.

A. Shutte, editor. *Philosophy for Africa*. Marquette University Press, 1995. ISBN 08-7462-6080.

D. Tody. The IRAF Data Reduction and Analysis System. In D. L. Crawford, editor, *Instrumentation in astronomy VI; Proceedings of the Meeting, Tucson, AZ, Mar. 4-8, 1986. Part 2 (A87-36376 15-35). Bellingham, WA,*

Society of Photo-Optical Instrumentation Engineers, 1986, p. 733., volume 627, page 733, 1986.

D. Tody. IRAF in the Nineties. In J. Barnes R. J. Hanisch, R. J. V. Brissenden, editor, *Astronomical Data Analysis Software and Systems II*, volume 52 of *ASPCS*, page 173, 1993.

P. A. Woudt. *Large Scale Structures behind the Southern Milky Way*. Ph.D. Dissertation, University of Cape Town, June 1998.

Appendix A

Selection of Utilised Abbreviations

Table A.1: Abbreviations used in this dissertation.

Abbreviation	Description
AAO	Anglo-Australian Observatory
ACO	Abell, Corwin and Olowin
ADU	Analog-to-Digital Unit
BTP	Behind The Plane
CIZA	Clusters in the Zone of Avoidance
DENIS	Deep Near Infrared Survey
DIRBE	Diffuse Infra Red Background Experiment
ESO	European Southern Observatory
ESO/SRC	ESO / United Kingdom Science Research Council
FWHM	Full Width at Half the Maximum
IRAF	Image Reduction and Analysis Facility
IRAS	Infrared Astronomical Satellite
IRAS PSC	Infrared Astronomical Satellite Point Source Catalogue
IRAS PSCz	IRAS PSC Redshift Survey
ISAAC	Infrared Spectrometer and Array Camera

Table A.1: (continued) Abbreviations used in this dissertation.

Abbreviation	Description
POSS	Palomar Observatory Sky Survey
PSC	Point Source Catalogue
PSF	Point Spread Function
REFLEX	ROSAT-ESO Flux Limited X-ray
RON	Readout Noise
ROSAT	Roentgen Satellite
ROSAT BSC	Roentgen Satellite Bright Source Catalogue
6dF	Six degree Field facility
SOFI	Son of ISAAC
2dF	Two degree Field facility
2dFGRS	2dF Galaxy Redshift Survey
2MASS	Two Micron All Sky Survey
WFI	Wide Field Imager

Appendix B

Changes made in this Dissertation

This chapter only applies at a later stage.

Appendix C

Vita

Karsten Markus was born in Thuine, Germany, on August 10th, 1974, as the son of Rudolf Bernhard Markus and Elisabeth Johanna Markus (neé Bonnekessen). After leaving the grammar schools Johanneum and Geor-

Figure C.1: The author, Karsten Markus

gianum in Lingen/Ems, Germany, he participated in the compulsory army service at the Luftlandebrigade 31 (paratroops) in Wildeshausen and Oldenburg, Germany. In 1995 he entered the Ruperto Carola in Heidelberg, Germany, where he obtained his Vordiplom in 1998. The following year, he entered the University of Cape Town, South Africa, and obtained a B.Sc. Hons. in Theoretical Physics and Astrophysics the same year. He has since been a part-time graduate student at the Department of Astronomy of the University of Cape Town and carried out observational work at observatories in France, Germany and South Africa.

Appendix D

Availability

A copy of this dissertation or a corrected version thereof should be available on the World Wide Web: http://www.karstenmarkus.de/publications/

Appendix E

Contact Details

Karsten Markus

Department of Astronomy
University of Cape Town
Rondebosch, Cape Town 7701
Republic of South Africa

Email: contact@karstenmarkus.de
WWW: karstenmarkus.de

Photometry of Elliptical Galaxies in Crowded Starfields

[Part III / III: Data Reduction Manual]

KARSTEN MARKUS

Department of Astronomy

University of Cape Town

Republic of South Africa

Cape Town & Berlin

01.12.2006

Abstract

Observations of nearby large-scale structures in the Zone of Avoidance have revealed a number of important findings. Amongst these were large-scale structures like the Norma cluster and the surmised Norma Supercluster. However, various difficulties arise when extragalactic objects are investigated close to the band of stars, dust and gas that form the Milky Way. The most severe of these problems, star crowding and Galactic extinction, are analysed in this study. Stars superimposed on a galaxy can cause significant deviations in the established surface brightness profiles of these galaxies. Furthermore, the light received from these galaxies is reduced by the increasing amount of dust and gas in the line of sight towards lower Galactic latitudes. In this study, a set of thirty elliptical galaxies in the central Norma cluster region was analysed by means of high quality optical and near infrared observational data. It is found that the determination and application of a pixel mask for interfering parts in the image offers sufficiently good results for moderate numbers of foreground stars and with relatively little effort. For heavy star crowding and awkwardly positioned stars or even other galaxies close to the investigated galaxy, a more accurate method was developed: the stars were modelled with a point spread function and thereafter subtracted. Subsequently, the $(R_c - K_s)$ colour (which is relatively insensitive to the choice of Galactic reddening law) and the colour excess were obtained. These were then compared with the most commonly used measure of extinction, the DIRBE/IRAS dust maps. The latter are, however, poorly calibrated at low Galactic latitude and are believed to overestimate the Galactic extinction at lower latitudes. The results obtained here do in fact show that the DIRBE/IRAS dust maps already slightly overestimate the Galactic extinction at the position of the central Norma cluster region.

Dedication

This thesis is dedicated to my parents,

Elisabeth Johanna Markus
née Bonnekessen –

and

Rudolf Bernhard Markus.

This thesis is also dedicated to the approximately 7 million South Africans who are expected to die within the next 10 years due to HIV and AIDS.

May the loss of wisdom and culture due to their deaths bring new thoughts and insights to the following generations.

Acknowledgments

Ubuntu ungamntu ngabanye abantu. [1]

There are innumerable people that – in one way or another – had influence on the positive outcome of my studies, and this dissertation in particular. Unfortunately, I will have to limit this little demonstration of gratitude to the most immediate supporters.

Professor Anthony – Tony – Patrick Fairall and Dr. Patrick Alan Woudt from the Astronomy Department at the University of Cape Town (UCT) will be the first ones to be mentioned. Both took very good care of me – against all odds. Tony, thanks a lot for being open to listening to me and for not getting tired of dealing with the various problems that occurred on and on. I also would like to emphasize that I have very much enjoyed your very good skills of 'explaining the local universe' and your interest in good quality education. Meeting you has left a deep impression on me. Patrick, the same holds for you. If it wasn't about your abilities to multitask and to turn problems into opportunities, the whole department would come to stand still. I will always be grateful to both of you for being your student and I am looking forward to working together with you in the future.

I would also like to mention Dr. Anja Schröder, who was a visiting astronomer at the UCT Astronomy Department in 2001. She may not have realised, but in her very kind way, she made me feel good about the things I was working on.

[1] Xhosa proverb: Ubuntu ungamntu ngabanye abantu – A person is only a person through other people; meaning that to develop as persons, we need to be empowered by others (Shuttle, 1995).

Meeting her has certainly put scientific work into a new perspective for me – Thank you!

Dr. Wolfgang Hasse from the Wilhelm-Foerster-Observatory (WFO) in Berlin, Germany, introduced me to quite a different scientific philosophy. Not only did I benefit from his theoretical knowledge, but also from his kind offer to join his working group at the WFO. Being a theoretical cosmologist, he showed great interest in my work and the discussions with him not seldomly opened my eyes as to where I was standing – literally. For this, a big "Danke!".

The most important person in my life, however, has been my friend and wife, Wilnelia Edith Adams. She was and still is the most valuable source of inspiration I have. Meeting her at UCT was a lucky chance in my life and I am happy that she offered me the opportunity of getting to know her better. Wilnelia, you may not be aware of this, but I do not regret a minute of the time I spent with you, be it in good or in bad times!

In terms of non-scientific support, I would first like to thank my family, and in particular my parents, Rudolf Markus and Elisabeth Markus. They never stopped believing in me and they supported me as much as they could. I will never forget this and I am proud to be your son!

Moreover, many friends and colleagues have been very encouraging in various ways. I will briefly mention a few representative names here, but the list is obviously incomplete. May those who are not mentioned forgive me for not doing so. I certainly should have mentioned you!

Joan **A**dams	Olivia Adams	Robert Adams
Rory Adams	William Adams	Wincia Adams
Marguerite Armstrong		
Frank **B**eier	Daniel Berdix	Andrea Bierau
Hermann Bonnekessen	Franz Bonnekessen	Hannah Bohle
Stefan Bubenzer	Prof. Buffler	
Michelle **C**lover	Lisa Crause	
Britta **D**eutsch	Hans-Joachim Döbler	
Prof. **F**airall	Prof. Feast	Julia Frantz
Jörn **G**reving		
Katrin **H**ammerstein	Dr. Hasse	Björn Heggemann
Dr. Hempe	Ulrike Hertschel	Frank Hermes
Prof. Hundinger		
Lesley **J**ennings	Birgit Joest	
Robert **K**astl	Volker Kathöfer	Dr. Kirstein
Thorsten Koch	Andreas Köster	Prof. Kraan Korteweg
Katya Kumkova Wolpert		
Regine **L**ord		
Anna **M**arkus	Elisabeth Markus	Oliver Markus
Rudolf Markus	Tanja Markus	Johannes Meier
Sabine Morgner		
Dr. **N**ickel	Sandra Nikolic	Prof. Nordmeier
Mark **P**ollmeier	Mellanie Pollmeier	Retha Pretorius
Tobias **R**odäbel		
Prof. **S**ahm	Katrin Sailer	Christian Schäfers
Christine Siewert	Dr. Schreiber	Dr. Schröder
Ralf Staudemeyer		
Helmut **T**hieke	Mia Thieke	Prof. Thomsen
Prof. **U**lmschneider		
Prof. **W**agner	Kerstin Wagner	Florian Weißbach
Dr. Wendt		

Utilised Data Sources

ArXiv e-print service:

See *http://lanl.arxiv.org/*.

Astrophysics Data System:

See *http://adswww.harvard.edu/*.

Coma cluster data:

Generously supplied by Dr. J. Lucey, Department of Physics, *University of Durham*, United Kingdom, see *http://www.dur.ac.uk/john.lucey/*.

Near infrared Norma cluster data:

Data obtained with *European Southern Observatory* facilities and generously supplied by Dr. A. C. Schröder, Department of Physics & Astronomy, *University of Leicester*, United Kingdom.

Milky Way image:

Generously supplied by Dr. A. Mellinger, see Mellinger (2000) and *http://home.arcor-online.de/axel.mellinger/*.

NED database:

NASA/IPAC Extragalactic Database, see *http://nedwww.ipac.caltech.edu/*.

Optical Norma cluster data:

Data obtained with *European Southern Observatory* facilities and generously supplied by Dr. P. A. Woudt, Astronomy Department, *University of Cape Town*, Republic of South Africa, see *http://monsa.ast.uct.ac.za/~pwoudt/*.

Redshift data:

Obtained with the *Anglo Australian Observatory 2dF* instrument and generously supplied by Dr. J. Lucey, Department of Physics, *University of Durham*, United Kingdom, see *http://www.dur.ac.uk/john.lucey/*.

SIMBAD database:

This research has made use of the *SIMBAD* database, operated at the *Centre de Données astronomiques de Strasbourg*, France, see *http://simbad.u-strasbg.fr/*.

ViZieR service:

This research has made use of the *ViZieR* service, operated at the *Centre de Données astronomiques de Strasbourg*, France,
see Ochsenbein et al. (2000) and *http://vizier.u-strasbg.fr/*.

Utilised Software

GALFIT software:

See *http://zwicky.as.arizona.edu/~cyp/work/galfit/galfit.html* and Peng et al. (2002).

GNUPlot software:

See *http://www.gnuplot.info/*.

Hierarch28 software:

Provided by the *European Southern Observatory*, see *http://archive.eso.org/saft/*

IRAF software:

IRAF is distributed by the *National Optical Astronomy Observatories*, which are operated by the *Association of Universities for Research in Astronomy, Inc.*, under cooperative agreement with the *National Science Foundation*. See *http://iraf.noao.edu/* and Tody (1986, 1993).

Killall software:

I kindly acknowledge Prof. McCall for the use of the *Killall* software.
also see Buta and McCall (1999).

Mac OS:

Developed by *Apple Computer, Inc.*, see *http://www.apple.com/*.

Physica software:

Provided by the *TRIUMPH Computing Services Group*,
see *http://www.triumf.ca/physica/html/homepage.html*.

RedHat Linux :

Provided by *Red Hat, Inc.*. See *http://www.redhat.com/*.

SAOImage DS9 software:

This research has made use of *SAOImage DS9*, developed by *Smithsonian Astrophysical Observatory*, see *http://hea-www.harvard.edu/RD/ds9/* and Joye and Mandel (2003).

SkyCat software:

Provided by the *European Southern Observatory*, see *http://archive.eso.org/skycat/*.

SM software:

Previously known as *SuperMongo*, see *http://www.astro.princeton.edu/~rhl/sm/* and Lupton and Monger (1997).

STSDAS & TABLES packages:

Products of the *Space Telescope Science Institute*, which is operated by *Association of Universities for Research in Astronomy, Inc.*, for *NASA*.
see *http://www.stsci.edu/resources/software_hardware/*.

Contents

List of Tables

List of Figures

Chapter 1

Introduction

This is the third part of three parts in which this dissertation is divided into. However, similar to Part II, it is considered to be only an attachment to Part I. The first part contains all details about the subject, data, analysis, results and the discussion. The second part contains plots and images of the galaxies which were investigated. These plots and images are not necessary for following the analysis and results shown in Part one, but they nonetheless offer information about the analysis that was applied to the data and can give more details about the galaxies that were processed.

In this part of this dissertation, more detailed information about how the data was processed and instructions on how to conduct similar investigations are given. This part is thus called the 'Data Reduction Manual'. It is a step by step guide through the processing. In connection with Part I, the given description should enable the reader to apply the the described techniques to any kind of data. All references made to directory structures or file names in this manual are the ones used by the author, but are chosen entirely arbitrarily and may be adjusted. For more information, e.g. on the data that was used for the analysis, the reader is referred to Part I and II of this dissertation.

All commands and tasks described in Chapters 2 to 6 are Image Reduction

and Analysis Facility[1] (*IRAF*)[2] commands, except where stated otherwise. Similarly, Chapter 7 contains *SM*[3] commands.

It is advisable to save and load the parameters of the different the *IRAF* tasks, to assure that parts of the data reduction can easily be repeated again at a later stage, if necessary. By using for instance `epar ellipse` and then `:w ellipse1.par` from within `epar`, the parameters for the `ellipse` task can be saved into `ellipse1.par`. The saved parameters can then be loaded at a later stage by entering `:r ellipse1.par` from within epar. To make the saving of parameters easier for the *DAOPHOT* package related functions, one is advised to look at the `setimpars` function (Davis, 1994).

[1] *IRAF* is distributed by the *National Optical Astronomy Observatories*, which are operated by the *Association of Universities for Research in Astronomy, Inc.*, under cooperative agreement with the *National Science Foundation* (Tody, 1986, 1993).
See also: http://iraf.noao.edu/

[2] For a description of abbreviations used in this dissertation, the reader is referred to Section A in the Appendix on page 87.

[3] *SM* was previously known as *SuperMongo*, see Lupton and Monger (1997)

Chapter 2

Preparation

To be able to apply the data reduction described in this manual, one has to prepare the images and collect information for each data set.

1. By using `imexamine` and the ,-key or the a-key, one can determine the centre of the galaxy and some initial values for the position angle and ellipticity of the galaxy. This information is needed later in Chapters 4 to 6 for the first initial fit of the isophotes.

   Using `imexamine` and the r-key or the a key on a series of bright, but non-saturated stars will give an estimate of the FWHM[1]. It is the last number stated on the very right. With `imexamine` and the m-key, the background count-rates for each image were determined. At ten different positions on the background of each image, i.e. in between the objects like stars and galaxies, a measurement was taken with `imexamine` and the m-key. This also gives the standard deviation of the background (`stddev` or σ), which is needed at a later stage.

   (Optional) One could compare this measured σ-value with the predicted value, by using

$$1 \cdot \sigma \approx \sqrt{\frac{s}{p} + \left(\frac{r}{p}\right)^2} = \frac{\sqrt{s \cdot p + r^2}}{p} \,,$$

[1] Full Width of Half the Maximum of a two-dimensional Gaussian fit to a star.

where s is the measured median sky value, p is the number of photons per ADU[2], i.e. the effective gain, and r is the effective readout noise (RON) (Davis, 1994, page 27).

2. For each image, subtract the background count rate, using `imarith`, to bring the background counts to zero.

3. If necessary, fix the header information. Due to the lack of keywords for the readout noise and the gain, this was necessary for instance for each of the WFI images. The keywords `egain` and `eron` were entered manually into the header, using `hedit`. The values for each chip were taken from the *WFI User Manual* (Baade, 1999, page 20) and as the images containing the galaxies consist of either four or five combined exposures, the effective values for gain and readout noise were calculated according to the formula for using a median combination method (Davis, 1994, page 20):

$$\text{gain}_{\text{eff}} = \frac{2 \cdot N}{3} \cdot \text{gain} \ ,$$

$$\text{RON}_{\text{eff}} = \sqrt{\frac{2 \cdot N}{3}} \cdot \text{RON} \ ,$$

where N is the number of images combined.

4. Using the task `imcopy`, one should cut out smaller sub-images out of large images, like the ones that were taken with the WFI instrument (Baade, 1999). These sub-images should be centred on the galaxy of interest and the size may vary according to the size of the galaxy, for instance between $800 \cdot 800$ pixels and $1600 \cdot 1600$ pixels. The galaxy should be well inside the borders of this sub-image.

5. Open and view the image with *DS9* to visually determine the diameter in pixel of the largest unsaturated stars. From this diameter D, one can calculate the psf-radius r_{PSF} needed later:

$$D = (2 \cdot r_{\text{PSF}}) + 1$$

[2] Analog-to-Digital Unit

6. The names for some keywords in the FITS image header need to be identified. The FITS image header can be viewed with `imhead`, and for the WFI images, the following keyword names were copied down from the corrected FITS image header:

   - Filter: `filter`
   - Observing time: `date-obs`
   - (Effective)[3] exposure time: `exptime`
   - (Effective)[4] airmass: `cairmass`
   - Readout noise: `eron`
   - Gain: `egain`

[3]For long exposures, say longer than a minute, the exposure time for the WFI is considered being equal the effective exposure time, see the *WFI User Manual* (Baade, 1999, page 9)

[4]The used WFI FITS images are a combination of several exposures and the effective airmass was calculated for the first exposure taken. Since all exposures were taken in a consecutive order, the airmass is thought to stay nearly constant during the observation of each WFI field that was observed. For further information on the WFI observations and WFI specific data reduction, the reader is referred to Part 1 of this dissertation.

Chapter 3

Sigma-Clipping

To be able to apply any of the in Chapters 4 to 6 described data reduction methods, one first has to produce a rough galaxy model which then has to be subtracted from the original image.

1. Display image `wkk5920_ks_orig.fits` using `display`. It will probably look somewhat like Figure 3.1 on page 8, which is the image used to demonstrate the effects of the Sigma-Clipping (*σ-Clipping*) and the Improved Point Spread Function Fitting (*iPSF-Fitting*) methods in this Chapter and Chapter 6, respectively.

2. Enter zero as background value into `bmodel`, or if the background was not subtracted as suggested in item 2 in Chapter 2 on page 4, enter the in Item 1 in Chapter 2 on page 3 previously determined value for the background count rate into `bmodel`.

   (Optional) Check the value by using `imexamine` and the `m`-key.

3. Check and if necessary enter parameters into `ellipse` or associated parameter files. The `nclip`, `usclip` and `lsclip` parameters are the relevant parameters for using the `ellipse`-internal σ-clipping. `usclip` and `lsclip` are the upper and lower σ-clipping limits, respectively and `nclip` gives the number of σ-clipping iterations.

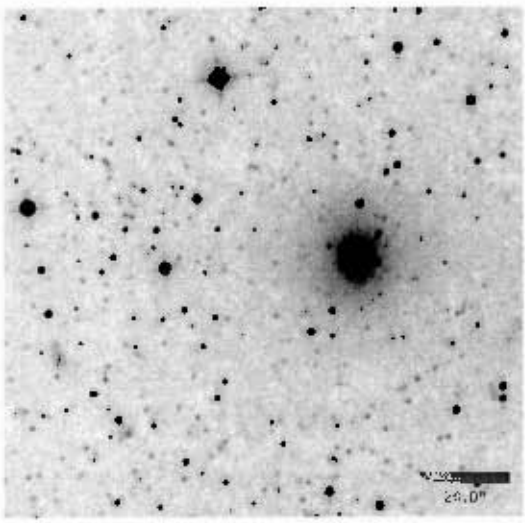

Figure 3.1: Galaxy WKK98 5920, original K_s band image.

```
integrm = mean
region  = no
nclip   = 50
usclip  = 3
lsclip  = 2
SMA     = 10
input   = isub....fits
output  = s...w....tab
```

4. Enter the following initial parameters into the ellipse task. ellip0 and pa0 can be taken from the results obtained in Item 1 in Chapter 2 on page 4:

```
x0      = ...
y0      = ...
ellip0  = ...
pa0     = ...
hellip  = no
hpa     = no
```

```
hcenter = no
xylearn = yes
recente = yes
maxSMA  = ...
```

5. Run `ellipse` and then `bmodel` on the resulting table, using the same background count value as used in Item 2. Adjust the parameters in Item 4 and the background value in `bmodel` and re-run the `ellipse` and `bmodel` tasks until the best possible fit is achieved. It is advisable that the `maxSMA` parameter mentioned in Item 4 is set to some large value, to ensure that the galaxy is modelled well into the background. The galaxy model should look like Figure 3.2 on page 9.

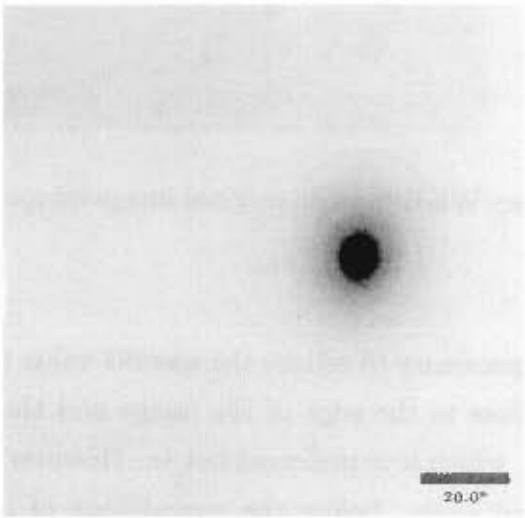

Figure 3.2: Galaxy WKK98 5920, *σ-Clipping* model of the galaxy as produced with the `ellipse`- and `bmodel` tasks.

Use the `isoexam` and `isoplot` tasks to examine the `ellipse` results.

It may also be necessary to change the values for `usclip` and `lsclip` and even the `SMA` parameter mentioned in Item 3.

6. Subtract the model from the original image, using `imarith`.

7. Re-run Items 4 to 6 and adjust the values in Item 4 and the background count value in `bmodel` until the galaxy model is as good as possible, i.e. in the resulting image from Item 6, the least possible remains and artefacts are visible. This gives a result similar to Figure 3.3 on page 10.

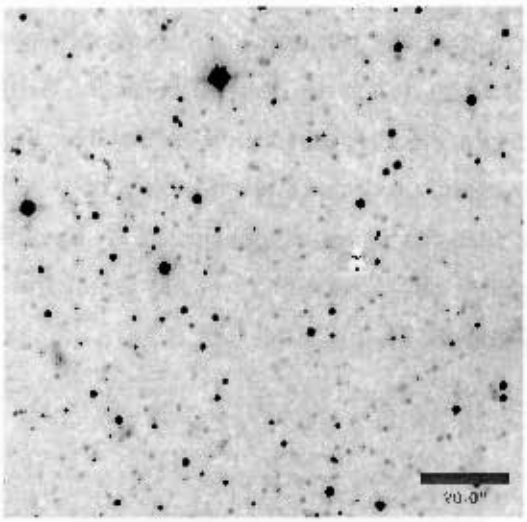

Figure 3.3: Galaxy WKK98 5920, original image minus the *σ-Clipping* galaxy model.

It may be necessary to reduce the `maxSMA` value in Item 4, if the galaxy model is close to the edge of the image and the edge is included into the model, which it is preferred not to. However this is at a later stage to be raised again, before the remodelling of the ellipse, i.e. for the *Star-Masking* method in Item 2 on page 39 in Chapter 5 and for the *PSF-Fitting* in Item 2 on page 32 in Chapter 4.

8. Copy the resulting file into a new file, using `cp` and display this file to look at residuals in the centre of the subtracted galaxy.
Also look for a free part of sky without stars or lines to cut out. Use this part for patching the centre of the subtracted galaxy with `imcopy`, for example:

```
cl> imcopy 1_k_nog.fits[200:290,140:160] 1_k_nogsen.fits[470:460,250:270]
```

Alternatively, one can use `imedit` to edit the remains left in the centre of the galaxy after subtraction of the model.

The resulting 'clean' image, i.e. without the galaxy, will look like Figure 3.4 on page 11.

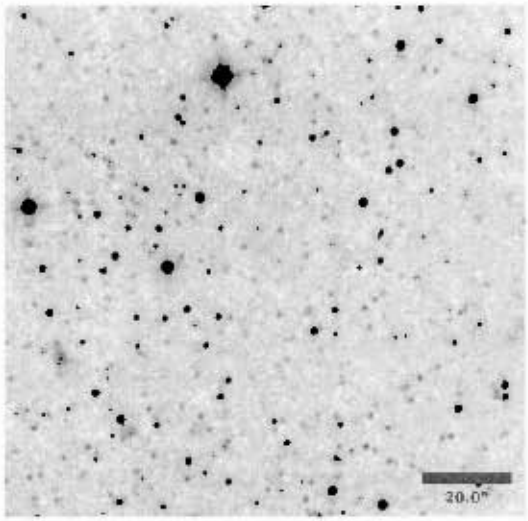

Figure 3.4: Galaxy WKK98 5920, resulting 'clean' image without a trace of the galaxy.

One has to look carefully for stars near the centre of the galaxy, since, for further processing of the images in Chapters 4 to 6, they mustn't be removed from the centre. This is for instance done by displaying the image with a large range in the count rate:

```
cl> display 1_k_nogsen.fits 1 zr- zs- z1=300 z2=10000
```

Here the parameters `z1` and `z2` have to be adjusted according to the brightness of the galaxy.

Alternatively, one can use *DS9* to open and view the image and to adjust the count rate.

Chapter 4

Point Spread Function Fitting

4.1 Point Spread Function Determination

1. Make a new directory and copy all relevant files obtained from Chapter 3 into this directory, e.g. the image, here `isub0701wkk6600.fits`. Enter this directory.

2. Display the image using `display`. It will look like Figure 4.1 on page 13.

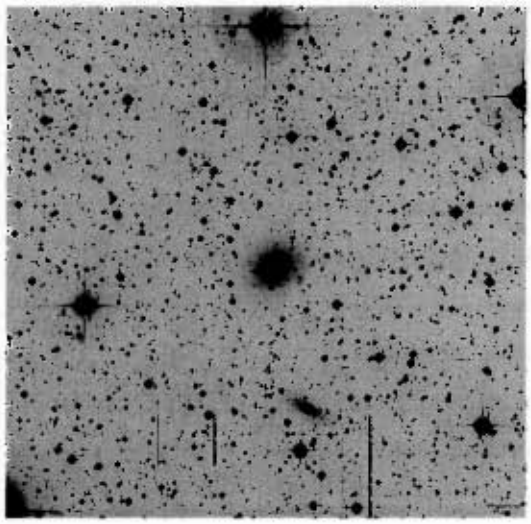

Figure 4.1: Galaxy WKK98 6600, original R_c band image.

3. Run `imexamine` on the image to get some values:

   - Use the `r`-key on the biggest, unsaturated stars to get the FWHM, it's the number on the very right side.
   - Zoom into the picture and estimate the radius of the biggest, not saturated stars.
   - Use the `h`-key to get the rough sky value, i.e. the maximum of the histogram plotted.

4. Enter the following parameters into `datapars`, `daopars`, `centerpars`, `fitskypars`, `photpars` and `findpars`:

```
datapars.fwhmpsf      = ...
datapars.sigma        = ...
datapars.datamin      = -20
datapars.datamax      = 60000

daopars.exposur       = exptime
daopars.airmass       = airmass
daopars.filter        = filter
daopars.obstime       = date-obs
daopars.ccdread       = ron
daopars.gain          = gain
daopars.recenter      = yes
daopars.fitsky        = yes
daopars.fitrad        = ...
daopars.psfrad        = 15
daopars.maxgrou       = 100
daopars.maxnsta       = 20000

centerpars.cbox       = ...
centerpars.calgorithm = none
```

```
fitskypars.annulus     = ...
fitskypars.dannulu     = ...

photpars.apertur       = ...

findpars.treshold      = ...
```

Here `sigma` is the value for the standard deviation σ (`stddev`) taken from Item 1 on page 3 in Chapter 2. `fwhmpsf` is the full width of the half maximum (FWHM) from Item 3 on page 14. The value for `datamin` is the minimum valid data count rate and similarly the value for `datamax` is the maximum valid data count rate.

Whichever of either the FWHM or 3 pixels is greater, it is used as the value for `fitrad`. The `psfrad` value is for faint star and it may be necessary to use a different value.

For the `cbox` parameter, twice the FWHM or 5 pixels is entered, whichever is greater, and for `annulus` and `dannulus` four times the FWHM are used.

Again, the larger value of either the FWHM or 3 pixels is used for the `apertur` parameter, and 3.5 is entered as an initial guess for the `treshold` value. This value needs to be adjusted though.

5. Enter `color=204` into `tvmark`.

6. To locate the stars in the image, run `daofind` on the image with the galaxy model subtracted from the original image, as described in Chapter 3, e.g. `s...w...minmodcen.fits`.

7. Using `display`, view the `s...w...minmodcen.fits` image without the galaxy in frame 1 of *DS9*. This image resulted from applying the σ-*Clipping* method described in Chapter 3 on page 7. Notice however that in this chapter, the galaxy and the instrument are different to

the ones used for the description of the *σ-Clipping*. The image will resemble Figure 4.2 on page 16.

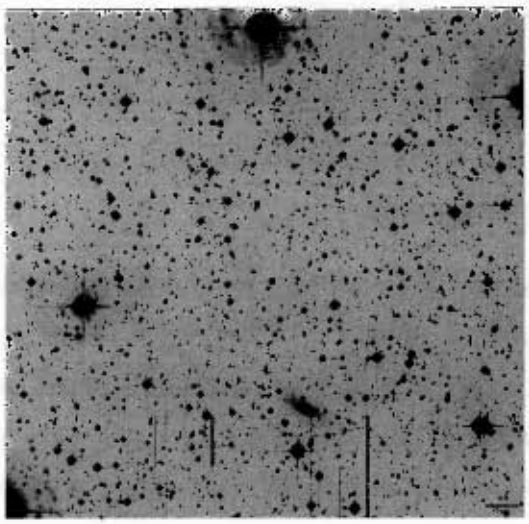

Figure 4.2: Galaxy WKK98 6600, 'clean' image without the galaxy, from applying the *σ-Clipping* described in Chapter 3 on page 7.

8. Use `tvmark 1 s...w...minmodcen` to display the coordinate(`.coo`) file and therefore the found stars.

   A different number of stars will be found at the edges of images for the different parts of the combined images, due to the different noise.

   For some reason, `tvmark` sometimes plots points at the edge of the screen, that do not represent the position of any objects.

9. Adjust the `treshold` parameter mentioned in Item 4 to find as many stars, yet as little noise as possible in the area in which the galaxy lies, and re-run sequence from Item 4, if necessary.

10. Display image `s...w...minmodcen.fits` using `display`.

11. Use `tvmark 1 s...w...minmodcen interactive+` to display the stars in the coordinate(`.coo`) file and to be able to interactively include or exclude stars from the set.

Check for and include stars left out close to the centre or very bright stars on the galaxy, using `tvmark`:

- Use the `l`-key to mark all found stars in the coordinate file on the display.
- Move cursor to desired unmarked objects and type `a`, type `d` for deleting unwanted objects.
- Type `q` to quit.

12. Run `phot s...w...minmodcen` to get the magnitudes of the stars.
13. Sort the stars in the resulting magnitude file from the `phot` task into five bins of different magnitude:

```
cl> pselect s...w...minmodcen.mag.1 s...w...mmcf.mag.1 "MAG != INDEF
        && MAG >= 22.0"
↩

cl> pselect s...w...minmodcen.mag.1 s...w...mmcm.mag.1 "MAG != INDEF
        && MAG >= 18.0 && MAG < 22.0"

↩

cl> pselect s...w...minmodcen.mag.1 s...w...mmcb.mag.1 "MAG != INDEF
        && MAG < 18.0"

↩

cl> pselect s...w...minmodcen.mag.1 s...w...mmcfm.mag.1 "MAG != INDEF
        && MAG >= 18.0"

↩

cl> pselect s...w...minmodcen.mag.1 s...w...mmcfmb.mag.1 "MAG != INDEF"

↩
```

In this case into three bins for bright (MAG $<$ 18), medium bright ($18 \leq$ MAG $<$ 22) and faint (MAG $\geq$ 22) stars, and two bins with the faint and medium bright together (MAG $\geq$ 18) and with all stars, except the ones that are not defined.

The range of these bins has to be adjusted. To do this first display the bright stars with `tvmark` and then the faint ones (leaves out the mid-range bin) and see from there.

14. Re-display image `isub....fits` using `display` and mark the faint stars, using `tvmark s...w...mmcf.mag.1`.

15. Enter `photfile = s...mmclmb.mag.1` into `psf`.

16. **First run of psf-function**

    Run `psf s...minmodcen` to produce a point spread function (PSF) for the faint stars. Make sure beforehand that `psfrad` in `daopars` is set to a value of ~ 15. for the faint stars. Choose at least five stars.

    - Out of the marked stars, position the cursor on one of the brightest ones, with as few neighbouring stars as possible and press the `a`-key.

      To view different plots, use the `c`-, `r`- and `m`-keys, for the plot with the `m`-key, one has further options, using the `w`-, `e`-, `s`- and `n`-keys.

    - To reject the star, press the `d`-key and to accept the star press the `a`-key again.

    - To list all psf-stars, type `l`.

    - To see the residuals for a star, move the cursor to that star and type `s`.

    - To fit the PSF, type `f`.

    - When done with selecting stars and fitting, press `w` to save the PSF.

    - To quit, type `q`

    (Optional) To view the PSF-image, one can use the `seepsf` task. A set of PSF-images is shown in Figure 6.1 on page 46. Although these were obtained in an iterative process, using the *iPSF-Fitting* method as described in Chapter 6 on page 43, they pretty much resemble what the PSF-images ought to look like from the iterative process described in this chapter.

17. Enter the following parameters into group, nstar and substar:

```
group.image       = s...minmodcen
group.photfile    = s...mmcf.mag.1

nstar.image       = s...minmodcen

substar.image     = s...minmodcen
substar.photfile  = s....nst.1
```

18. Run group, nstar and substar to subtract the faint stars.

19. Display the resulting image `s...minmodcen.sub.1.fits` with the faint stars subtracted, using `display` and see if the stars are well subtracted. It will look like Figure 4.3 on page 19.

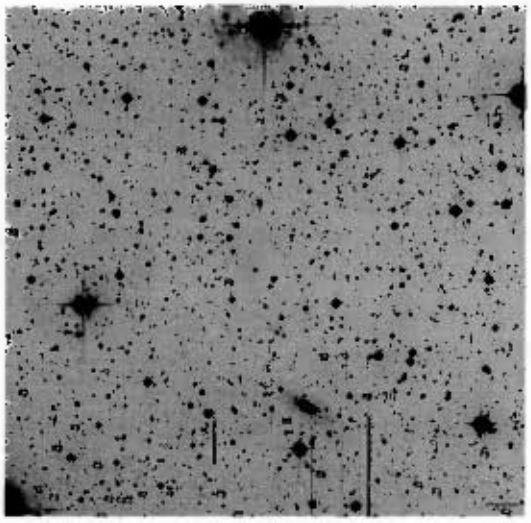

Figure 4.3: Galaxy WKK98 6600, image with galaxy and stars subtracted, after the first iteration of determining an appropriate PSF.

20. Mark the medium-bright stars, using `tvmark s.. w...mmcm.mag.1`.

21. Enter `image = s...minmodcon.sub.1` into `psf` and `psfrad = 30` into `daopars`, for the medium-bright stars. The `psfrad` value, however, needs to be adjusted.

22. **Second run of `psf`-function**

    Run `psf` to produce a point spread function (PSF) for the medium-bright stars and choose at least five stars:

    - Out of the marked stars, position the cursor on one of the brightest ones, with as few neighbouring stars as possible and press the a-key.

      To view different plots, use the `c`-, `r`- and `m` keys, for the plot with the `m`-key, one has further options, using the `w`-, `e`-, `s`- and `n`-keys.
    - To reject the star, press the `d`-key and to accept the star press the a-key again.
    - To list all `psf`-stars, type `l`.
    - To see the residuals for a star, move the cursor to that star and type `s`.
    - To fit the PSF, type `f`.
    - When done with selecting stars and fitting, press `w` to save the PSF.
    - To quit, type `q`.

    (Optional) To view the PSF image, one can use the `seepsf` task.

23. Enter the following parameters into `group`, `nstar` and `substar`:

```
group.psfimage     = s...minmodcon.sub.1.psf.1
group.photfile     = s...mmcfm.mag.1

nstar.psfimage     = s...minmodcon.sub.1.psf.1
```

```
substar.psfimage = s...minmodcen.sub.1.psf.1
substar.photfile = s....nst.2
```

24. Run group, nstar and substar to subtract the faint and medium-bright stars.

25. Display the resulting image `s...minmodcen.sub.2.fits` with the faint and medium-bright stars subtracted, using `display` and see if the stars are well subtracted. It will look like Figure 4.4 on page 21.

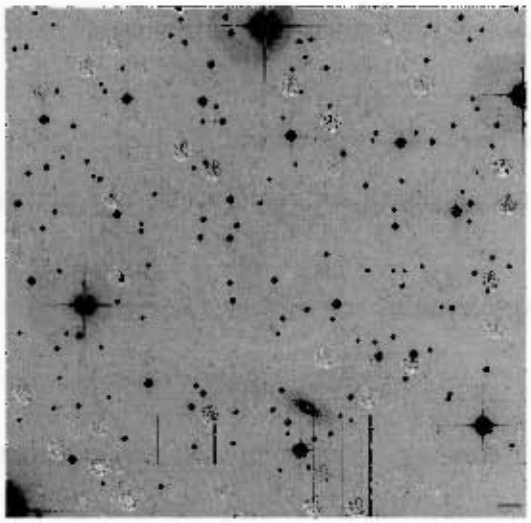

Figure 4.4: Galaxy WKK98 6600, image with galaxy and stars subtracted, after the second iteration of determining an appropriate PSF.

26. Mark the bright stars, using `tvmark s...w...mmcb.mag.2`.

27. Enter `image = s...minmodcen.sub.2` into `psf` and `psfrad = 45` into `daopars`, for the medium-bright stars. The `psfrad` value, however, needs to be adjusted.

28. **Third run of `psf`-function**

    Run `psf` to produce a point spread function (PSF) for the bright stars and choose at least five stars.

- Out of the marked stars, position the cursor on one of the brightest ones, with as few neighbouring stars as possible and press the a key.

  To view different plots, use the c-, r- and m-keys, for the plot with the m-key, one has further options, using the w , e , s- and n-keys.

- To reject the star, press the d-key and to accept the star press the a-key again.
- To list all psf-stars, type l.
- To see the residuals for a star, move the cursor to that star and type s.
- To fit the PSF, type f.
- When done with selecting stars and fitting, press w to save the PSF.
- To quit, type q.

(Optional) To view the PSF image, one can use the `seepsf` task.

29. Enter the following parameters into `group`, `nstar` and `substar`:

```
group.psfimage    = s...minmodcer.sub.2.psf.1
group.photfile    = s...mmcfm.mag.1

nstar.psfimage    = s...minmodcer.sub.2.psf.1

substar.psfimage  = s...minmodcen.sub.2.psf.1
substar.photfile  = s....nst.3
```

30. Run `group`, `nstar` and `substar` to subtract all stars, except the not defined ones.

31. Display the resulting image `s...minmodcer.sub.3.fits` with almost all stars subtracted, using `display` and see if the stars are well subtracted. It will look like Figure 4.5 on page 23.

The image might show obvious residuals.

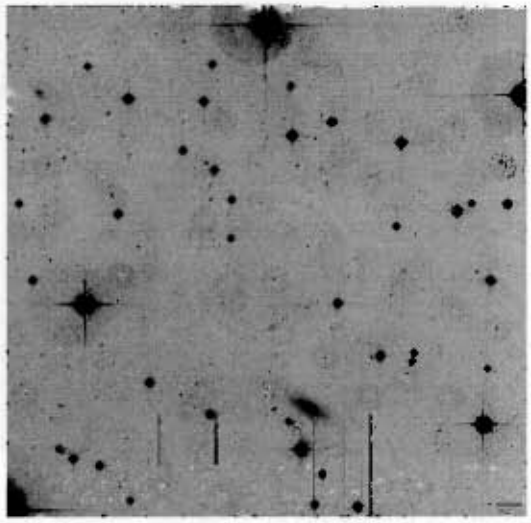

Figure 4.5: Galaxy WKK98 6600, image with galaxy and stars subtracted, after the third iteration of determining an appropriate PSF.

4.2 A better Galaxy Model

1. Run `substar` on the original image `isub....fits` to subtract all stars, except the not defined ones.

2. Display the resulting image `isub....sub.1.fits` with almost all stars subtracted from the original image, using `display` and see if the stars are well subtracted.

   As there are probably 'holes' in the galaxy and some obvious residuals, re-run `substar`, using a smaller `psfrad` in `daopars`, for instance a value of ~ 15.

3. If `substar` was re-run with a smaller `psfrad` in `daopars`, redisplay the resulting image `isub....sub.2.fits` with almost all stars subtracted by using `display` and see if the stars are well subtracted. It might look similar to Figure 4.6 on page 24.

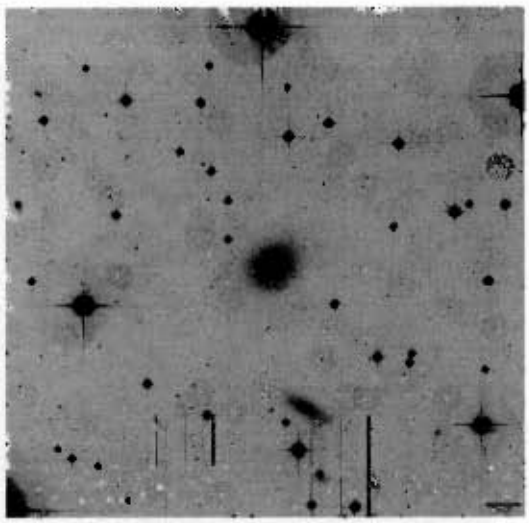

Figure 4.6: Galaxy WKK98 6600, original image with stars subtracted.

4. Enter parameters into `ellipse` or associated parameter files:

```
region    - no
nclip     = 50
input     = isub....sub.2
output    - isub....sub.2.tab
```

5. Confirm the following parameters in the `ellipse` task:

```
x0        = ...
y0        = ...
ellip0    = ...
pa0       = ...
hellip    = ...
hpa       = ...
hcenter   = ...
xylearn   = ...
recente   = ...
maxSMA    = ...
```

6. Run `ellipse`, adjust the parameters in item 5 and re-run the `ellipse` task until best possible fit achieved, i.e. with no or as little 'rings' and artefacts visible in item 9 as possible.

   Use `isoexam`- and `isoplot` tasks to examine the `ellipse`-results.

   (Optional) One could use the `tread` task, to look at the non ASCII-table `isub....sub.2.tab`; use `^D` and `q` to leave the displayed table.

7. Enter the following parameters into the `bmodel` task and then run the task. The resulting model could look like Figure 4.7 on page 25.

```
input      = isub...sub.2.tab
output     = isub...model.sub.2
```

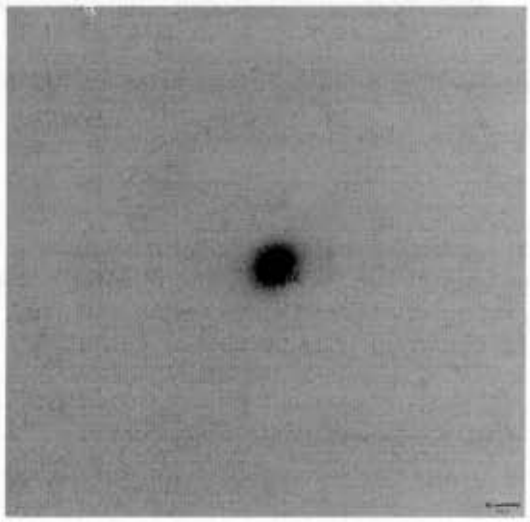

Figure 4.7: Galaxy WKK98 6600, galaxy model after subtracting the stars using the determined PSF.

8. Subtract the model from the original image:

```
cl> imarith isub....fits - isub...model.sub.2.fits isub...  zinmod.sub.2 fits
↩
```

9. Display `isub...minmod.sub.2.fits`, if necessary, adjust the background value and other parameters and re-run `bmodel` and `ellipse`. The resulting image could look like Figure 4.8 on page 26.

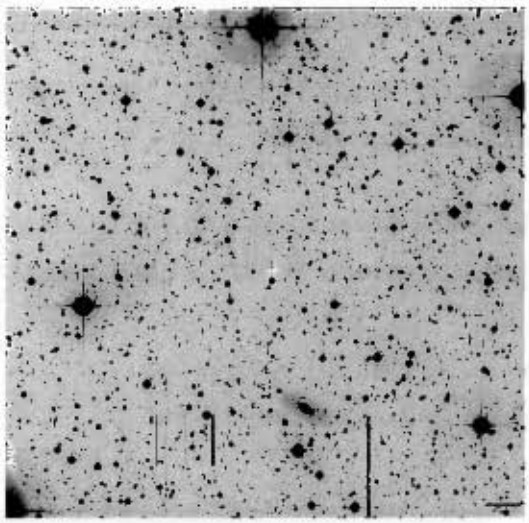

Figure 4.8: Galaxy WKK98 6600, image after subtracting the galaxy model and the stars using the determined PSF.

10. Copy `isub...minmod.sub.2.fits` into `isub...minmodcen.fits` and look at residuals in the centre of the subtracted galaxy and for a 'free' part of sky without stars or lines to cut out that part and to use it for patching the centre of the subtracted galaxy, for example:

```
cl> imcopy isub...minmod.sub.2.fits[700:790,440:460]
        isub...minmodcen.fits[770:860,350:370]
↩
```

11. Use `display` to display `isub...minmodcen.fits` and check if the centre is properly subtracted, as in Figure 4.9 on page 27.

4.3 Establishing Median and Pixel-Mask

1. Enter `image=isub...minmodcen.sub.2` into `substar`.

2. Run `substar` to subtract all, except the not defined stars.

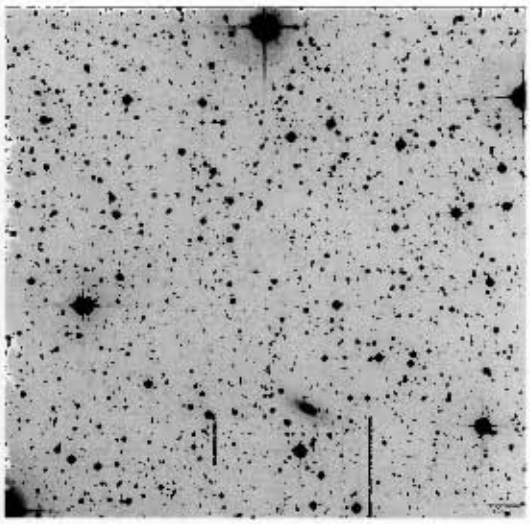

Figure 4.9: Galaxy WKK98 6600, new 'clean' image with stars and galaxy subtracted, after subtracting the galaxy model and the stars using the determined PSF.

3. Display resulting image `isub...minmod.sub.2.sub.1.fits` with almost all stars subtracted, using `display` and see if the stars are well subtracted.

4. Copy `isub...minmod.sub.2.sub.1.fits` into `isub...minmodcen.fits`.

5. Display this file and look at residuals in the centre of the subtracted galaxy.

   Also look for a 'free' part of sky without stars or lines to cut out that part and to use it for patching the centre of the subtracted galaxy, for example:

```
c!> imcopy isub...minmod.sub.2.sub.1.fits[700:790,440:460]
        isub...minmodcen.fits[770:860,350:370]
←
```

6. Use `display` to display `isub...minmodcen.fits` and check if the centre is properly subtracted, as in Figure 4.10 on page 28.

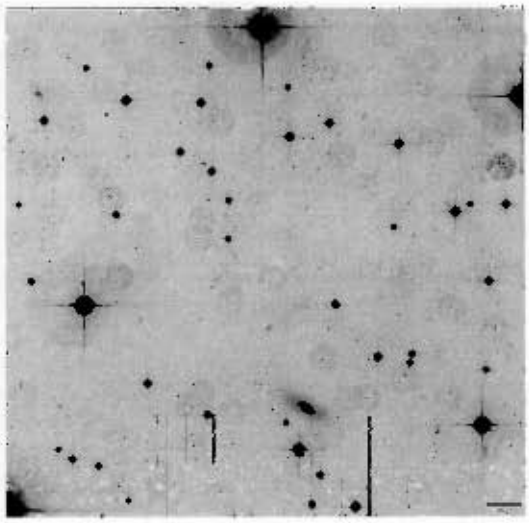

Figure 4.10: Galaxy WKK98 6600, new 'clean' image with stars and galaxy subtracted, after subtracting the galaxy model and the stars using the determined PSF.

7. Run `median` on the file `isub...minmodcen.fits`, which will result in an median-image similar to Figure 4.11 on page 29.

8. Figure 4.12 on page 29 shows the galaxy- and star-subtracted image `isub...minmodcen.fits` with the median subtracted:

```
cl> imarith isub...minmodcen.fits - isub...median.fits isub...mmcmm.fits
↩
```

9. Copy `isub...mmcmm.fits` into `isub...mmcmmbit.fits`.

10. Take the sigma from Item 1 on page 3 in Chapter 2 and use about $\sim 3 \cdot \sigma$ as threshold for pixels above and below the background noise to be raised to 65000 counts (for example $\sigma = 8 \Rightarrow$ lower = upper = 40):

```
cl> imreplace isub...mmcmmbit.fits 65000 lower=40
. .

cl> imreplace isub...mmcmmbit.fits 65000 upper=-40
. .

cl> imreplace isub...mmcmmbit.fits 0 upper=40
```

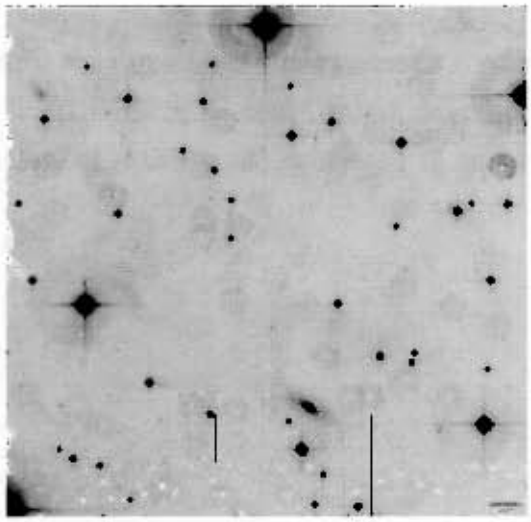

Figure 4.11: Galaxy WKK98 6600, median image obtained from the image with subtracted stars and galaxy.

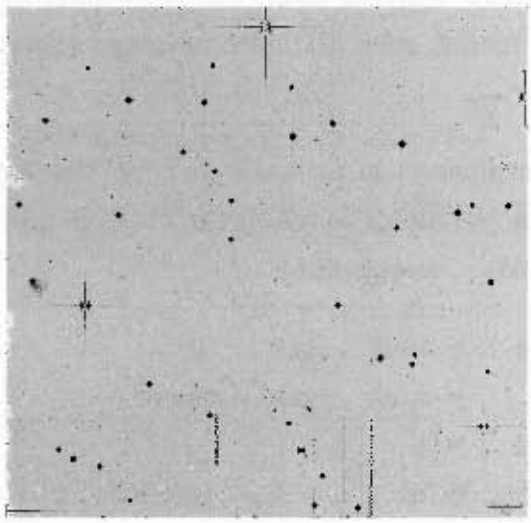

Figure 4.12: Galaxy WKK98 6600, the galaxy-, star- and median-subtracted image.

11. Display `isub...mmcmmbit` and redo sequence from item 9 onwards with a slightly different factor before σ in item 10, if necessary, until most of the stars but as little noise as possible is included.

Figure 4.13: Galaxy WKK98 6600, the pixel-mask derived from the image with the galaxy model, stars and median-image subtracted.

12. Change parameters in `ccdmask` and use the same root name for the mask as for the image to which the mask should be applied to (`isub...wkk...mmask.fit`):

```
image   = isub...bit
mask    = isub...wkk...mmask
ngood   = 1
ncmed   = 70
nlmed   = 70
ncsig   = 150
nlsig   = 150
```

13. Run `ccdmask`, if possible as a background task, as it takes quite long.

14. Subtract the median from the 'original-minus-stars' image. See Figure 4.14 on page 31 for a resulting image.

```
cl> imarith isub...wkk...sub.2.fits - isub...median.fits isub...mmask.fit
. .
```

Use three characters after the last dot in the resulting file.

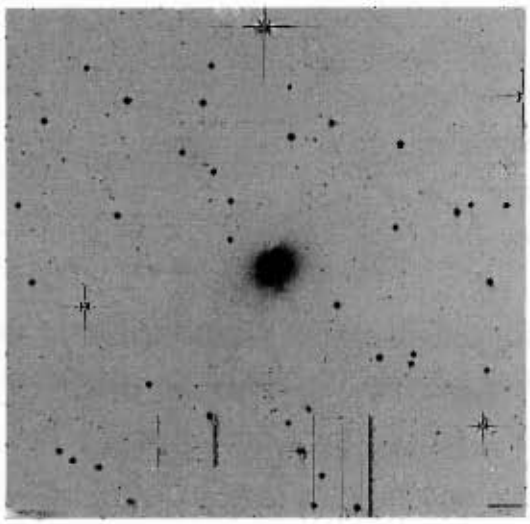

Figure 4.14: Galaxy WKK98 6000, original image with stars and the median subtracted.

4.4 The final Galaxy Model

1. Enter parameters into `ellipse` or associated parameter files:

```
region    = yes
nclip     = 0
input     = isub...mmask.fit
output    = isub...final.tab
```

The input file with three characters after the last dot.

2. Confirm the following parameters in the `ellipse` task:

```
x0          = ...
y0          = ...
ellip0      = ...
pa0         = ...
hellip      = ...
hpa         = ...
hcenter     = ...
xylearn     = ...
recente     = ...
maxSMA      = ...
```

3. Run `ellipse`, adjust the parameters in item 2 and re run the `ellipse` task until best possible fit achieved, i.e. with no or as little visible 'rings' as possible.

   Use `isoexam-` and `isoplot` tasks to examine the `ellipse`-results.

   Repeat from item 12 on page 30, if necessary.

   (Optional) One could use the `tread` task, to look at the non-ASCII-table `isub...wkk...final.tab`; use `^D` and `q` to leave the displayed table.

4. Enter the following parameters into the `bmodel` task and then run the task. The galaxy model should look like Figure 4.15 on page 33.

```
input       = isub...final.tab
output      = isub...finalmodel
```

5. Subtract the model from the original image:

```
cl> imarith isub...final.fits - isub...final-edu!.fits isub...finminmod.fits
--
```

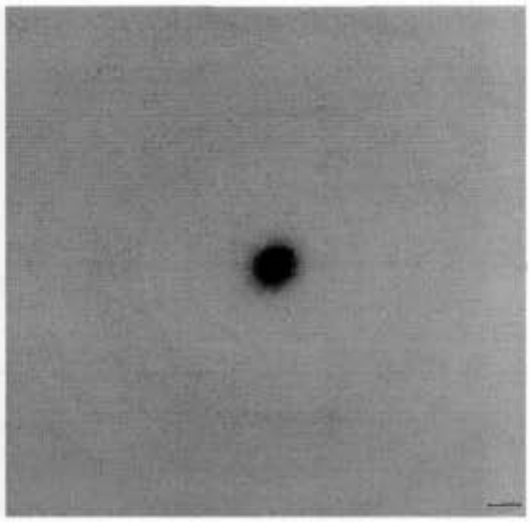

Figure 4.15: Galaxy WKK98 6600, *PSF-Fitting* model of the galaxy as produced with the `ellipse`- and `bmodel` tasks

6. Display `isub...finminmod.fits`, if necessary, adjust the background value and other parameters and re run `bmodel` and `ellipse`.

   Repeat from Item 12 on page 30, if necessary.

7. Enter parameters into `tdump`:

```
table    = isub...final.tab
cdfile   = isub...final.cd
pfile    = isub...final.p
datafil  = isub...final.dat
columns  = sma, intens, int_err, ellip, ellip_err,
           pa, pa_err, tflux_e, npix_e, ndata, nflag
```

8. Run `tdump` with `datafil=isub...final.dat` to create the ASCII table for further analysis with the *SM*-scripts described in Chapter 7 on page 73.

   (Optional) One can use the `tcreate` task to make a complete ASCII table out of the `....cd`, the `....p` and the `....dat` files produced by

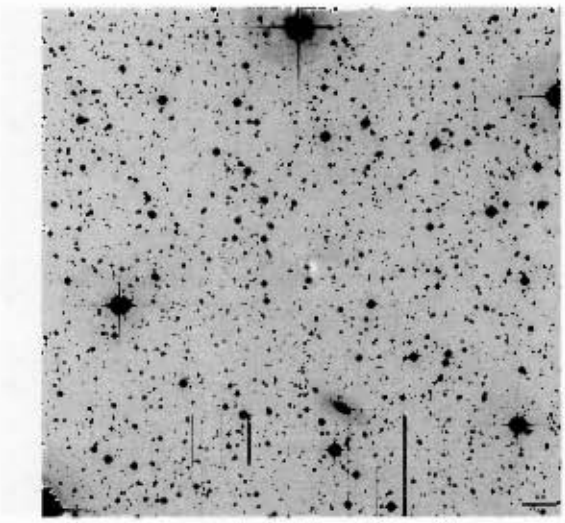

Figure 4.16: Galaxy WKK98 6600, original image minus the *PSF-Fitting* galaxy model.

`tdump`.

Chapter 5

Star-Masking

5.1 Pixel-Mask Determination

1. Copy the files `s...minmodcen.fits` and `isub....fits` into a newly made `usemasking` directory. Enter this directory and do all further *Star-Masking* calculations in this directory.

2. Copy the file `s...minmodcen.fits` into `s...minmodred.fits`. This is the resulting image from the *σ-Clipping* in Chapter 3 on page 7. Notice however that in this chapter, the instrument is different to the ones used for the description of the *σ-Clipping*. Also copy the original image `isub...wkk....fits` into `isub...wkk....fit` (three characters after the last dot). These images may look similar to the ones in Figure 5.2 on page 36 and Figure 5.1 on page 36, respectively.

3. Use about $5 \cdot \sigma$ (sigma from item 1 on page 3 in section 2) as threshold for pixels to be raised to 65000counts (for example $\sigma = 8 \rightarrow$ lower = upper = 44):

```
>>imreplace s...minmodred.fits 65000 lower=44
...

>>imreplace s...minmodred.fits 0 upper=44
...
```

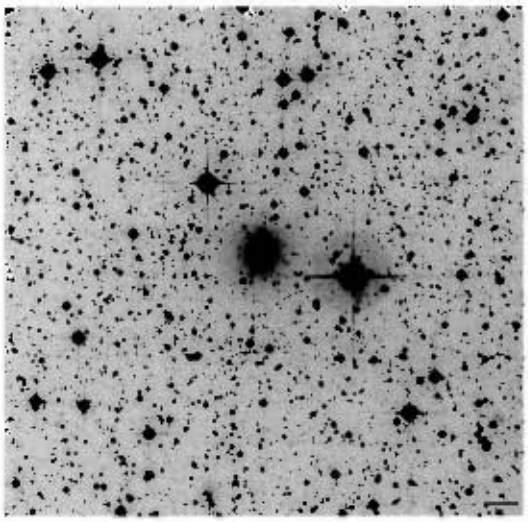

Figure 5.1: Galaxy WKK98 5920, original R_c band image.

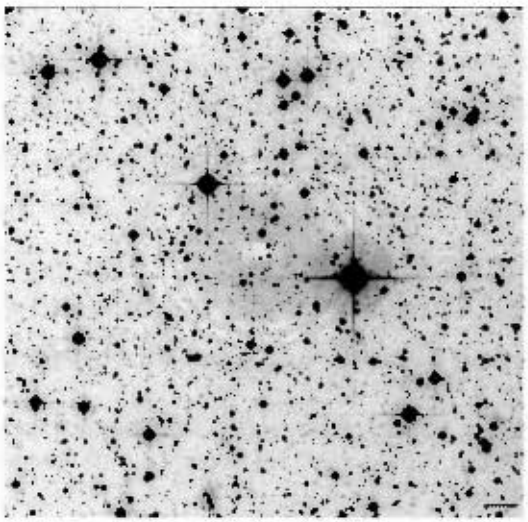

Figure 5.2: Galaxy WKK98 5920, 'clean' image without the galaxy, from applying the *σ-Clipping* described in Chapter 3 on page 7.

If the galaxy is close to the corner of the picture and there is an 'artificial' edge, due to the combination of several shifted images into one image, this edge must be masked out, using an appropriate value for `upper`:

```
>>imreplace s...minmodred.fits 65000 upper=-300
←
```

This must be done before the second call of `imreplace` mentioned above.

4. Display `s...minmodred` and redo sequence from item 2 onwards with a slightly different σ in item 3 until most of the stars but as little noise as possible is included. The resulting image will look similar to Figure 5.3 on page 37.

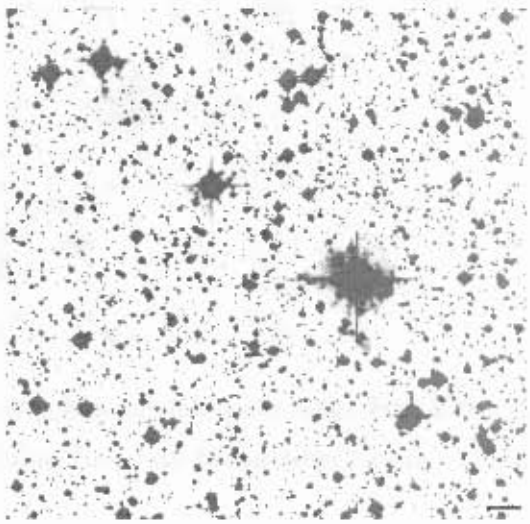

Figure 5.3: Galaxy WKK98 5920, the pixel-mask derived from the image with the *σ-Clipping* galaxy model subtracted.

5. Copy the file `s...minmodred.fits` into `s...minmodredc.fits`.

6. Copy the second row of pixels in the image into the first row, as for some reason the the whole first row of pixels is raised to 65000counts:

```
>>imcopy s...minmodredc.fits[1:1251,1250:1250]
         s...minmodredc.fits[1:1251,1251:1251]
. .
```

Do the same for other bad rows or columns going through the whole image, as the ccdmask task doesn't accept these values. If however the bad columns or rows go through the area where the galaxy is to be modelled, the lines are only to be removed for the part not needed for the galaxy model, for instance the top and bottom 200 rows. Figure 5.4 on page 38 shows a resulting image.

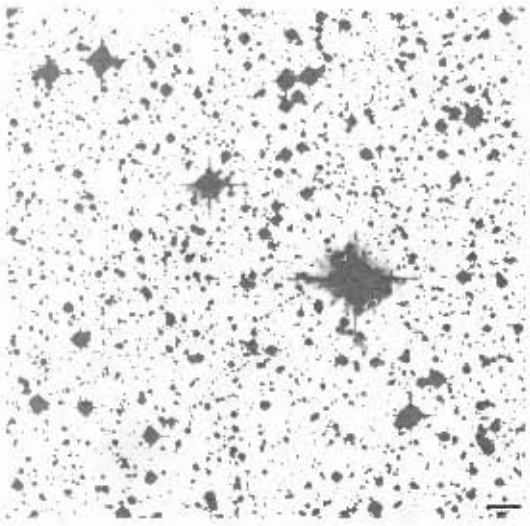

Figure 5.4: Galaxy WKK98 5920, the pixel mask derived from the image with the *σ-Clipping* galaxy model subtracted and bad pixel-columns removed.

7. Enter the following parameters into `ccdmask` and use the same root name for the mask as for the image the mask should be applied to (`isub...wkk....fits`):

```
image       = s...minmodredc
mask        = !sub...wkk...
ngood       = 1
```

```
lsigma    = 6
hsigma    = 6
ncmed     = 70
nlmed     = 70
ncsig     = 150
nlsig     = 150
```

Multiply the values for `ncmed`, `nlmed`, `ncsig` and `nlsig` by 2, 3 or 4, if necessary, to mask big parts – like galaxies or saturated stars – out of the image and to avoid the unfinished stop of the `ccdmask` task.

Be aware that each of these multiplications appears to be responsible for an grow of roughly a factor 10 in calculation time of the `ccdmask` task.

8. Run `ccdmask`, if possible as a background task, as it can take up to several hours or even a day, dependent on the capabilities of the computer used.

   Due to the long calculation time, it seems reasonable to copy the file `s...minmodredc.fits` onto another computer, for instance by using `ftp`, to run the `ccdmask` task on that computer with the same parameters as in item 7. The finished pixel-list file `isub...wkk....pl` can then later be copied back onto your computer for further calculations.

5.2 The final Galaxy Model

1. Enter parameters into `ellipse` or associated parameter files:

   ```
   region = yes
   nclip  = 0
   input  = isub....fit
   output = s...mask.tab
   ```

2. Confirm the following parameters in the `ellipse` task:

```
x0          = ...
y0          = ...
ellip0      = ...
pa0         = ...
hellip      = ...
hpa         = ...
hcenter     = ...
xylearn     = ...
recenter    = ...
maxSMA      = ...
```

3. Run `ellipse`, adjust the parameters in item 2 and re-run the `ellipse` task until best possible fit achieved, i.e. with no or as little visible 'rings' as possible.

   Use `isoexam` and `isoplot` tasks to examine the `ellipse`-results.

   (Optional) One could use the `tread` task, to look at the non-ASCII-table `s...w...mask.tab`; use `^D` and `q` to leave the displayed table.

4. Run `bmodel` with `input=s...mask.tab`, `output=s...mmodel.tab` and the value `background` for the background counts adjusted, usually by subtraction of about 10 of the previous value.

5. Subtract the model from the original image:

```
>>imarith isub...fit - s...w...mmodel.fits s...w...minmmod.fits
←
```

6. Display `s...w...minmmod.fits` and re-run items from 7 onwards, if necessary, for instance when the mask is not complete, change the parameters in `ccdmask` to obtain a different mask.

7. Enter parameters into `tdump`:

```
table       = s...mask.tab
cdfile      = s...mask.cd
```

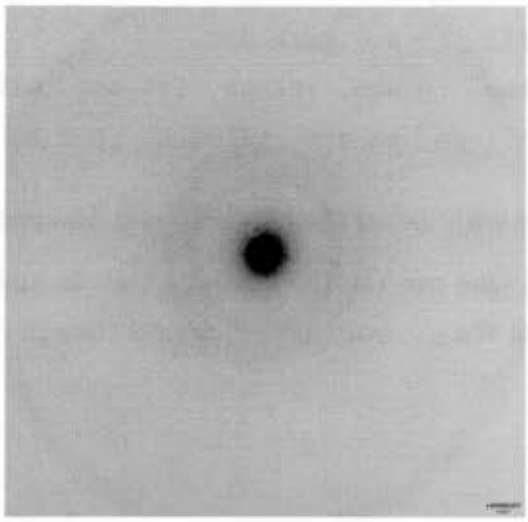

Figure 5.5: Galaxy WKK98 5920. *Star-Masking* model of the galaxy as produced with the `ellipse`- and `bmodel` tasks.

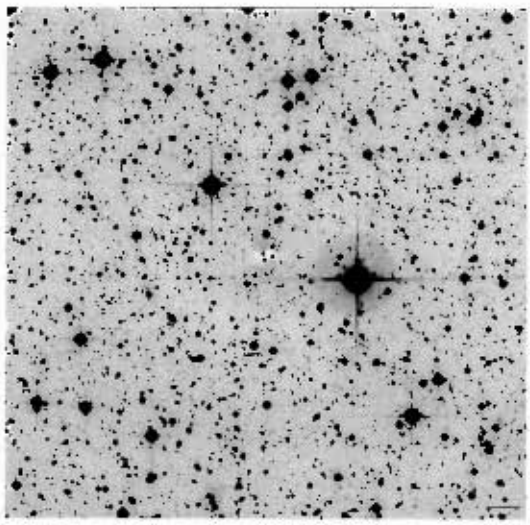

Figure 5.6: Galaxy WKK98 5920, original image minus the *Star-Masking* galaxy model.

```
pfile      = s...mask.p
datafil    = s...mask.dat
columns    = sma, intens, int_err, ellip, ellip_err,
         pa, pa_err, tflux_e, npix_e, ndata, nflag
```

8. Run tdump with datafil=s...mask.dat to create the ASCII-table.

   (Optional) One can use the tcreate task to make a complete ASCII-table out of the ....cd, the ....p and the ....dat files produced by tdump.

Chapter 6

Improved Point Spread Function Fitting

6.1 Point Spread Function Determination

1. Copy or rename the image of interest to some short name, like `k.fits`, and move this file into a new subdirectory. See Figure 3.1 on page 8 for an example of what the image may look like.

2. Make five further subdirectories within the new subdirectory:

   ```
   1_psf_fitting
   2_apply_killall
   3_get_galaxy_model
   4_apply_killall
   5_get_galaxy_model
   ```

3. Copy the file `k.fits` into each of these new subdirectories.

4. Enter the directory `1_psf_fitting` as the new working-directory.

5. Check and, if necessary, enter parameters into the `daofind`, `daopars`, `datapars`, `findpars`, `nstar`, `phot`, `photpars`, `psf` and `substar` parameter files:

```
daofind.verify    = yes
daofind.update    = yes
daofind.verbose   = yes
daofind.image     = k.noged

daopars.psfrad    = ...
daopars.fitrad    = ...
daopars.function  = ...

datapars.fwhm     = ...
datapars.sigma    = ...
datapars.datamin  = ...
datapars.datamax  = ...
datapars.ccdread  = ...
datapars.gain     = ...
datapars.exposur  = ...
datapars.airmass  = ...
datapars.filter   = ...
datapars.obstime  = ...

findpars.thresho  = ...

nstar.verify      = yes
nstar.groupfil    = k.noged.psg.1
nstar.image       = k.noged

phot.image        = k.noged
phot.verify       = yes
phot.update       = yes
phot.verbose      = yes
phot.graphic      = stdgraph
```

```
phot.display      = stdimage

photpars.aperture = ...

psf.image         = k.noged
psf.verify        = yes
psf.graphic       = stdgraph
psf.display       = stdimage
psf.psfimage      = k.noged.psf.1
psf.groupfil      = k.noged.psg.1
psf.opstfile      = k.noged.pst.1

substar.verify    = yes
substar.photfile  = default
substar.psfimage  = default
substar.image     = default
```

6. Run daofind on the k.noged image that resulted from applying the *σ-Clipping* in Section 3 on page 7. Figure 3.1 on page 11 shows such a result. Mark the found stars with tvmark, to see if too few or too many stars were found. Adjust the findpars.threshold value above and re run daofind, if necessary. One can also mark and delete stars interactively with tvmark, if necessary. The output of tvmark can be entered as a parameter output within tvmark.

7. Enter the FWHM value as aperture radii into daophot.photpars and run phot.

8. Use pselect to select bright stars within a range of magnitudes and display these stars with tvmark.

   One can use pstselect to find suitable PSF-stars to then display the found stars with tvmark.

9. **First run of psf-function**

   Run psf with a fitting radius of around the FWHM value and a small PSF radius, e.g. 14 instead of 20 pixel, and select at least 5 PSF-candidates without close neighbours.

   (Optional) To view the PSF-image, one can use the seepsf task.

   An example of the resulting PSF is is shown on the very left side of Figure 6.1 on page 46.

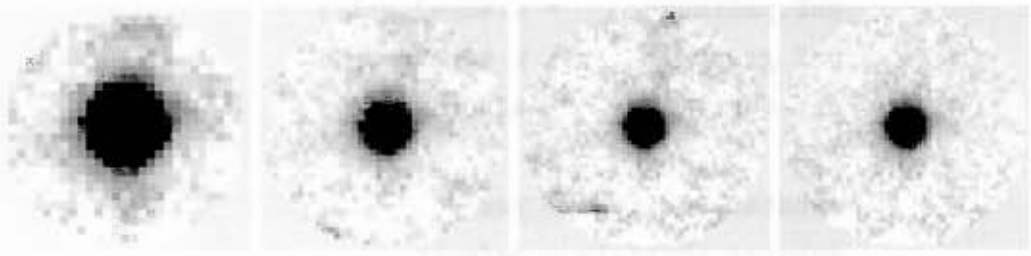

Figure 6.1: Galaxy WKK98 5920, evolution of a PSF. From left to right, resulting PSFs after the first, second, third and fourth run of psf are shown.

10. Run first nstar and then substar on the k.noged image with the small PSF-radius and display the resulting xxx.sub.1 image. Redo the PSF (see previous step) if stars are not nicely subtracted.

11. Delete the xxx.sub.1 file and remove the PSF-stars from within the r.noged.nst.1 file, by comparing the listed information with the information in the xxx.pst.1 file. Re-run substar and display the result to check. See Figure 6.2 on page 47 for an example.

12. Enter parameters into the nstar and psf parameter files:

```
nstar.groupfil    = k.noged.psg.2

psf.image         = k.noged.sub.1
psf.photfile      = k.noged.mag.1
```

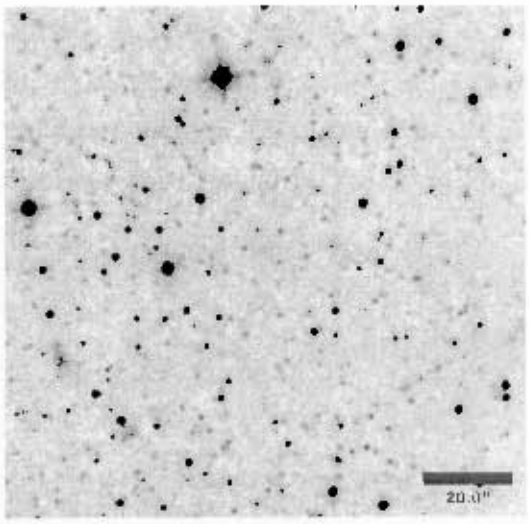

Figure 6.2: Galaxy WKK98 5920, after first run of psf. The closest neighbours of the selected PSF-stars were removed using the first PSF-model.

```
psf.psfimage    = k.noged.psf.2
psf.groupfil    = k.noged.psg.2
psf.opstfile    = k.noged.pst.2
```

13. **Second run of psf-function**

    Run psf again, this time with the normal PSF-radius, e.g. 20 pixel, and use a value for the datamin parameter that is several σ smaller, since the subtraction of stars has added some 'noise' to the image. Use the same PSF-stars as before (cf. Item 9 on page 46), or a subset thereof.

    (Optional) To view the PSF-image, one can use the seepsf task.

    The second from the left image in Figure 6.1 on page 46 shows an example.

14. Run first nstar and then substar on the k.noged image again with the normal PSF-radius and smaller value for the datamin parameter. Display the resulting xxx.sub.2 image and compare with the previous result from substar (cf. Item 10 on page 46).

15. Delete the `xxx.sub.2` file and remove the PSF-stars from within the `r.noged.nst.2` file, by comparing the listed information with the information in the `xxx.pst.2` file. Re-run `substar` and display the result to check. See Figure 6.3 on page 48 for an example.

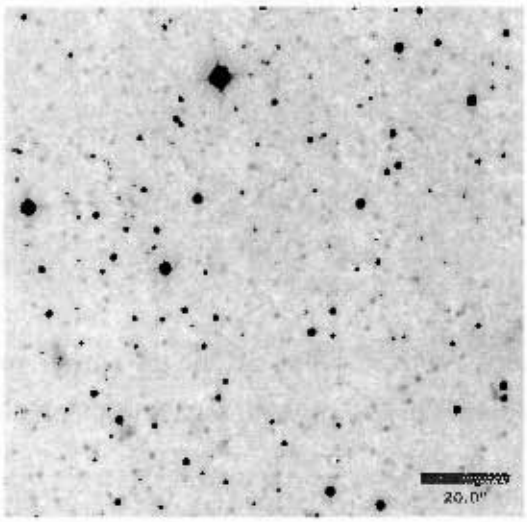

Figure 6.3: Galaxy WKK98 5920, after second run of `psf`. The close neighbours of the selected PSF-stars were removed using the second PSF-model.

16. Enter parameters into the `nstar` and `psf` parameter files:

```
nstar.groupfil    = k.noged.psg.3

psf.image         = k.noged.sub.2
psf.psfimage      = k.noged.psf.3
psf.groupfil      = k.noged.psg.3
psf.opstfile      = k.noged.pst.3
```

17. **Third run of `psf`-function**

    Yet again, run `psf`, now with a slightly bigger PSF-radius, e.g. 26 pixel, and use a value for the `datamin` parameter that is now even several σ smaller than before, since the subtraction of stars again has added some

'noise' to the image. Use the same PSF-stars as before (cf. item 13 on page 17), or a subset thereof.

(Optional) To view the PSF image, one can use the `seepsf` task.

See 6.1 on page 46, second from the right, for an example.

18. Run first `nstar` and then `substar` on the `k.noged` image again with the bigger PSF-radius and even smaller value for the `datamin` parameter. Display the resulting `xxx.sub.3` image and compare with the previous result from substar (cf. item 14 on page 17).

19. Delete the `xxx.sub.3` file and remove the PSF-stars from within the `r.noged.nst.3` file, by comparing the listed information with the information in the `xxx.pst.3` file. Re-run `substar` and display the result to check. See Figure 6.4 on page 49 for an example.

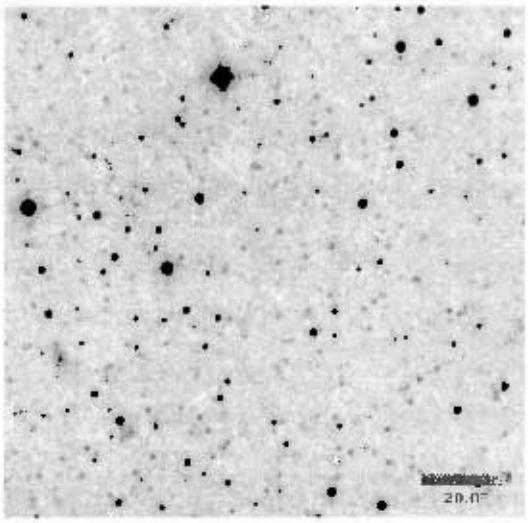

Figure 6.1: Galaxy WKK98 5920, after third run of psf. The neighbours of the selected PSF-stars were removed using the third PSF-model.

20. **Fourth run of psf-function**

21. Delete obvious remains and small left over stars at the edges of the

PSF-stars with `imedit` and save the result for example as `k.psfed`. See Figure 6.4 on page 49 for an example.

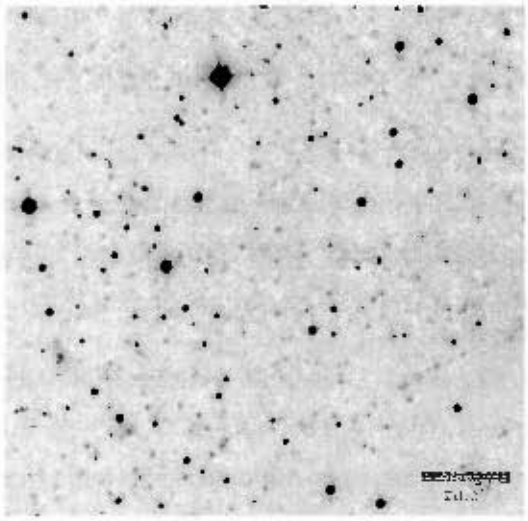

Figure 6.5: Galaxy WKK98 5920, after the surrounding of the PSF-stars has been 'cleaned' with `imedit`.

22. Enter parameters into the `psf` parameter files:

```
psf.image       = k.psfed
psf.psfimage    = k.psfed.psf.1
psf.groupfil    = k.psfed.psg.1
psf.opstfile    = k.psfed.pst.1
```

23. Now run `psf` again with the slightly bigger PSF-radius and use the several σ lower value for the `datamin` parameter. Use the same PSF-stars as before (cf. Item 17 on page 48), or a subset thereof.

    (Optional) To view the PSF-image, one can use the `seepsf` task.

    See 6.1 on page 46, the image on the very right, for an example.

24. Now copy the resulting `k.psfed.psf.1` file into the `2_apply_killall` directory. Rename it into `k.psf.1.fits` within the `2_apply_killall`

directory, make a copy of the file and label the copy `k.psf.2.fits`. Now copy the two files `k.psf.1.fits` and `k.psf.2.fits` into the `4_apply_killall` directory.

25. Copy the files `k.noged.fits` and `k.pars` into the `2_apply_killall` directory . The `k.pars` file can be typed in newly or taken from a previously worked on galaxy.

6.2 First run of *Killall*

1. Enter the directory `2_apply_killall` as the new working directory.

2. Enter all necessary information into a file `k.pars`, similar to the one shown here:

```
datapars.scale = 1.
datapars.fwhmpsf = 3.25
datapars.emission = yes
datapars.sigma = 6.7
datapars.datamin =  40.
datapars.datamax = 1000.
datapars.noise = "poisson"
datapars.ccdread = "ERON"
datapars.gain = "EGAIN"
datapars.readnoise = 0.
datapars.epadu = 1.
datapars.exposure = "EXPTIME"
datapars.airmass = "AIRMASS"
datapars.filter = "FILTER"
datapars.obstime = "UT"
datapars.itime = 1.
datapars.xairmass = INDEF
datapars.ifilter = "INDEF"
```

```
datapars.otime = "INDEF"
datapars.mode = "ql"
# EOF
findpars.threshold = 3.5
findpars.nsigma = 1.5
findpars.ratio = 1.
findpars.theta = 0.
findpars.sharplo = 0.2
findpars.sharphi = 1.
findpars.roundlo = -1.
findpars.roundhi = 1.
findpars.mkdetections = no
findpars.mode = "ql"
# EOF
centerpars.calgorithm = "centroid"
centerpars.cbox = 6.4
centerpars.cthreshold = 0.
centerpars.minsnratio = 1.
centerpars.cmaxiter = 10
centerpars.maxshift = 1.
centerpars.clean = no
centerpars.rclean = 1.
centerpars.rclip = 2.
centerpars.kclean = 3.
centerpars.mkcenter = no
centerpars.mode = "ql"
# EOF
fitskypars.salgorithm = "mode"
fitskypars.annulus = 10.
fitskypars.dannulus = 10.
fitskypars.skyvalue = 0.
```

```
fitskypars.smaxiter = 10
fitskypars.sloclip = 0.
fitskypars.shiclip = 0.
fitskypars.snreject = 50
fitskypars.sloreject = 3.
fitskypars.shireject = 3.
fitskypars.khist = 3.
fitskypars.binsize = 0.1
fitskypars.smooth = no
fitskypars.rgrow = 0.
fitskypars.mksky = no
fitskypars.mode = "ql"
# EOF
photpars.weighting = "constant"
photpars.apertures = "3.25"
photpars.zmag = 25.
photpars.mkapert = no
photpars.mode = "ql"
# EOF
daopars.function = "penny1"
daopars.varorder = 0
daopars.nclean = 0
daopars.saturated = no
daopars.matchrad = 3.
daopars.psfrad = 26.0
daopars.fitrad = 3.4
daopars.recenter = yes
daopars.fitsky = yes
daopars.groupsky = no
daopars.sannulus = 0.
daopars.wsannulus = 11.
```

```
daopars.flaterr = 0.75
daopars.proferr = 5.
daopars.maxiter = 50
daopars.clipexp = 6
daopars.cliprange = 2.5
daopars.mergerad = INDEF
daopars.critsnratio = 1.
daopars.maxnstar = 50000
daopars.maxgroup = 100
daopars.mode = "ql"
# EOF
```

3. Enter parameters into the `killall` parameter files:

```
killall.directory = /
killall.picture   = k.roged
killall.psf1      = k.psf.1
killall.psf2      = k.psf.2
killall.parameter = k.pars
killall.boxsize   = ...
killall.border    = ...
killall.xcentre   = ...
killall.ycentre   = ...
```

4. Run `killall` twice and look at the resulting `k.roged.rostr2` image as well as the other images produced by `killall`. If necessary re-run `killall` after adjusting the `killall` parameters and the parameter in the parameter file `k.pars`. For the `boxsize` parameter, use the maximum value, i.e. if possible the size of the image. If `boxsize` is significantly smaller than the longest side of the image to work on, the `border` parameter needs to be larger than zero. the exact size has to be established by viewing the results.

A set of resulting images can be seen in Figures 6.6 to 6.8 on pages 55 to 56, respectively.

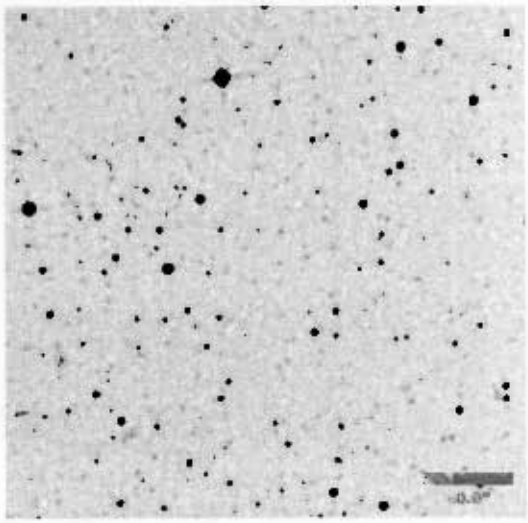

Figure 6.6: Galaxy WKK98 5920, *Killall* output image with all stars left in the image.

5. Copy the `k.pars` file into the directory `4_apply_killall` and copy the files `k.noged.nostr2`, `k.noged.allfits2` and `k.psf.2.fits` into the directory `3_get_galaxy_model`.

6.3 A better Galaxy Model

1. Enter the directory `3_get_galaxy_model` as the new working-directory.

2. Copy the `k.noged.allfits2` file into `k.imedfix` and edit this new file for instance with *Emacs*, so that the content is of the form 'x y 0 b', with the last row being '0 0 0 q'. Here x and y are the coordinates of the stars found by *Killall*. If many stars were found, it may be necessary to select the brightest 1500 or so stars with th `pselect`-function.

3. Enter parameters into the `imedit` parameter files:

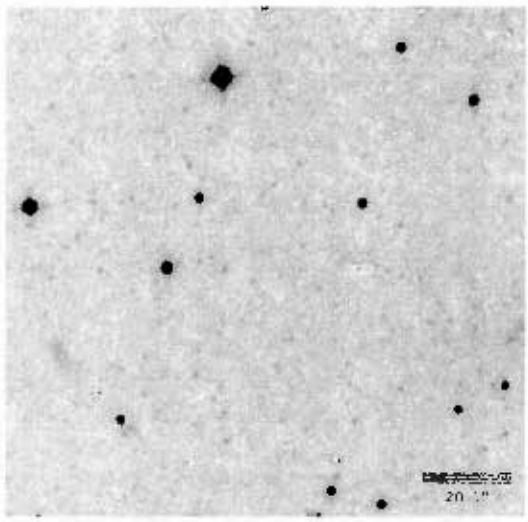

Figure 6.7: Galaxy WKK98 5920, *Killall* output image with all stars removed.

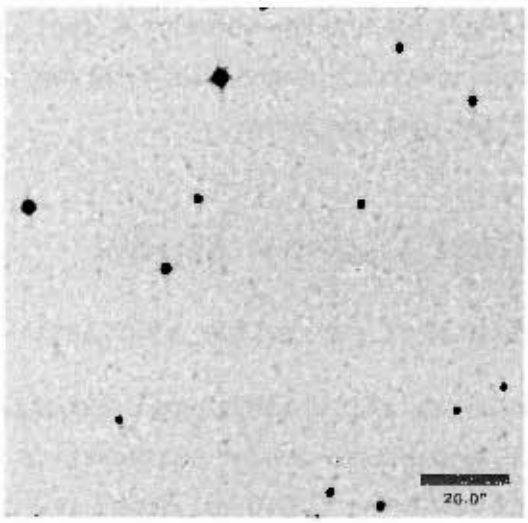

Figure 6.8: Galaxy WKK98 5920, *Killall* output image with the 'sky'.

```
imedit.input      - k.noged.nostr2
imedit.output     = k.nostr2.ed
imedit.cursor     - k.imedfix
imedit.display    = no
imedit.autodisp   = no
imedit.radius     - 7
```

It is important to set `display` and `autodispl` to `no`, since otherwise the process will take a long time or may even hang up.

4. Run `imedit` non-interactively to remove the remains from the star-reduction. See Figure 6.9 on page 57 for an example.

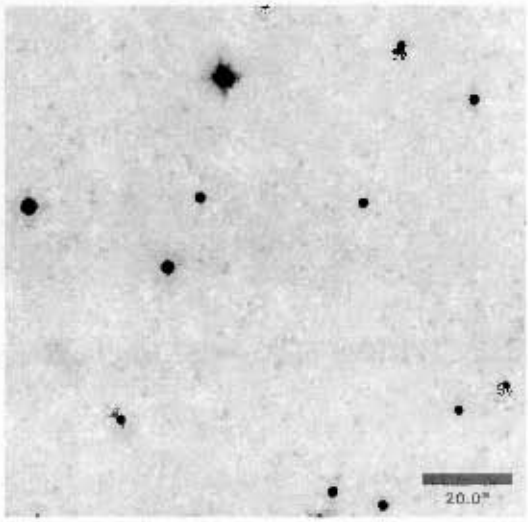

Figure 6.9: Galaxy WKK98 5920, after non-interactively 'cleaning' the image using the `imedit` task.

5. Set the `imedit` parameters to their default values by using `unlearn` and enter new values into the `imedit` parameter files:

```
imedit.input      = k.nostr2.ed
imedit.output     = k.nostr2.ed2
```

```
imedit.cursor     = k.imedfix
imedit.display    = yes
imedit.autodisp   = yes
imedit.radius     = 7
```

6. Now run `imedit` interactively to remove bright stars and spikes etc. See Figure 6.10 on page 58.

Figure 6.10: Galaxy WKK98 5920, after interactively 'cleaning' the image using the `imedit` task.

7. Enter `imarith k.noged.nostr2 - k.nostr2.ed2 k.diff` to produce a file containing the remains left, see Figure 6.11 on page 59 for an example.

8. Enter new values into the `substar` parameter files:

```
substar.image     = k
substar.photfile  = k.noged.allfits2
substar.psfimage  = k.psf.2
substar.verify    = yes
```

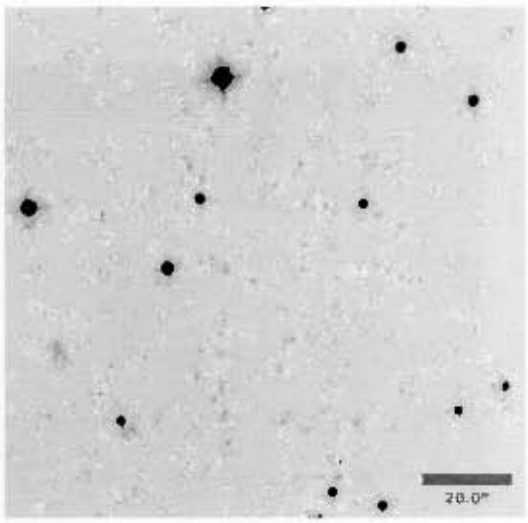

Figure 6.11: Galaxy WKK98 5920, image of remains left after running *Killall* and 'cleaning' the resulting image.

9. Run `substar` on the original image that contains the galaxy and enter the large PSF-radius and the high value for `datamin` that were used in Item 17 on page 48 when the function asks for it. Also enter a low value for `datamax`, e.g. 12000 counts. The result can be viewed in Figure 6.12 on page 60.

10. Now type `imarith k.sub.1 - k.diff k.goodsub` to produce the image that only contains the galaxy. See Figure 6.13 on page 60.

11. Sometimes some very high intensity pixels are left over after or produced during this procedure. These pixels can cause the `ellipse`-procedure not to produce a proper model when no *σ-Clipping* is applied. One can use `imedit` interactively to remove these pixels if they are not too close to the galaxy. However, if they are close or on top of the galaxy and editing becomes difficult or impossible, one can enter `imreplace k.goodsub xxx lower=12000` to lower the intensity of high-intensity pixels in the image. Here `xxx` is the average level of counts that is given in the area where the high-intensity pixels are.

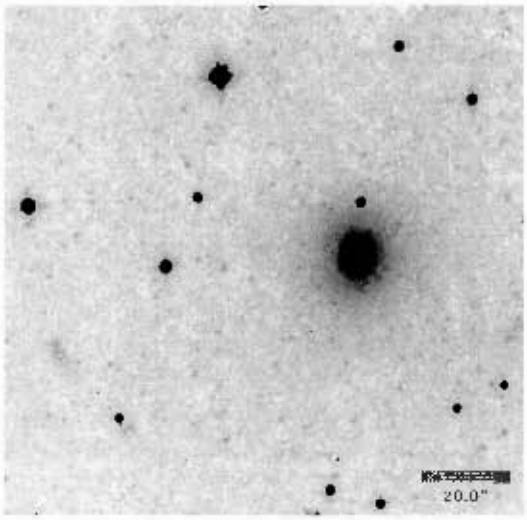

Figure 6.12: Galaxy WKK98 5920, original image with the stars subtracted.

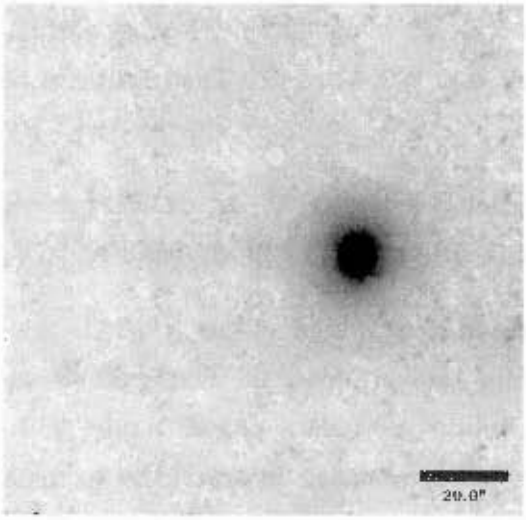

Figure 6.13: Galaxy WKK98 5920, original image 'cleaned', i.e. with the stars and remains subtracted.

i.e. the background. Doing this may cause the central region of the galaxy also to be altered. If this is the case, one has to copy the central region of the galaxy back into the `k.goodsub` image, using for instance `imcopy`. To be able to do this, making a copy of `k.goodsub` before applying `imreplace` is a good idea.

12. Enter new values into the `ellipse` and `bmodel` parameter files:

```
ellipse.input      = k.goodsub
ellipse.output     = e

magpar.mag0        = 25.

bmodel.table       = e
bmodel.output      = m
bmodel.background  = xxx
```

Here `xxx` is the value for the average background level.

13. Run `ellipse` and `bmodel` to determine a good galaxy model. If possible without *σ-Clipping*, i.e. with the `isophote.samplepar.nclip` parameter set to zero.

Use `isoexam` and `isoplot` tasks to examine the `ellipse`-results.

A resulting model is shown in Figure 6.14 on page 62.

14. Enter `imarith k.goodsub - m k.subnog` and check if the model of the galaxy is nicely subtracted. Re-run `ellipse` and `bmodel` after varying the `ellipse`- and `bmodel` parameters, if necessary. Figure 6.15 on page 62 shows the resulting image.

15. Type `imarith k - m k.nog` to subtract the model from the original image, see Figure 6.16 on page 63.

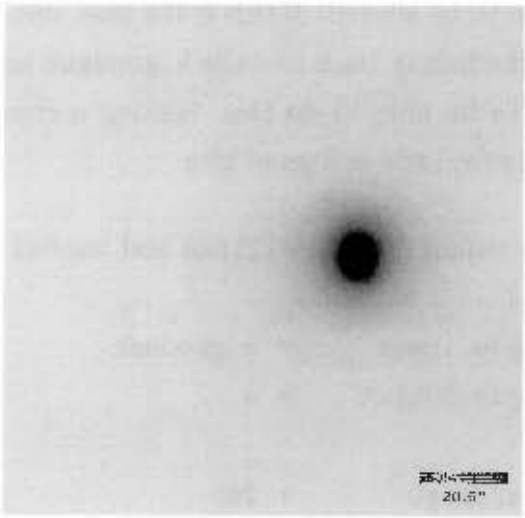

Figure 6.14: Galaxy WKK98 5920, improved galaxy model.

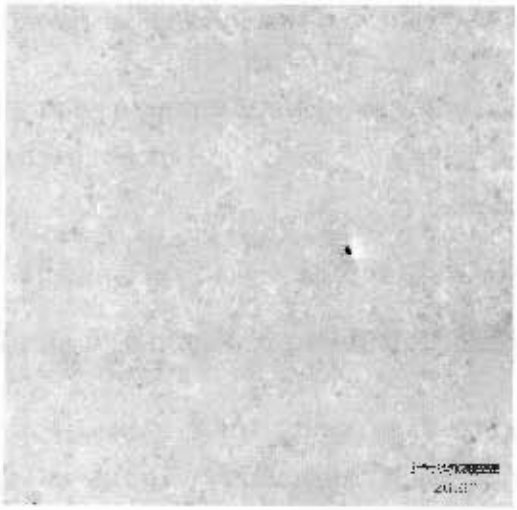

Figure 6.15: Galaxy WKK98 5920, 'clean' image minus the improved galaxy model.

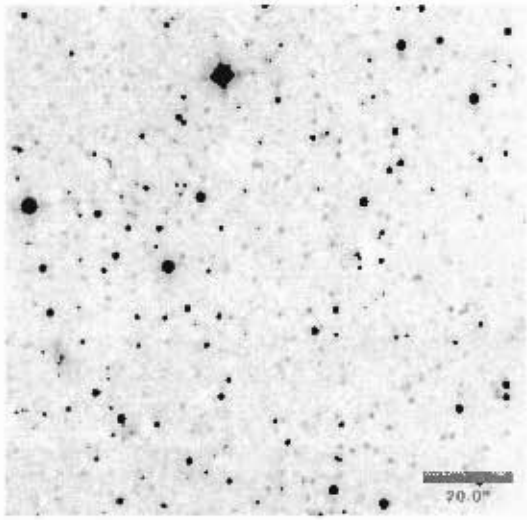

Figure 6.16: Galaxy WKK98 5920, original K_s band image minus improved galaxy model.

16. Remove the remains at the position of the centre of the galaxy after subtracting the model and save the resulting file as `k.noged.fits`, see Figure 6.17 on page 64. Copy this file into the directory `4_apply_killall`.

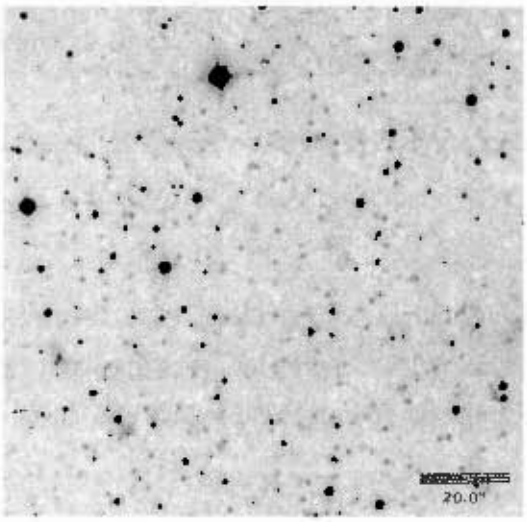

Figure 6.17: Galaxy WKK98 5920, original K_s band image minus improved galaxy model and removed remains in centre.

6.4 Second run of *Killall*

1. Enter the directory `4_apply_killall` as the new working-directory.

2. Start over once from Item 2 on page 51 up to Item 4 on page 54.

   A set of resulting images can be seen in Figures 6.18 to 6.20 on pages 65 to 66, respectively.

3. Copy the files `k.noged.nostr2`, `k.noged.allfits2` and `k.psf.2.fits` into the directory `5_get_galaxy_model`.

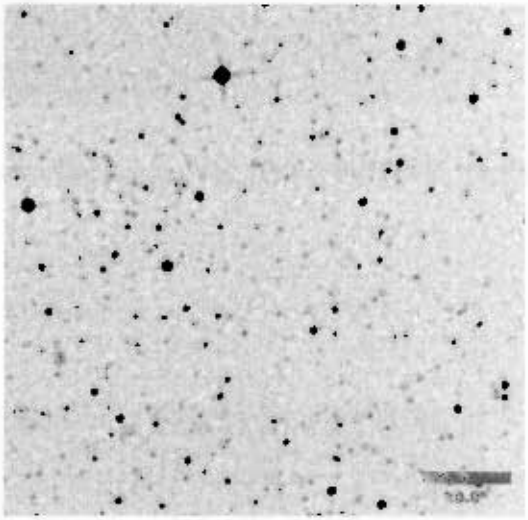

Figure 6.18: Galaxy WKK98 5920, *Killall* output image with all stars left in the image.

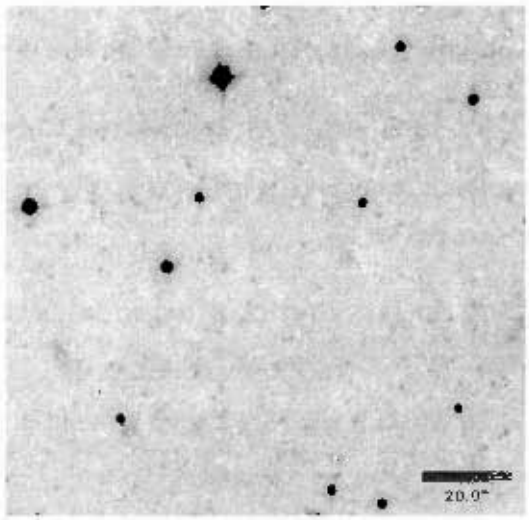

Figure 6.19: Galaxy WKK98 5920, *Killall* output image with all stars removed.

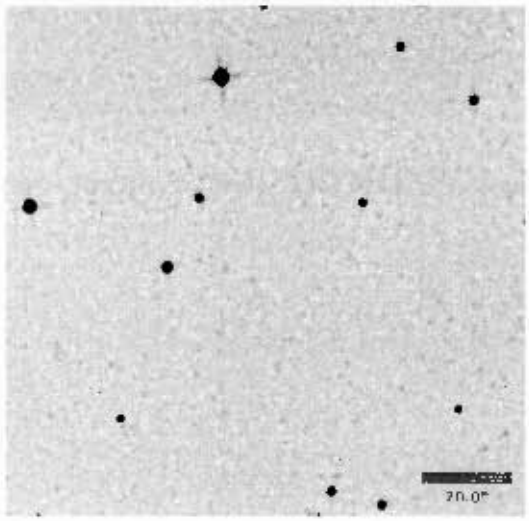

Figure 6.20: Galaxy WKK98 5920, *Killall* output image with the 'sky'.

6.5 The final Galaxy Model

1. Enter the directory `5_get_galaxy_model` as the new working-directory.

2. Repeat procedure once from Item 2 on page 55 up to Item 15 on page 61.

   A set of resulting images can be seen in Figures 6.21 to 6.28 on pages 67 to 71, respectively.

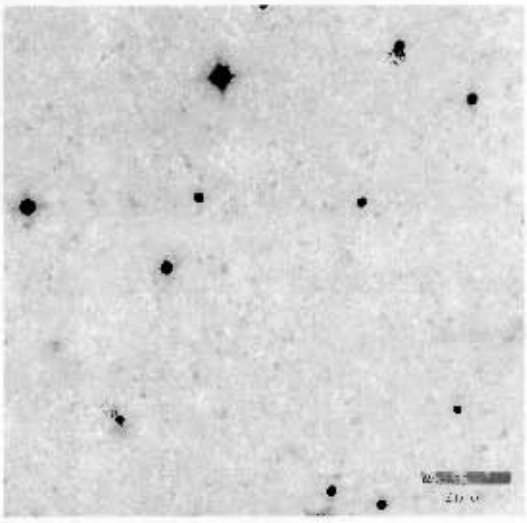

Figure 6.21: Galaxy WKK98 5920, after non-interactively 'cleaning' the image using the `imedit` task.

3. Use `tdump` to save the results from the model into an ASCII-table. For the *SM*-scripts described in Chapter 7 on page 73, the following parameters `sma`, `intens`, `int_err`, `ellip`, `ellip_err`, `pa`, `pa_err`, `tflux_e`, `npix_e`, `ndata` and `nflag` were saved into the file `wkk5920.ks.killall_table.dat`.

Figure 6.22: Galaxy WKK98 5920, after interactively 'cleaning' the image using the `imedit` task.

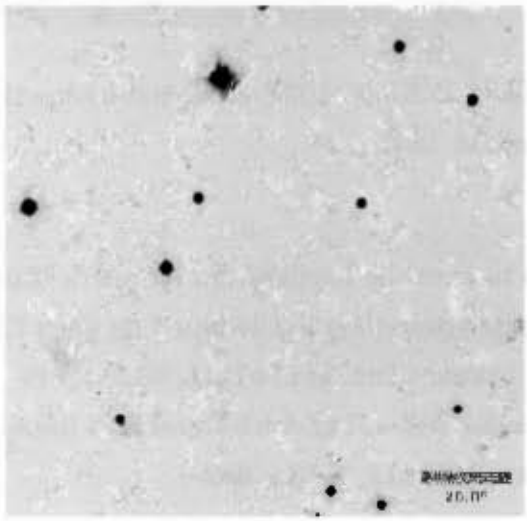

Figure 6.23: Galaxy WKK98 5920, image of remains left after running *Killali* and 'cleaning' the resulting image.

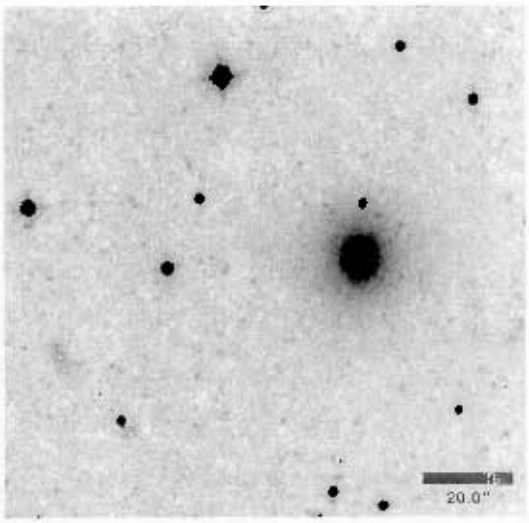

Figure 6.24: Galaxy WKK98 5920, original image with the stars subtracted.

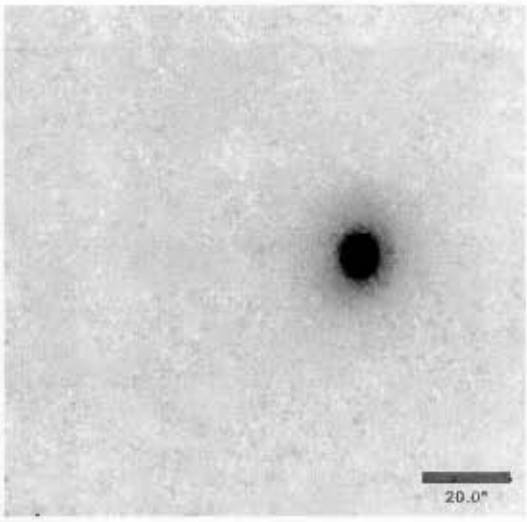

Figure 6.25: Galaxy WKK98 5920, original image 'cleaned', i.e. with the stars and remains subtracted.

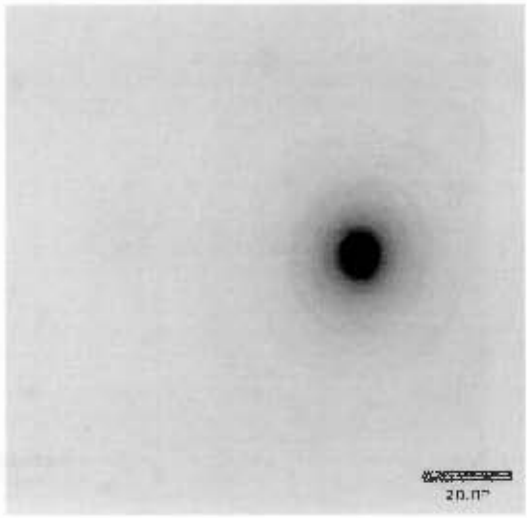

Figure 6.26: Galaxy WKK98 5920, final galaxy model

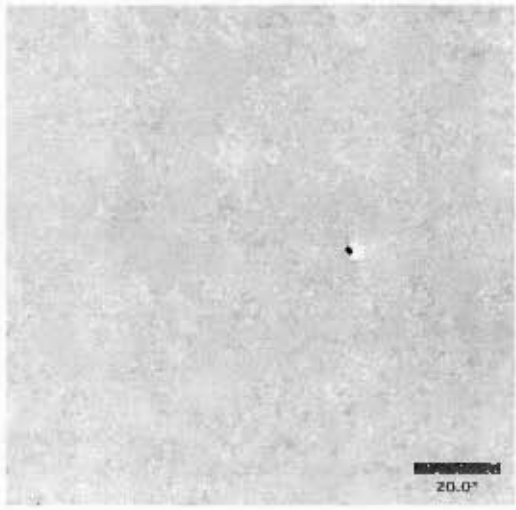

Figure 6.27: Galaxy WKK98 5920, 'clean' image minus the final galaxy model

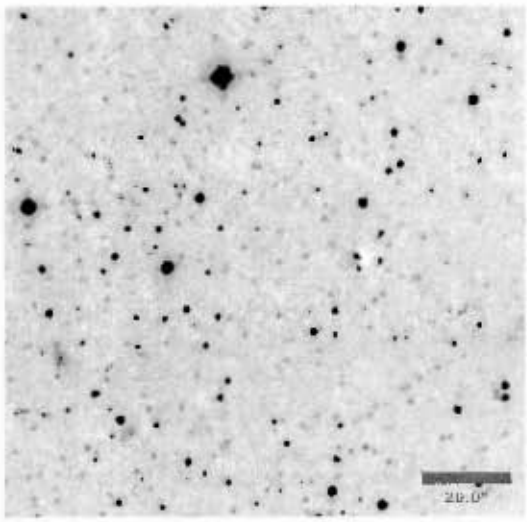

Figure 6.28: Galaxy WKK98 5920, original K_s band image minus final galaxy model

Chapter 7

SM Plotting

In this chapter, the *SM* routines are shown, that were used to produce the total isophotal and integrated magnitude plots, as well as position angle and ellipticity plots of a galaxy model, as derived from one of the methods given in Chapters 3 to 6. An example of these plots is given in Figure 7.1 on page 73.

Figure 7.1: Galaxy WKK98 5920. *SM* plots as produced by the *SM* scripts shown in this section.

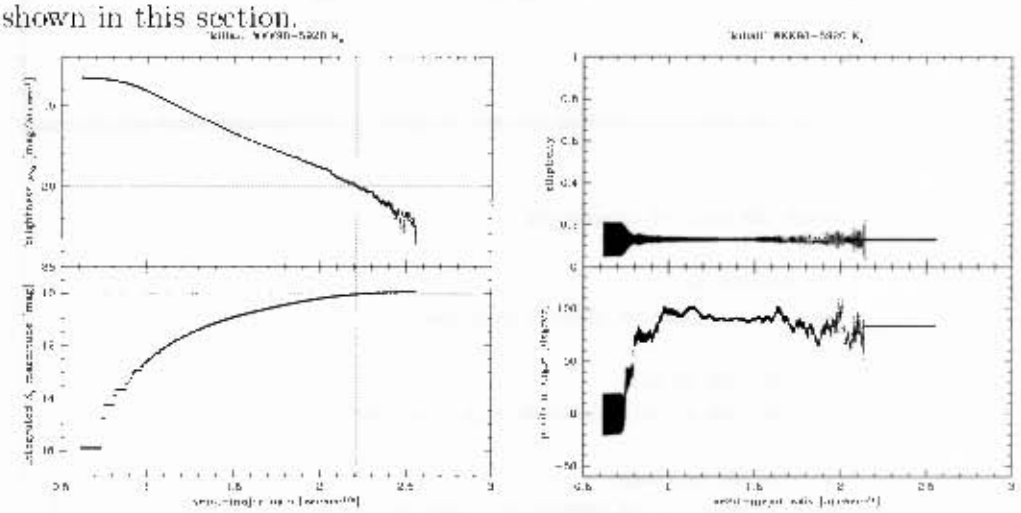

1. Assuming that *SM* is already installed on your system, one usually

enters `sm↩` at the command line in a new terminal window to start *SM*. All commands following are entered in the same window, but are now intercepted and executed by *SM*.

2. It is often most feasible, to produce files that contain consecutive commands. These files – or macros – can then be called from within *SM*. The first such file shown here contains the name definitions of the macros which will be used for calculating and plotting from within the *SM* environment. To make *SM* aware of all these programmes, one simply enters `macro read galaxy model_plotting_macros.sm↩` at the command line.

```
##########################################################################
#                                                                        #
#  This file contains macros for SM, to plot results from modelling      #
#  galaxies of the galaxy cluster AC03627.                               #
#                                                                        #
#                                                                        #
#                                                                        #
#                          Karaalan Markus                               #
#                       Department of Astronomy                          #
#                       University of Cape Town                          #
#                                                                        #
#                            09.11.2004                                  #
#                                                                        #
##########################################################################


########## WKK5920 ##########

plot_wkk5920.ks_kill
 execute "macros/plot_wkk5920.ks_killall.sm"

print_wkk5920.ks_kill
 execute "macros/print_wkk5920.ks_killall.sm"

plot_wkk5923.ks_rough
 execute  macros/plot_wkk5920.ks_rough.sm"

print_wkk5920.ks_rough
 execute "macros/print_wkk5920.ks_rough.sm"

plot_wkk5920.ks_1_killall
```

```
 execute "macros/plot_wkk5920.rc.11.51_killall.sm"

print_wkk5920.rc.11.51 killall
 execute "macros/print_wkk5920.rc.11.51_killall.sm"

plot_wkk5920.rc.11.51_rough
 execute "macros/plot_wkk5920.rc.11.51_rough.sm"

print_wkk5920.rc.11.51_rough
 execute "macros/print_wkk5920.rc.11.51_rough.sm"

plot_wkk5920.rc.11.51_mask
 execute "macros/plot_wkk5920.rc.11.51_mask.sm"

print_wkk5920.rc.11.51_mask
 execute "macros/print_wkk5920.rc.11.51_mask.sm"

plot_wkk5920.rc-ks.11.51_kill
 execute "macros/plot_wkk5920.rc-ks.11.51_killall.sm"

print_wkk5920.rc-ks.11.51_kill
 execute "macros/print_wkk5920.rc-ks.11.51_killall.sm"


########## WKK5972 ##########

plot_wkk5972.ks_kill
 execute "macros/plot_wkk5972.ks_killall.sm"
```

3. The second file shows a typical program which will be executed, once one of the macro names given in the previous file is called from within the *SM* environment, e.g. if `plot_wkk5920.ks_kill`↩ is entered at the command line.

```
##############################################################################
#                                                                            #
#  This file contains a macro for SM, to plot results from modelling         #
#  galaxies of the galaxy cluster ACO3627, using the 'killall'-method.       #
#                                                                            #
#                                                                            #
#                                                                            #
#                          Karskov, Markus                                   #
#                       Department of Astronomy                              #
#                       University of Cape Town                              #
```

```
#                                                                    #
#                              09.11.2004                            #
#                                                                    #
######################################################################
```

```
########## Data ##########

execute "macros/data_wkx5900.ks killall.sm"
```

```
########## Calculations and Constants SOFI ##########

execute "macros/calc+const_sofi.sm"
```

```
########## Isophotal Magnitude Plot ##########

device x11 -device 1 -bg white -g 500x700+600+0
erase

window 1 -2 1 2

execute "macros/plot_iso_mag_xs.sm"
```

```
########## Integrated Magnitude Plot ##########

window 1 -2 1 1

execute "macros/plot_int_mag_xs.sm"
```

```
########## Ellipticity Plot ##########

device x11 -device 2 -bg white -g 500x700+800+0
erase

window 1 -2 1 2

execute "macros/plot_ellip.sm"
```

```
########## Position Angle Plot ##########


window 1 -2 1 1

execute "macros/plot_pa.sm"
```

4. When the program listed above is executed, it imports several files, containing further code that is used by several similar programmes. By dividing the code into several files, it is possible to adjust small parts of the code, yet being able to use it for many programs.

   The first imported file contains definitions and parameters for one specific image and instrument. This is usually the only file where changes have to be made for each image.

```
##############################################################################
#                                                                            #
#                          Karsten Markus                                    #
#                      Department of Astronomy                               #
#                      University of Cape Town                               #
#                                                                            #
#                            09.11.2006                                      #
#                                                                            #
##############################################################################


########## Data ##########

# read data from killall procedure
data "data/tables_killall_models/wk45920.ks.killall_table.dat"

define galaxy "wk98 5920"
define galaxy_plot "WK98-5920"
define filter "Ks"
define filter_plot "K_s"
define field "0"
define field_plot " "
define ccd "0"
define ccd_plot " "
define procedure "killall"
define lower_pa_angle -60
define max_radius1_4 3.0
define max_iso_mag 12.0
```

```
define min_iso_mag 20.0
define max_int_mag 17.0
define min_int_mag 9.0
define vline_radius 2.21
define hline_int_mag 10.055
define first_line 2
define last_line 973

lines $first_line $last_line
read sma 1
read intens 2
read interr 3
read ellip 4
read elliperr 5
read pa 6
read paerr 7
read tflux 8
read npix 9
read nd 10
read nf 11

set kc0sofi =  99.319
set kc1sofi = -0.023
set kc2sofi = 0.05

set airmass = 1.229
set exp_time = 7.5
set sky = ((( 1.407) - (-2.855) + (-3.503) - (0.6253) + (-2.883)
        + (-1.727) - (3.625) + (1.872) + (-0.4056) + (-0.3795))/10)
# Remark: I used MEAN and a size of 10x10 pixels

echo
echo Data Set: $galaxy, $filter, $field, $procedure
echo estimated sky:
print '%5.3f' (sky)
echo
```

5. The second imported file contains further definitions and parameters for the specific kind of data and how to process the data. The information in this file is for one particular instrument, e.g. the SOFI instrument on the NTT, and a new file with changed parameters needs to be developed for a different instrument.

```
#################################################################################
#                                                                               #
```

```
#                              Karsten Markus                                  #
#                         Department of Astronomy                              #
#                         University of Cape Town                              #
#                                                                              #
#                              09.11.2004                                      #
#                                                                              #
################################################################################


########## Calculations ##########


set j_k = 1.0
set ri_sofi = j_k

set offset =  1*kc0_sofi - airmass*kc2_sofi - ri_sofi*kc1_sofi

set r_sma = 0.288*sma
set r_sma1_4 = r_sma**0.25

set m_iso = (offset - 2.5*lg((intens-sky)/((exp_time)*(0.288*0.288))))
set m_iso_pe1 = (offset - 2.5*lg((intens-sky+interr)/((exp_time)
                *(0.288*0.288))))
set m_iso_e1 = m_iso_pe1 m_iso
set m_iso_pe2 = (offset - 2.5*lg((intens-sky-interr)/((exp_time)
                *(0.288*0.288))))
set m_iso_e2 = m_iso-m_iso_pe2

set sum_int = (flux_e-(sky*npix))/exp_time
set m_int = offset-2.5*lg(sum_int)

set int2 = (intens-sky)*((nd+nf)/(exp_time))
set int2_e1 = (intens-sky-interr)*(nd+nf)/(exp_time)
set int2_e2 = (intens-sky-interr)*(nd+nf)/(exp_time)
set sum_int2 = cumulate(int2)
set sum_int2_e1 = cumulate(int2_e1)
set sum_int2_e2 = cumulate(int2_e2)
set m_int2 = offset - 2.5*lg(sum_int2)
set m_int2_e1 = m_int - offset - 2.5*lg(sum_int2_e1)
set m_int2_e2 = offset - 2.5*lg(sum_int2_e2) - m_int

print "output/"$galaxy.$filter.$field.$cnd.$procedure.int_mag.dat "
       %9.3f %9.3f %9.3f %9.3f %9.3f \n" {r_sma1_4 m_iso m_int
       m_iso_e1 m_iso_e2}
```

6. For plotting the data and the results from the calculation the next two files are imported. The first one contains information about the

plotting the isophotal magnitude.

```
###############################################################################
#                                                                             #
#                          Karsten Markus                                     #
#                       Department of Astronomy                               #
#                       University of Cape Town                               #
#                                                                             #
#                            09.11.2004                                       #
#                                                                             #
###############################################################################


############ Isophotal Magnitude Plot ##########

ltype 0
ctype black
limits 0.5 $max_radius1_4 $min_iso_mag $max_iso_mag
lweight 1
expand 1.001
box 0 2 0 0
toplabel '$procedure' $galaxy_plot $filter_plot $field_plot $ccd plot
ylabel brightness \mu{}_{Ks} [mag/arcsec^2]
ctype blue
ptype 12 3
expand 0.5
points r_smal_4 m_iso
lweight 0.05
errorbar r_smal_4 m_iso m_iso_e1 2
errorbar r_smal_4 m_iso m_iso_e2 4
lweight 1

ltype 1
relocate 0 20
draw 200 20
relocate $vline_radius 50
draw $vline_radius 0

ltype 0
expand 1.001
ctype black
```

7. The second file contains information about the plotting the integrated magnitude.

```
###############################################################################
#                                                                             #
```

```
#                          Karsten Markus                          #
#                      Department of Astronomy                     #
#                      University of Cape Town                     #
#                                                                  #
#                           09.11.2004                             #
#                                                                  #
####################################################################


########## Integrated Magnitude Plot ##########

ltype 0
ctype black
limits 0.5 $max_radius1_4 $max_int_mag $min_int_mag
lweight 1
expand 1.001
box 1 2 0 0
xlabel semi-major axis [arcsec^{1/4}]
ylabel integrated K_{s} magnitude [mag]

ctype blue
ptype 12 3
expand 0.5
points r_sma1_4 m_int

ltype 1
relocate $vline_radius 50
draw $vline_radius 0
relocate 0 $hline_int_mag
draw 100 $hline_int_mag

ltype 0
expand 1.001
ctype black
```

8. Finally, the last two files contain information about how to plot further properties of the galaxy. First the ellipticity.

```
####################################################################
#                                                                  #
#                          Karsten Markus                          #
#                      Department of Astronomy                     #
#                      University of Cape Town                     #
#                                                                  #
#                           09.11.2004                             #
#                                                                  #
####################################################################
```

```
############ Ellipticity Plot ##########

ltype 0
ctype black
limits 0.5 $max_radius1_4 0.0 1.0
lweight 1
expand 1.001
box 0 2 0 0
toplabel '$procedure' $galaxy_plot $filter_plot $field_plot $ccd plot
ylabel ellipticity

ctype blue
ptype 12 3
expand 0.6
points r_semi_4 ellip
lweight 0.05
error_y r_semi_4 ellip elliperr
lweight 1
expand 1.001
ctype black
```

9. Secondly the position angle of the galaxy.

```
##############################################################################
#                                                                            #
#                          Karsten Markus                                    #
#                      Department of Astronomy                               #
#                      University of Cape Town                               #
#                                                                            #
#                           09.11.2004                                       #
#                                                                            #
##############################################################################


########## Position Angle Plot #########

ltype 0
ctype black
define lower_plot_limit ($lower_pa_angle)
define upper_plot_limit ($lower_pa_angle+200)
limits 0.5 $max_radius1_4 $lower_plot_limit $upper_plot_limit
lweight 1
expand 1.001
box 1 2 0 0
ylabel position angle [degree]
```

```
xlabel semi-major axis (arcsec^(1/4))

ctype blue
ptype 12 3
expand 0.5

set i=1
define while_criteria "($last_line-$first_line)"

WHILE {i<$while_criteria} {
IF (pa[i]<$lower_pa_angle) {set pa[i] = pa[i]+180}
set i=i+1
}

points r_sma1_4 pa #IF (pa >= $lower_pa_angle)

lweight 0.05
error y r_sma1_4 pa paerr

lweight 1
expand 1.001
ctype black
```

10. The numerical results for the galaxy magnitudes are printed into a file, i.e. into the `output/wkk98_5920.Ks.0.0.killall.int_mag.dat` file, and can be examined or used for further analysis.

Bibliography

D. Baade. *Wide Field Imager User Manual.* European Southern Observatory, Garching, GER, 1.0.4 edition, May 1999. http://www.ls.eso.org/.

R. J. Buta and M. L. McCall. The IC 342/Maffei Group Revealed. *Astrophysical Journal Supplement Series*, 124:33, 1999.

Lindsey E. Davis. *A Reference Guide to the IRAF/DAOPHOT Package.* National Optical Astronomy Observatories, Tucson, USA, January 1994. http://iraf.noao.edu/.

W. A. Joye and E. Mandel. New Features of SAOImage DS9. In *ASP Conf. Ser. 295: Astronomical Data Analysis Software and Systems XII*, pages 489–+, 2003.

R. H. Lupton and P. Monger. *The SM Reference Manual*, 1997. http://www.astro.princeton.edu/~rhl/sm/sm.html.

A. Mellinger. Die Milchstraße im Computer. *Sterne und Weltraum*, 39:174, 2000.

F. Ochsenbein, P. Bauer, and J. Marcout. The VizieR database of astronomical catalogues. *Astronomy and Astrophysics Supplement Series*, 143: 23–32, 2000.

C. Y. Peng et al. Detailed Structural Decomposition of Galaxy Images. *Astronomical Journal*, 124:266–293, 2002.

A. Shuttle, editor. *Philosophy for Africa*. Marquette University Press, 1995. ISBN 08-7462-6080.

D. Tody. The IRAF Data Reduction and Analysis System. In D. L. Crawford, editor, *Instrumentation in astronomy VI; Proceedings of the Meeting, Tucson, AZ, Mar. 4-8, 1986. Part 2 (A87-36376 15-35). Bellingham, WA, Society of Photo-Optical Instrumentation Engineers, 1986, p. 733.*, volume 627, page 733, 1986.

D. Tody. IRAF in the Nineties. In J. Barnes R. J. Hanisch, R. J. V. Brissenden, editor, *Astronomical Data Analysis Software and Systems II*, volume 52 of *ASPCS*, page 173, 1993.

Appendix A

Selection of Utilised Abbreviations

Table A.1: Abbreviations used in this dissertation.

Abbreviation	Description
AAO	Anglo-Australian Observatory
ACO	Abell, Corwin and Olowin
ADU	Analog-to-Digital Unit
BTP	Behind The Plane
CIZA	Clusters in the Zone of Avoidance
DENIS	Deep Near Infrared Survey
DIRBE	Diffuse Infra-Red Background Experiment
ESO	European Southern Observatory
ESO/SRC	ESO / United Kingdom Science Research Council
FWHM	Full Width at Half the Maximum
IRAF	Image Reduction and Analysis Facility
IRAS	Infrared Astronomical Satellite
IRAS PSC	Infrared Astronomical Satellite Point Source Catalogue
IRAS PSCz	IRAS PSC Redshift Survey
ISAAC	Infrared Spectrometer and Array Camera

Table A.1: (continued) Abbreviations used in this dissertation.

Abbreviation	Description
POSS	Palomar Observatory Sky Survey
PSC	Point Source Catalogue
PSF	Point Spread Function
REFLEX	ROSAT-ESO Flux Limited X-ray
RON	Readout Noise
ROSAT	Roentgen Satellite
ROSAT BSC	Roentgen Satellite Bright Source Catalogue
6dF	Six degree Field facility
SOFI	Son of ISAAC
2dF	Two degree Field facility
2dFGRS	2dF Galaxy Redshift Survey
2MASS	Two Micron All Sky Survey
WFI	Wide Field Imager

Appendix B

Changes made in this Dissertation

This chapter only applies at a later stage.

Appendix C

Vita

Karsten Markus was born in Thuine, Germany, on August 10th, 1974, as the son of Rudolf Bernhard Markus and Elisabeth Johanna Markus (neé Bonnekessen). After leaving the grammar schools Johanneum and Geor-

Figure C.1: The author, Karsten Markus

gianum in Lingen/Ems, Germany, he participated in the compulsory army service at the Luftlandebrigade 31 (paratroops) in Wildeshausen and Oldenburg, Germany. In 1995 he entered the Ruperto Carola in Heidelberg, Germany, where he obtained his Vordiplom in 1998. The following year, he entered the University of Cape Town, South Africa, and obtained a B.Sc. Hons. in Theoretical Physics and Astrophysics the same year. He has since been a part-time graduate student at the Department of Astronomy of the University of Cape Town and carried out observational work at observatories in France, Germany and South Africa.

Appendix D

Availability

A copy of this dissertation or a corrected version thereof should be available on the World Wide Web: http://www.karstenmarkus.de/publications/

Appendix E

Contact Details

Karsten Markus

Department of Astronomy
University of Cape Town
Rondebosch, Cape Town 7701
Republic of South Africa

Email: contact@karstenmarkus.de
WWW: karstenmarkus.de